The Regulation of End Resection in the Repair of DNA Double-Strand Breaks

by

Andrew Jia-Jun Locke

A thesis submitted in partial fulfillment of the requirements for the degree of

Doctor of Philosophy

in

Cancer Sciences

Department of Oncology

University of Alberta

Abstract

DNA double-strand breaks (DSBs) are considered the most deleterious DNA lesions. Unrepaired or incorrectly repaired DSBs can lead to cell cycle arrest, apoptosis, or over time, the accumulation of mutations and chromosomal abnormalities that give rise to cancer. The repair of DSBs by homologous recombination (HR) requires the overall 5' to 3' enzymatic trimming of DNA away from the DSB, a process known as DNA end resection. Using a variety of biochemical and cell biological techniques on cultured human cell lines, the studies herein investigate how DNA end resection is regulated. This work places emphasis on the impact that post-translational modification (PTM) events, such as the conjugation of phosphoryl, ubiquitin, and SUMO moieties onto target proteins, have on the function of proteins involved in end resection. The work described in Chapter 3 reveals that BMI-1, a transcriptional repressor belonging to the Polycomb group of proteins, promotes DNA end resection and thus HR. Mechanistically, BMI-1 promotes end resection through inhibiting RNA polymerase II-dependent transcription, while also facilitating the deposition of ubiquitin onto residue K119 of histone H2A (H2AK119ub). Depletion of BMI-1 impairs the recruitment of the end resection-promoting factor CtIP to DSBs, and the H2AK119ub mark may mediate CtIP's accrual on chromatin, as CtIP can bind to ubiquitin directly. In Chapter 2, we uncover that CtIP itself is a target for modification by SUMO-2, particularly during the S phase of the cell cycle. CtIP SUMOylation is dependent on the E3 SUMO ligase PIAS4, and occurs primarily on residue K578. Relative to cells expressing wildtype CtIP, cells expressing CtIP with the K578R substitution mutation are impaired in DNA end resection and HR, are more sensitive to killing by the DSB-inducing drug camptothecin, and defective in protecting stalled replication forks from nucleolytic degradation. Lastly, in Chapter 4, we demonstrate that the E3 ubiquitin ligase and pro-resection factor RNF138 is modified by

ubiquitylation (at residue K158) and cyclin-dependent kinase-dependent phosphorylation (at residue T27). Preventing the occurrence of either PTM, by arginine and alanine substitution mutations, respectively, strongly reduces the ability for RNF138 to promote end resection and HR. Together, these findings uncover novel intricacies in the tightly orchestrated process of DNA end resection for the repair of DSBs.

Preface

The data presented in this thesis is a result of research collaborations, with contributions from members of Dr. Ismail Ismail's research group at the University of Alberta and two other research groups, those led by Dr. Jean-Yves Masson (CHU de Québec Research Center and Laval University Cancer Research Center, Université Laval, Québec City, Canada) and Dr. Mark Glover (Department of Biochemistry, University of Alberta). Chapters 2, 3, and 4 have been published in separate research articles. Beyond the sections detailed herein, the remainder of the thesis is original work by Andrew Locke with the exception of five schematic diagrams reproduced with permission from existing publications (**Figs. 1.1, 1.2, 1.3, 1.4, 1.5**). Generative artificial intelligence technologies were not used in the writing of any text in this thesis or its associated publications.

The section "BMI-1" (**Section 1.8.3**) contains modified text selections from an article published in the *International Journal of Molecular Sciences*, as Fitieh A., Locke A.J., Motamedi M., and Ismail I.H. (2021), "The Role of Polycomb Group Protein BMI1 in DNA Repair and Genomic Stability" (volume 22, issue 6, article 2976, DOI: 10.3390/ijms22062976). This review was written by Dr. Amira Fitieh, with editing performed by myself, Mobina Motamedi, and Dr. Ismail. I also prepared the schematic diagrams in the review.

Chapter 2 was published in *Nucleic Acids Research* as Locke A.J., Hossain L., McCrostie G., Ronato D.A., Fitieh A., Rafique T.A., Mashayekhi F., Motamedi M., Masson J.Y., and Ismail I.H. (2021), "SUMOylation mediates CtIP's functions in DNA end resection and replication fork protection" (volume 49, issue 2, pages 928 – 953, DOI: 10.1093/nar/gkaa1232). Dr. Ismail H. Ismail conceived, acquired funding for, and supervised the project, with Dr. Masson contributing experimental design and *in vitro* assay data, important conceptual insights, and critical feedback. I wrote most of the manuscript, with Drs. Ismail and Masson providing additional writing, and prepared the figures and figure legends for all data generated by our group. I designed and interpreted the experiments with Dr. Ismail, optimized, performed, and analyzed most of the experiments, and assisted with the remaining experiments from our group. Daryl Ronato expressed and purified proteins from *Sf*9 insect cells and performed *in vitro* resection and nuclease assays under the supervision of Dr. Masson. Lazina Hossain (additional His pull-down and immunoblot assays), Glynnis McCrostie (immunofluorescence and immunoblot assays), Tanzeem

Rafique (immunoblot and pulsed-field gel electrophoresis assays), Fatemeh Mashayekhi (immunofluorescence assays), Mobina Motamedi (immunoblot assays), and Dr. Ismail (DNA fiber assays) generated additional data. Dr. Amira Fitieh optimized the immunofluorescence assays. Dr. Fitieh (DNA fiber and laser microirradiation), Ms. Mashayekhi (immunofluorescence), and Ms. Motamedi (immunofluorescence, survival) also processed additional experimental data.

Chapter 3 was published in *Cell Reports* as Fitieh A., Locke A.J., Mashayekhi F., Khaliqdina F., Sharma A.K., and Ismail I.H. (2022), "BMI-1 regulates DNA end resection and homologous recombination repair" (volume 38, issue 12, article 110536, DOI: 10.1016/j.celrep.2022.110536). Dr. Ismail H. Ismail conceived, designed, acquired funding for, and supervised the project. Dr. Amira Fitieh spearheaded the work, optimizing, performing, analyzing and interpreting most of the experiments and writing the first draft of the manuscript. Fajr Khaliqdina performed additional immunoblot assays and initiated optimization of the Far Western blotting assay. Dr. Ajit Sharma, Fatemeh Mashayekhi and I carried out additional experiments for the revisions process. Dr. Sharma performed the chromatin immunoprecipitation and quantitative PCR assays, and Ms. Mashayekhi performed additional immunoblotting assays. I optimized, performed, and analyzed Far Western blotting and *in vitro* binding experiments that were designed by Dr. Ismail and I, carried out cell cycle profiling, and performed additional immunofluorescence and immunoblotting assays. In the manuscript, I contributed writing to the Discussion (**Section 3.5**), and wrote sections **3.1.2**, **3.1.3**, **3.3.12**, **3.3.13**, **3.4.7**, **3.4.8**, **3.5.1** and the legends to **Section 3.9.1**. I revised the Materials and Methods (**Section 3.3**) and main figure legends (**Section 3.4**), and edited the manuscript. I also revised the main figures, generated the schematic diagrams, prepared the supplementary/reviewer figures, and compiled the tables. Dr. Ismail and I responded to reviewer and editorial comments.

Chapter 4 is a previous version of a manuscript whose revised form is now published in the *Journal of Biological Chemistry* as Locke A.J., Abou Farraj, R., Tran C., Zeinali E., Mashayekhi F., Ali J.Y.H., Glover J.N.M., and Ismail I.H. (2024), "The role of RNF138 in DNA end resection is regulated by ubiquitylation and CDK phosphorylation" (volume 300, issue 3, article 105709, DOI: 10.1016/j.jbc.2024.105709). The section "RNF138" (**Section 1.8.4**) also contains modified text selections from the introduction of the same article. Dr. Ismail H. Ismail conceived, acquired funding for, and supervised the project, with Dr. Mark Glover providing important conceptual insights and critical feedback. Rabih Abou Farraj performed, interpreted,

and visualized the AlphaFold modeling and sequence alignments (**Figs. 4.1D, 4.4A,** and **4.S9**) under the supervision of Dr. Glover, and provided insights into RNF138 expression and purification. Dr. Ismail and I designed the experiments. I analyzed and interpreted the data, generated most of the figures, and wrote the bulk of the manuscript. I performed most of the experiments, many of which in collaboration with Mr. Abou Farraj or Caroline Tran, both of whom also helped with the maintenance of cell cultures. Mr. Abou Farraj and I conducted and analyzed immunofluorescence, clonogenic survival, and immunoblotting assays. Ms. Tran and I conducted immunoprecipitation, cycloheximide chase, His pull-down, and immunofluorescence assays. Jana Ali performed the laser microirradiation experiments. Eli Zeinali performed additional immunoprecipitation experiments. Fatemeh Mashayekhi performed the CDK2 *in vitro* kinase assay and additional immunoblotting assays. Dr. Ismail and I performed the homologous recombination reporter assay.

The Appendix contains a methods article published in *STAR Protocols* as Sharma A.K., Fitieh A.M., Locke A.J., Ali J.Y.H., and Ismail I.H. (2023), "Quantification of protein enrichment at site-specific DNA double-strand breaks by chromatin immunoprecipitation in cultured human cells" (volume 4, issue 1, article 101917, DOI: 10.1016/j.xpro.2022.101917). This publication describes the chromatin immunoprecipitation protocol used in Chapter 3. I contributed substantial original writing and extensive editing to the manuscript, and prepared seven of the figures.

Acknowledgements

This work would not have been possible without my supervisor, Dr. Ismail H. Ismail, to whom I am especially grateful for allowing me to join his research program. Ismail fostered a research environment that has been incredibly stimulating, rewarding, and full of camaraderie. As a mentor, he was always available for a scientific chat or phone call of technical suggestions for my experiments, sometimes as they were happening. Ismail also opened many opportunities for me to reach my highest potential, and gave me the independence to think and attempt new techniques on my own. Most importantly, he cared deeply for my wellbeing, giving me time to recharge, surprising me with his delicious home cooking, and supporting me through my recent health challenges. I thank Ismail for his nurturing guidance, his dedication to my success and that of our group, and for always being kind, patient, driven, and goal-oriented. His fearless leadership, ability to adapt to new situations, and resilience were not only instrumental to the completion and dissemination of this research, but are attributes I aspire to model in my own career.

I also wish to thank my supervisory committee members, Drs. Michael Weinfeld and Mark Glover, for their brilliant insights and suggestions during my committee meetings. I thank too our collaborators, Dr. Jean-Yves Masson (Université Laval) and again, Dr. Glover, whose guidance and feedback were vital to this work. I also thank the professors who served as examiners during my program: for my PhD defense, Drs. El Bachir Affar (Université de Montréal), Michael Hendzel and Kristi Baker; for my candidacy exam, Drs. Roseline Godbout and Ing Swie Goping. I am also grateful to Drs. Alan Underhill, Mary Hitt, and Gordon Chan, along with the Cancer Sciences Graduate Coordinating Committee, for monitoring my progress and providing critical feedback.

Biomedical research is difficult enough on its own but is much easier when you work with labmates that are caring about your success. I wish to acknowledge my colleagues Dr. Amira Fitieh, Fatemeh Mashayekhi, Elham Zeinali, and Rabih Abou Farraj, for whom I am honoured to have as my friends. The nicest people you will ever meet, they made every day a great day to come to the lab as they were committed to their work but loved to laugh and have fun. I especially thank Amira for encouraging me to pursue a PhD, giving me the nudge to embark on this academic adventure. I thank Fatemeh and Eli for their contagious enthusiasm, humour, and optimistic outlook, and Rabih for being an amazing collaborator and motivator. I have also been fortunate to work with some very bright and hardworking undergraduate students. I especially thank Caroline

Tran, Glynnis McCrostie, Mobina Motamedi, Jana Ali, Joseph Drake, Fajr Khaliqdina, Allison Tran, Adham Shousha, and Samantha Flint for their dedication and contributions to this research.

I extend my appreciation to the graduate and undergraduate students, post-doctoral fellows, lab staff, lab assistants, administrators, and faculty members in the Department of Oncology. Everyone that I have met has been immensely friendly, caring, and helpful, and I will deeply cherish the friendships and memories I made here and with the Oncology Graduate Students' Association. I am grateful to the research groups of Dr. Armin Gamper, Dr. Michael Chu, and Drs. Baker, Chan, Godbout, Hendzel, Weinfeld, and Underhill, who selflessly shared their reagents, consumables, equipment, and expertise. I thank Dr. Xuejun Sun and Gerry Barron for their guidance with microscopy, and Dr. Lei Li and Drs. Hendzel, Underhill, Gamper, and Chan for their critical feedback of our research. I am grateful to Dr. Anne Galloway, April Scott, Jola Paul, and Colleen Dluzewski for their exceptional work ethic in keeping our facilities operating smoothly. Dr. Galloway also performed cell sorting that was essential to these studies. Finally, I thank Dr. Godbout for her kindness and generosity – she has always been available for a friendly chat and I have always felt listened to and inspired after our conversations.

My family and friends have kept me grounded during this entire experience. I thank my grandparents and extended family for instilling in me an appreciation for education and inspiring me to be the best I can be. I thank my long-time friends for checking on me with their encouraging messages, and for excusing my tardiness at gatherings (often due to something happening in the lab). Most importantly, I am indebted to my brother, Kevin, and my parents, Fred and Sheila, for their unwavering and unconditional support, without a deep understanding of what my projects were or why the work required so much effort. Thank you all for your love and kindness.

I am grateful to the donors and funding agencies that supported this work. My stipend was supported by Dianne and Irving Kipnes (Rachel Mandel Scholarship in Lymphoma and Other Blood Cancers), the Yau Family Foundation, Robert Meltzer and the Meltzer family, the Faculty of Medicine & Dentistry (the 75th Anniversary Award), and the Government of Alberta (the Queen Elizabeth II Graduate Scholarship – Doctoral Level and the Alberta Graduate Excellence Scholarship). Research in this thesis was funded by a Canadian Institutes of Health Research (CIHR) Project Grant (MOP-365197), a Natural Sciences and Engineering Research Council (NSERC) Discovery Grant (RGPIN-2017-05752), and the Cancer Research Society (CRS, grant number 22019), all awarded to Dr. Ismail H. Ismail.

Table of Contents

List of Tables

List of Figures

Abbreviations

ɣH2AX: histone variant H2AX phosphorylated on Ser139
µL, mL: microliter, milliliter
µM, nM, mM, M: micromolar, nanomolar, millimolar, molar
µm: micrometer or micron
4-OHT: 4-hydroxytamoxifen
5-FU: 5-fluorouridine
53BP1: tumour protein p53 binding protein 1
Async: asynchronous
ATM: ataxia telangiectasia-mutated
ATP: adenosine triphosphate
ATR: ataxia telangiectasia-mutated and Rad3-related
ATRIP: ATR interacting protein
BAP1: BRCA1 associated protein-1
BARD1: BRCA1 associated RING domain 1
BLM: Bloom syndrome protein
BMI-1, BMI1: B-cell-specific Moloney murine leukemia virus integration region 1
bp: base pair
BRCA1: breast cancer type 1 susceptibility protein
BRCA2: breast cancer type 2 susceptibility protein
BrdU: 5-bromo-2'-deoxyuridine
BSA: bovine serum albumin
Cas9: CRISPR associated protein 9
CBX4: chromobox 4
CDK(s), CDK1, CDK2: cyclin-dependent kinase(s), cyclin-dependent kinase 1 or 2
ChIP: chromatin immunoprecipitation
Chk1: checkpoint kinase 1
Chk2: checkpoint kinase 2
CldU: 5-chloro-2'-deoxyuridine
CRISPR: clustered regularly interspaced short palindromic repeats
Co-IP: co-immunoprecipitation
CPT: camptothecin
CTD: C-terminal domain of RNAPII's large subunit
CtIP: C-terminal binding protein interacting protein
DAPI: 4',6-diamidino-2-phenylindole
DDR: DNA damage response
DMSO: dimethylsulfoxide
DNA: deoxyribonucleic acid
DNAPK: DNA-dependent protein kinase
DNAPKcs: DNAPK catalytic subunit
Dox: doxycycline
DRB: 5,6-dichloro-1-β-D-ribofuranosylbenzimidazole
DR-GFP: direct repeat GFP HR reporter system
DSB(s): DNA double-strand break(s)
dsDNA: double-stranded DNA

DUB(s): deubiquitylating enzyme(s)
E1, E2, E3: enzyme 1, 2, or 3 from the ubiquitin or SUMO conjugation pathways
EZH2: enhancer of zeste 2 polycomb repressive complex 2 subunit
G1: gap 1 phase in the cell cycle
G2: gap 2 phase in the cell cycle
GA: ginkgolic acid 15:1
GFP: green fluorescent protein
Gy: Gray
h: hour
H2A: histone H2A
H2AK119ub, H2AK119ub1: monoubiquitylated histone H2A on residue K119
HEK293: human embryonic kidney cell line
HA: human influenza hemagglutinin epitope tag
His PD: histidine tag pull-down (affinity purification procedure)
HR: homologous recombination, or homology-directed repair
HU: hydroxyurea
IB: immunoblot, Western blot
IdU: 5-iodo-2'-deoxyuridine
IF: immunofluorescence staining
IP: immunoprecipitation
IR: ionizing radiation
I-*Sce*I: intron-encoded homing endonuclease from *Saccharomyces cerevisiae* mitochondria I
JARID2: Jumonji/AT rich interactive domain 2
kDa: kilodalton
Ku: Ku70/Ku80 heterodimer
LacI: *lac* repressor protein
lacO: *lac* operator sequence
MAPK: mitogen-activated protein kinase
mCherry: monomeric Cherry
MEF: mouse embryonic fibroblast
min: minute
Mre11: meiotic recombination 11 homolog A
MRN: Mre11-Rad50-Nbs1
Nbs1: Nijmegen Breakage Syndrome 1
NHEJ: non-homologous end joining (canonical)
nt: nucleotide
ORF: open reading frame
P: phosphoryl-, phosphorylated
PALB2: partner and localizer of BRCA2
PARP(1): poly(adenosine diphosphate-ribose) polymerase (1)
PARPi: PARP inhibitors, PARP inhibition
PcG: Polycomb group
PCNA: proliferating cell nuclear antigen
PFGE: pulsed-field gel electrophoresis
PIAS1, PIAS4: protein inhibitor of activated signal transducer and activator of transcription 1 or 4

PIKK(s): phosphoinositide 3-kinase-related kinase(s) (family of kinases including DNAPKcs, ATM, and ATR)
PRC1, PRC2: Polycomb repressive complex 1 or 2
PTM(s): post-translational modification(s)
qPCR: quantitative PCR
Rad50: Rad50 (radiation-repair mutant 50) homolog
Rad51: Rad51 recombinase or Rad51 (radiation-repair mutant 51) homolog 1
RFP: red fluorescent protein
RING: really interesting new gene
RNA: ribonucleic acid
RNAPI, RNAPII: RNA polymerase I or II
RNF1, RNF2, RNF4, RNF8, RNF111, RNF138, RNF168: RING finger protein 1, 2, 4, 8, 111, 138, or 168
RPA: replication protein A complexes
RPA2: replication protein A subunit 2, also known as replication protein A 32 kDa subunit
rpm: revolutions or rotations per minute
S phase: DNA synthesis phase in the cell cycle
SAE1/2: SUMO activating enzyme 1/2
sfGFP: superfolder GFP (in **Chapter 4**, specifically refers to the FLAG, 8XHis, streptavidin binding peptide, and sfGFP-containing multifunctional tandem affinity purification (MAP) tag)
SDS-PAGE: sodium dodecyl sulfate polyacrylamide gel electrophoresis
SIM: SUMO-interacting motif
siRNA, si: short interfering RNA
SUMO, SUMO-1, -2, -3: small ubiquitin-like modifier, small ubiquitin-like modifier 1, 2, or 3
TREx: tetracycline regulated expression
TRI-DR-U2OS: U2OS cells stably expressing tetracycline (doxycycline)-inducible I-*Sce*I and the DR-GFP reporter
Ub: ubiquitin, ubiquityl-, ubiquitylated
UBC9, UBC13: ubiquitin conjugating enzyme 9 or 13 (note: UBC9 actually conjugates SUMO)
UIM: ubiquitin-interacting motif
USP48: ubiquitin specific peptidase 48
UV: ultraviolet light
U2OS, U-2 OS: osteosarcoma cell line
WT: wildtype
WRN: Werner syndrome protein
ZNF: zinc finger

Chapter 1 – Introduction

1.1 DNA Damage and Human Health

DNA (deoxyribonucleic acid) is the genetic material, encoding the information for the function of cells. DNA can be damaged by normal cellular metabolic processes and external agents such as chemotherapies and ionizing radiation (IR) (1). Such damage can present in a variety of changes: inter- and intrastrand cross-links, mispaired bases or misincorporated ribonucleotides from DNA replication, DNA-protein adducts, base adducts, chemical alterations to the bases and sugars, and strand breaks (2). As the genetic material, it is vital for cells to prevent damage to DNA and maintain its structure and sequence. To cope with and combat damaging insults, the cell is equipped with molecular programs to recognize, signal, and repair damage to DNA, jointly known as the DNA damage response (3). The DNA damage response also includes other actions, such as changes in transcriptional programs, the arrest of cell cycle progression (allowing time for DNA repair to occur), and the induction of apoptosis if the damage is excessive (preventing damaged DNA from being passed on to daughter cells) (4).

Left unrepaired, or if repaired incorrectly, DNA damage can lead to the accumulation of chromosomal abnormalities and mutations that may lead to cell cycle arrest and cell death, or over time, give rise to and contribute to the progression of cancer (5, 6). Indeed, cancer cells often lack genome stability and tolerate weakened DNA repair processes. This allows them to adapt to their environment and trigger the activation of other tumour-promoting oncogenes (7). Thus, the accurate and timely repair of DNA damage is crucial for preventing cancer. In support of this, loss of function mutations in DNA damage response genes can lead to rare diseases, many of which predispose patients to frequent, early-onset cancers (8). Some of these include ataxia telangiectasia

(9), Bloom syndrome (10), Nijmegen breakage syndrome (11), Fanconi anemia (12), xeroderma pigmentosum (13), Seckel syndrome (14), and constitutional mismatch repair deficiency (15).

On the contrary, once cancer has arisen, the induction of excessive DNA damage can slow the growth of or even kill tumour cells, a modality exploited by radio- and most chemotherapies (5). However, an overactive DNA damage response can circumvent responses to these therapies, promoting resistance to treatment and cancer progression (5). In fact, the DNA damage response is frequently dysregulated in cancer, seen by mutations in proteins mediating DNA repair (e.g. in BRCA1, the MRN complex, and Rad51), as well as changes to their expression in tumours (e.g. in Ku70/Ku80 and DNAPKcs) (16–19). Certainly, a more complete understanding of the intricacies by which the DNA damage response operates is needed to comprehend how cancers develop, as well as uncover new targets for cancer treatment. Perhaps in the future, such understanding will provide alternative therapeutics for when resistance to treatment emerges, and enable personalized medicine, where cancer patients receive the treatments for which they will respond best to.

1.2 DNA Double-Strand Breaks and Their Repair

Double-strand breaks (DSBs) are DNA lesions where both strands of DNA are severed on the phosphodiester backbone in close proximity. They are considered the most lethal type of DNA damage (20). As both strands are compromised, the continuity of the original DNA molecule is disrupted, each strand losing an intact template for repair. DSBs can be generated from collapsed replication forks, from exposure to IR, and when single-strand breaks arising from reactive oxygen species are closely spaced and on opposite DNA strands (21). They can also be generated by topoisomerase poisons. Topoisomerases relieve the topological strain induced from processes that wind and unwind DNA duplexes, such as DNA replication. They generate breaks in DNA strands to release torsional strain, then re-ligate the ends to re-establish the contiguity of the DNA molecule. Inhibitors of topoisomerases, such as camptothecin (CPT), can inhibit the re-ligation step (1), leaving topoisomerases bound to DNA that contains strand breaks. In the case of CPT, when a DNA replication fork passes through a CPT-stabilized single-strand break, this stalls and collapses the fork, generating a one- or single-ended DSB (22). While the DSBs described above are considered cytotoxic, please note that the formation of DSBs can also be programmed. DSBs are necessary intermediates in processes such as meiosis, along with the generation of diversity in the vertebrate adaptive immune system by V(D)J recombination and class switch recombination (23).

The repair of DSBs occurs by two major mechanisms depending on the cell cycle phase; appropriate choice of the pathway is critical for genomic stability (20). Throughout the cell cycle but predominantly in G1 phase ("Gap 1", the phase when eukaryotic cells are actively growing, between cell division and DNA replication), DSBs are repaired by non-homologous end joining (NHEJ) (24), where the two DNA ends flanking the break are directly ligated together (20) (**Fig.**

1.1, left). While its utility is its efficiency (DSBs repaired by NHEJ have a half-life of half an hour to 2 hours (25, 26)), NHEJ can sometimes be error-prone. If the two DSB ends are not chemically compatible for the ligation reaction, the ends may require processing by other enzymatic activities, resulting in insertions, deletions, or substitution mutations at the break site (23). Alternatively, as sequence homology is not a prerequisite for ligation (the NHEJ machinery cannot tell if both DNA ends originate from the same DSB (23)), chromosomal translocations can occur when ends from different genomic loci are inadvertently joined (27). DSBs can also be repaired by homologous recombination (HR), also known as homology-directed repair (20) (**Fig. 1.1**, right). Repair by HR relies on the availability of a donor sequence (in **Fig. 1.1**, the black DNA duplex, bottom right, is the donor sequence), typically the sister chromatid, a copy of each chromosome recently synthesized during S phase ("Synthesis" phase, where the entire genome is duplicated by the process of DNA replication). The sister chromatid thus serves as a template for the repair of the DSB site and its adjacent regions. As HR can restore the original sequence at the DSB, repair by HR is considered highly accurate (20). However, the dependence on the sister chromatid restricts HR to occur post-DNA replication, within the S and G2 ("Gap 2", the phase between DNA replication and cell division) phases of the cell cycle (24, 26, 28, 29). As the process of HR must search the genome for a region of homology to the DSB site, it requires more time relative to NHEJ (26, 30). In one study, HR took at least 7 hours to complete, unlike NHEJ, which took as little as half an hour (31).

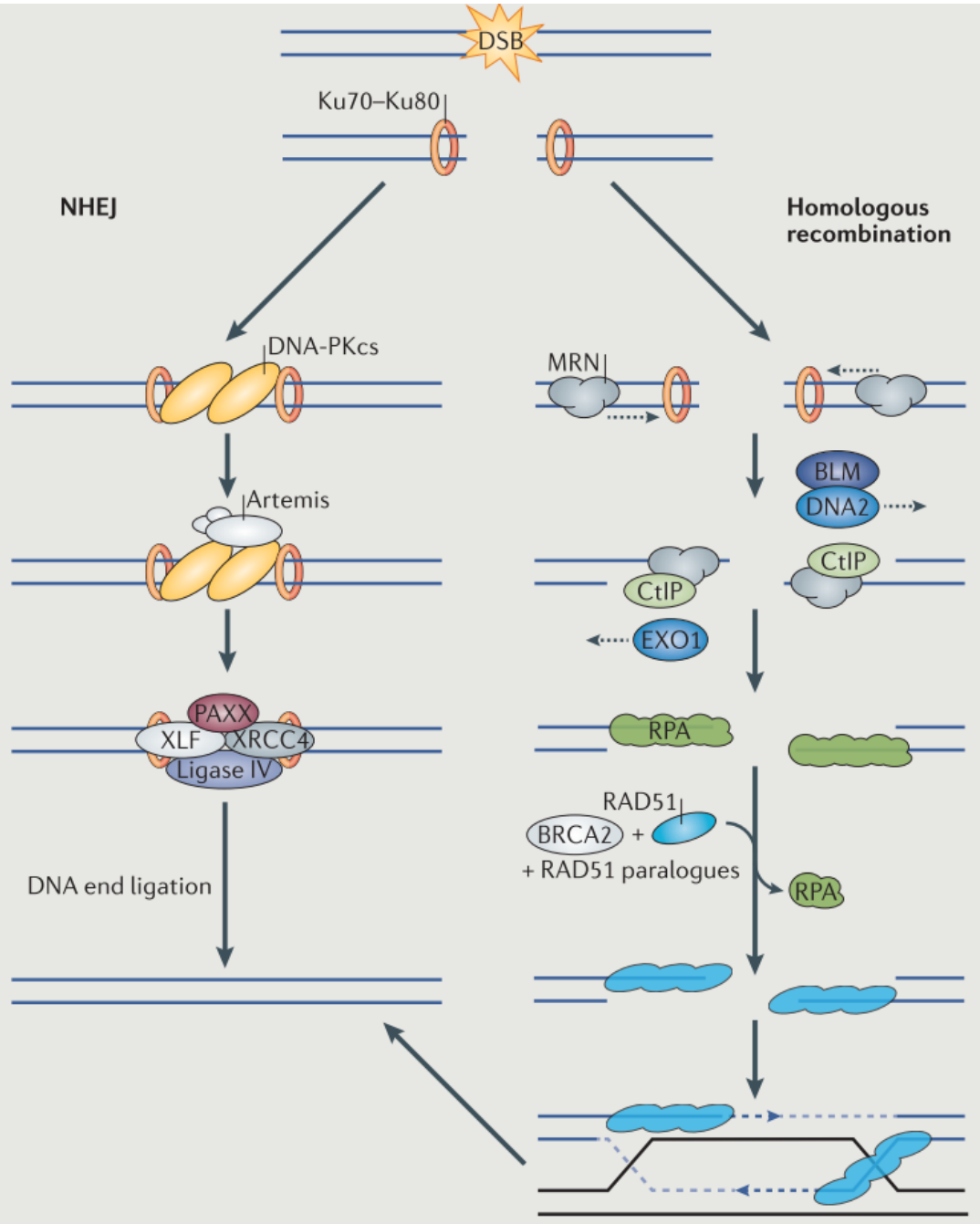

Figure 1.1: Repair of Double-Strand Breaks by Canonical NHEJ and HR, an Overview

Please see text for details. Reproduced with permission from Springer Nature (https://www.nature.com/nrm), from Petra Schwertman, Simon Bekker-Jensen, and Niels Mailand, "Regulation of DNA double-strand break repair by ubiquitin and ubiquitin-like modifiers", *Nature Reviews Molecular Cell Biology*, volume 17, issue 6, pages 379-394, 2016, Springer Nature (42), figure from Box 1.

Beyond NHEJ and HR, minor "backup" pathways exist to repair DSBs (32), such as single-strand annealing (SSA) and microhomology-mediated end joining (MMEJ, also known as alternative non-homologous end joining, or alt-NHEJ) (33), which will only be discussed briefly here. Overall, both utilize some components of the HR machinery and involve ligating DNA ends together (32). They each use 5'→3' end resection to generate single-stranded DNA (ssDNA) (33) (**Section 1.4**), exposing complementary sequences flanking the DSB. These regions of homology are then aligned and annealed, while the intervening non-complementary ssDNA is extruded as flaps and cleaved enzymatically, resulting in deletions in the DNA. The remaining gaps are filled in by DNA polymerases, and subsequently the DNA ends are sealed together by DNA ligases (32). These backup pathways utilize specific complements of proteins (32); for instance, MMEJ is Ku-independent (34, 35) (see **Section 1.3**), and involves PARP1 (poly(adenosine diphosphate-ribose) polymerase 1), the polymerase-helicase DNA polymerase theta (Pol Θ), and DNA Ligase III (36–41). For clarity, in this thesis, the term NHEJ refers to the major (canonical) NHEJ pathway, and does not refer to the backup pathways.

1.3 Canonical Non-Homologous End Joining

Canonical NHEJ is initiated when the highly abundant and ring-shaped Ku70/Ku80 (Ku) heterodimer senses and binds to the double-stranded DNA ends with high affinity (**Fig. 1.1**). The presence of Ku is critical for cells to perform canonical NHEJ (34, 43). Ku recruits a phosphoinositide 3-kinase-related kinase (PIKK) family member, the DNA-dependent protein kinase (DNAPK) catalytic subunit (DNAPKcs), activating its kinase activity (23). Both Ku and DNAPKcs are required for NHEJ and together form the DNAPK holoenzyme (44). DNAPK

activity phosphorylates many NHEJ factors as well as DNAPKcs itself. The proteins XRCC4 (X-ray repair cross complementing protein 4), XLF (XRCC4-like factor), and PAXX (paralogue of XRCC4 and XLF) then closely align the DNA ends, forming the synaptic complex (23) (**Fig. 1.1**). Recognizing Ku that is bound to a DSB, end ligation is then catalyzed by DNA Ligase IV, whose activity is enhanced by XRCC4 (44). While DNA Ligase IV can tolerate some mismatches between the DNA ends, in general it ligates a 5' phosphate group of one DNA end to a free 3' hydroxyl group on the other DNA end. The activities of other DNA end processing enzymes (e.g. Artemis, polynucleotide kinase phosphatase, aprataxin, DNA polymerases such as Pol λ and Pol μ) may be necessary (e.g. trimming, short resection, gap filling) to make the ends amenable for the ligation reaction (23).

1.4 DNA End Resection and Homologous Recombination

The initiation of HR requires the 5'→3' enzymatic, nucleolytic trimming of both DNA strands away from the site of damage, a process known as DNA end resection (45). This process produces 3' single-stranded DNA (ssDNA) overhangs (**Figs. 1.1 and 1.2**), structures that are not only poor substrates for the binding of Ku and the ligation step of canonical NHEJ (23) (**Fig. 1.2**, left side), but are required for the occurrence of HR downstream in the pathway (46).

End resection proceeds via two steps (47); the first step is known as short-range end resection (46), as the DNA strands are trimmed within the vicinity of the DSB (**Fig. 1.2**). Short-range end resection is initiated by the nuclease activities of the MRN (Mre11-Rad50-Nbs1) protein

complex, which binds the DNA ends of the DSB (45). Mre11 possesses the key endonuclease and 3'→5' exonuclease activities of the complex (48), while Rad50 contains ATPase activity and may bridge the DNA ends together (49). Nbs1 serves as an adaptor protein (45). Mre11's endonuclease activity nicks DNA internally 100 – 400 nucleotides (nts) away from the 5' terminated DSB end (47, 50), perhaps creating initiation sites for the action of downstream end resection factors (46) (see below), or to remove DNA-protein adducts (51, 52), excess Ku bound to DNA (53–57) (**Fig. 1.2**, right side; Ku and other protein blocks to end resection are represented by the blue oval labelled "Block"), or aberrant DNA secondary structures from the DSB (46). Mre11's 3'→5' exonuclease activity then takes over (48), initiating on nicks generated previously by its endonuclease activity (51) (**Fig. 1.2**, right side). *In vitro*, this exonuclease activity is promoted by Nbs1 and requires and proceeds toward protein-blocked ends (51). Notably, Mre11's endonuclease activity is only fully active when MRN is bound to the protein CtIP (C-terminal binding protein interacting protein), specifically when CtIP is phosphorylated (**Section 1.5.1**), with Nbs1 functioning to sense CtIP phosphorylation (51, 52, 58–61). As both Mre11's endo- and exonuclease activities are important for HR (48), CtIP is a critical regulator of whether end resection is initiated and if HR subsequently occurs (30).

In the second stage of end resection, known as long-range end resection, extensive 5'→3' trimming occurs to ~1000 nts (and potentially tens of thousands of nucleotides) distal from the DSB (46). This is carried out by the activities of two other nucleases, Dna2 and Exo1 (45, 47, 50, 62–64), with the actions of Dna2 being supported by the helicases BLM (Bloom syndrome protein) and WRN (Werner syndrome protein) (62, 65) (**Figs. 1.1 and 1.2**). The long-range resection factors are regulated by MRN/CtIP; for instance, CtIP recruits Dna2 to DSBs (64), and Exo1 recruitment to DSBs is MRN- and CtIP-dependent (63, 66). In *Saccharomyces cerevisiae*, the

equivalent of the MRN complex also promotes Dna2 and Exo1 loading at the DSB (67). *In vitro* studies further demonstrate that MRN stimulates Exo1 exonuclease activity and processivity (63), while CtIP constrains Exo1's exonuclease activity (66). CtIP also stimulates DNA unwinding by BLM, along with the nuclease and ssDNA translocase activities of DNA2 (68, 69). Ultimately, the resulting 3' ssDNA overhangs generated by end resection are coated by the heterotrimeric protein complex Replication Protein A (RPA) (**Figs. 1.1 and 1.2**), which binds tightly to ssDNA (70), protecting the overhangs from nucleolytic degradation and preventing association with complementary DNA sequences (46).

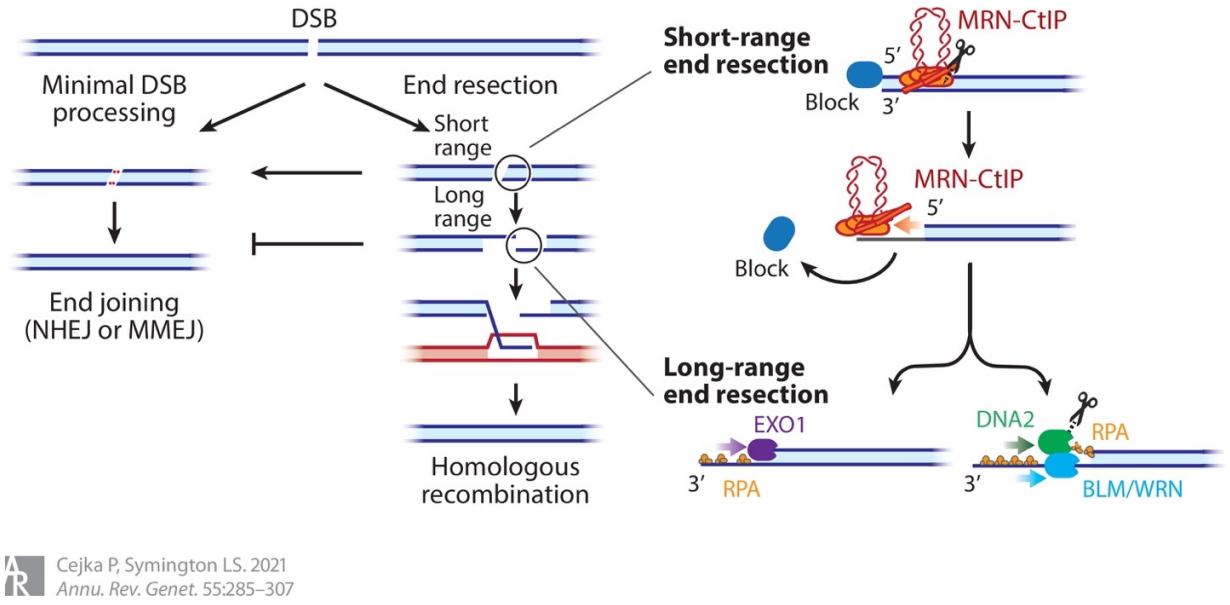

Figure 1.2: DNA End Resection

Please see text for details. Used with permission of Annual Reviews, Inc., from "DNA End Resection: Mechanism and Control", *Annual Review of Genetics*, Petr Cejka and Lorraine S. Symington, volume 55, issue 1, pages 285-307, 2021 (46), Fig. 1; permission conveyed through Copyright Clearance Center, Inc.

RPA is eventually replaced by the Rad51 recombinase protein (**Fig. 1.1**), a process mediated by the PALB2 (partner and localizer of BRCA2) and BRCA2 (breast cancer type 2 susceptibility protein) proteins (20). This entails destabilizing the interaction between RPA and ssDNA while having Rad51 interact with ssDNA. Processive Rad51 oligomerization assembles the ssDNA overhangs into nucleofilaments, mediating pairing, invasion, and strand exchange with the sister chromatid, searching within it for a region of homology to be used as a repair template (71) (**Fig. 1.1**, the black DNA duplex, bottom right, is the donor sequence). Rad51 activity is assisted by its paralogues, Rad51B, Rad51C, Rad51D, XRCC2, and XRCC3, which also integrate into the nucleofilament (71). After DNA synthesis to extend the invading strands and fill in any gaps, a series of nicking (performed by the structure-specific nuclease complexes Mus81-EME1 or SLX1-SLX4), reannealing, and ligation steps resolves the joined DNA molecules, completing the repair process (20, 71).

Other proteins contribute to the process of HR. For instance, the tumour suppressor protein BRCA1 (Breast Cancer Type 1 Susceptibility Protein), along with its binding partner BARD1 (BRCA1 Associated RING Domain 1), constitute a heterodimeric complex that promotes HR. BRCA1's role is multifaceted (**Fig. 1.5**): first, it antagonizes the activity of the pro-NHEJ protein 53BP1 (tumour protein p53 binding protein 1) (72, 73), excluding it from sites of DSB sites (74, 75) and thus directing repair pathway choice to HR (72–75) (**Section 1.6**). While BRCA1 is not essential for end resection (76), it accelerates its rate (77). BRCA1 also facilitates the BRCA2/PALB2-dependent loading of Rad51 onto RPA-bound ssDNA (78). BRCA1 is required for HR (79), and loss of BRCA1 results in genomic instability, the high frequency of mutations and chromosomal abnormalities (80).

1.5 Post-Translational Modifications

Overwhelming evidence indicates the appropriate and timely activity of DNA repair is controlled by reversible post-translational modifications (PTMs) (42, 81, 82). These are events where small chemical moieties (such as methyl, acetyl, phosphoryl, or adenosine diphosphate (ADP)-ribose) or proteins (such as ubiquitin) are covalently attached to or removed from biomolecules by targeted enzymatic activities. These conjugation (i.e. methylation, phosphorylation, ubiquitylation) and deconjugation events act as molecular switches that coordinate the activities of multiple proteins within space (e.g. proximal to the site of DNA damage, or propagated away from the site) and time (e.g. soon after the DNA lesion is detected, but not unnecessarily prolonged) (83, 84). PTMs have been found to facilitate protein-protein interactions, control enzymatic activity, alter protein localization to cellular compartments, and target proteins for degradation. Still, the direct impacts of PTMs on the functions of specific proteins are only beginning to be elucidated (81). Furthermore, mechanisms of how multiple PTMs occur on the same target molecule ("cross-talk"), and how different PTM combinations impact protein function, are still active areas of investigation. New findings continually reveal deeper regulatory complexities by PTMs. For example, phosphorylation (**Section 1.5.1**) was recently observed to occur directly on the ubiquitin modifier (**Section 1.5.2**) at residue Thr12, the phosphorylation reducing the ability for DSBs to be repaired by NHEJ and blocking the activity of a de-ubiquitylating enzyme (85).

1.5.1 Phosphorylation

The conjugation of phosphoryl groups ($-PO_3^{2-}$) imparts negative charge at the receiving amino acid residue (typically, a serine, threonine, or tyrosine residue). The presence of a

phosphoryl group can therefore permit or prevent protein-protein interactions by changing binding affinities, induce conformational arrangements in proteins, or trigger disorder-order transitions or *vice versa* (86). Protein kinases catalyze phosphorylation, whereas the removal of phosphoryl groups is catalyzed by protein phosphatases.

Three PIKK (phosphoinositide 3-kinase-related kinase) family members are involved in the DSB response: DNAPKcs, ATM (ataxia telangiectasia-mutated), and ATR (ataxia telangiectasia-mutated and Rad3-related) (87). These kinases are massive polypeptides that respond to various types of lesions. DNAPKcs and ATM both respond to DSBs, with DNAPKcs best known to coordinate the occurrence of NHEJ (87) (**Section 1.3**). Meanwhile, ATM-dependent phosphorylation activates a variety of HR factors, and promotes a signaling cascade on DSB-damaged chromatin leading to the recruitment of 53BP1 and BRCA1 to the DSB (**Sections 1.4 and 1.6**). ATM also phosphorylates checkpoint kinase 2 (Chk2) (88) and p53, which together activate a cellular program that promotes cell cycle arrest in G1 phase (preventing entry into mitosis), apoptosis (programmed cell death), or cellular senescence (87). ATR, on the other hand, is activated by UV-induced damage, as well as stretches of ssDNA coated by RPA complexes (89) next to double-stranded DNA. Such structures can arise from the uncoupling of helicases and polymerases during DNA replication (90) (**Section 1.7**) or DNA end resection (58, 89, 91) (**Section 1.4**). ATR phosphorylates checkpoint kinase 1 (Chk1) (92) and other substrates, leading to the halting of cell cycle progression and promoting actions to mitigate replication stress (**Section 1.7**). All three kinases are recruited and activated by cofactors that bind to chromatin (87): the Ku heterodimer activates DNAPKcs (93) (**Section 1.3**), the MRN complex activates ATM (94, 95), and ATRIP (ATR interacting protein) binds ssDNA-bound RPA to activate ATR (89).

Other kinases relevant to this study include the cyclin-dependent kinases (CDKs), which control transitions in the cell cycle. The kinase activities of some CDKs accumulate at specific cell cycle phases, and are stimulated when bound to their regulatory subunits, the cyclins (96, 97). The kinase activities of CDK2 and CDK1 trigger progression through the S, G2, and mitotic phases (96). To ensure HR can proceed during the S/G2, CDK-dependent phosphorylation events serve to activate HR and DNA end resection (98–100). Accordingly, players involved in DNA end resection, such as Mre11, Nbs1, CtIP, Dna2, and Exo1 are targets of CDK phosphorylation (61, 101–107). The association between BRCA1 and CtIP is also regulated by cell cycle-dependent phosphorylation (108).

One example of hyperphosphorylation in genome integrity is that of the RPA heterotrimer. RPA is hyperphosphorylated, particularly on the RPA2 subunit, in response to DNA damage (70). Conflicting studies have shown that all of ATR, ATM, and DNAPKcs can hyperphosphorylate RPA, while other groups have determined that the kinase is solely DNAPKcs (70). Phosphorylation is not required for RPA's initial interaction with DNA, but appears concurrent with DNA end resection and binding to ssDNA (70). Consequently, RPA2 phosphorylation is used as an indicator of end resection, as well as stalled replication forks formed during replication stress (58, 109) (**Section 1.7**). While numerous phosphorylation sites have been identified on RPA2 in response to DNA damaging agents, and phosphorylation-deficient RPA2 mutants have severe defects in HR and DNA replication, the function of RPA phosphorylation is still being uncovered (70, 110). A recent study of end resection reconstituted *in vitro* revealed that the activities of the BLM-bound nucleases Exo1 and Dna2 were inhibited when RPA was substituted with the hyperphosphorylated version (110). The function of RPA phosphorylation still demands further evaluation.

1.5.2 Ubiquitylation

The presence of a DSB is signaled through a cascade of ubiquitin conjugation events to proteins on chromatin (**Section 1.6**). Ubiquitin conjugation to proteins, or ubiquitylation, is now known to regulate DNA repair and numerous other processes in the cell, such as cell cycle progression, the stress responses to heat and nutrient starvation, and ribosome assembly (111). What is ubiquitin? Encoded by four genes in mammals (112, 113), ubiquitin is a highly conserved 76 amino acid protein in eukaryotes (114). It is conjugated to lysine residues on numerous target proteins via a glycine residue on its C-terminus (Gly76), generating an isopeptide linkage with the ε-amino group of the target lysine (42). Notably, histone H2A was the first protein found to be conjugated to the C-terminus of ubiquitin at an internal lysine residue (111, 115), an early example of histone modification (**Sections 1.5.4 and 1.6**). The full-length ubiquitin precursor is first processed by deubiquitylating enzyme (DUB)-dependent proteolytic cleavage at ubiquitin's di-glycine motif (116). Next, a series of three enzymatic steps leads to ubiquitin conjugation (117) (**Fig. 1.3**): E1s (ubiquitin activating enzymes) activate ubiquitin by catalyzing ATP-dependent adenylation, yielding ubiquitin adenylate which serves as the donor of ubiquitin onto the E1, forming a thioester linkage with the catalytic site cysteine residue (117). The E2s (ubiquitin conjugating enzymes) then catalyze a transesterification reaction, allowing ubiquitin to be transferred onto them, again onto a cysteine residue (117). More than 600 E3s (ubiquitin ligases) in the cell then act as "specificity factors", binding their cognate E2 along with the target protein for ubiquitylation (42). This allows ubiquitin to be transferred directly to the target via the E2 (the E3 serving as an adaptor), or after being transferred from the E2 to the E3 (the E3 serving as an intermediate in catalysis) (117). While there are three major classes of E3 ubiquitin ligases, the HECT E3s (homologous to the E6AP carboxyl terminus), RING E3s (really interesting new gene),

and RBR E3s (RING between RING) (117), the class most relevant to this discussion is the RING type E3 ligases. RING E3s contain a RING finger motif (primary sequence: Cys–X_2–Cys–$X_{9–39}$–Cys–$X_{1–3}$–His–$X_{2–3}$–Cys–X_2–Cys–$X_{4–48}$–Cys–X_2–Cys; X is any amino acid) where eight conserved cysteine (Cys) and histidine (His) residues coordinate two zinc cations, the motif folding into a compact domain (119). The RING finger recruits and orients the E2, promoting the direct transfer of ubiquitin to the target protein substrate (118). RING E3s can be monomers or homo- or heterodimers, with BRCA1/BARD1 and RNF2/BMI-1 (**Section 1.8.3**) being examples of heterodimeric RING E3s (75, 120–122).

Expanding the potential outcomes of ubiquitin signaling, ubiquitin itself has lysine residues, each of which can serve as sites for ubiquitin conjugation (42, 123) (**Fig. 1.3**). Thus, polyubiquitin chains can be assembled, and in different geometries. K48-linked ubiquitin chains are known to target proteins for degradation by the proteasome, whereas other linkages, such as K63-linked chains, are involved in assembling protein complexes and triggering signaling for DSB repair (42, 123, 124). Numerous ubiquitin binding domains have also been identified that allow proteins to recognize and bind to ubiquitylated proteins (125, 126). As well, like phosphorylation, ubiquitylation is reversible, with DUBs contributing to the dynamics of the modification by catalyzing ubiquitin removal from target proteins (116) (**Fig. 1.3**).

A current line of investigation involves the identification of novel E3 ubiquitin ligases functioning in DSB repair. Two chapters of this manuscript are centered on the activities of RING finger-containing E3 ubiquitin ligases at DSBs: that of the heterodimeric E3 RNF2/BMI-1, where the ligase activity of the RING E3 RNF2 is stimulated by its RING-containing binding partner BMI-1 (127–129) (**Chapter 3**), and RNF138 (**Chapter 4**). Both BMI-1 and RNF138 were recently characterized to have roles in DSB repair (130–133).

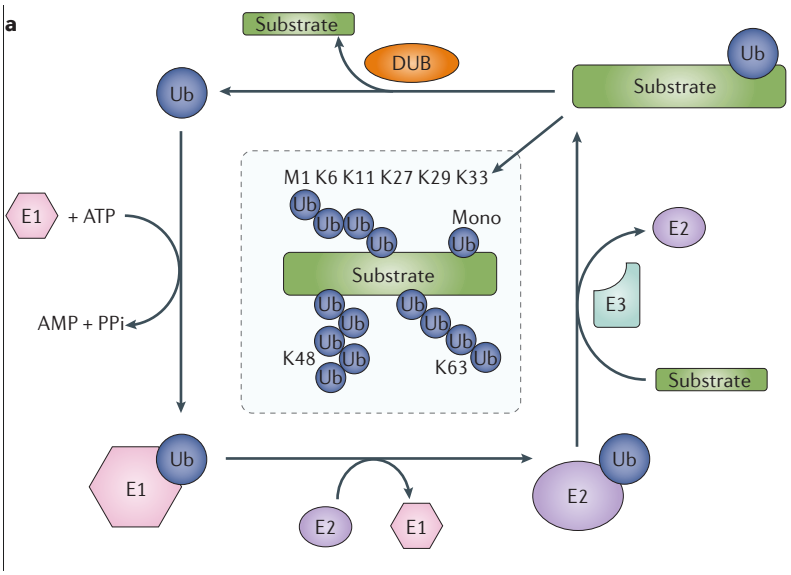

Figure 1.3: Ubiquitylation and Deubiquitylation

Please see text for details. Reproduced with permission from Springer Nature (https://www.nature.com/nrm), from Petra Schwertman, Simon Bekker-Jensen, and Niels Mailand, "Regulation of DNA double-strand break repair by ubiquitin and ubiquitin-like modifiers", *Nature Reviews Molecular Cell Biology*, volume 17, issue 6, pages 379-394, 2016, Springer Nature (42), figure a) from Box 2.

1.5.3 SUMOylation

SUMOylation is a ubiquitin-like PTM where SUMO (small ubiquitin-like modifier) proteins (~11-12 kDa) are covalently linked onto target proteins. It was first discovered to target the protein RanGAP1 to the cytoplasmic face of nuclear pore complexes (134, 135). The targets of SUMOylation are predominantly nuclear proteins (136–140), regulating processes such as DNA replication and the cell cycle, genome integrity, RNA splicing and metabolism, transcription, and nuclear and chromatin organization (140, 141). Molecularly, SUMO conjugation alters nuclear trafficking, localization to DNA damage, protein-protein interactions, protein stability, and enzymatic activity (134, 135, 142–162). Mammalian cells ubiquitously express three SUMO paralogues, SUMO-1, -2 and -3 (163), with SUMO-1 exhibiting 18% amino acid identity to

ubiquitin (134, 135). SUMO-2 and SUMO-3 have 92% sequence identity to each other (164, 165) and due to this similarity are often considered together as one group in SUMOylation studies (166). On the other hand, SUMO-1 shares 48% identity to SUMO-2/3 (164, 165). In human cells, SUMO-2/3 are expressed more abundantly than SUMO-1 (167). Indeed, SUMO-2 may be the most important paralogue, as mice lacking SUMO-2 die as embryos whereas those lacking SUMO-1 or SUMO-3 remain viable (168, 169). SUMO-1 and SUMO-2/3 can be conjugated to distinct targets, although there can be overlap, with some targets being modified by either (167, 170). Interestingly, a recent proteomic screen revealed DNA damage response proteins have a preference for binding SUMO-2 (and trimers of SUMO-2) over SUMO-1 (160).

Analogous to ubiquitylation, a cascade of E1, E2, and E3 enzymes and proteases catalyzes SUMOylation and deSUMOylation, respectively (164). Similar to ubiquitin, the SUMO proteins are also synthesized as precursors that are proteolytically cleaved by SUMO- (or sentrin)-specific proteases (SENPs) SENP1, -2, and -5 to expose a C-terminal diglycine motif necessary for conjugation (138, 171). The matured SUMOs are activated in an ATP-dependent manner by the E1 heterodimer SUMO-activating enzyme 1 (SAE1)/SAE2 and transferred to the sole SUMO E2 UBC9 (ubiquitin conjugating enzyme 9) (172). UBC9 transfers SUMO to lysine residues of the substrate, forming an isopeptide linkage between the C-terminal carboxyl group of SUMO and the ε-amino group of lysine (173). UBC9-dependent SUMO conjugation is an essential process, as mouse embryos deficient in UBC9 die early post-implantation (174). Unlike ubiquitylation, SUMOylation can occur at a consensus motif (ψ-K-x-E, with ψ representing a bulky, hydrophobic residue) (137). The lysine residue (K) within is the target for SUMOylation, although lysine modification within non-consensus sequences does also occur (136, 173, 175). *In vitro*, SAE1/SAE2 and UBC9 are sufficient to catalyze SUMOylation of substrate proteins (176, 177),

but *in vivo*, under thirty known E3 SUMO ligases (unlike the >600 E3 ubiquitin ligases) in human cells direct the substrate specificity of UBC9 and enhance the rate of SUMOylation (176, 178, 179). Similar to ubiquitin, SUMO chains can be conjugated to target proteins; SUMO-2/3 each contain an internal ψ-K-x-E motif, of which K11 acts an acceptor for the formation of poly-SUMO-2/3 chains (180, 181). As SUMO-1 lacks this motif, it was originally proposed to solely terminate SUMO-2/3 chains (181). However, chains containing SUMO-1, assembled on non-canonical acceptor lysine residues within SUMO-1, have been detected by mass spectrometry (139). SUMO moieties can also be removed from substrates; this is catalyzed by the SENP proteins as well (171). Mammals have six SENPs, SENP1, -2, -3, -5, -6, -7, all of which possess this isopeptidase activity within a conserved C-terminal catalytic domain (171).

SUMOylated proteins can be recognized by other proteins that contain SUMO-interacting motifs (SIMs), typically a stretch of 3-4 long hydrophobic amino acid residues followed by a string of acidic and serine or threonine residues, which facilitate non-covalent interactions with the SUMOs (182). One SIM-containing protein is RNF4 (RING finger protein 4), which functions as a SUMO-targeted E3 ubiquitin ligase (STUbL). With its four SIMs (183), RNF4 is recruited to proteins conjugated to poly-SUMO chains, facilitating their poly-ubiquitylation and subsequent proteasomal degradation (184–188). Another STUbL, RNF111, targets proteins linked to SUMO-1-capped poly-SUMO-2/3 chains for degradation (189), hinting that specific SUMO chain topologies can be recognized. The action of STUbLs exemplifies the connections between SUMO and ubiquitin signaling, allowing SUMOylated proteins to in turn be ubiquitylated.

SUMOylation has been implicated in DSB repair. The E3 SUMO ligases PIAS1 (protein inhibitor of activated signal transducer and activator of transcription 1) and PIAS4 are recruited to sites of DNA damage and mediate the formation of SUMO-1 and/or -2/-3 conjugates at these sites

(147). Moreover, depleting PIAS1 or PIAS4 reduces the frequency of HR and NHEJ, and sensitizes cells to DNA damage by IR and cisplatin (147, 149). Mechanistically, upon DNA damage, PIAS4 promotes RNF168 recruitment and the SUMOylation and recruitment of 53BP1 (**Section 1.6**), while both PIAS1 and PIAS4 promote the SUMOylation and recruitment of BRCA1 (147, 149) and the accumulation of RPA (147). Rad51 also contains a SUMO-1-interacting SIM, and the SIM, along with PIAS1 and PIAS4, are important for Rad51's accrual at sites of ultraviolet (UV) light irradiation (158). Other E3 SUMO ligases, such as CBX4 (chromobox 4) and TOPORS (topoisomerase I binding arginine/serine rich protein), are also involved in DNA repair and HR, respectively (131, 159). Other proteins involved in the response to DSBs are also targets of SUMOylation. These include ones involved in DSB signaling, like MDC1 (mediator of DNA damage checkpoint protein 1), 53BP1, and ATRIP (143–148), and in HR repair, such as BRCA1, the RPA complex, BLM, Dna2, Exo1, and Rad51 (147, 149–159). NHEJ (**Section 1.3**) also relies on SUMOylation, as overexpressing a SIM peptide to sequester SUMOylated proteins is sufficient to inhibit NHEJ (190), while mutating the SIM of the NHEJ factor XRCC4 disrupts its recruitment to sites of damage and its association with DNA Ligase IV (160). SUMOylation also promotes association of the Ku heterodimer with chromatin (161) and the nuclear localization of XRCC4 (162), actions of which serve to promote NHEJ. The NHEJ promoting factor RIF1 (**Section 1.6**), too, is SUMOylated by PIAS4, leading to the disassembly of DNA damage-induced RIF1 foci (146). On a broader scale, the STUbL RNF4 is recruited to sites of DNA damage in a PIAS1/4-dependent manner, controlling the turnover of the SUMO targets RPA and MDC1 and promoting both HR and NHEJ (144, 145, 187).

It is clear then that SUMOylation impacts many aspects of the DSB response. This increasing understanding of SUMOylation is bolstered by the emergence of high-throughput mass

spectrometric approaches for the identification of SUMO target proteins and modification sites (136, 175). Nevertheless, important, valuable work remains in identifying the critical residues of modification in other SUMO targets in DSB repair, and directly assessing the functional impacts of SUMOylation of these targets *in vivo*.

1.5.4 Histone Modifications

DNA molecules must be compacted to fit within the cell nucleus. To do so, DNA is wrapped around octameric complexes of histone proteins (1). The histone octamers typically contain two copies each of the core histone proteins H2A, H2B, H3, and H4. ~150 bp of DNA wrap less than two turns around one histone octamer; this complex is known as a nucleosome core particle (1). DNA (linker DNA) also connects neighbouring nucleosome core particles; together, a nucleosome core particle and its surrounding linker DNA comprise the nucleosome, a repeating unit along the length of DNA (1). Another histone protein, H1, binds where the linker DNA enters and exits the nucleosome core particle (191). The core histone H2A can also be substituted by variant histones (192, 193); for instance, in mammalian cell cultures, the H2A variant H2AX (**Section 1.6**) can constitute 2 – 25% of the total pool of H2A family members (194, 195).

The compaction of DNA into higher order chromatin structures poses an obstacle for nuclear processes which directly access the DNA sequence, like DNA replication, the transcription of genes (**Section 1.8.2**), and the repair of DNA lesions. Cells must manage accessing specific genomic loci quickly, without decondensing the entire genome. The solution to this exploits the unstructured N- and/or C-terminal tails of the core histones, which protrude away from the globular core of the nucleosome (1). As they are exposed to solvent, these tails are subject to PTMs, including (but not limited to) methylation, acetylation, phosphorylation, and ubiquitylation (196).

Histone PTMs can make chromatin more open (transcriptionally active, decondensed) or less accessible (transcriptionally repressed, condensed), permitting or restricting access to the DNA (197). This can be achieved either directly, by altering nucleosome-nucleosome or histone-DNA interactions, or indirectly, by promoting or preventing the recruitment of proteins whose activities affect chromatin accessibility (198). As an example, histone H3 that is acetylated at lysine residue K4 (H3K4ac) is enriched at the promoter sequences of actively transcribed genes; disrupting this modification prevents transcription of these genes (199). Conversely, genes occupied by nucleosomes where histone H3 is trimethylated at lysine K27 (H3K27me3) are transcriptionally repressed (200, 201).

Histone modifications can also recruit or block the binding of other protein factors, for instance those involved in DSB repair. One example is the modification of lysine K20 on histone H4. Newly synthesized nucleosomes are unmethylated on K20 (H4K20me0), but mono-, di- and eventually trimethylation of the site (H4K20me1/2/3) gradually occurs as cells progress through S, G2, mitosis and G1 phase (202, 203). Since "new" nucleosomes containing H4K20me0 are incorporated onto recently synthesized DNA, the presence of H4K20me0 marks newly synthesized chromatin and the availability of the sister chromatid. Recent reports show that H4K20me0 is recognized by the ankyrin repeat domain of the HR factor BARD1, facilitating its recruitment, along with that of its binding partner BRCA1, to chromatin during S/G2 (204–207) (**Section 1.4**). Remarkably, BARD1's ankyrin repeat domain does not bind to H4K20me2 (204, 205), one of the signals on chromatin recognized by the NHEJ-promoting factor 53BP1 (**Section 1.6**). This mechanism is consistent with the role of BRCA1-BARD1 in promoting HR during S/G2 phase, as the presence of H4K20-methylated nucleosomes prevents the recruitment of BRCA1-BARD1 to chromatin during G1 phase, when NHEJ is prevalent. As another example, acetylation at lysine

K16 on histone H4 (H4K16ac) prevents the association of 53BP1 (**Section 1.6**) with damaged chromatin (208, 209). Blocking the activity of the histone acetyltransferase enzyme TIP60 (60 kDa Tat-interactive protein) restores the formation of damage-induced 53BP1 foci (208). Meanwhile, blocking the activity of histone deacetylating enzymes, or mimicking H4 acetylation via a K16Q substitution mutation, reduces 53BP1 foci formation and end joining activity (209).

1.6 Signaling of Double-Strand Breaks

DSBs trigger cascades of PTMs on numerous proteins. These include phosphorylation events, catalyzed by the kinase ATM (94, 95), and ubiquitylation, mediated by the RING finger E3 ubiquitin ligases RNF8 and RNF168 (42). The DSB is first detected by the MRN complex, which recruits and activates ATM (**Fig. 1.4**). ATM phosphorylates the histone H2A variant H2AX on residue Ser139 (known as γH2AX) (194, 210), a signal that is further propagated megabases beyond the DSB by ATM activity (195, 211). As the tandem BRCA1 carboxy-terminus (BRCT) domains of the adaptor protein MDC1 (mediator of DNA damage checkpoint protein 1) recognize phosphorylated Ser139 on γH2AX, MDC1 is recruited to chromatin and then itself becomes phosphorylated, being in the vicinity of ATM (**Fig. 1.4**). Phosphorylated MDC1 recruits the ubiquitin E2/E3 pair UBC13-RNF8 (212–215). UBC13-RNF8 subsequently catalyzes the formation of K63-linked ubiquitin chains on histones (212–215), particularly histone H1 (216) (**Fig. 1.4**). These chains are recognized by and recruit the E3 ubiquitin ligase RNF168 (216, 217). RNF168 then amplifies the signal by promoting K63-linked ubiquitylation of H2A and other targets on damaged chromatin (42, 217, 218), while also catalyzing monoubiquitylation of histone H2A at lysine residues K13 and K15 (H2AK13ub, H2AK15ub) (219, 220) (Fig. 1.4). The surge

of RNF8/RNF168-driven ubiquitylation at the DSB site creates a platform for recruiting, among other proteins, two proteins that govern repair pathway choice: 53BP1 and BRCA1 (42, 212–215, 217, 218, 221, 222) (**Fig. 1.4**). 53BP1 recognizes a bivalent signal on chromatin: RNF168-generated H2AK15ub, and H4K20me2 (223–225) (green hexagon modification on H4, **Fig. 1.4**), which as described previously marks post-replicative chromatin (202, 203) (**Section 1.5.4**). RNF168 also promotes 53BP1 retention at DSBs by binding and ubiquitylating 53BP1 (226).

Both BRCA1 and 53BP1 exert antagonizing control over the choice of whether NHEJ or HR is performed (27, 72), regulating whether DNA end resection occurs (promoted by BRCA1) or does not (promoted by 53BP1) (72, 227) (**Fig. 1.5**). 53BP1 favours NHEJ by facilitating the protection of DNA ends and the inhibition of end resection (228–232). This is achieved by the sequential recruitment of other factors to chromatin: PTIP (PAX transactivation domain interacting protein 1) and RIF1 (RAP1-interacting factor 1), both of whom are recruited to ATM-phosphorylated 53BP1, the Shieldin complex (consisting of the subunits SHLD1, SHLD2, SHLD3, and REV7 (revertibility protein 7)), the CST (CTC1-STN1-TEN1) complex, and Pol α-primase (DNA polymerase alpha-primase). These factors may promote NHEJ in various ways (233, 234): occupying ssDNA to protect the DNA ends, inhibiting long-range end resection, suppressing Rad51 loading, and in the case of CST/Pol α-primase, performing local fill-in DNA synthesis to reduce the length of ssDNA overhangs generated by end resection (235, 236) (**Fig. 1.5**). On the other hand, in S/G2 phase, BRCA1, recruited to chromatin via BARD1's recognition of H4K20me0 (**Section 1.5.4**), counteracts 53BP1 activity by positioning 53BP1 away from DSB sites, enabling end resection and the initiation of HR (75, 237, 238). Mechanistically, BRCA1/BARD1 ubiquitylates H2A at lysine residues K125/K127/K129 (239), modifications recognized by the chromatin remodeller SMARCAD1 (SWI/SNF-related, matrix-associated actin-

dependent regulator of chromatin, subfamily A, containing DEAD/H Box-1), whose ATPase activity is required for repositioning 53BP1 (75, 237).

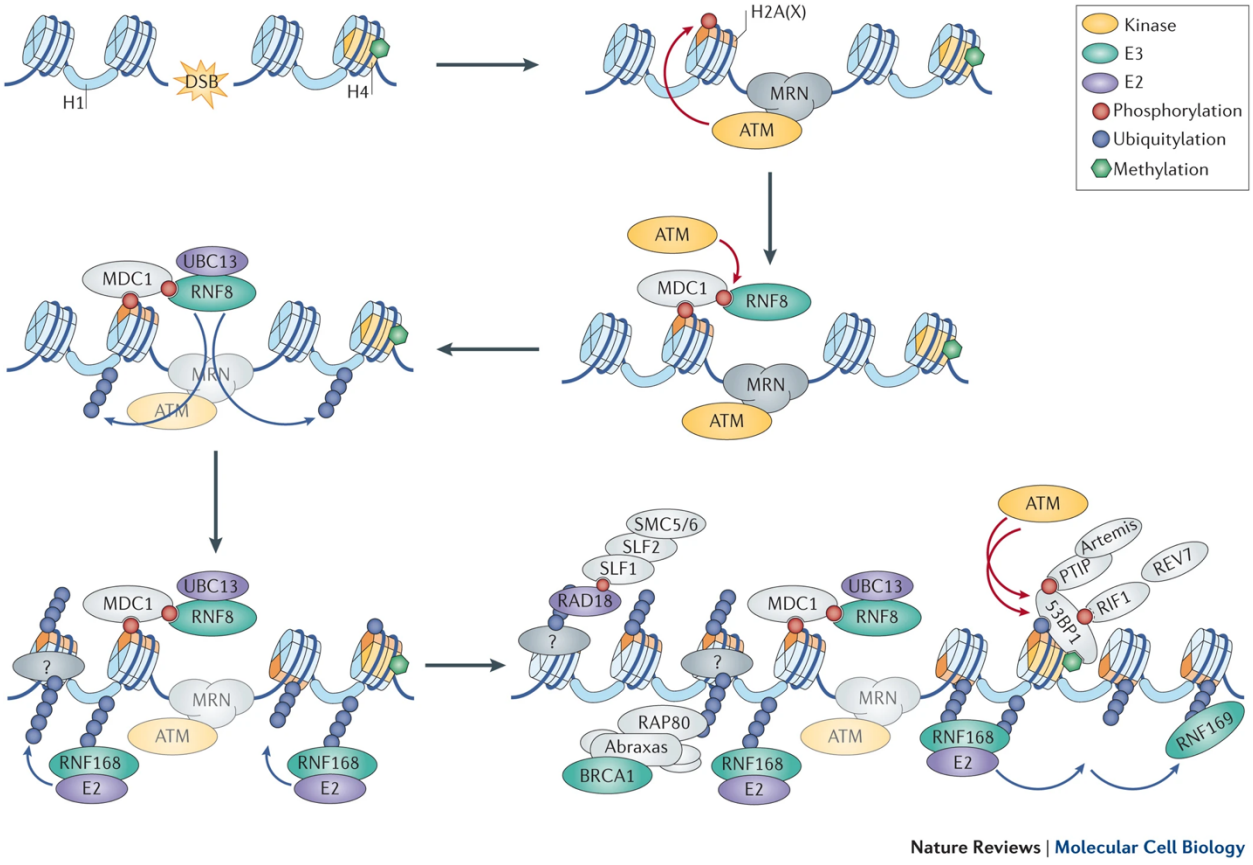

Figure 1.4: Signaling Events Induced by Double-Strand Breaks

Please see text for details. In this diagram, molecules or post-translational modifications not referred to in the text are not crucial to the discussion in this thesis. Reproduced with permission from Springer Nature (https://www.nature.com/nrm), from Petra Schwertman, Simon Bekker-Jensen, and Niels Mailand, "Regulation of DNA double-strand break repair by ubiquitin and ubiquitin-like modifiers", *Nature Reviews Molecular Cell Biology*, volume 17, issue 6, pages 379-394, 2016, Springer Nature (42), Fig. 2.

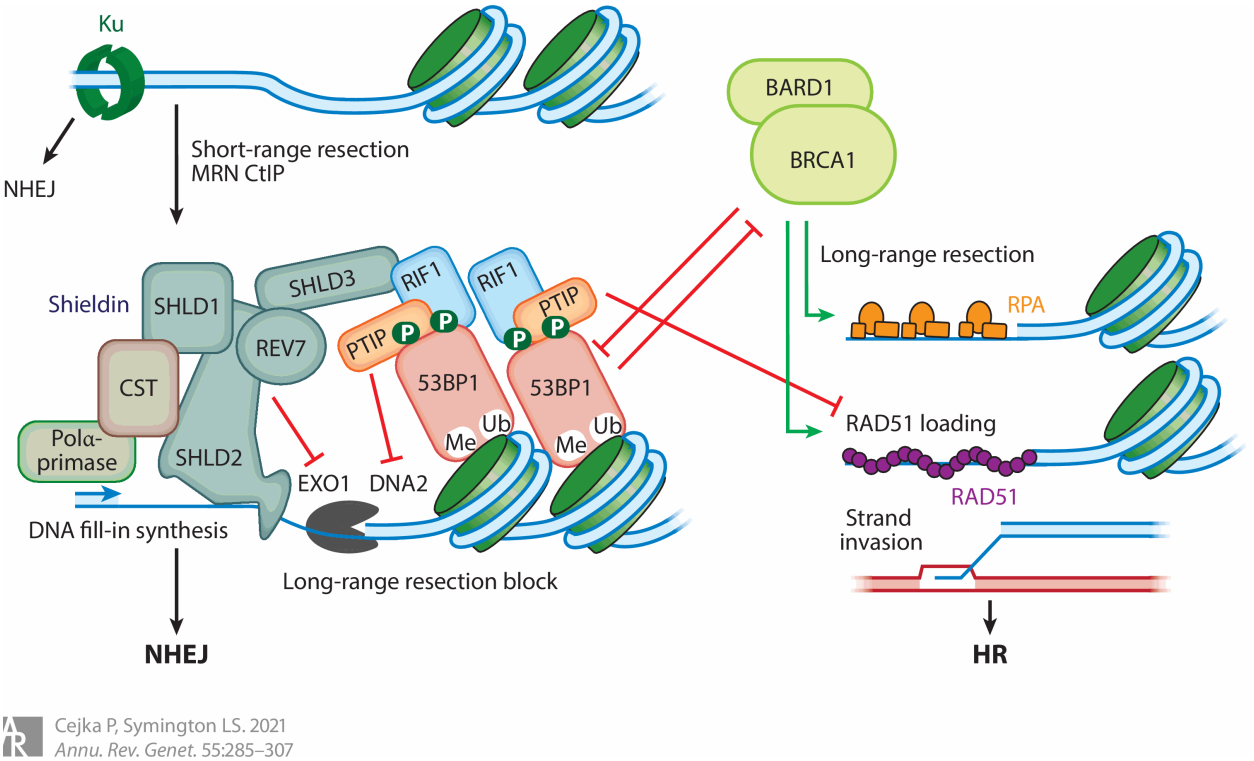

Figure 1.5: The Roles of BRCA1 and 53BP1 in Double-Strand Break Repair Pathway Choice

Please see text for details. Used with permission of Annual Reviews, Inc., from "DNA End Resection: Mechanism and Control", *Annual Review of Genetics*, Petr Cejka and Lorraine S. Symington, volume 55, issue 1, pages 285-307, 2021 (46), Fig. 2; permission conveyed through Copyright Clearance Center, Inc.

1.7 Replication Stress

The accurate completion of DNA replication in S phase is essential for cell growth and survival. Replication stress is described broadly as the slowing or halting of DNA synthesis and the disruption of error-free DNA replication (240). It can result from various endogenous impediments to the copying of DNA, such as depletion of the deoxyribonucleotide (dNTP) pools that are the building blocks for DNA, the misincorporation of ribonucleotides in DNA, DNA

secondary structures which prevent fork progression or cause slippage of the replication machinery, and unresolved DNA-protein complexes (241). Moreover, collisions between the DNA replication and transcription machineries (**Section 1.8.2**) can halt replication fork progression directly or generate DNA-RNA hybrids, where the extruded single-stranded DNA (ssDNA) is prone to damage that further hampers fork advancement. Replication stress is exacerbated in cancer cells (242, 243), where unrestrained tumour proliferation demands incessant DNA replication. Here, oncogene overexpression or activation promotes deregulated entry into the cell cycle, inappropriate firing of origins of replication, and consumption of dNTPs (240). Oncogene activation also increases global transcription (244) and thus the frequency of transcription-replication conflicts, and generates reactive oxygen species which damage DNA, further slowing replication (240, 241). Tumour cells can even have defects in the response to DNA damage, leaving unrepaired DNA lesions scattered across the genome that impede fork progression (245).

If unresolved, sustained replication stress may cause stalled DNA replication forks to eventually collapse, generating single-ended DSBs (241). To respond to replication stress, cells are dependent on the kinase ATR (241). ATR is activated by the presence of ssDNA next to newly replicated double-stranded DNA, which occurs when the replicative helicase proceeds to unwind the DNA duplex while the DNA polymerase has stalled and left behind (90). Activated ATR then triggers the replication stress response, buying time for the stress to become resolved and preventing further damage to the genome. ATR activity suppresses the firing of late replication origins, inhibits cell cycle progression, and stabilizes stalled replication forks, preventing them from recombination events and later aiding in their restart once the stressor is removed (241).

Intriguingly, under replication stress, the course of replication forks can be backtracked. Here, a four-way junction is formed, generated by the concerted annealing of the newly

synthesized strands and the re-annealing of the two template strands (246). This chicken-footed structure is believed to be protective, allowing fork progression to be restarted when conditions for replication have improved or when downstream roadblocks are removed or repaired. Unfortunately, this fork reversal mechanism can also have consequences, with the newly synthesized DNA becoming a target for nucleolytic degradation. If overactive, this degradation can lead to the loss of genetic information, contributing to genomic instability (247). Roles for BRCA1 and BRCA2 have been found in the response to replication stress, with the presence of BRCA1/2 protecting newly synthesized DNA at stalled replication forks from overactive nucleolytic degradation, such as that by Mre11 and Exo1 (248–252).

1.8 Proteins and Topics of Interest

The following section provides background information to proteins that are the focus of this thesis, in particular CtIP (**Chapters 2 and 3**), BMI-1 (**Chapter 3**), and RNF138 (**Chapter 4**).

1.8.1 CtIP

CtIP (C-terminal binding protein interacting protein) was originally identified as a transcriptional co-repressor for CtBP (adenovirus E1A C-terminal binding protein) (253) and an interactor of the G1/S transition-inhibiting factor retinoblastoma protein (Rb) (254). Simultaneously, a connection to DSB repair was revealed for CtIP when it was found to interact with BRCA1 (255). After being recruited to chromatin by the MRN complex and ATM activity and binding DNA (256), CtIP plays a crucial role in channeling repair pathway choice from NHEJ

to HR (30, 72) (**Section 1.4**). A critical factor to end resection (58), loss of CtIP impairs the generation of ssDNA (58, 256). As MRN endonuclease activity is fully active when bound to phosphorylated CtIP (52, 58, 61, 104), CtIP regulates whether end resection, and subsequently HR, occurs. CtIP also serves as a dynamic scaffold for bridging DNA ends and coordinating the assembly of protein complexes (257–263).

While most regions of CtIP are intrinsically disordered, CtIP's N-terminus is structurally ordered, containing an oligomerization domain (257–262). The C-terminus however contains a domain conserved across phyla from yeast to human (58, 59, 257). Emphasizing the importance of the C-terminus, patients with SCKL2 Seckel syndrome, a genetically inherited condition characterized by microcephaly, growth and neurological impairments, are mutated at the CtIP gene (*RBBP8)* and express a C-terminally truncated protein product (264). Cells expressing the SCKL2 CtIP mutant exhibit ATR signaling defects and DNA damage hypersensitivity (264). CtIP also contains residues that are targets for phosphorylation by the cyclin-dependent kinases (CDKs) and the PIKKs ATM and ATR (61, 105, 108, 265–267). In humans, CDK-phosphorylated CtIP is recognized by Nbs1 of the MRN complex, which then stimulates Mre11's endonuclease activity (52, 60, 105). In this way, Nbs1 transduces the activation of CtIP to that of MRN, allowing for cell cycle-dependent activation of MRN activity for DNA end resection and HR (46). Interestingly, CtIP can also be inhibited via phosphorylation by PLK1 (Polo-like kinase 1), a kinase that regulates the initiation and completion of mitosis, a time in the cell cycle when HR is inactive. PLK1 phosphorylates CtIP at residue Ser723, preventing it from supporting long-range end resection and HR, as Ser723-phosphorylated CtIP is deficient in stimulating Dna2 activity (268, 269) (**Section 1.4**).

While it is disputed in the field (261), human CtIP has been reported to possess an intrinsic 5' flap endonuclease activity that removes radiation-induced DNA lesions, protein-DNA adducts, and DNA secondary structures to allow end resection to occur (270–272). This endonuclease activity has also been implicated in the protection of stalled replication forks from degradation by nucleolytic activity (109).

1.8.2 Transcriptional Repression Near Double-Strand Breaks

Transcription is the process by which RNA (ribonucleic acid) is synthesized from the sequence of a DNA template. The transcription machineries involve RNA polymerase complexes, such as RNA polymerase II (RNAPII), which transcribes genes into the precursors that become messenger RNA, the sequences of which can be used for protein (1). RNA polymerases are bound to a multitude of other proteins. For instance, in the initiation of transcription, they are associated with transcriptional co-regulators (such as the Mediator complex), along with general transcription factors which bind the promoter sequences within genes and direct the RNA polymerases to transcription start sites (e.g. in the case of RNAPII, the general transcription factors include TFIIA, TFIIB, TFIID, TFIIE, TFIIF, and TFIIH) (1). Once transcription is initiated, RNA polymerases are associated with other proteins and protein complexes, such as transcription elongation factors, machineries involved in RNA processing (e.g. capping, splicing, polyadenylation), chromatin remodelers, and topoisomerases enzymes (1). Evidently, the transcription machinery encompasses a large assembly of factors engaged in numerous processes. Damaged or broken template DNA, or the machineries associated with repairing DSBs, may interfere with transcription, leading to the generation of aberrant RNA products. At the same time, the numerous processes and machineries that transcription is associated with may impede the progression of the DSB repair machinery

(273). In other words, the occurrence of DSBs could present a hurdle to transcription, and *vice versa*.

To avoid disruption to DSB repair, it would be logical for transcription to be halted in the vicinity of a DSB. In support of this notion, the transcription of ribosomal DNA genes by RNA polymerase I (RNAPI) was inhibited upon the induction of DSBs by ionizing radiation (IR), and this process was dependent on the activity of ATM kinase (274). IR prevented assembly of the RNAPI transcription initiation complex and displaced elongating RNAPI from chromatin (274). Later, the Soutoglou group observed the arrest of RNAPII-dependent transcription at genes next to DSBs induced by the action of the site-specific endonuclease I-*Ppo*I; this was dependent on the PIKK DNAPKcs (275). Next, the Greenberg laboratory generated a system where *Fok*I endonuclease could induce DSBs proximal to a reporter gene whose transcription was stimulated by doxycycline (**Fig. 3.4E**) (276). They observed ATM-dependent silencing of transcription of the reporter gene upon *Fok*I cleavage. Notably, transcriptional repression of the reporter gene only occurred when it was in *cis* to the DSB site (276). Excitingly, chromatin regions surrounding DNA damage sites have been observed to first expand, then undergo re-compaction, and later, hypercondensation, the condensation inducing signaling indicating the presence of the DSB (277–279). Other work demonstrates the DSB-induced establishment of repressive, compacted chromatin domains marked by H3K9me2/3 (279, 280). Combined, the findings indicate transcription repression is a key event in the response to DSBs.

1.8.3 BMI-1

The Polycomb group (PcG) of proteins encode transcriptional repressors that play essential roles in maintaining stem cell pluripotency by repressing developmental genes (281, 282). These

proteins were first discovered in the fruit fly *Drosophila melanogaster* as transcriptional regulators of key developmental genes known as homeobox (Hox) genes (283, 284). To regulate transcription, the PcG proteins form multimeric protein complexes called Polycomb repressive complexes (PRCs). Two major PRCs have been characterized so far, PRC1 and PRC2, and both alter chromatin to stably repress transcription at targeted genes (285, 286). The enzymatic activity of PRC2 is to trimethylate histone H3 at lysine 27 (H3K27me3), generating a transcriptionally repressive epigenetic mark (287). This is carried out by the methyltransferase activities of the enhancer of zeste (EZH1 or EZH2) subunits (286). PRC1, on the other hand, catalyzes the monoubiquitylation of histone H2A at lysine 119 (H2AK119ub1) (120, 121, 127), another epigenetic mark for transcriptional repression (288, 289).

The core components of the mammalian PRC1 system are RNF1 (also known as RING1A or RING1) and RNF2 (also known as RING1B or RING2) (290). These two proteins, each in complex with BMI-1 (B-cell-specific Moloney murine leukemia virus integration region 1), form the E3 ubiquitin ligases that catalyze the PcG-dependent ubiquitylation of histone H2A. RNF1, RNF2, and BMI-1 each contain a RING (really interesting new gene) domain and together embody the E3 ubiquitin ligase activity of PRC1. Of the three, RNF2 is the major ubiquitin ligase for H2A, while BMI-1 acts to stimulate the E3 activity of RNF2 (127, 288, 289). RNF1 is a less efficient H2A ubiquitin ligase and thus is not the main H2A E3. The combined action of the PRC complexes could lead to transcriptional repression through ubiquitylating histone H2A or by compacting chromatin independent of H2A ubiquitylation (291–294). These processes can on their own or together cause transcriptional repression; mechanisms may include blocking the movement of RNAPII during elongation, recruiting complexes that repress transcription, or inhibiting the recruitment of complexes required for transcription (291–294).

In addition to its role in gene repression, histone H2A ubiquitylation is implicated as an important post-translational modification in the regulation of the DNA damage response. RNF2-dependent H2AK119 ubiquitylation is induced at sites of ultraviolet light (UV)-induced DNA damage (295). As well, RNF2/BMI-1 contributes to DSB repair via histone H2A/H2AX ubiquitylation (130, 296–298). BMI-1 rapidly recruits to DNA lesions caused by local micro-irradiation via UV laser, ionizing irradiation (IR), and the replication fork stalling agent hydroxyurea (HU) in a number of cell types, including U2OS osteosarcoma cells, mouse embryonic fibroblasts (MEFs), HeLa, and $CD133^+$ glioblastoma multiforme (GBM) cells (130, 131, 297, 299, 300). The recruitment of the RNF2/BMI-1 E3 ubiquitin ligase is required for the monoubiquitylation of γH2AX and H2A, likely at K119, at DSBs in U2OS cells and MEFs, as downregulation of BMI-1 abolishes the modification at those sites (130, 296, 298). Of note, BMI-1's RING finger domain is required for its recruitment to DSBs (130, 297). The RING finger domain also mediates BMI-1's association with RNF2, and is therefore essential for BMI-1-associated E3 ligase activity (120, 121).

In support of the notion that BMI-1/H2A ubiquitylation is involved in DSB repair, BMI-1 downregulation compromises the survival of U2OS, Hela, and GBM cells in response to IR (130, 296, 297, 300, 301). Similarly, BMI-1-deficient MEFs display a two-fold reduction in the repair of DSBs induced by calicheamicin at 5 hours post-treatment, and the defects are rescued upon re-expression of BMI-1 (130). As well, knockdown of BMI-1 reduces HR-mediated DSB repair in human embryonic kidney HEK293T cells, as measured by an I-*Sce*l endonuclease-based *in vivo* HR assay (297). Interestingly, BMI-1 and recondensed chromatin facilitate the recruitment of BRCA1 (130, 279), which commits cells to repair DSBs using HR (74). In aggregate, the evidence supports the contributions of the BMI-1-associated E3 ligase activity to DSB repair.

More recent reports have found a role for PRC1 in repressing transcription at DSB sites. An initial report showed ATM and ubiquitylated H2A mediate local chromatin condensation at DSBs generated near sites of active transcription (273, 276, 302). Later, BMI-1 was revealed to have a major role in this process (302). The transcription elongation factor ENL (eleven–nineteen leukemia) is phosphorylated by ATM, enhancing an interaction with BMI-1 and thus recruiting PRC1 to chromatin. PRC1 then deposits H2AK119ub, enabling transcriptional silencing and allowing Ku70 to accrue at DSBs (302).

1.8.4 RNF138

RNF138 was first identified as a RING finger-containing E3 ubiquitin ligase that negatively regulates Wnt-β-catenin signaling (303). It was later found to be part of a subfamily of four E3 ubiquitin ligases with similar domain structure (304): an N-terminal RING domain, which interacts with the E2 ubiquitin conjugating enzyme, thereby promoting ubiquitin-transferring catalytic activity onto the substrate protein (133, 303, 304), three zinc finger domains, and a C-terminal ubiquitin-interacting motif. Beyond Wnt-β-catenin signaling, RNF138 contributes to the ubiquitylation of a variety of substrates in both physiological and pathological contexts. These range from a G2 phase/mitosis-specific E3 ubiquitin ligase (305), to voltage-gated calcium channels (306), to components of NFκB and Type I interferon signaling (307–310). RNF138 is also involved in spermatogenesis (311), B-cell malignancies (307), and mediating chemoresistance in glioblastoma and gastric cancer cells (312, 313).

Recent observations have linked RNF138 to the DNA damage response. Indeed, depleting RNF138 sensitizes cells to DNA damaging agents such as ionizing radiation, camptothecin (CPT),

cisplatin, mitomycin C (MMC), and methyl methanesulfonate (132, 133, 312–315). We and others have shown that RNF138's zinc finger (ZNF) domains mediate its recruitment to sites of DNA damage (132, 133, 315) and enable it to bind DNA (132, 133), preferring ssDNA overhangs over double-stranded DNA (132). The best characterized role for RNF138 in DNA repair is in promoting the occurrence of HR (132, 133, 314, 315). Loss of RNF138 impairs the recruitment of Rad51 to DSBs (132, 314), *in vivo* HR activity (132, 133, 315), and induces chromosomal aberrations upon treatment with MMC (314).

RNF138 firstly promotes HR by stimulating DNA end resection. Acting early in the process, it is recruited after Mre11 loading and nuclease activity but prior to the recruitment of CtIP (132, 133). With the UBE2D (ubiquitin conjugating enzyme E2 D) family of E2s, RNF138 mediates the ubiquitylation of CtIP, facilitating its accumulation at DSB sites (133). At the same time, RNF138 promotes the ubiquitylation of the Ku subunit Ku80, which evicts the Ku heterodimer from chromatin (132). Ku, which recognizes DSB ends and assembles the NHEJ machinery (23, 34, 232), is highly abundant (316). As such, Ku is recruited to DSB sites independent of the cell cycle phase (132). As persistently bound Ku is an impediment to end resection, it must be displaced from chromatin for DNA end resection to begin (317–320). These combined actions – promoting recruitment of CtIP, an activator of end resection, and facilitating the dissociation of Ku, which inhibits resection (317, 318) – ensure end resection can proceed.

More downstream in the HR pathway, another target of RNF138-dependent ubiquitylation is Rad51D, a paralogue of the Rad51 recombinase (314, 315). Rad51D may contribute to Rad51 filament assembly, mediating the formation of Rad51 foci in response to IR (321). Although it is not clear how Rad51D ubiquitylation contributes to HR (314), Rad51D recruitment to DNA damage was found to depend on RNF138 (315).

1.9 Study Overview and Aims

The work described in Chapters 2-4 are investigations into the mechanisms by which DNA end resection is regulated. These studies address two broad questions. First, what other protein players regulate DNA end resection, and how do they do so (mainly, **Chapter 3**)? And secondly, how are proteins in DNA end resection regulated by PTMs (**Chapters 2, 3, and 4**)?

In Chapter 2, treating cells with an inhibitor of SUMOylation processes revealed that the formation of irradiation-induced foci of CtIP was dependent on SUMOylation events. We hypothesized that CtIP was indeed a target for SUMOylation, finding that it is indeed a SUMO-2 substrate. We proceeded to characterize the conditions upon which CtIP is SUMOylated, identify protein and signaling factors that this SUMOylation depends upon, and address if other PTMs alter CtIP SUMOylation. We later assessed potential contributions of CtIP SUMOylation to genome integrity using a SUMOylation-deficient mutant of CtIP.

For Chapter 3, our group previously found that the protein BMI-1 was recruited to sites of DNA damage, with loss of BMI-1 impacting the recruitment of other DSB repair proteins, such as 53BP1 and BRCA1, and sensitizing cells to killing by ionizing radiation (130, 131). BMI-1 also promoted γH2AX ubiquitylation (130). Surmising that BMI-1 aids in the repair of DSBs, we extended upon these observations. We tested whether BMI-1 impacts the occurrence of HR, finding that it does indeed, and that it also promotes DNA end resection. We later explored potential mechanisms by which BMI-1 impacts resection, asking whether its activities in transcriptional inhibition, and the generation of the H2AK119ub mark, play a role.

In Chapter 4, we continued our group's investigations into the role of RNF138 in end resection. How RNF138 activity is controlled in HR has not been extensively investigated, but a tantalizing hint comes from the observation that ionizing radiation-induced RNF138-dependent

activity occurs in S/G2, but not G1 phase (132). We hypothesized that RNF138 activity might be under cell cycle regulation to coincide with the onset of HR. Noting a putative cyclin-dependent kinase (CDK) phosphorylation motif within, we suspected RNF138 was regulated by CDK-dependent phosphorylation. We therefore tested if RNF138 is indeed phosphorylated by CDKs, and asked if ubiquitylation also plays a role in regulating its activity. We later examined the impacts of these PTMs on RNF138's functions, particularly its abilities to facilitate end resection and HR.

Chapter 2 – SUMOylation Mediates CtIP's Functions in DNA End Resection and Replication Fork Protection

2.1 Summary

Double-strand breaks and stalled replication forks are a significant threat to genomic stability that can lead to chromosomal rearrangements or cell death. The protein CtIP promotes DNA end resection, an early step in homologous recombination repair, and has been found to protect perturbed forks from excessive nucleolytic degradation. However, it remains unknown how CtIP's function in fork protection is regulated. Here, we show that CtIP recruitment to sites of DNA damage and replication stress is impaired upon global inhibition of SUMOylation. We demonstrate that CtIP is a target for modification by SUMO-2 and that this occurs constitutively during S phase. The modification is dependent on the activities of cyclin-dependent kinases and the PI-3-kinase-related kinase ATR on CtIP's carboxyl-terminal region, an interaction with the replication factor PCNA, and the E3 SUMO ligase PIAS4. We also identify residue K578 as a key residue that contributes to CtIP SUMOylation. Functionally, a CtIP mutant where K578 is substituted with a non-SUMOylatable arginine residue is defective in promoting DNA end resection, homologous recombination, and in protecting stalled replication forks from excessive nucleolytic degradation. Our results shed further light on the tightly coordinated regulation of CtIP by SUMOylation in the maintenance of genome stability.

2.2 Introduction

The accurate transmission of genetic information to progeny is essential for living organisms. In eukaryotic cells, two problems that arise include double-strand breaks (DSBs), toxic DNA lesions where the phosphodiester backbone is severed in both strands (322), and replication stress, conditions that slow or halt replication fork progression (241). Both must be resolved to maintain the integrity of the genome.

To repair DSBs, cells in S/G_2 phase rely on homologous recombination (HR) (20). Here, 5'–3' nucleolytic trimming away from the DSB, known as DNA end resection, yields 3' single-stranded DNA (ssDNA) overhangs that are bound by RPA complexes (323). Short-range end resection is initiated by the nuclease activities of the MRN (Mre11-Rad50-Nbs1) complex and stimulated by the MRN co-factor CtIP ((carboxy-terminal binding protein) interacting protein) (52, 58, 324), after which exonucleases Dna2 and Exo1 catalyze long-range resection up to hundreds of nucleotides away from the DSB in collaboration with BLM and WRN helicases (45). End resection can be negatively regulated by the activities of PARP1 (325), DNA helicase B (326), and the Shieldin complex (234). Eventually, RPA coating the ssDNA overhangs is removed by PALB2-BRCA2 (78) to facilitate Rad51-mediated invasion and use of the sister chromatid as a template for error-free repair (20).

On the other hand, to deal with replication stress, the course of replication forks can be reversed by the assembly of a protective four-way junction, made possible by coordinated annealing of the newly synthesized strands and re-annealing of the template strands (246). Fork progression can later be restarted when replicative conditions are improved or downstream obstacles are repaired (246). Despite replication fork reversal being a well-known phenomenon (327, 328), knowledge of its mechanisms is incomplete and is currently an area of active research

(247). Intriguingly, HR proteins have been implicated in fork reversal and restart. Rad51 has been found to mediate fork reversal (329), while also, along with BRCA1 and BRCA2, to protect reversed forks from excessive degradation by the nuclease activities of Mre11 and Dna2 (249, 250, 330–333), both of which are end resection factors in HR (45).

Recent evidence demonstrates a role for the end resection factor CtIP at the replication fork, beyond its established role in promoting end resection for HR (252, 334–337). For example, CtIP was found to be enriched at ongoing replication forks in a proteomic screen (334), and was also found to interact with PCNA (proliferating cell nuclear antigen) (335), a clamp protein that enhances the processivity of DNA polymerases in DNA replication (338). This interaction targeted CtIP to foci of active DNA replication (335). While disrupting the interaction suppressed proliferation, caused cell cycle arrest, and induced DNA damage and a checkpoint response (335), the function of the interaction remains unknown. More recently, CtIP was shown to protect nascent DNA in reversed forks from excessive Dna2-dependent degradation in response to replication stress, independent of its role in HR-related end resection (336). Still, it is not clear how CtIP's fork protective function is regulated.

The activity of HR proteins is tightly controlled by various reversible post-translational modifications (PTMs) by chemical groups (e.g. phosphorylation) or proteins (e.g. ubiquitylation) (339), and CtIP is no exception. It is ubiquitylated by BRCA1 (340) and RNF138 (133), the latter of which targets it to DSB sites. CtIP is also phosphorylated by the DNA damage sensing kinases ATM (ataxia telangiectasia mutated) and ATR (ataxia telangiectasia and Rad3-related), and cyclin-dependent kinases (CDKs), the phosphorylations promoting its role in end resection and mediating its interaction with BRCA1 (61, 105, 108, 266, 267, 341). Another modification, SUMOylation, describes the conjugation of members of the small ubiquitin-like modifier (SUMO) protein family

onto target proteins. Analogous to ubiquitylation, a cascade of E1, E2, and E3 enzymes catalyzes the covalent linkage of SUMO isoforms onto protein substrates, and SUMO-specific proteases facilitate SUMO removal from these modified targets (342). While conjugation of SUMO proteins to other HR proteins has been shown to regulate protein stability, activity, nuclear trafficking, and protein-protein interactions (148, 152–155, 157), the role of SUMOylation in CtIP function is just beginning to be uncovered (343), and so far SUMOylation has not been linked to CtIP's function in replication fork protection. In this study, we demonstrate that CtIP is modified by SUMO-2 in S phase in an ATR- and CDK-dependent manner and is mediated by an interaction with PCNA. We further implicate PIAS4 as a SUMO E3 ligase for CtIP during S phase, and identify a key site for CtIP SUMOylation at residue K578. Functionally, we demonstrate K578 SUMOylation promotes CtIP's function at halted replication forks in protecting nascent DNA from uncontrolled degradation, and in HR by stimulating DNA end resection. Our findings suggest SUMOylation is a mechanistic link between CtIP's established interaction with PCNA to its ability to regulate fork stability during replication stress.

2.3 Materials and Methods

2.3.1 Plasmids, siRNAs, Site-Directed Mutagenesis, Transfections

pCAGGS empty vector and pCAGGS-I-*Sce*I were gifts from Jeremy Stark (City of Hope Comprehensive Cancer Center). Plasmids encoding Gam1-WT (wildtype) or -L258A/L265A were gifts from Susanna Chiocca (European Institute of Oncology IRCCS, Milan). FLAG-CtIP and a series of internal deletion mutants (D1 to D6) (344) were kind gifts from Junjie Chen (University of Texas). pICE-HA-CtIP-siR-WT (Addgene plasmid #82030; http://n2t.net/addgene:82030; RRID:Addgene_82030) and pICE-HA-CtIP-siR-S664A-S679A-S745A (Addgene plasmid #82031; http://n2t.net/addgene:82031; RRID:Addgene_82031) (53) were gifts from Patrick Calsou. FLAG-hPIAS4 (Addgene plasmid #15208; http://n2t.net/addgene:15208; RRID:Addgene_15208) (345) was a gift from Ke Shuai. siRNA-resistant N-terminally GFP-tagged CtIP plasmids (GFP-CtIP) of wildtype (WT), -7KR, -K896R, -6KR, -T847A, and -T847E were generous gifts from Pablo Huertas (University of Sevilla). RFP-PCNA was a gift from Michael Hendzel (University of Alberta). Custom siRNA duplexes were obtained from Sigma-Aldrich (**Table 2.1**) and transfected 48 hours prior using Lipofectamine RNAiMax Transfection Reagent (Invitrogen, Thermo-Fisher) according to the manufacturer's instructions. CtIP siRNA was transfected at 20 – 25 nM. If two transfections were required, 10 nM siCtIP was used for a second transfection 24 hours after the first one. All other siRNAs were used at 20 – 50 nM. Mutagenesis was performed using the Quikchange II XL (Agilent) and Q5 (New England Biolabs) site-directed mutagenesis kits according to the manufacturers' instructions, generating GFP-CtIP-T859A, -T859E, Δ515-518, -K578R, -K578R-K896R, -7KR-R578K, -N181A, -N181A-K578R, -N289A-H290A, and -N289A-H290A-K578R, as well as pICE-HA-CtIP-siR-K578R (**Table 2.2**). Plasmids containing the desired mutations were verified by Sanger sequencing performed at The

Applied Genomics Core (University of Alberta) (**Table 2.3**). Unless indicated otherwise, DNA plasmids were transfected using Effectene Transfection Reagent (Qiagen) 16 – 24 hours prior to cell harvest.

2.3.2 Human Cell Lines and Tissue Culture

U-2 OS, HEK293, HeLa, and HeLa His_{10}-SUMO-2 were cultured at 37°C in a humidified atmosphere containing 5% CO_2 in low glucose DMEM (Dulbecco's Modified Eagle's medium) supplemented with 10% fetal bovine serum (Gibco), 50 units/mL penicillin and 50 µg/mL streptomycin (Life Technologies). U-2 OS cells stably expressing the DR-GFP cassette were a gift from Jeremy Stark (City of Hope Comprehensive Cancer Center). U-2 OS cells stably expressing GFP-CtIP were a gift from Steve Jackson (University of Cambridge). U-2 OS cells stably expressing Mre11-GFP were a gift from Dorthe Helena Payne-Larsen (Danish Cancer Society Research Center). HeLa cells stably expressing 10x-histidine-tagged SUMO-2 from a pLV-CMV-His_{10}-SUMO-2-IRES-GFP construct (HeLa His_{10}-SUMO-2) (346) or not (parental HeLa) were gifts from Alfred C.O. Vertegaal (Leiden University). U-2 OS cells stably expressing GFP-tagged CtIP constructs were generated by transient lipofection of the constructs followed by selection in 850 µg/mL G418 (Thermo-Fisher). Cells were seeded to achieve 70-90% final confluency at the time of harvest.

2.3.3 Pharmacological Treatments

Unless indicated otherwise, all inhibitors were purchased from Millipore-Sigma or Selleck Chemicals. Inhibitors were diluted in warmed (37°C) tissue culture medium (low glucose DMEM supplemented with 10% fetal bovine serum), with working concentrations and treatment times

indicated in the figure legends. For vehicle controls, the same dilutions were performed using the solvent of the inhibitor (either DMSO or water). As the activity of ginkgolic acid 15:1 (GA, Cayman Chemical) was inactivated in the presence of serum (data not shown), cells were rinsed twice in phosphate buffered saline (PBS) prior to treatment with GA to remove residual serum left from the culture medium. GA treatment solutions were prepared by diluting GA into serum-free warmed DMEM and added to near-confluent cell monolayers.

2.3.4 *In vivo* Gene Conversion Homologous Recombination Reporter Assay

U-2 OS stably expressing the DR-GFP cassette **(Fig. 2.S9A)** were transfected with I-*Sce*I using a Gene Pulser Xcell Electroporation System (Bio-RAD). Cells were harvested 24 hours later, after which flow cytometry was performed using a BD FACSCanto II (BD Biosciences) to detect GFP^+ cells upon gating for forward and side scatter.

2.3.5 Pulsed-Field Gel Electrophoresis Assay

90% confluent U-2 OS cells grown on 6 cm dishes were treated as indicated and then trypsinized. 1 X 10^6 cells per condition were resuspended into 25 µL of PBS, then embedded into 60 µL of molten 0.9% Low Melting Point Agarose (Invitrogen) in 0.5X TAE Buffer (20 mM Tris pH 8.5, 10 mM acetic acid, 0.5 mM EDTA). The mixture was cast into a mold on ice to form a gel plug of volume 80 µL. Each plug was then digested with agitation at 32°C in 0.5 mL of PFGE Lysis Buffer (100 mM EDTA, pH 8.0, 1% N-laurylsarcosine, 0.2% sodium deoxycholate, 1 mg/mL Proteinase K) for 48 hours. The treated plugs were then washed three times 15 minutes each in TE Buffer (20 mM Tris-HCl pH 8.0, 50 mM EDTA) with gentle agitation at room temperature, then cut in half. The half-plugs were electrophoresed at 14°C, in duplicate, in a 0.9% Certified

Megabase Agarose (Bio-RAD)/0.5X TAE gel containing 0.25 μg/mL ethidium bromide via the CHEF-DR III Variable Angle System (Bio-RAD). The running parameters were as follows: Block 1 (9 hours, 120° included angle, 5.5 V/cm, 30-18s switch time); Block 2 (6 hours, 117° included angle, 4.5 V/cm, 18-9s switch time); Block 3 (6 hours, 112° included angle, 4.0 V/cm, 9-5s switch time). Resolved gels were visualized on a Typhoon 9400 Variable Mode Imager (GE Healthcare), then quantified with ImageQuant 5.2 (GE Healthcare).

2.3.6 *In Vitro* SUMOylation Assay

An *in vitro* SUMO-2 conjugation kit (K-715) was purchased from Boston Biochem. Reactions were assembled on ice using 2 μL of each component if needed (buffer, E1, E2, SUMO-2, Mg^{2+}-ATP) and 140 ng of recombinant glutathione S-transferase (GST)-tagged human CtIP (Abnova). The volume was completed to 20 μL with laboratory-grade water. Reactions were allowed to proceed for 1 hour at 37°C, then quenched by adding 6.7 μL of 4X SDS Sample Buffer, along with 2-mercaptoethanol to a concentration of 5%, then heating at 95°C for 5 minutes. The mixtures were resolved by SDS-PAGE and immunoblotted to detect the reaction components.

2.3.7 Cell Cycle Synchronization

HeLa His_{10}-SUMO-2 cells were synchronized to the G_1/S transition by double thymidine block. In brief, the cells were seeded to 40-50% confluency and 4 mM deoxythymidine was added to the culture media for 14 to 18 hours (first block). The cells were then released to progress through the cell cycle with 2 washes in PBS and cultured in warmed culture media for 8 to 12 hours. 4 mM deoxythymidine was added to the culture media for another 14 to 18 hours (second block). The cells were then released by 2 washes in PBS and replacing with warmed culture media for the

duration needed for the required cell cycle phase (e.g. 3 hours for mid-S phase, at least 11 hours for G_1 phase). If necessary, siRNA and DNA plasmid transfections were performed during release from the first thymidine block. U-2 OS cells were synchronized to S phase in the same manner, except they were released for 4 hours after double thymidine block instead of 3 hours.

2.3.8 His Pull-Down of His_{10}-SUMO-2 Conjugates by Ni-NTA Affinity Purification

Samples were processed in a protocol adapted from Tatham and Hay (347). HeLa His_{10}-SUMO-2 cells from 2 10 cm dishes or 1 15 cm dish were harvested by trypsinization and divided into three fractions: 5% was saved for cell cycle analysis by flow cytometry (Fraction C), 10% for input control (Fraction I), and 85% for His pull-down (Fraction H). Fraction C was resuspended into ice cold 70% ethanol in PBS and processed for DNA content analysis, whereas fractions I and H were pelleted and frozen in liquid nitrogen; all were stored at -80°C. Samples of Fraction H were resuspended into 10 mL of ice cold fresh Guanidine Lysis Buffer (6 M guanidine-HCl, 100 mM sodium phosphate buffer pH 8.0, 10 mM Tris, 5 mM imidazole, 5 mM 2-mercaptoethanol), sonicated for 1 minute at amplitude 50 on a Model 705 Sonic Dismembrator fitted with a microtip probe (Fisher Scientific), and centrifuged at 1450g for 15 min. The lysate was then mixed with 200 – 300 µL of Ni-NTA agarose beads (Qiagen) pre-equilibrated in Guanidine Lysis Buffer and agitated overnight at 4°C. The beads were washed once in Guanidine Wash Buffer (6 M guanidine-HCl, 100 mM sodium phosphate buffer pH 8.0, 10 mM Tris, 0.1% Triton X-100, 10 mM imidazole, 5 mM 2-mercaptoethanol), once in Urea Wash Buffer A (8 M urea, 100 mM sodium phosphate buffer pH 8.0, 10 mM Tris, 0.1% Triton X-100, 10 mM imidazole, 5 mM 2-mercaptoethanol), and 3 times in Urea Wash Buffer B (8 M urea, 100 mM sodium phosphate buffer pH 6.3, 10 mM Tris, 0.1% Triton X-100, 5 mM 2-mercaptoethanol); all buffers were prepared immediately before use.

On occasion, the imidazole concentration in buffers was raised to 20 mM for increased stringency. The beads were then eluted with agitation in Ni-NTA Elution Buffer (150 mM Tris-HCl pH 6.7, 200 mM imidazole, 5% sodium dodecyl sulfate, 30% glycerol, 0.05% bromophenol blue, 5% 2-mercaptoethanol) for 30 minutes at 60°C. Samples of Fraction I were resuspended into 2X SDS-PAGE Sample Buffer (125 mM Tris pH 6.8, 4% sodium dodecyl sulfate, 20% glycerol, 0.1% bromophenol blue, 5% 2-mercaptoethanol), heated for 2 minutes at 95°C, and ultrasonicated in a Bioruptor (Diagenode) for 30 minutes (each cycle: 30 seconds on, 30 seconds off). For subsequent SDS-PAGE and immunoblotting, volumes representing ~16 - 22-fold more of starting cellular content were loaded for Fraction H relative to Fraction I to enable suitable detection of the SUMOylated proteins, unless indicated otherwise.

2.3.9 DNA Content Analysis for Cell Cycle Profiling

Cells were fixed in 70% ethanol in 1X PBS overnight. They were then washed once in PBS, then treated with 100 µg/mL RNase A in PBS containing 3.8 mM sodium citrate for 30 minutes at 37°C with agitation. Propidium iodide was added to a final concentration of 50 µg/mL and incubated with the cells for 30 minutes. Flow cytometry was performed on the processed samples using a BD FACSCanto II (BD Biosciences) to detect propidium iodide fluorescence upon gating for forward and side scatter.

2.3.10 Fractionation for Chromatin Enrichment

Cell pellets were resuspended into ice cold Extraction Buffer (25 mM HEPES pH 7.9, 300 mM sucrose, 50 mM NaCl, 1 mM EGTA, 3 mM $MgCl_2$, 0.5% IGEPAL CA-630) supplemented with cOmplete protease inhibitor cocktail, phosSTOP phosphatase inhibitor cocktail (both from Roche),

and 25 mM N-ethylmaleimide (NEM) and tumbled end-over-end for 20 minutes at 4°C. Samples were then centrifuged at 20,000g for 20 minutes at 4°C, after which the supernatant was recovered as the soluble fraction. The pellet, representing the chromatin-enriched fraction, was then resuspended into the buffer of choice and sonicated with a Model 705 Sonic Dismembrator fitted with a microtip probe (Fisher Scientific).

2.3.11 Co-Immunoprecipitation (Co-IP) Assay

Cell pellets from 10 cm dishes were resuspended into 200 µL of ice-cold RIPA buffer (50 mM Tris-HCl pH 7.4, 150 mM NaCl, 1% IGEPAL CA-630, 0.25% sodium deoxycholate, 0.1% SDS, 1 mM EDTA) supplemented with 50 mM NEM, 2X cOmplete, and 1X phosSTOP (both Roche) protease and phosphatase inhibitor cocktails. After agitation on ice for 30 minutes, samples were clarified by centrifugation at 20,000g at 4°C, upon which 10% of the supernatant was saved for the input control. The remainder of the supernatant was diluted in ice-cold Dilution Buffer (150 mM NaCl, 10 mM Tris-HCl pH 7.5, 0.5 mM EDTA) supplemented with 25 mM NEM, 1X cOmplete, and 1X phosSTOP to a final volume 1.7 mL. This was mixed with 25 µL of Dilution Buffer-equilibrated GFP- or RFP-Trap agarose beads (Chromotek) and tumbled overnight. The beads were washed once in Dilution Buffer, then 3 times in Wash Buffer (500 mM NaCl, 10 mM Tris-HCl pH 7.5, 0.5 mM EDTA), before sample elution into 2X Sample Buffer (125 mM Tris-HCl pH 6.8, 4% sodium dodecyl sulfate, 20% glycerol, 0.1% bromophenol blue, 5% 2-mercaptoethanol) at 95°C for 10 minutes. Analysis of IP and input fractions was performed via SDS-PAGE and immunoblotting. For Co-IP experiments involving GFP-CtIP-Δ515-518, RIPA was replaced with NETMN buffer (500 mM NaCl, 1 mM EDTA, 50 mM Tris-HCl pH 7.4, 2.5

mM MgCl2, 0.5% IGEPAL CA-630) (335), which was then adjusted to a composition similar to Dilution Buffer prior to mixing with the beads.

2.3.12 SDS-PAGE and Immunoblotting

Unless indicated otherwise, cell lysates were prepared by resuspending cell pellets into 2X SDS-PAGE Sample Buffer (125 mM Tris-HCl pH 6.8, 4% sodium dodecyl sulfate, 20% glycerol, 0.1% bromophenol blue, 5% 2-mercaptoethanol), heating for 2 minutes at 95°C, and sonicating with a Model 705 Sonic Dismembrator fitted with a microtip probe (Fisher Scientific), generating whole cell extract. Lysates were electrophoresed in 5 to 15% polyacrylamide mini-gels handcast in 0.1% sodium dodecyl sulfate (SDS) and Tris buffer (pH 6.8 for stacking layer, pH 8.8 for resolving) in running buffer (25 mM Tris-HCl pH 8.3, 192 mM glycine, 0.1% SDS), then wet transferred onto nitrocellulose membrane in transfer buffer (25 mM Tris-HCl pH 8.3, 192 mM glycine, 20% methanol) for 6 hours at 50 V or 90 minutes at 110 V. Total protein on membranes was visualized and quantified by staining with REVERT Total Protein Stain (LI-COR Biosciences). For immunoblot, membranes were blocked in 4% fish skin gelatin in Tris buffered saline (TBS) at room temperature and incubated in primary antibodies (**Table 2.4**) diluted in TBS + 0.1% Tween-20 (TBST) overnight at 4°C or 1 hour at room temperature. They were then washed in TBST, incubated for 1 hour with secondary antibodies conjugated to horseradish peroxidase (HRP) or IRDye 680RD and 800CW (all LI-COR Biosciences) (**Table 2.5**) in TBST at room temperature, and rinsed in TBST and TBS. Amersham ECL Prime Western Blotting Detection Reagent (GE Healthcare) was used to detect HRP according to the manufacturer's instructions. Immunoblots were acquired on the Odyssey Fc Imaging System (LI-COR Biosciences) and quantified by densitometry using Image Studio software (LI-COR Biosciences). When necessary, membranes

were stripped in a buffer containing 1% SDS and 100 mM glycine, pH 2.2, for 1 hour prior to re-blocking and re-probing with the appropriate primary and secondary antibodies.

2.3.13 Immunofluorescence (IF) Staining

U-2 OS cells were seeded onto #1½ cover slips (Electron Microscopy Sciences) at least 24 hours prior to experimental treatments. For detection of native 5-bromo-2'-deoxyuridine (BrdU) foci, cells were seeded in media supplemented with 10 µg/mL BrdU 36 hours prior to the experimental treatment. After the necessary treatments, they were incubated in the appropriate extraction buffer (**Table 2.6**), rinsed twice in ice cold PBS, fixed in 2% paraformaldehyde in PBS for 20 minutes, and quenched for 10 minutes in 100 mM NH_4Cl in PBS. Incubations in primary antibodies (**Table 2.4**) were performed overnight at 4°C. Next, the cells were placed in PBS + 0.1% Tween-20 (PBST) for 5 minutes, rinsed 6 times in PBS, and incubated with the appropriate secondary antibodies (**Table 2.5**) diluted in PBS for 1 hour at room temperature. The cells were then incubated in PBST containing 10 ng/µL DAPI for 20 minutes, rinsed 6 times in PBS, and mounted on microscopy slides in 2% propyl gallate in PBS with 10% DMSO/80% glycerol as the solvent. Images were acquired on an upright fluorescence microscope (Zeiss AxioImager.Z1) with a Plan Apochromat 1.4 N.A. 63X oil immersion objective lens via MetaMorph (Molecular Devices, LLC) using a Prime 95B camera (Teledyne Photometrics). Scale bars in all micrographs represent 10 µm. Nuclear foci in fluorescence microscopy images were quantified by the Granularity application in MetaXpress 6 software (Molecular Devices, LLC) or using Imaris software (Oxford Instruments). All images within the same experiment were scaled evenly for brightness and contrast.

2.3.14 Laser Microirradiation

U-2 OS cells were cultured on 35-mm culture dishes containing a coverslip mounted on the bottom of the dish (MatTek Corporation) 48 hours before the experiment and transfected with siRNA to CtIP. They were then transfected with the appropriate GFP-CtIP constructs ~16 hours before irradiation. Prior to imaging, the media was replaced with Phenol Red-free DMEM supplemented with 2 mM L-glutamine, 10% FBS, and 14 mM HEPES. Cells were then treated with 0.5 µg/ml Hoechst 33258 for 20 – 30 minutes, washed with PBS, then placed on the stage of a spinning disk (Ultraview, Perkin-Elmer) inverted microscope (Axiovert 200M, Carl Zeiss, with a 40X/1.3 N.A. Plan-Neofluar oil immersion objective lens) equipped with an electron-multiplying charge-coupled device (EM-CCD) camera (ORCA-FLASH-4.0; Hamamatsu Photonics). DSBs were generated along a 0.2 – 1 µm wide region across the nucleus of a single living cell by excitation of the Hoechst 33258 dye using a 405 nm laser line. The laser output was set to 10% (unless stated otherwise), and 10 iterations were used to generate localized DNA damage. GFP fluorescence imaging was recorded using 500 – 800 ms exposure times for 5 – 6 minutes using Volocity software (Perkin-Elmer). The mean accumulation ± standard deviation of GFP-CtIP from at least 24 – 48 cells pooled from three independent experiments was then plotted.

2.3.15 Clonogenic Survival Assay

Parental or GFP-CtIP-expressing stable cell lines of U-2 OS were transfected with CtIP or non-targeting siRNA in two rounds, 24 hours apart. ~40 hours after the first transfection, cells were seeded in duplicate into 6 cm dishes at ≥400 cells per dish and allowed to settle at 37°C for 6 to 8 hours, after which they were treated with camptothecin at the indicated concentrations for 1 hour at 37°C. The media in each dish was then replaced, and colonies were allowed to form over 9 –

11 days at 37°C. The colonies were fixed and visualized in 0.5% crystal violet/25% methanol. Colonies containing at least 50 cells were then scored and counted, and the surviving fraction was calculated accordingly (348).

2.3.16 DNA Fiber Assay

U-2 OS cells were pulse-labeled with two thymidine analogs: first 20 μM 5-iodo-2'-deoxyuridine (IdU; Sigma-Aldrich), then 250 μM 5-chloro-2'-deoxyuridine (CldU; Sigma-Aldrich), each for 30 minutes at 37°C. Cells were washed twice with PBS after each pulse-labeling and then treated with 2 mM hydroxyurea (HU) for 4 hours. The cells were then collected and resuspended in PBS at 100,000 cells/mL. 2 μL of the cell suspension was mixed with 10 μL of DNA Fiber Lysis Buffer (200 mM Tris-HCl pH 7.5, 50 mM EDTA, 0.5% SDS) on a glass slide. After 2 minutes, the slides were tilted at a 45° angle for spreading by gravity, and the resulting DNA spreads were air dried for 40 minutes, fixed in 3:1 methanol/acetic acid for 10 minutes, and stored at 4°C. The DNA fibers were denatured with 2.5 M hydrochloric acid for 1 hour, washed with PBS, and blocked with 5% BSA in PBS containing 0.1% Tween-20 for 1 hour. DNA immunostaining was then performed with a rat anti-BrdU/CldU antibody to detect CldU and mouse anti-BrdU/IdU antibody to detect IdU (**Table 2.4**) in a humidified chamber for 2 hours at room temperature. The following secondary antibodies were then bound for 1 hour at room temperature: chicken anti-rat—Alexa Fluor 488 and goat anti-mouse—Alexa Fluor 546 (**Table 2.5**). The slides were air dried and mounted in ProLong Gold Antifade Mountant (Invitrogen, Thermo-Fisher). Images were sequentially acquired with an upright fluorescence microscope (Zeiss AxioImager.Z1) with a Plan Neofluar 1.3 N.A. 40X oil immersion objective lens via MetaMorph (Molecular Devices, LLC) using a Prime 95B camera (Teledyne Photometrics). The DNA tract lengths were measured with ImageJ software

(version 1.51k), and the pixel length values converted into micrometers using the scale bars generated by the microscope. $n \geq 150$ fiber tracts were scored for each data set. Scatterplots display the mean value and standard deviation.

2.3.17 Protein Expression and Purification

The MRN (Mre11, Rad50 and Nbs1) complex was expressed in *Sf*9 insect cells and purified according to an established protocol (349). Dna2 was expressed in *Sf*9 cells and purified as described (350). For two-step affinity purification of recombinant WT- and K578R-CtIP, *Sf*9 cells were infected with GST-CtIP-10XHis baculovirus. 72 hours post-infection, cells were collected by centrifugation and the pellet was frozen on dry ice. To induce CtIP phosphorylation (pCtIP), the *Sf*9 culture was supplemented with 25 nM okadaic acid (Sigma) 4 hours before harvest (i.e. 68 hours after viral infection) followed by treatment with 1 μM camptothecin (Sigma) 1 hour before harvest (i.e. 71 hours after viral infection). Cells were lysed in Buffer 1 (1X PBS supplemented with 150 mM NaCl, 1 mM EDTA, 0.05% Triton X-100, and 1 mM DTT) supplemented with cOmplete protease inhibitor cocktail (Roche) and homogenized 10 times with a Dounce homogenizer (Pestle A). The cell lysate was incubated with 1 mM $MgCl_2$ and 2.5 U/mL benzonase nuclease at 4°C for 1 hour followed by centrifugation at 90,000g for 1 h. The soluble cell extract was then incubated with 1 mL of glutathione-sepharose beads for 90 min at 4°C with gentle rotation. The beads were washed twice with Buffer 1, and incubated with Buffer 2 (Buffer 1 with 5 mM ATP and 15 mM $MgCl_2$) for 1 hour at 4°C. The beads were then washed twice with Buffer 1 supplemented with 350 mM NaCl and once with P5 Buffer (50 mM sodium phosphate pH 7.0, 500 mM NaCl, 10% glycerol, 0.05% Triton X-100, 5 mM imidazole), then incubated with 60 U/mL PreScission protease (GE Healthcare Life Sciences) in P5 Buffer overnight at 4°C to cleave off the

GST tag. Supernatant was then collected and completed to 10 mL with P5 Buffer before incubating for 1 hour at 4°C with 400 µL of TALON bead slurry (Clontech) equilibrated in P5 Buffer. The TALON beads were washed twice with P30 buffer (50 mM sodium phosphate pH 7.0, 500 mM NaCl, 10% glycerol, 0.05% Triton X-100, 30 mM imidazole) before eluting the bound protein twice in one bead volume of P500 buffer (50 mM sodium phosphate pH 7.0, 500 mM NaCl, 10% glycerol, 0.05% Triton X-100, 500 mM imidazole). Eluted protein was then dialysed in the storage buffer (20 mM Tris pH 7.4, 200 mM NaCl, 10% glycerol, 1 mM DTT) and stored in aliquots at -80°C.

2.3.18 MRN Endonuclease Assay

The dsDNA substrate used in this reaction was prepared as described (52). The MRN endonuclease assay was performed in a reaction buffer consisting of 25 mM MOPS pH 7.0, 60 mM KCl, 1 mM $MnCl_2$, 5 mM $MgCl_2$, 0.2% Tween-20, 2 mM DTT, 2 mM ATP, and 100 nM of 5'-radiolabeled 70 bp dsDNA substrate blocked with 15 nM streptavidin for 5 min at room temperature. The indicated concentration of purified CtIP was added to the reaction and incubated at 37°C for 5 min. Where indicated, 20 nM of purified MRN was added and the reaction was allowed to proceed for a further 30 min at 37°C. Reactions were deproteinized in one-fifth volume of Stop Buffer (20 mM Tris-HCl pH 7.5, 2 mg/mL proteinase K) for 30 min at 37°C. An equal volume of 100% formamide was added to each reaction, and the samples were boiled at 95°C for 3 min before loading onto an 8% acrylamide/urea gel and running at 75 W for 60 min. The gel was dried on DE81 paper (Whatman) and signals were detected by autoradiography. Densitometric analyses were performed using the FLA-5100 phosphorimager (Fujifilm) and quantitated using the Image Reader FLA-5000 v1.0 software.

2.3.19 Dna2 and CtIP Nuclease Assay

The nuclease assay was performed in a reaction buffer consisting of 25 mM MOPS pH 7.0, 60 mM KCl, 5 mM $MgCl_2$, 0.2% Tween-20, 2 mM DTT, 2 mM ATP, and 100 nM of 5'-radiolabeled flap DNA substrate. The indicated concentration of purified Dna2 or CtIP protein was added to the reaction and incubated at 37°C for 30 min followed by deproteinization in one-fifth volume of Stop Buffer (20 mM Tris-HCl pH 7.5, 2 mg/mL Proteinase K) for 30 min at 37°C. An equal volume of 100% formamide was added to each reaction, and the samples were boiled at 95°C for 3 min before loading onto an 8% acrylamide/urea gel and running at 75 W for 60 min. The gel was dried on DE81 paper (Whatman) and signals were detected by autoradiography. Densitometric analyses were performed using the FLA-5100 phosphorimager (Fujifilm) and quantitated using the Image Reader FLA-5000 v1.0 software. The flap DNA substrate was made by annealing JYM925 (GGGTGAACCTGCAGGTGGGCAAAGATGTCCTAGCAATGTAATCGTCAAGCTTTATGCCGT) and JYM926 (ACGCTGCCGAATTCTACCAGTGCCAGCGACGGACATCTTTGCCCACCTGCAGGTTCACCC).

2.3.20 Image and Data Processing

Raw microscopic and immunoblot images were adjusted for brightness and contrast in Adobe Photoshop then arranged and labeled in Adobe Illustrator. Scale bars on micrographs represent 10 µm. Immunoblots were displayed avoiding saturation when possible. Graphs and scatterplots were generated in Prism (Graphpad) and display the mean and standard deviation (error bars). Two-tailed, unpaired, non-parametric Student's *t*-tests (Mann-Whitney) were performed in Prism

to determine statistical significance. Asterisks depict statistically significant differences: ns (not significant), * ($p \leq 0.05$), ** ($p \leq 0.01$), *** ($p < 0.001$), **** ($p < 0.0001$). Schematic diagrams were prepared in Adobe Illustrator.

2.4 Results

2.4.1 SUMOylation Events Mediate Homologous Recombination

Currently, the role of SUMOylation in the regulation of homologous recombination (HR) proteins is not well understood. We thus sought to identify potential SUMO targets in the HR pathway and characterize how SUMOylation could affect their function. To screen for SUMO targets, we utilized ginkgolic acid 15:1 (GA), an inhibitor of global protein SUMOylation that interferes with formation of the E1-SUMO intermediate and does not affect ubiquitylation (351). We chose to block SUMOylation with acute GA treatment as opposed to short interfering RNA (siRNA)-mediated depletion of UBC9 (the sole E2 enzyme in the SUMOylation cascade) to avoid issues associated with RNA interference, namely incomplete knock-down, off-target effects, and cellular adaptation mechanisms from prolonged knockdown. We first confirmed that treating U-2 OS cells with GA was able to reduce the presence of higher-order SUMO conjugates via immunoblot (**Fig. 2.1A**), validating the effectiveness of the inhibitor. To determine if SUMOylation events mediate the process of HR, we performed a gene conversion assay in U-2 OS cells stably expressing the DR-GFP reporter construct (U-2 OS DR-GFP) (352) in the presence or absence of GA. Expressing I-*Sce*I endonuclease in these cells generates a site-specific DSB within the reporter construct, which when repaired by HR results in expression of a functional

green fluorescent protein (GFP) product (**Fig. 2.S9A**). The number of GFP^+ cells, measured by flow cytometry, was used as a readout of the frequency of HR events. Indeed, treating the cells with GA reduced the number of GFP^+ cells in a dose-dependent manner relative to cells treated with vehicle control (DMSO) (**Fig. 2.1B**). Since HR is active during the S and G_2 stages of the cell cycle, we wondered if treating cells with GA could be altering the cell cycle distribution. To address this, we treated U-2 OS cells with GA and quantified their DNA content by propidium iodide staining and flow cytometry. The chosen concentrations of GA did not drastically alter the proportion of cells within G_1, S, and G_2 phase (**Fig. 2.1C**), confirming that the inhibition of HR in U-2 OS DR-GFP was not due to GA biasing cells to the G_1 stage. To verify that the GA-dependent reduction in HR frequency was due to the inhibition of SUMOylation, we used another inhibitor of SUMOylation, the avian adenoviral protein Gam1 (Gallus anti-morte 1) (353, 354). Mechanistically, Gam1 inhibits SUMOylation by binding to the SUMO E1 heterodimer SAE1/SAE2 and recruiting it to an elongin/cullin E3 ubiquitin ligase complex, targeting it for proteasomal degradation. Gam1 expression also promotes proteasomal degradation of the SUMO E2 UBC9 (355, 356), and all these activities are abrogated in the L258A/L265A (LL/AA) mutant of Gam1 (354–356). After confirming that Gam1 expression was able to reduce protein levels of UBC9 (**Fig. 2.S9B**), and only slightly increased the proportion of cells in G_1 phase (**Fig. 2.S9C**), we co-expressed in U-2 OS DR-GFP cells I-*Sce*I with either wildtype (WT)- or LL/AA-Gam1. Expressing WT-, but not LL/AA-Gam1, led to a reduction in the frequency of HR similar to treatment with GA (**Fig. 2.1B**). Hence, HR is regulated by SUMOylation events, as it can be inhibited both by GA treatment and by Gam1 expression.

2.4.2 DNA End Resection and CtIP Recruitment are Regulated by SUMOylation Events

We next sought to map out which players in the HR pathway were potentially impacted upon inhibition of SUMOylation by GA. We reasoned that certain disruptions in function could be visualized by defects in the accumulation of HR proteins at sites of DNA damage in response to camptothecin (CPT) or ionizing radiation (IR). Starting at the assembly of Rad51 nucleofilaments, a downstream event in HR, we observed that GA treatment inhibited the formation of Rad51 foci in U-2 OS cells in response to IR, despite the cells still incurring DSBs, as visualized by the formation of γH2AX foci (**Fig. 2.1D**). This validated that HR as a process was inhibited by GA, agreeing with the reduction in HR frequency seen in the U-2 OS DR-GFP reporter cells (**Fig. 2.1B**). As H2AX is a substrate for SUMOylation itself (357), γH2AX foci intensity could be altered in the presence of GA and not reflect the true extent of the DNA damage load. We thus resorted to using pulsed-field gel electrophoresis (PFGE) to measure the degree of DSBs induced by IR in the presence or absence of GA. Interestingly, GA alone and in combination with IR exacerbated the proportion of broken DNA in U-2 OS cells (**Fig. 2.1E-F**), suggesting more DSBs were in fact induced with GA present. Thus the reduction in Rad51 foci observed with GA treatment reflects a true inhibition in Rad51 function, as the GA-treated cells had incurred even more DSBs than those treated with vehicle control. We then hypothesized that the reduction in Rad51 foci could, at least in part, be a result of hindered DNA end resection, an event upstream of Rad51 filament assembly. End resection generates single-stranded DNA (ssDNA) overhangs that are protected from nucleolytic degradation by the recruitment of RPA complexes (323), so we chose to detect both RPA and ssDNA foci as readouts of functional end resection. Treating U-2 OS cells with GA reduced the intensity of RPA foci formed in response to CPT (**Fig. 2.1G**), and reduced CPT-induced 5-bromo-2'-deoxyuridine (BrdU) foci detected under non-denaturing

conditions (**Figs. 2.1H, 2.S9D**), exposure of which represents ssDNA. As a control, by PFGE, we detected more DSB damage inflicted in cells treated with CPT and GA than CPT alone (**Fig. 2.1E-F**), emphasizing the true reduction in RPA and BrdU foci seen upon GA treatment. In line with this, expression of Gam1 also strongly inhibited the formation of RPA (**Fig. 2.S9E**) and native BrdU foci (**Fig. 2.S9F**). Although transient Gam1 expression slightly increased the proportion of cells in G_1 (**Fig. 2.S9C**), our use of CPT as a damaging agent ensured damage was only inflicted on cells within S phase (358). Together, our findings suggest end resection is dependent on SUMOylation events, which, when inhibited, result in less ssDNA and reduced RPA recruitment to sites of damage. We hypothesized that this impairment in end resection could be due to defects in the recruitment of the end resection machinery to DSBs. We proceeded by examining the ability for the MRN complex components Nbs1 and Mre11 as well as MRN co-factor CtIP (52) to form IR-induced foci in the presence of GA, selecting U-2 OS cell lines stably expressing GFP-tagged versions of CtIP and Mre11 to improve detection of IR-dependent foci over background. While the intensity and number of Mre11-GFP (**Fig. 2.S9G**) and Nbs1 (**Fig. 2.S9H**) foci were not substantially altered by GA treatment, the intensity of GFP-CtIP foci was notably inhibited in the presence of GA (**Fig. 2.1I**), suggesting less CtIP was being recruited to DSB sites upon inhibition of SUMOylation. Thus, we conclude end resection is dependent on SUMOylation, and one explanation may lie in a defect in CtIP recruitment to DSB sites upon shutdown of SUMOylation.

Since CtIP has also been found to function at the replication fork (252, 334–337), we tested if conditions that induce replication stress also promoted the formation of CtIP foci. Treating U-2 OS cells with CPT at low concentrations (359) and the deoxynucleotide triphosphate (dNTP) pool-depleting agent hydroxyurea (HU) (360), both of which induce replication stress, led to the recruitment of CtIP into distinct foci in a dose-dependent manner (**Fig. 2.S10A**). Interestingly,

treatment with GA reduced the intensity of these foci, suggesting CtIP recruitment to sites of replication stress is also mediated by SUMOylation processes (**Fig. 2.S10B**). In summary, CtIP forms foci both when DSBs and replication stress are induced, and in both cases this recruitment is dependent on SUMOylation events.

Figure 2.1

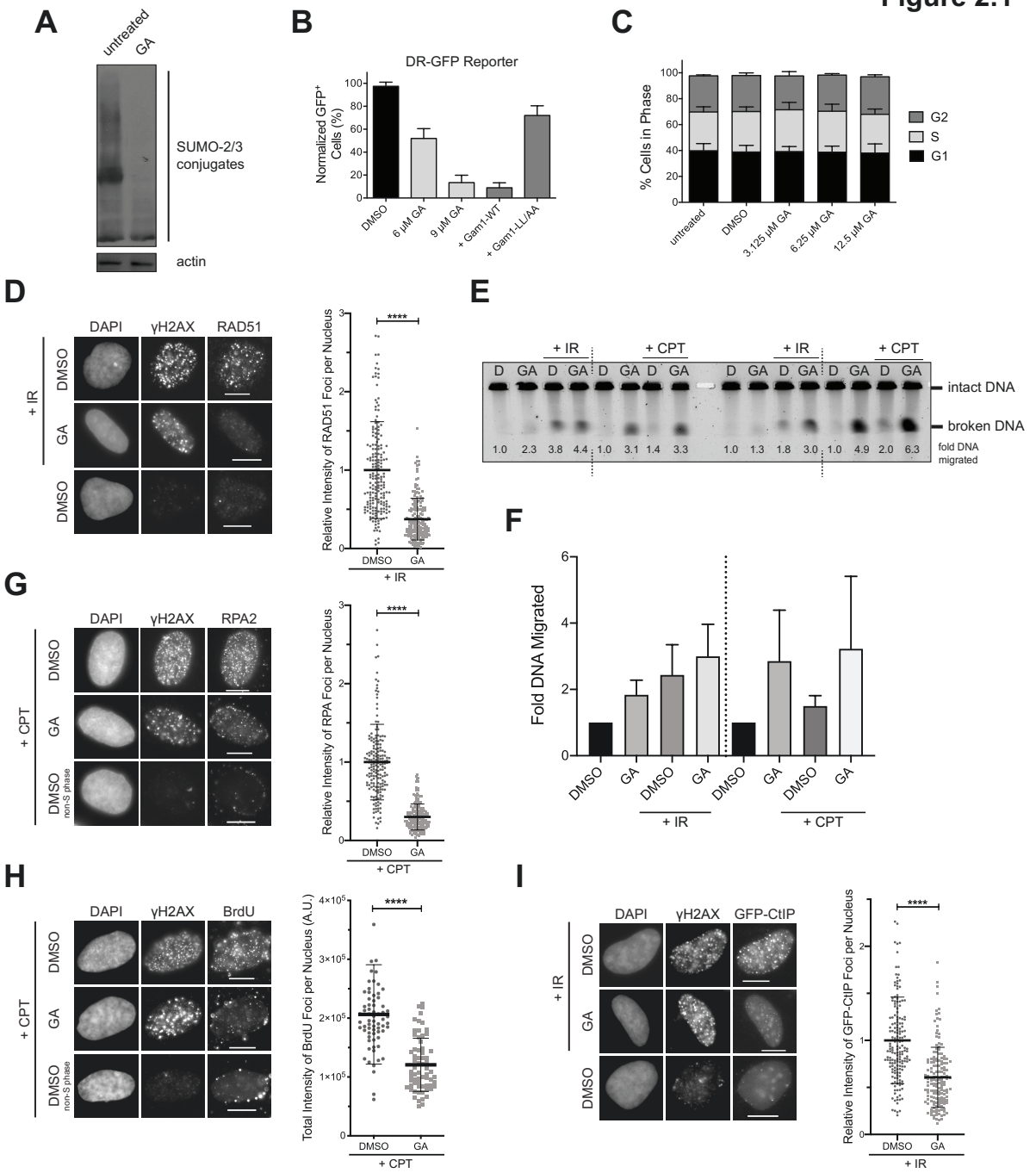

Figure 2.1: SUMOylation Events Mediate Homologous Recombination and DNA End Resection

A) U-2 OS cells were treated with ginkgolic acid 15:1 (GA) at 25 μM for 3 hours. A reduction in SUMO-2/3 conjugates is seen upon GA treatment by immunoblot. **B)** DR-GFP homologous recombination reporter assay in U-2 OS cells stably expressing the DR-GFP cassette. I-*Sce*I was expressed for 24 hours in the presence of 0.025% DMSO (vehicle control), GA at the indicated concentrations, or co-expression of FLAG-tagged wildtype (WT) Gam1 or the LL/AA mutant.

The means from 2 independent experiments are displayed. **C)** U-2 OS cells were treated with 0.025% DMSO or GA at the indicated concentrations for 24 hours and processed for DNA content analysis. Shown are the means from 3 independent experiments. **D)** U-2 OS cells were pre-treated with 12 μM GA or 0.024% DMSO for 1 hour, subjected to 10 Gy of IR or not, and recovered for 3 hours in the presence of GA. Immunofluorescence (IF) micrographs presented are representative of at least 4 independent experiments (left panel). The total Rad51 foci intensity was quantified from ≥179 Rad51 foci-positive cells per condition from 3 independent experiments (right panel). **E)** U-2 OS cells were pre-treated with 0.024% DMSO (D) or 12 μM GA (GA) for 2 hours, then either exposed to 20 Gy of ionizing radiation (IR), treated with 1 μM CPT for 1 hour in the presence of DMSO or GA, or not. 1 X 10^6 cells per condition were embedded into agarose plugs and digested with Proteinase K. Each plug was cut in half, and both halves were resolved by pulsed-field gel electrophoresis. The representative gel shown has duplicate halves from one experiment run simultaneously (left and right). Intensities of the migrated and immobile DNA bands were quantified and used to calculate relative DNA migration, which is presented below each lane and indicates the quantity of DSBs induced. **F)** Quantification of relative DNA migration from the gel in **E)**, averaged with data from a second independent replicate. **G) and H)**: Left panels: IF micrographs of U-2 OS cells pre-treated with 12 μM GA or 0.024% DMSO for 2 hours, after which 1 μM camptothecin (CPT) was added for an additional hour. As only cells in S phase are sensitive to CPT, cells that did not respond to CPT are also presented. Right panels: In **G)**, ≥178 γH2AX$^+$ cells per condition from 3 independent experiments were quantified for total RPA2 foci intensity. In **H)**, ≥66 γH2AX$^+$ cells per condition from 1 experiment were quantified for total BrdU foci intensity. Cells in **H)** were cultured in BrdU-containing media prior to treatment. **I)** IF micrographs (left panel) of U-2 OS cells stably expressing GFP-CtIP pre-treated with 12 μM GA or 0.024% DMSO for 1 hour, subjected to 10 Gy of IR or not, and recovered for 4 hours in the presence of GA. Right panel: the total GFP-CtIP foci intensity was quantified from ≥158 GFP-CtIP foci-positive cells per condition from 3 independent experiments. Micrographs in **G) - I)** are representative of the results from at least 6 independent experiments.

2.4.3 CtIP is a Target for SUMO-2 Modification

With this evidence as groundwork, we hypothesized that CtIP is a substrate for SUMOylation. To examine if CtIP is a potential substrate for SUMOylation, we performed an *in vitro* SUMOylation assay (**Fig. 2.2A)**. Indeed, recombinant CtIP was modified by multiple SUMO-2 moieties in the presence of SUMO E1 SAE1/SAE2 and E2 UBC9, and the reaction was dependent on ATP. We then moved to detect and characterize CtIP SUMO modification *in vivo*. To enable this, we obtained HeLa cells stably expressing decahistidine-tagged SUMO-2 (HeLa His_{10}-SUMO-2) at modest levels (346, 361). The presence of the His_{10}-tag and slight increase in expression of SUMO-2 in HeLa His_{10}-SUMO-2 cells was confirmed via immunoblot relative to

the parental HeLa cells (**Fig. 2.S11A**). Conceptually, the expression of His_{10}-tagged SUMO-2 allows all SUMO-2 conjugates in the cell to be labeled with the His_{10} tag. Lysis of the cells under strongly denaturing conditions (6 M guanidium-HCl) prevents reversal of SUMOylation by denaturing SUMO proteases, while subsequent nickel affinity purification isolates the fraction of cellular proteins that are His_{10}-tagged SUMO-2 conjugates (347). We first verified that Ni-NTA purification ("His pull-down", or His PD) of HeLa His_{10}-SUMO-2 lysates was able to enrich for His_{10}-SUMO-2 conjugates (**Fig. 2.S11B**). Next, to detect if CtIP is SUMOylated *in vivo*, we split asynchronous HeLa and HeLa His_{10}-SUMO-2 cells into two fractions, one which was processed as whole cell extract, while the remainder was processed for Ni-NTA purification. SDS-PAGE and immunoblotting of both fractions revealed that CtIP was detected in the His pull-down fraction in HeLa His_{10}-SUMO-2 cells but not parental HeLa cells, despite similar levels of expression in the whole cell extract (**Fig. 2.2B**), as was the case for RanGAP-1, a known target for SUMOylation (347). Moreover, CtIP in the His pull-down fraction exhibited a slower electrophoretic migration (near 150 kDa) compared to CtIP in the whole cell extract (~125-130 kDa) (**Fig. 2.2C**), the increase in molecular weight supportive of the linkage of one or two SUMO-2 moieties onto the protein (347). Subsequent densitometric quantification of CtIP in the His pull-down fraction versus whole cell extract suggested only 2.5 – 5% of endogenous CtIP was modified by SUMO-2 at the steady state, reflecting the low abundance of the modified form. Supportive that the ~150 kDa species observed was indeed SUMO-2-modified CtIP, we first found that the signal intensity could be reduced in a dose-dependent manner in the presence of GA (**Fig. 2.S11C**). Second, to ensure the immunoreactive bands detected were in fact CtIP, we validated the specificity of our CtIP antibody. The antibody could not detect a truncated CtIP mutant missing residues 732 – 892 (D6) (344) (**Fig.**

2.S11D), consistent with it being raised to bind the CtIP C-terminus (362). Thus, CtIP is a target for SUMOylation in the cell, with a small fraction of CtIP being modified by SUMO-2 *in vivo*.

We next characterized if SUMOylated CtIP was localized to chromatin. HeLa His_{10}-SUMO-2 lysates were separated into chromatin-enriched and soluble fractions which were then subjected to His pull-down to enrich for SUMO-2 modified proteins. We observed that the majority of CtIP partitioned into the soluble fraction. Although a small fraction of CtIP remained chromatin-bound, this fraction was enriched for SUMOylated species (**Fig. 2.2D**). This suggests that SUMOylated CtIP is bound to chromatin, indicating that SUMOylation of CtIP may be important for its function, either allowing it to be targeted to chromatin, or being SUMOylated once it is recruited to chromatin. In summary, CtIP is a SUMO-2 substrate both *in vitro* and *in vivo*, and SUMO-2-modified CtIP is enriched on chromatin.

Figure 2.2

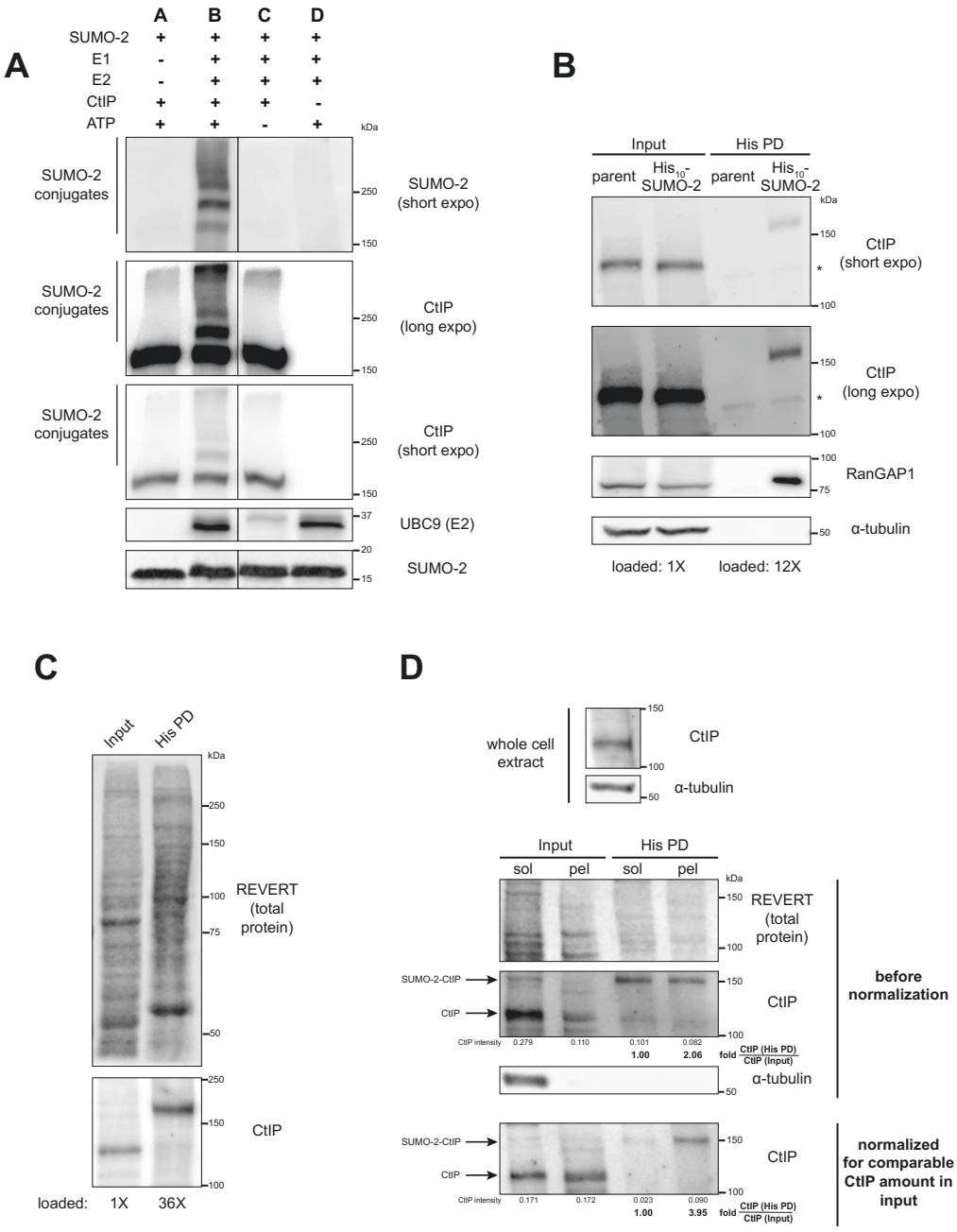

Figure 2.2: CtIP is a Target for SUMO-2 Modification

A) *In vitro* reactions assembled using a SUMO-2 conjugation kit and recombinant glutathione S-transferase (GST)-tagged human CtIP were resolved by SDS-PAGE and immunoblotted. Despite even input of UBC9 into the reactions, less UBC9 was consistently detected by immunoblot in Reaction C; we speculate the antibody used preferentially recognizes auto-SUMOylated UBC9, which is absent when ATP is eliminated from the reaction (Reaction C). The solid line defines where an intervening lane was spliced out of the image. The immunoblot shown is representative

of 6 independent experiments. **B)** HeLa cells expressing 10XHis-tagged SUMO-2 (His_{10}-SUMO-2) or parental HeLa cells were portioned into input and His pull-down (His PD) fractions and processed as whole cell extracts or Ni-NTA affinity purifications, respectively, then resolved by SDS-PAGE. Shown is a representative result of 2 independent experiments. * indicates a non-specific immunoreactive band. Corresponds to **Fig. 2.S11B**. **C)** As in **B)** but with His_{10}-SUMO-2 cells only, representative of at least 3 independent experiments. **D)** 10% of a cell pellet of HeLa His_{10}-SUMO-2 cells was lysed as the whole cell extract (top panel); the remainder was fractionated for chromatin enrichment. 1/9 of each of the resulting soluble (sol) and chromatin-enriched pellet (pel) fractions was saved to represent the input prior to His PD. The remainder was processed for His PD, and all fractions were resolved by SDS-PAGE. For the first run (middle panel), the His PD fractions contain 32X more of the starting amount of sample relative to the input. In the second run (bottom panel), the pellet fraction (for input and His PD portions) was loaded to represent a similar starting amount of CtIP as the soluble fraction. Shown is a representative result of 2 independent experiments.

2.4.4 Analysis of CtIP SUMOylation Status in S Phase and in Response to Double Strand Breaks and Replication Stress

Having detected low abundance CtIP SUMOylation, we proceeded to investigate if the modification could be enhanced in response to DNA damage. As CtIP plays a crucial role in the repair of DSBs (58), we tested if its SUMOylation would increase in response to DSBs, similar to BRCA1, which is SUMOylated in response to IR (147). Exposure to IR did not drastically increase the degree of SUMOylated CtIP as detected by His pull-down (**Fig. 2.3A**), despite equal pull-down efficiency between the Ni-NTA purification samples, as detected by the reversible total protein stain REVERT. Nor was SUMOylation status noticeably altered in response to IR for the end resection factors Mre11 and Nbs1, although there was a noticeable induction for BRCA1 SUMOylation as expected (147) (**Fig. 2.S12A**). Similarly, treatment with other DSB inducing agents including CPT, etoposide, and phleomycin did not increase levels of SUMO-2 CtIP (**Fig. 2.3B**). We reasoned that the lack of response in CtIP was because our experiments had been conducted on asynchronous cells, which are primarily in G_1 phase (**Fig. 2.3C**), and that if CtIP SUMOylation was involved in end resection as a part of HR that it would be more apparent in cells in the S and G_2 phases, when HR occurs. As such, we synchronized HeLa His_{10}-SUMO-2 cells to

the G_1/S transition via double thymidine block. The cells were then collected after being released from thymidine block for various times, allowing them to progress to different stages of the cell cycle. Samples collected after each timepoint were fractioned and processed either for His pull-down or as whole cell extracts, or for DNA content analysis by propidium iodide staining. DNA content analysis confirmed the cells had indeed been synchronized to various cell cycle stages (**Fig. 2.3C**), and immunoblot analysis demonstrated no substantial changes in His_{10}-SUMO-2 expression levels over the phases (**Fig. 2.S12B**). Intriguingly, the degree of CtIP modified by SUMO-2 was dependent on the cell cycle stage, increasing and peaking considerably at S phase (3 hours post-release) while decreasing as the cells progressed through G_2 and reaching a minimum in G_1 phase, despite less drastic fluctuations in total CtIP expression over the cell cycle (**Figs. 2.3D and 2.S12C**). This induction of CtIP SUMOylation reflected a ~2-3-fold increase in SUMO-2-CtIP compared to asynchronous cells. Observing the large impact the cell cycle stage can have on SUMOylation, we next tested if cells synchronized to S or G_1 phase would respond to DSBs by further upregulating CtIP SUMOylation. Still, inducing DSBs via IR did not increase CtIP SUMOylation, whether the cells were synchronized to S or G_1 phase (**Fig. 2.S12D**). The induction of SUMOylation in S phase suggested that CtIP was SUMOylated in response to active DNA replication or replication stress. We consequently examined if there were alterations in CtIP SUMOylation in response to externally applied replication stress. His pull-down experiments on asynchronous cells revealed a surprising reduction in SUMO-2-CtIP upon treatment with HU, aphidicolin (a DNA polymerase inhibitor), and low concentration CPT, all inducers of replication stress, despite steady expression levels of CtIP (**Fig. 2.3E**). In support of this, we observed a time-dependent reduction in SUMO-2-CtIP over 4 hours of HU treatment (**Fig. 2.3F**). Thus, CtIP

modification by SUMO-2 occurs constitutively in S phase, and this modification is not detectably induced by DSB damage, but is reduced during exogenous replication stress.

Figure 2.3

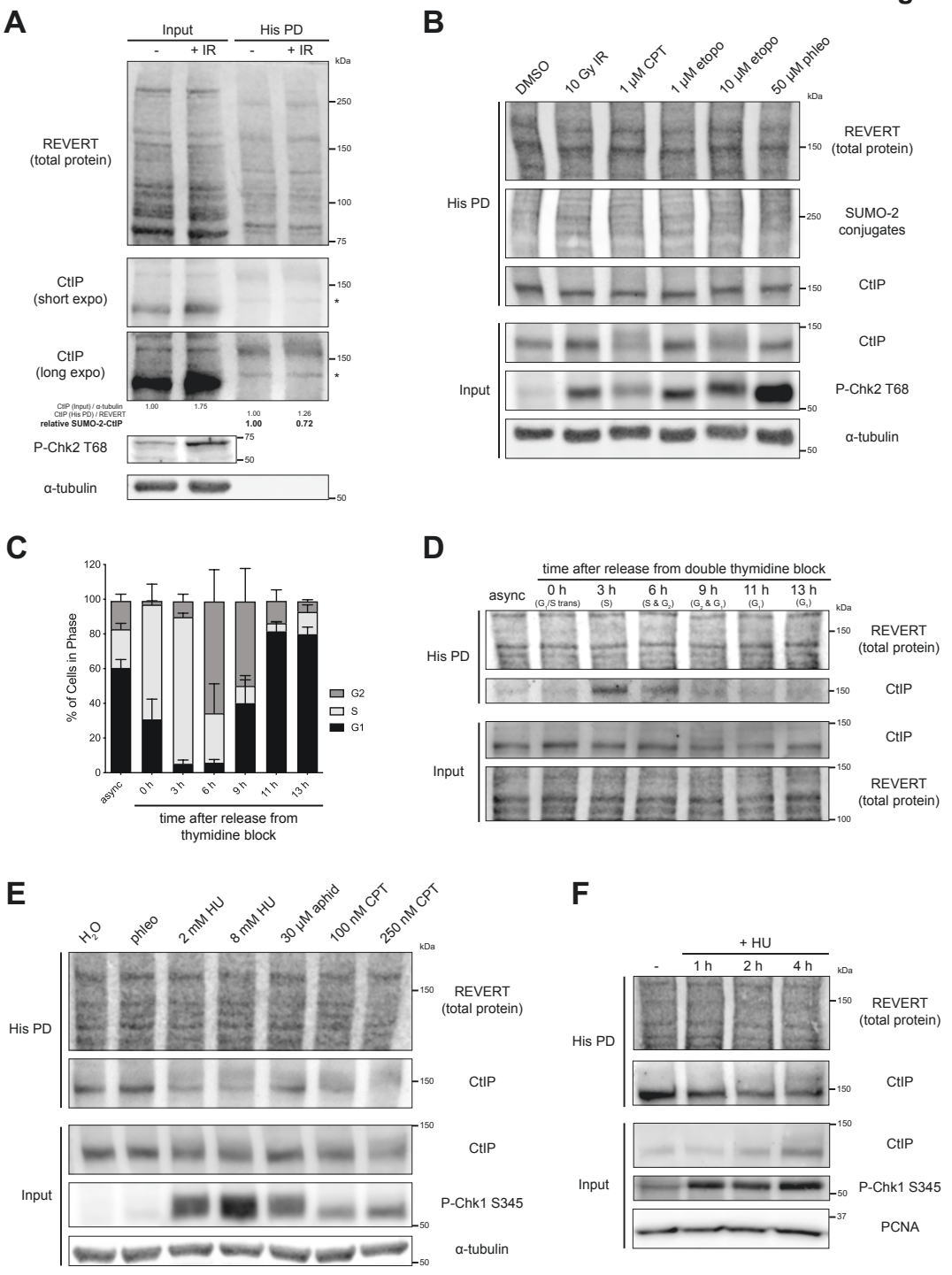

Figure 2.3: Analysis of CtIP SUMOylation Status in S Phase and in Response to Double-Strand Breaks and Replication Stress

A), B), D), E), F): HeLa His_{10}-SUMO-2 cells were treated as indicated, portioned into input and His PD fractions and processed accordingly before SDS-PAGE and immunoblotting. Chk2 and Chk1 phosphorylation were used as readouts for the induction of DSBs or replication stress, respectively. **A)** Asynchronous cells were subjected to 10 Gy of IR or not and allowed to recover for 1 hour. Shown is a representative result of 3 independent experiments. * indicates a non-specific immunoreactive band. Corresponds to **Fig. 2.S12A**. **B)** Asynchronous cells were exposed to 10 Gy of IR and allowed to recover for 1 hour, or subject to CPT, etoposide (etopo), or phleomycin (phleo) at the indicated concentrations for 1 hour. Shown is a representative result of 4 independent experiments. CtIP typically exhibits smearing upon treatment with high dose CPT (147) and etoposide (input fraction). **C)** HeLa His_{10}-SUMO-2 cells were left asynchronous (async) or synchronized by double thymidine block and released for various timepoints to reach different cell cycle phases, then a portion was processed for DNA content analysis. Shown are the means from 3 independent experiments. **D)** As in **C)**, but this time processed for immunoblot of input and His PD fractions. Shown is a representative result of 3 independent experiments. **E)** Asynchronous cells were subject to 25 μM phleomycin for 1 hour or the indicated replication stress inducing agents for 4 hours. 0.8% H_2O served as the vehicle control; aphidicolin (aphid); hydroxyurea (HU). Shown is a representative result of 3 independent experiments. **F)** Asynchronous cells were treated with 2 mM HU for the indicated timepoints or not treated for 4 hours. Shown is a representative result of at least 3 independent experiments.

2.4.5 SUMOylation of CtIP in S Phase is Dependent on Cyclin-Dependent Kinase and ATR Activities and an Interaction with PCNA

As we only observed an induction of CtIP SUMOylation during S phase, we focused on characterizing this occurrence, seeking to identify factors that mediate it. We first examined the C-terminus of human CtIP, which contains a Sae2-like domain evolutionarily conserved among CtIP orthologues in vertebrates and in budding and fission yeast (58) (**Fig. 2.S13A**). To determine if the residues in the C-terminus could potentially play a role in the ability for CtIP to be SUMOylated, we compared the ability of full length (WT) and C-terminally-truncated CtIP (D6, missing residues 732 – 892) to be modified by SUMO-2. FLAG-tagged-WT- and D6-CtIP were transiently expressed in S phase synchronized HeLa His_{10}-SUMO-2 cells and processed for His pull-down. While both constructs were expressed at similar levels, SUMOylation of the D6 mutant was almost abolished relative to WT-CtIP (**Fig. 2.4A**). While we could not rule out that certain lysine residues within the region deleted in D6 (161 residues) were SUMOylation sites or if the

D6 mutant was altered in its ability to interact with DNA (258, 261), one explanation could be that residues within the C-terminus, upon modification by phosphorylation, could be promoting CtIP's SUMOylation. Indeed, the C-terminus of CtIP contains serine and threonine residues that are sites of phosphorylation and regulate the function of CtIP in HR repair (61, 105, 267) (**Fig. 2.S13A**). Kinases that target these sites include the DNA damage sensing kinases ATM and ATR, which control the cellular response to DNA damage and replication stress, respectively (87), and the cyclin-dependent kinases (CDKs), which govern temporal progression of the cell cycle (363). Given that CtIP SUMOylation occurs during S phase, and that the C-terminus contains several CDK sites (61, 105), we predicted that inhibiting the activity of CDKs would block bulk CtIP SUMOylation. In agreement, HeLa His_{10}-SUMO-2 cells synchronized to S phase and treated with two broad-acting CDK inhibitors that inhibit CDK2, which mediates progression through late G_1 and S phase (364), roscovitine and AZD5438 (365, 366), exhibited reduced CtIP SUMOylation compared to the vehicle control (**Fig. 2.4B**). We verified the acute treatments had little immediate impact on the cell cycle distribution and that the inhibitors were active (**Figs. 2.S13B-C**). Interestingly, RO-3306, an inhibitor specific to CDK1, a CDK active in the transition from late G_2 to mitosis (367), exhibited much less of an inhibitory effect (**Fig. 2.4B**). This suggests CDKs other than CDK1, perhaps CDK2, may be phosphorylating CtIP and facilitating its SUMOylation. We further confirmed the role of CDK activity in CtIP SUMOylation by obtaining mutants of GFP-tagged CtIP at a conserved CDK site, T847 (**Fig. 2.S13A**), whose phosphorylation promotes DNA end resection (61, 267). We first verified that GFP-WT-CtIP could indeed be SUMOylated itself *in vivo*, as a clear shift in molecular weight was observed when the construct was expressed in HeLa His_{10}-SUMO-2 cells and subjected to His-tag purification (**Fig. 2.S13D**). The detected immunoblot signal was specific to the CtIP portion of the construct, since it was not seen when

GFP empty vector was transfected instead. To test the role of T847 in CtIP SUMOylation, GFP-CtIP-WT or mutants where T847 was substituted with alanine (loss of function, T847A) or glutamate (phosphomimic, T847E) were expressed in HeLa His_{10}-SUMO-2 cells synchronized to S phase. By His-tag pull-down, the T847A mutant had partially reduced SUMOylation compared to WT-CtIP, and this was partially restored in the T847E mutant (**Fig. 2.4C**). Thus, phosphorylation of CtIP by CDKs, at T847 and potentially other CDK sites, mediates its SUMOylation in S phase.

As the C-terminus of CtIP also contains residues that are targets for phosphorylation by ATM and ATR (61, 105, 266, 267, 341), we next pursued if the activities of these kinases could be prerequisites for CtIP SUMOylation. To address this, HeLa His_{10}-SUMO-2 cells were synchronized to S phase while being treated acutely with inhibitors to ATM (KU-55933), ATR (ETP-46464 and VE-821), and the related DNA-dependent protein kinase catalytic subunit (DNAPKcs) (NU-7441), and SUMOylated CtIP was isolated by His pull-down. Importantly, we verified that the chosen compounds only exerted minimal effects on the cell cycle profile (**Fig. 2.S13E**), and were effective at inhibiting their target kinases (**Figs. 2.S13F-I**). ETP-46464 and VE-821 treatment reduced CtIP SUMOylation (**Fig. 2.4D**), suggesting that ATR-dependent phosphorylation events on CtIP could be regulating its SUMOylation. To confirm this, we obtained an HA-tagged CtIP mutant where three previously identified S/TQ sites (the consensus sequence phosphorylated by ATM and ATR (368)), S664, S679, and S745 (105, 266, 341) (**Fig. 2.S13A**), were mutated to alanine (53). In HeLa His_{10}-SUMO-2 cells, exogenous HA-CtIP-WT was SUMOylated more than its S664A/S679A/S745A counterpart (**Fig. 2.4E**). This was seen in both asynchronous and S phase-synchronized cells, with the difference more obvious in cells in S phase, supporting the cell cycle-dependent nature of CtIP SUMOylation. Another S/TQ site on

CtIP is T859 (**Fig. 2.S13A**), whose phosphorylation by ATR upon DSB formation allows CtIP to bind to chromatin and activate end resection (267). Bulk SUMOylation of CtIP in S phase was not impacted in a mutant with T859 mutated to alanine, T859A (**Fig. 2.S13J**), indicating this particular site is dispensable for the CtIP SUMOylation observed. Thus, ATR-dependent phosphorylation of CtIP, potentially at residues S664A, S679A, and/or S745A, but not at T859, mediates constitutive CtIP SUMOylation in S phase.

Our observations that CtIP forms foci during replication stress, and is SUMOylated during S phase in a CDK- and ATR-dependent manner, are compatible with the finding that CtIP interacts with the DNA polymerase processivity factor PCNA (335). The study found a putative PCNA-interacting protein domain (PIP-Box (369)) within CtIP at residues 518-537 (**Fig. 2.S13A**). This PIP-Box resides in a region of CtIP dubbed the Replication Foci Targeting Sequence (RFTS, residues 505-546) (335). The RFTS was found to be sufficient for binding PCNA as well as targeting CtIP to $BrdU^+$ foci of active DNA replication. Deleting residues 515-518 near and within the PIP-Box disrupted the interaction of the RFTS fragment with PCNA, and prevented RFTS from being targeted to replication foci (335). We hypothesized that the interaction between PCNA and CtIP facilitates its SUMOylation, perhaps by helping recruit CtIP to sites of DNA replication or replication stress. We first verified that both proteins do interact as reported. We co-expressed monomeric red fluorescent protein (RFP)-tagged PCNA and GFP-CtIP in U-2 OS cells and performed co-immunoprecipitation (Co-IP) experiments. Immunoprecipitating GFP-CtIP co-purified RFP-PCNA (**Fig. 2.4F**), and *vice versa* (**Fig. 2.S14A**), confirming the two proteins associate with each other. By Co-IP, we also found that the Δ515-518 mutation in CtIP (**Fig. 2.S13A**) could partially disrupt its interaction with PCNA (**Fig. 2.4G**), in support of the previous findings (335). To study the impact of disrupting the PCNA-CtIP interaction on CtIP

SUMOylation, we expressed in S phase-synchronized HeLa His_{10}-SUMO-2 cells GFP-CtIP-Δ515-518. The His pull-down assay revealed the Δ515-518 mutant was markedly less SUMOylated than GFP-CtIP-WT (**Fig. 2.4H**), suggesting the interaction with PCNA promotes CtIP SUMOylation. In summary, we have shown that conjugation of SUMO-2 to CtIP in S phase is promoted by residues in its C-terminus, particularly those that are targets of the activities of the CDKs and ATR kinase, as well as residues 515-518, which may act by enhancing an interaction with PCNA.

Figure 2.4

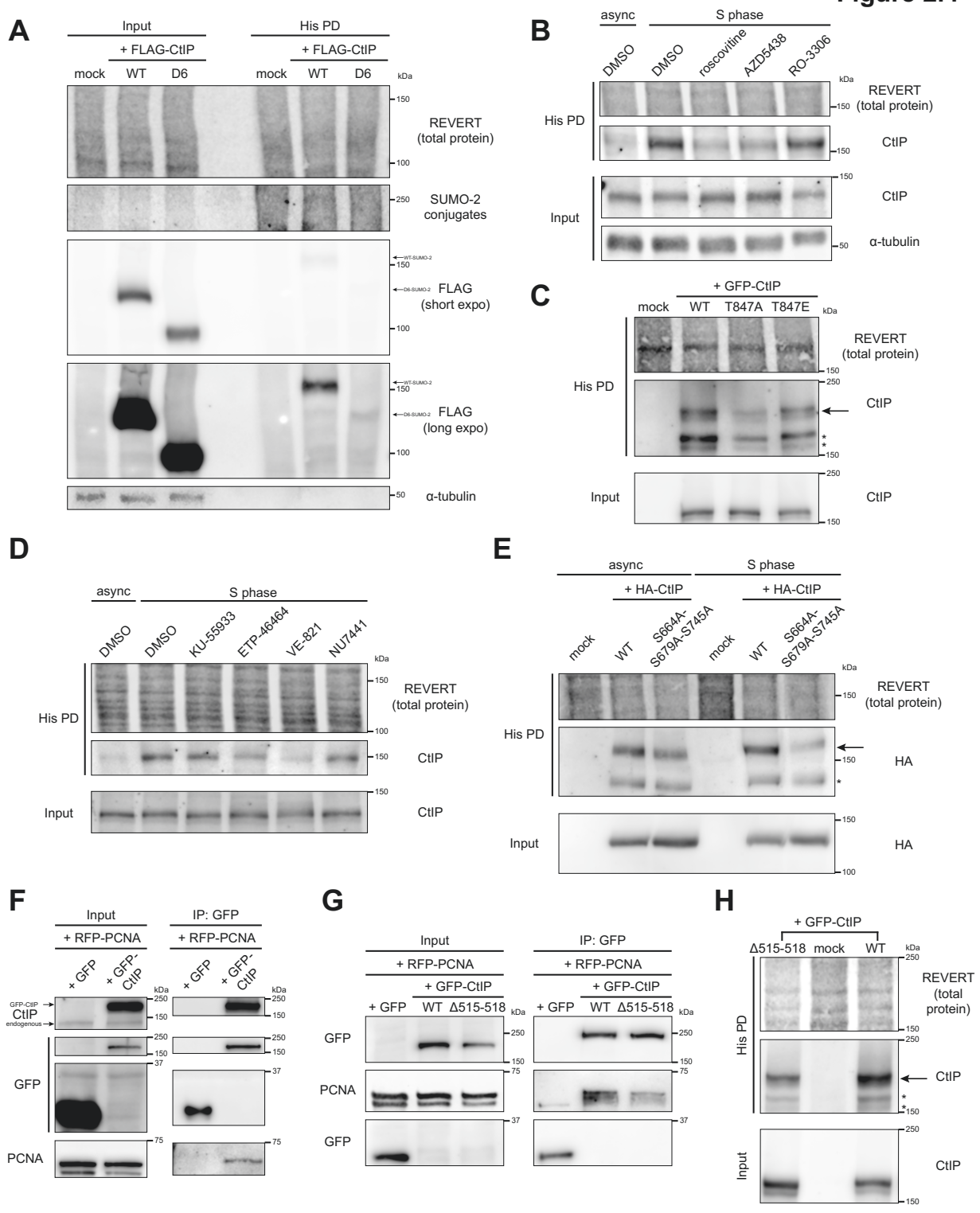

Figure 2.4: SUMOylation of CtIP in S Phase is Dependent on Cyclin-Dependent Kinase and ATR Activities and an Interaction with PCNA

A) – E), H) HeLa His_{10}-SUMO-2 cells were treated as indicated, portioned into input and His PD fractions and processed accordingly before SDS-PAGE and immunoblotting. * indicates an exogenous CtIP immunoreactive band that is not of interest; we speculate it is either lower molecular weight SUMO-2-modified CtIP or unmodified tagged-CtIP retained in the His PD fraction due to overexpression. **A)** HeLa His_{10}-SUMO-2 cells were transfected with FLAG-tagged wildtype (WT) CtIP or a C-terminal truncation mutant (D6) (see **Fig. 2.S15A**) or mock transfected. Shown is a representative result of 4 independent experiments. **B)** HeLa His_{10}-SUMO-2 cells were synchronized by double thymidine block and released to mid-S phase for 1 hour in plain media, then for 2.5 hours in the presence of 0.1% DMSO (vehicle control), 25 μM roscovitine, 2.5 μM AZD5438, or 10 μM RO-3306. Asynchronous cells (async) were treated in 0.1% DMSO for 2.5 hours. Shown is a representative result of 3 independent experiments. **C)** HeLa His_{10}-SUMO-2 cells were synchronized to mid-S phase. 24 hours prior to harvest, they were transfected with GFP-CtIP-WT or substitution mutants at residue T847, or mock transfected. Shown is a representative result of 2 independent experiments. **D)** HeLa His_{10}-SUMO-2 cells were left asynchronous or synchronized by double thymidine block and released for 3 hours to mid-S phase in the presence of 0.2% DMSO, 10 μM KU-55933 (ATM inhibitor), 20 μM ETP-46464 or 20 μM VE-821 (ATR inhibitors), or 1 μM NU-7441 (DNAPKcs inhibitor). Shown is a representative result of at least 4 independent experiments. **E)** HeLa His_{10}-SUMO-2 cells were cells were left asynchronous or synchronized to mid-S phase. 24 hours prior to harvest, they were transfected with HA-tagged WT-CtIP or an alanine substitution mutant at residues S664, S679, and S745, or mock transfected. Shown is a representative result of 2 independent experiments. **F)** U-2 OS cells were co-transfected with RFP-PCNA and either GFP empty vector or GFP-CtIP and processed for immunoprecipitation (IP) of GFP. Prior to IP, a portion of lysate was saved as an input control. **G)** As in **F**), except cells were depleted of endogenous CtIP by siRNA, then co-transfected with RFP-PCNA and either GFP empty vector, GFP-CtIP-WT or -Δ515-518. Shown is a representative result of at least 6 **(F)** or 3 **(G)** independent experiments. **H)** HeLa His_{10}-SUMO-2 cells were synchronized to mid-S phase. 24 hours prior to harvest, they were transfected with GFP-CtIP-WT or the Δ515-518 deletion mutant. Shown is a representative result of 2 independent experiments.

2.4.6 SUMOylation of CtIP in S Phase is Dependent on the E3 SUMO Ligase PIAS4

Next, we investigated which E3 SUMO ligase(s) could be SUMOylating CtIP in S phase. Our candidates were PIAS1 and PIAS4, which have been implicated in SUMOylation events at DSB sites (147, 149), and CBX4, which was recently reported to mediate CtIP's role in end resection (343). siRNAs targeting each of the three E3 ligases were transfected into HeLa His_{10}-SUMO-2 cells as they were being synchronized to S phase, and His pull-down was performed to enrich SUMO-2-CtIP. While each E3 ligase was knocked down sufficiently, depleting PIAS1 upregulated CtIP expression levels, while depleting PIAS4 and CBX4 downregulated them (**Fig.**

2.5A, first run). When these fluctuations in basal CtIP expression were accounted for, depleting PIAS4, but not PIAS1 or CBX4, inhibited CtIP SUMOylation in S phase (**Fig. 2.5A**, second run). Importantly, the effect of PIAS4 knockdown on CtIP SUMOylation was not due to substantial changes in the cell cycle profile (**Fig. 2.5B**). To complement the depletion experiment, overexpression of FLAG-tagged PIAS4 in the same cells enhanced the abundance of SUMO-2-CtIP, despite even loading of samples into the His pull-down fraction (**Fig. 2.5C**). Notably, this effect was more pronounced in cells synchronized to S phase relative to asynchronous cells, underscoring the notion that PIAS4 SUMOylates CtIP during S phase. As an E3 SUMO ligase for CtIP, we then predicted that PIAS4 would interact with CtIP, and pursued Co-IP experiments to test this. Indeed, GFP-tagged CtIP was able to co-immunoprecipitate endogenous PIAS4 in U-2 OS cells (**Fig. 2.5D**). In addition, a U-2 OS cell line stably expressing GFP-CtIP-WT (**Fig. 2.S14B**) co-immunoprecipitated more PIAS4 when it had been synchronized to S phase than when it was grown asynchronously (**Fig. 2.5E**), congruent with the rise in CtIP SUMOylation we observe during S phase (**Figs. 2.3D, 2.S12C**). Intriguingly, inducing replication fork stalling with HU caused a dose-dependent dissociation of PIAS4 from GFP-CtIP (**Fig. 2.5F**), consistent with the reduction in CtIP SUMOylation seen in the presence of HU and other replication stress agents (**Figs. 2.3E-F**). All in all, the Co-IP experiments support the notion that PIAS4 associates with CtIP during S phase to promote its SUMOylation. Combining them with the PIAS4 depletion and overexpression experiments, we conclude that PIAS4 is the main E3 ligase for SUMOylating CtIP in S phase.

Figure 2.5

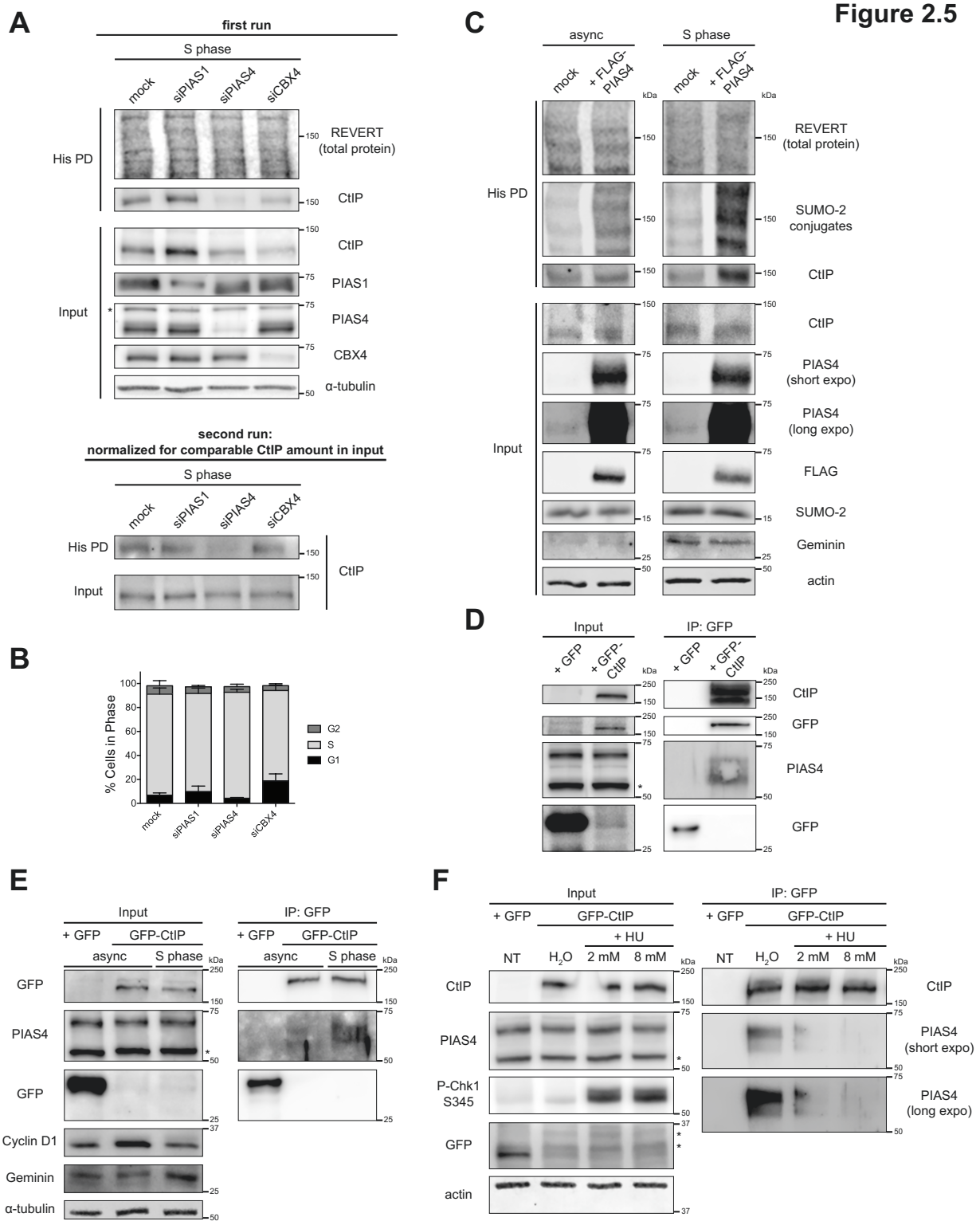

Figure 2.5: SUMOylation of CtIP in S Phase is Dependent on the E3 SUMO Ligase PIAS4

A) HeLa His_{10}-SUMO-2 cells were transfected twice 24 hours apart with siRNAs targeting either PIAS1 (at 50 nM), PIAS4 (at 40 nM), or CBX4 (at 40 nM), or mock transfected, while being

synchronized by double thymidine block. 48 hours after the first transfection, the cells were released for 3 hours to approach mid-S phase, portioned into input control and His PD fractions, and processed for whole cell lysis or Ni-NTA affinity purification (top panel). A second run (bottom panel) was performed where the input and His PD portions were normalized to accommodate for alterations in CtIP expression resulting from the depletion of the various E3 SUMO ligases. Shown is a representative result of 3 independent experiments. **B)** As in **A)**, but using the portion of cells processed for DNA content analysis. Shown are the means of 3 independent experiments. **C)** HeLa His_{10}-SUMO-2 cells were left asynchronous or synchronized to S phase. 24 hours prior to harvest, they were transfected with FLAG-tagged human PIAS4 or mock transfected. The cells were portioned and processed as input controls or for His PD. Shown is a representative result of 2 independent experiments. **D)** U-2 OS cells were transfected with GFP-CtIP or GFP empty vector and processed for IP of GFP. Prior to IP, a portion of lysate was saved as an input control. Shown is a representative result of at least 4 independent experiments. **E)** U-2 OS cells stably expressing GFP-CtIP were left asynchronous or synchronized to S phase and processed for IP of GFP. U-2 OS cells transfected with GFP empty vector served as a control. Shown is a representative result of at least 4 independent experiments. **F)** Asynchronous U-2 OS cells stably expressing GFP-CtIP were treated for 4 hours with HU at the indicated concentrations or 0.8% H_2O (vehicle control) and processed for IP of GFP. U-2 OS cells transfected with GFP empty vector served as a control. Shown is a representative result of at least 4 independent experiments. * indicates a non-specific immunoreactive band. Geminin and Cyclin D1 are markers for S and G_1 phases, respectively.

2.4.7 K578 is a Key CtIP SUMOylation Site

Having narrowed down specific factors involved in SUMOylating CtIP in S phase, we wished to determine which particular lysine residue(s) CtIP was SUMOylated on. Recent work from Pablo Huertas' group uncovered a role for CtIP SUMOylation on residue K896 (343). Using GPS-SUMOsp2.0 software to predict putative SUMOylation sites on CtIP, Soria-Bretones and colleagues selected seven residues as potential SUMO sites: K46, K449, K578, K705, K709, K802, and K896 (**Fig. 2.6A**) (343). Interestingly, they observed that substituting K896 with the positively-charged but non-SUMOylatable arginine residue yielded functional defects, preventing CtIP's recruitment to an I-*Sce*I-induced DSB, impairing DNA end resection and Rad51 accumulation, and increasing genomic instability, although having little impact on the CtIP SUMOylation detectable by immunoblot (Supplementary Figure 3G in their report) (343). To further refine which of the six remaining residues selected by Soria-Bretones *et al.* were potential

SUMOylation sites, we used an internal deletion panel of FLAG-tagged CtIP constructs, of which the D6 construct described earlier is a part of (344), to assess which regions of CtIP mediated its bulk SUMOylation. Along with D6, the panel consisted of mutants with large deletions that overlap with the remaining sites chosen by Soria-Bretones *et al*.: D3 (residues 369 – 495 deleted), D4 (496 – 695 deleted), and D5 (695 – 778 deleted) (**Fig. 2.S15A**). We ignored construct D1 (17 – 160 deleted) as we did not wish to interfere with CtIP's N-terminal oligomerization region, shown to be important for CtIP function (258, 261, 344). Despite variable expression of each construct in HeLa His_{10}-SUMO-2 cells, mutants D4 and D6 showed pronounced inhibition of SUMOylation, unlike D3 and D5 (**Fig. 2.S15B**). Having already observed an impact of the C-terminus on CtIP SUMOylation via D6 (**Fig. 2.4A**), the dramatic loss of SUMOylation in D4 suggested residue K578, or potentially other residues within 496 – 695, could be potential SUMOylation sites or be mediating CtIP SUMOylation.

After obtaining the arginine substitution mutants of GFP-CtIP used by Soria-Bretones *et al.* in their study (343), we proceeded to evaluate which of the seven predicted residues were SUMOylation sites on CtIP. We expressed the mutants in HeLa His_{10}-SUMO-2 cells synchronized to S phase, and subjected the cells to His-tag purification. Consistent with Soria-Bretones and coworkers (343), a mutant where all seven predicted sites had been substituted with arginine (7KR) (**Fig. 2.6A**) strongly reduced the amount of SUMOylated GFP-CtIP enriched in the His pull-down fraction relative to WT-CtIP (**Fig. 2.6B**), suggesting one or more of the seven predicted residues was responsible for the majority of CtIP SUMOylation. We did not observe a reduction of SUMOylation in the K896 mutant, while the 6KR mutant (where six of the predicted sites except K896 were mutated to arginine) (**Fig. 2.6A**) sharply diminished CtIP SUMOylation to a level similar to that of 7KR (**Fig. 2.6B**). This suggests that K896's contribution to bulk CtIP

SUMOylation is very minor, and that one or more of the remaining six sites is instead responsible. With residues K449, K705, K709 located within internal deletions in mutants that did not reduce CtIP SUMOylation (D3 and D5), and K578 located within the deleted residues of mutant D4, which showed remarkable loss of SUMOylation (**Fig. 2.S15B**), we moved to investigate if K578 specifically was a CtIP SUMOylation site.

The K578R mutant of GFP-CtIP was generated by site-directed mutagenesis and transfected into S phase-synchronized HeLa His_{10}-SUMO-2 cells. Relative to GFP-CtIP-WT, K578R abolished SUMOylation to an extent similar to the 7KR mutant (**Fig. 2.6C**), suggesting K578 is a major site responsible for CtIP SUMOylation. In addition, unlike the K896R single mutant, a double mutant where both K578 and K896 were mutated to arginine (K578R-K896R) (**Fig. 2.6A**) exhibited a similar reduction in SUMOylation as both the K578R and 7KR mutants (**Fig. 2.6D**), emphasizing the key contribution of K578 to bulk CtIP SUMOylation. To determine if K578 alone was responsible for bulk SUMOylation, or if the remaining predicted sites contributed, we generated a mutant that would allow only K578 to be SUMOylatable out of the seven predicted sites. The mutant, 7KR-R578K, was prepared by reverting residue R578 to lysine in the 7KR construct (**Fig. 2.6A**). Upon expression in S phase or asynchronous HeLa His_{10}-SUMO-2 cells, the reversion partially restored CtIP SUMOylation, but not to the extent of WT-CtIP (**Figs. 2.6E, 2.S15C**). This confirmed that K578 was a SUMOylatable residue, while suggesting its SUMOylation is a pre-requisite for SUMOylation events on the other six residues to constitute the rest of CtIP SUMOylation. To recapitulate the effect of K578R in a construct that did not utilize a bulky GFP tag, we incorporated the mutation into HA-tagged CtIP, observing yet again a substantial loss in SUMO-2-modified CtIP in the presence of K578R, even in cells that were asynchronous (**Fig. 2.S15D**). Finally, we sought to demonstrate the importance of K578 in

CtIP SUMOylation by aligning amino acid sequences of CtIP orthologues using Clustal Omega. Consistently, K578, amid the canonical ψ-K-x-E SUMOylation motif (136, 137, 370) (with ψ representing a bulky, hydrophobic amino acid), is conserved among mammalian orthologues of CtIP as well as in chicken (**Fig. 2.S15E**). Taken together, our data uncover a novel SUMOylation site for CtIP at residue K578. Moreover, they reveal a dynamic interplay between SUMO sites, with K578 SUMOylation serving as a prerequisite for SUMOylation on other residues, a role not detectably manifested by K896.

Figure 2.6

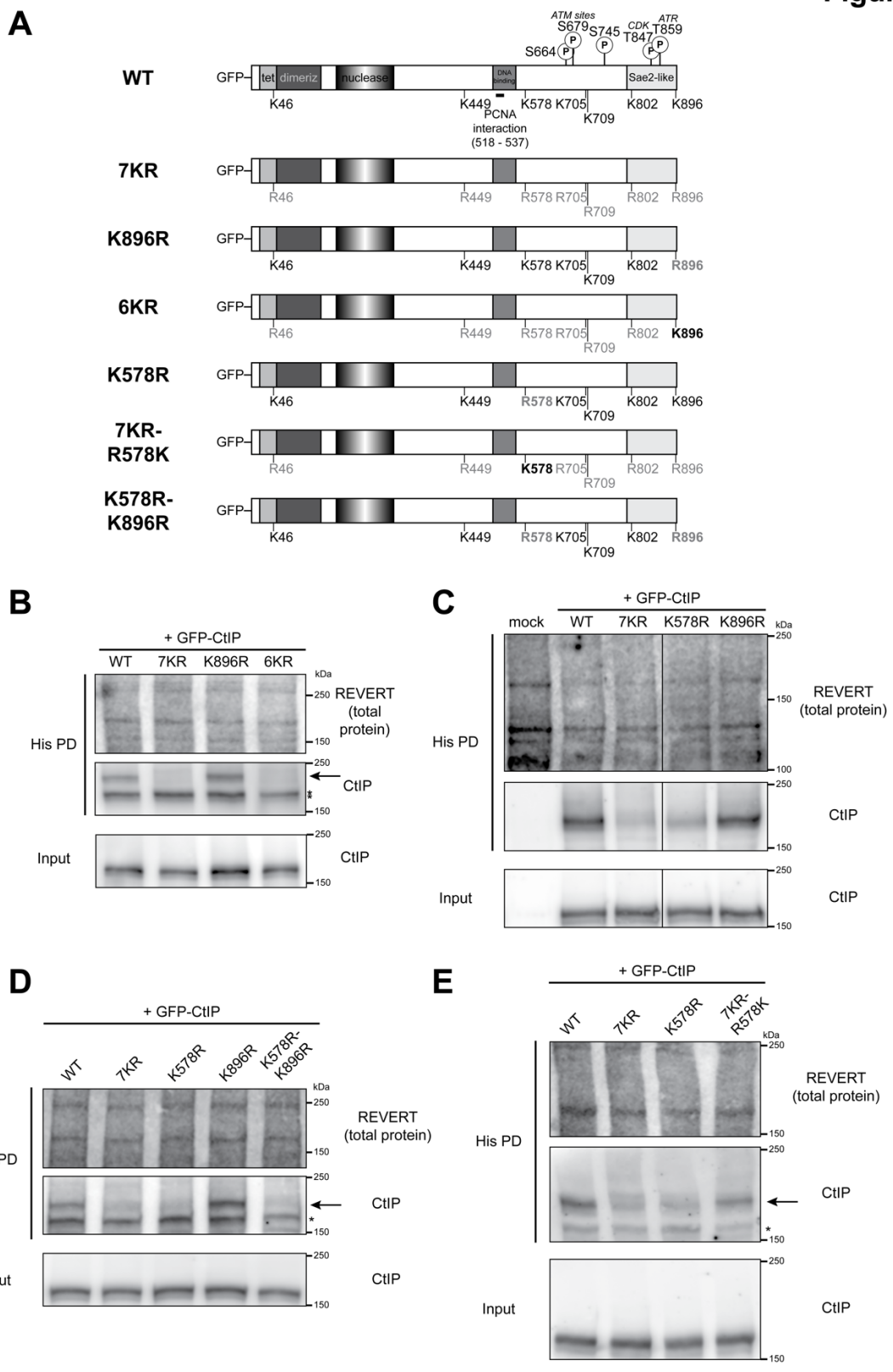

Figure 2.6: K578 is a Key CtIP SUMOylation Site

A) Schematic diagrams of CtIP domain structure of wildtype (WT) CtIP and relevant phosphorylation and SUMOylation sites in this study, along with residues substituted in the corresponding site mutants of GFP-tagged CtIP. "Tet": tetramerization domain; "dimeriz": dimerization domain; "nuclease": endonuclease domain, "PCNA interaction": also known as PIP-Box. In **B) to E)**, HeLa His_{10}-SUMO-2 cells were synchronized to mid-S phase. 24 hours prior to harvest, they were transfected with the indicated GFP-CtIP constructs, then portioned into input control and His pull-down (His PD) fractions and processed accordingly. * indicates an exogenous CtIP immunoreactive band that is not of interest; it may be lower molecular weight SUMO-2-modified CtIP, or unmodified GFP-CtIP retained in the His PD fraction due to high expression. **B)** Shown is a representative result of 3 independent experiments. **C)** The solid line defines where an intervening lane was spliced out of the image. Shown is a representative result of 3 independent experiments. **D)** Shown is a representative result of 2 independent experiments. **E)** Shown is a representative result of 3 independent experiments.

2.4.8 Cells Expressing K578R Mutant CtIP Show Defects in DNA End Resection and Homologous Recombination

We next sought to study the functional effects of CtIP reduced in SUMOylation using the mutants K578R and Δ515-518 (mutant with attenuated PCNA interaction, **Fig. 2.4G**). We first asked if cells expressing these mutants exhibited a defect in DNA end resection. To do this, we generated U-2 OS cell lines stably expressing siRNA-resistant GFP-CtIP-WT, -K578R, -K896R, and -Δ515-518 (**Fig. 2.S14B**). The cells were then depleted of endogenous CtIP with siRNA, and treated with CPT to induce end resection, which we measured by quantifying native BrdU (**Fig. 2.7A**) and RPA (**Fig. 2.7B**) foci in $\gamma H2AX^+$ cells. Parental U-2 OS cells were capable of forming native BrdU and RPA foci in response to CPT, but this was severely impaired when CtIP was depleted. Expressing WT-CtIP could restore these foci to similar levels as parental cells, but adding back K578R or Δ515-518 could not, or caused only a slight rescue of foci formation, indicating both mutants were defective in promoting end resection. Critically, the K896R mutant also could not recover RPA and BrdU foci to levels in cells expressing WT-CtIP, in line with the findings of Soria-Bretones *et al* (343).

We then explored mechanistically how K578R and Δ515-518 are unable to promote end resection. We first asked if both mutants were capable of being recruited to sites of DNA damage generated by laser microirradiation. GFP-CtIP-K578R was recruited and retained on laser tracks efficiently, with similar kinetics as GFP-CtIP-WT (**Figs. 2.S16A-B**), indicating impaired recruitment was not a factor in its inability to promote end resection, and that SUMOylation on K578 is not required for CtIP's recruitment to sites of damage. On the other hand, the Δ515-518 mutant recruited poorly to laser-damaged DNA, providing an explanation for its inability to stimulate resection. We thus continued investigating functional impacts of the K578R mutation, hypothesizing that SUMOylation at K578 could be promoting CtIP's known interactions with the MRN complex and BRCA1. By Co-IP, the K578R mutant co-immunoprecipitated all the aforementioned proteins as efficiently as WT-CtIP (**Fig. 2.S16C**), implying CtIP's association with these proteins is not dependent on the K578 residue being a functional modification site. Seeing no alteration in recruitment or protein interactions, we resorted to reconstituting end resection *in vitro* to see if K578R-CtIP was impaired in its ability to stimulate the MRN complex in cleaving streptavidin-blocked double-stranded DNA (52). We successfully expressed and purified phosphorylated WT- and K578R-CtIP and the MRN complex in *Sf*9 cells (**Figs. 2.S16D-E**). To our surprise, both phosphorylated WT- and K578R-CtIP were capable of stimulating MRN endonuclease activity, and to a similar extent (**Fig. 2.S16F**). However, as we could not detect higher molecular weight forms of purified CtIP indicative of SUMOylation (**Fig. 2.S16D**), it is likely that most of the purified CtIP was not SUMOylated and that a difference in SUMOylation status did not exist between WT- and K578R-CtIP. Nevertheless, our *in vitro* data demonstrates that the K578R mutant is inherently as capable of stimulating MRN activity as WT-CtIP, therefore its defect in promoting end resection *in vivo* is not due to a change in catalytic activity arising from

the arginine substitution. This suggests that for WT-CtIP in the cell, SUMO modification at K578 may promote conformational changes that alter MRN activity, or alter CtIP's interactions with other proteins. Perhaps it is these changes that fully activate CtIP's ability to stimulate MRN-dependent resection, and these changes are lost when the K578 site is not modifiable.

We next wondered if there were further functional impacts from the loss in end resection in cells expressing K578R-CtIP. As end resection is an initiating step in homologous recombination (20), we predicted that the process of HR would be disrupted if end resection was impaired. To test this, we performed the DR-GFP HR reporter assay (**Fig. 2.S9A**) in cells depleted of endogenous CtIP and complemented with either HA-tagged WT- or K578R- siRNA-resistant CtIP (**Figs. 2.7C, 2.S15D**). As expected, the frequency of HR events was dramatically decreased in cells depleted of CtIP. Fittingly, expressing HA-CtIP-WT was able to rescue HR almost to levels seen in cells treated with non-targeting siRNA, while expressing HA-CtIP-K578R was strikingly unable to, demonstrating the significance of CtIP SUMOylation at K578 on proper HR function. Taking this further, we anticipated that cells expressing K578R-CtIP, with their diminished end resection and consequently HR capacities, would be more sensitive to DNA damage by DSBs. To address this, we performed a clonogenic survival assay on CtIP-depleted stable cell lines expressing GFP-CtIP-WT or -K578R and challenged with CPT (**Figs. 2.7D, 2.S14B**). Accordingly, unlike WT-CtIP expressing cells, those expressing the CtIP-K578R mutant were as sensitive to CPT as parental U-2 OS cells depleted of CtIP with siRNA. This sensitivity was also seen for the Δ515-518 mutant, which is impaired in recruitment to sites of DNA damage, SUMOylation, and thus DNA end resection (**Figs. 2.S16A-B, 2.4H, 2.7A-B**). To summarize, modification of CtIP at residue K578 by SUMOylation promotes DNA end resection, and

substituting K578 with arginine results in impaired end resection and HR activity and poorer survival in response to CPT.

Figure 2.7

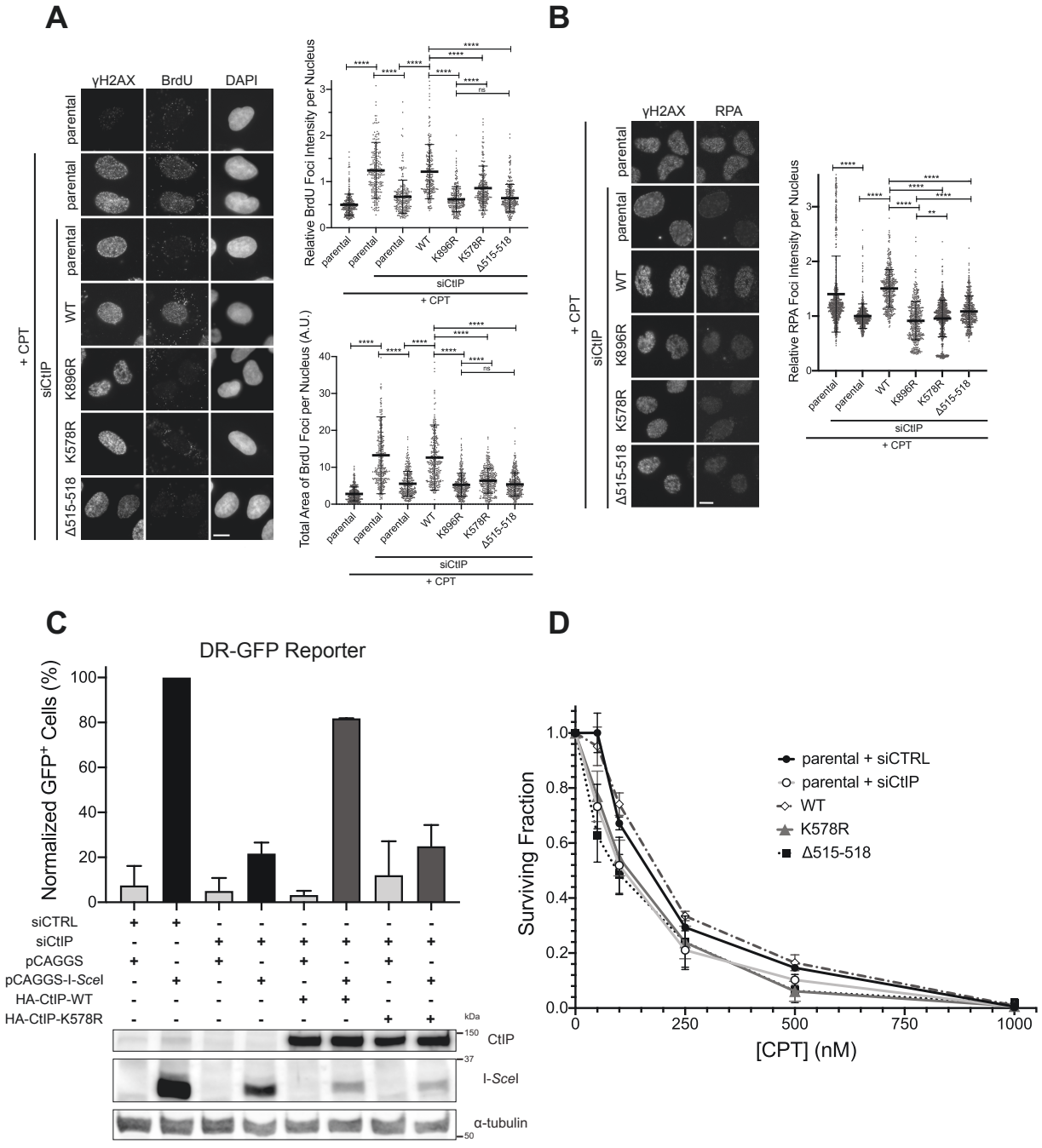

Figure 2.7: Cells Expressing K578R Mutant CtIP Show Defects in DNA End Resection and Homologous Recombination

A) Left panel: parental U-2 OS cells or U-2 OS stably expressing the indicated siRNA-resistant GFP-CtIP constructs were transfected with siRNA to CtIP (or not) and treated with 1 μM CPT for 1 hour (or not), then processed for IF staining. Cells were cultured in BrdU-containing media prior to treatment with CPT. Cells sensitive to CPT (seen by the induction of γH2AX foci, with the exception of the untreated condition) were quantified for BrdU foci (right panels). IF micrographs are representative of 3 independent experiments; 249 to 299 cells per condition from 2 independent experiments (total foci intensity) and 299 to 340 cells per condition from 3 independent experiments (total foci area) were quantified. **B)** Similar to **A)** but without BrdU in the culture media, and IF staining for RPA2 instead of BrdU. Micrographs are representative of 4 independent experiments; 467 to 748 cells per condition from 3 to 4 independent experiments were quantified for total RPA2 foci intensity. Asterisks depict statistically significant differences as determined by a two-tailed, unpaired, non-parametric Student's *t*-test (Mann-Whitney): ns (not significant), ** ($p<0.01$), **** ($p<0.0001$). **C)** DR-GFP homologous recombination reporter assay in U-2 OS stably expressing the DR-GFP cassette. The cells were transfected with non-targeting (siCTRL) or CtIP-targeting (siCtIP) siRNA. 24 hours later, they were transfected with the same siRNAs, and either pCAGGS empty vector or pCAGGS-I-*Sce*I, in combination with siRNA-resistant constructs encoding HA-CtIP-WT or -K578R or not. GFP^+ cells were assessed via flow cytometry 24 hours later. Data presented are the means of 2 independent experiments (top panel). An immunoblot confirming the transfection combinations for one experiment is presented beneath (bottom panel). **D)** Clonogenic survival assay of parental U-2 OS transfected with siCTRL or siCtIP, or U-2 OS cell lines stably expressing GFP-CtIP-WT, -K578R, or Δ515-518 and transfected with siCtIP. Cells were treated with CPT at the indicated concentrations for 1 hour, and colonies were allowed to form over ~10 days. Survival data is presented as mean ± standard deviation from 3 independent experiments.

2.4.9 K578 is Not Required for CtIP Recruitment During Replication Stress or its Interaction with PCNA

The fact that CtIP SUMOylation decreases in the presence of HU, aphidicolin, and low dose CPT (**Figs. 2.3E-F**) suggests SUMO-2 modification may mediate CtIP's functions in the response to replication stress. We thus performed experiments to explore the functional consequences of an inability to SUMOylate CtIP in the context of replication stress. We previously found that CtIP is recruited to sites of replication stress, seen by its ability to form foci in response to HU and low dose CPT (**Fig. 2.S10A**). We then asked how a loss of SUMOylation at K578 would impact CtIP recruitment to stalled replication forks. We depleted endogenous CtIP in U-2 OS cells stably expressing GFP-CtIP-WT or -K578R, then treated them with HU and evaluated their abilities to form foci. U-2 OS stably expressing the PCNA interaction mutant GFP-CtIP-

Δ515-518 (**Fig. 2.4G**) were also used in these experiments, as previous observations showed the interaction with PCNA recruits CtIP to active replication centers (335). In response to HU, cells expressing K578R-CtIP exhibited a partial reduction in foci-forming ability compared to WT-CtIP, as opposed to those expressing Δ515-518, which were severely inhibited (**Fig. 2.S17A)**. While this indicates an interaction with PCNA is needed for CtIP recruitment to sites of replication stress, in line with the literature (335), it is clear that unlike the Δ515-518 mutant, SUMOylation of CtIP at K578 is dispensable for recruitment to these sites.

Earlier, we also observed that the interaction with PCNA promotes CtIP SUMOylation (**Figs. 2.4G-H**). We next pursued the converse question: if SUMOylation at K578R impacts CtIP's interaction with PCNA, both under normal and replication stress conditions. We performed co-immunoprecipitations in U-2 OS cells depleted of endogenous CtIP and transfected with RFP-PCNA and GFP-CtIP-WT or -K578R. Both the forward and reverse Co-IPs did not show a reduction in the CtIP-PCNA interaction for K578R-CtIP relative to WT at the steady state, unlike the Δ515-518 mutant (**Figs. 2.S17B-D**). Moreover, the interaction of GFP-CtIP and endogenous PCNA was not altered in the presence of replication stress induced by HU, whether WT- or K578R-CtIP was immunoprecipitated as the bait (**Fig. 2.S17E**). Thus, we conclude residue K578 is not required for the interaction between CtIP and PCNA.

2.4.10 CtIP-K578R Expression Phenocopies a Fork Protection Defect in CtIP-Depleted Cells During Replication Stress

A recent study demonstrated that CtIP protects stalled replication forks from degradation (336). Here, the presence of CtIP limited stalled replication forks from over-resection by Dna2 exonuclease and prevented genomic instability, virtues lost when mutations that abrogate CtIP's apparent intrinsic flap endonuclease activity were introduced (270, 272, 336). We therefore sought

to determine if SUMOylation of CtIP at K578 could play a role in replication fork protection, despite the K578R mutant still being able to recruit to replication foci (**Fig. 2.S17A**). To directly visualize the impact of K578R substitution on fork dynamics, we performed the DNA fiber spreading assay. Briefly, we sequentially pulse-labeled newly synthesized DNA using two halogenated nucleosides (5-chloro-2'-deoxyuridine (CldU) first, then 5-iodo-2'-deoxyuridine (IdU) second), then treated with HU to stall replication fork progression and potentially initiate nascent strand degradation (**Fig. 2.8A**; the typical appearance of spread fibers is shown in **Fig. 2.S18A**). The ratio of the resulting IdU and CldU tract lengths in the spread DNA fibers was then used as a readout for replication fork protection; IdU/CldU ratios near 1 reflected little or no degradation (fork protection), whereas ratios <1 indicated degradation of newly synthesized DNA. The assay was performed on U-2 OS cells depleted of endogenous CtIP and complemented with WT- or mutant GFP-CtIP. Consequently, depleting CtIP consistently reduced the IdU/CldU ratio from ~1 to 0.5-0.7, and the ratio was restored to 0.91 when GFP-CtIP-WT was added back (**Fig. 2.8B**), confirming the reported loss of fork protection in the absence of CtIP (336). Interestingly, expressing the 7KR mutant could not restore fork protection, nor could K578R-CtIP. However, the 7KR-R578K mutant recovered the IdU/CldU ratio to near WT levels (**Fig. 2.8B**). This implicates K578 as the residue among the seven predicted SUMOylation sites that mediates CtIP's role in replication fork protection. In support of a role for CtIP SUMOylation in fork protection, the Δ515-518 mutant, which interacts less with PCNA and is inhibited in SUMOylation (**Figs. 2.4G-H**), reduced the IdU/CldU ratio in a similar manner to CtIP-K578R (**Fig. 2.8C**), although the value was slightly higher, perhaps because K578 was still intact as a SUMOylation site. Secondly, depleting SUMO E2 UBC9 also produced the nascent DNA degradation phenotype (**Fig. 2.S18B**), suggesting SUMOylation events in general promote fork protection. Thirdly, as PIAS4

SUMOylates CtIP in S phase (**Fig. 2.5**), we predicted that reducing PIAS4 levels would lead to more nascent DNA degradation. Certainly, knockdown of PIAS4 reduced the IdU/CldU ratio relative to mock transfected cells, but not to the extent of cells expressing the K578R mutant (**Fig. 2.8D**), suggesting fork protection overall is mediated by PIAS4 and other E3 SUMO ligases. Critically, however, depleting PIAS4 while expressing K578R-CtIP resulted in an IdU/CldU ratio similar to expressing the K578R mutant alone (**Fig. 2.8D**), demonstrating that CtIP modification at K578 and PIAS4 activity reside within the same pathway and are epistatic. Together, our DNA fiber data demonstrate that an inability to SUMOylate CtIP results in defective fork protection in response to HU, with the CtIP-K578R mutant phenocopying the fork over-resection defect seen by the loss of CtIP.

Since the purported flap endonuclease activity of CtIP (270, 272) was reported to mediate CtIP's role in replication fork protection (336), we were curious if SUMOylation at K578 controls this activity. The apparent endonuclease activity can be inhibited by loss of function mutations at residues N181 or N289 and H290 (270, 272). We thus generated both mutants in GFP-CtIP by site-directed mutagenesis, along with double mutants combining "nuclease deficiency" with K578R (N181A-K578R, N289A-H290A-K578R). As a control, we found that neither of the solely "nuclease-deficient" mutants were impacted in the ability to be SUMOylated during S phase in HeLa His_{10}-SUMO-2 cells, unlike K578R (**Fig. 2.S18C**). Only the "nuclease-deficient"-K578R double mutants were strongly reduced in CtIP SUMOylation, and to the same level as K578R alone (**Fig. 2.S18C**), indicating that ablation of K578 was responsible for the reduction in SUMOylation. Intriguingly, K578R, both "nuclease-deficient" mutants, and the "nuclease-deficient"-K578R combination mutants all showed similar IdU/CldU ratios (**Fig. 2.8E**). This suggests that both SUMOylation at K578 and the functions of residues N181 and N289/H290 are

within the same pathway. While this implies K578 SUMOylation could control CtIP's purported endonuclease activity, we could not test the idea, as we were unable to detect any flap endonuclease activity in purified CtIP to start (**Fig. 2.S18D**). Nevertheless, this experiment shows K578 SUMOylation is epistatic with whatever functions residues N181 and N289/H290 mediate, and our evidence overall implicates K578 SUMOylation in the mechanism by which CtIP protects stalled replication forks from over-resection.

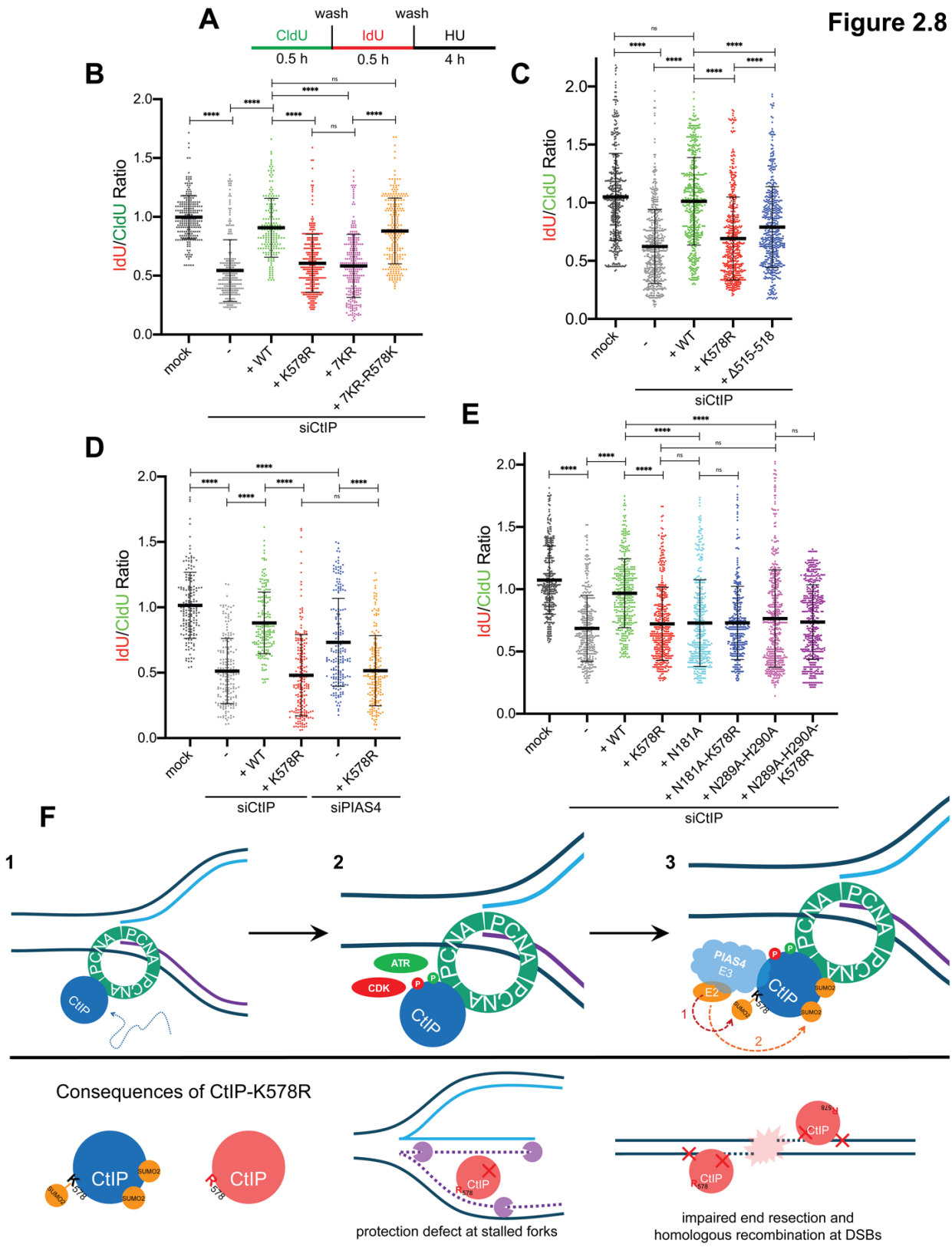

Figure 2.8: CtIP-K578R Expression Phenocopies a Fork Protection Defect in CtIP-Depleted Cells During Replication Stress

A) Labeling and 2 mM HU treatment protocol for all DNA fiber experiments performed. **B) – E)** IdU/CldU ratio scatterplots of spread DNA fibers from U-2 OS cells transfected with siRNA targeting CtIP or PIAS4 or mock-transfected ~48 hours prior to labeling, transfected with the indicated GFP-CtIP constructs or not (-) ~16 hours prior to labeling, then treated according to **A)**. The mean and standard deviation are displayed. Asterisks depict statistically significant differences as determined by a two-tailed, unpaired, non-parametric Student's *t*-test (Mann-Whitney): ns (not significant), **** ($p<0.0001$). **B)** 182 to 290 fibers per condition were sourced from 2 independent experiments. **C)** 476 to 520 fibers per condition were sourced from 2 independent experiments. **D)** 169 to 204 fibers per condition were sourced from 2 independent experiments. **E)** 332 to 423 fibers per condition were sourced from 2 independent experiments. **F)** Schematic diagram of the model of the data. See text for details.

2.5 Discussion

In this study, we sought to find potential SUMO targets in the HR pathway and characterize how SUMOylation could affect their function. Use of the SUMOylation inhibitor GA suggested CtIP was a substrate for SUMOylation, as its recruitment to sites of DSBs was impaired upon GA treatment, along with the process of DNA end resection, which CtIP is known to promote (52, 58, 324) (**Figs. 2.1G-I, 2.S9D**). By nickel affinity purification of His_{10}-SUMO-2ylated proteins, we later detected DSB damage-independent (**Figs. 2.3A-B, 2.S12D**) and constitutive (**Figs. 2.2B-D**) CtIP SUMOylation *in vivo*. In line with this, a recent report by Soria-Bretones *et al*. also found CtIP to be constitutively SUMOylated, and at similar levels with or without DNA damage (343). Soria-Bretones and coworkers showed that this was mediated by the E3 SUMO ligase CBX4, which when depleted inhibited DNA end resection (343). Furthermore, they found that SUMOylation at the near-C-terminal residue K896 was required for proficient DNA end resection, Rad51 foci formation, maintenance of genomic stability, and CtIP's recruitment to I-*Sce*I-generated DSBs, as these were all inhibited in cells expressing the K896R mutant but could be rescued when SUMO-1 was fused to the C-terminus of CtIP (343). In our study, we establish a

cell cycle dependency for CtIP SUMOylation, with the modification strikingly stimulated during S phase (**Figs. 2.3D and 2.S12C**). We then uncovered a SUMOylation site on CtIP, K578, that sits within a canonical ψ-K-x-E SUMOylation motif (**Fig. 2.S15E**). Comparing our findings, we and Soria-Bretones *et al*. show that constitutive CtIP SUMOylation at residues K578 or K896 (343) is important for DNA end resection, and to similar extents (**Figs. 2.7A-B**). It might be that both sites are functionally critical to promote end resection, thus end resection is blocked whenever one or the other site is ablated. More enticingly, however, it could be that K896 SUMOylation controls end resection, but that K578 SUMOylation is a prerequisite for K896 SUMOylation (see below). Meanwhile, our studies do report contrasting results for the dependence of SUMOylation on CDK phosphorylation at T847, where we find T847 phosphorylation does partially mediate SUMOylation (**Fig. 2.4C**). Additionally, CtIP SUMOylation was promoted by the E3 ligase PIAS4, not CBX4, in our study (**Figs. 2.5A,C**). These two contradictions could be a result of our emphasis on S phase-synchronized cells and the SUMO isoform SUMO-2. We reason that PIAS4 SUMOylates CtIP in S phase, and speculate additional SUMOylation by CBX4 could then prepare CtIP to function in DNA end resection.

CtIP's function in end resection is tightly governed by multiple PTMs, including phosphorylation (61, 105, 267), ubiquitylation (133), and SUMOylation (343). For instance, CDK phosphorylation of T847 (and its equivalent in the *S. cerevisiae* orthologue) restricts end resection activity to the S and G_2 cell cycle stages (61, 104). Furthermore, ATR phosphorylation at T859 enables CtIP recruitment to DNA to activate end resection (267). Our work reveals a dynamic interplay between the PTMs on CtIP. Firstly, our data indicates CDK- and ATR-mediated phosphorylations promote CtIP SUMOylation during S phase (**Figs. 2.4B-E**), suggesting phosphorylation events are upstream of CtIP SUMOylation. In support of this, both kinase

activities were linked for CtIP phosphorylation in *Xenopus* oocytes, where phosphorylation at the residue corresponding to CDK site T847 preceded ATR phosphorylation at the equivalent of T859 (267). In addition, a connection between CDK activity and human CtIP SUMOylation was found in a mass spectrometry screen, where peptides of K578-SUMOylated CtIP were co-modified with CDK-dependent phosphorylation, and CtIP SUMOylation at different sites was altered in the presence of a CDK inhibitor (140). Secondly, we uncover mechanistic intricacies in CtIP SUMOylation. Unlike the K896R mutation, the K578R substitution dramatically reduces CtIP SUMOylation (**Figs. 2.6C-E, 2.S15C-D**), while combining both mutations in the K578R-K896R double mutant reduces CtIP SUMOylation to a level similar to K578R alone (**Figs. 2.6A,D**). This suggests SUMOylation on K896 is likely a low abundance modification, perhaps only for the fraction of CtIP engaged in end resection (343), and is consistent with Soria-Bretones *et al*. who found the K896R mutant exhibited similar SUMOylation levels as WT-CtIP (343). Astonishingly, we found that K578 contributes prominently to CtIP SUMOylation not only as a SUMOylation site, but by priming SUMOylation *en masse* at other residues within CtIP when it is SUMOylated. This was inferred from the observation that the K578R single mutant reduces SUMOylation levels similar to that of the 7KR mutant (where all seven potential SUMOylation sites are blocked), yet the 7KR-R578K mutant (where of the seven blocked SUMOylation sites, only K578 was restored) could only partially rescue SUMOylation levels to that of WT-CtIP (**Figs. 2.6A,E, 2.S15C**). Thus it appears at least some of the other six putative sites contribute to CtIP SUMOylation, but in a manner dependent on the SUMOylation of K578. It may be that SUMOylation at K578 is a prerequisite for activatory conformational changes in CtIP that then allow other lysine residues to become accessible for SUMOylation.

While HR proteins are involved in fork reversal and restart (247, 249, 250, 330–332), their precise roles and regulation at replication forks are poorly understood compared to their functions at DSBs. Our data fosters three implications for CtIP in fork biology. Firstly, our findings illustrate the importance of CtIP's interaction with PCNA (335). We demonstrate that disrupting the interaction via Δ515-518 (**Figs. 2.4G, 2.S17D**) prevents CtIP recruitment to sites of DNA damage as well as replication stress foci (**Figs. 2.S8A-B, 2.S17A)**. Interestingly, while CtIP-Δ515-518 exhibits a recruitment defect, this is not manifested in the K578R mutant (**Figs. 2.S16A-B, 2.S17A)**, implying that the inhibition of CtIP recruitment upon GA treatment (**Figs. 2.1I, 2.S10B**) may depend on SUMOylation on other sites of the protein, or perhaps multiple other SUMOylation events beyond those on CtIP. That CtIP-K578R is markedly less SUMOylated than WT, beyond the contribution of the K578 site alone (**Figs. 2.6C-E, 2.S15C-D**), but still is recruited efficiently also suggests complete SUMOylation is not required for CtIP accumulation at sites of replication stress or DNA damage. This supports the notion that CtIP SUMOylation occurs downstream of its accrual on chromatin. We propose then that the PCNA-CtIP interaction targets CtIP to actively replicating DNA for rapid responses to DNA damage and replication stress. This could then allow CtIP to be SUMOylated (**Fig. 2.4H**), which we find is critical for its functions in DNA end resection and fork protection (**Figs. 2.7A-B, 2.8B-D**). While a portion of the Δ515-518 mutant is still chromatin-enriched (**Fig. 2.S14B**), perhaps localizing CtIP to PCNA brings CtIP in the vicinity of PIAS4 for its SUMOylation, in line with a report that PCNA can be SUMOylated by PIAS4 (371). Second of all, our data demonstrate that SUMOylation of K578 is necessary and sufficient for protecting stalled replication forks from excessive nucleolytic degradation (**Fig. 2.8**). This is made evident with the 7KR-R578K (**Fig. 2.8B**) mutant being proficient in fork protection, despite ablation of the remaining six potential SUMOylation sites (**Fig. 2.6A**). While K578R and point

mutants causing CtIP to be "nuclease-deficient" (270, 272) were epistatic in the fork degradation phenotype (**Fig. 2.8E**), we were unable to detect this intrinsic endonuclease activity in purified CtIP (**Fig. 2.S18D**) and thus could not determine if SUMOylation regulated the activity. Other groups have not been able to detect nuclease activity in CtIP or its orthologues (52, 261, 324). We therefore speculate SUMOylation triggers conformational changes that control CtIP's function as a co-factor for an associated endonuclease activity. This activity promotes fork protection and is somehow mediated by residues N181 and N289/H290 within CtIP, perhaps by facilitating protein-protein interactions. Thirdly, the increase in CtIP SUMOylation during S phase (**Figs. 2.3D, 2.4B,D, and 2.S12C-D**) raises the intriguing possibility that CtIP could play a role in DNA replication. This is bolstered by evidence that CtIP interacts constitutively with the processivity factor PCNA (335), an observation we have reproduced (**Figs. 2.4F, 2.S14A**), forms foci at sites of active DNA replication (335) and during replication stress (**Fig. 2.S10A**), is recruited to ongoing replication forks as detected by iPOND (isolation of proteins on nascent DNA) (334), and that SUMOylated CtIP is enriched on chromatin (**Fig. 2.2D**) and is promoted by CDK activity (**Figs. 2.4B-C**). Notably, we find that replication stress inducing agents reduce CtIP SUMOylation (**Figs. 2.3E-F**), and fittingly HU treatment causes the dissociation of the E3 SUMO ligase PIAS4 from CtIP (**Fig. 2.5F**). Consistent with this, a mass spectrometry study detected K578 as a SUMOylation site on CtIP, and classified it as a dynamically regulated site, being markedly deSUMOylated in response to HU treatment at 2 and 24 hours (361). Thus, it appears CtIP is SUMOylated during fork progression, but this is reduced during prolonged fork stalling. Perhaps these changes in SUMOylation level switch CtIP between different roles depending on the conditions at the fork. Interestingly, while we observe a reduction in CtIP SUMOylation in response to HU (**Fig. 2.3F**), the SUMOylation-deficient CtIP-K578R mutant still exhibits a fork

protection defect (**Figs. 2.8B-E**). This suggests CtIP must first be SUMOylated in S phase, then deSUMOylated during prolonged fork stalling, in order to protect halted forks from nascent DNA strand degradation.

Taken together, our data supports the following model (**Fig. 2.8F**). CtIP is recruited to chromatin by an interaction with PCNA, which facilitates its targeting to active DNA replication foci during S phase. CDK-dependent phosphorylation events (at T847 and other residues), along with ATR-dependent phosphorylation (at sites such as S664, S679, and/or S745), predispose CtIP for constitutive modification by SUMO-2 during S phase. This SUMOylation is facilitated by the E3 SUMO ligase PIAS4. SUMOylation on residue K578 then licenses CtIP to be SUMOylated on other sites. SUMOylated CtIP is an activated version of the protein that promotes DNA end resection, and subsequently HR, and prevents over-resection of newly synthesized DNA at stalled replication forks, functions that are disrupted when K578 is not modifiable by SUMOylation (**Fig. 2.8F**). Overall, our data provide a link between CtIP SUMOylation and fork protection (336). Our work expands the functions of SUMOylation in regulating CtIP beyond its recruitment to DSBs, promotion of end resection (343), and solubility (372), and validates K578 as a *bona fide* SUMOylation site with functional impacts.

2.6 Funding

This research is supported by an NSERC (Natural Sciences and Engineering Research Council of Canada) Discovery Grant (RGPIN-2017-05752) and a CIHR (Canadian Institutes of Health Research) Project Grant (MOP-365197), both awarded to I.H.I, and a CIHR Foundation grant (FDN-388879) awarded to J.-Y.M. A.J.L. was supported by an Alberta Graduate Excellence

Scholarship and Queen Elizabeth II Graduate Scholarship (Doctoral) from the Government of Alberta, a 75th Anniversary Award from the Faculty of Medicine & Dentistry, the Dr. Herbert Meltzer Memorial Fellowship, and the Yau Family Foundation Award. L.H. was supported by a Faculty of Medicine & Dentistry/Alberta Health Services Graduate Student Recruitment Studentship (Doctoral). D.A.R. is a recipient of an FRQS PhD studentship. T.A.R. was supported by the Alberta Cancer Foundation/Antoine Noujaim Entrance Award. J.-Y.M holds a Tier I Canada Research Chair in DNA Repair and Cancer Therapeutics.

2.7 Acknowledgements

We are especially grateful to Dr. Pablo Huertas for providing the GFP-CtIP constructs. We thank Dr. Michael Hendzel and Dr. Lei Li for critical feedback to the manuscript, Dr. Xuejun Sun for assistance with data quantitation, Dr. J.N. Mark Glover, Dr. Michael Weinfeld, and Dr. Cody W. Lewis for insightful suggestions. We also thank Dr. Shirin Bonni for guidance to PIAS1/4 constructs, Youssef Ismail for writing Python code to quantify laser microirradiation recruitment data, and Samantha Flint, Ugbad Hassan, and Badri Forghani for technical support.

2.8 Conflict of Interest

The authors declare no conflicts of interest.

2.9 Author Contributions

A.J.L. designed experiments, performed most of the experiments, and analyzed and interpreted data. L.H. performed some His pull-down and immunoblot assays. G.M. performed immunofluorescence and immunoblot assays. D.A.R. performed protein purification and *in vitro* resection and nuclease assays. A.F. optimized immunofluorescence assays and processed DNA fiber and laser microirradiation data. T.A.R. performed immunoblot and pulsed-field gel electrophoresis assays. F.M. performed immunofluorescence assays and processed immunofluorescence data. M.M. performed immunoblot assays and processed immunofluorescence and survival data. J.-Y.M. designed experiments and supervised D.A.R. I.H.I. conceived and supervised the project, designed experiments, performed DNA fiber assays, and analyzed and interpreted data. A.J.L. and I.H.I. wrote and revised the manuscript. All authors have read and approved the revised manuscript.

2.10 Supplementary Data

Supplementary figures (**Figs. 2.S9 – 2.S18**) and tables (**Tables 2.1 – 2.6**) are provided in support of the main figures (**Figs. 2.1 – 2.8**).

2.10.1 Supplementary Figures

Figure 2.S9

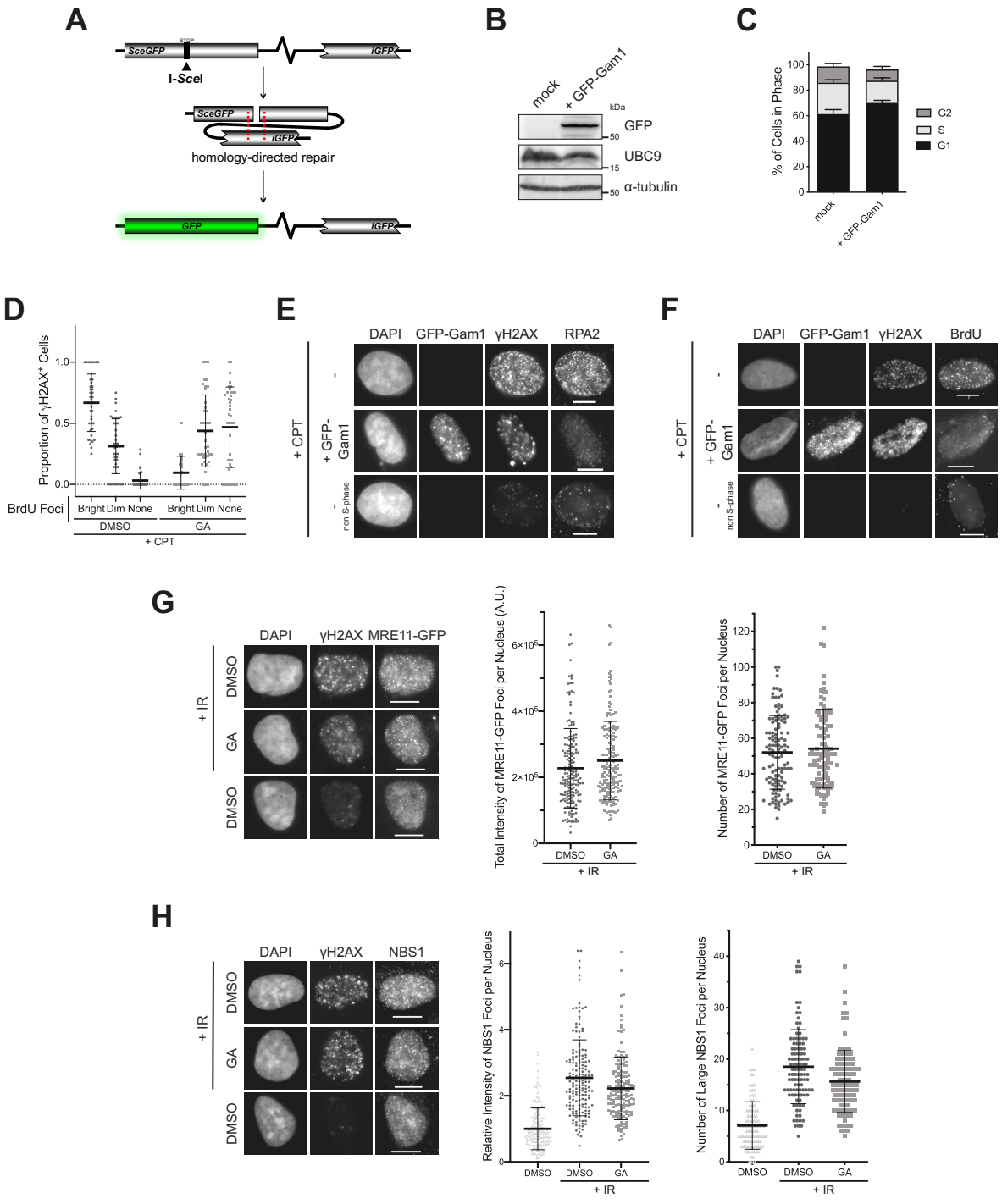

Figure 2.S9: Related to Figure 2.1

A) Schematic representation of the DR-GFP homologous recombination reporter cassette (352). The reporter contains two copies of a modified GFP gene, both of which are mutated to produce non-fluorescent protein products. One incorporates an I-*Sce*I cutting site containing two stop codons (*SceGFP*); the other encodes an internal fragment of GFP (*iGFP*). Expression of I-*Sce*I

endonuclease generates a double-strand break in *SceGFP*. Repair of the break by gene conversion produces functional GFP. **B)** Immunoblot showing reduction in UBC9 expression 24 hours after transfecting GFP-tagged Gam1 into HeLa cells, representative of 2 independent experiments. **C)** HeLa cells were transfected with GFP-Gam1 or mock transfected. The cells were harvested 24 hours later and processed for DNA content analysis. Shown are the averages of 3 independent experiments. **D)** Quantitation of BrdU foci intensity in U-2 OS cells cultured in BrdU-containing media, pre-treated for 1 hour with 12 μM GA or 0.025% DMSO, and stimulated for 1 hour in 1 μM CPT in their presence. Evenly scaled IF images of both conditions were compared in tandem, and all $\gamma H2AX^+$ cells were scored for their relative BrdU foci intensity (bright, dim, or no foci). The proportions of cells in each category were calculated per field of view. 40 fields of view pooled from 4 independent experiments were scored per condition. **E) and F)** IF micrographs of U-2 OS cells transfected or not with GFP-Gam1 for 24 hours, after which 1 μM CPT was added for 1 hour. As only cells in S phase are sensitive to CPT, cells that did not respond to CPT are also presented. In **F)**, cells were cultured in BrdU-containing media prior to treatment. Shown are representative images from 3 **(E)** and 2 **(F)** independent experiments. **G) and H)** IF micrographs of U-2 OS cells stably expressing Mre11-GFP **(G)** or plain U-2 OS cells **(H)** pre-treated with 12 μM GA or 0.025% DMSO for 1 hour, subjected to 10 Gy of IR or not, and recovered for 2 hours in the presence of GA or DMSO. Left panel: representative images from at least 6 independent experiments. Center and right panels: quantifications of total foci intensity (pooled from 3 independent experiments; ≥175 cells per condition for Mre11-GFP, ≥153 cells per condition for Nbs1) and foci count (1 experiment; ≥114 cells per condition for Mre11-GFP, ≥103 cells per condition for Nbs1). In **G)**, Mre11-GFP foci were quantified from Mre11-GFP foci-positive cells, whereas in **H)**, Nbs1 foci were quantified from all cells.

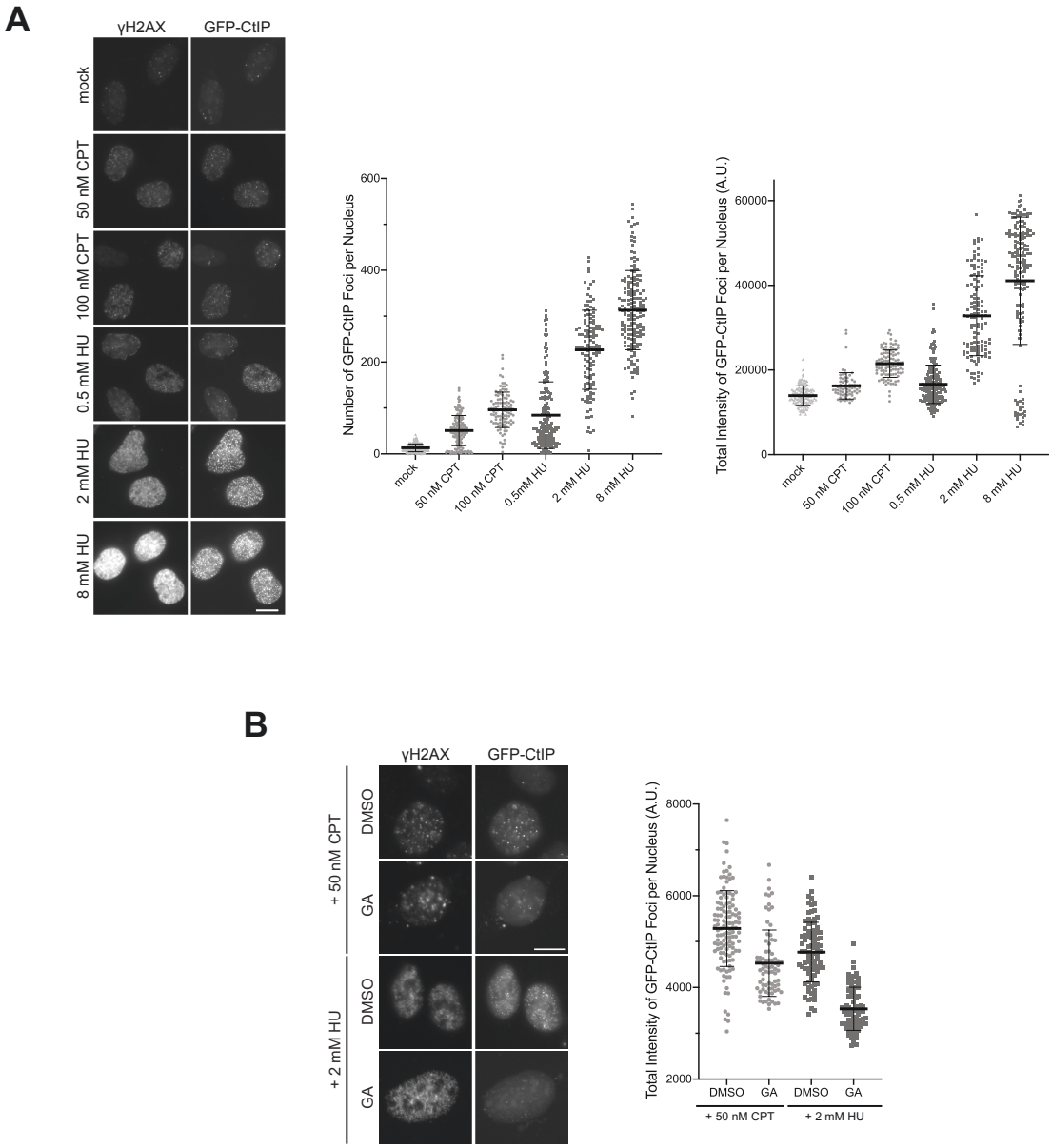

Figure 2.S10: Related to Figure 2.1

A) U-2 OS cells stably expressing GFP-CtIP were treated with the indicated concentrations of CPT or HU for 4 hours and processed for IF staining. Shown are representative images from 2 independent experiments, and GFP-CtIP foci quantifications from 70 – 186 γH2AX^{+} cells per condition from 1 experiment. All images were scaled evenly for brightness and contrast. **B)** U-2 OS cells stably expressing GFP-CtIP were pre-treated for 30 minutes with 10 μM GA, then treated for 4 hours with 50 nM CPT or 2 mM HU in the presence of GA and processed for IF staining. Shown are representative images from 2 independent experiments, and GFP-CtIP foci quantifications from 75 – 123 γH2AX^{+} cells per condition from 1 experiment. All images were scaled evenly for brightness and contrast.

Figure 2.S11

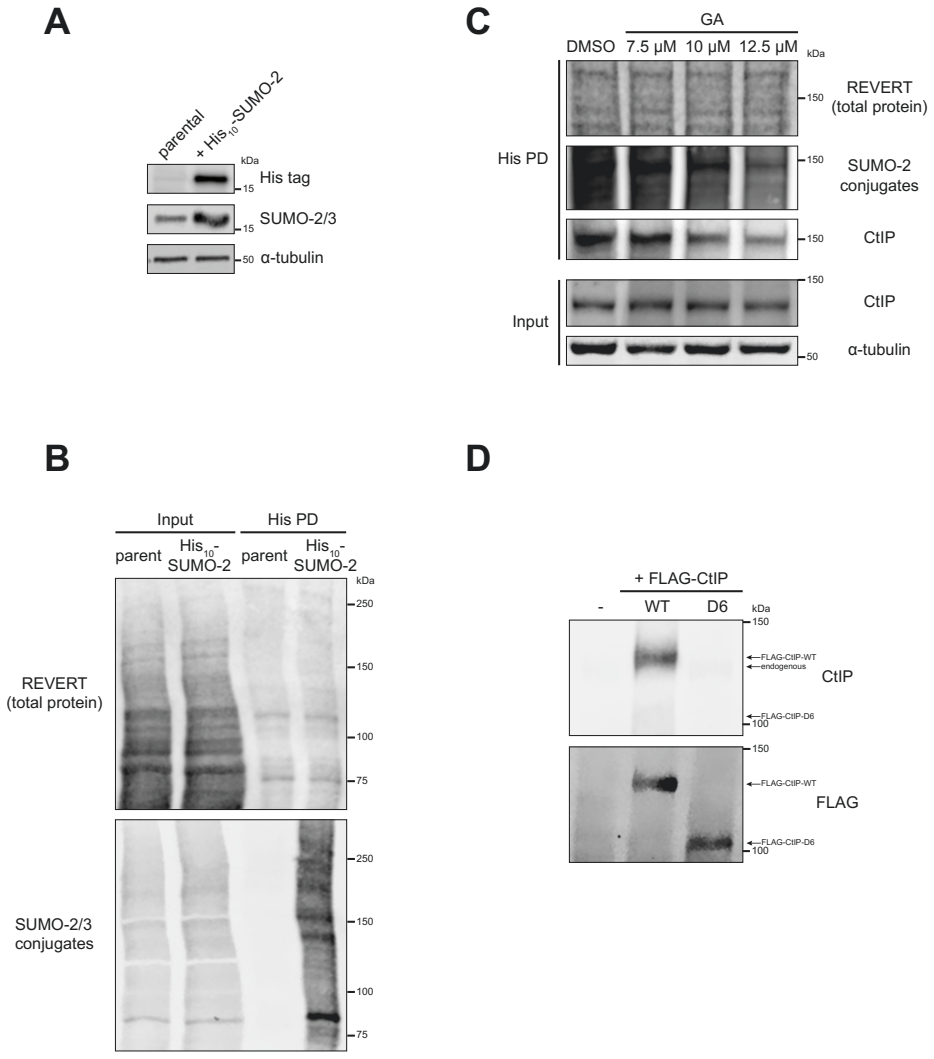

Figure 2.S11: Related to Figure 2.2

A) Immunoblot verifying the expression of His_{10}-SUMO-2 in HeLa His_{10}-SUMO-2 cells. **B)** HeLa cells expressing 10XHis-tagged SUMO-2 (His_{10}-SUMO-2) or HeLa cells they were derived from (parent) were portioned into input and His PD fractions and processed accordingly. The His PD fraction was processed using buffers containing 20 mM imidazole, and the fraction loaded represents 12X more of the starting amount of sample relative to the input. Shown is a representative result of 3 independent experiments. Corresponds to **Fig. 2.2B**. **C)** HeLa His_{10}-SUMO-2 cells were treated with GA at the indicated concentrations for 2 hours, then portioned into input and His PD fractions and processed accordingly before SDS-PAGE and immunoblotting. Shown is a representative result of 3 independent experiments. **D)** Lysates from HeLa His_{10}-SUMO-2 cells expressing FLAG-tagged wildtype CtIP (WT) or a C-terminal truncation mutant (D6) (see **Fig. 2.S15A**) were blotted for CtIP or FLAG to demonstrate the specificity of the CtIP antibody for the CtIP C-terminus. Shown is a representative result of 3 independent experiments.

Figure 2.S12

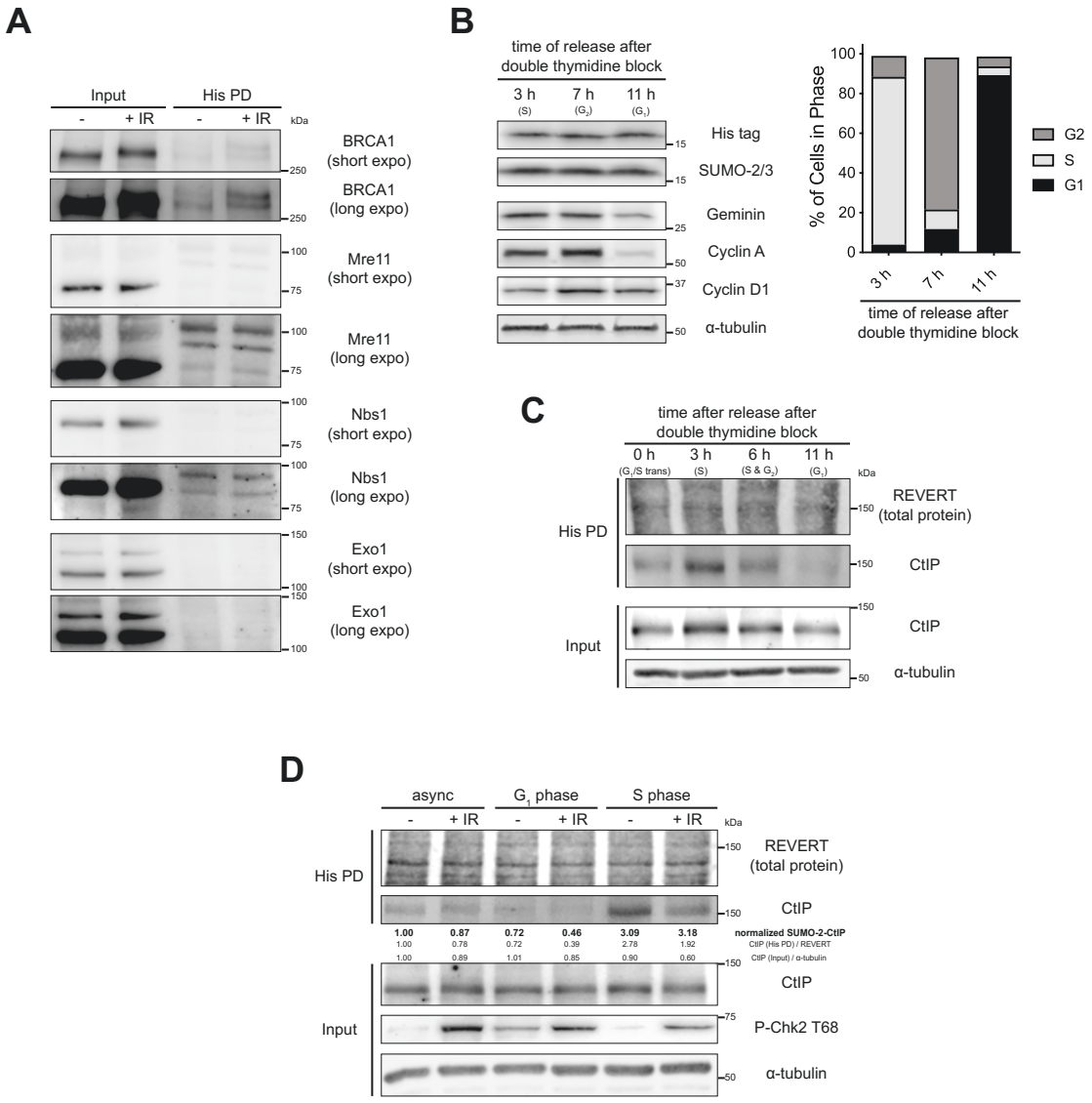

Figure 2.S12: Related to Figure 2.3

For **A), C), and D)**, HeLa His_{10}-SUMO-2 cells were treated as indicated, portioned into input control and His PD fractions, processed accordingly for whole cell lysis or Ni-NTA affinity purification, then resolved by SDS-PAGE. **A)** Cells were subjected to 10 Gy of IR or not and allowed to recover for 1 hour. Corresponds to **Fig. 2.3A**. **B)** HeLa His_{10}-SUMO-2 cells were synchronized by double thymidine block and released for either 3 (mid-S phase), 7 (early G_2 phase), or 11 hours (G_1 phase). The resulting cell lysates were blotted for the expression of His_{10}-SUMO-2 and cell cycle markers (Geminin, for S phase; Cyclin A, for G_2 phase; Cyclin D1, for G_1 phase) (left panel). Right panel: the corresponding cell cycle profiles by DNA content analysis. **C)** HeLa His_{10}-SUMO-2 cells were synchronized by double thymidine block and released for various timepoints to reach different cell cycle phases (0 h for the G_1/S transition, 3 h for mid-S phase, 6 h for S and G_2 phases, 11 h for G_1 phase). **D)** Cells were left asynchronous or synchronized by double thymidine block with release for 2 (mid-S phase) or 12 hours (G_1 phase),

after which they were subjected to 10 Gy of IR or not and allowed to recover for 1 hour. Shown is a representative result of 2 independent experiments.

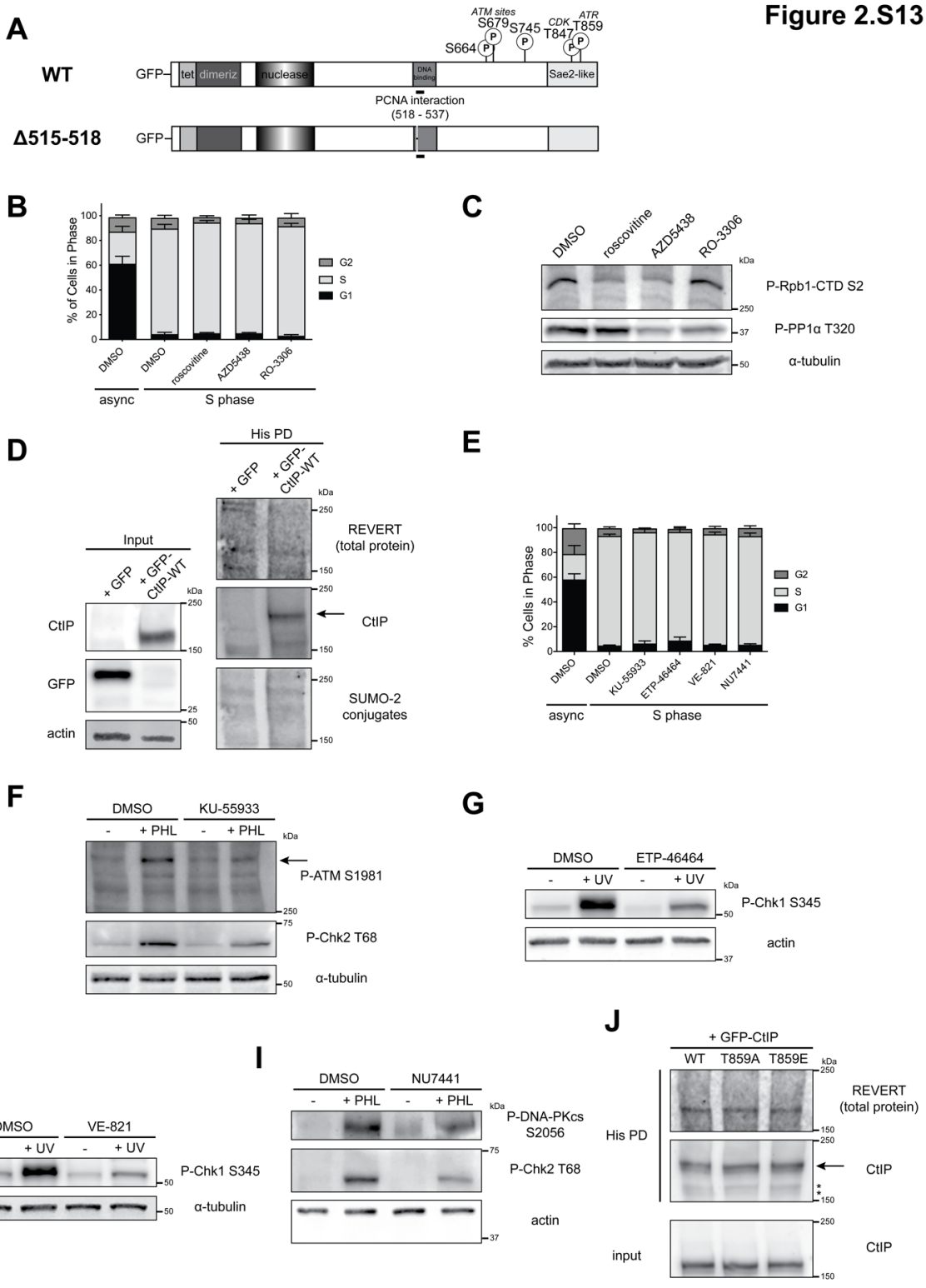

Figure 2.S13: Related to Figure 2.4

A) Schematic diagrams of the domain structure of GFP-CtIP-WT and the internal deletion mutant -Δ515-518 along with relevant phosphorylation sites. "Tet": tetramerization domain; "dimeriz": dimerization domain; "nuclease": endonuclease domain, "PCNA interaction": also known as PIP-Box. **B)** Cells were treated as in **Fig. 2.4B** and processed for DNA content analysis. Shown are the means of 2 independent experiments. **C)** Lysates of HeLa His_{10}-SUMO-2 cells treated for 2.5 hours in 0.1% DMSO, 25 μM roscovitine, 2.5 μM AZD5438, or 10 μM RO-3306 were blotted for the phosphorylation of CDK substrates. Ser2 in the heptapeptide repeats of the RNA polymerase II subunit Rpb1 C-terminal domain (CTD) is phosphorylated by CDK9 (373), which is a target of roscovitine and AZD5438 (365, 366). Thr320 of protein phosphatase 1 alpha (PP1α) is phosphorylated by CDK1 (374), which is a target of AZD5438 and the target for RO-3306 (366, 367). **D)** Immunoblot of input and His PD fractions of HeLa His_{10}-SUMO-2 cells transfected with empty vector GFP or GFP-CtIP-WT. **E)** Cells were treated as in **Fig. 2.4D** and processed for DNA content analysis. Shown are the means of 2 to 4 independent experiments. **F) - I)** Immunoblots of cells treated with 10 μM KU-55933, 20 μM ETP-46464, 20 μM VE-821, or 1 μM NU7441 for 1 hour, then supplemented with 25 μM phleomycin (PHL) for 30 minutes **(F)** or 1 hour **(I)**, or treated with 82 J/m^2 of ultraviolet light (UV) and recovered for 1 hour in their presence **(G, H)**. **J)** Immunoblot of input and His PD fractions of HeLa His_{10}-SUMO-2 cells synchronized to mid-S phase and transfected with GFP-CtIP-WT or substitution mutants at residue T859. Shown is a representative result of 3 independent experiments. * indicates an exogenous CtIP immunoreactive band that is not of interest; we speculate it is either lower molecular weight SUMO-2-modified CtIP, or unmodified tagged-CtIP retained in the His PD fraction due to overexpression.

Figure 2.S14

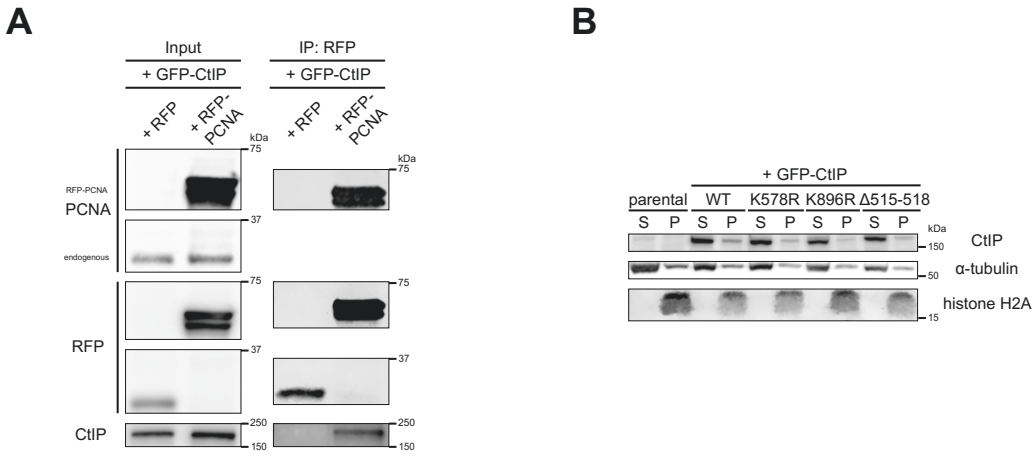

Figure 2.S14: Related to Figure 2.4

A) U-2 OS cells were transfected with GFP-CtIP and either monomeric red fluorescent protein (RFP) empty vector or RFP-PCNA and processed for immunoprecipitation (IP) for the RFP tag. Prior to IP, a portion of lysate was saved as an input control. Shown is a representative result of at least 6 independent experiments. **B)** Chromatin fractionation experiment, with resulting soluble (S) or chromatin-enriched (P, pellet) fractions for U-2 OS cells stably expressing GFP-CtIP-WT, -K578R, -K896R, or -Δ515-518, or the parental U-2 OS cells. Histone H2A and α-tubulin serve as markers for the chromatin-enriched and soluble fractions, respectively.

Figure 2.S15

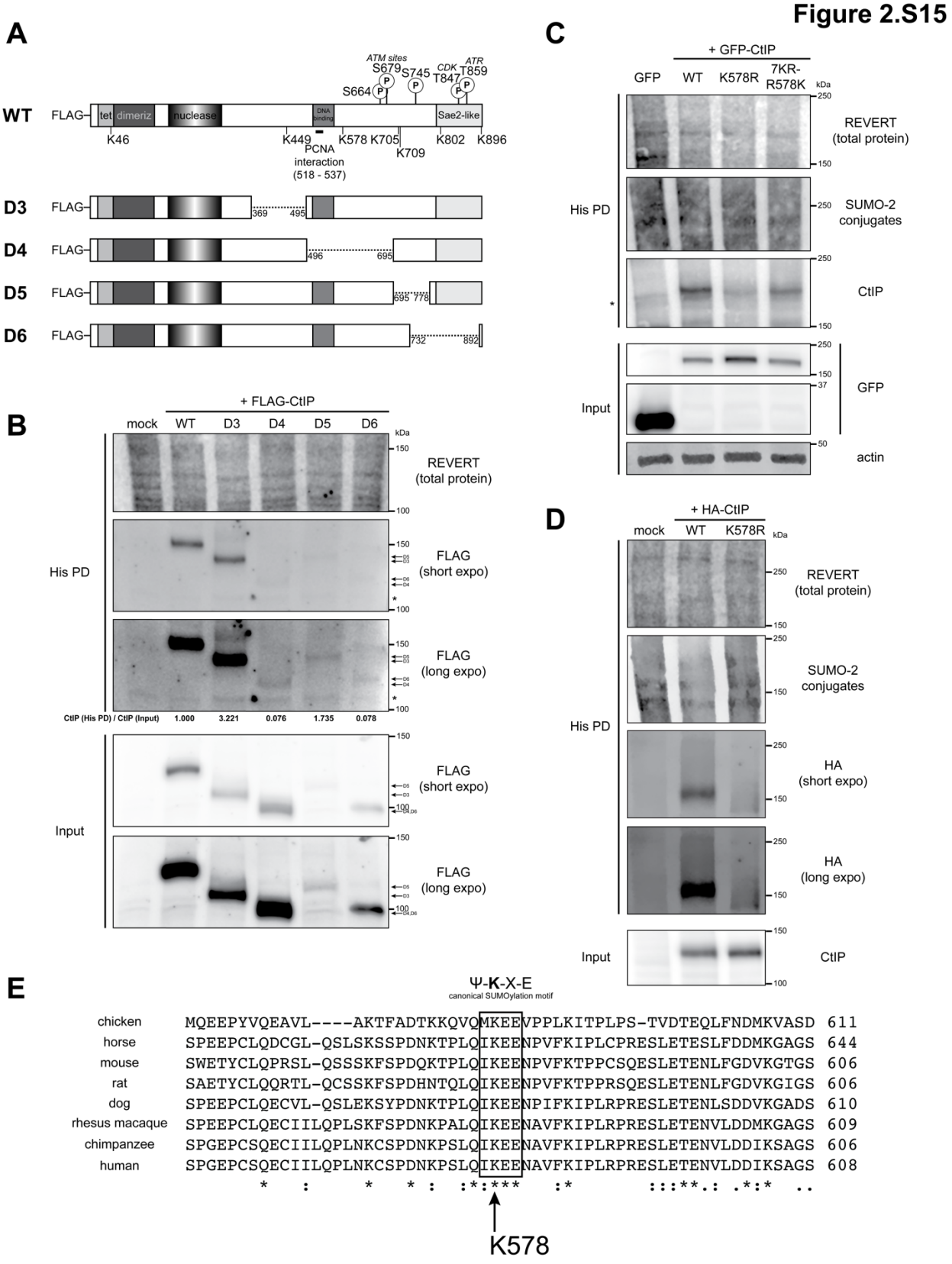

Figure 2.S15: Related to Figure 2.6

A) Schematic diagrams of CtIP domain structure of FLAG-tagged wildtype (WT) CtIP and a panel of corresponding internal deletion mutants (D3 to D6); the regions deleted are denoted by the dotted line. Also indicated in the WT schematic are relevant phosphorylation and SUMOylation sites in this study. "Tet": tetramerization domain; "dimeriz": dimerization domain; "nuclease": endonuclease domain, "PCNA interaction": also known as PIP-Box. **B)** HeLa His_{10}-SUMO-2 cells were synchronized to mid-S phase. 24 hours before harvest, they were transfected with FLAG-CtIP-WT or the internal deletion mutants D3, D4, D5, and D6, then portioned into input control and His PD fractions and processed accordingly. Shown is a representative result of 2 independent experiments. * indicates a non-specific immunoreactive band. **C)** Asynchronous HeLa His_{10}-SUMO-2 cells were transfected with GFP empty vector or the indicated GFP-CtIP constructs, portioned into input control and His PD fractions, and processed accordingly. **D)** Asynchronous HeLa His_{10}-SUMO-2 cells were transfected with the indicated HA-tagged CtIP constructs, portioned into input control and His pull-down (His PD) fractions, and processed accordingly. **E)** Clustal Omega (European Bioinformatics Institute, European Molecular Biology Laboratory) multiple sequence alignment was performed on the amino acid residue sequences of CtIP orthologues. The conserved lysine residue at K578 (in human CtIP) and the surrounding canonical SUMOylation motif are highlighted. * indicates complete identity; **:** indicates conservative substitutions; **-** indicates the residue is absent.

Figure 2.S16

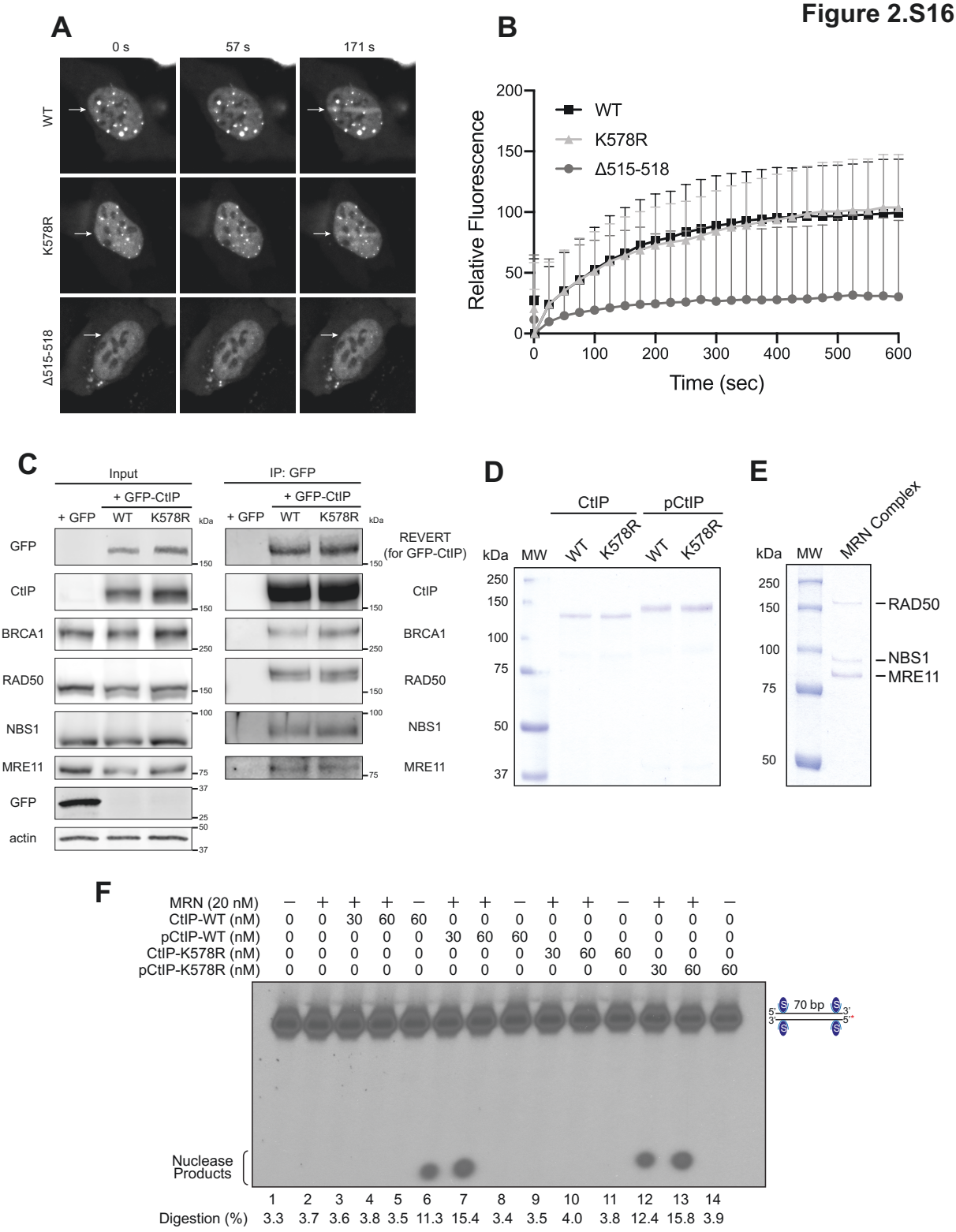

Figure 2.S16: Related to Figure 2.7

A) and B) Live cell time-lapse laser microirradiation experiments performed on U-2 OS cells depleted of endogenous CtIP with siRNA and transfected with siRNA-resistant GFP-CtIP-WT, -K578R, or -Δ515-518. **A)** shows images representative of the results from at least 3 independent experiments; white arrows indicate the linear region of laser microirradiation. **B)** displays the mean relative fluorescence intensity at the microirradiated region of 24 – 48 cells sourced from 3 independent experiments. **C)** HEK293 cells depleted of endogenous CtIP by siRNA were transiently transfected with GFP empty vector or GFP-CtIP-WT or -K578R, then immunoprecipitated (IP) for GFP. Prior to IP, a portion of lysate was saved as an input control. SDS-PAGE and immunoblotting were then performed on both input and IP fractions. The blots displayed are representative of at least 2 independent experiments. **D) and E)** Coomassie Brilliant Blue-stained SDS-PAGE gels showing purification of CtIP-WT- and -K578R or their phosphorylated versions (pCtIP) **(D)** or the MRN complex **(E)** from *Sf*9 cells. MW: molecular weight standards. **F)** *In vitro* MRN endonuclease assay utilizing the products of **D)** and **E)** on a 5'-labeled streptavidin (S)-blocked 70 base pair (bp) double-stranded DNA substrate.

Figure 2.S17

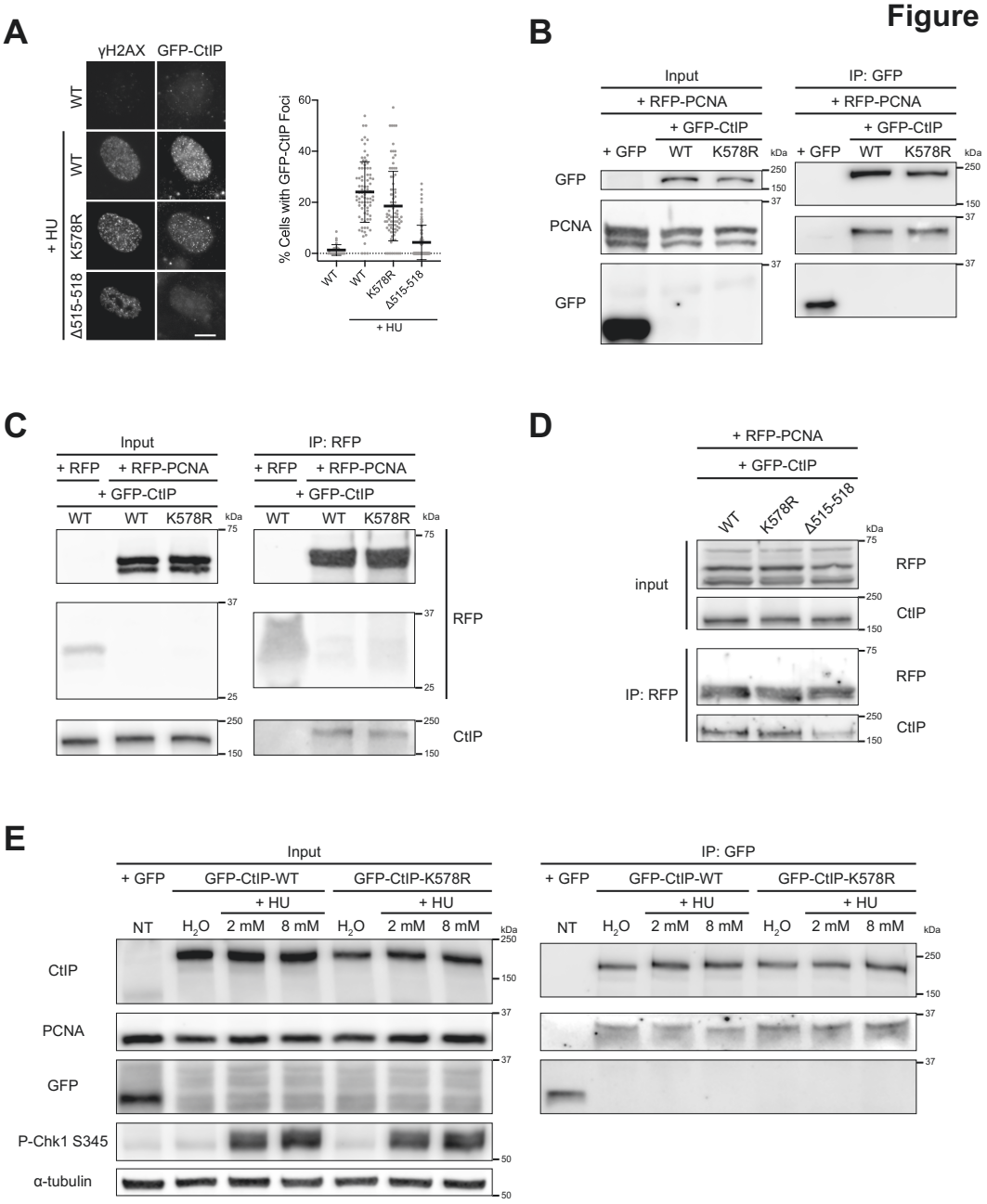

Figure 2.S17: K578 is Not Required for CtIP Recruitment During Replication Stress or its Interaction with PCNA

A) Stable cell lines expressing GFP-CtIP-WT, -K578R, or Δ515-518 were transfected with siRNA to CtIP and then treated or not with HU for 4 hours, then processed for IF staining. Left panel: representative images of the results from 4 independent experiments. Right panel: 826 to 1678 cells (for all except the untreated condition, these were γH2AX$^+$ cells) from 83 to 86 fields of view from 4 independent replicates were scored for the appearance of GFP-CtIP foci. **B)** U-2 OS cells were depleted of endogenous CtIP by siRNA and transfected with RFP-PCNA and either GFP empty vector or siRNA-resistant GFP-CtIP-WT or -K578R. A portion of lysate was saved as an

input control, after which the remainder was processed for IP of the GFP tag. The result shown is representative of at least 4 independent experiments. **C)** U-2 OS cells stably expressing GFP-CtIP-WT or -K578R were depleted of endogenous CtIP by siRNA, then transfected with either RFP-PCNA or RFP empty vector and processed for IP of the RFP tag. Prior to IP, a portion of lysate was saved as an input control. The result shown is representative of at least 4 independent experiments. In the IP fraction, the RFP empty vector pulled down is 57.6% of the amount of RFP-PCNA-WT and -K578R pulled down. **D)** U-2 OS cells were co-transfected with RFP-PCNA and GFP-CtIP-WT, -K578R, or -Δ515-518 and processed for IP of the RFP tag. Prior to IP, a portion of lysate was saved as an input control. The result shown is representative of 2 independent experiments. **E)** U-2 OS cells stably expressing GFP-CtIP-WT or -K578R were depleted of endogenous CtIP by siRNA then treated for 4 hours with 2 or 8 mM HU or 0.8% H_2O (vehicle control). U-2 OS cells without siRNA treatment and transfected with GFP empty vector served as a control sample. A portion of lysate was saved as an input control, after which the remainder was processed for IP of the GFP tag to detect co-immunoprecipitation of endogenous PCNA. The result shown is representative of 2 independent experiments.

Figure 2.S18

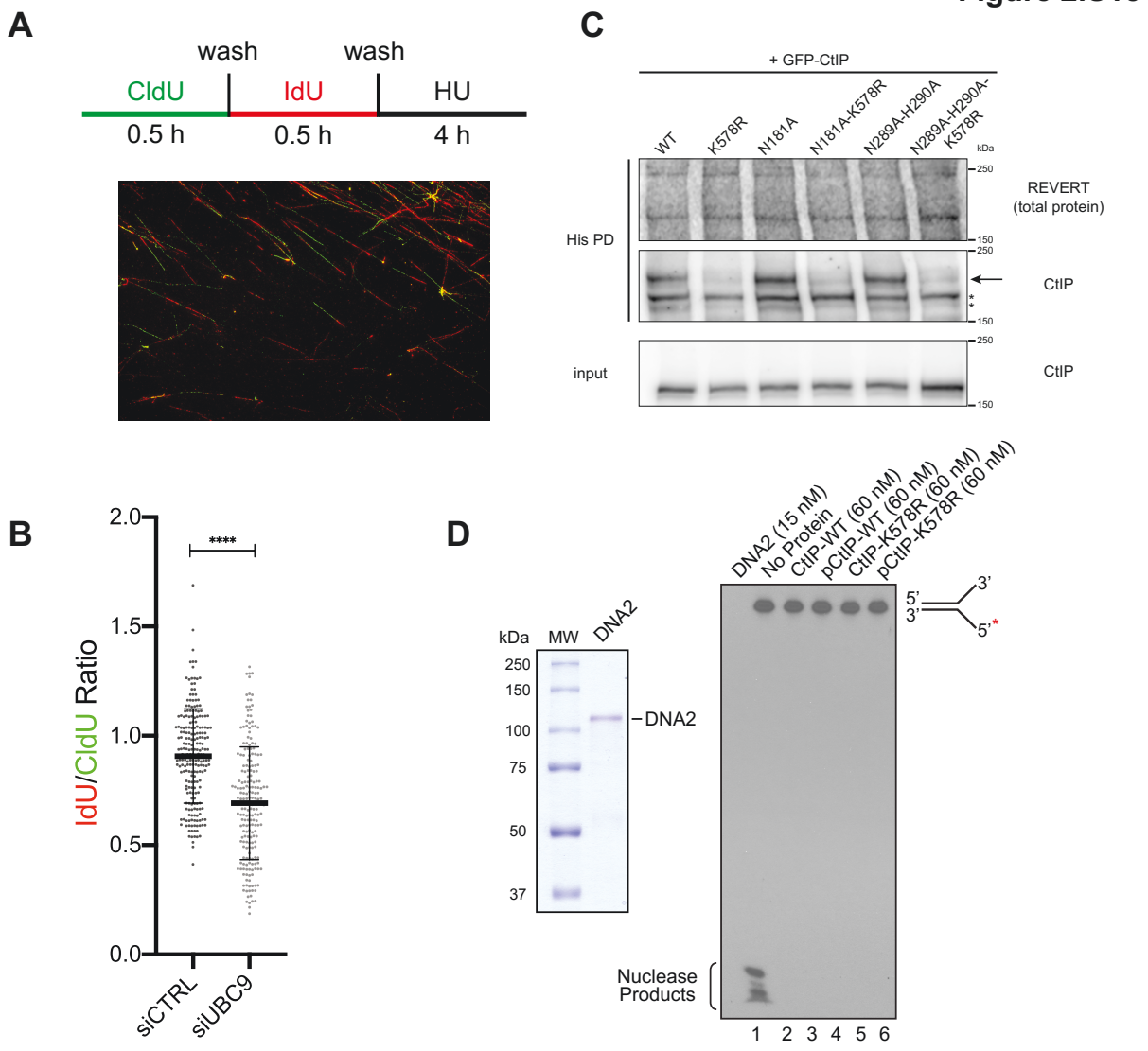

Figure 2.S18: Related to Figure 2.8

A) Top panel: Labeling protocol for all DNA fiber experiments performed: cells were pulse-labeled with 5-chloro-2'-deoxyuridine (CldU) for 30 minutes, then with 5-iodo-2'-deoxyuridine (IdU) for 30 minutes, then treated with 2 mM HU for 4 hours to promote fork stalling. Bottom panel: a typical image of gravity-spread DNA fibers used for quantification of the IdU (labeled in red) / CldU (labeled in green) tract length ratio. **B)** IdU/CldU ratio scatterplot of spread DNA fibers from U-2 OS cells transfected with non-targeting siRNA (siCTRL) or siRNA directed to UBC9 (siUBC9) and treated according to **A)**. 210 to 222 fibers per condition were sourced from 2 independent experiments. **C)** HeLa His_{10}-SUMO-2 cells were transfected with the indicated GFP-CtIP constructs during synchronization to mid-S phase, then harvested. Cell pellets were portioned into input control and His PD fractions and processed accordingly. Shown is a representative result of at least 2 independent experiments. * indicates an exogenous CtIP immunoreactive band that is not of interest; we speculate it is either lower molecular weight SUMO-2-modified CtIP, or

unmodified tagged-CtIP retained in the His PD fraction due to overexpression. **D)** Left panel: Coomassie Brilliant Blue-stained SDS-PAGE gel showing purification of Dna2 from *Sf*9 cells. Right panel: *in vitro* endonuclease assay utilizing Dna2 or phosphorylated (pCtIP) or not WT- or K578R-CtIP (**Fig. 2.S16D**) on a 5'-labeled flap DNA substrate. Dna2 activity was used as a positive control for nuclease activity. MW: molecular weight standards.

2.10.2 Supplementary Tables

Table 2.1: siRNAs

Target	Sense Sequence (5'-3')	Manufacturer	Reference
CtIP	GCUAAAACAGGAACGAAUC	Millipore Sigma	(343)
PIAS1	GGAUCAUUCUAGAGCUUUA	Millipore Sigma	(147)
PIAS4	GGAGUAAGAGUGGACUGAA	Millipore Sigma	(147)
CBX4	GUACUACUACCAGCUCAACUU	Millipore Sigma	(343, 375)
UBC9	CAAAAAAUCCCGAUGGCAC	Millipore Sigma	(376)
Negative Control siRNA	N/A	Qiagen	#1022076

Table 2.2: Primers for Site-Directed Mutagenesis

Mutant	Template	Source for Template	Primer Sequences (5'-3')	Kit
GFP-CtIP-T859A	GFP-CtIP-WT	(343)	Forward:CTTTCCATACAAGTCTGAGCGGAAGGAAAACCAACTTCC Reverse:GGAAGTTGGTTTTCCTTCCGCTCAGACTTGTATGGAAAG	QC
GFP-CtIP-T859E	GFP-CtIP-WT	(343)	Forward:AATATAACCTCTTTCCATACAAGTCTGCTCGGAAGGAAAACCAACTTCCCAAAAATT Reverse:AATTTTTGGGAAGTTGGTTTTCCTTCCGAGCAGACTTGTATGGAAAGAGGTTATATT	QC
GFP-CtIP-Δ515-518	GFP-CtIP-WT	(343)	Forward:GTGACTCTTTATGAGGCTTTG Reverse:GTTTTTAGAAGTCTCACTTCC	Q5
GFP-CtIP-K578R	GFP-CtIP-WT	(343)	Forward:GACAGCATTTTCTTCTCTTATTTGTAATGATGGTTTATTGTCTGGAGA Reverse:TCTCCAGACAATAAACCATCATTACAAATAAGAGAAGAAAATGCTGTC	QC
HA-CtIP-K578R	pICE-HA-CtIP-siR-WT	Addgene #82030	Forward:ATTACAAATAAGAGAAGAAAATGCTG Reverse:GATGGTTTATTGTCTGGAG	Q5
GFP-CtIP-K578R-K896R	GFP-CtIP-K896R	(343)	Forward:ATTACAAATAAGAGAAGAAAATGCTG Reverse:GATGGTTTATTGTCTGGAG	Q5
GFP-CtIP-7KR-R578K	GFP-CtIP-7KR	(343)	Forward:TTACAAATAAAAGAAGAAAATGCTG Reverse: TGATGGTTTATTGTCTGG	Q5
GFP-CtIP-N181A	GFP-CtIP-WT	(343)	Forward:AAGAAAGGAGGCCCCCCATGTCCGATAC Reverse: CGTAGCCGGTTAACGCCA	Q5
GFP-CtIP-N181A-K578R	GFP-CtIP-K578R	generated for this report	Forward:AAGAAAGGAGGCCCCCCATGTCCGATAC Reverse: CGTAGCCGGTTAACGCCA	Q5
GFP-CtIP-N289A-H290A	GFP-CtIP-WT	(343)	Forward:TCTGGAAGGAGCTGCCAAGAAACAGCCTTTTGAG Reverse:CAGTGGTAGAGCTCATCAC	Q5
GFP-CtIP-N289A-H290A-K578R	GFP-CtIP-K578R	generated for this report	Forward:TCTGGAAGGAGCTGCCAAGAAACAGCCTTTTGAG Reverse:CAGTGGTAGAGCTCATCAC	Q5

Primers were custom synthesized by Millipore Sigma.
QC: Quikchange II XL Site Directed Mutagenesis Kit (Agilent)
Q5: Q5 Site-Directed Mutagenesis Kit (New England Biolabs).

Table 2.3: Primers for DNA Sequencing

Primer	Primer Sequence (5'-3')
CtIP 199 Forward	AGGGAACAGCAGAAAGTCCT
CtIP 692 Reverse	CTTTGGTCATAAGTGTCAGCTAC
CtIP 1523 Reverse	CCTTGGCTTTTCTCTTGACG
CtIP 1973 Forward	ATCCGGGAGCAGACCTTTC
CtIP 2289 Reverse	AGTGTGTAGTTTCTTTGTGGCA
CtIP 2409 Forward	GGAGAGAAGAAAACTGCTTGGG

Primers were custom synthesized by Millipore Sigma.

Table 2.4: Primary Antibodies

Antigen	Host	Manufacturer	Catalogue Number	Application
β-Actin	rabbit	Millipore Sigma	A5060	IB (1:5000)
Phospho-ATM at S1981	mouse	Active Motif	39529	IB (1:2500)
BRCA1	rabbit	Bethyl Laboratories	A301-377A	IB (1:3000)
BrdU	mouse	GE Healthcare / Millipore Sigma	GERPN202	IF (1:750)
BrdU (for CldU)	rat	Abcam	ab6326	Fiber (1:100)
BrdU (for IdU)	mouse	BD Biosciences	347580	Fiber (1:100)
CBX4	rabbit	Atlas Antibodies / Millipore Sigma	HPA008228	IB (1:2000)
Phospho-Chk1 at S345	rabbit	Cell Signaling Technology	2348	IB (1:4000)
Phospho-Chk2 at T68	rabbit	Cell Signaling Technology	2197	IB (1:1000)
CtIP	mouse	Active Motif	61141	IB (1:16000)
CtIP	rabbit	Abcam	ab155988	IB (1:16000)
Cyclin A	rabbit	Santa Cruz Biotechnology	sc-751	IB (1:1000)
Cyclin D1	rabbit	Santa Cruz Biotechnology	sc-718	IB (1:1000)
Phospho-DNAPKcs at S2056	rabbit	Abcam	ab18192	IB (1:3000)
Exo1	rabbit	Bethyl Laboratories	A302-640A	IB (1:2000)
FLAG tag	mouse	Sigma	F1804	IB (1:2000)
Geminin	rabbit	Cell Signaling Technology	5165	IB (1:1000)
GFP	mouse	Santa Cruz Biotechnology	sc-9996	IB (1:2000)
HA tag	mouse	BioLegend	901501	IB (1:1000)
His-probe	mouse	Santa Cruz Biotechnology	sc-8036	IB (1:500)
Histone H2A	rabbit	Upstate / Millipore Sigma	07-146	IB (1:2000)
Phospho-Histone H2AX at S139 (γH2AX)	rabbit	Active Motif	39118	IF (1:2000)

Phospho-Histone H2AX at S139 (γH2AX)	mouse	Millipore Sigma	05-636-I	IF (1:2000)
I-*Sce*I	rabbit	Abcam	ab216263	IB (1:1000)
Mre11	mouse	GeneTex	GTX70212	IB (1:3000)
Nbs1	rabbit	Novus Biologicals	NB100-143	IB (1:6000) IF (1:500)
PCNA	mouse	Santa Cruz Biotechnology	sc-56	IB (1:2000)
PIAS1	rabbit	Abcam	ab32219	IB (1:1000)
PIAS4	rabbit	Abcam	ab58416	IB (1:3000)
Phospho-PP1α at T320	rabbit	Abcam	ab62334	IB (1:30000)
Rad50	mouse	Abcam	ab89	IB (1:4000)
Rad51	rabbit	Santa Cruz Biotechnology	sc8349	IF (1:200)
RanGAP-1	mouse	ThermoFisher Scientific	33-0800	IB (1:1000)
Phospho-Rpb1-CTD at S2	mouse	BioLegend	920204	IB (1:1000)
RFP	rabbit	Abcam	ab62341	IB (1:2000)
RPA2	mouse	Abcam	ab2175	IF (1:2000)
SUMO-2/3	mouse	Cytoskeleton	ASM23	IB (1:2500)
α-Tubulin	mouse	GeneTex	GTX628802	IB (1:10000)
α-Tubulin	mouse	Millipore Sigma	T6074	IB (1:10000)
α-Tubulin	mouse	Millipore Sigma	T6199	IB (1:5000)
UBC9	rabbit	Cell Signaling Technology	4786	IB (1:2000)

IB: immunoblot; IF: immunofluorescence; Fiber: DNA fiber assay

Table 2.5: Secondary Antibodies

Antibody Conjugate	Manufacturer	Catalogue Number	Application
chicken anti-rat—Alexa Fluor 488	ThermoFisher Scientific	A-21470	Fiber (1:300)
goat anti-mouse—Alexa Fluor 546	ThermoFisher Scientific	A-21123	Fiber (1:300)
goat anti-mouse—HRP	LI-COR	926-80010	IB (1:5000)
goat anti-rabbit—HRP	LI-COR	926-80011	IB (1:5000)
donkey anti-mouse—IRDye 680RD	LI-COR	926-68072	IB (1:20000)
donkey anti-rabbit—IRDye 680RD	LI-COR	926-68073	IB (1:20000)
donkey anti-mouse—IRDye 800CW	LI-COR	926-32212	IB (1:20000)
donkey anti-rabbit—IRDye 800CW	LI-COR	926-32213	IB (1:20000)
donkey anti-mouse—Alexa Fluor 488	ThermoFisher Scientific	A-21202	IF (1:1000)
donkey anti-mouse—Alexa Fluor 594	ThermoFisher Scientific	A-21203	IF (1:1000)
donkey anti-rabbit—Alexa Fluor 594	ThermoFisher Scientific	A-21207	IF (1:1000)
donkey anti-rabbit—Alexa Fluor 647	ThermoFisher Scientific	A-31573	IF (1:300)
goat anti-mouse—Alexa Fluor 647	Abcam	ab150115	IF (1:300)

HRP: horseradish peroxidase; IB: immunoblot; IF: immunofluorescence; Fiber: DNA fiber assay

Table 2.6: Extraction Buffers for Immunofluorescence Staining

Molecule	Buffer Composition	Conditions
GFP-CtIP, Rad51, RPA, Native BrdU	25 mM HEPES pH 7.9, 300 mM sucrose, 50 mM NaCl, 1 mM EDTA, 3 mM $MgCl_2$, 0.5% Triton X-100	ice-cold 2 times, 3 minutes each
Mre11-GFP	20 mM HEPES pH 7.5, 20 mM NaCl, 5 mM $MgCl_2$, 0.5% Nonidet P-40	ice-cold 2 times, 3 minutes each
Nbs1	10 mM HEPES pH 7.0, 300 mM sucrose, 100 mM NaCl, 3 mM MgCl2, 0.7% Triton X-100, 0.3 mg/mL RNase A (added fresh)	room temperature 2 times, 5 minutes each

Chapter 3 – BMI-1 Regulates DNA End Resection and Homologous Recombination Repair

3.1 Highlights

3.1.1 Summary

BMI-1 is an essential regulator of epigenetic silencing during development. Recently, the role of BMI-1 in the DNA damage response (DDR) has gained much attention, but the exact mechanism of how BMI-1 participates in the process is unclear. Here, we establish a role for BMI-1 in the repair of DNA double-strand breaks (DSBs) by homologous recombination (HR), where it promotes DNA end resection. Mechanistically, BMI-1 mediates DNA end resection by facilitating the recruitment of CtIP, thus allowing RPA and Rad51 accumulation at DNA damage sites. Interestingly, treatment with transcription inhibitors rescues the DNA end resection defects of BMI-1-depleted cells, suggesting BMI-1-dependent transcriptional silencing mediates DNA end resection. Moreover, we find that H2A ubiquitylation at K119 (H2AK119ub) promotes end resection. Taken together, our results identify BMI-1-mediated transcriptional silencing and promotion of H2AK119ub deposition as essential regulators of DNA end resection and thus the progression of HR.

3.1.2 Key Findings

- BMI-1 promotes homologous recombination repair via its RING domain.
- BMI-1 and the H2AK119ub histone mark promote DNA end resection.
- The end resection defect from BMI-1 depletion is rescued by inhibiting RNA Pol II.
- The resection factor CtIP is recruited to H2AK119ub-modified chromatin *in vivo*.

3.1.3 In Brief

Fitieh *et al.* report the Polycomb group protein BMI-1 promotes homologous recombination (HR) repair of DNA double-strand break lesions. BMI-1 promotes DNA end resection, an event preceding HR, by inhibiting RNA polymerase II-dependent transcription, and by facilitating deposition of the H2AK119ub chromatin mark, which helps recruit the resection factor CtIP.

3.1.4 Graphical Summary

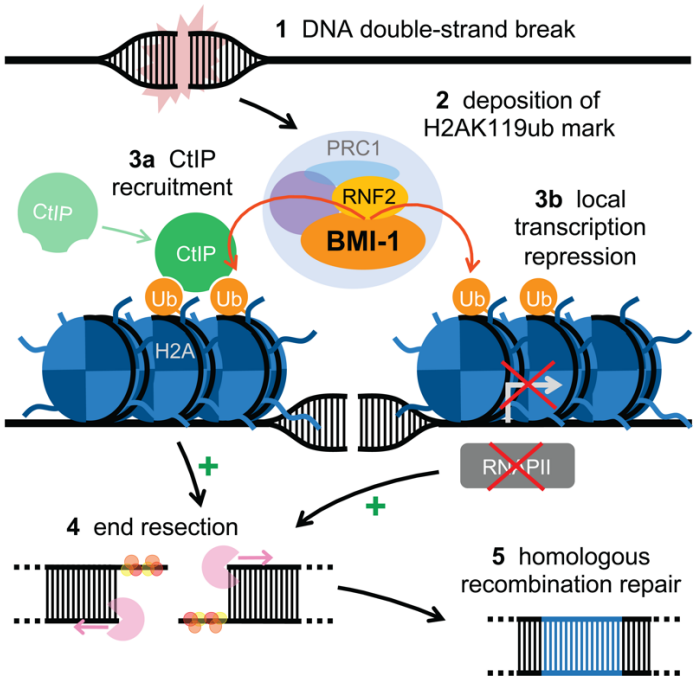

Figure 3.1: Graphical Summary – Chapter 3

3.2 Introduction

Intrinsic and extrinsic damaging agents constantly attack DNA. To combat the harmful consequences of DNA damage, cells have developed a signal transduction network, the DNA damage response (DDR), that is activated upon DNA damage to restore the genome to its original state. An important event in the DDR is the conjugation of ubiquitin to histones H2A and H2AX (130, 213, 217, 220, 296, 298). Histone H2A can be ubiquitylated at different sites, resulting in distinct physiological consequences for DNA repair. In response to DNA double-strand breaks (DSBs), ubiquitylation at lysine residues 125/127/129 by the BRCA1/BARD1 E3 ubiquitin ligase promotes repair by homologous recombination (HR) (377), whereas ubiquitylation at lysine 13/15 by RNF168 seems to promote non-homologous end joining (NHEJ) (220, 378). H2A can also be monoubiquitylated on lysine K119 (H2AK119ub) (379) for the epigenetic silencing of transcription, the modification promoted by Polycomb group (PcG) protein containing complexes, in particular Polycomb Repressive Complex 1 (PRC1) (380–382). H2AK119ub is dependent on the PRC1 subunit BMI-1, which forms a heterodimer with and stimulates the H2AK119-targeting E3 ubiquitin ligase activity of RNF2, another PRC1 subunit (383–385). Intriguingly, RNF2/BMI-1 has also been implicated in DSB repair, with its E3 ubiquitin ligase activity toward H2AK119 being important for this function (130, 296–298, 301).

In response to DNA damage, cells trigger rapid and transient transcriptional pauses in the flanking chromatin to prevent collisions between DNA repair and transcription machineries at damage sites (386–389). The DSB-induced halting of transcription depends on the DDR kinase ATM and involves H2AK119ub (390). The function of PcG proteins in gene silencing, along with the enrichment of the repressive H2AK119ub mark at DSB sites (390, 391), suggest PcG proteins could be involved in damage-dependent transcriptional silencing. Indeed, both BMI-1 and EZH2

(enhancer of zeste 2), a component of PRC2, another Polycomb repressive complex, are required for damage-induced transcriptional silencing (297, 386–389, 391–393). Other mechanistic insights have been gained: H2AK119ub deposition at DSBs depends on the PBAF (polybromo-associated BRG1-associated factor) chromatin remodeling complex and is important for repair of DSBs in close proximity to the transcription machinery, likely through promoting NHEJ (386, 387). Furthermore, the transcriptional elongation factor ENL (eleven–nineteen leukemia) is phosphorylated by ATM in response to DSBs (391), enabling a direct interaction with BMI-1 and promoting H2AK119ub deposition and transcriptional silencing. Still, the role of H2AK119ub in the DDR is still not well understood. One possibility could be that it shields the break site from intrusion of the transcription machinery, establishing a H2AK119ub-dependent barrier of silenced transcription at a defined distance from the break site (394–396). Another possibility is that transcription repression and CtIP-dependent DNA end resection (the 5'→3' generation of single-stranded DNA (ssDNA) overhangs (397), an early step in HR) regulate one another. For instance, depletion of the NuRD (nucleosome remodeling and deacetylase) chromatin remodeler subunit CHD4 (chromodomain helicase DNA binding protein 4) impairs the recruitment and phosphorylation of the ssDNA binding complex RPA, indicating a defect in DNA end resection (398). Overall, although it seems transcriptional silencing is crucial to establish a chromatin compartment amenable to DSB repair, the exact mechanism is unknown, and the interdependencies of end resection and transcriptional silencing need further resolution.

3.3 Materials and Methods

3.3.1 Cell Lines

All cells were cultured at 37°C and in a humidified atmosphere with 5% CO_2. Cell lines used have not been authenticated. U2OS (female in origin) and HEK293 (female in origin) cells were cultured in low glucose DMEM (Dulbecco's Modified Eagle's medium) containing 10% fetal bovine serum (FBS). U2OS cells stably expressing GFP-CtIP were a gift from Steve Jackson (University of Cambridge) and cultured in low glucose DMEM with 10% FBS. U2OS cells stably integrated with the *lacO* array and doxycycline-inducible transcription reporter construct (p3216PECMS2β) at a single locus (U2OS 2-6-3 cells) (399) were a gift from Roger Greenberg (University of Pennsylvania) and maintained in low glucose DMEM with 10% FBS. U2OS 2-6-3 cells stably expressing ER-mCherry-LacI-*Fok*I-DD (208), rtTA, and YFP-MS2 were a gift from Roger Greenberg (University of Pennsylvania) and maintained in low glucose DMEM with 10% charcoal-stripped FBS, 2 μg/mL puromycin, 100 μg/mL hygromycin, and 400 μg/mL G418. In these cells, active transcription at the reporter locus was induced by adding 2 μg/mL doxycycline (Dox, Sigma) to the culture media for 3 hours, after which *Fok*I activity was induced by further adding 1 μM Shield-1 (Selleck Chemicals) and 1 μM 4-hydroxytamoxifen (4-OHT, Sigma) to the culture media for an additional 4 hours. Culture and induction conditions for DR-GFP U2OS cells, U2OS-DSB reporter cells that stably express ER-mCherry-LacI-*Fok*I-DD, and *Asi*SI-ER U2OS cells are described below in the assays requiring them. BMI-1 CRISPR/Cas9 knockout DR-GFP U2OS cells were prepared by co-transfecting into DR-GFP U2OS cells hCas9 (a gift from George Church (Addgene plasmid #41815; http://n2t.net/addgene:41815; RRID:Addgene_41815) (400) and guide RNA (gRNA)-expressing plasmids (gBlocks were ordered from Integrated DNA Technologies (IDT) and cloned into the pCR-Blunt II-TOPO vector (Invitrogen) by TOPO cloning;

gRNA #1 forward sequence: CACCGAACGTGTATTGTTCGTT; gRNA #1 reverse sequence: AAACGGTAACGAACAATACACGTTC; gRNA #2 forward sequence: CACCGTGGTCTGGTCTTGTGAAC; gRNA #2 reverse sequence: AAACAGTTCACAAGACCAGACCAC), selecting for G418 resistance, and isolating a single clone devoid of BMI-1 protein expression.

3.3.2 siRNA, Plasmids, and Transfection

Two different BMI-1 siRNAs (#1, #2) were obtained from Dharmacon. siRNA #1 was the default siRNA for BMI-1. Control siRNA and all other siRNAs were synthesized by Sigma. siRNA transfections were performed at a final concentration of 20 nM siRNA using Lipofectamine RNAiMax (Invitrogen) as a transfection reagent, according to the manufacturer's instructions. Unless indicated otherwise, cells were induced with DNA damage and harvested within 48 – 52 hours post-siRNA transfection. pCAGGS empty vector and pCAGGS-I-*Sce*I for the DR-GFP reporter assay were gifts from Jeremy Stark (City of Hope). The Myc-BMI-1 domain deletion mutants were generated in a previous report (130). The GFP-BAP1 (401) and HA-JARID2-N (1-541) expression constructs (402) were gifts from Dr. Keith Wilkinson (Emory University) and Dr. Neil Brockdorff (Oxford University), respectively. FLAG-HA-USP48 was a gift from Wade Harper (403) (Addgene plasmid #22585; http://n2t.net/addgene:22585; RRID:Addgene_22585). mCherry-LacI-RNF8, -RNF2-WT and -C90S were gifts from Dr. Nico Dantuma (Karolinska Institutet). The GFP-CtIP plasmid was a gift from Pablo Huertas (University of Sevilla). GFP-RNF138-WT and -dUIM were generated in a previous report (132). The panel of FLAG-CtIP-WT and internal deletion mutants was a gift from Junjie Chen (University of Texas) (344). p3XFLAG-Gateway (FLAG empty vector) was a gift from Gordon Chan (University of Alberta). Unless stated

otherwise, U2OS and HEK293 cells were transfected using Effectene transfection reagent (Qiagen) according to the manufacturer's instructions and collected 16-24 hours later. All mock transfections contained the transfection reagent but no nucleic acid.

3.3.3 Cell Treatments

For ionizing radiation treatment (IR), cells were irradiated at a dose rate of 0.8 Gy/min at room temperature using a model CS-600 ^{137}Cs irradiator (Picker). Cells were treated with camptothecin (CPT) at 1 μM for 1 hour. Unless indicated otherwise, cells were treated with PTC-209 at 10 μM for 18 hours prior to induction of DNA damage. Unless indicated otherwise, 0.05% DMSO was used as the vehicle control. Transcription was inhibited by treatment with 100 μM DRB for 3 hours or 10 μg/mL α-amanitin for 1 hour. The ATM inhibitor (ATMi) was KU-55933 and was used at 10 μM. Pharmacological inhibitors were maintained in the culture media during induction of DNA damage.

3.3.4 Immunoblotting

Unless indicated otherwise, cells were harvested into Laemmli Buffer (62.5 mM Tris-HCl, pH 6.8, 2% sodium dodecyl sulfate (SDS), 10% glycerol, 0.05% bromophenol blue, 5% 2-mercaptoethanol), sonicated with a Model 705 Sonic Dismembrator fitted with a microtip probe (Fisher Scientific), and heated at 95°C for 10 minutes yielding whole cell extracts. The extracts were resolved by SDS polyacrylamide gel electrophoresis (SDS-PAGE). After electrotransfer at 110 V for 1 hour onto nitrocellulose membrane (0.2 μm pore size) in transfer buffer (25 mM Tris-HCl, pH 8.3, 192 mM glycine, 20% methanol), the membranes were blocked with 5% fish skin gelatin in Tris-buffered saline (TBS) (50 mM Tris-HCl, pH 7.5, 150 mM NaCl) for 1 hour at room

temperature and next incubated overnight at 4°C with primary antibodies diluted in TBS containing 0.1% Tween-20 (TBST). A panel of commercially available primary antibodies directed against various DNA damage and Polycomb group proteins were used (**Table 3.1**). Next, the membranes were washed with TBST 3 times, 10 minutes each, and incubated with secondary antibodies conjugated to horseradish peroxidase enzyme (HRP) or the fluorescent dyes IRDye 800CW or IRDye 680RD (LI-COR Biosciences) diluted in TBST. After 3 more washes with TBST, IRDye fluorescence or HRP activity were detected using the Odyssey® Fc Imaging System (LI-COR Biosciences). HRP activity was stimulated upon adding the substrate for the enhanced chemiluminescent reaction (Amersham ECL Western Blotting Detection Reagent, GE Healthcare). Densitometric quantification of immunoblot band intensities was performed Image Studio software (LI-COR Biosciences). Immunoblots for H2AK119ub and histone H2A were performed on histone preps prepared as follows prior to SDS-PAGE: cell pellets were lysed in an ice-cold hypotonic lysis buffer (50 mM NaCl, 25 mM HEPES, pH 7.9, 300 mM sucrose, 1 mM EGTA, 3 mM $MgCl_2$, 0.5% IGEPAL CA-630, 2X cOmplete, 1X phosSTOP (both Roche)), after which the insoluble chromatin pellet from centrifugation at 14,000 rpm was subjected to acid extraction and trichloroacetic acid (TCA)-precipitation (404) prior to resuspension in water and then Laemmli Buffer at a final concentration of 1X.

3.3.5 HR Reporter Assay

DR-GFP U2OS cells were obtained from Dr. Jeremy Stark and cultured in high glucose DMEM supplemented with 10% FBS. 24 hours post-siRNA transfection (if RNA interference was required), the cells were electroporated with 7 μg of pCAGGS or pCAGGS-I-*Sce*I using a GenePulser II electroporator (Bio-Rad) (280 V, 975 μF). When needed, 4 μg of Myc-tagged BMI-

1-wildtype or the domain deletion constructs were included in the electroporation. HR efficiencies were analyzed by flow cytometry 24 hours later using a FACSCanto II (BD Biosciences) and expressed as the percentage of GFP-positive cells.

3.3.6 Cell Cycle Profiling

Cells were suspended into 70% ethanol in 1X PBS and incubated for at least 1 hour at -20°C for fixation/permeabilization. They were then washed in PBS, and treated for 30 minutes with 100 µg/mL RNase A in PBS supplemented with 3.8 mM sodium citrate during end-over-end rotation at room temperature. Propidium iodide was then added to a final concentration of 50 µg/mL, and the samples were rotated end-over-end, again at room temperature, for at least 30 minutes before flow cytometry analysis of propidium iodide intensity using a FACSCanto II (BD Biosciences).

3.3.7 Immunofluorescence (IF) Staining

Cells were cultured on #1½ cover slips (Electron Microscopy Sciences), treated as indicated, and fixed with 4% (w/v) paraformaldehyde in PBS (phosphate-buffered saline, pH 7.4) for 20 minutes at room temperature (unless indicated otherwise). Cells were then permeabilized with PBS containing 0.5% Tween-20 for 5 minutes. Next, coverslips were washed twice with PBS and incubated with an appropriate primary antibody at room temperature for 1 hour or overnight at 4°C. Coverslips were rinsed with PBS containing 0.1% Tween-20 and washed twice with PBS before a 30 minute incubation with the appropriate fluorescent dye-conjugated secondary antibodies. Cells were rinsed with PBS containing 0.1% Tween-20 and washed twice with PBS, prior to staining with 10 ng/uL DAPI for 20 minutes and again rinsing in PBS + 0.1% Tween-20. Coverslips were mounted onto slides in 2% propyl gallate in a base of PBS dissolved in 10%

DMSO 80% glycerol. Fluorescence microscopy images were acquired using MetaMorph (Molecular Devices, Inc.) controlling an Axio Imager.D2m microscope (Carl Zeiss, Inc.) equipped with a 14-bit charge-coupled device camera (Cascade; Photometrics). For higher-magnification images, a 1.4 NA Plan-Apochromat 63× objective lens (Carl Zeiss, Inc.) was used. All images in a single figure panel were acquired under the same exposure settings and enhanced for brightness and contrast using the same parameters. Composite figures of collected images were assembled in Photoshop 2020 (Adobe). Scale bars in micrographs represent a width of 10 μm.

3.3.8 Detection of Nuclear Foci by IF Staining

The methods described are additions to the procedure for IF staining described above. For IF detection of RPA2, CtIP, BRCA1, Rad51, BMI-1, and H2AK119ub foci, cells were induced for DNA damage as indicated (if needed) then pre-extracted with cold RPA Extraction Buffer (50 mM NaCl, 25 mM HEPES, pH 7.9, 300 mM sucrose, 1 mM EDTA, 3 mM $MgCl_2$, 0.5% Triton X-100) twice, 3 minutes each, on ice. This was followed by 3 PBS washes and subsequent fixation. For native immunostaining of incorporated BrdU, cells were grown in the presence of 10 μg/mL BrdU (Sigma) for 30 hours prior to induction of DNA damage as indicated. Cells were sequentially extracted with two buffers (extraction buffer 1: 100 mM NaCl, 10 mM PIPES, pH 7.0, 300 mM sucrose, 3 mM $MgCl_2$, 1 mM EGTA, and 0.5% Triton X-100; extraction buffer 2: 10 mM NaCl, 10 mM HEPES, pH 7.5, 3 mM $MgCl_2$, 1% IGEPAL CA-630, 0.5% sodium deoxycholate) on ice, 10 minutes each. Cells were washed 3 times with PBS followed by fixation.

3.3.9 Chromatin Immunoprecipitation (ChIP)

The enrichment of RPA2, CtIP and Rad51 near a sequence-defined DSB site was determined quantitatively by ChIP followed by qPCR in U2OS-DSB reporter cells that stably express ER-mCherry-LacI-*Fok*I-DD (208), a gift from Roger Greenberg (University of Pennsylvania). These cells were maintained in low glucose DMEM supplemented with 10% charcoal-stripped FBS, 2 μg/mL puromycin and 100 μg/mL hygromycin. *Fok*I activity was induced by treatment with 0.5 μM Shield-1 and 300 nM 4-OHT for 3 hours. ChIP and qPCR were performed to loci p1 and p4 near the induced DSB site. The chromatin occupancy near several known *Asi*S1 cleavage sites with initiated RNAPII was determined by ChIP followed by qPCR in U2OS cells stably expressing HA-tagged *Asi*SI-ER (*Asi*SI-ER U2OS) (195), a gift from Dr. Gaelle Legube (Université Paul Sabatier). These cells were maintained in low glucose DMEM containing 10% FBS and 2 μg/mL puromycin. *Fok*I activity was induced by treatment with 300 nM 4-OHT for 3 hours. Regardless of the cell line, cells were grown in 15 cm dishes. After induction, they were washed 2-3 times with PBS. Cells were crosslinked with 1% (w/v) paraformaldehyde in PBS for 10 minutes at room temperature, then glycine was added to a final concentration of 125 mM in PBS to quench the crosslinking reaction for 5 minutes. Cells were scraped into 10 mL of ice-cold PBS and pelleted by cold centrifugation (1000 rpm for 5 minutes). The cell pellet was resuspended in at least 10 volumes of Swelling Buffer (50 mM NaCl, 25 mM HEPES, pH 7.9, 300 mM sucrose, 1 mM EDTA, 3 mM $MgCl_2$, 0.5% Triton X-100), incubated on ice for 10 minutes, homogenized 10-20 times up and down with a Dounce homogenizer, and centrifuged (2000 rpm, 5 minutes, 4°C) to collect isolated nuclei. The nuclear pellet was resuspended in Sonication Buffer (140 mM NaCl, 50 mM HEPES, pH 7.9, 1 mM EDTA, 1% Triton X-100, 0.1% sodium deoxycholate, 1% SDS, 2X cOmplete and 1X phosSTOP (both inhibitor cocktails from Roche) for 10 minutes on ice, and

sonicated at 4°C using a Bioruptor (Diagenode; 15 cycles of 30 sec on, then 30 sec off) to obtain ~200 to 500 bp chromatin fragments. The samples were then centrifuged at 14,000 rpm for 15 minutes at 4°C, after which the supernatant consisting of fragmented chromatin was collected. The supernatant was then pre-cleared by incubation with magnetic Protein G-coupled Dynabeads (Invitrogen) for 2 hours under constant rotation at 4°C. The precleared supernatant was diluted with Dilution Buffer (140 mM NaCl, 50 mM HEPES, pH 7.9, 1 mM EDTA, 1% Triton X-100, 0.1% sodium deoxycholate, 2X cOmplete and 1X phosSTOP) to achieve a final SDS concentration of 0.1% prior to antibody incubation, then incubated with pre-bound antibody–Protein G-Dynabead complexes (containing 2 – 4 μg of antibody) overnight at 4°C under constant rotation. The beads were washed once in low-salt buffer (50 mM NaCl, 20 mM Tris-HCl, pH 8.1, 2 mM EDTA, 1% Triton X-100, 0.1% SDS), once in high-salt buffer (500 mM NaCl, 20 mM Tris-HCl, pH 8.1, 2 mM EDTA, 1% Triton X-100, 0.1% SDS), once in LiCl buffer (250 mM LiCl, 10 mM Tris-HCl, pH 8.0, 1 mM EDTA, 1% IGEPAL CA-630, 1% sodium deoxycholate), and twice in TE buffer (10 mM Tris-HCl, pH 8.0, 1 mM EDTA). The washed beads were then eluted twice into 100 μL of Elution Buffer (1% SDS, 100 mM $NaHCO_3$), and the crosslinks were reversed by overnight incubation at 65°C in Reversal Buffer (0.1 mg/mL RNase A, 0.2 mg/mL Proteinase K, 300 mM NaCl in Elution Buffer). The resulting DNA was purified with QIAquick PCR purification columns (Qiagen), and subjected to qPCR on a 7900HT Fast instrument using the Fast SYBR Green-based detection system (both Applied Biosystems). The primers used were proximal to the cleavage sites by *Asi*SI or *Fok*I (195, 208) and are listed in **Table 3.2**. ChIP data are the mean and standard deviation of three independent experiments.

3.3.10 Quantifying *in vivo* DNA end resection by qPCR

*Asi*SI-ER U2OS (195) cells were treated or not with 300 nM 4-OHT for 4 hours to induce nuclear translocation and DNA cleavage by the stably-expressed *Asi*SI-ER restriction enzyme. The cells were harvested by trypsinization, centrifuged, and DNA from the cell pellet was purified via the DNeasy Blood & Tissue Kit (Qiagen) according to the manufacturer's instructions (the RNAse A incubation step was added as recommended by the manufacturer). The single-stranded DNA generated proximal to two *Asi*SI-induced DSBs within the genome ('Chr 1 DSB' at Chr1:89231183 (405), and 'Chr 22 DSB' at chr22:38864102 – 38864108 (406) was analyzed using the procedure described by Zhou *et al*. (405), with the following modifications. For each sample, 140 ng of extracted DNA was subjected to RNase H treatment for 15 minutes, and digested at 37°C overnight in a 30 µL volume reaction with 16 U of either *Bsr*GI or *Ban*I enzyme (New England Biolabs) or neither (mock digested). Samples were heat inactivated at 65°C, and analyzed by qPCR. 3 µL of the samples (20 ng) were used as templates in 10 µL qPCR reactions to measure resection at loci 335 nt to Chr 1 DSB and 200 nt to Chr 22 DSB (primers are indicated in **Table 3.2**). For each sample, ΔCt was calculated by subtracting the Ct value of the mock-digested sample from the Ct value of the digested sample. The percentage of ssDNA generated by resection at selected sites (ssDNA %) was calculated with the following equation: ssDNA % = 1/(2^(ΔCt-1) + 0.5)*100 (405).

3.3.11 Co-Immunoprecipitation (Co-IP)

U2OS cells were collected in PBS and lysed in IP Lysis Buffer (150 mM NaCl, 10 mM Tris-HCl, pH 7.3, 12.5% glycerol, 0.1 mM EDTA, 0.75 mM $MgCl_2$, 0.5% IGEPAL CA-630, 1X protease inhibitor cocktail (EDTA-free cOmplete, Roche), 1 mM phenylmethylsulfonyl fluoride, 50 mM

sodium fluoride, 25 mM β-glycerophosphate, 50 U/mL Benzonase) for 30 minutes on ice and clarified by centrifugation. ~1 mg of the protein lysate was used per immunoprecipitation. As an input control, 5% of the clarified lysate was collected and denatured in Laemmli Buffer (to a final concentration of 62.5 mM Tris-HCl, pH 6.8, 2% SDS, 10% glycerol, 0.05% bromophenol blue, 5% 2-mercaptoethanol), for 10 minutes at 95°C. Non-specific binding of proteins to the beads was reduced by incubating samples with 50 µL of magnetic Protein G-coupled Dynabeads (Invitrogen) for 1 hour, rotating at 4°C, prior to immunoprecipitation (pre-clearing). Protein extracts were incubated with 50 µL of anti-CtIP- or anti-H2AK119ub-Protein G-Dynabead complexes for 2 hours at 4°C. After carefully washing the beads 3 times with IP lysis buffer, bound proteins were eluted in 2X Laemmli Buffer (125 mM Tris-HCl, pH 6.8, 4% sodium dodecyl sulfate, 20% glycerol, 0.1% bromophenol blue, 5% 2-mercaptoethanol) and denatured at 95°C for 10 minutes. Subsequent SDS-PAGE and immunoblot enabled analysis of immunoprecipitated protein complexes.

3.3.12 Direct Binding Assay

10 cm dishes of HEK293 cells transfected with 1 ug of pEGFP-C1 or 3 µg of GFP-CtIP and were lysed in 350 µL of ice-cold NETN-300 buffer (300 mM NaCl, 1 mM EDTA, 20 mM Tris-HCl, pH 7.4 at 4°C, 0.5% IGEPAL CA-630) supplemented with cOmplete and phosSTOP protease and phosphatase inhibitors (Roche). After clarification of the lysate by centrifugation, the NaCl concentration was adjusted to 150 mM, after which 25 µL of buffer-equilibrated GFP Selector beads (NanoTag Biotechnologies) were added to immunoprecipitate GFP or GFP-CtIP by overnight end-over-end rotation at 4°C. Either the entire volume of lysate from a 10 cm dish (GFP-CtIP) or a quarter of that volume (GFP) of cells was used per immunoprecipitation (IP), each IP

was then used for a single binding reaction. The beads were washed 3 times in cold NETN-300, then once in cold TBS, and once in cold Binding Buffer (50 mM HEPES, pH 7.5 at 4°C, 150 mM Na^+, 125 mM Cl^-, 20% glycerol, 0.05% IGEPAL CA-630, 0.05% 2-mercaptoethanol added fresh). The beads were then rotated end-over-end in 300 µL of cold Binding Buffer containing 2.5 µg of the chosen ubiquitylated H2A peptide (UbiQ) (**Table 3.3)**, 12.5 µg of biotinylated H2A-C-terminal peptide (Bio Basic Canada Inc.), or neither for 2 hours at 4°C. After 4 washes in cold Binding Buffer, immobilized proteins/peptides were eluted from the beads into 2X Laemmli Buffer for 15 minutes at 95°C. The eluates were subsequently resolved by SDS-PAGE, with components detected by immunoblot or blotting using streptavidin-HRP conjugate (GE Healthcare).

3.3.13 Far Western Blotting Assay

HEK293 cells were transfected with the FLAG-CtIP deletion panel, pEGFP-C1, GFP-CtIP, -RNF138-WT or -dUIM in 10 cm dishes. GFP construct-expressing cells were lysed and immunoprecipitated as in the Direct Binding Assay but washed instead 3 times in cold NETN-500 buffer (500 mM NaCl, 1 mM EDTA, 20 mM Tris-HCl, pH 7.4 at 4°C, 0.5% IGEPAL CA-630) prior to their elution into 2X Laemmli Buffer. FLAG-CtIP-expressing cells were lysed in 300 µL of ice-cold NETMN buffer (500 mM NaCl, 1 mM EDTA, 50 mM Tris-HCl, pH 7.4 at 4°C, 2.5 mM $MgCl_2$, 0.5% IGEPAL CA-630) containing cOmplete and phosSTOP protease and phosphatase inhibitors (Roche). After clarification of the lysate by centrifugation, the buffer composition was adjusted to 150 mM NaCl, ~20 mM Tris-HCl, 0.3% IGEPAL CA-630, ~0.7 mM EDTA, ~0.5 mM $MgCl_2$, after which 30 µL of anti-FLAG M2 magnetic beads (Sigma) were added to the entire volume of lysate for overnight immunoprecipitation with end-over-end rotation at 4°C. The magnetic beads were then washed 3 times in cold TBS prior to elution into 2X Laemmli

Buffer. All eluates (or 1 μg of bovine serum albumin, BSA) were subsequently resolved by SDS-PAGE and transferred onto Immobilon-FL PVDF membrane (Millipore). REVERT total protein stain (LI-COR Biosciences) was used to verify suitable electrotransfer. The transferred proteins were then denatured and renatured by incubating the membrane using the AC buffers, temperatures, and timing described in Wu *et al.* (407), with the exception that 1 mM dithiothreitol was substituted with 1 mM 2-mercaptoethanol. Renaturation in AC buffer containing no guanidinium-HCl was performed at 4°C overnight. The membrane was then blocked in Far Western Binding Buffer (50 mM HEPES, pH 7.5 at 4°C, 150 mM Na^+, 125 mM Cl^-, 20% glycerol, 0.05% IGEPAL CA-630) containing 5% skim milk powder (milk) for 2 hours at 4°C, and incubated overnight at 4°C with 10 μg of recombinant HA-tagged human ubiquitin (BostonBiochem) diluted in 15 mL of Far Western Binding Buffer containing 2% milk. After 3 15-minute washes in Far Western Washing Buffer (150 mM NaCl, 50 mM Tris-HCl, pH 7.5, 20% glycerol, 0.05% Tween-20) at room temperature, the membrane was incubated overnight at 4°C in rabbit anti-HA antibody (Abcam, ab9110) diluted 1:1000 in Far Western Binding Buffer containing 3% milk. This was followed by 3 15-minute washes in Far Western Washing Buffer, incubation for 1 hour with goat anti-rabbit—HRP secondary antibody (LI-COR Biosciences) diluted 1:5000 in Far Western Binding Buffer, and 3 15-minute washes in Far Western Washing Buffer, all at room temperature, after which the membrane was subjected to chemiluminescent development (ECL reagent, GE Healthcare). To strip off bound HA-ubiquitin, the membrane was incubated for 1 hour in 6 M guanidinium-HCl, rinsed in double-distilled water, and air-dried overnight. The membrane was then rehydrated and subjected to conventional immunoblotting (described above), using either mouse anti-FLAG or mouse anti-GFP antibodies to detect immobilized proteins. If the membrane

was to be re-immunoblotted for other epitopes on the immobilized proteins, it was stripped again using 6 M guanidinium-HCl prior to.

3.3.14 Quantification and Statistical Analysis

Information regarding the number of independent biological replicates performed (n) that the figure represents or that is included in graphs shown is found in the corresponding figure legend (in both main and supplementary figures). The remaining statistical details are described here. Graphs were generated using Prism version 8 (GraphPad), with error bars representing the standard deviation from the mean value. For IF micrographs, quantification of nuclear foci intensity was performed using the Granularity application in MetaXpress 6 software (Molecular Devices, LLC). Typically, 100-120 cells (minimum: 86 cells, maximum: 276 cells) were quantified per condition. The resulting values (integrated intensity of foci per nucleus) were then normalized to the average integrated intensity of foci per nucleus value for the control condition (e.g. control siRNA or DMSO vehicle control) and plotted in a scatterplot, with each point shown representing a single nucleus. The parameter of % positive cells was determined by manually scoring ~200 cells per condition from IF images. Colocalization between channels of IF micrographs was represented by the Pearson correlation coefficient calculated using ImageJ software. Analysis of statistical significance was performed in Prism version 8 (GraphPad) and is presented in the graphs, with ns denoting not significant, * denoting $p \leq 0.05$, ** denoting $p \leq 0.01$, *** denoting $p < 0.001$, and **** denoting $p < 0.0001$. Two-tailed, unpaired, parametric *t* tests (unpaired *t* test) were used for qPCR data presented in **Figs. 3.3B, 3.3D, 3.3F, 3.4D, and 3.4H**. Two-tailed, unpaired, non-parametric *t* tests (Mann-Whitney test) were used for nuclear foci intensity data in **Figs. 3.3A, 3.3C, 3.3E, 3.4A, 3.5C-D, 3.S9F, and 3.S10E**.

3.4 Results

3.4.1 Depletion of BMI-1 Inhibits DNA Repair by HR

To investigate the role of BMI-1 in HR repair, we depleted BMI-1 levels by two different short interfering RNAs (siRNAs) in U2OS osteosarcoma cells stably expressing the DR-GFP (Direct Repeat-GFP) reporter system (408). This reporter system exploits an I-*Sce*I restriction site situated in one of two mutated green fluorescent protein (GFP) genes oriented as direct repeats. Expression of I-*Sce*I generates a site-specific DSB, which, when repaired through HR, results in functional GFP expression (**Fig. 3.2A**). We verified that our siRNAs could reduce BMI-1 protein levels (**Fig. 3.2B**) and monitored their impact on the cell cycle in U2OS cells. siRNA #1 had no impact on the cell cycle distribution, whereas siRNA #2 slightly increased the proportion of cells in S phase (**Fig. 3.2C**). Consistent with its role as a downstream HR effector, knockdown of Rad51 (**Fig. 3.S9A**) strongly decreased the frequency of HR (**Fig. 3.2D**). Depleting BMI-1 with both BMI-1 siRNAs led to a considerable repression of HR, the total GFP-positive population decreasing from 8.3% to 3.2% and 2.65% (**Fig. 3.2D**). Importantly, this repressive effect was not due to indirect effects on the cell cycle, as it did not result in a higher proportion of cells in G1 phase (which is refractory to HR) (**Fig. 3.2C**). Moreover, siRNA-mediated depletion of BMI-1 did not alter Rad51 expression, indicating that the repression of HR was not due to loss of Rad51 (**Fig. 3.S9B**). To confirm the role of BMI-1 in HR, we used two complementary approaches. First, we generated BMI-1 knockout (KO) DR-GFP U2OS cells via CRISPR/Cas9-mediated gene editing (**Fig. 3.S9C**). Consistent with the notion of a function for BMI-1 in HR, BMI-1 knockout cells exhibited a defect in HR repair (**Fig. 3.2E**). Second, we used the newly identified small molecule inhibitor of BMI-1 developed by PTC Therapeutics, PTC-209, that reduces BMI-1 expression post-transcriptionally (409). Several studies have shown PTC-209 is a potent and specific inhibitor

of BMI-1 *in vitro* and *in vivo* (409–411). Treating U2OS cells with PTC-209 reduced BMI-1 expression without affecting that of Rad51 (**Fig. 3.2F**) and abolished the H2AK119ub mark (**Fig. 3.S9D**). Similar to BMI-1 knockdown and knockout, PTC-209 treatment decreased the frequency of HR (**Fig. 3.2G**). This effect was also not due to an altered cell cycle profile (**Fig. 3.S9E**). BMI-1 contains an N-terminal RING finger domain (RING), which closely interacts with the RING finger of RNF2, the dimer of the two RING domains being sufficient for H2A ubiquitylation (120, 121). It also contains a central helix-turn-helix-turn-helix-turn domain (H-T) and a C-terminal proline- and serine-rich PEST-like domain (**Fig. 3.2H**). To confirm a direct role for BMI-1 in HR, and identify the domains required for BMI-1 function in HR, we expressed Myc-tagged BMI-1 deletion mutants lacking the PEST-like (dPEST), RING (dRING), or H-T (dH-T) domains in DR-GFP U2OS cells depleted of BMI-1. Overexpressing full-length BMI-1 (WT), BMI-1-dPEST, and BMI-1-dH-T, but not BMI-1-dRING, rescued the downregulation of HR in BMI-1 knockdown cells (**Fig. 3.2I**), suggesting BMI-1's RING domain is required for its ability to promote HR. Consistently, our findings demonstrate that BMI-1 promotes efficient HR repair.

Figure 3.2

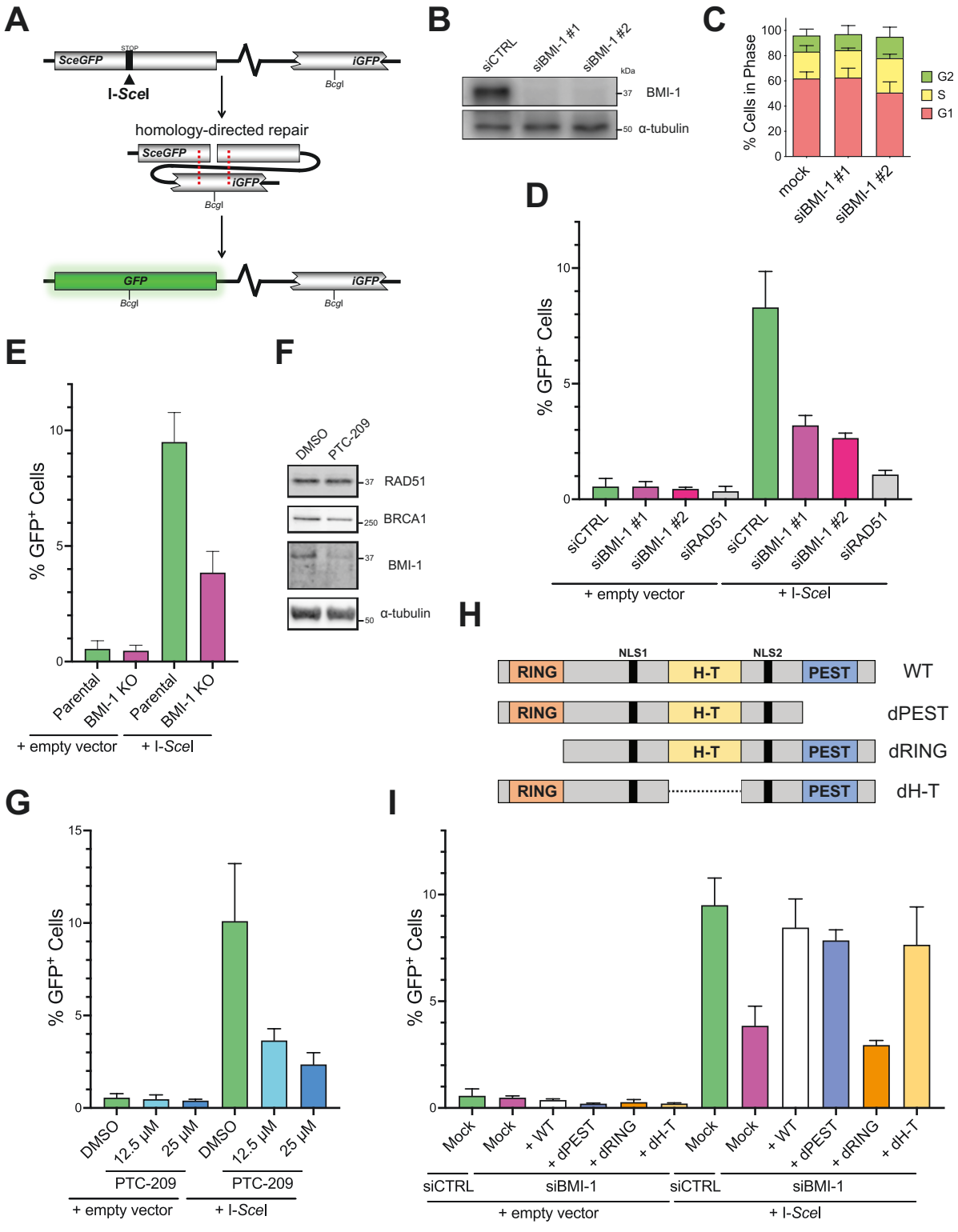

Figure 3.2: Depletion of BMI-1 Inhibits DNA Repair by HR

A) Schematic of the DR-GFP reporter locus used to measure HR activity. **B)** Immunoblots of whole cell extracts from U2OS transfected with control siRNA (siCTRL) or siRNAs targeting BMI-1. **C)** Cell cycle profiles of U2OS cells mock transfected or transfected with BMI-1 siRNA. **D)** DR-GFP U2OS cells treated with siRNA for 24h were transfected with I-*Sce*I or empty vector for another 24h. GFP-positive cells were quantified by flow cytometry. **E)** HR reporter assay in parental DR-GFP U2OS or those with BMI-1 knocked out by CRISPR/Cas9. **F)** Immunoblots of U2OS treated with PTC-209 or DMSO. **G)** HR reporter assay in DR-GFP U2OS transfected with I-*Sce*I or empty vector for 6h then treated with PTC-209 or 0.1% DMSO for 24h. **H)** Schematics of BMI-1 domain deletion constructs. **I)** HR reporter assay in DR-GFP U2OS transfected with siRNA for 24h, then transfected with Myc-BMI-1-wildtype (WT) or deletion constructs and empty vector or I-*Sce*I for 24h. (B, F): representative results from 3 biological replicates; (C): 3 biological replicates pooled together; (D-E, G, I): 2 biological replicates pooled together. Error bars represent the standard deviation of the mean.

3.4.2 BMI-1 Regulates HR Repair at the Step of DNA End Resection

We next investigated which step BMI-1 might be acting in HR repair. We first monitored the accumulation of Rad51 at DNA damage sites in U2OS cells via immunofluorescence (IF) staining. The induction of Rad51 foci by the topoisomerase I inhibitor camptothecin (CPT) was reduced in cells depleted of BMI-1 by siRNA (**Fig. 3.3A**). The effect was specific because knockdown of BMI-1 did not inhibit the ability for cells to form γH2AX foci, a marker for DSBs (**Fig. 3.3A**), nor alter Rad51 expression (**Fig. 3.S9B**). Similar results were obtained using cells treated with PTC-209 (**Figs. 3.3A**, **3.2F**). We also examined Rad51 recruitment to DNA adjacent to DSBs induced at an integrated transgene in cells stably expressing mCherry-LacI-*Fok*I (the U2OS-DSB reporter system (208)). We performed chromatin immunoprecipitation (ChIP) for Rad51 at two loci proximal to the *Fok*I-induced DSB site. Rad51 recruitment to these sites was inhibited upon depleting BMI-1 via siRNA or PTC-209 treatment (**Fig. 3.3B**), recapitulating our findings seen via IF staining (**Fig. 3.3A**) and consistent with the inhibition of HR upon BMI-1 depletion (**Fig. 3.2**).

We decided to probe further upstream in the HR pathway, asking if the Rad51 recruitment defect could be an indirect effect of BMI-1 acting at an earlier stage in HR. Interestingly, the

recruitment of BRCA1 to CPT-induced DSBs was also significantly impaired upon reducing BMI-1 via siRNA and PTC-209 (**Fig. 3.S9F**), despite the treatments not affecting BRCA1 expression (**Figs. 3.S9B, 3.2F**). As BRCA1 acts at both early and later stages of HR, we next examined if events preceding BRCA1 activity were impacted upon BMI-1 reduction. BMI-1 knockdown or PTC-209 treatment had no discernible impact on the formation of damage-induced Mre11 or Nbs1 foci (**Figs. 3.S9G-H**), suggesting a role for BMI-1 downstream of the MRN complex but upstream of the action of BRCA1 in HR.

Resection from DSB ends is a critical initial reaction in HR and occurs downstream of MRN recruitment but upstream of Rad51. We thus asked if the action of BMI-1 could be at the level of DNA end resection. The progress of end resection was visualized by IF staining for the accumulation of the RPA complex at sites of DSBs. RPA is an essential HR protein complex with a high binding affinity to ssDNA (412), therefore its accumulation serves as a readout for the extent of resection. Inhibiting BMI-1 expression by PTC-209 or siRNA markedly reduced the accrual of RPA subunit RPA2 (**Fig. 3.3C**), as well as that of the end resection factor CtIP (**Fig. 3.3E**), to sites of CPT-induced damage. A similar result was obtained for both proteins via ChIP in the U2OS-DSB system (**Figs. 3.3D and 3.3F**), confirming BMI-1 reduction impairs CtIP and RPA recruitment to DSBs. Since phosphorylated CtIP activates Mre11 of the MRN complex to initiate DNA end resection (52, 58, 59), a tempting model is that depleting BMI-1 results in an inability to recruit CtIP to the MRN situated at DSBs, preventing the progression of end resection.

To confirm end resection is regulated by BMI-1, we resorted to three other methods to monitor its progress. First, we used a 5-bromo-2'-deoxyuridine (BrdU)-based IF assay for visualizing the ssDNA overhangs that are products of resection. BrdU is incorporated into cellular DNA upon its addition to the growth medium. Under native conditions, the BrdU epitope is only

accessible within ssDNA, so detection of BrdU without acid denaturation can visualize resected DNA. In line with our observations for RPA2 foci, reducing BMI-1 levels by siRNA or PTC-209 substantially inhibited the formation of BrdU foci (**Fig. 3.4A**).

In the presence of DSBs, both histone H2AX and RPA2 are phosphorylated by the DDR kinases ATM, ATR, and DNA-dependent protein kinase, with RPA2 phosphorylation serving as a readout for DNA end resection (413, 414). By an immunoblotting approach, we observed that pharmacological or siRNA depletion of BMI-1 impaired RPA2 phosphorylation, detected using a phospho-specific antibody and by the slower electrophoretic migration of a portion of total RPA2 (**Figs. 3.4B-C**). Because we did not observe impairment of γH2AX in response to CPT treatment (**Fig. 3.4B**), we reasoned that the reduced RPA2 phosphorylation was from inefficient generation of ssDNA and impaired recruitment of RPA2 to DSBs, where it is highly accessible to the DDR kinases, rather than to impaired function of the kinases. As a control, we verified that depleting CtIP, which is required for efficient resection, could prevent CPT-induced RPA2 phosphorylation at S4/S8 (**Fig. 3.S10A**), as previously reported (58). Furthermore, the phosphorylation of checkpoint kinase 1 (Chk1), a target for ATR kinase activity upon ATR associating with RPA-coated ssDNA (58, 89, 91), was impaired in PTC-209 treated cells stimulated with CPT (**Fig. 3.4C**), illustrating the consequences of the block in resection on DNA damage signaling.

As a third approach, we used an established qPCR-based assay to measure the ssDNA present upon the induction of defined DSBs within the genome (405). Here, we used the *Asi*SI-ER system, in which the restriction endonuclease *Asi*SI is fused to the estrogen receptor hormone-binding domain (ER) and stably expressed in U2OS cells (195). Treatment with 4-hydroxytamoxifen (4-OHT) induces *Asi*SI translocation to the nucleus, where it can generate DSBs (**Fig. 3.S10B**). We found that BMI-1 depletion by both siRNA and PTC-209 significantly reduced

the ssDNA near two *Asi*SI cut sites (**Fig. 3.4D**), again demonstrating BMI-1 reduction inhibits DNA end resection. Altogether, our data show BMI-1 regulates HR by promoting DNA end resection, particularly by promoting the recruitment of CtIP but not regulating that of Nbs1 or Mre11.

3.4.3 Transcriptional Silencing at DSBs Requires BMI-1 but Not CtIP

We turned to study the interplay between transcriptional silencing and end resection. ATM-dependent transcription silencing occurs in *cis* to DSBs, and this is dependent on ATM, H2AK119ub, and BMI-1 and RNF2 (276, 302, 415). Intriguingly, in budding yeast, DNA end resection has been shown to regulate transcriptional silencing at sites of DNA damage (416). We thus wondered if this occurred in human cells, and as CtIP has also been characterized as a transcriptional co-repressor (263), if it could also be promoting transcriptional silencing at DSBs prior to regulating DNA resection. We knocked down CtIP in the context of a reporter system that visualizes transcriptional repression adjacent to DSBs (276, 399) (**Fig. 3.4E**). This U2OS cell line stably expresses ER-mCherry-LacI-*Fok*I-DD, which can be induced to cut at the reporter locus' *lacO* tandem array upon Shield-1 and 4-OHT treatment (208). Downstream of the *lacO* array, doxycycline treatment induces transcription of CFP-SKL, whose messenger RNA contains stem-loop repeats that are recognized by the stably expressed yellow fluorescent protein-tagged viral coat protein MS2 (YFP-MS2) (**Fig. 3.4E**). As reported (276), induction of *Fok*I activity inhibited the production of nascent transcripts from the reporter locus, seen by YFP-MS2 signal, and inhibiting ATM activity strongly restored transcription near the DSB site (**Figs. 3.4F-G**). Another study implicated RNF2/BMI-1 in DSB-proximal H2AK119 ubiquitylation and transcriptional repression using a comparable reporter (302). Supporting these findings, BMI-1 depletion by

siRNA and PTC-209 appreciably de-repressed transcription near the DSB (**Figs. 3.4F-G**). On the contrary, depleting CtIP did not affect transcriptional repression near the DSB site. While this result is consistent with a previous observation (276), we chose to confirm it using a complementary approach in case loss of nascent RNA production was due to the stalling of RNA polymerase II (RNAPII) after DNA damage (301). We monitored by ChIP the presence of active, initiated RNAPII near three *Asi*SI-generated DSBs (417) by detecting serine 5 (S5)-phosphorylated heptapeptide repeats at the C-terminal domain of RNAPII's large subunit (CTD) (**Fig. 3.S10B**). As expected, phospho-S5-CTD-RNAPII was impaired at *Asi*SI-generated break sites, indicating efficient inhibition of transcription around DSBs (**Fig. 3.4H**). However, while BMI-1 depletion restored accumulation of active RNAPII to levels prior to DSB induction, CtIP depletion could not, implying efficient transcriptional silencing near DSBs despite the absence of CtIP (**Fig. 3.4E**). Using two approaches, we thus conclude and reaffirm that CtIP does not promote transcriptional silencing proximal to DSBs, unlike BMI-1.

Figure 3.3

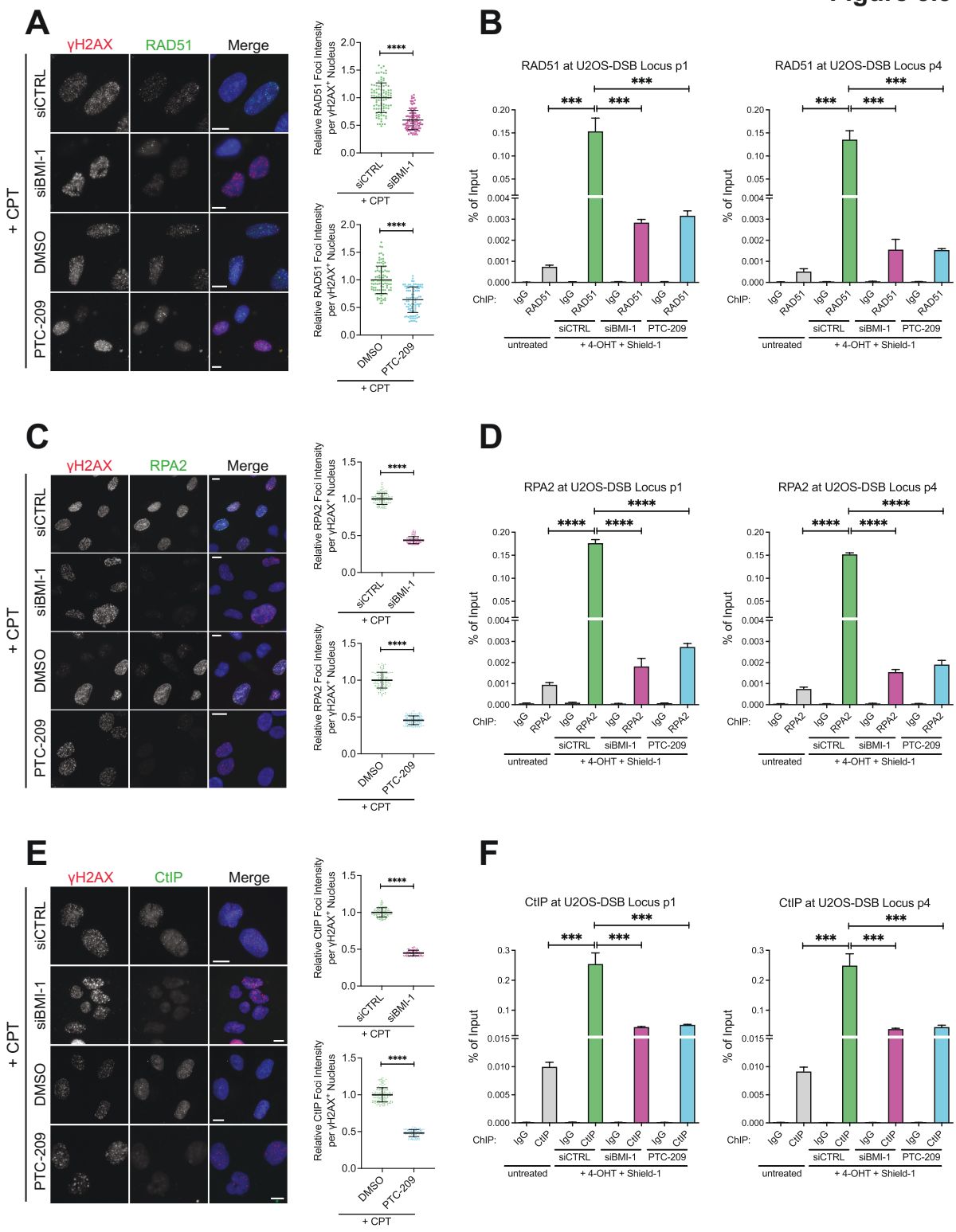

Figure 3.3: BMI-1 Mediates the Accrual of HR Repair Factors

A), C), E) U2OS cells were treated with siRNA for 48h, or 0.05% DMSO or 10 μM PTC-209 for 18h, then 1 μM CPT was applied for 1h. Cells were processed for immunofluorescence (IF) staining of damage-induced foci as indicated. Left: representative images; right: scatterplots of relative integrated intensity of nuclear foci in $\gamma H2AX^{+}$ cells; each point is from one cell. **B), D), F)** U2OS-DSB reporter cells stably expressing ER-mCherry-LacI-*Fok*I-DD were treated or not with siRNA for 48h or 10 μM PTC-209 for 18h. *Fok*I activity at the *lacO* array was induced for 3h by adding 4-OHT and Shield-1. The accrual of the indicated proteins at two loci proximal to the DSB site (p1, p4) was quantified by ChIP. (A, C, E): representative results from ≥3 biological replicates; (B, D, F): 3 biological replicates pooled together. Error bars represent the standard deviation from the mean. *** $p < 0.001$; **** $p < 0.0001$. Scale bars: 10 μm.

Figure 3.4

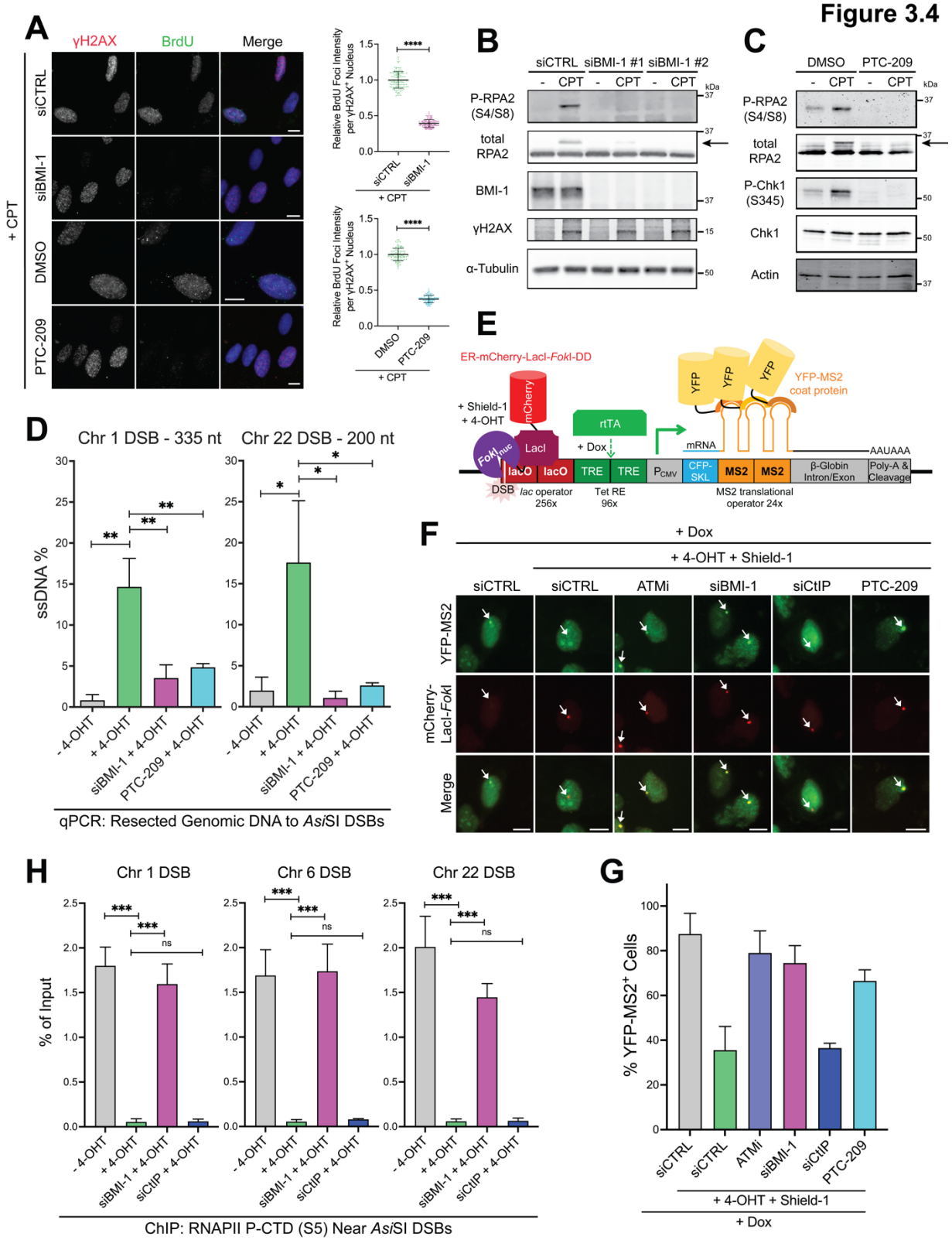

Figure 3.4: BMI-1 Regulates DNA End Resection; Transcriptional Silencing at DSBs Requires BMI-1 but Not CtIP

A) U2OS cells cultured in the presence of BrdU were treated with siRNA, DMSO, or PTC-209. 1 μM CPT was added to the media 1h prior to IF staining. Quantifications as in **Fig. 3.3A**. **B), C)** Immunoblot analysis of U2OS treated with siRNA (B) or PTC-209 (C) then treated 1h with CPT. Arrows denote the slower migration of phospho-RPA2. **D)** qPCR detection of resected DNA near two *Asi*SI-induced DSB sites in *Asi*SI-ER U2OS cells treated with BMI-1 siRNA or PTC-209; *Asi*SI activity was induced by 4-OHT. **E)** Schematic of the DSB-proximal transcription reporter in U2OS 2-6-3 cells stably expressing ER-mCherry-LacI-*Fok*I-DD, rtTA, and YFP-MS2. **F)** Cells in E) were treated with siRNAs or PTC-209. Transcription at the reporter locus was induced with doxycycline (Dox) for 3h. *Fok*I activity was then induced for 4h by adding 4-OHT/Shield-1 to the media, after which the cells were fixed and imaged. Treatment with ATM inhibitor (ATMi) was done during *Fok*I induction. Arrows denote the reporter locus. **G)** Quantification of YFP-MS2^{+} cells in F). **H)** ChIP was used to quantify initiated RNAPII at loci proximal to three *Asi*SI-induced DSB sites in *Asi*SI-ER U2OS cells treated with or without the indicated siRNA; *Asi*SI activity was induced by 4-OHT. (A-C, F): representative results from ≥3 biological replicates; (D, H): 3 biological replicates pooled together; (G): 2 biological replicates pooled together. Error bars represent the standard deviation from the mean. ns: not significant; * $p \leq 0.05$; ** $p \leq 0.01$; *** $p < 0.001$; **** $p < 0.0001$. Scale bars: 10 μm.

3.4.4 BMI-1-Mediated Transcriptional Silencing Promotes DNA End Resection

We next tested whether BMI-1-mediated transcriptional silencing regulates DNA end resection. We first examined the impact of broad transcriptional inhibition on the occurrence of resection. We acutely inhibited RNAPII activity in U2OS cells with α-amanitin or 5,6-dichloro-1-β-D-ribofuranosylbenzimidazole (DRB). Effective RNAPII inhibition with these agents was confirmed by assessing 5-fluorouridine (5-FU) incorporation in cells, which marks nascent RNA (**Fig. 3.S10C**). We measured DNA end resection by IF for native BrdU or RPA2 foci formation in cells pre-treated with DRB or α-amanitin and subjected to CPT. Proficient and enhanced resection was observed using either inhibitor (**Figs. 3.5A-D**), indicating transcriptional repression promotes end resection. As BMI-1 mediates transcriptional silencing near DSBs (**Figs. 3.4F-H**) and promotes resection (**Figs. 3.3C-D, 3.4A-D**), we hypothesized that the end resection defect in BMI-1-depleted cells could be rescued by concurrent transcriptional inhibition, bypassing the dependence on BMI-1. We thus pre-treated BMI-1 siRNA-transfected cells with DRB or α-amanitin, then monitored native BrdU and RPA2 foci formation in response to CPT. Indeed,

inhibiting transcription sufficiently rescued the end resection defects caused by BMI-1 deficiency (**Figs. 3.5E-H**). We also examined if CtIP localization to DSB sites (presumably to maintain actively proceeding resection) could be restored in BMI-1-depleted cells upon transcriptional inhibition. Combining BMI-1 siRNA with DRB treatment partially rescued CtIP foci formation in response to CPT (**Figs. 3.S10D-E**). Overall, we conclude that DNA end resection is promoted by BMI-1-mediated transcriptional repression.

3.4.5 H2A Ubiquitylation at K119 is Important for DNA End Resection

As BMI-1 promotes H2AK119 ubiquitylation (128, 379), we wished to determine if H2AK119ub was also involved in resection. To this aim, we used two different tools to curtail the response to H2AK119ub in cells. First, we overexpressed GFP-tagged BAP1, a deubiquitylating enzyme that upon overexpression will reduce the H2AK119ub mark (418, 419) (**Fig. 3.6A)**, a consequence we confirmed by immunoblotting (**Fig. 3.6B**). As a control, we verified that our H2AK119ub antibody was specific to the modification, as BMI-1 depletion via PTC-209 or siRNA, and siRNA-mediated depletion of RNF2, were all able to reduce detection of the modification, despite even loading of histone H2A (**Fig. 3.S9D**). Secondly, we made use of an HA-tagged N-terminal fragment of PRC2 cofactor JARID2, HA-JARID2-N, which contains a ubiquitin interacting-motif (UIM) that binds to H2AK119ub (402) (**Fig. 3.6A)**. We reasoned that expressing HA-JARID2-N would sequester H2AK119ub-dependent signaling events but not reduce H2AK119ub levels, the latter of which was confirmed by immunoblot (**Fig. 3.6B**). Interestingly, both GFP-BAP1 and HA-JARID2-N overexpression inhibited the formation of damage-induced RPA2 foci, similar to the knockdown of BMI-1 (**Figs. 3.6C-D**). Importantly, both manipulations did not impact the expression of total RPA2 (**Fig. 3.6B**), eliminating the possibility

that the lack of RPA2 foci was from reduced expression of the protein. As well, the effect was specific to H2AK119ub, as overexpressing USP48, a deubiquitylase for ubiquitylation at residues K125/K127/K129 on H2A (420) (**Fig. 3.6A)**, was unable to inhibit RPA2 foci formation (**Figs. 3.6C-D**). The effect of GFP-BAP1 and HA-JARID2-N overexpression was also not due to cell cycle changes, as transfecting the constructs did not increase the proportion of cells in G1 phase, which would prevent end resection (**Fig. 3.6E**). Corroborating our IF results, overexpressing GFP-BAP1 or HA-JARID2-N reduced RPA2 phosphorylation detected by immunoblot (**Fig. 3.6F**), again suggesting disrupting the H2AK119ub signal inhibited DNA end resection. Interestingly, both constructs also impaired the phosphorylation of Chk1 (**Fig. 3.6F**), in line with the loss of RPA2 recruitment to chromatin (**Figs. 3.6C-D**) and upholding our observation that BMI-1 depletion abrogates Chk1 signaling (**Fig. 3.4C**). Presumably, inhibiting resection by disrupting H2AK119ub prevents RPA binding, blocking subsequent ATR activation and Chk1 phosphorylation. Taken together, these experiments suggest that the H2AK119ub mark is required for efficient DNA end resection.

Figure 3.5

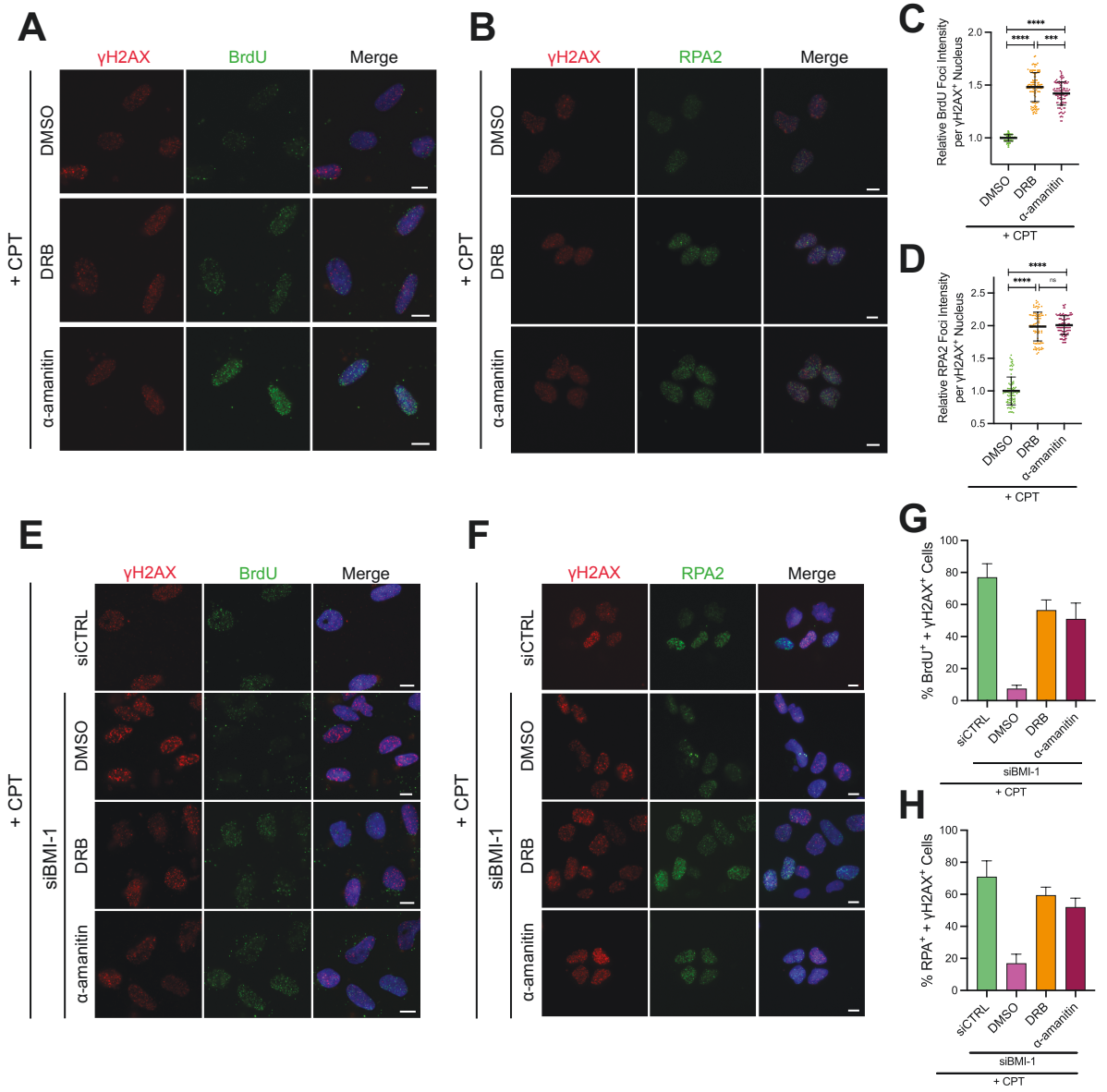

Figure 3.5: BMI-1-Mediated Transcriptional Silencing Promotes DNA End Resection

A) U2OS cells were treated with 0.1% DMSO or 100 μM DRB for 3h or 10 μg/mL α-amanitin for 1h, after which 1 μM CPT was added to the media for 1h. BrdU was added to the culture media 30h prior to CPT treatment. Cells were processed for IF staining. **B)** As in A) except without addition of BrdU. **C), D)** Scatterplots of relative integrated intensity of nuclear foci in γH2AX$^+$ cells from A) and B), respectively. Each point is from one cell. **E), F)** As in A) or B) but in cells transfected with the indicated siRNA 48h prior to CPT treatment. **G), H)** Quantifications of foci-positive γH2AX$^+$ cells from E) and F), respectively. (A-F): representative results from ≥3 biological replicates; (G, H): 2 biological replicates pooled together. Error bars represent the standard deviation from the mean. ns: not significant; *** $p < 0.001$; **** $p < 0.0001$. Scale bars: 10 μm.

Figure 3.6

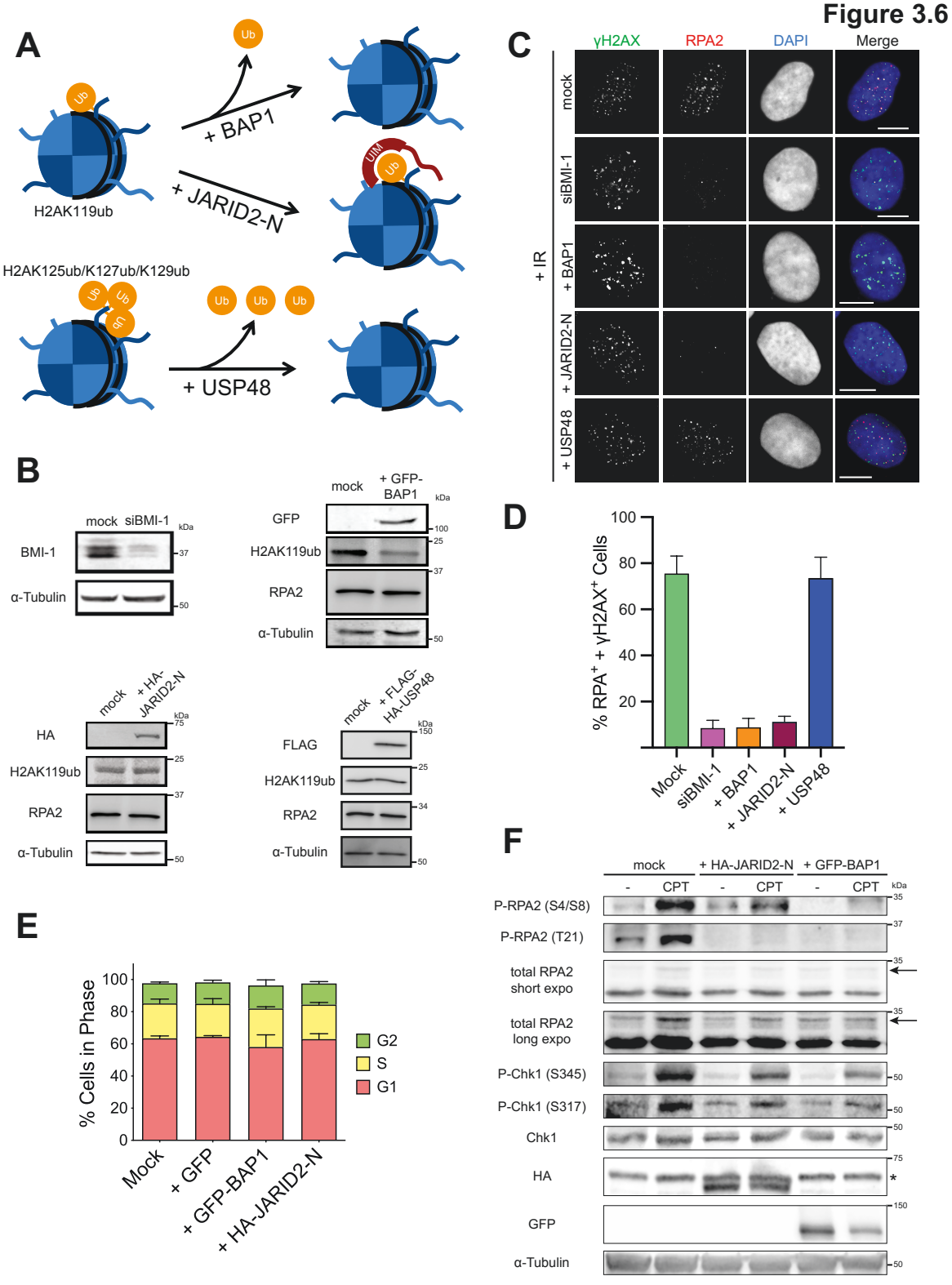

Figure 3.6: H2A Ubiquitylation at K119 is Important for DNA End Resection

A) Depiction of the activities of the DNA constructs used in this figure. **B)** Immunoblot analysis of U2OS transfected with the indicated DNA constructs or BMI-1 siRNA. **C)** IF images of U2OS cells transfected with BMI-1 siRNA or the DNA constructs indicated before exposure to 10 Gy of ionizing radiation and allowing 3h for recovery. **D)** Quantifications of RPA2 foci-positive γH2AX^{+} cells from C). **E)** Cell cycle profiles of U2OS cells transfected with GFP, GFP-BAP1, HA-JARID2-N, or neither. **F)** Immunoblot analysis of U2OS cells transfected with GFP-BAP1 or HA-JARID2-N or neither and treated with 1 μM CPT for 1h. Arrows denote slower migration of phospho-RPA2. *: non-specific signal. (B, F): representative results from ≥2 biological replicates; (C): representative results from ≥3 biological replicates; (D, E): 2 biological replicates pooled together. Error bars represent the standard deviation from the mean. Scale bars: 10 μm.

3.4.6 CtIP is Recruited to H2AK119ub-Modified Chromatin Upon RNF2 Tethering

As H2AK119ub is important for resection, and BMI-1 depletion impairs CtIP recruitment to DSBs (**Figs. 3.3E-F**), and given the BMI-1 dependent enrichment of H2AK119ub at DSBs (302), we hypothesized that CtIP is recruited to DSBs in part by recognizing H2AK119ub. We asked whether tethering RNF2, the main E3 ubiquitin ligase for depositing H2AK119ub, is sufficient to recruit CtIP to chromatin. To test this, we utilized an *in vivo* targeting system for tethering proteins-of-interest to chromatin (**Fig. 3.7A**). This system uses a protein-of-interest fused to the *lac* repressor LacI and mCherry in cell lines with a genomic locus containing tandem *lacO* repeats (421). To target RNF2 to chromatin and visualize the event, we expressed in U2OS cells containing a *lacO* array (399) a fusion protein of RNF2-LacI-mCherry (**Fig. 3.7A**). To rule out the contribution of other H2A ubiquitylation sites, we also expressed a similar fusion containing instead RNF8, which promotes H2A ubiquitylation at K13/K15. A previous report using these constructs saw a concentration of ubiquitylated H2A at the *lacO* array dependent on their E3 ubiquitin ligase activities (422). We observed that immobilizing RNF2 to chromatin induced CtIP recruitment to the array, which colocalized with a distinct focus of H2AK119ub (**Figs**. **3.7A-C**). As a control, the accrual of CtIP and H2AK119ub did not occur at the array when either LacI-mCherry alone or RNF8-LacI-mCherry were expressed (**Figs**. **3.7A-C**). As well, when

catalytically dead RNF2 (RNF2-C90S) was tethered, CtIP accumulation at the array was reduced to the background level (**Figs**. **3.7A-C**), coincident with the basal level of H2AK119ub at the array. These data indicate local concentration of the H2AK119ub mark is sufficient to induce CtIP accumulation on chromatin, even in the absence of DNA damage.

The data suggests CtIP may interact with H2AK119ub. Indeed, immunoprecipitation (IP) of H2AK119ub pulled down endogenous CtIP (**Fig. 3.7D**), and the reciprocal IP of CtIP pulled down K119ub-modified H2A (**Fig. 3.7E**). Thus CtIP and H2AK119ub interact, with the interaction being DNA damage independent. To substantiate our results, we performed colocalization analysis by IF on unperturbed U2OS cells. Both BMI-1 and CtIP were concentrated in several larger foci reminiscent of PcG bodies (423) (**Fig. 3.S11A**). In addition, H2AK119ub foci colocalized with CtIP foci, despite the absence of DNA damage (**Fig. 3.S11B**), reiterating that CtIP interacts with K119ub-modified H2A.

3.4.7 CtIP Binds to Ubiquitin

To investigate if CtIP can directly bind K119-ubiquitylated H2A, we performed a direct binding assay between GFP-tagged CtIP and a biotinylated peptide of the H2A C-terminal tail conjugated to ubiquitin at the K119 position (H2A-C-term-K119ub). GFP alone or GFP-CtIP were expressed in HEK293 cells and coupled onto agarose beads by anti-GFP immunoprecipitation, which distinctly enriched them from the cell lysate (**Fig. 3.S11C**). While the K119-ubiquitylated H2A peptide exhibited a weak non-specific interaction with GFP, substituting GFP with a similar amount of GFP-CtIP enriched binding 2.36-fold (**Figs. 3.7F, 3.S11E**), suggesting CtIP can indeed bind H2AK119ub. The binding was also specific to the ubiquitin moiety, as GFP-CtIP did not detectably bind the unmodified H2A-C-term peptide, even though a comparable amount was used

in the binding reaction (**Fig. 3.7F**). This indicates that, at least under these conditions, CtIP binding to H2A-C-term-K119ub is by recognition of ubiquitin, and not to additional features found in the H2A C-terminal tail. In support of this, GFP-CtIP could bind the same peptide but ubiquitylated at residue K118, as well as a K13-ubiquitylated H2A-N-terminal peptide, despite input of equal amounts of all three peptides into the reaction (**Figs. 3.S11D-E**). It is possible the binding of CtIP may be more specific to H2AK119ub *in vivo* (**Figs. 3.7B-C**), with the interaction mediated by structural elements present only in a nucleosomal context, or requiring other histone post-translational modifications as pre-requisites. Nevertheless, our results suggest CtIP can recognize ubiquitin.

To unequivocally demonstrate that CtIP directly binds ubiquitin, we performed Far Western blotting analysis (407) by incubating membrane-immobilized FLAG-tagged CtIP with HA-tagged ubiquitin. Indeed, robust HA-ubiquitin binding was observed to FLAG-CtIP, and not to bovine serum albumin loaded in far excess to FLAG-CtIP, indicating the interaction with CtIP was specific (**Fig. 3.S12A**). As confirmation, we performed Far Western blotting with GFP or GFP-CtIP immobilized on the membrane. HA-ubiquitin capably bound to GFP-CtIP but not to free GFP (**Fig. 3.S12B**), although the bound HA signal was substantively weaker compared to when FLAG-CtIP was immobilized, likely due to interference from the sizable GFP tag. Notably, HA-ubiquitin also bound to GFP-tagged RNF138 (132, 133), but not to a version deleted of its ubiquitin-interacting motif (dUIM) (**Figs. 3.S13A-B**), lending credence to the *bona fide* binding between ubiquitin and CtIP.

Figure 3.7

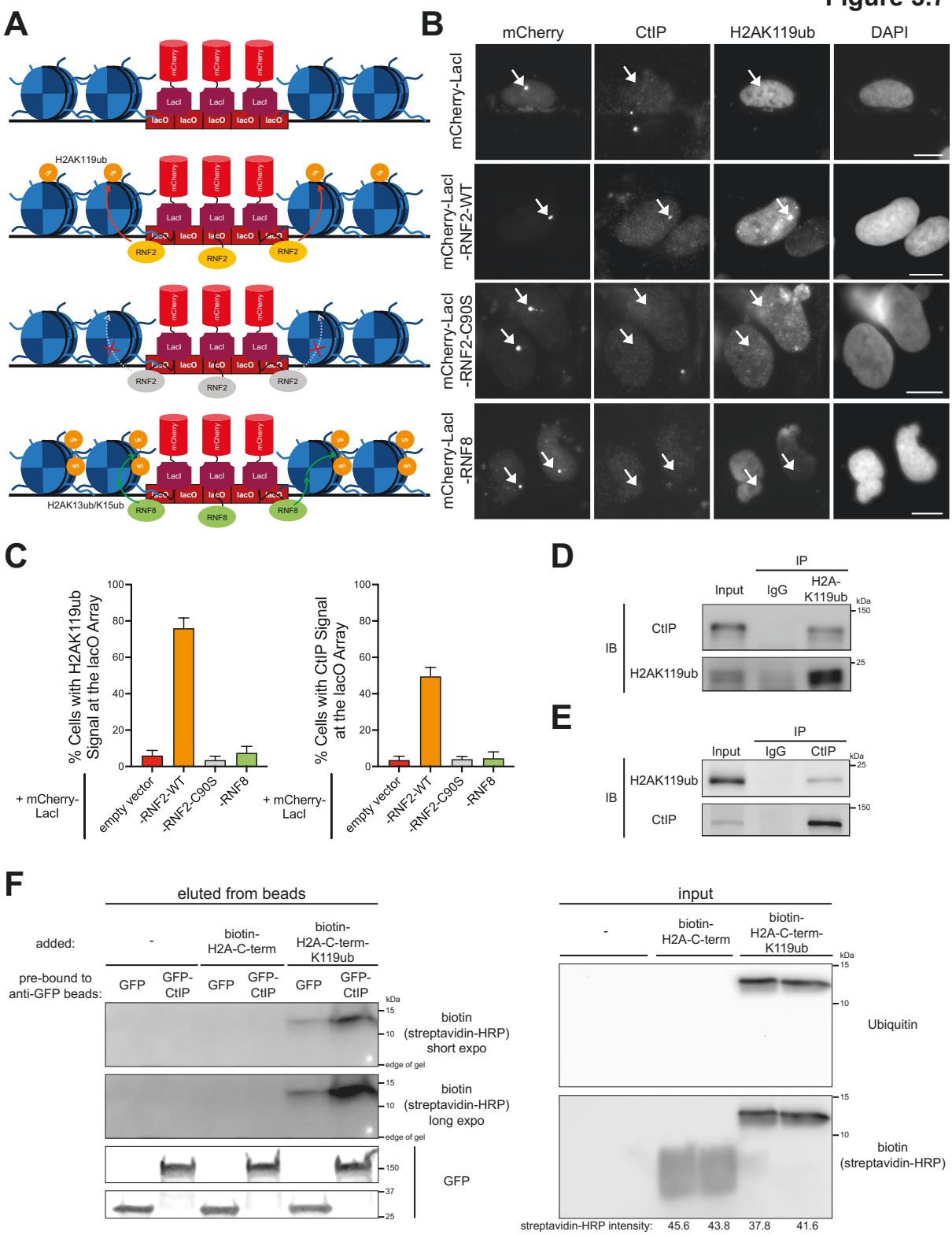

Figure 3.7: CtIP is Recruited to H2AK119ub-Modified Chromatin Upon RNF2 Tethering

A) Schematic of the DNA constructs used in B)-C) and their tethering to the *lacO* array in U2OS 2-6-3 cells. **B)** Images of U2OS 2-6-3 cells transfected with the mCherry-LacI constructs as indicated and immunostained for CtIP and H2AK119ub. Arrows denote accumulation of the mCherry-LacI fusions at the *lacO* array. **C)** Quantifications of cells with H2AK119ub or CtIP signal accumulating at the *lacO* array from B). **D)** Co-IP of untreated U2OS lysate where H2AK119ub was immunoprecipitated (IP'd). IB: immunoblot. **E**) As in D) except CtIP was IP'd. **F)** GFP or GFP-CtIP were IP'd onto anti-GFP-agarose beads and mixed with biotinylated H2A-C-terminal peptides with or without ubiquitin conjugated at K119 for 2h at 4°C. The bead eluate (left) and peptide input (right) were analyzed by immuno- and streptavidin blot. (B, D-E): representative results from ≥3 biological replicates; (C): 2 biological replicates pooled together; (F): representative results from 3 biological replicates. Error bars represent the standard deviation from the mean. Scale bars: 10 μm.

3.4.8 Multiple Regions of CtIP Possess the Capacity to Bind Ubiquitin

We proceeded to investigate which domains of CtIP are required for binding ubiquitin. We performed the same Far Western assay, this time utilizing a panel of FLAG-CtIP internal deletion mutants (344) (**Figs. 3.S14A-B**). To our surprise, while most of the internal deletion mutants (all except D3) were modestly reduced in their ability to bind HA-ubiquitin relative to full-length CtIP, none of them strongly inhibited ubiquitin binding (**Figs. 3.8A, 3.S14A**). We infer then that CtIP possesses the capacity for ubiquitin binding at multiple regions along its length. Perhaps stark reductions in ubiquitin binding were not observed as the loss of ubiquitin binding from a deleted region could be compensated by ubiquitin binding domains still present in other regions. In support of our findings for internal deletion mutant D2 (residues 133-369 deleted) (**Fig. 3.S14A**), a CtIP mutant deleted of residues 153-322 was still capable of binding ubiquitin (424). While further investigations are required to understand how CtIP recognizes ubiquitin, it is clear CtIP binds to ubiquitin. Perhaps one aspect of BMI-1's role in HR is to promote deposition of H2AK119ub, the modification serving to further recruit CtIP to the site of damage for the promotion of DNA resection (**Fig. 3.8B**).

Figure 3.8

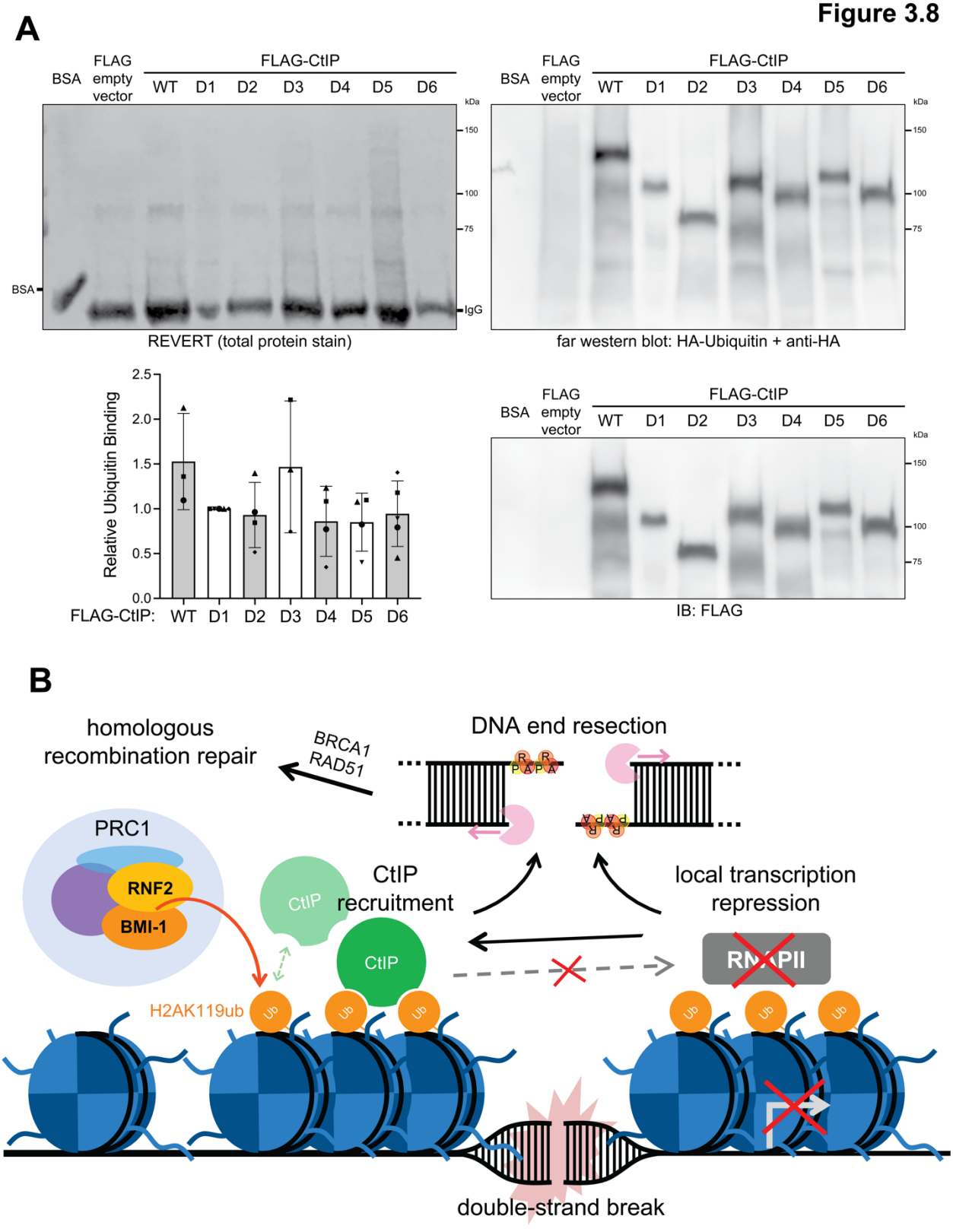

Figure 3.8: Multiple Regions of CtIP Possess the Capacity to Bind Ubiquitin

A) Far Western Blot assay. Albumin (BSA) or immunoprecipitates of FLAG empty vector or FLAG-CtIP-WT or its internal deletion mutants were immobilized and renatured on PVDF membrane, then incubated with recombinant HA-ubiquitin. After immunoblotting for HA (top right), the membrane was stripped in guanidinium-HCl and immunoblotted for FLAG (bottom right). Densitometric measurements of HA signal were normalized to those of FLAG signal to quantify ubiquitin binding to CtIP (bottom left); data from 3 to 5 biological replicates were pooled. Images are representative of ≥3 biological replicates. Error bars represent the standard deviation of the mean. **B)** Model; see text for details.

3.5 Discussion

Upon DNA damage, cells transiently repress local transcription at damage sites to prevent spatial clashes between the repair and active transcription machineries (273, 301, 415, 425). Accumulating evidence is shedding light on the tightly coordinated interplay between the transcription and DSB repair machineries (302, 426). Intriguingly, BMI-1 and RNF2, core members of PRC1, have been found to play a role in DSB repair, with this role linked to E3 ubiquitin ligase activity toward H2AK119 (130, 296–298, 301). In support of this, we demonstrate that the occurrence of HR is dependent on BMI-1 (**Fig. 3.2**). BMI-1's role in HR is likely dependent on its promotion of RNF2's E3 ligase activity, as a RING domain-deleted BMI-1 could not rescue HR in BMI-1 depleted cells (**Fig. 3.2I**). Precisely how BMI-1 promotes DSB repair remained unclear, thus we sought to gain mechanistic insights into if BMI-1's activities in H2AK119ub generation and transcriptional repression played a role.

BMI-1 promotes the recruitment of CtIP to DSB sites (**Fig. 3.3E**). With Mre11/Nbs1 accumulation at DSBs unaffected by loss of BMI-1 (**Figs. 3.S9G-H**), and with CtIP being essential for end resection (58), we speculate the defect exhibited in end resection upon BMI-1 depletion is at least in part from preventing CtIP localization to sites of damage. This may not be completely

unexpected, as links between the PRC1 complex and CtIP have been found in the past. One report showed CtIP is constitutively SUMOylated at lysine 896 (K896), and this is facilitated by the PRC1 component CBX4 (343). SUMO conjugation to K896 is important for its function in resection, as depleting CBX4 or replacing K896 with an arginine residue inhibited DNA end resection and Rad51 foci formation. Relatedly, the SUMO E3 ligase function of CBX4 was first identified through its substrate CtBP, an interactor of CtIP and transcriptional co-repressor (177, 253, 427). As CBX4 also promotes the SUMOylation of BMI-1, facilitating its recruitment to DSBs (131), it is possible that CBX4-mediated BMI-1 and CtIP SUMOylation are interconnected. Supporting this notion, CBX4 depletion strongly impairs RPA and Rad51 foci formation (343), similar to BMI-1 depletion (**Fig. 3.3**). CBX4 may therefore regulate DNA end resection by modulating the functions of its downstream targets BMI-1 and CtIP, raising the question of whether CBX4, BMI-1, and CtIP constitute a common axis that controls HR. As CBX4 and BMI-1 interact (428), could the inhibition of CtIP accrual from BMI-1 depletion be a consequence of BMI-1 loss on CBX4 activity? We think this is unlikely, as CBX4 recruitment to DNA damage is independent of BMI-1 (131). Moreover, we and others have shown that drastically reducing CtIP SUMOylation (using the K578R substitution) does not impair rapid recruitment of CtIP to DNA damage (429, 430).

Another link between PRC1 and CtIP comes from their localization to similar nuclear compartments. Indeed, CtBP1 localizes to nuclear bodies containing CtIP and BMI-1 in the absence of DNA damage, although the function of these complexes is still unknown (427, 431). We confirmed this observation, detecting colocalization between CtIP and BMI-1 or H2AK119ub **(Figs. 3.S11A-B)**. These data led us to speculate that CtIP interacts with H2AK119ub constitutively and that the interaction mediates its function in DNA end resection. Co-

immunoprecipitation experiments detected an interaction between CtIP and H2AK119ub, while concentrating H2AK119ub on chromatin recruited CtIP in the absence of DNA damage (**Fig. 3.7**). In support, perturbing the H2AK119ub signal blocked end resection (**Fig. 3.6**). We later found that CtIP directly binds to ubiquitin (**Figs. 3.S12, 3.S13**), an observation previously reported in two studies (424, 432). As both reports could not find conserved ubiquitin binding domains within the CtIP primary sequence, we attempted to identify a ubiquitin-binding region of CtIP using a panel of internal deletion mutants. Surprisingly, each mutant was able to bind ubiquitin, with only a minor reduction of binding in most (**Fig. 3.8A**). Thus, CtIP recognizes ubiquitin through multiple regions distributed over its primary sequence, consistent with predictions of CtIP's structure to be highly disordered (257, 262). Perhaps these multiple regions, combined with CtIP's ability to form homotetramers (258), create a high avidity trap to concentrate it at the numerous ubiquitin moieties deposited near the DSB site (42). This insight adds another mechanism to the growing list of mechanisms by which CtIP is recruited to sites of DNA damage, which include DNA binding (256, 258, 259, 261), interactions with the MRN complex and ATM (256), its own ubiquitylation (133, 340), and an interaction with PCNA (335).

Beyond generating the H2AK119ub mark for CtIP recruitment, BMI-1-mediated transcriptional silencing also promotes end resection and CtIP recruitment to DSBs (**Figs. 3.5E-H, 3.S10D-E**). These data may suggest an alternate mechanism for CtIP recruitment to DSBs independent of the H2AK119ub mark, as here BMI-1 was depleted. It may be that BMI-1 establishes a transcription barrier (433) distant from the DSB that is conductive to CtIP recruitment, controlled DNA end resection, and assembly of the HR machinery. Conversely, it is clear that CtIP, and by extension end resection, is dispensable for DSB-induced transcription silencing. Knockdown of CtIP, unlike that of BMI-1, was unable to de-repress transcription or the

localization of active RNAPII near induced DSBs (**Figs. 3.4F-H)**. This is in contrast to *Saccharomyces cerevisiae*, where end resection is required for DSB-induced transcriptional inhibition (416).

Taken together, our data support a model of how BMI-1 regulates HR repair (**Fig. 3.8B**). BMI-1-mediated transcriptional repression and deposition of H2AK119ub promote DNA end resection, allowing for the downstream accrual of RPA, BRCA1, and Rad51 at DNA damage sites and the progression of HR. H2AK119ub could enhance resection by recruiting the essential resection factor CtIP, which directly binds to ubiquitin moieties generated at the DSB site upon the localization of RNF2/BMI-1 (130), perhaps along with other ubiquitin moieties on chromatin-bound proteins (42). Our data provide deeper mechanistic insights into the involvement of BMI-1 in DSB repair, revealing a tight interplay between the transcriptional silencing machinery and DNA end resection.

3.5.1 Limitations of the Study

Somewhat surprisingly, we observed through direct binding assays that CtIP capably binds to ubiquitylated peptides of H2A's tails, regardless of the position of the modification. This result could arise from the use of free peptides of the H2A tails in our binding reactions. Perhaps CtIP may show more specificity to H2AK119ub in the context of intact nucleosomes. We also note that treatment with DRB or α-amanitin alone substantially enhanced RPA2 and BrdU foci intensity in response to CPT, suggesting barriers for initiating resection could be lower upon inhibiting RNAPII-dependent transcription globally. Fewer active transcription complexes could reduce steric hindrance or topological stress on chromatin, increasing its accessibility to DDR factors and the resectosome. For instance, chromatin regions enriched in RNAPII are refractory to γH2AX

spreading (195). Thus, the rescue of BrdU, RPA2, and CtIP foci from combining BMI-1 depletion with transcription inhibitors could be inflated. Nevertheless, the rescue of CtIP foci highlights the existence of alternate mechanisms of CtIP recruitment to DSBs in the absence of BMI-1 activity, such as direct DNA binding (discussed above).

3.6 Acknowledgements

This research was funded by CIHR (Canadian Institutes of Health Research), grant number MOP-365197, CRS (Cancer Research Society), grant number 22019, and NSERC (Natural Sciences and Engineering Research Council of Canada), grant number RGPIN-2017-05752, awarded to I.H.I. A.L. was supported by the Dr. Herbert Meltzer Memorial Fellowship, the Yau Family Foundation Award, and the Rachel Mandel Scholarship in Lymphoma and Other Blood Cancers. F.M. is supported by a Terry Fox Research Institute Marathon-of-Hope Graduate Studentship.

3.7 Declaration of Interests

The authors declare no conflicts of interest.

3.8 Author Contributions

A.F. performed most of the experiments and wrote the manuscript. A.J.L. performed *in vitro* binding experiments. F.M. and F.K. performed immunoblotting experiments. A.S. conducted ChIP experiments. I.H.I. conceived and supervised the project. A.F., A.J.L., and I.H.I generated the figures and revised the manuscript.

3.9 Supplementary Data

Supplementary figures (**Figs. 3.S9 – 3.S14**) and tables (**Tables 3.1 – 3.3**) are provided in support of the main figures (**Figs. 3.2 – 3.8**).

3.9.1 Supplementary Figures

Figure 3.S9

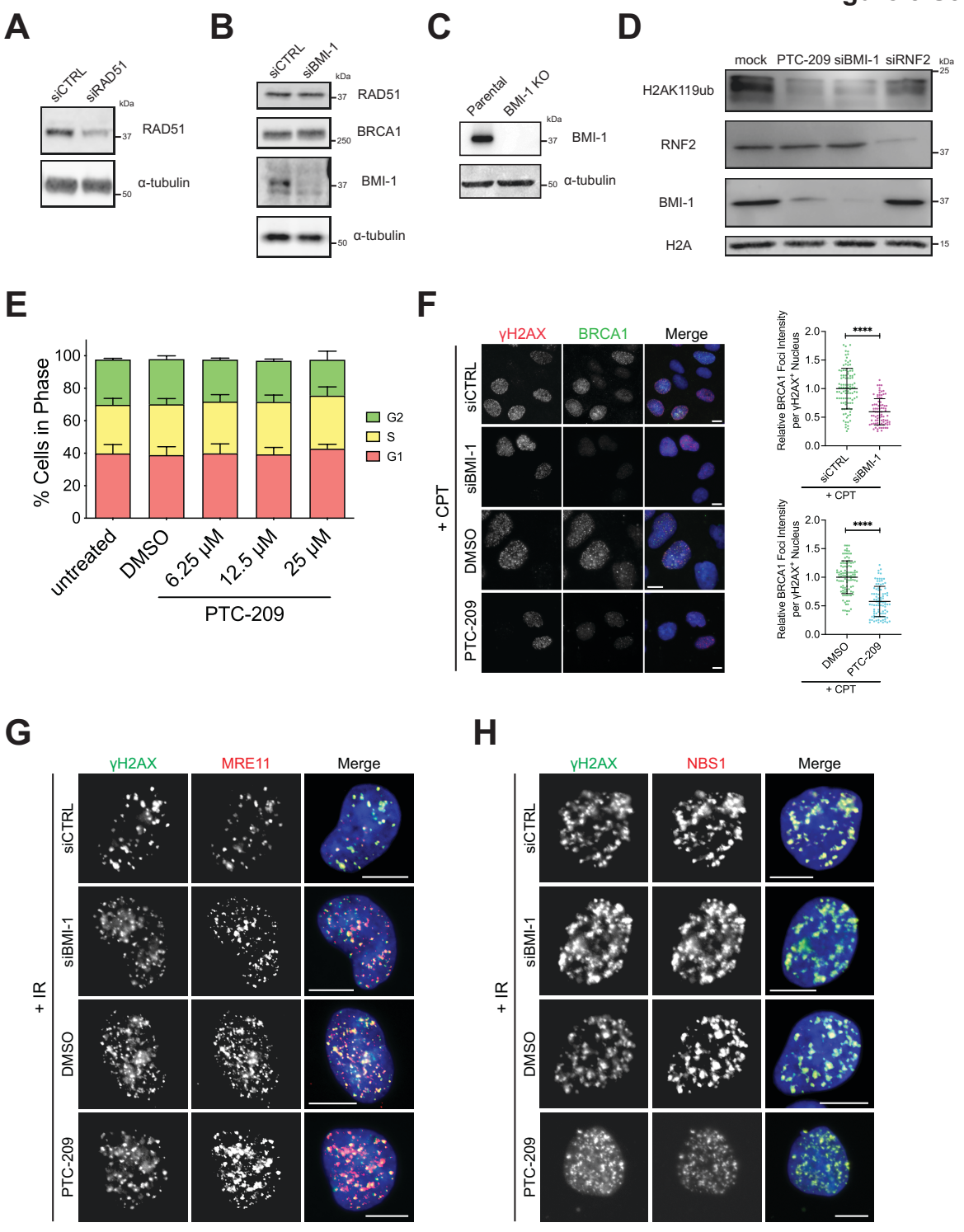

Figure 3.S9: Cellular Depletion of BMI-1; BMI-1 Mediates the Accrual of BRCA1 but Not Mre11 and Nbs1, Related to Figures 3.2 and 3.3

A) Immunoblots of whole cell extracts from DR-GFP U2OS transfected with control siRNA (siCTRL) or siRNA targeting Rad51. α-tubulin served as the loading control. **B)** Immunoblot analysis of BMI-1, Rad51, and BRCA1 protein expression in U2OS cells treated with control siRNA or siRNA targeting BMI-1. **C)** Immunoblot analysis of parental DR-GFP U2OS cells or those with CRISPR/Cas9-mediated knockout (KO) of BMI-1. **D)** U2OS cells were mock transfected or transfected with siRNA targeting BMI-1 or RNF2 for 48h, or treated with 10 μM PTC-209 for 18h and split into two portions, one where whole cell extract was prepared (to probe for BMI-1 and RNF2 expression) and another which was subjected to hypotonic lysis, acid extraction and subsequent TCA precipitation of histones (to probe for H2AK119ub and histone H2A). Both portions were subjected to SDS-PAGE and immunoblotting. **E)** Cell cycle profiles of U2OS cells treated with 0.1% DMSO or PTC-209 at the indicated concentrations for 18h. Cells were processed for propidium iodide staining and analyzed by flow cytometry. **F)** U2OS cells were treated with siRNA for 48h, or 0.05% DMSO or 10 μM PTC-209 for 18h. 1 μM CPT was then added to the media for 1h to induce DNA damage, after which cells were processed for immunofluorescence (IF) staining of damage-induced foci. Left: representative images; right: scatterplots of relative integrated intensity of nuclear foci in $\gamma H2AX^+$ cells; each point is from one cell. **G) and H)** Images of cells treated as in F) but with 10 Gy of ionizing radiation (IR) as the source of DNA damage, followed by a 1h recovery prior to processing for IF. (A-C): representative results from ≥2 biological replicates; (D, F-H): representative results from ≥3 biological replicates; (E): 3 biological replicates pooled together.

Figure 3.S10

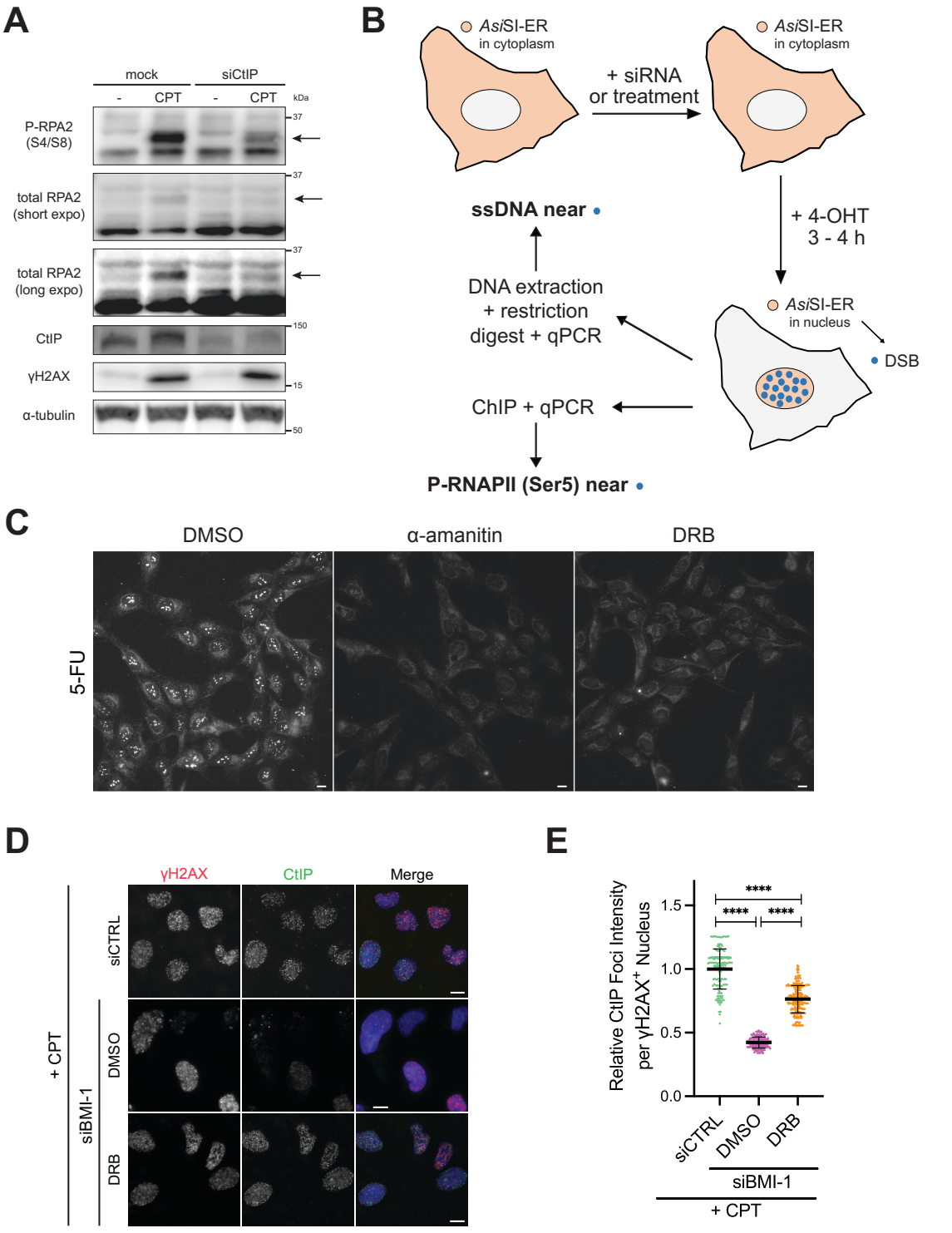

Figure 3.S10: BMI-1 Promotes DNA End Resection Through Transcriptional Silencing, Related to Figures 3.4 and 3.5

A) Immunoblot analysis of U2OS cells transfected with siRNA targeting CtIP or not, then treated with 1 μM CPT or not for 1h. Arrows denote the slower migration of phospho-RPA2 (P-RPA2 S4/S8). **B)** Workflow for using *Asi*SI-ER U2OS cells to measure DNA occupancy with initiated RNAPII (via ChIP) or the presence of resected DNA (via qPCR) near *Asi*SI-generated DSBs. *Asi*SI-ER is cytosolic, but rapidly translocates to the nucleus upon the addition of 4-hydroxytamoxifen (4-OHT), inducing sequence-specific DSBs at defined locations in the genome. **C)** U2OS cells were treated with either 0.1% DMSO or 100 μM DRB for 3h or 10 μg/mL α-amanitin for 1h, then labeled for 10 min with 2 mM 5-fluorouridine (5-FU) to visualize sites of ongoing transcription. Cells were fixed in ice-cold methanol and immunostained with an anti-BrdU antibody. Inhibition of transcription can be seen by the loss of nucleolar staining. **D)** U2OS cells transfected with the indicated siRNA for 48h were treated with 0.1% DMSO or 100 μM DRB for 3h, after which 1 μM CPT was added to the media for 1h. Cells were processed for IF staining. **E)** Scatterplot of relative integrated intensity of CtIP foci in $\gamma H2AX^{+}$ cells from D); each point is from one cell. (A, C-E): representative results from 2 biological replicates.

Figure 3.S11

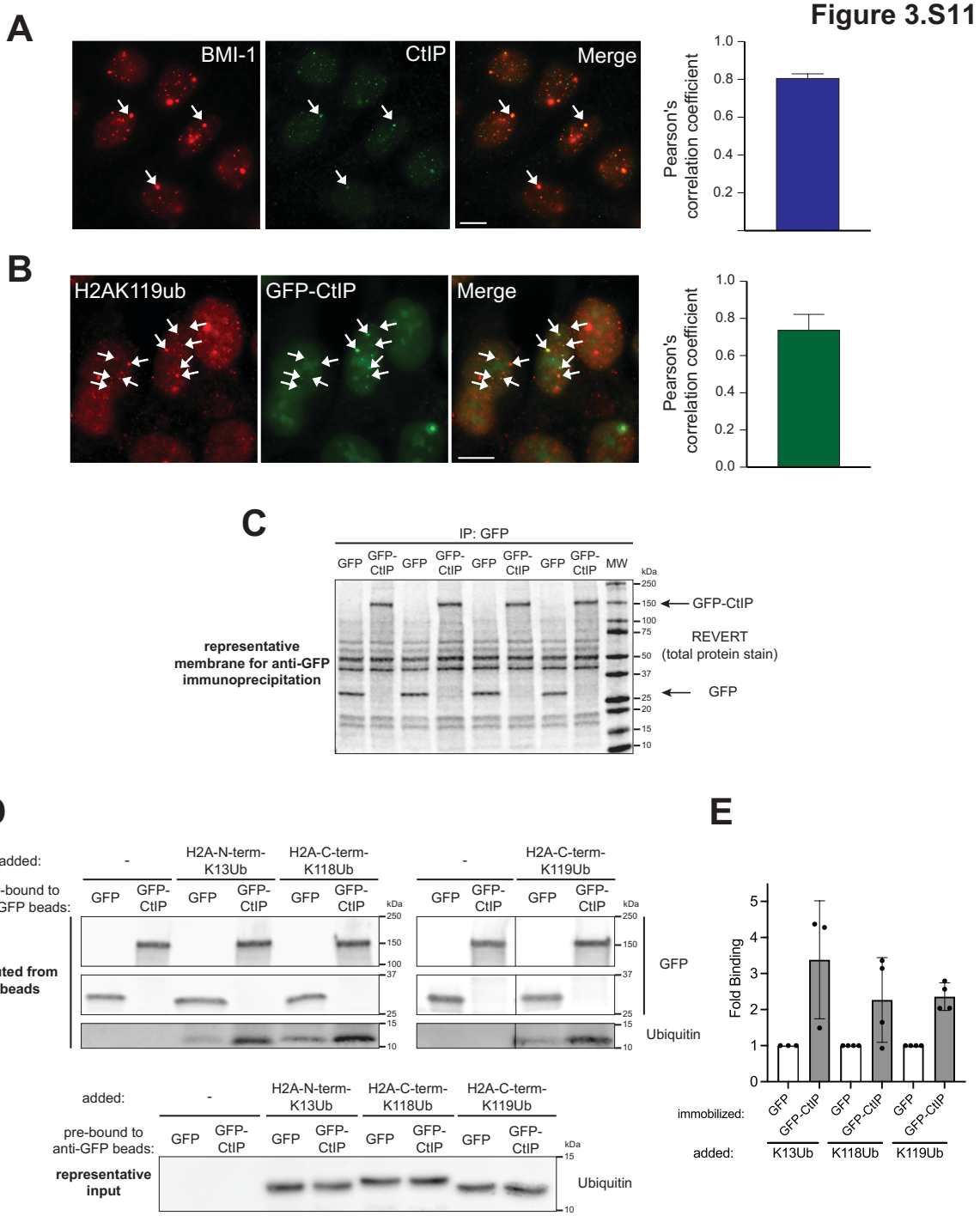

Figure 3.S11: CtIP Colocalizes with H2AK119ub and Binds to Ubiquitylated H2A Peptides, Related to Figure 3.7

A) Colocalization of endogenous CtIP and endogenous BMI-1 in unperturbed U2OS cells processed for immunofluorescence staining. Left: representative image with arrows pointing to examples where foci in both channels colocalize; right: average Pearson's correlation coefficient

between the two channels. **B)** As in A), except that U2OS cells stably expressing GFP-CtIP were used to show CtIP colocalization to endogenous H2AK119ub. CtIP foci were visualized using GFP-CtIP due to the lack of a commercially available rabbit anti-CtIP antibody that detects CtIP speckles in cells. **C)** Representative nitrocellulose membrane from SDS-PAGE of the GFP immunoprecipitation products used to perform the direct binding assay, stained with REVERT total protein stain. GFP or GFP-CtIP were expressed in HEK293 cells and coupled onto agarose beads by anti-GFP immunoprecipitation, which enriched them from the cell lysate, seen by the highly abundant and comparable levels of free GFP and GFP-tagged CtIP. **D)** GFP or GFP-CtIP were immunoprecipitated onto anti-GFP-agarose beads and mixed with 2.5 μg of ubiquitylated H2A peptides for 2h at 4°C. SDS-PAGE and immunoblotting were performed to detect immobilized proteins/peptides. The bead eluate (top) and peptide input (bottom) were analyzed by immunoblot. **E)** Quantification of ubiquitylated H2A peptide binding efficiency from independent replicates of D). Densitometric measurements of ubiquitin signal (ubiquitylated H2A peptide) in the eluate were divided by those of GFP signal in the eluate. Binding to GFP-CtIP was then normalized to non-specific binding in the GFP only control for the same H2A peptide. (A, B): representative results from ≥2 biological replicates; (C): representative results from ≥6 biological replicates; (D): representative results from ≥3 biological replicates; (E): ≥3 biological replicates pooled together.

Figure 3.S12

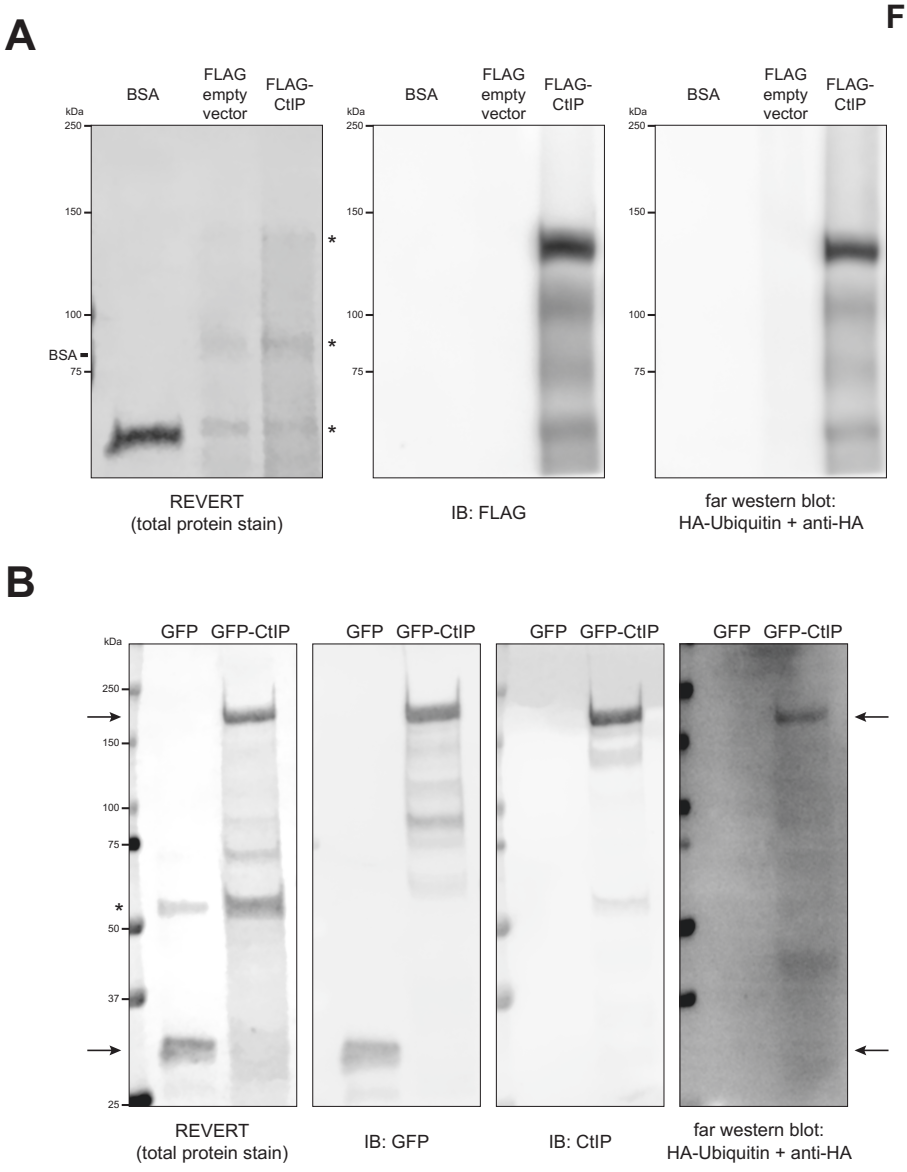

Figure 3.S12: Ubiquitin Binds to CtIP, Related to Figure 3.8

Far Western blot assays. "Prey" proteins were resolved by SDS-PAGE, transferred to PVDF membrane, and renatured, then the membrane was incubated with recombinant HA-ubiquitin ("bait"). After immunoblotting for HA ("far western blot"), the membrane was stripped in guanidinium-HCl and re-immunoblotted for the presence of the "prey" proteins. An interpretation of direct binding would require HA signal to overlay the position of a "prey" band on the membrane. **A)** Bovine serum albumin (BSA) and immunoprecipitates of FLAG empty vector and FLAG-CtIP served as the "prey" proteins. *: non-specific signals. Representative result of 3 biological replicates. **B)** Immunoprecipitates of GFP and GFP-CtIP served as the "prey" proteins (positions indicated by arrows). Representative result of 3 biological replicates.

Figure 3.S13

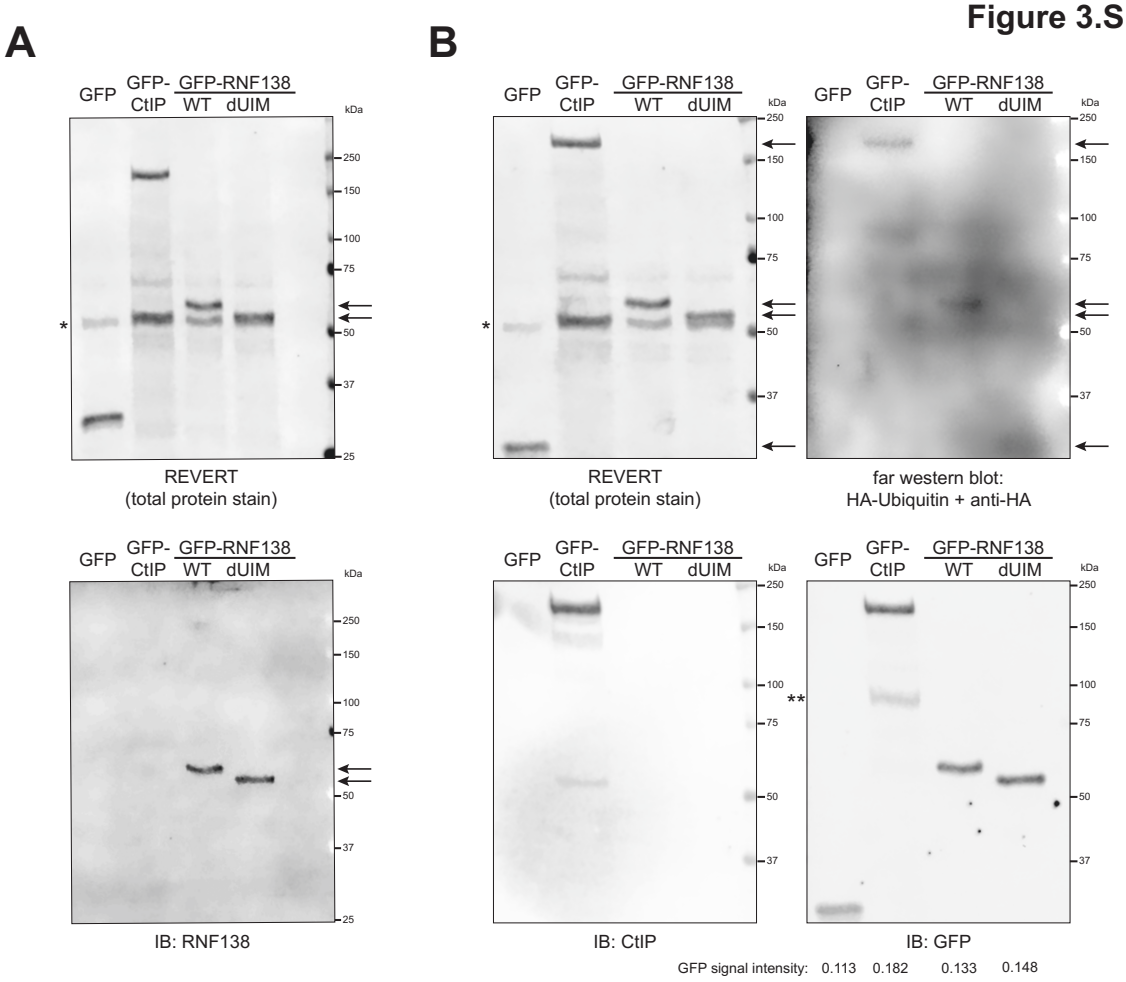

Figure 3.S13: Ubiquitin Binds to GFP-CtIP, Related to Figure 3.8

A) Enrichment of GFP or GFP-tagged proteins from cell lysate via anti-GFP immunoprecipitation. Immunoprecipitates were processed by SDS-PAGE and transferred to PVDF. The membrane was stained with REVERT total protein stain, then immunoblotted for RNF138. **B)** Far Western blot assay as in **Figure 3.S12**. GFP, GFP-CtIP, -RNF138-WT, and -RNF138-dUIM served as the "prey" proteins (positions indicated by arrows); HA-ubiquitin was the "bait". *: non-specific signal; **: likely degradation product of GFP-CtIP. Representative result of 2 biological replicates.

Figure 3.S14

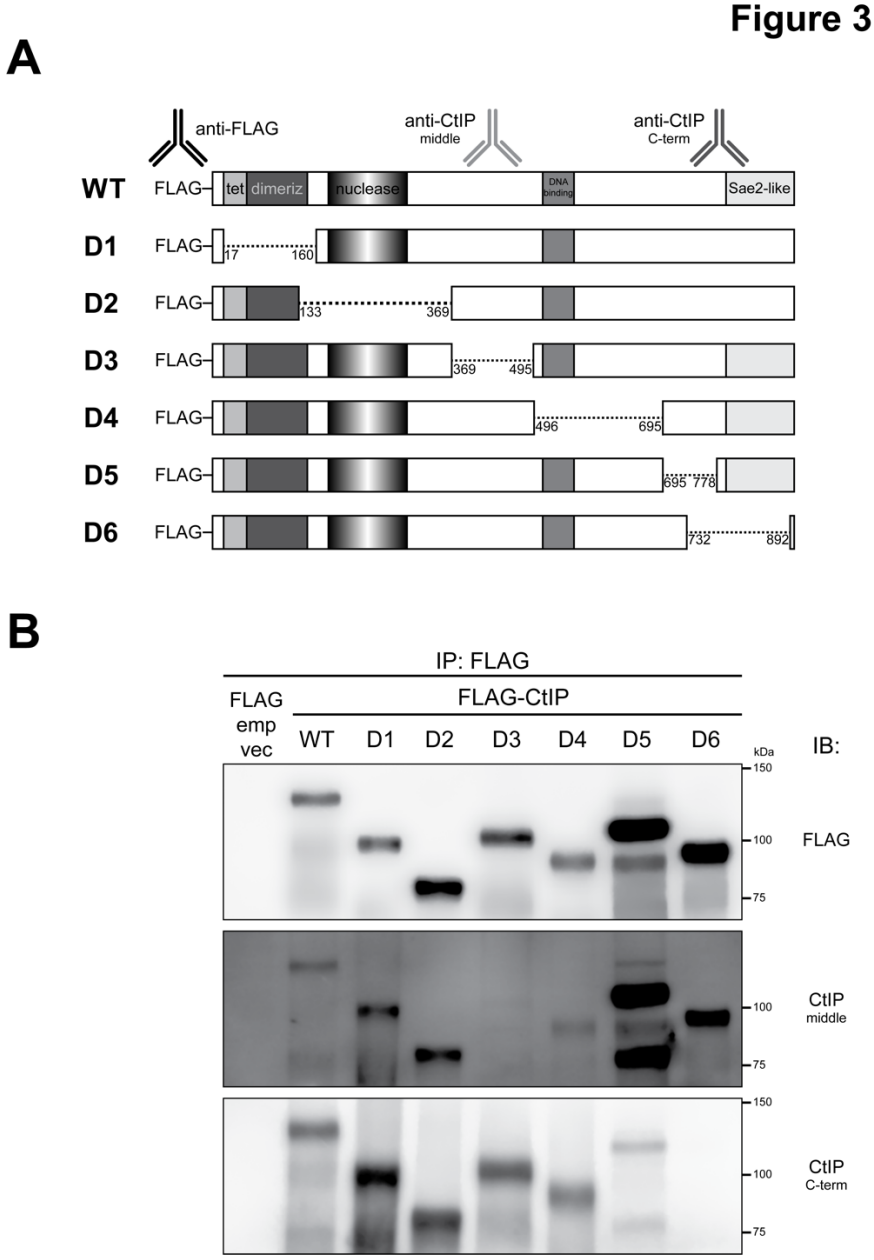

Figure 3.S14: A Panel of CtIP Internal Deletion Mutants, Related to Figure 3.8

A) Schematic diagram of the FLAG-CtIP internal deletion panel (Yuan and Chen, 2009) and approximate binding locations of antibodies used for immunoblot in B). **B)** Individual members of the FLAG-CtIP internal deletion mutant panel, full-length (WT) CtIP, or a FLAG empty vector plasmid were isolated by FLAG immunoprecipitation and resolved by SDS-PAGE. Successive immunoblots were performed using antibodies raised against the FLAG epitope (recognizes all constructs), the middle region of CtIP (recognizes all except D3), and the CtIP C-terminus (recognizes D5 weakly, does not recognize D6). The membrane was stripped in guanidium-HCl and air-dried between immunoblots.

3.9.2 Supplementary Tables

Table 3.1: Key Resources Table

REAGENT or RESOURCE	SOURCE	IDENTIFIER
Antibodies		
rabbit anti-BMI-1 (IF)	Bethyl Laboratories	Cat#A301-694A
mouse anti-BMI-1, F6 (IB)	Abcam	Cat#ab14389
rabbit anti-RNF2, D22F2 (IB)	Cell Signaling Technology	Cat#5694
mouse anti-H2AK119ub, E6C5 (IF)	Millipore Sigma	Cat#05-678
rabbit anti-H2AK119ub, D27C4 (IB, IP)	Cell Signaling Technology	Cat#8240
rabbit anti-Histone H2A, acidic patch (IB)	Millipore Sigma	Cat#07-146
mouse anti-α-Tubulin, B-5-1-2 (IB)	Millipore Sigma	Cat#T6074
rabbit anti-phospho-H2AX at S139 (γH2AX) (IF)	Active Motif	Cat#39118
mouse anti-phospho-H2AX at S139 (γH2AX), JBW301 (IF, IB)	Millipore Sigma	Cat#05-636-I
rabbit anti-Rad51, H-92 (IB, IF, ChIP)	Santa Cruz Biotechnology	Cat#sc8349
rabbit anti-BRCA1 (IB)	Bethyl Laboratories	Cat#A301-377A
mouse anti-BRCA1, D-9 (IF)	Santa Cruz	Cat#sc-6954
rabbit anti-Mre11 (IF)	Bethyl Laboratories	Cat#A303-998A
rabbit anti-Nbs1 (IF)	Novus Biologicals	Cat#NB100-143
mouse anti-CtIP, 14-1 (IB, IF, ChIP, IP)	Active Motif	Cat#61141
rabbit anti-CtIP C-term, EPNCIR160 (IB)	Abcam	Cat#155988
rabbit anti-CtIP Middle (IB)	Millipore Sigma	Cat#SAB3500491
mouse anti-BrdU (IF for BrdU)	Cytiva Life Sciences	Cat#GERPN202
mouse anti-BrdU, BU-33 (IF for 5-FU)	Millipore Sigma	Cat#B2531
mouse anti-RPA2, 9H8 (IB, IF, ChIP)	Abcam	Cat#ab2175
rabbit anti-phospho-RPA2 at S4/S8 (IB)	Bethyl Laboratories	Cat#A300-245A
rabbit anti-phospho-RPA2 at T21, EPR2846(2) (IB)	Abcam	Cat#ab109394
mouse anti-Chk1, 2G1D5 (IB)	Cell Signaling Technology	Cat#2360
rabbit anti-phospho-Chk1 at S345, 133D3 (IB)	Cell Signaling Technology	Cat#2348
rabbit anti-phospho-Chk1 at S317 (IB)	Cell Signaling Technology	Cat#2344
mouse anti-RNA polymerase II phospho-S5 at CTD repeats (YSPTSPS), 4H8 (ChIP)	Abcam	Cat#ab5408
mouse anti-HA, HA.11, 16B12 (IB)	BioLegend	Cat#901501
rabbit anti-HA (IB, Far Western Blot)	Abcam	Cat#ab9110
mouse anti-FLAG, M2 (IB)	Millipore Sigma	Cat#F1804
mouse anti-GFP, B-2 (IB)	Santa Cruz Biotechnology	Cat#sc-9996
mouse anti-Ubiquitin, P4D1 (IB)	Santa Cruz Biotechnology	Cat#sc-8017
rabbit anti-RNF138 (IB)	St. John's Laboratory	Cat#STJ112342
goat anti-mouse—HRP (IB)	LI-COR	Cat#926-80010
goat anti-rabbit—HRP (IB)	LI-COR	Cat#926-80011
donkey anti-mouse—IRDye 680RD (IB)	LI-COR	Cat#926-68072
donkey anti-rabbit—IRDye 680RD (IB)	LI-COR	Cat#926-68073
donkey anti-mouse—IRDye 800CW (IB)	LI-COR	Cat#926-32212
donkey anti-rabbit—IRDye 800CW (IB)	LI-COR	Cat#926-32213

donkey anti-mouse—Alexa Fluor 488 (IF)	Thermo Fisher	Cat#A-21202
donkey anti-mouse—Alexa Fluor 594 (IF)	Thermo Fisher	Cat#A-21203
donkey anti-rabbit—Alexa Fluor 594 (IF)	Thermo Fisher	Cat#A-21207
donkey anti-rabbit—Alexa Fluor 647 (IF)	Thermo Fisher	Cat#A-31573
goat anti-mouse—Alexa Fluor 647 (IF)	Abcam	Cat#ab150115
Bacterial and Virus Strains		
DH5α *E. coli* Competent Cells for plasmid prep	Thermo Fisher	Cat#18265017
Chemicals, Peptides, and Recombinant Proteins		
DMSO	Sigma	Cat#D8418; CAS: 67-68-5
PTC-209	Calbiochem	Cat#530154; CAS: 315704-66-6
Camptothecin	Selleck Chemicals	Cat#S1288; CAS: 7689-03-4
KU-55933 (ATM inhibitor)	Calbiochem	Cat#118500; CAS: 587871-26-9
Shield-1	Clontech (Takara)	Cat#632189; CAS: 914805-33-7
4-Hydroxytamoxifen	Sigma	Cat#H7904; CAS: 68047-06-3
Doxycycline	Sigma	Cat#D9891; CAS: 24390-14-5
α-Amanitin	Calbiochem	Cat#129741; CAS: 23109-05-9
5,6-Dichloro-1-β-D-ribofuranosylbenzimidazole (DRB)	Sigma	Cat#D1916; CAS: 53-85-0
5-Fluorouridine	Sigma	Cat#F5130; CAS: 316-46-1
5-Bromo-2'-deoxyuridine (BrdU)	Sigma	Cat#B5002; CAS: 59-14-3
Effectene Transfection Reagent	Qiagen	Cat#301425
Lipofectamine RNAiMax Transfection Reagent	Thermo Fisher	Cat#13778075
cOmplete Protease Inhibitor Cocktail, EDTA-free	Roche	Cat#11873580001
phosSTOP	Roche	Cat#04906837001
RNase A	Thermo Fisher	Cat#12091021
Propidium Iodide	Thermo Fisher	Cat#P1304MP; CAS: 25535-16-4
Dynabeads™ Protein G	Thermo Fisher	Cat#10003D
Anti-FLAG M2 Magnetic Beads	Millipore Sigma	Cat#M8823
GFP Selector beads	NanoTag Biotechnologies	Cat#N0310
Streptavidin-HRP Conjugate	Cytiva Life Sciences	Cat#GERPN1231
Recombinant Human HA-Ubiquitin	Boston Biochem (R&D Systems)	Cat#U-110
Revert 700 Total Protein Stain for Western Blot Normalization	LI-COR	Cat#926-11011
Amersham ECL Prime Western Blotting Detection Reagent	Cytiva Life Sciences	Cat#RPN2236
Critical Commercial Assays		
GeneJET Plasmid Miniprep Kit	Thermo Fisher	Cat#K0502
Zero Blunt TOPO PCR Cloning Kit	Thermo Fisher	Cat#451245
QIAquick PCR Purification Kit	Qiagen	Cat#28104

Experimental Models: Cell lines		
U2OS	ATCC	Cat#HTB-96; RRID:CVCL_0042
DR-GFP U2OS	Jeremy Stark (408)	N/A
DR-GFP U2OS BMI-1 CRISPR KO	This study	N/A
U2OS stably expressing GFP-CtIP	Stephen Jackson (58)	N/A
U2OS 2-6-3	Roger Greenberg (399)	N/A
U2OS-DSB reporter cells stably expressing ER-mCherry-LacI-*Fok*I-DD	Roger Greenberg (208)	N/A
U2OS 2-6-3 stably expressing ER-mCherry-LacI-*Fok*I-DD, rtTA, and YFP-MS2	Roger Greenberg (208)	N/A
*Asi*SI-ER U2OS	Gaelle Legube (195)	N/A
HEK293	ATCC	Cat#CRL-1573; RRID:CVCL_0045
Oligonucleotides		
Control siRNA: CGUACGCGGAAUACUUCGAdTdT	(58)	N/A
siRNA to Rad51: GAGCUUGACAAACUACUUCdTdT	(58)	N/A
siRNA to BMI-1 #1	Dharmacon	Cat#J-005230-10-0005
siRNA to BMI-1 #2	Dharmacon	Cat#J-005230-09-0005
siRNA to CtIP: GCUAAAACAGGAACGAAUCdTdT	(58)	N/A
Recombinant DNA		
pCAGGS	Jeremy Stark (408)	N/A
pCAGGS-I-*Sce*I	Jeremy Stark (408)	N/A
Myc-BMI-1-WT	Goberdhan Dimri, Ismail H. Ismail (130)	N/A
Myc-BMI-1-dRING	Goberdhan Dimri, Ismail H. Ismail (130)	N/A
Myc-BMI-1-dPEST	Goberdhan Dimri, Ismail H. Ismail (130)	N/A
Myc-BMI-1-dH-T	Goberdhan Dimri, Ismail H. Ismail (130)	N/A
GFP-BAP1	Keith Wilkinson (401)	N/A
HA-JARID2-N (1-541)	Neil Brockdorff (402)	N/A
FLAG-HA-USP48	Addgene (403)	RRID:Addgene_22585
mCherry-LacI-RNF2-WT	Nico Dantuma (422)	N/A
mCherry-LacI-RNF2-C90S	Nico Dantuma (422)	N/A
mCherry-LacI-RNF8	Nico Dantuma (422)	N/A
GFP-CtIP	Pablo Huertas (58)	N/A
GFP-RNF138-WT	Ismail H. Ismail (130)	N/A
GFP-RNF138-dUIM	Ismail H. Ismail (130)	N/A
FLAG-CtIP-WT	Junjie Chen (344)	N/A
FLAG-CtIP-D1	Junjie Chen (344)	N/A
FLAG-CtIP-D2	Junjie Chen (344)	N/A
FLAG-CtIP-D3	Junjie Chen (344)	N/A
FLAG-CtIP-D4	Junjie Chen (344)	N/A
FLAG-CtIP-D5	Junjie Chen (344)	N/A

FLAG-CtIP-D6	Junjie Chen (344)	N/A
hCas9	Addgene (400)	RRID:Addgene_41815
Software and Algorithms		
LI-COR Image Studio Software	LI-COR	RRID:SCR_015795
MetaMorph Microscopy Automation and Image Analysis Software	Molecular Devices	RRID:SCR_002368
MetaXpress 6	Molecular Devices	RRID:SCR_016654
ImageJ	https://imagej.net	RRID:SCR_003070
GraphPad Prism 8	GraphPad	RRID:SCR_002798
BD FACSCalibur Flow Cytometry System	BD Biosciences	RRID:SCR_000401
Other		
Gene Pulser Xcell Electroporation System	Bio-RAD	Cat#165-2661
CS-600 ^{137}Cs irradiator	Picker	N/A
Fisherbrand Model 705 Sonic Dismembrator	Fisher Scientific	N/A
Diagenode Bioruptor Homogenizer	Diagenode	N/A
Mini-PROTEAN Tetra Handcast Systems	Bio-RAD	N/A
Trans-Blot Transfer Medium nitrocellulose membrane	Bio-RAD	Cat#162-0112
Immobilon®-FL PVDF Membrane	Millipore-Sigma	Cat#IPFL00010
LI-COR Odyssey Fc Imaging System	LI-COR	N/A
Zeiss Axio Imager Z1 Upright Fluorescence Microscope	ZEISS	N/A
Applied Biosystems 7900HT Fast Real-Time PCR System	Applied Biosystems	RRID:SCR_018060

Table 3.2: Primers

Name	DNA Sequence (5'→3')*	Ref	Cell Line	Assay
primer set p1: for	GGAAGATGTCCCTTGTATCACCAT	(208)	U2OS-DSB + ER-mCherry-LacI-*Fok*I-DD	ChIP (**Fig. 3.3**)
primer set p1: rev	TGGTTGTCAACAGAGTAGAAAGTGAA			
primer set p4: for	CCACCTGACGTCTAAGAAACCAT			
primer set p4: rev	GATCCCTCGAGGACGAAAGG			
Chr 1 DSB 335 nt: for	GAATCGGATGTATGCGACTGATC	(405)	U2OS ER-*Asi*SI	qPCR for ssDNA (**Fig. 3.4**)
Chr 1 DSB 335 nt: rev	TTCCAAAGTTATTCCAACCCGAT			
Chr 22 DSB 200 nt: for	ACCATGAACGTGTTCCGAAT	(406)		
Chr 22 DSB 200 nt: rev	GAGCTCCGCAAAGTTTCAAG			
Chr1 89231183: for	GATTGGCTATGGGTGTGGAC	(195)		ChIP (**Fig. 3.4**)
Chr1 89231183: rev	CATCCTTGCAAACCAGTCCT			
Chr6 90404906: for	TGCCGGTCTCCTAGAAGTTG			
Chr6 90404906: rev	GCGCTTGATTTCCCTGAGT			
Chr22 21292316: for	TGGCTGGAACTGCTTTCTTT			
Chr22 21292316: rev	GGTGAGTGAATGAGCTGCAA			

*all primers custom synthesized by Sigma

Table 3.3: Peptides

Name	Origin	Sequence***	Amino Acid Residues	Molecular Weight (kDa)	Manufacturer & Catalogue ID	Purity (%)	Solvent	Stock Conc. (µg/µL)
Biotin-H2A-C-term	human H2A, residues 112-126**	**Biotin**-Ahx-QAVLLPKKTESHHKA	15	1.91324	Bio Basic Canada Inc. (Markham, CAN) custom product	96.02	H_2O	2.5
H2A-N-term-K13Ub	human H2A, residues 5-21**	KQGGKARAK(-**Ub**)AKTRSSRA ubiquitin conjugated at K13 via an isopeptide bond	17 (peptide) + 76 (ubiquitin)	10.36	UbiQ (Amsterdam, NL) # UbiQ-172	≥90%	50 mM HEPES pH 8.0, 100 mM NaCl, 2.5% DMSO in H_2O	0.5
H2A-C-term-K118Ub	human H2A, residues 112-126**	QAVLLPK(-**Ub**)KTESHHKA ubiquitin conjugated at K118 via an isopeptide bond	15 (peptide) + 76 (ubiquitin)	11.1	UbiQ (Amsterdam, NL) # UbiQ-060	≥95%	50 mM HEPES pH 8.0, 100 mM NaCl, 2.5% DMSO in H_2O	0.5
H2A-C-term-K119Ub	human H2A, residues 112-126**	QAVLLPKK(-**Ub**)TESHHKA ubiquitin conjugated at K119 via an isopeptide bond	15 (peptide) + 76 (ubiquitin)	10.22	UbiQ (Amsterdam, NL) # UbiQ-061	≥95%	50 mM HEPES pH 8.0, 100 mM NaCl, 2.5% DMSO in H_2O	0.5
Biotin-H2A-C-term-K119Ub	human H2A, residues 112-129**	**Biotin**-Ahx-QAVLLPKK(-**Ub**)TESHHKAKGK ubiquitin conjugated at K119 via an isopeptide bond	18 (peptide) + 76 (ubiquitin)	10.88	UbiQ (Amsterdam, NL) # UbiQ-185	≥95%	50 mM HEPES pH 8.0, 100 mM NaCl, 1.25% DMSO in H_2O	0.5

**amino acid count ignores initiator methionine
***Ahx: 6-amino-hexanoic acid linker

Chapter 4 – The Role of RNF138 in DNA End Resection is Regulated by Ubiquitylation and CDK Phosphorylation

4.1 Summary

Double-strand breaks (DSBs) are DNA lesions that pose a significant threat to genomic stability. The repair of DSBs by the homologous recombination (HR) pathway is preceded by DNA end resection, the 5' to 3' nucleolytic degradation of DNA away from the DSB. We and others previously identified a role for RNF138, a RING finger E3 ubiquitin ligase, in stimulating DNA end resection and HR. Yet, little is known about how RNF138's function is regulated in the context of DSB repair. Here, we show that RNF138 is phosphorylated at residue T27 by cyclin-dependent kinase (CDK) activity during the S and G2 phases of the cell cycle. We also observe that RNF138 is ubiquitylated constitutively, with ubiquitylation occurring in part on residue K158 and rising during the S/G2 phases. Interestingly, RNF138 ubiquitylation decreases upon genotoxic stress. By mutating RNF138 at residues T27, K158, and the previously identified S124 ATM phosphorylation site (Han *et al.*, *PLOS One*, 2016), we find that post-translational modifications at all three positions mediate DSB repair. Cells expressing the T27A, K158R, and S124A variants of RNF138 are impaired in DNA end resection, HR activity, and are more sensitive to ionizing radiation compared to those expressing wildtype RNF138. Our findings shed more light on how RNF138 activity is controlled by the cell during HR.

4.2 Introduction

DNA double-strand breaks (DSBs) occur when both DNA strands are severed in close proximity and are considered the most dangerous DNA lesion (434). They are mainly repaired by two major mechanisms, namely homologous recombination (HR) and non-homologous end joining (NHEJ). HR typically uses the sister chromatid as a template for repair (71). As the sister chromatid is generated upon DNA replication, this restricts HR activity to the S and G2 phases of the cell cycle (24, 435). HR commences with DNA end resection, the 5' to 3' nucleolytic degradation of DNA away from the DSB (46). The process generates 3' single-stranded DNA (ssDNA) overhangs which are rapidly coated by RPA (replication protein A) complexes (46). End resection is initiated by the nuclease activities of the MRN (Mre11-Rad50-Nbs1) complex (46), the Mre11 endonuclease activity being activated upon binding to CtIP (51, 52, 58). The overhangs are further extended by the exonucleases Exo1 and Dna2 (46), after which RPA is exchanged for the Rad51 recombinase. Rad51 activity then drives the search for the homologous locus in the sister chromatid, initiating strand invasion and the eventual restoration of the site of damage by DNA synthesis (71).

If DSBs are instead repaired by NHEJ, the two DNA ends are directly ligated together once they are made to be chemically compatible by end processing (23). NHEJ requires binding of the DNA ends by the Ku70-Ku80 (Ku) heterodimer (316), which serves as a platform to assemble the NHEJ machinery (23, 34, 232). NHEJ is active during all phases of the cell cycle (435), but is especially important in G1 phase as that is when HR is not active. The decision of whether to perform NHEJ or HR is a dynamic process governed by multiple decision points (436). End resection biases cells to performing HR, as the resulting ssDNA overhangs are not amenable to ligation by NHEJ, and Ku itself has low affinity to ssDNA (316). However, Ku recruits to DSBs

regardless of the cell cycle phase (132), and its presence on chromatin is a block to end resection (317, 318). Thus, the removal of Ku is required for both end resection and HR to proceed (317, 318).

A recurring theme in the regulation of DSB repair is post-translational modification (PTM), the reversible covalent conjugation of protein or chemical groups onto biomolecules. PTMs include phosphorylation, catalyzed by kinases such as the cyclin-dependent kinases (CDKs) (363), and by members of the PI-3-kinase-related kinase (PIKK) family, such as ATM, which is activated by DNA damage (87). Ubiquitylation also plays major roles in the DSB response (42). Here, the ubiquitin protein is conjugated to its target substrates through sequential activity of three classes of enzyme, E1, E2 and E3. We and others have shown that the E3 ubiquitin ligase RNF138 promotes HR (132, 133, 314, 315). Originally found to inhibit Wnt-β-catenin signaling (303), RNF138 belongs to a family of E3s with similar domain structure (304). This includes an N-terminal RING (Really Interesting New Gene) finger domain, which interacts with the E2 ubiquitin conjugating enzyme (133, 303, 304), three zinc finger (ZNF) domains, and a C-terminal ubiquitin-interacting motif (UIM) (**Fig. 3.S13**). The zinc finger domains mediate its recruitment to DNA damage (132, 133, 315) and bind DNA (132, 133), showing preference for ssDNA overhangs (132). Mechanistically, RNF138 promotes HR by stimulating DNA end resection (132, 133). It promotes the ubiquitylation of Ku80, which evicts Ku from chromatin (132). It also mediates the ubiquitylation of CtIP, facilitating CtIP's accumulation at DSB sites (133). These parallel actions – promoting the recruitment of CtIP, a stimulator of resection, and facilitating the dissociation of Ku, which blocks resection – help ensure end resection can proceed (437). Downstream of end resection, a third target of RNF138-dependent ubiquitylation was found to be Rad51D (314, 315), a Rad51 paralogue that may contribute to Rad51 filament assembly (321). Although it is not clear

how Rad51D ubiquitylation contributes to HR (314), the recruitment of Rad51D to DNA damage is dependent on RNF138 (315).

While it is established that RNF138 participates in HR, how its activity is controlled in HR has not been extensively investigated. Intriguingly, in response to IR, RNF138-dependent ubiquitylation of Ku80 occurs in S/G2 phase, but not G1 phase (132). This hints RNF138 activity might be under cell cycle regulation to coincide with the onset of HR. We also wondered if RNF138 could be regulated by ubiquitin conjugation. In this study, we find that RNF138 is phosphorylated in S and G2 phase by CDK activity on residue T27, and is also ubiquitylated on residue K158. Both sites mediate RNF138 function in DSB repair, as cells expressing the T27A and K158R mutants exhibit defective DNA end resection, HR activity, and heightened sensitivity to ionizing radiation relative to those expressing wildtype RNF138. We also investigate whether the same processes are impacted by mutations at S124, a previously identified ATM phosphorylation site on RNF138 (315). Our findings uncover how RNF138 activity is governed by the cell, providing more insight into its contribution to DSB repair.

4.3 Materials and Methods

4.3.1 DNA Constructs and siRNAs

The FLAG-RNF138 vector (containing the full-length RNF138 open reading frame (ORF) and a single FLAG tag (DYKDDDDK) directly C-terminal to it, within the AbVec2.0 expression vector) was a gift from Michael Hendzel (University of Alberta). pEGFP-RNF138-WT and -ΔUIM (with the RNF138 ORF C-terminal of the GFP tag) were generated previously (132); the ΔUIM mutant contains residues 1-228 of full-length RNF138. pCDNA3-HA-ubiquitin-WT and -L73P (both

containing residues 2-76 of ubiquitin) plasmids were gifts from Tony T. Huang (New York University School of Medicine) (438). pcDNA4-TO-hygromycin-sfGFP-MAP was a gift from Dannel McCollum (Addgene plasmid # 44100; http://n2t.net/addgene:44100; RRID:Addgene_44100) (439). The siRNA-resistant RNF138 ORF was inserted into the pcDNA4-TO-hygromycin-sfGFP-MAP vector between the superfolder GFP (sfGFP)-N175 and His_8 modules by GenScript Biotech (Piscataway, New Jersey, USA), producing the pcDNA4-TO-hygromycin-sfGFP-RNF138-MAP (abbreviated sfGFP-RNF138) construct. The siRNA-resistant RNF138 ORF was inserted into the pmCherry-C1 vector by Biomatik Corporation (Kitchener, Ontario, Canada), producing the mCherry-RNF138 construct. The sfGFP-RNF138-T27A, -S124A, and -K158R mutants were generated by GenScript Biotech. All other mutants were generated using the Q5 Site-Directed Mutagenesis Kit (New England Biolabs) according to the manufacturer's instructions. Sequences were verified by Sanger sequencing performed by the Molecular Biology Service Unit (Dept. of Biological Sciences, University of Alberta). DNA primers used for Sanger sequencing (**Table 4.1**) and site-directed mutagenesis (**Table 4.2**) and siRNA (**Table 4.3**) were custom synthesized by Sigma-Aldrich (St. Louis, Missouri, USA).

4.3.2 Cell Lines, Tissue Culture, and Transfection of Nucleic Acids

All cells were maintained at 37°C in a humidified atmosphere containing 5% CO_2. Unless indicated, all cells were cultured in low glucose Dulbecco's Modified Eagle's medium (DMEM) supplemented with 10% fetal bovine serum (FBS, Gibco), 50 units/mL penicillin and 50 µg/mL streptomycin (both Gibco). Cells approaching confluency were detached using trypsin-EDTA solution, 0.25% (Sigma-Aldrich) prior to subculture. All cell lines were tested for *Mycoplasma* using DAPI staining. HeLa cells were a gift from Alfred C.O. Vertegaal (Leiden University). The

HeLa HB-ubiquitin cell line (440) was a gift from Peter Kaiser (University of California, Irvine). HEK293 cells were a gift from Michael Hendzel (University of Alberta). U2OS cells stably expressing doxycycline-inducible I-*Sce*I and the DR-GFP reporter (TRI-DR-U2OS) were a gift from Philipp Oberdoerffer (Johns Hopkins University) (279). U2OS cells stably integrated with FRT (flippase recognition target) sites and the TetR tetracycline repressor-expressing pcDNA6/TR vector (U2OS-TREx cells) were a gift from Armin Gamper (University of Alberta). The Flp recombinase (Flp-In) system was not exploited to generate stable cell lines in U2OS-TREx. Instead, pcDNA4-TO-hygromycin-sfGFP-RNF138-MAP constructs were stably integrated into U2OS-TREx cells upon transient transfection and selection in DMEM supplemented with 10% charcoal-stripped FBS (Sigma-Aldrich) and 200 μg/mL hygromycin B (Invitrogen). To enrich for cells expressing the sfGFP-RNF138 constructs, 5 μg/mL doxycycline (Sigma-Aldrich) was added to the culture medium for 20-24 hours, then GFP^+ cells were isolated by fluorescence-activated cell sorting (FACS). U2OS-TREx cells stably expressing RNF138 constructs were maintained in DMEM with 10% FBS, 150 to 200 μg/mL hygromycin B, and 10 μg/mL blasticidin S (Gibco). Unless indicated otherwise, plasmid DNA was transfected into cells using Effectene Transfection Reagent (Qiagen) according to the manufacturer's instructions 18-24 hours before assays were performed. siRNA was transfected into freshly seeded cells using Lipofectamine RNAiMax Transfection Reagent (Invitrogen) once ~48 hours before assays were to be performed. Unless indicated otherwise, siRNA (**Table 4.3**) to RNF138 was transfected at a final concentration of 60 nM, while siRNAs to CDK1 and CDK2 were transfected at a final concentration of 50 nM. Control siRNA targeting luciferase was transfected at the same final concentration as the targeted siRNA.

4.3.3 Cell Cycle Synchronization

HeLa cells were synchronized by the double thymidine block method. Thymidine (4 mM final concentration) was added to the culture medium of asynchronous cells at ~40% confluency for 16-18 hours (block #1). The cells were then washed twice with room temperature sterile PBS, replaced with warmed DMEM + 10% FBS, and incubated at 37°C (release). 7-8 hours post-release, cells were transfected with DNA constructs, if necessary. 2-3 hours post-transfection (or 9-11 hours post-release), thymidine (4 mM final concentration) was again added to the culture medium and kept for 12-14 hours (block #2). At this point the cells were considered synchronized to the G1/S transition. To allow synchronous progression through the cell cycle, the cells were released by 2 washes with ice-cold PBS followed by 37°C incubation in warm DMEM + 10% FBS. Cells were then harvested at various timepoints post-release to enrich for specific cell cycle phases (e.g. 3 hours for S phase, 7 hours for G2 phase, 11 hours for G1 phase).

4.3.4 Harvesting Cells

For HEK293, the cells were dislodged from the culture vessel by flushing the surface with the culture medium. Cells were then pelleted by centrifugation at 525*g* for 5 minutes at 4°C. The other cell lines were dislodged via trypsinization: they were washed twice in ice-cold PBS (137 mM NaCl, 2.7 mM KCl, 10 mM Na_2HPO_4, 1.8 mM KH_2PO_4, pH 7.4), detached with trypsin-EDTA solution, 0.25% (Sigma-Aldrich) at 37°C for 5 minutes, resuspended into 4 volumes of ice-cold DMEM + 10% FBS, and pelleted by centrifugation at 525*g* for 5 minutes at 4°C. All cells were then resuspended into ice-cold PBS and centrifuged again (525*g*, 5 minutes, 4°C). After removing the supernatant, the pellet was flash frozen in liquid nitrogen before storage at -80°C.

4.3.5 Cell Cycle Profiling by Flow Cytometry

If needed, this procedure was performed during the above cell harvesting method. When cells were resuspended in PBS after the first centrifugation, 10-20% of the cell pellet was saved. To this fraction, much of the supernatant was removed, after which the cells were vortexed into an ice-cold mixture of PBS prepared with 70% ethanol as the solvent. The cells were fixed by -20°C incubation for at least 30 minutes. The cells were washed once in PBS, then tumbled end-over-end for 30 minutes at room temperature in PBS containing 100 µg/mL RNase A (Invitrogen) and 3.8 mM sodium citrate. Propidium iodide was added to a final concentration of 50 µg/mL, and the cells were again tumbled end-over-end at room temperature for at least 30 minutes. The propidium iodide intensity was then measured for single cells by flow cytometry using a FACSCanto II (BD Biosciences).

4.3.6 Cell Treatments

All inhibitors were purchased from Millipore-Sigma or Selleck Chemicals and dissolved in DMSO (or, for hydroxyurea, water). Inhibitors were diluted in warmed (37°C) culture medium immediately prior to cell treatment. Vehicle controls contained only the solvent of the inhibitors diluted to the same extent. Unless indicated otherwise, cells were treated with the following concentrations of inhibitors: 25 µM roscovitine, 2.5 µM AZD5438, 10 µM RO-3306, 10 µM SB203580. For treatment with ultraviolet light (UV), cell monolayers were washed in PBS, which was then removed, and exposed to 20 seconds of UV (equivalent to ~60 J/m^2). The culture medium was quickly re-added and cells were incubated at 37°C for 1 hour after which they were harvested. For treatment with ionizing radiation, cells were exposed to 10 Gy from a ^{60}Co source (Gammacell 220 Irradiation Unit, purchased 1978, Atomic Energy of Canada Limited), allowed to recover for

1 hour at 37°C, then harvested. For the remaining DNA damaging agents, cells were replaced with culture medium containing the agents and incubated at 37°C (1 μM camptothecin for 1 hour; 25 μM phleomycin for 1 hour; 2 mM hydroxyurea for 4 hours), then harvested.

4.3.7 Preparation of Whole Cell Extracts

Frozen pellets (obtained from the above cell harvesting protocol) were resuspended into ice-cold High SDS Lysis Buffer (25 mM HEPES pH 7.4, 500 mM NaCl, 2% sodium dodecyl sulfate, 1% Triton X-100, 0.5% sodium deoxycholate, 1 mM EDTA) supplemented with 2X cOmplete protease inhibitor cocktail, EDTA-free (cOmplete, Roche) and 1X phosSTOP phosphatase inhibitor cocktail (phosSTOP, Roche). The mixture was then sonicated with a Fisher Scientific Model 705 Sonic Dismembrator with microtip probe (at amplitude 1 to 5, for 1 minute). 4X SDS Sample Buffer (250 mM Tris pH 6.8, 8% sodium dodecyl sulfate, 40% glycerol, 0.2% bromophenol blue) was then added to attain a final concentration of 1X, while 2-mercaptoethanol (BME) was added to a final concentration of 5%. The samples were treated at 95°C for 5 minutes at 900 rpm on a ThermoMixer F1.5 (Eppendorf) prior to resolution by SDS-PAGE (sodium dodecyl sulfate polyacrylamide gel electrophoresis).

4.3.8 SDS-PAGE and Immunoblotting

Samples were loaded into hand-cast mini-gels comprising Tris (37.5 mM, pH 8.8 for the resolving layer; 12.5 mM, pH 6.8 for the stacking layer), 0.1% sodium dodecyl sulfate (SDS), and 5-12% polyacrylamide. Precision Plus protein dual color standards (Bio-Rad) were loaded as the molecular weight ladder. Electrophoresis was performed at 150 V in Running Buffer (25 mM Tris pH 8.3, 192 mM glycine, 0.1% SDS). The resolved proteins were then wet electro-transferred onto

0.2 μm nitrocellulose membrane for 1 hour at 110 V in Transfer Buffer (25 mM Tris pH 8.3, 192 mM glycine, 20% methanol). To perform immunoblot, the nitrocellulose was first blocked in 4% fish skin gelatin (FSG) dissolved in TBS (50 mM Tris pH 7.5, 150 mM NaCl) at room temperature. TBS with 5% bovine serum albumin (BSA) was used as the blocking solution when phospho-specific antibodies were used as the primary antibody. The primary antibodies (**Table 4.4**) were diluted in freshly prepared TBS + 0.1% Tween-20 (TBST). For phospho-specific antibodies, 5% BSA was included in this solution, while for the anti-RNF138 antibodies, 2% FSG was included. The diluted antibodies were incubated with the membranes for either 1 hour at room temperature or overnight at 4°C under gentle rocking. The membranes were then shaken in TBST (3 times, 10 minutes each), incubated for 1 hour at room temperature with horseradish peroxidase (HRP)-, IRDye 680RD- or IRDye 800CW-conjugated secondaries (all LI-COR Biosciences) in TBST under gentle rocking, and shaken in TBST (3 times, 10 minutes each) and TBS (once, 10 minutes). HRP activity was detected by incubating the membranes in Amersham ECL Prime Western Blotting Detection Reagent (Cytiva) for 2 minutes. Enhanced chemiluminescence (HRP) or fluorescence (IRDye) signals were acquired on the Odyssey Fc Imaging System and quantified by densitometry with Image Studio software (both LI-COR Biosciences). If re-probing was required, membranes were treated with Stripping Buffer (100 mM glycine pH 2.2, 1% SDS) for 30 minutes with vigorous shaking, rinsed with distilled water, and air-dried overnight. They were then re-blocked and probed with the necessary primary and secondary antibodies. To ensure immunoblots for loading controls of whole cell extracts (actin, tubulin) and immunoprecipitations (anti-GFP on GFP-RNF138, anti-FLAG on FLAG-RNF138) could be quantified without saturation, in such situations primary antibodies were used at low concentrations (**Table 4.4**) and blots were detected via fluorescence (IRDye) instead of enhanced chemiluminescence.

4.3.9 FLAG Immunoprecipitation

Pellets of FLAG-RNF138-expressing HeLa cells from a 100 mm dish were resuspended into ice-cold NETN-500 (50 mM Tris pH 8.0 at 4°C, 500 mM NaCl, 0.5% IGEPAL CA-630, 1 mM EDTA) supplemented with fresh 2X cOmplete, 1.25X phosSTOP, and 50 mM N-ethylmaleimide (NEM) and shaken on ice (250 rpm, 20 minutes). The lysate was clarified by centrifugation at 20000*g* for 15 minutes at 4°C, and the resulting pellet was discarded. 10% of the supernatant was saved as an input control and mixed with an equal volume of 2X SDS Sample Buffer (125 mM Tris pH 6.8, 4% sodium dodecyl sulfate, 20% glycerol, 0.1% bromophenol blue) along with BME to a final concentration of 5%. The input control was then heated to 95°C for 5 minutes at 900 rpm on a ThermoMixer F1.5. The remaining supernatant (90%) was diluted to reduce the NaCl concentration to 150 mM, then mixed with 20 µL of anti-FLAG M2 magnetic beads (Sigma) that were pre-washed twice in ice-cold TBS + 0.5% IGEPAL CA-630 (TBSN). The mixture was tumbled end-over-end for 2 hours at 4°C. Non-specific binding was removed by 4 washes in ice-cold TBSN. Each wash involved vortexing for 20 seconds, centrifuging at 2700*g* for 2 minutes, placing the sample on a magnetic rack, and aspirating the supernatant. Bound proteins were eluted off the beads by adding 2X SDS Sample Buffer and heating for 10 minutes at 95°C at 1200 rpm (ThermoMixer F1.5). The eluate and input control fractions were then processed for SDS-PAGE and immunoblotted. For the eluate fraction, the modification of interest (e.g. phosphorylation) was blotted for first, then the membrane was stripped and re-probed to detect immunoprecipitated FLAG-RNF138.

4.3.10 Co-Immunoprecipitation

Pellets of GFP construct-expressing HEK293 cells from a 100 mm dish were processed as in the procedure for GFP Immunoprecipitation (**Section 4.3.12**), with the following changes: NETN-150 (50 mM Tris pH 8.0 at 4°C, 150 mM NaCl, 0.5% IGEPAL CA-630, 1 mM EDTA) was used in place of RIPA Buffer, 20 µL of GFP Selector agarose beads (NanoTag Biotechnologies, Göttingen, Germany) were used, and the beads were washed 4 times with only NETN-150 to remove non-specific interactions.

4.3.11 Isolation of Ubiquitin Conjugates by Nickel Affinity Purification

HeLa HB-ubiquitin cells from 150 mm dishes were harvested as described above, except prior to pelleting for flash freezing, the cells were resuspended into ice-cold PBS and 10% of each sample was taken out to serve as the input control. All samples were then pelleted by centrifugation (525*g*, 5 minutes, 4°C) and flash frozen in liquid nitrogen before storage at -80°C. The 10% input control was processed separately for lysis to prepare whole cell extract (as above) while the remainder was processed for nickel affinity purification, described here. All buffers were prepared at most 4 hours before use. All washes entailed vortexing in the indicated buffer for at least 20 seconds, centrifugation at 750*g* for 2 minutes, and removal of the supernatant via vacuum aspiration. Cell pellets were dissociated into ice-cold Guanidine Lysis Buffer (6 M guanidine-HCl, 100 mM sodium phosphate buffer pH 8.0, 10 mM Tris, 5 mM imidazole, 5 mM BME) by vortex and sonicated for 1 minute (amplitude 25, Fisher Scientific Model 705 Sonic Dismembrator with microtip probe). The lysate was then mixed with 150 µL of Ni-NTA agarose beads (Qiagen) that were pre-washed three times in Guanidine Lysis Buffer. The mixture was agitated on a rocker for 4 hours at room temperature. Non-specific interactions were removed with sequential washes at

room temperature: once in Guanidine Wash Buffer (6 M guanidine-HCl, 100 mM sodium phosphate buffer pH 8.0, 10 mM Tris, 10 mM imidazole, 0.1% Triton X-100, 5 mM BME), once in pH 8 Urea Wash Buffer (8 M urea, 100 mM sodium phosphate buffer pH 8.0, 10 mM Tris, 10 mM imidazole, 0.1% Triton X-100, 5 mM BME), and three times in pH 6.3 Urea Wash Buffer (8 M urea, 100 mM sodium phosphate buffer pH 6.3, 10 mM Tris, 0.1% Triton X-100, 5 mM BME). Bound proteins were eluted off the beads with Ni-NTA Elution Buffer (150 mM Tris pH 6.7, 200 mM imidazole, 5% sodium dodecyl sulfate, 30% glycerol, 0.05% bromophenol blue, 5% BME) at 60°C for 30 min on a ThermoMixer F1.5 (Eppendorf) at 1200 rpm and resolved by SDS-PAGE for subsequent immunoblotting.

4.3.12 GFP Immunoprecipitation

Pellets of GFP construct-expressing HEK293 cells from a 100 mm dish were resuspended into ice-cold RIPA Buffer (50 mM Tris pH 7.4 at 4°C, 150 mM NaCl, 1% IGEPAL CA-630, 1% sodium deoxycholate, 0.1% SDS, 1 mM EDTA) supplemented with fresh 2X cOmplete, 1.25X phosSTOP, and 50 mM NEM and shaken on ice (250 rpm, 20 minutes). The lysate was centrifuged (20000*g*, 15 minutes, 4°C), and the pellet discarded. 10% of the supernatant was taken out as an input control and processed as in the FLAG Immunoprecipitation procedure (**Section 4.3.9**). The remaining supernatant (90%) was mixed with 15 µL of GFP Selector agarose beads (NanoTag Biotechnologies, Göttingen, Germany) that were pre-washed twice in ice-cold RIPA Buffer, then tumbled end-over-end at 4°C for 1 hour. To remove non-specific binding, the beads were washed twice in ice-cold RIPA Buffer, then 4 times in ice-cold Stringent Wash Buffer (50 mM Tris pH 8.0 at 4°C, 2 M NaCl, 1% IGEPAL CA-630, 0.25% sodium deoxycholate, 0.1% SDS, 1 mM EDTA). Each wash involved vortexing for 20 seconds, centrifuging at 3000*g* for 2 minutes, and aspirating

the supernatant. Bound proteins were eluted by adding to the beads 2X SDS Sample Buffer with 5% BME and heating on the Thermomixer (95°C, 30 minutes, 1200 rpm). Both the input and eluate fractions were then subjected to SDS-PAGE and immunoblot analysis. For the eluate fraction, the modification of interest (e.g. ubiquitylation) was blotted for first, then the membrane was stripped and re-probed to detect the immunoprecipitated GFP-tagged protein.

4.3.13 Cycloheximide Chase Assay

HEK293 cells were transfected with the indicated GFP-RNF138 DNA constructs. 20 hours later, cycloheximide was added to the culture medium to 100 μg/mL with or without MG132 (5 μM final concentration). Cells were incubated for various timepoints up to 16 hours and then harvested. Whole cell extracts were prepared, and protein expression levels were analyzed by fluorescence-based immunoblotting, with GFP intensity normalized to the intensity of actin.

4.3.14 Laser Microirradiation of Live Cells

U2OS cells were seeded on 35 mm glass-bottom dishes (MatTek Corporation). 24 hours later, they were transfected with 200 ng of the indicated DNA construct and incubated for ~16 hours. Prior to imaging, cells were pre-sensitized with 0.5 μg/mL Hoechst 33258 for 30 min at 37°C, washed with PBS, and replaced with warmed phenol red-free DMEM containing 25 mM HEPES + 10% FBS (both Gibco). The dishes were maintained at 37°C in a humidified 5% CO_2 atmosphere while being imaged on a Nipkow spinning disk confocal system (UltraVIEW ERS, Perkin-Elmer) mounted on an Axiovert 200M inverted microscope (Zeiss) and equipped with an sCMOS camera (Prime BSI, Photometrics). Localized DNA damage was induced in a single 1 μm thick line spanning the width of the cell nucleus using a 5 mW 405 nm diode laser coupled to a FRAP

(fluorescence recovery after photobleaching) module (UltraVIEW Photokinesis, PerkinElmer) with the following settings: 20% power output, 20 iterations. The GFP fusion proteins were then excited with a 488 nm argon laser and seen through a 63X, 1.4 numerical aperture oil immersion DIC Plan-Apochromat objective lens (Zeiss). Time-lapse images in the GFP emission channel were recorded using Volocity 6.3 software (PerkinElmer). The fluorescence intensity at the laser stripe over time was determined via Image J software. Measurements from 30-75 cells pooled from three independent experiments were averaged.

4.3.15 Immunofluorescence Staining

Stable cell lines generated in U2OS-TREx were seeded onto sterilized glass coverslips (#1.5 thickness, Electron Microscopy Sciences) and transfected with siRNA 1 hour later. ~28 hours post-transfection, 5 μg/mL doxycycline was added to the culture medium for ~16 hours to induce sfGFP-RNF138 expression. After a 1-hour treatment with 1 μM camptothecin, the cells were washed twice with ice-cold PBS, then incubated twice, 3 minutes each, with ice-cold RPA Extraction Buffer (25 mM HEPES pH 7.9 at 4°C, 300 mM sucrose, 50 mM NaCl, 0.5% Triton X-100, 1 mM EDTA, 3 mM $MgCl_2$). They were then washed again twice with ice-cold PBS prior to fixation at room temperature for 20 minutes in 2% paraformaldehyde in PBS. The reaction was quenched for 10 minutes in 100 mM NH_4Cl in PBS, and the cells were permeabilized for 5 minutes in PBS + 0.5% Tween-20. The cells were then incubated with primary antibodies (**Table 4.4**) for 1 hour at room temperature or overnight at 4°C, incubated in PBS + 0.1% Tween-20 for 5 minutes, washed 6 times in PBS, and incubated with secondary antibodies for 1 hour at room temperature. All antibodies were diluted in PBS, and antibody incubations were performed with the coverslips being inverted into 75 μL droplets of the antibody solution. The cells were then counterstained in

10 ng/μL DAPI in PBS for 20 minutes, washed 6 times in PBS, and mounted onto microscopy slides in Mounting Medium (2% propyl gallate in PBS prepared with 10% DMSO and 80% glycerol as the solvent). Images were acquired on a fluorescence microscope (Zeiss AxioImager.Z2) using version 7.10.4 of MetaMorph software (Molecular Devices). The microscope utilized a 1.4 numerical aperture 40X oil immersion DIC M27 Plan-Apochromat objective lens (Zeiss) and Prime BSI sCMOS camera (Teledyne Photometrics). Extraction-resistant nuclear foci were quantified using the Cell Intensity Mean of Vesicles feature of the Statistics module of Imaris x64 software version 9.9.1 (Oxford Instruments).

4.3.16 *In vivo* Homologous Recombination (DR-GFP) Reporter Assay

Per condition, ~4 X 10^6 TRI-DR-U2OS cells were electroporated with 60 nM siRNA and if necessary, 2 μg of mCherry-RNF138 DNA via a 4D-Nucleofector X Unit (program CM-104) with SE Cell Line 4D-Nucleofector X Kit L (both Lonza Bioscience). 8 hours post-transfection, 1 μg/mL doxycycline (Dox) was added to the culture medium for 24 hours to induce expression of I-*Sce*I. The culture medium was then replaced and cells were cultured without doxycycline for another 24 hours. Cells were collected according to the above cell harvesting procedure except that instead of being flash frozen, the cells were vortexed into 2% paraformaldehyde in PBS and incubated for 20 minutes for fixation. The cells were then washed 3 times in PBS. The frequency of GFP^+ cells was measured by flow cytometry (FACSCanto II, BD Biosciences) on at least 100,000 cells.

4.3.17 Clonogenic Survival Assay

Stable cell lines of U2OS-TREx were seeded in 100 mm dishes and transfected with siRNA 1 hour later. ~40 hours post-transfection, the cells were detached by trypsinization and kept on ice. The cell density was measured on an automated cell counter (Corning) equipped with CytoSMART Cloud (CytoSMART Technologies). Cells were then seeded in duplicate onto 60 mm dishes and incubated at 37°C with or without 5 µg/mL doxycycline for ~16 hours. The number of cells seeded per dish were as follows: parental + siCTRL – 900 cells, parental or sfGFP-RNF138-WT + siRNF138 – 4000 cells, all other cell lines + siRNF138 – 12000 cells. The dishes were exposed to up to 5 Gy of ionizing radiation from a ^{60}Co source (Gammacell 220 Irradiation Unit, purchased 1978, Atomic Energy of Canada Limited), after which the culture medium was replaced. The cells were incubated at 37°C for 7-10 days; 5 µg/mL doxycycline was included in the medium if sfGFP-RNF138 expression was required. The medium was then removed and cells were fixed and stained in 0.5% crystal violet/25% methanol. Colonies of ≥50 cells were counted. The surviving fraction was calculated by dividing the number of colonies formed at a given dose by the number that formed at 0 Gy.

4.3.18 Sequence Alignment

Amino acid sequences of RNF138 orthologues were obtained from UniProt, aligned with Clustal Omega (European Bioinformatics Institute, European Molecular Biology Laboratory), and annotated in ESPript 3.0 (441).

4.3.19 AlphaFold Modeling

RNF138 modeling and predictions were performed using the ColabFold implementation of AlphaFold (https://github.com/sokrypton/ColabFold) (442–445). The AlphaFold_MMseqs2 Google Colab notebook (version 1.5.2) was used as previously described (446). Confidence metrics were plotted with Microsoft Excel (version 2204) and Morpheus (https://software.broadinstitute.org/morpheus).

4.3.20 Image and Data Processing

Raw micrographs and immunoblot scans were adjusted with the Levels tool and cropped in Adobe Photoshop 2023 and 2021, respectively. For immunofluorescence micrographs, images from the same biological replicate were scaled to identical settings. For GFP immunoprecipitation assays, GFP-RNF138 ubiquitylation was quantified from densitometry readings of immunoblots with Image Studio software (LI-COR Biosciences). HA signal from immunoprecipitates was normalized to the GFP signal immunoprecipitated. All graphs were generated in Prism 9 (GraphPad) and display the mean with error bars showing the standard deviation. Unless indicated otherwise, ordinary one-way ANOVA with Šídák's multiple comparisons test was performed to determine statistical significance. Asterisks depict statistically significant differences: ns (not significant), * ($p \leq 0.05$), ** ($p \leq 0.01$), *** ($p < 0.001$), **** ($p < 0.0001$). Figures were arranged and labeled using Adobe Illustrator 2023.

4.4 Results

4.4.1 RNF138 Protein Expression is Maintained Over the Course of the Cell Cycle

To ascertain how RNF138 is regulated, we first asked if its expression was controlled in a cell cycle-dependent manner. As the expression of the HR factor BRCA1 peaks during the S and G2 phases (447–449), we surmised RNF138 protein levels could behave similarly, coinciding with its role in mediating Ku80 ubiquitylation and eviction from chromatin in S/G2 (132). We chose to examine RNF138 expression in HeLa cells as they can be efficiently synchronized to the G1/S transition by double thymidine block. HeLa can then be released for different timepoints to approach specific cell cycle phases (450). Flow cytometric analysis confirmed that the chosen timepoints sufficiently enriched for cells in either S, G2 or G1 phase (**Fig. 4.1A**). When whole cell extracts from these samples were immunoblotted, we detected a prominent immunoreactive band above 25 kDa in all cell cycle phases (**Fig. 4.1B**). As RNF138's molecular weight is predicted to be 28 kDa, and transfecting cells with short interfering RNA (siRNA) targeting both coding and non-coding regions of the *RNF138* gene reduced detection of the band (**Fig. 4.S8A**), the immunoblot signal just above 25 kDa represents endogenous RNF138. Interestingly, while a minor increase in RNF138 expression was seen at G2 phase, RNF138 was still adequately expressed in G1 phase, and overall, substantial changes in expression were not seen at any particular phase (**Fig. 4.1C**). We thus conclude that in HeLa cells, RNF138 protein expression is relatively constant over the course of the cell cycle.

4.4.2 RNF138 is Phosphorylated at Residue T27 by CDK-Dependent Activity

We reasoned RNF138 activity might be regulated during the cell cycle by a different mechanism. Transitions in the cell cycle are controlled by cyclin-dependent kinases (CDKs),

whose activities accumulate at specific phases, and are stimulated when bound to their regulatory subunits, the cyclins (96, 97). CDK activity promotes HR and DNA end resection (98–100), and players in DNA end resection such as Mre11, Nbs1, CtIP, Dna2, and Exo1 are indeed targets of CDK phosphorylation (61, 101–107). Analysis of RNF138's primary structure revealed a single putative CDK consensus phosphorylation motif (S/T-P-X-K/R) (97), with the potential phosphorylation site at threonine 27 (T27). This motif is conserved in RNF138 orthologues spanning *Xenopus laevis*, chicken, and mammals (**Fig. 4.1D**), and was predicted to be the only CDK site on RNF138 by the algorithm GPS 6.0 (451) (**Fig. 4.S8B**). Further, the AlphaFold prediction of RNF138's structure shows T27, despite being located within the RING domain, is solvent-accessible and potentially available for phosphorylation (**Figs. 4.S9A-E**). T27 is also at the centre of a positively charged surface of the RING (K26, R40, K41, R48, R80) (**Figs. 4.S9B**), the addition of a phosphoryl group potentially altering electrostatics in the region. We thus hypothesized RNF138 is phosphorylated at residue T27 by CDK activity.

To uncover if RNF138 was phosphorylated, we first transfected HeLa cells with FLAG-tagged RNF138, and performed anti-FLAG immunoprecipitation to enrich for exogenous RNF138. Expressing FLAG-RNF138 yielded a protein that migrated at 37 kDa upon sodium dodecyl sulfate polyacrylamide gel electrophoresis (SDS-PAGE) (**Fig. 4.1E**), despite RNF138 being predicted to be 28 kDa. While endogenous RNF138 migrated at the expected position upon SDS-PAGE (**Figs. 4.1B, 4.S8A**), immunoprecipitated FLAG-RNF138 was detected at 37 kDa by an anti-RNF138 antibody (**Fig. 4.S10A**). We thus attribute the reduced electrophoretic mobility of FLAG-RNF138 to the FLAG tag, speculating the tag's five negatively charged aspartate residues hinder SDS binding to the protein, impeding its migration during electrophoresis. We next immunoblotted the FLAG immunoprecipitates for the presence of phospho-threonine immediately

N-terminal of a proline residue (phospho-Thr-Pro, or P-TP), a motif shared by the substrates of both CDKs and mitogen-activated protein kinases (MAPKs). We observed P-TP signal on FLAG-RNF138 (**Fig. 4.1E**), suggesting RNF138 was a substrate for phosphorylation at TP sites. To detect if RNF138 was phosphorylated in a cell cycle-dependent manner, we transfected HeLa cells with FLAG-RNF138 and synchronized them to S, G2, or G1 phase. The cells were suitably enriched for the phases of interest, although the synchronization efficiency was less than in untransfected HeLa cells (**Fig. 4.1F**, compare to **Fig. 4.1A.**), likely from minor cytotoxicity resulting from FLAG-RNF138 overexpression. FLAG immunoprecipitation revealed P-TP signal that peaked at S phase and progressively weakened as cells approached the G2 and then G1 phases (**Fig. 4.1G**). In support of this, P-TP signal was partially reduced in cells that were not synchronized by double thymidine block (**Fig. 4.1G**), which primarily contain cells in G1 phase (**Fig. 4.1F**). Importantly, the P-TP signal occurred at 37 kDa, and did not appear in immunoprecipitates from untransfected cells (**Figs. 4.1E, 4.1G**), indicating the P-TP signal was associated with FLAG-RNF138. We thus conclude RNF138 is phosphorylated in a cell cycle-dependent manner, with the modification occurring primarily in S and G2 phase.

CDK2 and CDK1 activity trigger progression through the S and G2 phases (96). To confirm that the P-TP signal observed on RNF138 was dependent on CDK activity, we treated HeLa cells expressing FLAG-RNF138 with roscovitine and AZD5438, inhibitors that target both CDK1 and CDK2 activity (365, 366), and RO-3306, an inhibitor of CDK1 activity (367). The P-TP signal in FLAG immunoprecipitates was reduced upon treatment with each inhibitor (**Fig. 4.1H**). As a control, treating the cells with an inhibitor of MAPK activity did not affect the P-TP signal, indicating the phosphorylation on RNF138 arose solely from CDK-dependent activity (**Fig. 4.S10B**). We also assessed the P-TP signal on FLAG-RNF138 when cells were transfected with

siRNA targeting CDK1 or CDK2. Knocking down either kinase capably reduced RNF138 TP-phosphorylation (**Fig. 4.1I**). While CDK1 or CDK2 depletion did decrease the proportion of cells in S or G2 phase, in both cases from 49.5% to ~45% (**Fig. 4.S10C**), accounting for this difference still resulted in the P-TP signal dropping ~50% when either CDK was depleted (**Fig. 4.1I**). Thus, the P-TP signal on RNF138 is dependent on CDK1 and CDK2. In support of a role for CDK2 in RNF138 phosphorylation, CDK2 and its binding partner Cyclin A could co-immunoprecipitate with RNF138 (**Fig. 4.1J**), indicating RNF138 may form a complex with CDK2-Cyclin A. Overall, our findings suggest RNF138 is phosphorylated by the action of CDK1 and CDK2.

To demonstrate T27 is the site of TP phosphorylation on RNF138, we ablated the site by mutating T27 to a non-phosphorylatable alanine residue (T27A) in the FLAG-RNF138 construct. P-TP signal was severely impaired in immunoprecipitates of T27A relative to wildtype (WT) FLAG-RNF138 (**Fig. 4.1K**). At first, we could not completely eliminate P-TP signal from the T27A mutant (**Fig. 4.1K**, centre panel), speculating residual signal arises from other proteins co-precipitating with FLAG-RNF138 at the same molecular weight. In line with this, loading a smaller amount of the immunoprecipitates for SDS-PAGE completely abrogated P-TP signal in the T27A mutant (**Fig. 4.1K**, right panel). Altogether, our results suggest RNF138 is phosphorylated at position T27 in a CDK1- and CDK2-dependent manner.

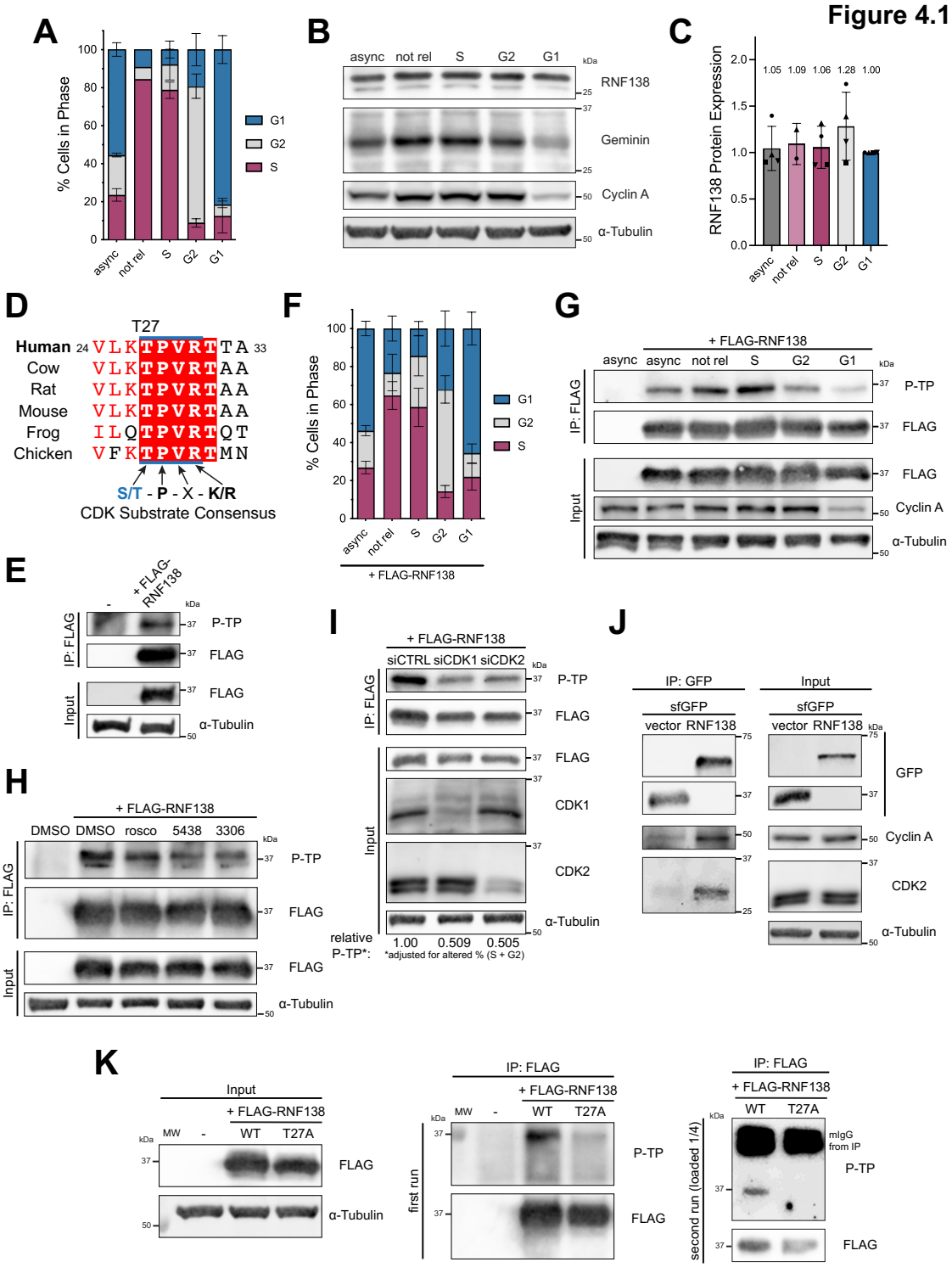

Figure 4.1: RNF138 is Phosphorylated by CDK-Dependent Activity

A) Flow cytometric analysis of propidium iodide signal in HeLa cells that were left asynchronous (async) or were synchronized by double-thymidine block without release (not rel) or with release to the S, G2, and G1 phases. **B)** Immunoblot (IB) of whole cell extracts from cells treated as in A).

Geminin expression was used to confirm enrichment for cells in S phase, while Cyclin A expression was used to confirm enrichment in the S/G2 phases. **C)** Quantification of endogenous RNF138 expression from B). RNF138 expression was normalized to α-tubulin levels. **D)** Clustal Omega amino acid sequence alignment of the CDK consensus phosphorylation motif from human RNF138 and its orthologues. UniProt accession numbers are indicated in **Fig. 4.4A**. **E)** FLAG immunoprecipitation (IP) from asynchronous HeLa cells expressing FLAG-RNF138, immunoblotted for phosphorylated-TP sites (P-TP). **F)** As in A), but with HeLa transfected with FLAG-RNF138 during the first release step of double thymidine block. **G)** FLAG IP and IB of cells processed as in F). **H)** FLAG-RNF138-expressing asynchronous HeLa cells treated with the CDK inhibitors roscovitine (rosco), AZD5438, or RO-3306 or vehicle control (DMSO) for 4 hours before harvest, FLAG IP, and IB. **I)** HeLa cells were transfected with siRNA (si) to luciferase (CTRL), CDK1 or CDK2 and FLAG-RNF138 DNA and subjected to FLAG IP and IB. Quantification of relative P-TP signal is adjusted for the altered proportion of cells in S or G2 phase resulting from knockdown of CDK1 or CDK2 from the same biological replicate (**Fig. 4.S8E**). **J)** GFP co-immunoprecipitation for endogenous CDK2 and Cyclin A in HEK293 cells transfected with sfGFP-MAP-tagged (439) RNF138 or the empty vector (vector). **K)** As in E), but with FLAG-RNF138-WT and -T27A. The IP eluate was loaded at different volumes (first, second runs). mIgG: mouse anti-FLAG immunoglobulin G fragments used for IP detected by the secondary antibody. Shown are representative results from at least 2 (I), 3 (G, H, K), at least 3 (E, J), and 4 (B) biological replicates. Averages were calculated from at least 2 (C) or at least 5 (F) biological replicates pooled together.

4.4.3 RNF138 is a Target for Polyubiquitylation

The repair of DSBs is coordinated by a cascade of ubiquitylation events, contributing to protein recruitment to sites of damage, the assembly and disassembly of complexes involved in repair, and protein turnover (42, 227). We consequently were curious if RNF138 was also a target of ubiquitylation. Previously, we studied SUMOylation of CtIP in HeLa cells stably expressing His-tagged SUMO-2; SUMO-2 is a ubiquitin-like modifier also conjugated to proteins (430). From these cells, we isolated the pool of His-tagged proteins by nickel affinity purification ("His pull-down"), which represented those that had incorporated SUMO-2. We attempted to use the same strategy to study the ubiquitylation of endogenous RNF138, this time using HeLa cells stably expressing 6xHis-biotin-tagged ubiquitin (HeLa HB-ubiquitin) (440), with the goal of exploiting the 6xHis component for nickel affinity purification. Nickel beads could successfully enrich ubiquitylated proteins from extracts of these cells relative to plain HeLa cells not expressing HB-

ubiquitin (**Fig. 4.S10D**). However, despite our best efforts, we were unable to detect ubiquitylated RNF138 in the His pull-down fraction, even though RNF138 expression was observed in whole cell extracts (**Fig. 4.S10D**, rightmost panel). Monoubiquitylated RNF138 should increase in molecular weight by ~10 kDa, and such a species (~38 kDa) was not clearly observed in HeLa HB-ubiquitin relative to plain HeLa cells (**Fig. 4.S10D**). Perhaps ubiquitylated RNF138 is of low abundance, such that these species are below the detection limit of our immunoblotting approach. The issue is exacerbated by RNF138 antibodies detecting non-specific signals during immunoblotting (**Fig. 4.S10D**, rightmost panel). It is difficult to discern which higher order species in the His pull-down arise from ubiquitylated RNF138 or are simply non-specific in nature, complicating our analysis. Thus, in our hands, we do not consider His pull-down a viable approach to study RNF138 ubiquitylation.

As an alternate strategy to detect RNF138 ubiquitylation, we turned to exogenous co-expression of green fluorescent protein (GFP)-tagged RNF138 and HA-tagged ubiquitin (HA-Ub) in cells followed by GFP immunoprecipitation. This approach would boost expression of both ubiquitin and RNF138, improving the detection of ubiquitylated RNF138. In addition to WT-ubiquitin, we also used an HA-tagged mutant, with leucine 73 substituted with proline (HA-Ub-L73P), that is conjugable to substrates but resistant to deubiquitinating enzymes (438). We hoped this would stabilize ubiquitylated RNF138, increasing the likelihood of its detection. We also performed these experiments in HEK293 cells, which capably tolerated overexpression of GFP-RNF138. GFP-RNF138 was isolated by immunoprecipitation with anti-GFP beads under stringent conditions. Eluates from the beads were then processed for SDS-PAGE and subjected to immunoblotting for the HA tag. When HA-Ub-WT and GFP-RNF138 were co-expressed, we detected a smear of immunoreactivity to HA appearing under 75 kDa and extending beyond 250

kDa, where the signal greatly intensified (**Fig. 4.2A**), strongly suggesting GFP-RNF138 (theoretically ~55 kDa in size but migrating at ~63 kDa to start) was polyubiquitylated. This signal was absent in cells when HA-Ub-WT was co-expressed with empty vector GFP (**Fig. 4.2A**). Notably, higher order HA signal was also present when the same experiment was performed with HA-Ub-L73P (**Fig. 4.2A**). Similar to before, this signal was much reduced when GFP was used in place of GFP-RNF138. However, using HA-Ub-L73P shifted the bulk of the HA smear between <75 to ~150 kDa, and reduced the intensity of the signal appearing >250 kDa (**Fig. 4.2A**). At lower molecular weights, the smear resolved to a distinct laddering pattern perhaps revealing different species of ubiquitylated RNF138, each band suggestive of a different number of ubiquitin moieties attached to the protein. The discrepancy in how RNF138 conjugates appear using HA-Ub-WT or -L73P is consistent with the observation that L73P-Ub is conjugated to targets less efficiently than WT-Ub *in vitro* (438). On ubiquitin, L73 sits in a hydrophobic patch used by some E3 ligases to assemble polyubiquitin chains, and the proline substitution disrupts hydrophobic packing in this region (438). In our case, it is clear expressing L73P- instead of WT-Ub restricts the extent by which RNF138 can be polyubiquitylated, but it is still polyubiquitylated nonetheless. Continuing on, to confirm RNF138 is ubiquitylated, we observed that the ladder of HA signal in immunoprecipitates of GFP-RNF138 was absent if HA-Ub-L73P was not transfected into cells (**Fig. 4.2B**), indicating the signal resulted from HA-Ub-L73P co-expression. We also co-expressed a truncated GFP-RNF138 deleted of its UIM (ΔUIM) (**Figs. 4.S10E, 3.S13**) with HA-Ub-L73P. Here, the bands in the HA-Ub ladder exhibited a downward shift in size relative to those from GFP-RNF138-WT, consistent with the decrease in molecular weight resulting from deleting the UIM (**Fig. 4.2C**). This definitively showed that the HA signal on GFP-RNF138 arises from

ubiquitylation events on RNF138 itself, and not from proteins that are inadvertently co-immunoprecipitated. We thus conclude that RNF138 is constitutively polyubiquitylated in cells.

Figure 4.2

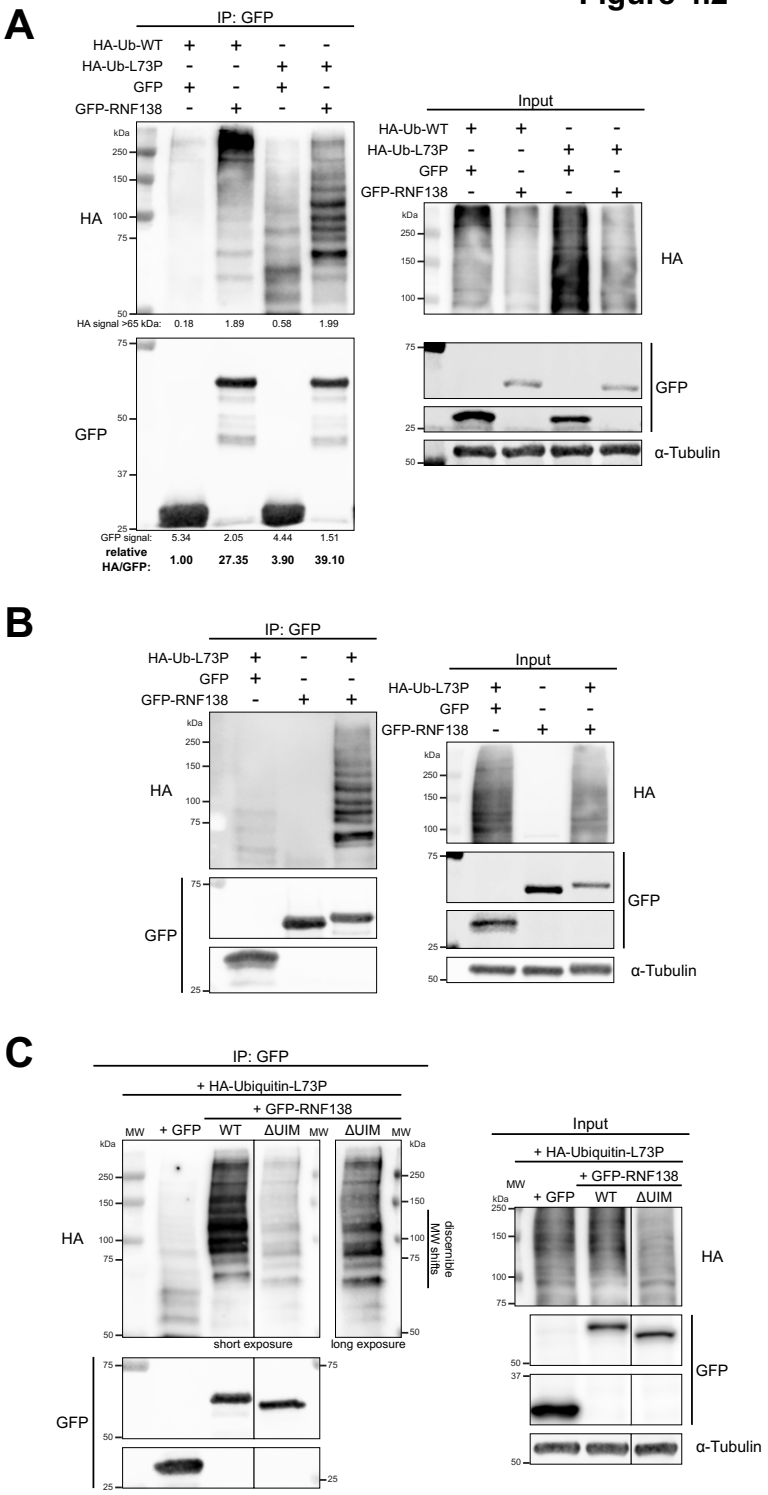

Figure 4.2: RNF138 is Constitutively Polyubiquitylated

Stringent GFP immunoprecipitations (IP) were performed for HEK293 cells expressing **A)** HA-Ub-WT or -L73P and GFP-RNF138 or free GFP, **B)** GFP or GFP-RNF138 with or without HA-Ub-L73P, or **C)** HA-Ub-L73P with GFP or GFP-RNF138-WT or -ΔUIM, the products of which were then immunoblotted. Shown are representative results from at least 4 biological replicates (each of A, B, C). MW: molecular weight standards.

4.4.4 Insights into the Dynamics of RNF138 Ubiquitylation

Having determined that RNF138 is a target for ubiquitylation, we sought to understand how different cellular conditions would affect RNF138 ubiquitylation. We first asked if the cell cycle factored into the degree of RNF138 ubiquitylation. We synchronized HeLa cells to the S, G2, and G1 phases, and during the process co-expressed in them low levels of HA-Ub-WT and GFP-RNF138. Despite transfecting in low levels of GFP-RNF138, its expression was slightly cytotoxic to HeLa, resulting in a reduction in synchronization efficiency (**Fig. 4.3A**, compare with **Fig. 4.1A**). Still, GFP immunoprecipitation consistently revealed more RNF138 ubiquitylation in samples enriched for S phase cells compared to ones enriched for G1 phase cells (**Fig. 4.3B-C**). As well, samples enriched for cells in G2 had similar or greater levels of ubiquitylation than those enriched for S phase cells (on average, 1.986 times more). We infer then that RNF138 ubiquitylation is cell cycle-dependent, with ubiquitylation increasing in S and G2 phase and decreasing in G1 phase.

We also examined if genotoxic stress would alter RNF138 ubiquitylation. We expressed HA-Ub-WT and GFP-RNF138 in HEK293 cells and treated the cells with various DNA damaging agents. We used ionizing radiation from a gamma source (IR) and phleomycin (phleo) to induce DSBs. We also treated cells with ultraviolet light (UV), along with the replication stress-inducing agents camptothecin (CPT, which also induces DSBs) and hydroxyurea (HU). Treating cells with any of the agents reduced the signal of higher order HA-Ub on GFP-RNF138 (**Figs. 4.3D-E**). This

was not due to variable expression of HA-Ub-WT between the samples, as signals from HA-Ub-WT conjugates were comparable in whole cell extracts (**Fig. 4.3D**). Therefore, DNA damage induces a reduction in RNF138 ubiquitylation. Overall, our data reveal differential ubiquitylation of RNF138 depending on cell status, with ubiquitylation rising when cells are in S/G2 phase and lessening upon genotoxic stress.

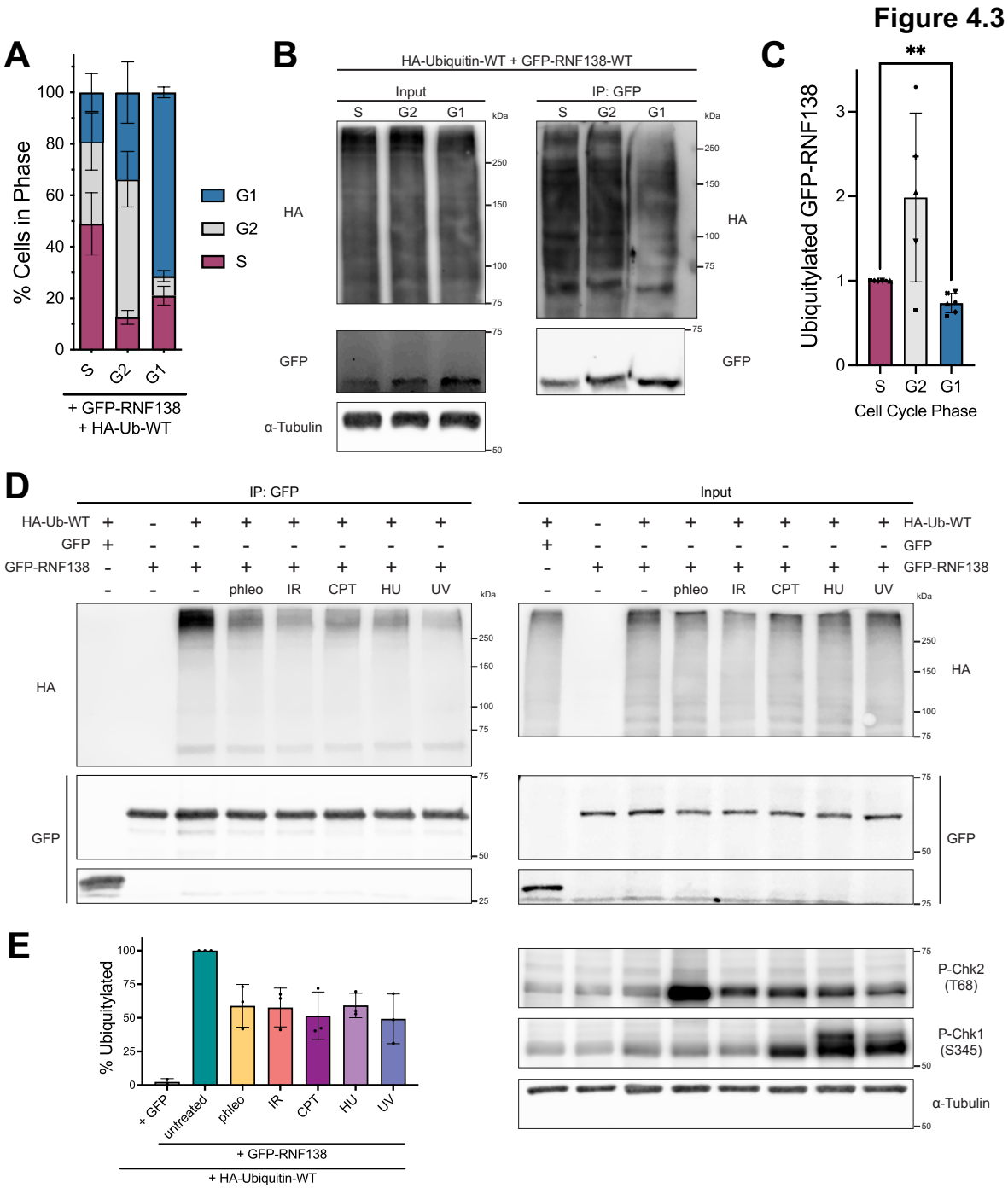

Figure 4.3: The Dynamics of RNF138 Ubiquitylation Upon Cell Cycle Progression and DNA Damage

A) Flow cytometric analysis of propidium iodide signal in HeLa cells synchronized by double-thymidine block and release. The cells were transfected with GFP-RNF138 and HA-ubiquitin-WT during the first release. **B)** GFP immunoprecipitation (IP) assay from cells treated as in A). **C)** Quantification of ubiquitylated GFP-RNF138 from B). HA signal in the IP fraction was normalized

to GFP signal in the IP fraction. **: a paired, two-tailed, parametric *t*-test comparing the S and G1 phase conditions for ubiquitylated GFP-RNF138 gives $p = 0.0043$ ($p \leq 0.01$). **D)** HEK293 cells were transfected with HA-ubiquitin-WT and GFP or GFP-RNF138 and exposed to phleomycin (phleo), ionizing radiation (IR), camptothecin (CPT), hydroxyurea (HU), or ultraviolet light (UV). The cells were then subjected to GFP immunoprecipitation and immunoblot analysis. Chk1 and Chk2 phosphorylation (P) at S345 and T68, respectively, are markers for activation of the DNA damage response. **E)** Quantification of D) as per C). Shown are representative results from 3 (D) and at least 6 (B) biological replicates. Averages were calculated from 3 (E), at least 4 (A), or at least 5 (C) biological replicates pooled together. A paired, two-tailed, parametric *t*-test was performed in C).

4.4.5 K158 is a Site of RNF138 Ubiquitylation

Four proteomic screens have identified residue K158 as a ubiquitylation site on RNF138 expressed in HEK293, HeLa cells, and Jurkat cells (452–455). K158 was also a site of ubiquitylation in a study that found RNF138 promotes oncogenic signaling in lymphomas expressing the L265P-mutated MyD88 (307). Interestingly, the K158 residue is conserved across RNF138 orthologues (**Fig. 4.4A**). It is also predicted to be solvent-exposed (**Figs. 4.S9A, 4.S9C-E**), in line with it being accessible for modification. To determine if K158 was indeed a ubiquitylation site in our system, we generated a K158R mutant of GFP-RNF138, the arginine substitution maintaining the positive charge but ablating the site of ubiquitylation. GFP immunoprecipitates of the construct exhibited a notable reduction in HA-Ub signal relative to WT-RNF138 when co-expressed with HA-Ub-L73P (**Fig. 4.4B**), substantiating K158 as a site for RNF138 ubiquitylation.

As polyubiquitin chains are known to target proteins for degradation by the proteasome (123), we determined the impact of disrupting K158 ubiquitylation on RNF138 stability by a cycloheximide chase assay. We expressed GFP-RNF138-WT or -K158R in HEK293 cells, inhibited protein synthesis with cycloheximide, and monitored exogenous RNF138 levels over time. We found that the K158R mutant was turned over at a reduced rate compared to WT-RNF138

(**Figs. 4.4C-D**). In the same experiment, we also inhibited proteasome activity with the compound MG132. MG132 treatment partially and fully restored WT- and K158R-RNF138 stability, respectively (**Figs. 4.4C, 4.4E**), indicating RNF138 turnover is at least partly dependent on proteasomal activity. Taken together, these findings indicate K158 is a site of constitutive ubiquitylation on RNF138, and modification of this site by ubiquitin can promote proteasome-mediated turnover of the protein.

Figure 4.4

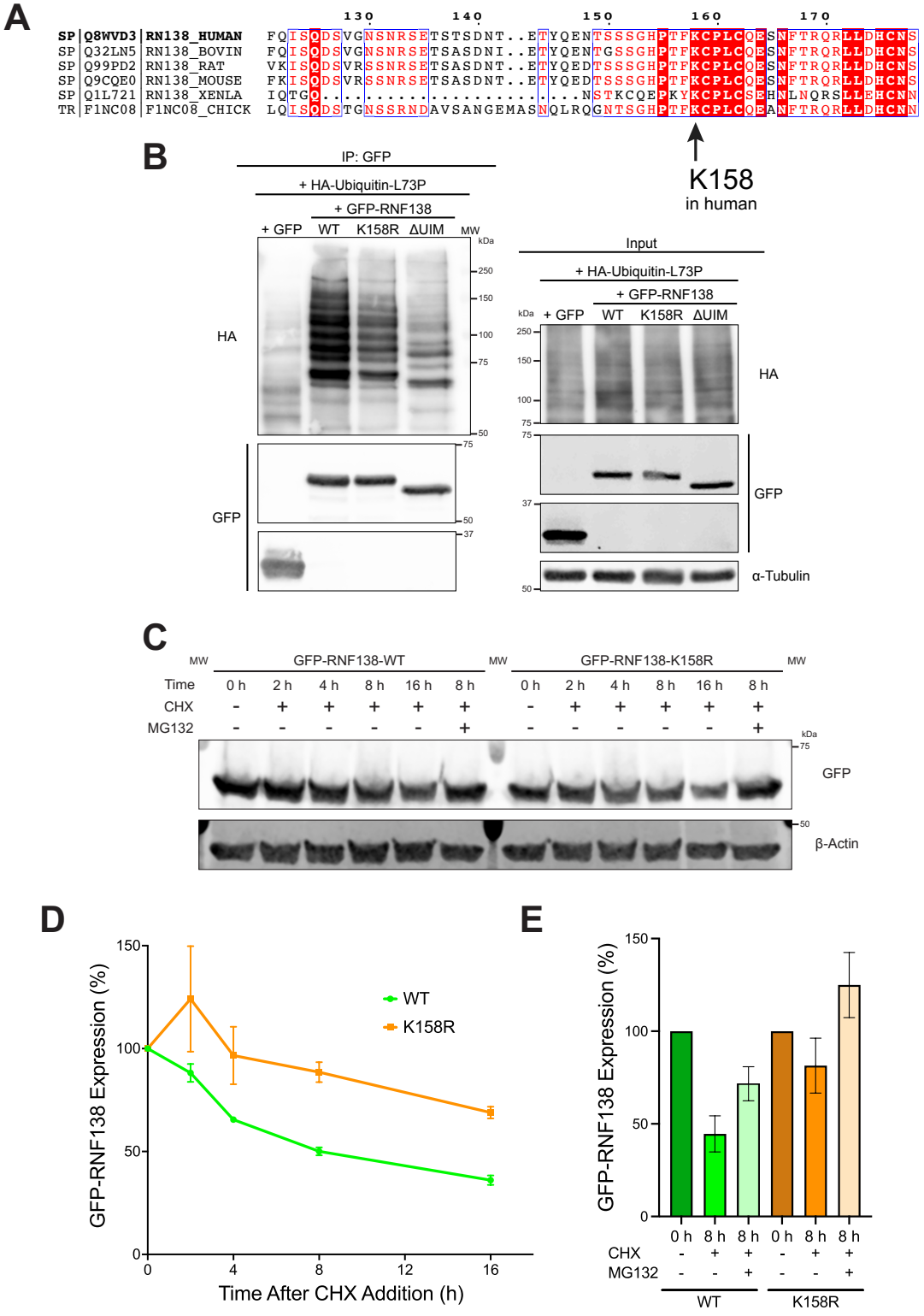

Figure 4.4: K158 is a Site of RNF138 Ubiquitylation

A) Clustal Omega amino acid sequence alignment of the region containing the K158 residue from human RNF138 with its orthologues. **B)** Stringent GFP immunoprecipitation (IP) was performed for HEK293 cells transfected with HA-Ub-L73P and GFP or GFP-RNF138-WT, -K158R, or -ΔUIM and then immunoblotted. **C)** Immunoblot of whole cell extracts of HEK293 cells transfected with GFP-RNF138-WT or -K158R and treated with cycloheximide (CHX) with or without MG132 for various timepoints. **D) and E)** Quantifications of C). Shown are representative results from 2 (C) and at least 5 (B) biological replicates. Averages in D) and E) are of 2 biological replicates pooled together. MW: molecular weight standards.

4.4.6 T27 and K158 are Not Required for the Recruitment of RNF138 to Sites of Damage

We so far observed CDK-dependent phosphorylation of RNF138 on residue T27 and, in support of previous findings (307, 452–455), ubiquitylation on RNF138 at K158. To study how these post-translational modifications impact RNF138's function in the DSB response, we continued our investigations in U2OS osteosarcoma cells, a standard cell line used to study the DSB response. The three zinc finger domains (ZNF1, ZNF2, and ZNF3) are together essential for targeting RNF138 to DNA damage sites (132). ZNF2 and ZNF3 are predicted to pack together in a single domain; this ZNF2/3 domain is flexibly tethered to the rest of the protein by a long linker (**Figs. 4.S9A, 4.S9C-E**). As K158 is situated immediately N-terminal of ZNF2 in RNF138 (**Fig. 4.5A**), we asked if ubiquitylation at K158 might contribute to RNF138 recruitment to DNA damage. We transiently transfected U2OS cells with minimal amounts of DNA encoding GFP-RNF138-WT or -K158R. To induce DNA damage, we pre-sensitized cells with Hoescht 33358, then irradiated nuclei with a stripe of 405 nm light. Timelapse fluorescence imaging was used to monitor the recruitment of the fusion proteins to the regions of damage over 5 minutes. Both GFP-RNF138-WT and -K158R effectively accumulated at laser stripes (**Fig. 4.5B**), although the K158R mutant exhibited a minor impairment when the recruitment kinetics were examined (~25% decrease in signal relative to WT at 200 s) (**Fig. 4.5C**). We conclude then that the K158 site promotes but is not essential for RNF138's accumulation on damaged DNA.

We next asked if T27 played a role in RNF138 recruitment to damage. This time, we generated phospho-ablating alanine (T27A) and phospho-mimicking glutamate (T27→E27, T27E) substitutions for T27 in the context of GFP-RNF138. While the WT and T27A GFP-RNF138 constructs were capably enriched at laser-microirradiated stripes (**Fig. 4.5D**), the T27A mutant displayed a subtle defect in retention over time (~10% decrease in signal relative to WT at 240 s) (**Fig. 4.5E**). Meanwhile, the T27E variant accumulated at laser stripes, but exhibited a slight defect in accrual (14.75% decrease in signal relative to WT at 100 s) and a discernible defect in retention (36.22% decrease in signal relative to WT at 300 s) (**Figs. 4.5D-E**). It appears then that a permanent negative charge at T27 may impact sustained localization of RNF138 to chromatin, perhaps owing to electrostatic repulsion impacting DNA binding potentially contributed by the positively charged surface of the RING domain (**Figs. 4.S9A-B**). Regardless, it is clear the function of residue T27 is not required for RNF138's localization to sites of DNA damage. Collectively, these data suggest modifications at K158 and T27 are not required for RNF138's accrual at DNA damage, but may have minor roles in promoting recruitment to (K158) and regulating retention on (T27) chromatin.

Figure 4.5

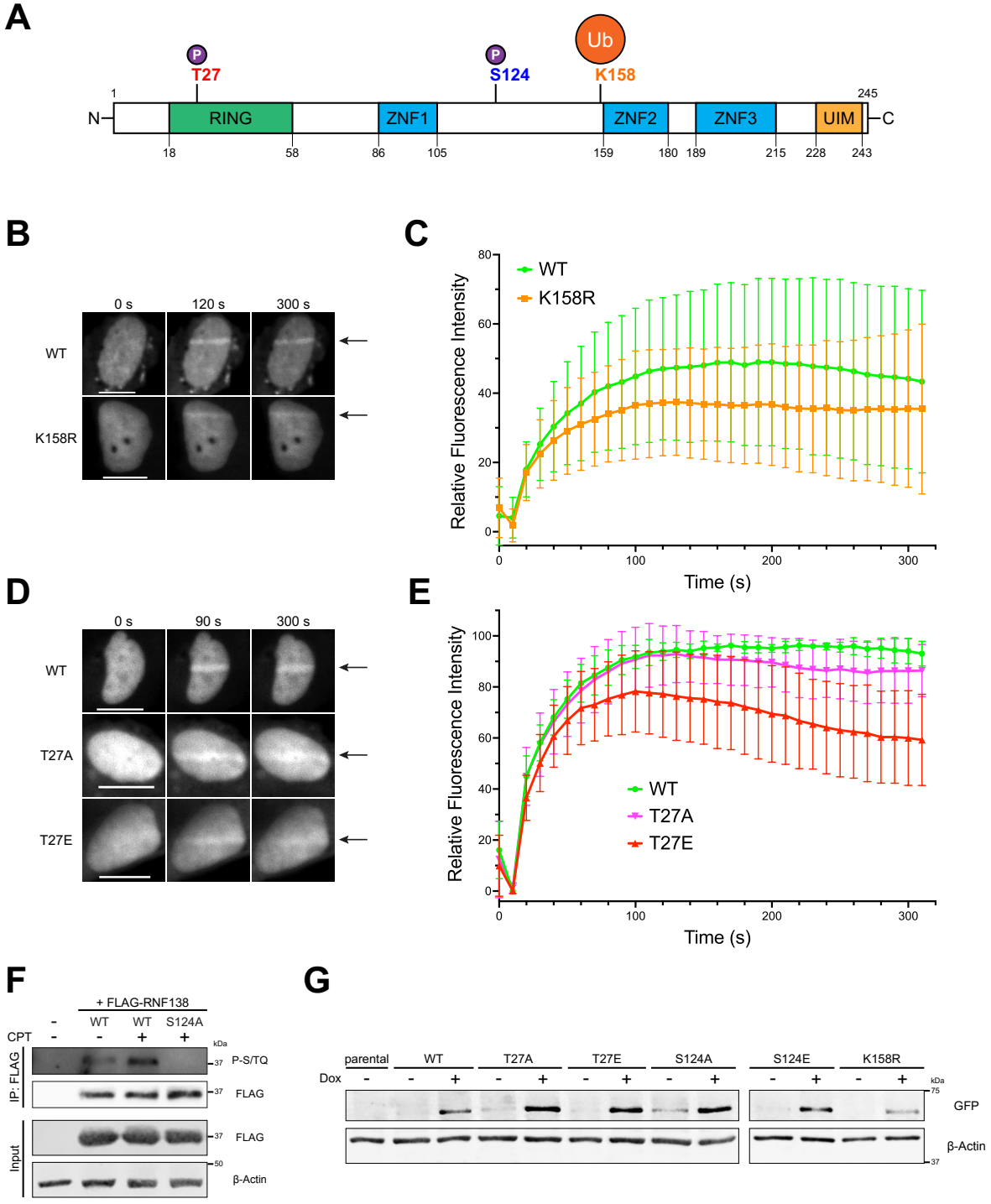

Figure 4.5: Recruitment Kinetics of RNF138 Mutants at T27 and K158 to Sites of DNA Damage; Stable Expression of T27, S124, and K158 Variants in U2OS-TREx Cells

A) Schematic diagram of the structural domains in wildtype (WT) RNF138 and the positions of the post-translational modification sites investigated. **B)** Representative micrographs of live U2OS

cells transfected with GFP-RNF138-WT or -K158, microirradiated in a line across the nucleus with a 405 nm laser, and monitored by time-lapse microscopy (arrow: region irradiated). **C)** Quantification of relative fluorescence intensity over time at the microirradiated region in B). The relative recruitment kinetics of 30 cells per construct, pooled from 3 biological replicates, were averaged. **D)** As in B) but for U2OS expressing GFP-RNF138-WT, -T27A, and -T27E. **E)** Quantification of relative fluorescence intensity over time at the microirradiated region in D). For a single replicate, the mean recruitment kinetics of ~25 cells were calculated for each construct. The normalized means from 3 biological replicates were then averaged and plotted (~75 cells total per construct). **F)** FLAG immunoprecipitation (IP) and subsequent immunoblot (IB) of HeLa cells expressing FLAG-RNF138-WT or -S124A and treated with camptothecin (CPT) or not for 1 hour. **G)** IB of parental or stable sfGFP-RNF138 variant-expressing U2OS-TREx cells induced with doxycycline (Dox) or not. Shown are representative results from 2 (F), 3 (B, D), and at least 7 (G) biological replicates. Scale bars denote 10 μm.

4.4.7 The RNF138 PTM Sites T27, S124 and K158 are Important for DNA End Resection

An additional residue on RNF138, S124, has been reported to be phosphorylated in an ATM kinase- and DNA damage-dependent manner (315). S124 resides in the long, flexible linker between ZNF1 and ZNF2 (**Figs. 4.5A, 4.S9A, 4.S9C-E**), so it would also be available for phosphorylation. We confirmed that S124 was the sole DNA damage-induced phosphorylation site on RNF138 by immunoblotting immunoprecipitates of FLAG-RNF138-WT and -S124A for the phosphorylated PIKK substrate consensus motif (phospho-Ser/Thr-Gln, or P-S/TQ) (**Fig. 4.5F**). Treating HeLa cells with CPT induced S/TQ phosphorylation on FLAG-RNF138-WT, while this signal was completely abolished in the S124A mutant. While it has been reported that the S124A mutant is proficient in recruitment to laser-microirradiated stripes (315), the effects of S124 phosphorylation on other aspects of HR have not been investigated.

As RNF138 promotes DNA end resection in HR (132, 133), we next examined what impact mutations at T27, S124, and K158 would have on the efficiency of DNA end resection. We opted for a simultaneous knockdown and complementation approach in U2OS cells, depleting endogenous RNF138 and re-expressing exogenous, siRNA-resistant WT-RNF138 or versions

where the PTM sites were mutated. We employed the tetracycline regulated expression (TREx) system to enable inducible expression of exogenous RNF138 in the bulk of cells. This system was comprised of U2OS cells stably expressing the TetR tetracycline repressor (U2OS-TREx) being transfected with the pCDNA4-TO-hygromycin-sfGFP-MAP vector (439). The vector contains Tet operator sequences which are bound by TetR, enabling transcriptional repression of the encoded transgene in the absence of tetracycline or doxycycline, but inducible expression in their presence. Using this vector, we generated U2OS-TREx cells stably expressing siRNA-resistant RNF138-WT or its mutants tagged with all four of the FLAG, 8XHis, streptavidin binding peptide (SBP), and superfolder GFP (sfGFP) tags (439). When induced with doxycycline, these cell lines produced fusion proteins of ~65 kDa (**Fig. 4.5G**), from here on referred to as sfGFP-RNF138 constructs. The WT and K158R variants of RNF138 were expressed at similar levels as measured by quantitative immunoblotting (**Figs. 4.5G, 4.S10F**). On the other hand, the T27A, T27E, S124A, and S124E mutants were expressed, on average, 2.7-3.7 times higher than WT. We attempted to adjust the doxycycline concentrations to induce similar expression levels of the variants, but these differences could not be eliminated at the concentrations tested (0.1 μg/mL – 5 μg/mL) (**Fig. 4.S10G**). Perhaps the differences in expression reflect other factors among the cell lines, such as the frequency of vector integration or integration in heterochromatic versus euchromatic regions. Nonetheless, we achieved inducible expression of exogenous RNF138 in U2OS-TREx cells, and importantly the expression levels of WT/K158R, T27A/T27E, and S124A/S124E were comparable within each pair, respectively.

With the TREx system ready, we examined the ability for U2OS-TREx cells expressing these mutants to undergo end resection in response to treatment with CPT. CPT was chosen as it inhibits DNA Topoisomerase I (TOP1), stabilizing TOP1 cleavage complexes that, upon collision

with a DNA replication fork, are converted into single-ended DSBs (456). In this way, CPT-induced DSBs are generated in an S phase-dependent manner (456), biasing repair pathway choice to DNA end resection and HR. To monitor end resection, we detected the occurrence of ssDNA by immunofluorescence staining (IF). U2OS-TREx cells were labeled with the brominated nucleoside 5-bromo-2'-deoxyuridine (BrdU), which is incorporated into DNA. The process of resection generates ssDNA, exposing an epitope on BrdU that can be detected by IF under non-denaturing conditions. The appearance of BrdU foci in response to CPT is thus indicative of active DNA end resection (457, 458). As expected, treating parental U2OS-TREx cells with CPT significantly increased the intensity of BrdU foci (**Figs. 4.S11A-B, 4.6A-C**). In accordance with RNF138 being shown to promote DNA end resection (132, 133), this intensity was significantly reduced when the cells were transfected with siRNA targeting RNF138 (**Figs. 4.S11A-B, 4.6A-C**). We next performed flow cytometric analysis to check if the difference was due to changes in the ratio of S phase cells. Depleting RNF138 in U2OS-TREx did not substantially alter the proportion of cells in S phase (**Fig. 4.S11E**). Therefore, the change in BrdU focal intensity did not arise from a shift in the frequency of S phase-cycling cells, rather reflecting a perturbation in efficient DNA end resection.

We next examined the impact of RNF138 mutations on DNA end resection. U2OS-TREx cells were depleted of endogenous RNF138 and complemented with WT or mutated sfGFP-RNF138 by treatment with doxycycline. In agreement with T27 being an important phosphorylation site, average BrdU focal intensity in the cell line expressing the T27A mutant was substantially reduced compared to cells expressing WT-RNF138, and at levels barely above that of the same cells not treated with CPT (**Fig. 4.6A**), indicating dramatically reduced end resection. The contrary was observed for the T27E mutant, with mean BrdU focal intensity extensively

higher than WT (**Fig. 4.6A**). Perhaps the negatively charged glutamate substitution results in constitutively active RNF138, constantly promoting resection. Hence, the phosphorylation of RNF138 at T27 plays a crucial role in RNF138's ability to promote DNA end resection. Performing the same assay on the S124A mutant showed reduced BrdU focal intensity relative to WT (**Fig. 4.6B**), demonstrating a role for S124 phosphorylation in RNF138 function. Interestingly, unlike T27E, the S124E mutation was unable to restore BrdU focal intensity (**Fig. 4.6B**). Perhaps glutamate substitution at S124 is insufficient to cause the same conformational changes elicited by serine phosphorylation. Nevertheless, the fact that both S124A and S124E mutations reduce BrdU intensity underscores the importance of the S124 site in RNF138 function. We also performed the same assay for the K158R substitution mutant. U2OS-TREx cells expressing sfGFP-RNF138-K158R exhibited reduced intensity in BrdU foci relative to cells expressing WT (**Fig. 4.6C**), indicating K158 plays a role in RNF138's ability to promote DNA end resection. As a control, we confirmed that concurrently depleting endogenous RNF138 while inducing expression of sfGFP-RNF138-WT with doxycycline did not severely alter the proportion of cells in S phase (**Fig. 4.S11E**). We also checked if this proportion was affected by expressing any of the RNF138 mutants. The S phase fraction was similar (~31-37%) among all the U2OS-TREx cell lines, whether expression of the sfGFP-RNF138 mutants was induced or not (**Fig. 4.S11F**). Thus, the observed differences in BrdU focal intensity were not from cells being more or less responsive to CPT from changes in the fraction in S phase.

As active end resection generates ssDNA overhangs that are rapidly coated and protected by the binding of RPA complexes (46, 458–460), we asked if the observed changes in BrdU focal intensity would correlate with RPA binding. To do so, we performed a similar IF assay in U2OS-TREx, this time detecting extraction-resistant foci of the RPA complex subunit RPA2 in response

to CPT. As seen with BrdU foci (**Figs. 4.S11A-B, 4.6A-C**), knocking down RNF138 reduced RPA focal intensity (**Figs. 4.S11C-D, 4.6D-F**), indicating the inhibition of end resection. Notably, CPT-induced RPA focal intensity was partially rescued upon concurrent expression of sfGFP-RNF138-WT (**Figs. 4.6D-F**). As well, the T27A, S124A, and K158R variants exhibited significantly reduced RPA2 focal intensity relative to WT-RNF138 (**Figs. 4.6D-F**). Likewise, RPA2 focal intensity was rescued by the T27E mutant, but not by the S124E mutant (**Fig. 4.6D**). Our results with RPA2 foci thereby recapitulate our findings seen with native BrdU foci.

The N-terminal region of RPA2 is phosphorylated by the PIKKs in response to DNA damage (414). As Ser4 and Ser8 phosphorylation on RPA2 (P-S4/S8-RPA2) is dependent on CtIP (58, 133) and occurs after the binding of RPA complexes to ssDNA (414, 461, 462), it has been used as a readout for end resection (61, 133). To further support that end resection is regulated by PTMs on RNF138, we detected CPT-induced P-S4/S8-RPA2 in the same cell lines by immunoblot (**Figs. 4.7A-B**). Consistent with our previous findings (132), cells transfected with siRNA to RNF138 exhibited reduced RPA2 phosphorylation upon stimulation with CPT. Cells knocked down of RNF138 and expressing sfGFP-RNF138-T27A, -S124A, -S124E, or -K158R could not restore P-S4/S8-RPA2 to the levels seen with WT-RNF138, agreeing with our IF data with BrdU and RPA2 foci. In fact, the cells exhibited P-S4/S8-RPA2 levels below that of parental U2OS-TREx cells treated with RNF138-targeting siRNA. Unlike the IF data however, the T27E mutant did not recover P-S4/S8-RPA2 to levels near or above WT-RNF138 (**Figs. 4.7A-B, 4.6A, 4.6D**). It may be that the resection induced by T27E, seen by IF, somehow cannot trigger RPA2 phosphorylation as effectively as having a phosphoryl group on T27, and that RPA2 phosphorylation requires events additional to RPA binding ssDNA. Still, this data reveal the importance of the T27 site in early RNF138-dependent DSB signaling. Overall, the analysis of

BrdU foci, RPA2 foci, and phospho-RPA2 levels suggest phosphorylation at T27 and S124 and ubiquitylation at K158 are important for RNF138's role in promoting DNA end resection.

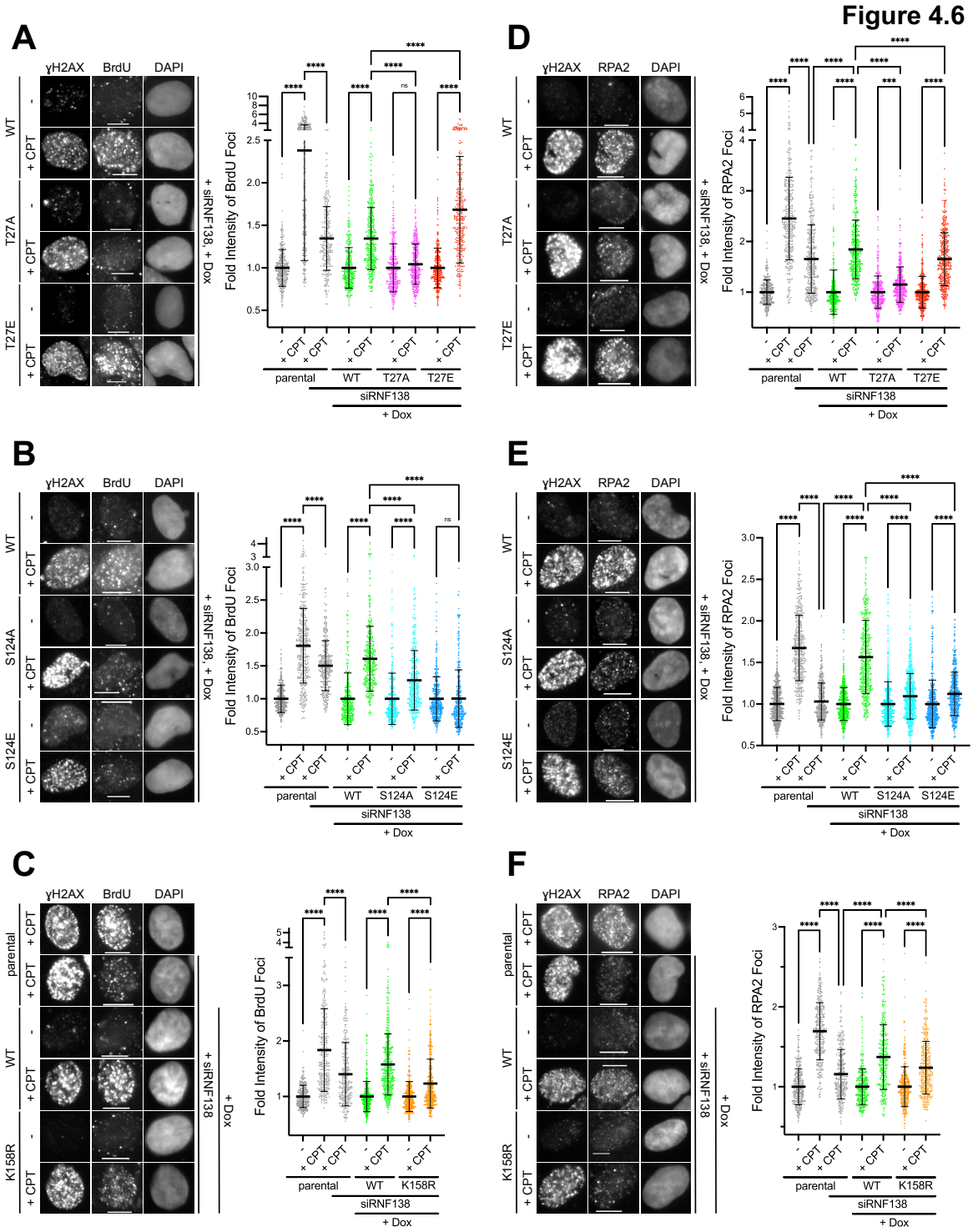

Figure 4.6: The RNF138 PTM Sites T27, S124 and K158 are Important for DNA End Resection

A), B), C) Left panel: Representative BrdU immunofluorescence (IF) micrographs of sfGFP-RNF138 variant-expressing U2OS-TREx cells transfected with siRNA to RNF138 (siRNF138) and treated with doxycycline (Dox) to induce expression of sfGFP-RNF138 from a single biological replicate. C) includes parental U2OS-TREx cells transfected with or without siRNF138. In all, cells were treated with camptothecin (CPT) or not for 1 hour. ɣH2AX was used to indicate DNA damage, while DAPI stain labeled the nucleus. Right panel: quantifications of relative intensity of nuclear BrdU foci. For CPT-treated cells, only ɣH2AX$^+$ cells were quantified. The fluorescence intensities of foci for conditions within a given cell line were normalized to each other, with the average fluorescence intensity set at 1 for the untreated sample (no CPT). Averages were derived from the focal intensity of at least 150 cells each from 2 biological replicates (at least 300 cells total per condition). **D), E), F)** As in A)-C), but performing IF for RPA2 foci. Scale bars denote 10 μm. See **Fig. 4.S11A-D** for additional representative micrographs from experiments depicted in **Figs. 4.6A-B, 4.6D-E**. In all, ordinary one-way ANOVA with Šídák's multiple comparisons test was performed to determine whether differences between conditions were statistically significant. ****: p values were <0.0001. For A), ns: $p = 0.8921$. For B), ns: $p > 0.9999$. For D), ***: $p = 0.0002$.

4.4.8 T27, S124 and K158 on RNF138 are Important for HR and Cell Survival

In HR, the processes of homology search, strand invasion, and DNA synthesis occur downstream of DNA end resection (71). As T27, S124, and K158 affected the efficiency of end resection, we next determined if the frequency of HR was impacted by the same mutations. To do so, we used the direct repeat GFP (DR-GFP) reporter assay (408), utilizing U2OS cells integrated with two repeats of the GFP open reading frame (ORF) (**Fig. 4.7C**). These copies are mutated such that neither produces a fluorescent protein product; the upstream copy contains stop codons and a recognition site for the restriction endonuclease I-*Sce*I, while the downstream copy is truncated, with the N- and C-terminal regions removed. Expression of I-*Sce*I induces a site-specific DSB in the upstream copy of the GFP ORF. If the DSB is repaired by HR using the downstream copy as a template, the sequence encoding intact, fluorescent GFP is generated. Consequently, the proportion of GFP$^+$ cells after I-*Sce*I expression reflects the efficiency of HR. We generated siRNA-resistant, mCherry-tagged constructs of WT-RNF138 and its PTM site mutants (T27A, T27E, S124A, S124E, K158R), then transfected them into TRI-DR-U2OS cells stably expressing doxycycline-

inducible I-*Sce*I and depleted of endogenous RNF138. As expected, I-*Sce*I induction alone markedly increased the frequency of GFP^+ cells, and this frequency was sharply inhibited when the cells were depleted of RNF138 (132) (**Fig. 4.7D**). Consistent with our IF data for end resection detected by RPA2 foci (**Figs. 4.6D-F, 4.S11C-D**), adding back mCherry-RNF138-WT and -T27E in the presence of RNF138 siRNA partially rescued the frequency of HR to levels seen in cells expressing endogenous RNF138 (**Fig. 4.7D**). On the other hand, cells expressing the -T27A, -S124A, and -K158R mutants exhibited severely reduced HR frequencies (**Fig. 4.7D**). Interestingly, the S124E mutant was fully capable of restoring HR frequency, in fact to levels surpassing that of WT-RNF138, similar to the T27E mutant (**Fig. 4.7D**). It appears that in this specific context (DR-GFP reporter assay, mCherry-tagged RNF138), S124E resembles the actions of constitutively phosphorylated RNF138. Thus, the T27, S124, and K158 sites are important for RNF138's ability to promote HR.

With end resection and the occurrence of HR dependent on the aforementioned PTM sites, we asked if cell survival upon DNA damage would also be impacted by mutations at the sites. To do so, we performed clonogenic survival assays on U2OS-TREx cells treated with IR. Knocking down RNF138 impeded the colony forming ability of parental U2OS-TREx cells (**Fig. 4.7E**), in line with previous observations (132, 133). This was not due to indirect effects on the cell cycle from RNF138 depletion, as the proportion of cells in S or G2 phase (and therefore conducive to HR) increased slightly when RNF138 was depleted (**Fig. 4.S11B**). Conversely, clonogenic survival was partly rescued in sfGFP-RNF138-WT-expressing U2OS-TREx cells depleted of endogenous RNF138 (**Fig. 4.7E**). As a control, when doxycycline was not added to the culture medium, preventing expression of sfGFP-RNF138-WT, survival was reduced (**Fig. 4.7E**). Again, these effects were not from indirect changes on the cell cycle, as the S/G2 fraction of cells was similar

whether doxycycline was added or not (**Fig. 4.S11E**). Having confirmed that survival to IR is dependent on RNF138, we tested how the PTM site mutants would fare in colony forming ability using U2OS-TREx cells stably expressing the sfGFP-RNF138 variants. Consistent with our IF results for resection (**Figs. 4.6A-F**), cells expressing the T27A, S124A, S124E, and K158R mutants exhibited relative surviving fractions similar to or below that of parental U2OS-TREx cells depleted of RNF138 at 1, 2, and 3 Gy (**Fig. 4.7F**). At the same doses, cells expressing the T27E mutant showed intermediate survival, greater than the former mutants but less than WT-RNF138. None of these effects were from fluctuations in the cell cycle distribution, as the stable cell lines did not show appreciable differences in the S/G2 phase fraction (~58% to 63.6%) upon doxycycline induction (**Fig. 4.S11F**).

All in all, these data exemplify the role of the T27, S124, and K158R residues in promoting HR and cellular survival in the face of DSBs. They are also mostly concordant with the phenotypes observed for the mutants in DNA end resection, assayed by RPA2 and BrdU foci formation (**Figs. 4.6A-F, 4.S11A-D**).

Figure 4.7

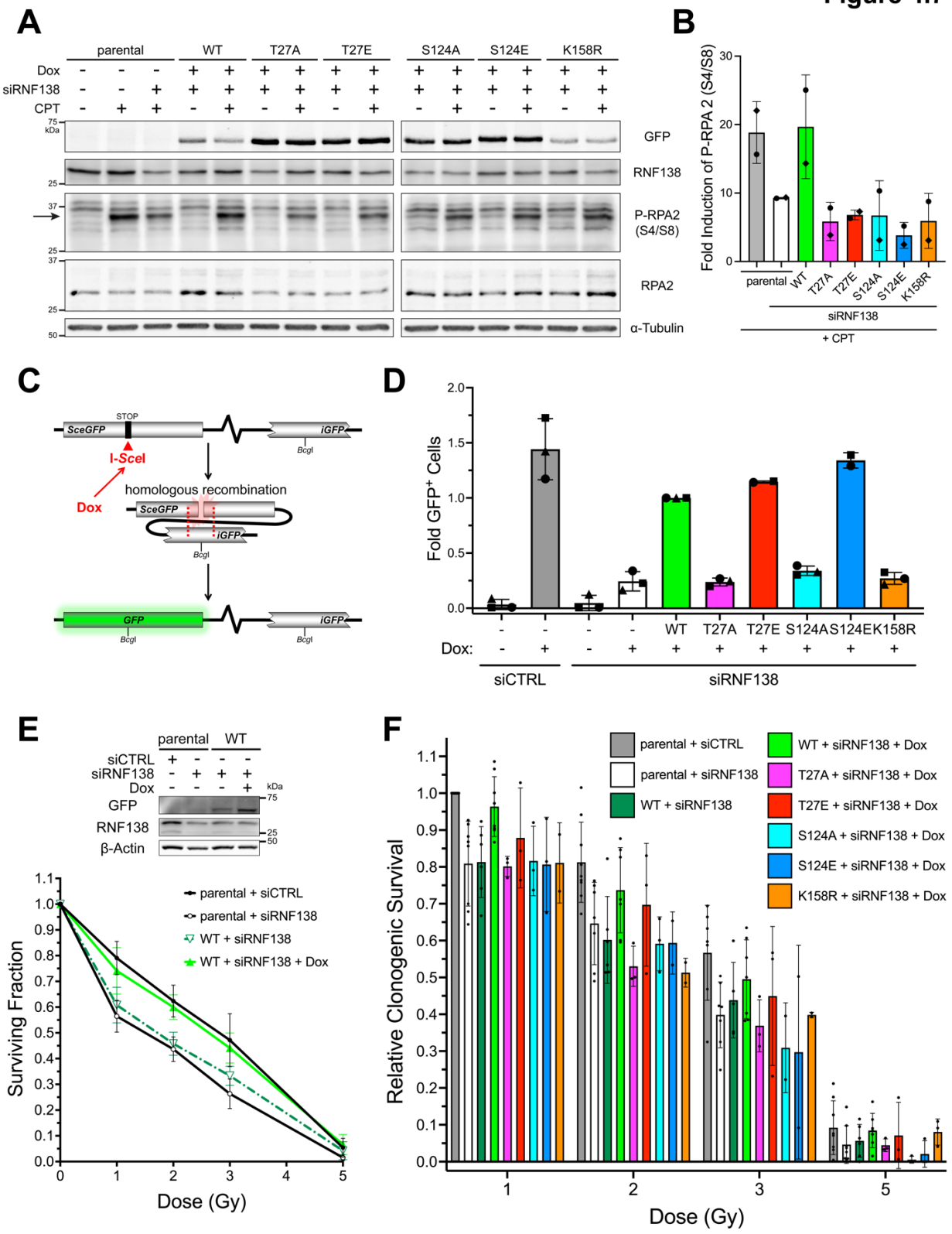

Figure 4.7: T27, S124 and K158 on RNF138 are Important for RPA2 Phosphorylation, HR Activity, and Cell Survival

A) Immunoblot of whole cell extracts of parental or sfGFP-RNF138 variant-expressing U2OS-TRex cells transfected with or without siRNA to RNF138 and treated with camptothecin (CPT) or not for 1 hour. Arrow: main band for P-RPA (S4/S8); note its reduced electrophoretic mobility compared to unmodified RPA2. **B)** Quantification of fold induction of P-RPA2 (S4/S8) signal from A). P-RPA2 (S4/S8) signal was normalized to that of RPA2 expression. The resulting values from CPT-treated samples were then ratioed to those left untreated. **C)** Schematic diagram of the DR-GFP reporter assay in TRI-DR-U2OS cells expressing doxycycline (Dox)-inducible I-*Sce*I. **D)** DR-GFP reporter assay in TRI-DR-U2OS cells transfected with siRNA to luciferase (siCTRL) or RNF138 (siRNF138) and complemented with siRNA-resistant mCherry-RNF138 variants or not. GFP^+ cells were quantified by flow cytometry. **E)** Bottom: Clonogenic survival assay for parental or sfGFP-RNF138-WT-expressing U2OS-TREx cells transfected with siCTRL or siRNF138, induced with Dox if necessary, and treated with increasing doses of ionizing radiation. Top: immunoblot of endogenous and exogenous RNF138 expression of cells used for the clonogenic survival assay at time of irradiation. **F)** Clonogenic survival assay for parental or sfGFP-RNF138 variant-expressing U2OS-TRex cells transfected with siCTRL or siRNF138, induced with Dox or not, and treated with increasing doses of ionizing radiation. Within each biological replicate, the surviving fractions obtained were normalized to the surviving fraction of the parental cells + siCTRL + 1 Gy IR condition. A) is a representative result from at least 2 biological replicates. Averages were calculated from 2 (B), at least 2 (D, F), and at least 6-10 (E) biological replicates pooled together.

4.5 Discussion

Multiple reports have implicated a role for RNF138 in the DNA damage response (132, 133, 312–315). As an E3 ubiquitin ligase, RNF138 facilitates the ubiquitylation of Ku80, CtIP, and Rad51D, actions that promote the occurrence of HR (132, 133, 314, 315). Little however is known about how its activity is regulated in the context of DSB repair. While RNF138 was reported to be phosphorylated by ATM in response to IR at position S124 (315), the functional significance of this modification remained unclear, as it did not affect RNF138's recruitment to sites of DNA damage (315). Furthermore, as RNF138 stimulates Ku80 ubiquitylation in S/G2, but not G1 phase (132), it appeared RNF138 activity could be regulated by the cell cycle, although how this occurred was not previously explored. Thus, we sought to elucidate additional mechanisms by which

RNF138 could be regulated. In HeLa cells, we detected a slight increase in RNF138 protein levels during G2 phase (**Fig. 4.1C**), consistent with the reported increase in RNF138 messenger RNA transcripts in G2 (305). However, RNF138 protein was expressed throughout the cell cycle, and at relatively constant levels (**Figs. 4.1A-C**). As HR is specific to the S/G2 phases (436), we speculate RNF138 expression in G1 may serve its roles outside of HR, such as binding interactors and ubiquitylating substrates in NFκB or Wnt-β-catenin signaling (303, 307–309). Regardless, it became clear that factors beyond protein level regulate RNF138 activity in HR. We located a putative CDK substrate consensus motif within RNF138's amino acid sequence (**Fig. 4.1D**). In addition, RNF138 was a hit in proteomic screens for ubiquitylated proteins (452–455), and ubiquitylation events are well known to govern the response to DSBs (42). We therefore addressed if ubiquitylation and CDK-dependent phosphorylation occurred on RNF138 and were involved in its function in HR.

We report here that RNF138 is phosphorylated in a CDK-dependent manner. This phosphorylation peaked during S phase, was dependent on CDK1 and CDK2, occurred on residue T27 (**Figs. 4.1G-I**), and, importantly, stimulated RNF138-mediated DNA end resection (**Figs. 4.6A, 4.6D, 4.7A-B**). While the precise mechanism by which CDK phosphorylation activates RNF138 requires further study, it aligns with a pro-resection function for CDK activity in S/G2. RNF138 has been shown to mediate ubiquitylation of the pro-resection factor CtIP, enabling CtIP's recruitment to DSBs (133). RNF138-dependent ubiquitylation of Ku80 also promotes the eviction of the DNA end-protecting and NHEJ-promoting (34, 232) Ku heterodimer from chromatin (132). As Ku displacement is required for DNA end resection to begin (317, 318), this contributes a second mode to trigger end resection. Notably, CtIP itself is phosphorylated by CDK activity, the phosphorylated version activating the endonuclease activity of Mre11 to initiate DNA end

resection (51, 52, 60, 61, 104, 105). The Ku heterodimer is also a substrate for CDK activity; Ku70 is phosphorylated by CDK1 and CDK2 during S, G2, and M phase (463), and in budding yeast, CDK-phosphorylated Yku80 promotes HR and impairs NHEJ (319). Phosphorylated Ku, similar to ubiquitylated Ku (320), has been found to dissociate from DNA (317, 463). The evidence points to a model where concerted CDK activity in S and G2, acting on multiple fronts, like RNF138, CtIP, Ku, and other resection factors (101–103, 106, 107), culminates to drive the process of DNA end resection. Interestingly, our laser microirradiation data also suggests that beyond promoting DNA end resection, T27 phosphorylation may serve a minor role in regulating RNF138's retention on chromatin (**Figs. 4.5D-E**).

We also find that RNF138 is constitutively polyubiquitylated, with K158 serving as a site of modification (**Figs. 4.2A-C, 4.4B**). This is in line with a recent report identifying K158 as a ubiquitylation site on RNF138, with the K158R substitution able to suppress negative regulation of oncogenic MyD88 signaling (307). As the K158R mutant could not completely eliminate HA-Ub-L73P signal in GFP-RNF138 immunoprecipitates (**Fig. 4.4B**), there are likely other residues by which RNF138 is ubiquitylated. Indeed, four additional lysine residues on RNF138 (K26, K41, K94, K107) were detected to be ubiquitylated in one proteomic screen (454). Yet, K158 is probably an abundant site for ubiquitylation, as it was the only ubiquitylation site predicted by UbPred software (307), and was consistently ubiquitylated in four proteomic screens, detected in three of these as the only site of modification on RNF138 (452–455). Phenotypically, despite exhibiting reduced turnover and prolonged stability, the K158R mutant was still clearly defective in promoting DNA end resection (**Figs. 4.4C-D, 4.6C, 4.6F, 4.7A-B**). Although K158 was not essential for RNF138 recruitment to laser stripes, the K158R mutant also showed a minor impairment in recruitment (**Fig. 4.5C**), and this change could contribute at least partly to the defect

in end resection. Overall, the data suggests ubiquitylation on K158 activates RNF138 for end resection. This is supported by the increase in ubiquitylated RNF138 in the S and G2 phases (**Figs. 4.3B-C**), overlapping with the times end resection and HR are active. As RNF138 is appreciably expressed during all cell cycle phases (**Fig. 4.1C**), we suspect the enhanced ubiquitylation in S/G2 serves more to activate the protein for end resection and HR rather than actively target it for proteasomal degradation. Further study, particularly of the linkages in the ubiquitin chains conjugated to RNF138, is required to validate this idea. We also observed that RNF138 ubiquitylation was reduced upon DSBs, UV, and replication stress (**Figs. 4.3D-E**). In support of this, a proteomic screen found ubiquitylation at K158 was reduced 3 hours after HEK293 cells were exposed to UV irradiation (452). Since K158 ubiquitylation promotes DNA end resection (**Figs. 4.6C, 4.6F, 4.7A-B**), the reduction in ubiquitylation, seen after 1 hour of genotoxic stress (**Figs. 4.3D-E**), may reflect a negative regulatory mechanism, constraining RNF138 activity after actions to resolve the. stress have commenced. For HR, this might prevent overstimulation of DNA end resection, which could lead to a loss of genetic information. Uncontrolled resection might also deplete local RPA pools, causing aberrant annealing, secondary structures, and degradation in unprotected ssDNA (460). Together, our data suggest RNF138 is regulated by ubiquitylation, with ubiquitin conjugation to K158 serving to activate the protein in DSB repair.

Our work thus identifies two additional PTMs that contribute to RNF138's function in DSB repair, the aforementioned K158 ubiquitylation and CDK-dependent T27 phosphorylation. Both promote RNF138's role in stimulating DNA end resection, as the T27A and K158R variants inhibit RNF138-dependent resection in response to CPT (**Figs. 4.6A, 4.6C-D, 4.6F, 4.7A-B**). Using the S124A mutant, we also demonstrate S124 phosphorylation positively regulates RNF138's role in end resection (**Figs. 4.6B, 4.6E, 4.7A-B**), providing functional significance to the known ATM-

dependent modification (315). Aligning with these observations, the T27A, S124A, and K158R mutations dramatically reduced HR frequency *in vivo* (**Fig. 4.7D**) and sensitized cells to DNA damage by IR (**Fig. 4.7F**), suggesting the defects in end resection translated to negative consequences downstream. Supporting the importance of T27 phosphorylation, the phospho-mimicking T27E variant could restore DNA end resection, HR, and clonogenic survival (**Figs. 4.6A, 4.6D, 4.7D, 4.7F**), despite having a partial defect in retention on chromatin (**Figs. 4.5D-E**). Intriguingly, like T27E, the S124E mutant was also capable of restoring HR (**Fig. 4.7D**), although it was unable to rescue end resection and clonogenic survival (**Figs. 4.6B, 4.6E, 4.7A-B, 4.7F**). We note that the end resection and survival assays were conducted with sfGFP-RNF138, while the HR reporter assay utilized the mCherry-RNF138 fusion. Beyond the different fluorescent proteins, the sfGFP construct also contains three other epitope tags (439). We speculate construct-specific conformational differences could explain the discrepancy in results for S124E. Alternatively, it could be that the S124E variant does not sufficiently promote end resection yet is capable of activating HR through a separate mechanism. Indeed, we did not assess if the stability or recruitment of Rad51D, another target of RNF138 ubiquitylation in HR (314, 315), were impacted by the PTM site mutations in RNF138. We thus cannot conclude if the effects on HR and survival arise solely from changes in end resection or if alterations in Rad51D activity also contribute. Nevertheless, our functional readouts reiterate that PTMs at T27, S124, and K158 are important to the role of RNF138 in protecting cells from DSBs.

Our data ultimately point to a scenario where phosphorylations at T27 and S124 and ubiquitylation at K158 all positively regulate RNF138 activity in end resection and HR. This may enable RNF138 to integrate signals of both DNA damage and cell cycle stage, ensuring it is fully active when DSB breaks occur during S/G2 phase. An attractive idea is that cell cycle-dependent

ubiquitylation and CDK-dependent T27 phosphorylation prime RNF138 to function in S/G2. ATM-dependent phosphorylation at S124, triggered by DSBs, could perhaps give the final go-ahead signal to license RNF138 activity. This of course needs to be tested, and further study is needed to decipher the mechanisms by which the PTMs stimulate RNF138 and if they may influence each other. In the end, our data provide additional intricacies to the tightly orchestrated molecular events triggered upon DSB damage.

4.6 Funding

Funding for this work was provided by a CIHR (Canadian Institutes of Health Research) Project Grant (grant number 154485) to I.H.I., a CIHR Project Grant (grant number 168972) to J.N.M.G., an NSERC (Natural Sciences and Engineering Research Council of Canada) Discovery Grant (RGPIN-2017-05752) to I.H.I., and CRINA (Cancer Research Institute of Northern Alberta) Bridge Funding to I.H.I. provided by Terry and Betty Davis. A.J.L. was supported by the Rachel Mandel Scholarship in Lymphoma and Other Blood Cancers, the Dr. Herbert Meltzer Memorial Fellowship, and the Yau Family Foundation Award.

4.7 Acknowledgements

We are grateful to Joseph Drake, Allison Tran, Adham Shousha, Kristi Baker, and Anne Galloway for technical assistance. We also thank Fatemeh Mashayekhi for assistance with foci quantitation using Imaris software.

4.8 Conflict of Interest

The authors declare that they have no conflicts of interest with the contents of this article.

4.9 Author Contributions

A.J.L. analyzed the data and performed most of the experiments, often with assistance from co-authors (described below). R.A.F. conducted AlphaFold modeling and sequence alignments. R.A.F. and A.J.L. performed immunofluorescence, immunoblotting, and clonogenic survival assays. C.T. and A.J.L. performed immunoprecipitation, cycloheximide chase, and His pull-down assays. J.Y.H.A. performed laser microirradiation experiments. I.H.I and A.J.L. performed the HR reporter assay. A.J.L. and I.H.I. designed the experiments and wrote the manuscript. J.N.M.G. supervised R.A.F. I.H.I. conceived and supervised the project. All authors have read and approved the manuscript.

4.10 Supplementary Data

Supplementary figures (**Figs. 4.S8 – 4.S11**) and tables (**Tables 4.1 – 4.4**) are provided in support of the main figures (**Figs. 4.1 – 4.7**).

4.10.1 Supplementary Figures

Figure 4.S8

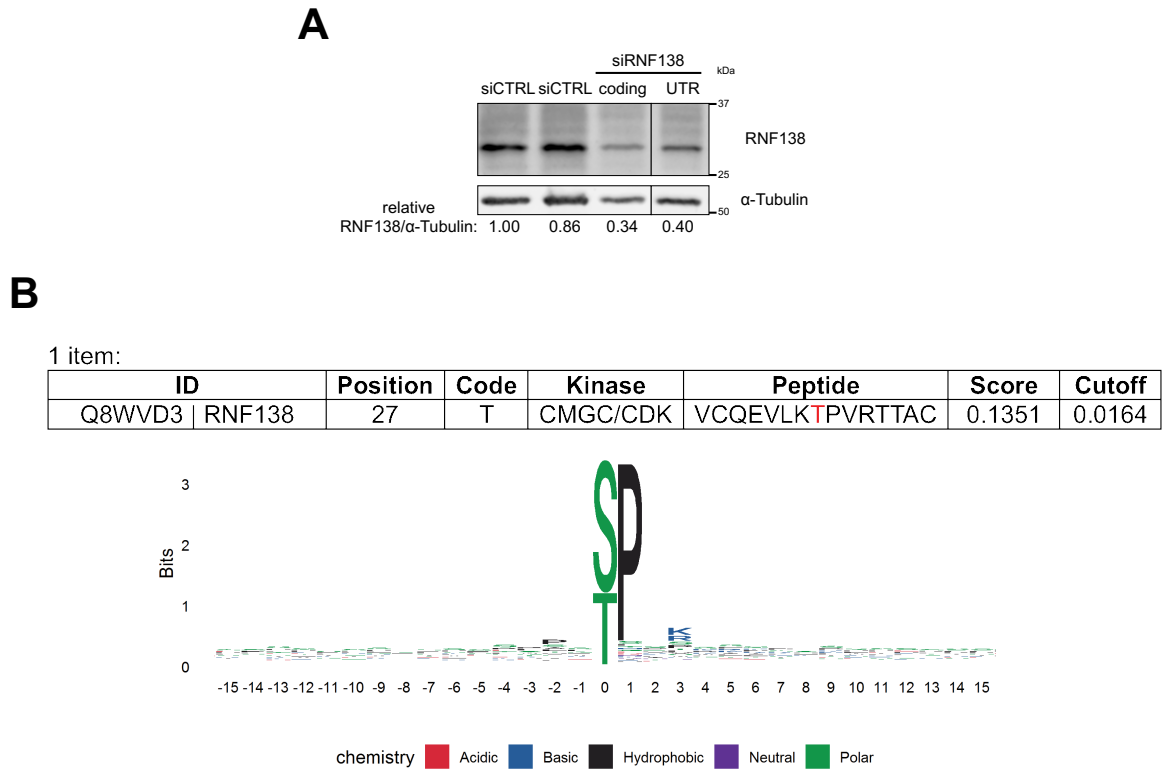

Figure 4.S8: Related to Figure 4.1

A) Immunoblots (IBs) of U2OS cells were transfected with siRNA targeting luciferase (siCTRL) or the *RNF138* gene (siRNF138) within its coding or 3' untranslated region (UTR). **B)** Results from the scan of the primary sequence of full-length human RNF138 by the GPS (Group-based Prediction System) 6.0 web server (451) for consensus phosphorylation motifs of the cyclin-dependent kinase (CDK) subset of the CMGC family of kinases (http://gps.biocuckoo.cn/online.php).

Figure 4.S9

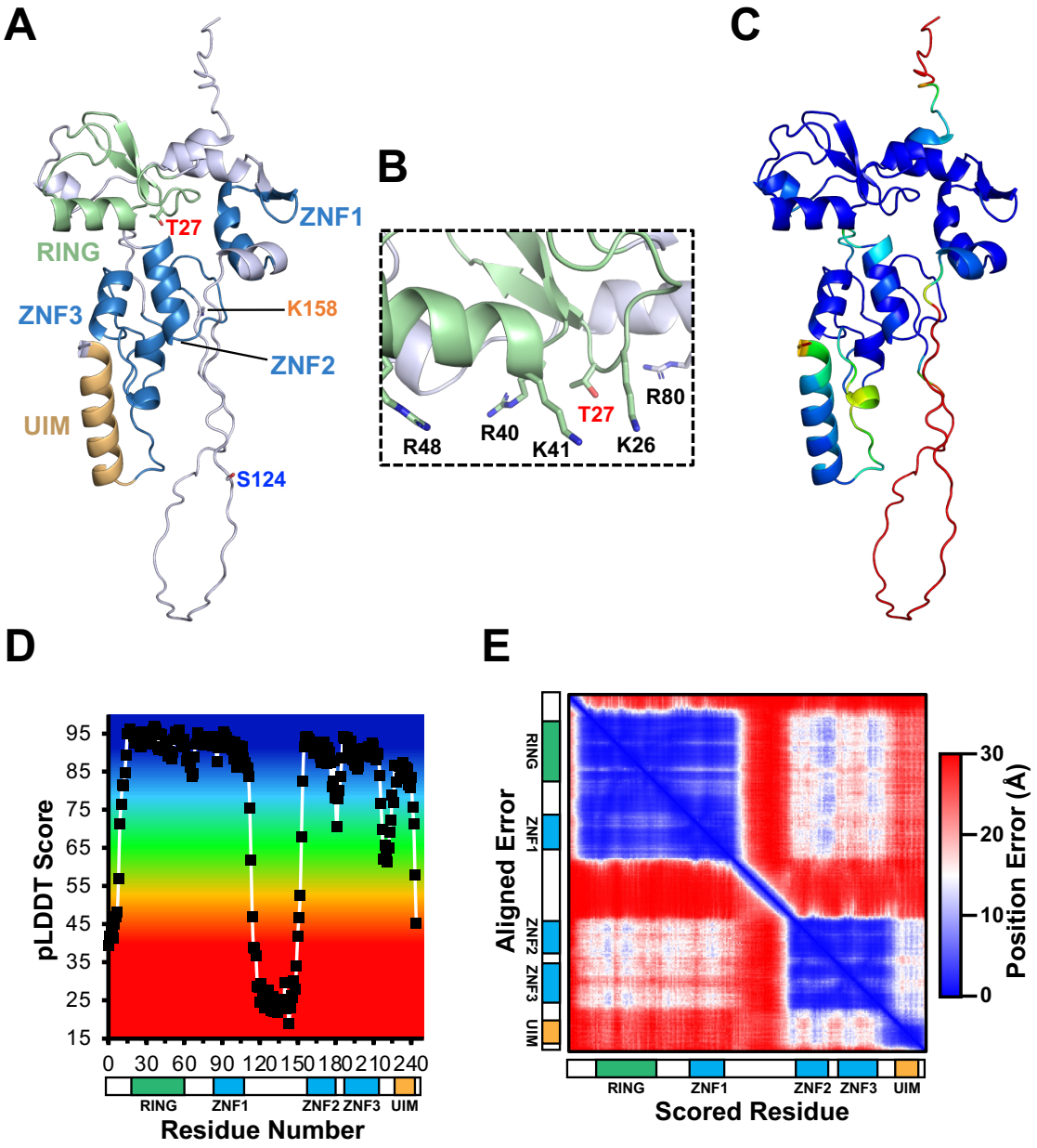

Figure 4.S9: AlphaFold-Predicted Model of RNF138's Structure

A) Predicted model (442, 444, 445) of human RNF138 (UniProt accession Q8WVD3) with individual domains coloured respectively: linkers in white, RING in green, zinc fingers (ZNF) in blue, ubiquitin-interacting motif (UIM) in dark yellow. The RING domain folds onto ZNF1, linked together by a hinge-like linker. A longer linker (54 residues) connects the N-terminal RING and ZNF1 to ZNF2 and ZNF3, which appear to pack and form a folded structure and are followed by the UIM. The post-translational modification sites described in this study are highlighted: T27 (red), S124 (dark blue), and K158 (orange). **B)** Closeup view of residue T27 in A), highlighting positive residues in close proximity and forming a positively charged surface in the RING domain.

C), D) Predicted Local Distance Difference Test (pLDDT) (464) plot of the predicted model of RNF138. pLDDT scores range from 0 to 100, where scores above 70 indicate a high level of confidence in the position of the Cα atom, and scores above 90 indicate a high level of confidence in the placement of side chain atoms. Scores below 50 are generally considered as indications of low confidence and suggest disorder (464). Dark blue and red correspond to high confidence (>90) and low confidence (<50) pLDDT scores, respectively. The colour gradient on the graph (D) corresponds to the same colour scheme in panel C). Overall, the model was predicted with high confidence with a median pLDDT of 88.9. The residues in the N-terminal RING domain and ZNF1 had consistently high pLDDT high values. Notably, T27 had a score of 91.6. The linker connecting the N-terminal domains to the C-terminal domains was predicted with low confidence, suggesting flexibility within those residues. S124 is positioned in the flexible linker with a pLDDT score of 26.05, suggesting a dynamic or flexible region (442–444, 464). The C-terminal zinc fingers and UIM were predicted with high confidence. Interestingly, residue K158, preceding ZNF2, had a pLDDT score of 94.12. **E)** Plot representing the predicted alignment error (pAE) for the predicted structure of RNF138. In contrast to pLDDT, which measures local confidence, pAE is a long-range domain position confidence metric that calculates the confidence of each residue in relation to all other residues (442–445). It quantifies the predicted error in Angstroms (Å) for residue *x* if the model were aligned onto the true structure at residue *y*. The pAEs within the N-terminal domains of RNF138 were of high confidence, with a median predicted error of 2.82 Å. The flexible linker connecting the N-terminal and C-terminal domains had high predicted error, with a median pAE value of 22.36 Å, further suggesting a flexible region in the protein. The C-terminal domains had a median pAE of 5.1 Å, suggesting a high confidence prediction. pAE is practical for measuring and analyzing both intra- and interposition confidence because it does not impose the requirement for the residues to belong to the same monomer (442, 443). Although the N- and C-terminal domains are within the same monomer and appear to fold and interact, they are separated by the large flexible linker. The pAE error between the N-terminal domains and C-terminal domains is relatively high (16.77 Å) due to the dynamic linker making it difficult to confidently predict residues involved in the interaction between the N- and C-terminal domains. Overall, this modeling suggests RNF138 is a flexible and dynamic protein accessible to post-translational modification.

Figure 4.S10

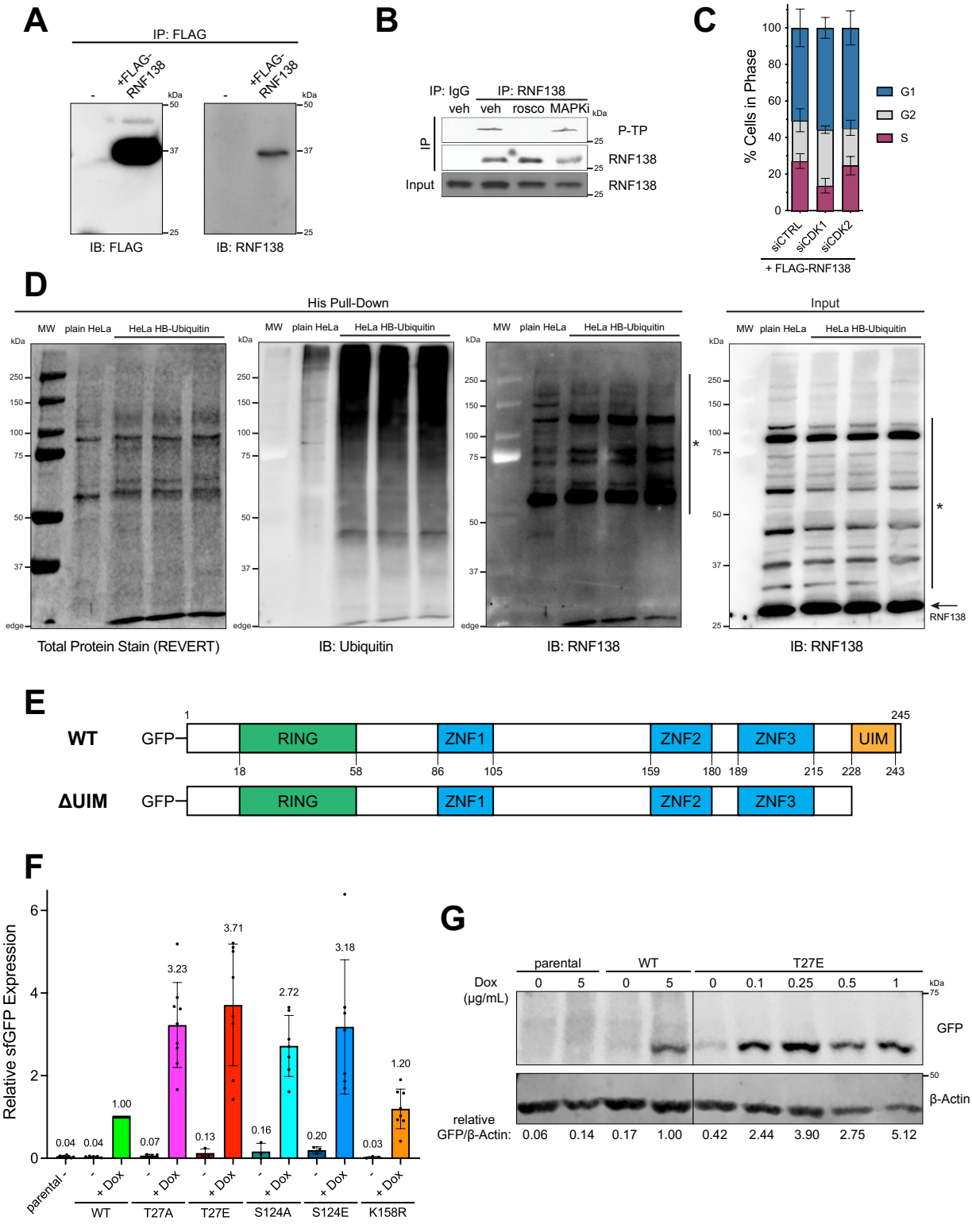

Figure 4.S10: Related to Figures 4.1, 4.2 and 4.5

A) FLAG immunoprecipitates (IPs) of HEK293 cells expressing FLAG-RNF138 or not were immunoblotted for the FLAG epitope or RNF138 (Abcam antibody). **B)** G2-synchronized HeLa cells were treated with 0.2% DMSO vehicle control (veh), 50 μM roscovitine (rosco), or the MAP kinase inhibitor SB203580 (MAPKi) at 10 μM for 4 hours. Cell extracts were then IP'd for RNF138 or with control immunoglobulin G (IgG) and immunoblotted for phosphorylated TP sites (P-TP) or RNF138. **C)** Flow cytometric analysis of propidium iodide signal in HeLa cells treated as in **Fig. 4.1I**. Averages in C) were calculated from 3 biological replicates pooled together. **D)** 90% of a single pellet of plain HeLa cells and 3 cell pellets of HeLa stably expressing 6XHis-biotin-ubiquitin (HeLa HB-ubiquitin) was subjected to nickel affinity purification ("His pull-down"), while the remaining 10% was processed to generate whole cell extract (input). The samples were resolved by SDS-PAGE and transferred to nitrocellulose membrane. The His pull-down fraction was first stained for total protein with REVERT total protein stain (LI-COR Biosciences), then immunoblotted (IB'd) for RNF138, and finally stripped and IB'd for ubiquitin. For the remaining 10% of cells, whole cell extracts were prepared for the input control (rightmost panel) and IB'd for RNF138. Note the RNF138 antibody detects other species beyond RNF138 (*). RNF138 itself (predicted molecular weight: 28 kDa) is detected just above 25 kDa (arrow). MW: molecular weight standards. **E)** Schematic diagrams of the structural domains in wildtype (WT) and the ΔUIM mutant of GFP-tagged RNF138. **F)** Quantification of IBs (such as **Fig. 4.5G**) for doxycycline (Dox)-inducible expression of sfGFP-RNF138 variants in U2OS-TRex cells stably integrated with their DNA. **G)** Example titration of Dox concentrations to induce sfGFP-RNF138-WT and -T27E expression, detected by IB. D) is a representative result from at least 6 biological replicates. Averages in F) were calculated from at least 7 biological replicates pooled together.

Figure 4.S11

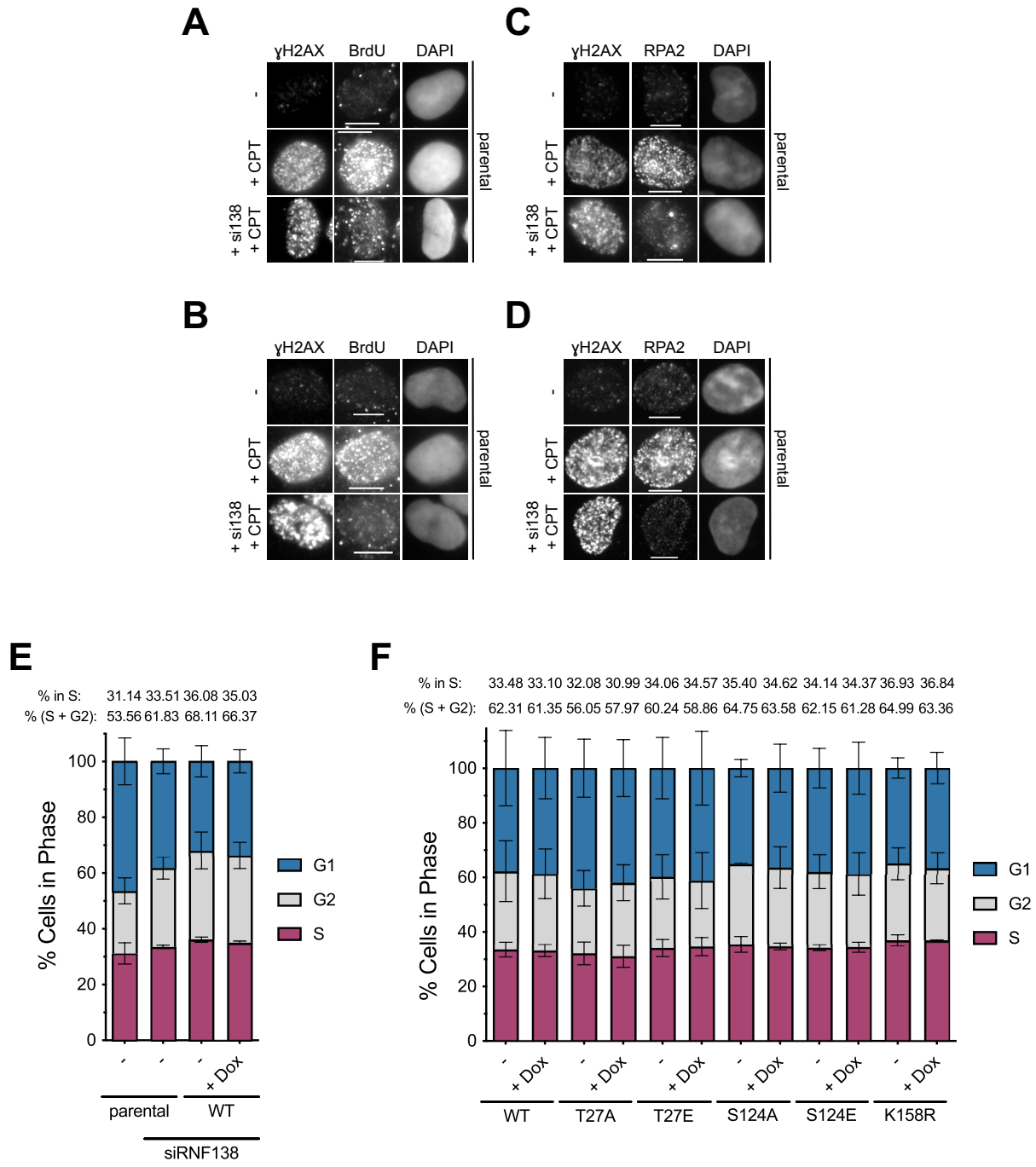

Figure 4.S11: Related to Figures 4.6 and 4.7

A) and B) Additional representative micrographs from **Fig. 4.6**. Representative BrdU immunofluorescence (IF) micrographs of parental U2OS-TRex cells transfected with or without siRNA to RNF138 (siRNF138) and treated with camptothecin (CPT) or not for 1 hour. ɣH2AX was used to indicate DNA damage, while DAPI stain labeled the nucleus. Micrographs are derived from the same biological replicates presented in the left panels of **Fig. 4.6A** (A) and **Fig. 4.6B** (B),

respectively. **C) and D)** As per A) and B), but for RPA2 foci instead. Micrographs are derived from the same biological replicates presented in the left panels of **Fig. 4.6D** (C) and **Fig. 4.6E** (D), respectively. **E)** Flow cytometric analysis of propidium iodide signal in parental or sfGFP-RNF138-WT-expressing U2OS-TRex cells transfected with siRNA to RNF138 or not, and with or without doxycycline (Dox) induction. **F)** Flow cytometric analysis of propidium iodide signal in sfGFP-RNF138 variant-expressing U2OS-TRex cells induced with Dox or not. Averages were calculated from 2 (F) or at least 2 (E) biological replicates pooled together. Scale bars denote 10 μm.

4.10.2 Supplementary Tables

Table 4.1: Primers for DNA Sequencing

Name	Sequence (5' – 3')	Construct	Direction
RNF138 21 For	GGCCACGTCCTACACCGA	any containing RNF138	forward
RNF138 210 For	ACGGGCCTTAGACCTTGAAA	any containing RNF138	forward
RNF138 169 Rev	ATAGGGGACAATGTGCTCCG	any containing RNF138	reverse
FLAG-RNF138 845 Rev	TGAAATTTGTGATGCTATTGCTTT	FLAG-RNF138	reverse
pEGFP-C1 For	CATGGTCCTGCTGGAGTTCGTG	GFP-RNF138	forward
pEGFP-C1 Rev	CAGGTTCAGGGGGAGGTGTGG	GFP-RNF138	reverse

Table 4.2: Primers for Q5 Site-Directed Mutagenesis (New England Biolabs)

Mutation	Templates	Sequences of Primer Pairs (5' – 3')	Annealing Temp.
RNF138-T27A	FLAG-RNF138-WT, GFP-RNF138-WT, mCherry-RNF138-WT	Forward: GGTGCTCAAAgcgCCCGTGCGGA Reverse: TCCTGACAGACGGGGCAGTAG	72°C
RNF138-T27E	GFP-RNF138-WT, sfGFP-RNF138-WT, mCherry-RNF138-WT	Forward: GGTGCTCAAAgagCCCGTGCGGAC Reverse: TCCTGACAGACGGGGCAG	67°C
RNF138-K158R	GFP-RNF138-WT, mCherry-RNF138-WT	Forward: CCTACTTTTaggTGTCCCCTG Reverse: ATGACCAGAAGAACTTGTATTC	60°C
RNF138-S124A	mCherry-RNF138-WT	Forward: CTTTCAGATCgctCAAGATTCAG Reverse: TTTGGAATGATAGAAGAAACAC	58°C
RNF138-S124E	sfGFP-RNF138-WT, mCherry-RNF138-WT	Forward: CTTTCAGATCgagCAAGATTCAGTAGGG Reverse: TTTGGAATGATAGAAGAAACAC	57°C

Table 4.3: siRNAs

Name	Target	Sense Sequence (5' – 3')
siCTRL	Luciferase (negative control)	CGUACGCGGAAUACUUCGA
siRNF138	RNF138 coding region (133)	CCAAACUGCUGUUGAAGAA
siRNF138 UTR (used only in Fig. 4.S8A)	RNF138 3' UTR (sequences were selected by Dharmacon Inc.)	The following siRNAs pooled together: GGAGGGAAUUGUAUUGAUA AAAGAGUGGUGUUUACUAU GGGAAUAGGGAUAGACUUU AGCCAUACAUCUUAAUGAA
siCDK1	CDK1	CCUAGUACUGCAAUUCGGGAAAUUU

All siRNAs were synthesized by Sigma-Aldrich and included [dTdT] overhangs.

Table 4.4: Antibodies

Antibody	Source	Catalogue Number	Identifier	Dilution (Application)
rabbit anti-β-actin	Sigma	A5060	RRID:AB_476738	1:10000 – 1:20000 for 1 hour (IB)
mouse anti-BrdU	Cytiva Life Sciences	RPN202	RRID:AB_2314032	1:1000 overnight (IF)
mouse anti-CDK1	Santa Cruz Biotechnology	sc-54	RRID:AB_627224	1:1000 overnight (IB)
rabbit anti-CDK2	Santa Cruz Biotechnology	sc-163	RRID:AB_631215	1:1000 overnight (IB)
rabbit anti-phospho-Chk1 (Ser345)	Cell Signaling Technology	2348	RRID:AB_331212	1:5000 for 1 hour (IB)
rabbit anti-phospho-Chk2 (Thr68)	Cell Signaling Technology	2197	RRID:AB_2080501	1:1000 overnight (IB)
rabbit anti-Cyclin A	Santa Cruz Biotechnology	sc-751	RRID:AB_631329	1:1000 overnight (IB)
mouse anti-FLAG tag	Millipore Sigma	F1804	RRID:AB_262044	1:4000 – 1:8000 for 1 hour (IB)
rabbit anti-FLAG tag	Cell Signaling Technology	14793	RRID:AB_2572291	1:4000 – 1:8000 for 1 hour (IB)
rabbit anti-Geminin	Cell Signaling Technology	5165	RRID:AB_10623289	1:1000 overnight (IB)
mouse anti-GFP	Santa Cruz Biotechnology	sc-9996	RRID:AB_627695	1:2000 – 1:6000 for 1 hour (IB)
rabbit anti-GFP	Proteintech	50430-2-AP	RRID:AB_11042881	1:5000 for 1 hour (IB)
rabbit anti-phospho-H2AX (Ser139)	Cell Signaling Technology	2577	RRID:AB_2118010	1:3000 for 1 hour (IF)
rabbit anti-HA tag	Abcam	ab9110	RRID:AB_307019	1:4000 – 1:8000 overnight (IB)
rabbit anti-RNF138	St John's Laboratory	STJ112342	RRID:AB_2938982	1:1000 – 1:4000 overnight (IB)
rabbit anti-RNF138 (used only in Fig. S3A)	Abcam	ab92730	RRID:AB_2238719	1:1000 overnight (IB)
mouse anti-RPA2	Abcam	ab2175	RRID:AB_302873	1:8000 for 1 hour (IF) 1:2000 overnight (IB)
rabbit anti-phospho-RPA2 (Ser4/Ser8)	Bethyl Laboratories	A300-245A	RRID:AB_210547	1:4000 – 1:12000 overnight (IB)
rabbit anti-phospho-Ser/Thr (P-S/TQ; ATM/ATR substrate)	Cell Signaling Technology	2851	RRID:AB_330318	1:1000 overnight (IB)
mouse anti-phospho-Thr-Pro (P-TP)	Cell Signaling Technology	9391	RRID:AB_331801	1:500 – 1:1000 overnight (IB)
mouse anti-α-Tubulin	Genscript	A01410	RRID:AB_1968943	1:20000 – 1:25000 for 1 hour (IB)
mouse anti-Ubiquitin	Santa Cruz Biotechnology	sc-8017	RRID:AB_2762364	1:1000 overnight (IB)
donkey anti-mouse IgG—IRDye 680RD	LI-COR Biotechnology	926-68072	RRID:AB_10953628	1:20000 for 1 hour (IB)
donkey anti-rabbit IgG—IRDye 680RD	LI-COR Biotechnology	926-68073	RRID:AB_10954442	1:20000 for 1 hour (IB)
donkey anti-mouse IgG—IRDye 800CW	LI-COR Biotechnology	926-32212	RRID:AB_621847	1:20000 for 1 hour (IB)

donkey anti-rabbit IgG—IRDye 800CW	LI-COR Biotechnology	926-32213	RRID:AB_621848	1:20000 for 1 hour (IB)
goat anti-mouse IgG—HRP	LI-COR Biotechnology	926-80010	RRID:AB_2721263	1:5000 for 1 hour (IB)
goat anti-rabbit IgG—HRP	LI-COR Biotechnology	926-80011	RRID:AB_2721264	1:5000 for 1 hour (IB)
goat anti-mouse IgG—Cy3	Jackson ImmunoResearch Laboratories	115-165-146	RRID:AB_2491007	1:500 for 1 hour (IF)
goat anti-rabbit IgG—Alexa Fluor 647	Invitrogen	A-21244	RRID:AB_2535812	1:250 for 1 hour (IF)

- IF = immunofluorescence staining; IB = immunoblot
- 1 hour = 1 hour incubation at room temperature is preferable
- Overnight = overnight incubation at 4°C is preferable

Chapter 5 – Discussion

5.1 Summary of Findings and a Consolidated Model

The overarching goal of this work was to study how DNA end resection, the process by which nucleolytic activity results in the 5'→3' degradation of both DNA strands away from the DSB site, is controlled. We sought to investigate a) if other protein players regulate DNA end resection, and b) how known proteins involved in DNA end resection might be regulated by PTMs. Overall, we uncovered that BMI-1, as a protein involved in the response to DSBs, promotes end resection, and provide mechanistic insights into how this occurs. The work presented also reveals additional protein targets of SUMOylation (CtIP), ubiquitylation (RNF138), and phosphorylation (RNF138) in DSB repair, with direct impacts on end resection when the sites of these modifications are disrupted.

In Chapter 2, we find that SUMOylation regulates end resection (465, 466) by directly impacting the function of the pro-resection factor and MRN cofactor, CtIP. We characterized the conditions by which CtIP is modified by SUMOylation, finding that it is conjugated with SUMO-2 during S phase (**Section 2.4.4**) and that this is dependent on the E3 SUMO ligase PIAS4, an interaction with the DNA replication factor PCNA, and occurs after prior ATR and CDK activity on CtIP (**Sections 2.4.5 and 2.4.6**). Importantly, we identify that CtIP is primarily SUMOylated at an internal residue, K578 (**Section 2.4.7**), one that, at the time, had not been linked to CtIP function (343). Phenotypically, we observe that K578 SUMOylation is important for DNA end resection, the occurrence of HR repair, and the protection of stalled replication forks from nucleolytic degradation (**Sections 2.4.8 and 2.4.10**).

Next, in Chapter 3, we dissected what roles the transcriptional repressor protein BMI-1 could have in DSB repair by depleting BMI-1 via RNA interference or treatment with the compound PTC-209, finding that BMI-1 promotes HR and end resection (**Sections 3.4.1 and 3.4.2**). Probing further, we show that BMI-1-dependent transcriptional silencing promotes end resection, as the inhibition of end resection by BMI-1 depletion can be overcome by treatment with transcription inhibitors (**Section 3.4.4**). At the same time, BMI-1's promotion of H2AK119ub deposition contributes to end resection (**Section 3.4.5**) by recruiting CtIP, which we observe has multiple regions that bind ubiquitin (**Sections 3.4.2, 3.4.6, 3.4.7, and 3.4.8**). Together, these findings reveal mechanistic insights into how BMI-1 regulates end resection. They also reinforce the notion that CtIP binds ubiquitin (424, 432), giving rise to the exciting possibility that the general accumulation and propagation of ubiquitin at sites of DNA damage (42) plays at least some role in recruiting CtIP.

Finally, in Chapter 4, we observe that the stimulatory role for the E3 ubiquitin ligase RNF138 in end resection is controlled both by ubiquitylation and CDK-dependent phosphorylation events. Interestingly, RNF138 ubiquitylation is increased during the S and G2 phases but decreased upon prolonged genotoxic stress (**Section 4.4.4**), hinting it may serve as a switch to prime and restrict RNF138 activity, respectively. Such a pattern is reminiscent of that for CtIP SUMOylation, where CtIP is SUMOylated in S phase, with SUMO modification being reduced during prolonged replication stress (**Section 2.4.4**). Certainly, further investigation is needed to conclude whether conjugation and (seemingly) deconjugation of SUMO or ubiquitin function hand in hand to modulate RNF138 or CtIP activity, respectively. Clearer, however, is the essential role of phosphorylation on RNF138 activity in end resection and the progression of HR (**Sections 4.4.7 and 4.4.8**). For example, phospho-ablating mutations at the T27 (by CDK1/2-dependent activity,

Section 4.4.2) and S124 (by ATM (315)) sites abrogate HR-dependent gene conversion, but it can be rescued to levels beyond that of wildtype RNF138 by phospho-mimicking substitutions at both positions (**Section 4.4.8**).

A model for the activation of end resection in DSB repair can be proposed by consolidating the data presented here and from the literature. Here, these events are arranged sequentially for simplicity, but it is likely that many of them are occurring rapidly, simultaneously, and interdependently in the cell. Upon the induction of a DSB during the S and G2 phases, the Ku heterodimer and the MRN complex are among the earliest proteins to be recruited to the site of damage (and independently of each other) (54, 55, 316, 467–470). The binding of MRN to chromatin is sufficient to recruit and activate ATM kinase (94, 95). The presence of Ku is a physical block to end resection (67, 317, 318, 405, 471) and biases cells to perform NHEJ (30, 34, 43, 232), thus Ku must be removed from chromatin for end resection and HR to occur in S/G2 (48, 53–57, 132, 472, 473). RNF2/BMI-1 is recruited to chromatin in an ATM-dependent manner (297, 302), downstream of the MRN complex but upstream of the DSB signaling proteins BRCA1 (**Chapter 3**) and 53BP1, whose early recruitment to DNA damage is dependent on BMI-1 (130). After MRN begins early processing of the DSB ends, generating short stretches of ssDNA, RNF138 is recruited to the ssDNA ends by its three ZNF domains (132, 437). During S/G2, RNF138 is phosphorylated at residue T27 by CDK1/2 activity (96) and ubiquitylated; one site of RNF138 ubiquitylation is residue K158 (**Chapter 4**). Activated ATM also phosphorylates RNF138 at S124 (315). The combined action of these three PTMs may cause conformational changes that fully activate RNF138 as an E3 ubiquitin ligase (**Chapter 4**). The Ku subunit Ku80 (132) is then ubiquitylated by the UBE2D ubiquitin E2s and RNF138 (133), promoting the dissociation of Ku from chromatin and removing its block on end resection (132). Around the

DSB site, RNF2/BMI-1 then deposits the H2AK119Ub mark on histone H2A and facilitates transcriptional repression (276, 302). Repressing transcription may clear the DSB site of "traffic", the transcription complexes that could impede the assembly of the DSB signaling and DNA end resection machinery (195), allowing CtIP to better access chromatin (**Chapter 3**). CtIP is then recruited to the vicinity of the DSB, perhaps in part by its ability to bind to ubiquitin and thus H2AK119Ub ((424, 432) and **Chapter 3**). The ubiquitylation of CtIP by UBE2Ds/RNF138 further promotes CtIP accrual on chromatin (133). As well, in S phase, CtIP interacts with PCNA ((335) and **Chapter 2**) that is enriched on chromatin to support DNA replication (338), localizing even more CtIP to the DSB. On chromatin, CtIP is SUMOylated by the SUMO E3 ligase PIAS4 ((429) and **Chapter 2**). SUMOylation on residue K578 promotes additional SUMOylation events on CtIP (**Chapter 2**), perhaps on residue K896 and potentially involving the SUMO E3 ligase CBX4 (343). CtIP SUMOylation is enhanced by CDK2-dependent phosphorylation at residue T847, along with ATR-dependent phosphorylation on residues S664, S679, and S745 (**Chapter 2**). This ATR activity may arise from replication stress (in S phase) and/or the RPA-bound short ssDNA regions (87) already generated by limited MRN activity. Chromatin-bound and phosphorylated CtIP then binds the MRN complex, fully activating MRN's endonuclease activity (51, 52, 58–61) to initiate DNA end resection and further remove Ku-bound DNA proximal to the DSB. MRN/CtIP-dependent short-range resection is then followed by long-range end resection catalyzed by Exo1, Dna2, BLM, and WRN (233). By mechanisms that are currently unclear, K578-SUMOylated CtIP stimulates DNA end resection, and the resulting ssDNA overhangs are bound by RPA complexes (**Chapter 2**). RPA is eventually exchanged with Rad51, forming nucleofilaments that will undergo the HR process (71). Regulatory signals to shut off excessive end resection may include the deSUMOylation of CtIP, which can also occur upon sustained

replication stress (**Chapter 2**), and the deubiquitylation of RNF138 (**Chapter 4**). Collectively, the findings in this body of work shed more light on the molecular signals and events governing the occurrence of DNA end resection.

5.2 Additional Discussion and Future Directions – CtIP SUMOylation

Our observation that residue K578 is a critical SUMOylation site on CtIP has been supported by a study from Jun Huang's group, published soon after the release of our article (429). The study proposes that ATM activity on CtIP both supports end resection (for the repair of the DSB) but also suppresses uncontrolled, excessive resection. Many of the findings in Chapter 2 were recapitulated in this report, including that CtIP is modified by SUMO-2 on chromatin (in their report, preferentially by SUMO-2/3 over SUMO-1); that PIKK-dependent activity on CtIP is a prerequisite for SUMOylation; that K578 and not K896 is the main residue for CtIP SUMOylation; that PIAS4, and not CBX4, is the SUMO E3 ligase involved in bulk CtIP SUMOylation; and that disrupting the K578 SUMOylation site does not impair CtIP recruitment to laser stripes, but reduces repair by HR and clonogenic survival to DNA damage (429). Fascinating, new insights from the Huang group include that PIAS4 preferentially interacts with ATM-phosphorylated CtIP, and that the STUbL RNF4 recognizes K578-SUMOylated-CtIP, resulting in CtIP's polyubiquitylation and, presumably, proteasomal degradation (429). A few differences lie in the Huang group's observations: that CtIP SUMOylation is induced upon treatment with CPT, ionizing radiation, and etoposide, but not hydroxyurea (in our study, DSB-

inducing agents did not stimulate CtIP SUMOylation, although passing through S phase did, while treatment with hydroxyurea reduced CtIP SUMOylation), and that ATM hyperphosphorylation stimulates SUMOylation (in our study, ATR was the PIKK involved) (429). These discrepancies may be explained by cell line-specific differences, in that we performed our SUMOylation His pull-down assays in HeLa cells expressing low levels of His-tagged SUMO-2 (346), whereas the Huang group used HEK293T cells or HeLa cells infected with a lentiviral vector expressing SUMO-2. The difference may also lie in the expression levels of SUMO-2, as the creators of our HeLa line sorted the cells for those low in SUMO-2 expression (346). As cell sorting was not mentioned in the Huang group's report, it may be that their cells presented with high levels of SUMO-2. In addition, the Huang group reported the K578R mutant of CtIP is recruited/retained more on laser microirradiated chromatin than wildtype CtIP (in our study, wildtype and K578R-CtIP had similar recruitment kinetics to laser stripes) (429). Moreover, cells expressing K578R-CtIP exhibited brighter RPA2 foci in response to CPT (we reported dimmer RPA2 foci) (429). These observations are summarized in their model, that preventing CtIP SUMOylation averts RNF4-mediated ubiquitylation (and presumably proteasomal degradation), thus stabilizing CtIP and increasing its retention at sites of damage and prolonging end resection (429). We again note that the Huang group performed these functional experiments using cell lines stably expressing CtIP by lentiviral and retroviral infection (429), where the genetic construct of interest can be integrated into the host cell genome at high efficiency (474). When stable cell lines were used for our experiments, they were generated by lipofection and stable expressors were subsequently selected with antibiotics over a few weeks. Thus, it could be that the expression levels of CtIP are lower in our experiments with stable cell lines (exemplified by our cells' faint GFP-CtIP fluorescence) relative to those used in the Huang group's report (presumably, an overexpression

system), explaining these opposing observations. (We also note that Pablo Huertas' group did not observe an induction of CtIP SUMOylation with ionizing radiation in HEK293T cells transfected with His-tagged SUMO-1/-2 and GFP-CtIP by the calcium phosphate method (343).) Nevertheless, both our and the Huang group's models can co-exist, in that SUMOylation at K578 plays dual roles – activating CtIP for stimulating DNA end resection, as we found, but also targeting CtIP for RNF4-dependent turnover to prevent excessive chromatin localization and uncontrolled end resection, as found by the Huang group. As well, both our reports emphatically demonstrate the importance of SUMOylation in regulating CtIP function, and that chromatin binding and PIKK-dependent phosphorylation events precede CtIP SUMOylation.

The observation that the near C-terminal residue K896 is a minor SUMOylation site on CtIP has now been shown by three independent groups, our group and those of Pablo Huertas and Jun Huang (343, 429). Yet, cells expressing the K896R mutant show strong defects in end resection and the formation of RPA and Rad51 foci in response to IR (343). Conversely, RPA and Rad51 foci formation can be rescued upon C-terminal fusion of SUMO-1 to K896R-CtIP (343). We demonstrated that cells expressing K578R-mutated CtIP are also deficient in DNA end resection in response to CPT (**Section 2.4.8, Figs. 2.7A-B**). To compare the contributions of the K578 and K896 residues to end resection, we also examined the formation of CPT-induced BrdU foci for cells expressing CtIP-K578R, -K896R, or the -K578R-K896R double mutant (**Fig. 5.1A-B**). Expressing the K896R mutant abrogated BrdU foci intensity and area to the extent of CtIP knockdown, consistent with the notion that K896R SUMOylation is essential for DNA end resection (343). On the other hand, expressing the K578R mutant strongly reduced BrdU foci and area, but not to the extent of the K896R mutant. Meanwhile, expressing the K896R-K578R double mutant reduced BrdU foci and area to the level of the K896R single mutant (**Fig. 5.1A-B**). Thus,

between the two residues, K896 is more important for CtIP's ability to promote BrdU foci formation, and both residues may act within the same pathway. Still, the individual contributions of K578 and K896 to end resection have not been fully explored. This could be assessed by performing similar BrdU or RPA foci formation and DR-GFP HR reporter assays in cells expressing the GFP-CtIP-6KR or -7KR-R578K mutants (**Fig. 2.6A**), where of the canonical SUMOylation sites, CtIP is left with only functional ones at the K578 or K896 positions. Whether SUMOylation on K578 is a pre-requisite for K896 SUMOylation also requires further investigation, perhaps with mass spectrometry to detect the K896 modification, which is of low abundance and cannot be detected by immunoblotting Ni^{2+}-affinity purified His-SUMO conjugates for GFP-CtIP (**Fig. 2.6C-D**, (343)).

Figure 5.1

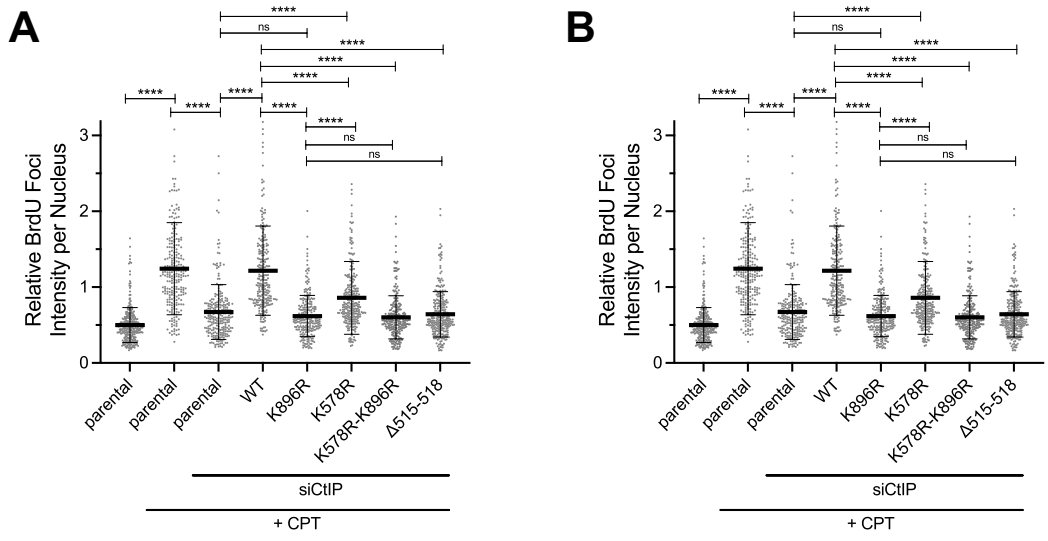

Figure 5.1: Assessing the Impact of K578R and K896R Mutations of CtIP on DNA End Resection, as Measured by CPT-Induced BrdU Foci

A) and B) Parental U-2 OS cells or U-2 OS stably expressing the indicated siRNA-resistant GFP-CtIP constructs were transfected with siRNA to CtIP (or not), cultured in BrdU-containing media, treated with 1 μM CPT for 1 hour (or not), then processed for IF staining. $\gamma H2AX^+$ cells (with the

exception of the untreated condition) were quantified for BrdU foci intensity (A) or area (B). This figure contains data presented already (**Fig. 2.7**) but with the inclusion of data for the K578R-K896R double mutant.

Other future work in this study could further examine how CtIP SUMOylation at K578 supports DNA end resection. While we did not observe a difference in the ability for CtIP to interact with the members of the MRN complex in the K578R mutant (**Fig. 2.S16C)**, these co-immunoprecipitation experiments were done in unperturbed cells. Instead, they could be attempted in cells synchronized to S phase and/or treated to induce DNA damage. As well, beyond the MRN complex, interactions with other resection factors, such as BLM, Dna2, Exo1, and RPA complex, should be examined. Alternatively, the fraction of SUMOylated CtIP could be boosted for such interaction studies. For instance, instead of performing co-immunoprecipitations in cells overexpressing GFP-CtIP, CtIP could instead be overexpressed and affinity purified from suspension cultures (such as *Sf*9 or Expi293F cells), be SUMOylated *in vitro*, and immobilized as bait in binding experiments with cell extracts. This would ensure the interactions detected (or lost) result from the presence of SUMO groups on CtIP. With this method, various K→R substitution mutants of CtIP could also be purified and then subjected to *in vitro* SUMOylation, allowing interrogation of whether protein interactions with SUMO-CtIP differ if only K578 or K896, or both together, are modified with SUMO. The paralogue of SUMO could also be varied (i.e. SUMO-1 versus SUMO-2). If *in vitro* SUMOylation proves difficult, an alternative strategy could entail SUMOylating overexpressed CtIP in a site-specific manner *in vivo*, using an approach combining site-directed mutagenesis, genetic code expansion, and sortase-mediated SUMOylation (475). This CtIP could then be subjected to affinity purification for use in binding assays. Intriguingly, the *S. cerevisiae* homologue of Mre11 has been found to recruit to poly-SUMO chains and contains a functional SIM (SUMO-interacting motif) (476). Relatedly, a recent proteomics

screen in HeLa cells found the components of the MRN complex bind very tightly to SUMO-2 and SUMO-2 chains (Mre11, for instance, binds with a higher affinity for SUMO-2 chains than RNF4 itself) (160). It could well be that the induction of CtIP SUMO-2ylation serves to recruit it to MRN, triggering the formation of the MRN-CtIP complex necessary for the initiation of end resection.

Other investigations could be performed with purified and subsequently *in vitro* SUMOylated CtIP to assess exactly how SUMO-CtIP promotes resection. Numerous *in vitro* assays have been developed to monitoring resection activity with purified proteins. These could include the MRN clipping assay (**Fig. 2.S16F)** (52), the MRN endonuclease assay (324), the CtIP "nuclease" assay (**Fig. 2.S18D)**, helicase/nuclease assays for Dna2 (477), and the DNA curtain approach for monitoring resection on single molecules of DNA (110). CtIP and its homologue in *S. cerevisiae* have also been shown to form tetramers, an action critical for end resection, HR, and DSB repair and dependent on CtIP's N-terminal domain (258, 259, 261, 344). It would be interesting to examine if *in vitro* SUMOylation enhances or disrupts the ability by which purified CtIP assembles in tetramers, measured using SEC-MALS (size exclusion chromatography coupled to multi-angle light scattering). Intriguingly, while residue K578 does not lie near the N-terminal domain of CtIP, residue K46, another putative SUMOylation site, resides within CtIP's tetramerization motif (**Fig. 2.S15A**).

5.3 Additional Discussion and Future Directions – BMI-1 and End Resection

The link between transcription and DSB repair is certainly complicated (478, 479). While we and others (276, 302, 415, 480) have reported a role for BMI-1-dependent transcriptional repression in promoting HR, an interesting conundrum has risen: the notion that active transcription serves to promote HR. Indeed, active RNA polymerase II (RNAPII) localizes to DSBs and is recruited by the MRN complex (481, 482). MRN also has the capacity to melt DNA ends at DSBs, promoting RNAPII transcription (483). As well, DSBs that occur within highly transcribed regions of chromatin are preferentially repaired by HR instead of NHEJ (484). Transcription can generate nascent RNAs that anneal to one strand of the DNA duplex. This pairing forms structures known as R-loops, which consist of the hybrid duplex of DNA-RNA with the remaining DNA strand being displaced. Indeed, DNA-RNA hybrids are enriched around DSB sites (482). RNA transcripts themselves, when artificially tethered near DSBs, enhance the ability of Rad51 to form displacement loops, a key step in the process of HR that precedes homology search (485). RNA polymerase III, too, has also been found to be an essential factor for end resection and HR, generating RNA transcripts at DSBs and forming DNA-RNA hybrids which may protect the 3' ssDNA overhang remaining after end resection (486). How can one reconcile the positive roles of both active transcription and transcriptional repression (480) in the occurrence of HR? This might all come down to timing. While DNA-RNA hybrids and R-loops promote HR, perhaps transcriptional repression is eventually needed to suppress their formation after end resection is initiated. This reasoning is supported by additional data suggesting negative consequences of these structures. For instance, the DNA-RNA hybrids themselves must form but also not persist, as both deleting or overexpressing RNase H, a ribonuclease that degrades DNA-

RNA hybrids, leads to the inhibition of HR (482). Likewise, senataxin, a helicase that unwinds DNA-RNA hybrids, is also recruited to DSBs at actively transcribed regions of the genome, promoting the recruitment of Rad51 and preventing inappropriate translocation events (406). As well, the stabilization of DNA-RNA hybrids impairs the recruitment of RPA, suggesting the transcripts do compete with RPA for binding ssDNA overhangs (482). Thus, the ATM-dependent silencing of transcription in the vicinity of DSBs, of which BMI-1 contributes to (276, 302, 415, 480), may act as a regulatory mechanism to prevent the unnecessary formation of R-loops once the process of repair has begun.

Future directions in the study of H2AK119ub in end resection could first determine if CtIP itself preferentially recognizes the H2AK119ub mark or just binds to ubiquitin in general. While we were able to detect CtIP binding to ubiquitylated peptides representing the H2A tails, in these experiments CtIP did not show a clear preference for H2AK119ub (**Figs. 3.S11D-E**). Perhaps performing a similar experiment, but mixing purified CtIP with reconstituted nucleosome core particles (85) containing the H2AK119ub mark (instead of ubiquitylated peptides) will address this question within the correct structural context of the nucleosome. A second remaining query includes identifying regions of CtIP that can bind ubiquitin. While none of the CtIP internal deletion mutants strongly impaired ubiquitin binding (**Section 3.4.8**), one could instead utilize individual fragments representing ~100 amino acid regions along the length of CtIP as "prey" proteins for Far Western blotting. The CtIP primary sequence could also be scanned for potential ubiquitin binding domains (126). A previous report found a novel ubiquitin-interacting motif (UIM) in the PRC2 component JARID2 that facilitates an interaction with H2AK119ub, its UIM having sequence similarity to a non-canonical UIM in DNMT1 (DNA methyltransferase 1) (402). A manual scan of the CtIP primary sequence revealed four sequences with some semblance to

features of JARID2-like UIMs (402) (**Fig. 5.2**). Putative UIMs #1-3 do not overlap with well-characterized CtIP domains (e.g., oligomerization, endonuclease, DNA binding, conserved region with *S. cerevisiae*), while #4 partially overlaps with a region known to stimulate Dna2 activity (68). *In vitro* binding assays using biotinylated peptides of these sequences and free ubiquitin could be performed to determine if they truly bind ubiquitin, and particularly, H2AK119ub.

Lastly, the exact mechanism by which BMI-1 mediates transcriptional repression at DSBs remains unclear (**Section 3.4.4**) and should be further explored. In embryonic stem cells, the H2AK119ub mark is essential for maintaining the repression of PcG target genes, the deposition of H2AK119ub stabilizing both the occupancy of PRC1 and PRC2 at these sites (294). Certainly, PRC1 components, including the homologue of BMI-1 in *Drosophila*, can compact chromatin *in vitro* (487, 488), but PRC1-induced compaction is independent of its activity in ubiquitylating H2A (489, 490). At transcriptionally active loci, DSB induction prevents the decondensation (opening) of chromatin induced by transcription up to several kilobases distal of the site of damage (276). DSB-induced transcriptional silencing is also dependent on the generation of H2AK119ub, and the removal of ubiquitin from H2A (by the deubiquitylating enzyme USP16, or ubiquitin specific peptidase 16) is linked to the restart of transcription once the DSBs are prevented from occurring (276). While the deposition of H2AK119ub near DSBs is dependent on BMI-1 and RNF2 (302), it has not been established whether BMI-1 (or other PRC1 components) directly promotes chromatin compaction in the vicinity of the DSB (276). To visualize if chromatin compaction events are driven by BMI-1, live cell imaging could be performed on the targeted DSB system (U2OS cells with the integrated *lacO* array and inducible LacI-*Fok*I, **Fig. 3.4E**). The area of the *lacO* array could be measured over time in the presence of PTC-209 or siRNAs targeting BMI-1 (276). Alternatively, the same cells could be used, but co-expressing a photoactivatable or

photoswitchable fluorescent protein-tagged histone H2B (278); activation of the fusion protein's fluorescence in the area surrounding the *lacO* array would allow monitoring of chromatin area after the induction of DSBs. To determine the direct impacts of localized H2AK119ub generation, further fluorescence microscopy or chromatin immunoprecipitation experiments could be performed in U2OS 2-6-3 cells (which contain the *lacO* array) expressing wildtype or catalytically-dead RNF2-LacI (**Fig. 3.7A**). This would enable asking if concentrating H2AK119ub on chromatin can evict RNAPII (and other transcriptional machinery) locally, perhaps freeing space for end resection factors to accrue near the DSB.

Figure 5.2

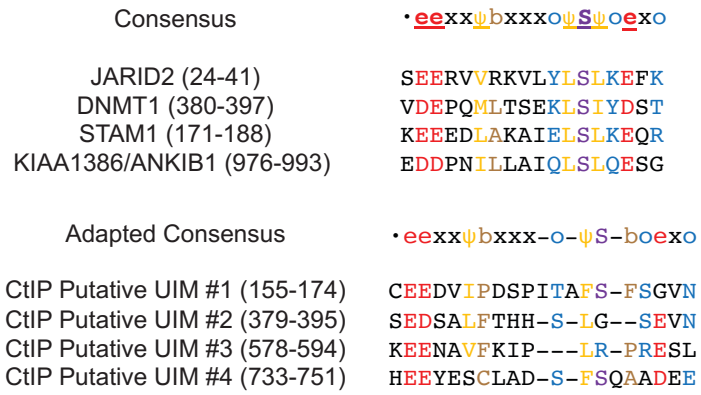

Figure 5.2: Putative JARID2-Like UIMs in CtIP

Top: amino acid sequence alignment of the N-terminal JARID2 ubiquitin-interacting motif (UIM) to other proteins containing a single-sided UIM (402). Bottom: Amino acid sequence alignment of four segments of CtIP containing elements of the JARID2 UIM. • = residue preceding the UIM; e (and red) = negatively charged residue; x = any amino acid; ψ (and yellow) = large hydrophobic residue; b (and brown) = hydrophobic residue; o (and blue) = hydrophilic residue.

5.4 Future Directions – RNF138 Ubiquitylation and Phosphorylation

Future work in the RNF138 study will first gain insights into the ubiquitylation of RNF138. As we suspect increased ubiquitylation in S/G2 serves to activate RNF138 rather than target it for proteasomal degradation, support for this notion could come from identifying the ubiquitin chain linkages that occur on RNF138. GFP immunoprecipitations could be performed on HEK293 cells co-expressing GFP-RNF138 and HA-Ub, then be probed with antibodies recognizing specific ubiquitin chain linkages. Alternatively, in the same assay, HA-Ub could be replaced with mutants where ubiquitin's internal lysines are individually substituted with arginine (i.e. HA-Ub-K48R or -K63R), inhibiting the formation of chains with those linkages. Conversely, mutants with every lysine replaced with arginine except for one (e.g. ubiquitin with lysine only at position 63 (HA-Ub-K63only)), could be co-expressed with GFP-RNF138. Such approaches would enable biochemical characterization of the ubiquitin linkages occurring on RNF138.

Another avenue of interest would identify the E3 ubiquitin ligase responsible for ubiquitylating RNF138. As RNF138 is an E3 ligase, it would be interesting to test if ubiquitylations on the protein in fact arise from autocatalytic activity. This could be answered by impairing the function of the RING domain by mutating residues chelating its Zn cations (e.g. RNF138-C18A-C54A, or -H36A-C39S (303, 314)), then determining if ubiquitin signals would still be detected on immunoprecipitates of GFP-RNF138. If autocatalysis does not contribute to RNF138 ubiquitylation, other candidates for E3 ligases of RNF138 could be assessed by depleting them with siRNA and again detecting RNF138 ubiquitylation. One candidate E3 is A20, a protein that inhibits NFκB signaling (491). In B cell malignancies, A20's E3 activity is involved in ubiquitylating RNF138, suppressing the oncogenic activity of L265P-mutated MyD88 (307).

Interestingly, A20 was found to negatively regulate DSB signaling in a manner independent of its catalytic activity. Mechanistically, A20 inhibits H2A ubiquitylation and the accumulation of RNF168 and 53BP1 by directly binding RNF168 (492). Another E3 ligase candidate could be the SCF (Skp1 – Cullin 1 – F-box protein) complexes, multi-subunit E3 ligase complexes involved in ubiquitylation events during cell cycle progression from late G1 phase to early M phase (493). While SCF complexes all share the same core components, the F-box protein is variable and determines substrate specificity. Our interest in SCFs comes from the fact that RNF138 ubiquitylation is upregulated during S/G2 (**Figs. 4.3B-C**). This coincides with when both HR and SCF activity are occurring in the cell. Indeed, SCF complexes have been linked to the occurrence of DNA end resection and HR (494–497). For example, in G2 phase, CtIP is stabilized from degradation by an SCF complex with Skp2 as the F-box protein (SCF^{Skp2}), and knockdown of Skp2, Skp1, or Cullin 1 inhibits DNA end resection in G2 phase (494). Skp2 also promotes K63-linked ubiquitylation of the MRN subunit Nbs1, triggering recruitment of the PIKK ATM to DSB sites (497). SCF^{Fbx12} is required for the ubiquitylation and dissociation of Ku80 from DNA (320, 496), and ubiquitylation and degradation of the resection exonuclease Exo1 depends on Cullin 1 activity, serving to restrict end resection (495). Certainly, testing if RNF138 is a SCF substrate is warranted given the increasing evidence for SCF involvement in end resection and DSB signaling.

Our study reveals that both ubiquitylation and CDK-mediated phosphorylation on RNF138 are cell cycle-dependent. Both ubiquitylation and TP motif phosphorylation were augmented during S/G2, with ubiquitylation peaking at G2 phase and TP phosphorylation peaking at S phase (**Figs. 4.3B-C, 4.1G**)). This gives rise to a third line of investigation: the alluring possibility that the PTMs may be dependent on each other. We previously reported that CtIP SUMOylation, a ubiquitin-like modification, was dependent on CDK activity and a functional CDK substrate

consensus motif on CtIP (**Section 2.4.5**). Perhaps the same holds true for RNF138, that there is interplay between the PTM events. This could be tested by measuring how much the T27A mutant is ubiquitylated relative to WT-RNF138, or if the K158R mutant exhibits altered TP phosphorylation to WT, in both asynchronous cells or cells enriched for particular cell cycle phases. Similar experiments could also reveal whether S124 phosphorylation depends on prior T27 phosphorylation or K158 ubiquitylation, given that the latter PTMs occur constitutively with cell cycle progression. Intriguingly, in the AlphaFold model of RNF138, residues K26 and K41 in RNF138 lie in close proximity to residue T27 (**Figure 4.S9**). By mass spectrometry, both K26 and K41 were detected to be ubiquitylated (454), and our data indicates K158 is not the only ubiquitylation site on RNF138 (**Sections 4.4.5, 4.5**). The AlphaFold model predicts T27 is accessible to solvent, but that the proline and arginine residues of the CDK phosphorylation motif are buried, perhaps hindering RNF138's recognition by CDKs. In order for CDKs to phosphorylate T27, the RING domain would have to be unfolded. Perhaps ubiquitylation at K26 and/or K41 serves this purpose, causing conformational changes that unfold the RING domain, permitting full accessibility of RNF138's consensus phosphorylation motif to CDK activity. Therefore, closer examination of the contributions of K26 and/or K41 to RNF138 ubiquitylation, and if T27 phosphorylation is dependent on one or both lysine sites being intact, is certainly of great interest. If interplay is observed between any sites, functional assays could confirm this by determining if the PTMs exert their effects epistatically instead of additively (i.e. comparing CPT-induced RPA focal intensity for variants with double versus single PTM site mutations, such as RNF138-T27A-K158R to -T27A and -K158R). We have already begun work on this question, performing the DR-GFP HR reporter assay with empty vector mCherry or siRNA-resistant mCherry-RNF138 containing single, double- or triple mutations among the sites T27, S124, and K158R in cells

depleted of endogenous RNF138. We observe that ablating mutations at any of the sites, all three, or any combination of two of the sites cannot rescue the frequency of HR to the extent of wildtype RNF138, generating HR frequencies similar to when RNF138 is depleted (**Fig. 5.3**). Thus, it seems that all three sites are essential for the activation of RNF138 in HR and function within the same pathway. Disrupting any site prevents the full activation of RNF138 (**Fig. 5.3**), and we are now exploring if interplay exists between the sites. Another exciting question lies in whether there is hierarchical importance to the phosphorylations in stimulating RNF138, or if they are equivalent in that capacity. This could be tested for instance by comparing the mutants T27A, S124A, T27A-S124A, T27E, S124E, T27E-S124A, T27A-S124E, and T27E-S12EA all in the same setting of the HR reporter assay.

Figure 5.3

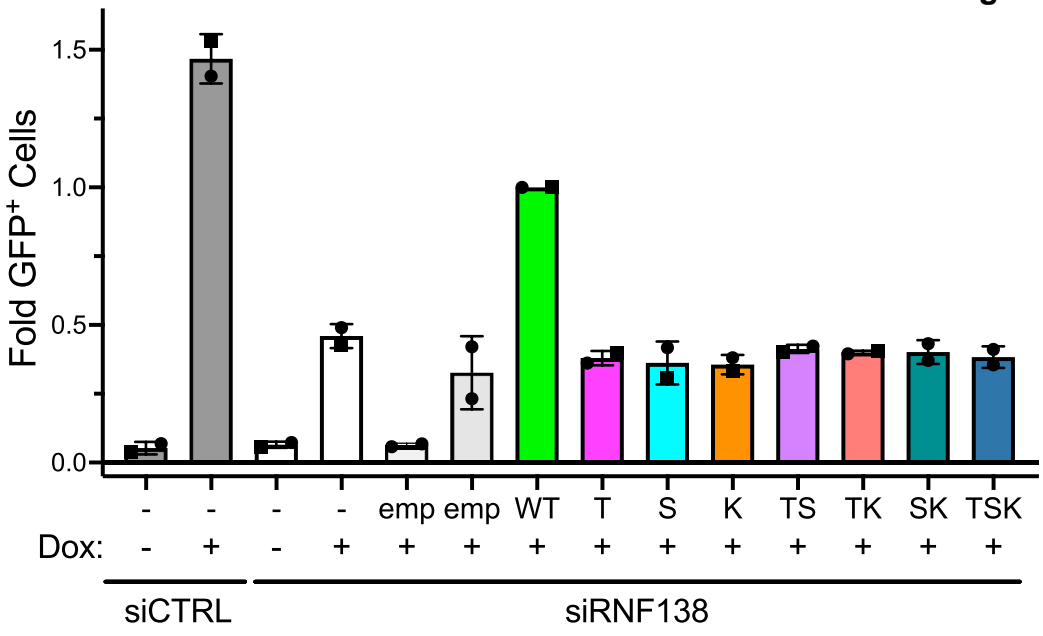

Figure 5.3: Effect of Single, Double, or Triple Mutations on RNF138 at T27, S124 and/or K158 on the Occurrence of HR

DR-GFP reporter assay in TRI-DR-U2OS cells transfected with siRNA to luciferase (siCTRL) or RNF138 (siRNF138) and complemented with mCherry empty vector (emp) or siRNA-resistant mCherry-RNF138 variants or not, performed as in Chapter 4. I-*Sce*I expression was induced by

doxycycline. GFP^+ cells were quantified by flow cytometry. T: T27A, S: S124A, K: K158R, TS: T27A-S124A, TK: T27A-K158R, SK: S124A-K158R, TSK: T27A-S124A-K158R. Averages were calculated from 2 biological replicates pooled together.

Our study also reveals RNF138 ubiquitylation is reduced upon genotoxic stress (**Figs. 4.3D-E**). Thus, a fourth line of investigation would ask if this decrease is associated with the activity of deubiquitylating enzymes (DUBs). Intriguingly, A20, which promotes RNF138 ubiquitylation in B cell malignancies (307), is also a DUB (491, 498). We could therefore determine if A20 may serve as a DUB for RNF138 in DSB repair by monitoring RNF138's ubiquitylation upon A20 depletion and overexpression. If A20 does not appear to act on RNF138, candidate DUBs could be identified in a mass spectrometric screen for proteins that interact with RNF138 after DNA damage. RNF138 phosphorylation on S124 (**Fig. 4.5F**, and (315)), which is induced upon DNA damage and ATM-dependent, may also be relevant in this question. Using the S124A mutant, we could test if S124 phosphorylation is a pre-requisite for the drop in RNF138 ubiquitylation upon DNA damage. Perhaps S124 phosphorylation could be promoting the association of DUB proteins with RNF138, facilitating its deubiquitylation, a model that would of course require further study.

As both the T27A and S124A mutations block RNF138-dependent end resection and HR (**Figs. 4.6A-B, 4.6D-E, 4.7A-B, 4.7D**), one final aspect of study could be determining how RNF138 phosphorylation positively regulates its activity. It could be that phosphorylated RNF138 interacts more strongly with its substrates to facilitate their ubiquitylation, a notion that could be tested by co-immunoprecipitation analysis. Alternatively, another idea is that the phosphoryl groups activate RNF138's E3 ligase activity, enabling ubiquitylation of its substrates (132, 133, 314, 315) and culminating in the occurrence of HR. Interestingly, the activity of the E3 ubiquitin ligase RNF4 was found to be primed by S phase-specific, CDK-dependent phosphorylation (499).

As well, T27 is located within the RING ("catalytic") domain of RNF138 (**Fig. 4.5A**). An enticing experiment would see if purified RNF138, when phosphorylated *in vitro* by CDK-cyclin activity, exhibits enhanced E3 ubiquitin ligase activity. Such activity could be measured *in vitro* by detecting RNF138 autoubiquitylation in the presence of the E1 UBE1, the E2 UBE2D, ATP, and ubiquitin (133, 303). The data would provide mechanistic insight into the regulation of RNF138 by phosphorylation. To begin this work, we attempted to overexpress His- or glutathione S-transferase (GST)-tagged RNF138 for purification from *E. coli* and mammalian Expi293F cells, respectively. Such efforts have so far encountered difficulties, with the purification products from bacterial expression being unstable and prone to aggregation, while the mammalian expression system has yielded inadequate transfection efficiency for protein purification. Clearly, such efforts will require further optimization. In summary, the findings from our investigation into RNF138 regulation raise many more exciting questions regarding the control of RNF138 function.

5.5 Potential Applications

5.5.1 BMI-1 Overexpression in Cancer

As a transcriptional repressor, BMI-1 can have myriad effects on the complement of genes transcribed. It is not surprising then that BMI-1 plays a role in the self-renewal of stem cells and cancer stem cells (500), and regulates cancer cell proliferation, migration, invasion, and chemoresistance (501, 502). BMI-1 is overexpressed in numerous cancers, including gastric, ovarian, breast, lung, head and neck, lymphoma, chronic myeloid leukemia, and acute myeloid leukemia (501, 502). In B cell leukemia and lymphoma, the BMI-1 gene itself is subject to a

chromosomal translocation to the IgH locus, which may cause deregulation of BMI-1 expression or activity (503). The compounds PTC-209 and PTC-596, which inhibit BMI-1 transcription and protein expression, respectively, have also been shown to inhibit the self-renewal of colorectal cancer-initiating cells (409) or induce apoptosis in acute myeloid leukemia progenitor cells (504). At the time of writing, PTC-596 is being evaluated as a treatment option in clinical studies of glioma, ovarian cancer, and leiomyosarcoma patients (clinicaltrials.gov).

We have shown that BMI-1 activates HR (**Chapter 3**). When the appropriate repair template (sister chromatid) is used and undamaged, the use of HR ensures high fidelity repair of the DSB. However, the genome contains many repetitive elements, and overactive HR, seen in actively dividing cells, combined with the use of inappropriate repair templates, can lead to large deletions, duplications, and chromosomal translocations (505, 506). These processes contribute to loss of heterozygosity (the loss of an allele of a gene) and aneuploidy (changes in chromosome number), genomic rearrangements which potentiate carcinogenesis (505, 506). We speculate that a potential consequence of high BMI-1 expression could be dysregulated HR, a factor that should be considered when treating patients battling BMI-1-overexpressing tumours with DSB-inducing therapies, and especially with the BMI-1 inhibitor PTC-596.

5.5.2 Dysregulation of SUMOylation in Cancer

SUMOylation is dysregulated in many cancers, and often manifests as overexpression of the SUMOylation machinery (507), suggesting upregulated SUMOylation dynamics provides a selective advantage to cancers. In multiple myeloma (MM), the second most frequent hematological malignancy in adults (508, 509), the SUMO E2 UBC9 and the E3 SUMO ligases PIAS1 and RanBP2 (RAN binding protein 2) are upregulated in MM cell lines and patient samples

relative to normal plasma cells (510, 511), as is the SUMO protease SENP1 (512). PIAS1 and UBC9 expression were correlated with patient survival: of MM patients treated with the chemotherapy melphalan, 80% of those with low levels of both proteins were living 6 years after starting treatment, contrasted to 45% for those that expressed high levels of PIAS1 and UBC9 (510). Experimentally, MM cells overexpressing a dominant-negative UBC9 were less viable than those expressing the wildtype version (510), indicating their reliance on UBC9 activity for survival. Relatedly, in a different study, silencing SENP1 induced apoptosis and abrogated proliferation in MM cells (512).

TAK-981 is an inhibitor of the SUMO activating enzyme (SAE1/SAE2) (513, 514), and enhances sensitivity of MM cells to the therapies lenalidomide and dexamethasone (515, 516). Currently, TAK-981 is being evaluated in clinical studies as a treatment for head and neck cancer, advanced solid tumours, non-Hodgkin lymphoma, and refractory MM (clinicaltrials.gov). We have demonstrated that the progression of HR and the formation of CtIP, RPA, and Rad51 foci are inhibited upon inhibition of global SUMOylation (**Sections 2.4.1, 2.4.2**). Perhaps the inhibition of HR, and the many other nuclear processes SUMOylation facilitates, contribute to the action of TAK-981 in re-sensitizing refractory MM cells to therapies. Because HR relies on SUMOylation, we also predict that TAK-981 should sensitize tumour cells to DSB-inducing and other DNA damaging therapies. Like clinical use of the BMI-1 inhibitor (PTC-596), the inhibition of HR in tumours (and normal tissues) should be considered as a consequence when treating patients with TAK-981.

5.5.3 Treatment of HR-Deficient Tumours with PARP Inhibitors, and Tumour-Specific Mutations of CtIP and RNF138

A recent advance in the targeted treatment of cancer is the use of poly(adenosine diphosphate-ribose, or PAR) polymerase (PARP) inhibitors (PARPi) to treat tumours defective in HR repair (517–519). These include ovarian, breast, and pancreatic cancers mutated in the HR proteins BRCA1 or BRCA2 (519). As HR-proficient cells (the normal tissue) are spared, the action of PARPi on HR-deficient tumour cells is an example of synthetic lethality, where coincident disruption of two genes (i.e. a PARP enzyme and BRCA1 or BRCA2) causes cell killing, but disrupting only one gene (i.e. the PARP enzyme or BRCA1/2 alone) preserves cell viability (519). The enzyme PARP1 is the most characterized of the PARPs and is a sensor for DNA breaks (520). It participates in several processes, such as antagonizing DNA end resection (325), single-strand break repair, base excision repair, the ligation of Okazaki fragments on the lagging strand during DNA replication, microhomology-mediated end joining, and the restart of DNA replication after fork stalling (519). Interestingly, PARP1 is recruited to DSBs very rapidly (similarly to Ku) (469) and facilitates the recruitment of Mre11 and Nbs1 to DNA damage sites (521). PARPi are purported to act by several mechanisms in HR-deficient cells: 1) the inhibition of single-strand break repair and the subsequent accumulation of single-strand breaks, which may be converted to DSBs (518); 2) the trapping of PARP on DNA, a lesion that stalls DNA replication forks, generating DSBs that, in the absence of functional HR, are repaired erroneously by NHEJ and cause catastrophic genomic instability (517, 522); 3) the toxic hyperactivation of NHEJ (523); and 4) the impaired ligation of Okazaki fragments and increased replication fork progression (524), generating ssDNA gaps in DNA (525). As truncation mutations in PALB2 (partner and localizer of BRCA2), another protein that participates in HR, also lead to PARPi sensitivity (526), it is likely that reduced expression or inactivation of HR proteins in general sensitizes cells to PARPi.

Perhaps tumours with inactivated RNF138 or BMI-1 could be sensitized to killing by PARPi, although this requires further testing. However, for CtIP, it has been reported that its expression is low in breast cancer patients, and this may present a clinical benefit, as PARPi are more cytotoxic to CtIP-depleted cells and xenograft tumour models in mice, which are HR-deficient due to reduced CtIP (527).

The emergence of next-generation sequencing of cancer genomes will continue to transform patient care in the clinic (528). Determining mutations present in tumour cells will help diagnose and predict therapeutic vulnerabilities in cancer. Perhaps in the future, a better understanding of structure-function relationships in the biology of CtIP, RNF138, and BMI-1 will predict if specific mutations render the proteins functional, partially functional, or impaired in activity. Knowing the impact of such mutations in patient tumours could then be used to determine, for example, whether the tumour cells are HR-deficient or HR-proficient, and subsequently, sensitive or not to PARPi, thus dictating treatment regimens.

As we have identified critical PTM sites in CtIP and RNF138 (**Chapter 2, Chapter 4**), one might ask if any tumours have mutations at such sites. A scan of cancer genomics datasets in cBioPortal (529–531) does not reveal substitution mutations disrupting the K578 SUMOylation site in tumours, presumably because the site is critical for bulk CtIP SUMOylation (**Section 2.4.7**). However, substitutions were found in the K896 SUMOylation site (343) (K896T, in squamous cell lung carcinoma) and the putative SUMOylation site centered at K449 (E451K, in invasive lobular breast carcinoma). Furthermore, a recent report screened early-onset breast cancer patients with functional BRCA1 and BRCA2 proteins for mutations in CtIP (532). One frequently occurring mutation was a deletion at E804 (532), perhaps abolishing the use of the putative K802 SUMOylation site. Interestingly, cells expressing this variant were proficient for end resection

and HR and did not show any increase in PARPi sensitivity (532). However, the mutated CtIP could not associate with newly replicated DNA, could not form Rad51 foci in response to HU, and had a partial defect in protecting stalled replication forks from degradation (532). This study illustrates the value of systematically determining the effects mutations have on protein function *in situ*. It also reveals that the functions of CtIP in end resection and replication fork protection are separable; unlike K578 (**Section 2.4.8 and 2.4.10)**, if K802 is a true CtIP SUMOylation site, K802 SUMOylation is involved in the fork protection roles of CtIP but not the HR promoting roles. As for RNF138, scanning cBioPortal (529–531) reveals a splice variant of RNF138 that bypasses the T27 site altogether in T-lymphoblastic leukemia and lung adenocarcinoma, as well as a missense mutation at Q125 (Q125E) that disrupts the canonical SQ ATM phosphorylation site based around S124. While we speculate these versions of RNF138 escape cell cycle or DNA damage-dependent control of activity, the true impact of these mutations must be evaluated *in situ*. Ultimately, our identification of critical PTM sites on CtIP and RNF138 may provide insights into alterations in function seen for variants of the proteins in cancer.

5.5.4 CtIP and CRISPR/Cas9-Based Technologies

The development of CRISPR (clustered regularly interspaced short palindromic repeats)/Cas9 (CRISPR associated protein 9) and related technologies has revolutionized gene editing by its simple customizability (533). The system utilizes the bacterial Cas9 nuclease to generate site-specific DSBs, the cut site dictated by a synthesized guide RNA molecule that base pairs to a target DNA sequence, upon which it binds and stimulates Cas9 activity (533). In cells, the DSB is then repaired by HR and NHEJ, with NHEJ-dependent repair potentially generating small insertions and deletions and disrupting the locus of interest. However, if a donor DNA

template is provided for repair of the DSB, cells may use HR to repair the break, replacing it with the sequence of the exogenous DNA and thus editing the locus of interest (533). As a result, the typical goal of CRISPR/Cas9 procedures is to harness HR for repair of the Cas9-generated break, rather than relying on NHEJ. As CtIP stimulates end resection and the occurrence of HR, a recent report found that fusing the N-terminal ~300 amino acids of CtIP (encompassing the oligomerization domain) to Cas9 helped tether endogenous CtIP to the genetic locus to be edited. This increased the likelihood of HR, enhancing the desired efficiency of transgene integration of CRISPR by at least two-fold (534). A similar approach by fusing full-length CtIP to Cas9 yielded enhanced HR/NHEJ ratios of 4.5- to six-fold (535). More recently, fusing Cas9 with both CtIP and nuclease-dead (RING domain-deleted) RNF168 also improved editing accuracy (536). Given that the MRN complex recognizes SUMO-2 (160, 537), that CtIP SUMOylation is important for end resection (**Chapter 2**, (343, 429)), and that SUMO-1 fusion to the CtIP C-terminus is feasible and can rescue end resection in K896R-mutated CtIP (343), it may be worth fusing SUMO-2 to the C-terminus of Cas9-CtIP. This might further increase the efficiency by which CRISPR/Cas9-generated breaks are repaired by end resection and HR.

References

1. Voet, D., Voet, J. G., and Pratt, C. W. (2016) *Fundamentals of Biochemistry: Life at the Molecular Level, 5th Edition: Life at the Molecular Level*, Wiley
2. Tiwari, V., and Wilson, D. M. 3rd (2019) DNA Damage and Associated DNA Repair Defects in Disease and Premature Aging. *Am J Hum Genet*. **105**, 237–257
3. Jackson, S. P., and Bartek, J. (2009) The DNA-damage response in human biology and disease. *Nature*. **461**, 1071–1078
4. Zhou, B.-B. S., and Elledge, S. J. (2000) The DNA damage response: putting checkpoints in perspective. *Nature*. **408**, 433–439
5. Torgovnick, A., and Schumacher, B. (2015) DNA repair mechanisms in cancer development and therapy . *Frontiers in Genetics* . **6**, 157
6. Hanahan, D., and Weinberg, R. A. (2011) Hallmarks of cancer: the next generation. *Cell*. **144**, 646–674
7. Tian, H., Gao, Z., Li, H., Zhang, B., Wang, G., Zhang, Q., Pei, D., and Zheng, J. (2015) DNA damage response--a double-edged sword in cancer prevention and cancer therapy. *Cancer Lett*. **358**, 8–16
8. Sharma, R., Lewis, S., and Wlodarski, M. W. (2020) DNA Repair Syndromes and Cancer: Insights Into Genetics and Phenotype Patterns . *Frontiers in Pediatrics*
9. Meyn, M. S. (1993) High spontaneous intrachromosomal recombination rates in ataxia-telangiectasia. *Science*. **260**, 1327–1330
10. Ellis, N. A. (1996) Mutation-causing mutations. *Nature*. **381**, 110–111
11. Weemaes, C. M., Hustinx, T. W., Scheres, J. M., van Munster, P. J., Bakkeren, J. A., and Taalman, R. D. (1981) A new chromosomal instability disorder: the Nijmegen breakage syndrome. *Acta Paediatr Scand*. **70**, 557–564
12. Fanconi, G. (1927) Familiare infantile perniciosaartige Anamia (pernicioses Blutbild und Konstitution). *Jahb Kinderheikd*. **117**, 257–280
13. Hebra, F. (1866) *On diseases of the skin, including the exanthemata*, New Sydenham Society

14. O'Driscoll, M., Ruiz-Perez, V. L., Woods, C. G., Jeggo, P. A., and Goodship, J. A. (2003) A splicing mutation affecting expression of ataxia-telangiectasia and Rad3-related protein (ATR) results in Seckel syndrome. *Nat Genet*. **33**, 497–501
15. Wimmer, K., and Kratz, C. P. (2010) Constitutional mismatch repair-deficiency syndrome. *Haematologica*. **95**, 699–701
16. Prakash, R., Zhang, Y., Feng, W., and Jasin, M. (2015) Homologous recombination and human health: the roles of BRCA1, BRCA2, and associated proteins. *Cold Spring Harb Perspect Biol*. **7**, a016600
17. Cerbinskaite, A., Mukhopadhyay, A., Plummer, E. R., Curtin, N. J., and Edmondson, R. J. (2012) Defective homologous recombination in human cancers. *Cancer Treat Rev*. **38**, 89–100
18. Cancer Genome Atlas Research Network (2011) Integrated genomic analyses of ovarian carcinoma. *Nature*. **474**, 609–615
19. Sishc, B. J., and Davis, A. J. (2017) The role of the core non-homologous end joining factors in carcinogenesis and cancer. *Cancers (Basel)*. 10.3390/cancers9070081
20. Chapman, J. R., Taylor, M. R. G., and Boulton, S. J. (2012) Playing the End Game: DNA Double-Strand Break Repair Pathway Choice. *Mol Cell*. **47**, 497–510
21. Jeggo, P. A., and Löbrich, M. (2007) DNA double-strand breaks: Their cellular and clinical impact? *Oncogene*. **26**, 7717–7719
22. Saleh-Gohari, N., Bryant, H. E., Schultz, N., Parker, K. M., Cassel, T. N., and Helleday, T. (2005) Spontaneous Homologous Recombination Is Induced by Collapsed Replication Forks That Are Caused by Endogenous DNA Single-Strand Breaks. *Mol Cell Biol*. **25**, 7158–7169
23. Stinson, B. M., and Loparo, J. J. (2021) Repair of DNA Double-Strand Breaks by the Nonhomologous End Joining Pathway. *Annu Rev Biochem*. **90**, 137–164
24. Rothkamm, K., Krüger, I., Thompson, L. H., and Löbrich, M. (2003) Pathways of DNA double-strand break repair during the mammalian cell cycle. *Mol Cell Biol*. **23**, 5706–5715
25. Mladenov, E., and Iliakis, G. (2011) Induction and repair of DNA double strand breaks: The increasing spectrum of non-homologous end joining pathways. *Mutation Research - Fundamental and Molecular Mechanisms of Mutagenesis*. **711**, 61–72

26. Karanam, K., Kafri, R., Loewer, A., and Lahav, G. (2012) Quantitative Live Cell Imaging Reveals a Gradual Shift between DNA Repair Mechanisms and a Maximal Use of HR in Mid S Phase. *Mol Cell*. **47**, 320–329
27. Shibata, A. (2017) Regulation of repair pathway choice at two-ended DNA double-strand breaks. *Mutation Research - Fundamental and Molecular Mechanisms of Mutagenesis*. **803–805**, 51–55
28. Zierhut, C., and Diffley, J. F. X. (2008) Break dosage, cell cycle stage and DNA replication influence DNA double strand break response. *EMBO J*. **27**, 1875–1885
29. Hartlerode, A., Odate, S., Shim, I., Brown, J., and Scully, R. (2011) Cell cycle-dependent induction of homologous recombination by a tightly regulated I-SceI fusion protein. *PLoS One*. **6**, e16501
30. Shibata, A., Conrad, S., Birraux, J., Geuting, V., Barton, O., Ismail, A., Kakarougkas, A., Meek, K., Taucher-Scholz, G., Löbrich, M., and Jeggo, P. A. (2011) Factors determining DNA double-strand break repair pathway choice in G2 phase. *EMBO J*. **30**, 1079–1092
31. Mao, Z., Bozzella, M., Seluanov, A., and Gorbunova, V. (2008) Comparison of nonhomologous end joining and homologous recombination in human cells. *DNA Repair (Amst)*. **7**, 1765–1771
32. Sallmyr, A., and Tomkinson, A. E. (2018) Repair of DNA double-strand breaks by mammalian alternative end-joining pathways. *J Biol Chem*. **293**, 10536–10546
33. Truong, L. N., Li, Y., Shi, L. Z., Hwang, P. Y.-H., He, J., Wang, H., Razavian, N., Berns, M. W., and Wu, X. (2013) Microhomology-mediated End Joining and Homologous Recombination share the initial end resection step to repair DNA double-strand breaks in mammalian cells. *Proc Natl Acad Sci U S A*. **110**, 7720–7725
34. Fattah, F., Lee, E. H., Weisensel, N., Wang, Y., Lichter, N., and Hendrickson, E. A. (2010) Ku regulates the non-homologous end joining pathway choice of DNA double-strand break repair in human somatic cells. *PLoS Genet*. **6**, e1000855
35. Bennardo, N., Cheng, A., Huang, N., and Stark, J. M. (2008) Alternative-NHEJ is a mechanistically distinct pathway of mammalian chromosome break repair. *PLoS Genet*. 10.1371/journal.pgen.1000110

36. Wang, M., Wu, W., Wu, W., Rosidi, B., Zhang, L., Wang, H., and Iliakis, G. (2006) PARP-1 and Ku compete for repair of DNA double strand breaks by distinct NHEJ pathways. *Nucleic Acids Res*. **34**, 6170–6182

37. Simsek, D., Brunet, E., Wong, S. Y.-W., Katyal, S., Gao, Y., McKinnon, P. J., Lou, J., Zhang, L., Li, J., Rebar, E. J., Gregory, P. D., Holmes, M. C., and Jasin, M. (2011) DNA ligase III promotes alternative nonhomologous end-joining during chromosomal translocation formation. *PLoS Genet*. **7**, e1002080

38. Yousefzadeh, M. J., Wyatt, D. W., Takata, K., Mu, Y., Hensley, S. C., Tomida, J., Bylund, G. O., Doublié, S., Johansson, E., Ramsden, D. A., McBride, K. M., and Wood, R. D. (2014) Mechanism of Suppression of Chromosomal Instability by DNA Polymerase POLQ. *PLoS Genet*. **10**, e1004654

39. Wyatt, D. W., Feng, W., Conlin, M. P., Yousefzadeh, M. J., Roberts, S. A., Mieczkowski, P., Wood, R. D., Gupta, G. P., and Ramsden, D. A. (2016) Essential Roles for Polymerase θ-Mediated End Joining in the Repair of Chromosome Breaks. *Mol Cell*. **63**, 662–673

40. Black, S. J., Ozdemir, A. Y., Kashkina, E., Kent, T., Rusanov, T., Ristic, D., Shin, Y., Suma, A., Hoang, T., Chandramouly, G., Siddique, L. A., Borisonnik, N., Sullivan-Reed, K., Mallon, J. S., Skorski, T., Carnevale, V., Murakami, K. S., Wyman, C., and Pomerantz, R. T. (2019) Molecular basis of microhomology-mediated end-joining by purified full-length Polθ. *Nat Commun*. **10**, 4423

41. Luedeman, M. E., Stroik, S., Feng, W., Luthman, A. J., Gupta, G. P., and Ramsden, D. A. (2022) Poly(ADP) ribose polymerase promotes DNA polymerase theta-mediated end joining by activation of end resection. *Nat Commun*. 10.1038/s41467-022-32166-7

42. Schwertman, P., Bekker-Jensen, S., and Mailand, N. (2016) Regulation of DNA double-strand break repair by ubiquitin and ubiquitin-like modifiers. *Nat Rev Mol Cell Biol*. **17**, 379–394

43. Cheng, Q., Barboule, N., Frit, P., Gomez, D., Bombarde, O., Couderc, B., Ren, G.-S., Salles, B., and Calsou, P. (2011) Ku counteracts mobilization of PARP1 and MRN in chromatin damaged with DNA double-strand breaks. *Nucleic Acids Res*. **39**, 9605–9619

44. Davis, A. J., and Chen, D. J. (2013) DNA double strand break repair via non-homologous end-joining. *Transl Cancer Res*. **2**, 130–143

45. Symington, L. S. (2016) Mechanism and regulation of DNA end resection in eukaryotes. *Crit Rev Biochem Mol Biol*. **51**, 195–212
46. Cejka, P., and Symington, L. S. (2021) DNA End Resection: Mechanism and Control. *Annu Rev Genet*. **55**, 285–307
47. Garcia, V., Phelps, S. E. L., Gray, S., and Neale, M. J. (2011) Bidirectional resection of DNA double-strand breaks by Mre11 and Exo1. *Nature*. **479**, 241–244
48. Shibata, A., Moiani, D., Arvai, A. S., Perry, J., Harding, S. M., Genois, M. M., Maity, R., van Rossum-Fikkert, S., Kertokalio, A., Romoli, F., Ismail, A., Ismalaj, E., Petricci, E., Neale, M. J., Bristow, R. G., Masson, J. Y., Wyman, C., Jeggo, P. A., and Tainer, J. A. (2014) DNA Double-Strand Break Repair Pathway Choice Is Directed by Distinct MRE11 Nuclease Activities. *Mol Cell*. **53**, 7–18
49. Hopfner, K.-P., Craig, L., Moncalian, G., Zinkel, R. A., Usui, T., Owen, B. A. L., Karcher, A., Henderson, B., Bodmer, J.-L., McMurray, C. T., Carney, J. P., Petrini, J. H. J., and Tainer, J. A. (2002) The Rad50 zinc-hook is a structure joining Mre11 complexes in DNA recombination and repair. *Nature*. **418**, 562–566
50. Zhu, Z., Chung, W.-H., Shim, E. Y., Lee, S. E., and Ira, G. (2008) Sgs1 Helicase and Two Nucleases Dna2 and Exo1 Resect DNA Double-Strand Break Ends. *Cell*. **134**, 981–994
51. Deshpande, R. A., Lee, J. H., Arora, S., and Paull, T. T. (2016) Nbs1 Converts the Human Mre11/Rad50 Nuclease Complex into an Endo/Exonuclease Machine Specific for Protein-DNA Adducts. *Mol Cell*. **64**, 593–606
52. Anand, R., Ranjha, L., Cannavo, E., and Cejka, P. (2016) Phosphorylated CtIP Functions as a Co-factor of the MRE11-RAD50-NBS1 Endonuclease in DNA End Resection. *Mol Cell*. **64**, 940–950
53. Chanut, P., Britton, S., Coates, J., Jackson, S. P., and Calsou, P. (2016) Coordinated nuclease activities counteract Ku at single-ended DNA double-strand breaks. *Nat Commun*. **7**, 12889
54. Whelan, D. R., and Rothenberg, E. (2021) Super-resolution mapping of cellular double-strand break resection complexes during homologous recombination. *Proc Natl Acad Sci U S A*. **118**, 1–12
55. Wu, D., Topper, L. M., and Wilson, T. E. (2008) Recruitment and dissociation of nonhomologous end joining proteins at a DNA double-strand break in Saccharomyces cerevisiae. *Genetics*. **178**, 1237–1249

56. Langerak, P., Mejia-Ramirez, E., Limbo, O., and Russell, P. (2011) Release of Ku and MRN from DNA ends by Mre11 nuclease activity and Ctp1 is required for homologous recombination repair of double-strand breaks. *PLoS Genet*. 10.1371/journal.pgen.1002271

57. Myler, L. R., Gallardo, I. F., Soniat, M. M., Deshpande, R. A., Gonzalez, X. B., Kim, Y., Paull, T. T., and Finkelstein, I. J. (2017) Single-Molecule Imaging Reveals How Mre11-Rad50-Nbs1 Initiates DNA Break Repair. *Mol Cell*. **67**, 891-898.e4

58. Sartori, A. A., Lukas, C., Coates, J., Mistrik, M., Fu, S., Bartek, J., Baer, R., Lukas, J., and Jackson, S. P. (2007) Human CtIP promotes DNA end resection. *Nature*. **450**, 509–514

59. Zdravkovi, A. (2021) A conserved Ctp1 / CtIP C-terminal peptide stimulates Mre11 endonuclease activity. 10.1073/pnas.2016287118/-/DCSupplemental.Published

60. Anand, R., Jasrotia, A., Bundschuh, D., Howard, S. M., Ranjha, L., Stucki, M., and Cejka, P. (2019) NBS1 promotes the endonuclease activity of the MRE11-RAD50 complex by sensing CtIP phosphorylation. *EMBO J*. 10.15252/embj.2018101005

61. Huertas, P., and Jackson, S. P. (2009) Human CtIP mediates cell cycle control of DNA end resection and double strand break repair. *Journal of Biological Chemistry*. **284**, 9558–9565

62. Mimitou, E. P., and Symington, L. S. (2008) Sae2, Exo1 and Sgs1 collaborate in DNA double-strand break processing. *Nature*. **455**, 770–774

63. Nimonkar, A. V, Genschel, J., Kinoshita, E., Polaczek, P., Campbell, J. L., Wyman, C., Modrich, P., and Kowalczykowski, S. C. (2011) BLM-DNA2-RPA-MRN and EXO1-BLM-RPA-MRN constitute two DNA end resection machineries for human DNA break repair. *Genes Dev*. **25**, 350–362

64. Hoa, N. N., Kobayashi, J., Omura, M., Hirakawa, M., Yang, S.-H., Komatsu, K., Paull, T. T., Takeda, S., and Sasanuma, H. (2015) BRCA1 and CtIP Are Both Required to Recruit Dna2 at Double-Strand Breaks in Homologous Recombination. *PLoS One*. **10**, e0124495

65. Sturzenegger, A., Burdova, K., Kanagaraj, R., Levikova, M., Pinto, C., Cejka, P., and Janscak, P. (2014) DNA2 cooperates with the WRN and BLM RecQ helicases to mediate long-range DNA end resection in human cells. *J Biol Chem*. **289**, 27314–27326

66. Eid, W., Steger, M., El-Shemerly, M., Ferretti, L. P., Peña-Diaz, J., König, C., Valtorta, E., Sartori, A. A., and Ferrari, S. (2010) DNA end resection by CtIP and exonuclease 1 prevents genomic instability. *EMBO Rep*. **11**, 962–968

67. Shim, E. Y., Chung, W.-H., Nicolette, M. L., Zhang, Y., Davis, M., Zhu, Z., Paull, T. T., Ira, G., and Lee, S. E. (2010) Saccharomyces cerevisiae Mre11/Rad50/Xrs2 and Ku proteins regulate association of Exo1 and Dna2 with DNA breaks. *EMBO J.* **29**, 3370–3380

68. Ceppi, I., Howard, S. M., Kasaciunaite, K., Pinto, C., Anand, R., Seidel, R., and Cejka, P. (2020) CtIP promotes the motor activity of DNA2 to accelerate long-range DNA end resection. *Proc Natl Acad Sci U S A*. **117**, 8859–8869

69. Daley, J. M., Jimenez-Sainz, J., Wang, W., Miller, A. S., Xue, X., Nguyen, K. A., Jensen, R. B., and Sung, P. (2017) Enhancement of BLM-DNA2-Mediated Long-Range DNA End Resection by CtIP. *Cell Rep*. **21**, 324–332

70. Byrne, B. M., and Oakley, G. G. (2019) Replication protein A, the laxative that keeps DNA regular: The importance of RPA phosphorylation in maintaining genome stability. *Semin Cell Dev Biol*. **86**, 112–120

71. Wright, W. D., Shah, S. S., and Heyer, W. D. (2018) Homologous recombination and the repair of DNA double-strand breaks. *Journal of Biological Chemistry*. **293**, 10524–10535

72. Escribano-Díaz, C., Orthwein, A., Fradet-Turcotte, A., Xing, M., Young, J. T. F., Tkáč, J., Cook, M. A., Rosebrock, A. P., Munro, M., Canny, M. D., Xu, D., and Durocher, D. (2013) A Cell Cycle-Dependent Regulatory Circuit Composed of 53BP1-RIF1 and BRCA1-CtIP Controls DNA Repair Pathway Choice. *Mol Cell*. **49**, 872–883

73. Feng, L., Li, N., Li, Y., Wang, J., Gao, M., Wang, W., and Chen, J. (2015) Cell cycle-dependent inhibition of 53BP1 signaling by BRCA1. *Cell Discov*. **1**, 15019

74. Chapman, J. R., Sossick, A. J., Boulton, S. J., and Jackson, S. P. (2012) BRCA1-associated exclusion of 53BP1 from DNA damage sites underlies temporal control of DNA repair. *J Cell Sci*. **125**, 3529–3534

75. Densham, R. M., Garvin, A. J., Stone, H. R., Strachan, J., Baldock, R. A., Daza-Martin, M., Fletcher, A., Blair-Reid, S., Beesley, J., Johal, B., Pearl, L. H., Neely, R., Keep, N. H., Watts, F. Z., and Morris, J. R. (2016) Human BRCA1–BARD1 ubiquitin ligase activity counteracts chromatin barriers to DNA resection. *Nat Struct Mol Biol*. **23**, 647

76. Polato, F., Callen, E., Wong, N., Faryabi, R., Bunting, S., Chen, H.-T., Kozak, M., Kruhlak, M. J., Reczek, C. R., Lee, W.-H., Ludwig, T., Baer, R., Feigenbaum, L., Jackson, S., and Nussenzweig, A. (2014) CtIP-mediated resection is essential for viability and can operate independently of BRCA1. *Journal of Experimental Medicine*. **211**, 1027–1036

77. Cruz-García, A., López-Saavedra, A., and Huertas, P. (2014) BRCA1 accelerates CtIP-Mediated DNA-end resection. *Cell Rep*. **9**, 451–459

78. Ducy, M., Sesma-Sanz, L., Guitton-Sert, L., Lashgari, A., Gao, Y., Brahiti, N., Rodrigue, A., Margaillan, G., Caron, M.-C., Cote, J., Simard, J., and Masson, J.-Y. (2019) The Tumor Suppressor PALB2: Inside Out. *Trends Biochem Sci*. **44**, 226–240

79. Chen, C.-C., Feng, W., Lim, P. X., Kass, E. M., and Jasin, M. (2018) Homology-Directed Repair and the Role of BRCA1, BRCA2, and Related Proteins in Genome Integrity and Cancer. *Annu Rev Cancer Biol*. **2**, 313–336

80. Deng, C. X., and Scott, F. (2000) Role of the tumor suppressor gene Brca1 in genetic stability and mammary gland tumor formation. *Oncogene*. **19**, 1059–1064

81. Polo, S. E., and Jackson, S. P. (2011) Dynamics of DNA damage response proteins at DNA breaks: a focus on protein modifications. *Genes Dev*. **25**, 409–433

82. Bergink, S., and Jentsch, S. (2009) Principles of ubiquitin and SUMO modifications in DNA repair. *Nature*. **458**, 461–467

83. Psakhye, I., and Jentsch, S. (2012) Protein group modification and synergy in the SUMO pathway as exemplified in DNA repair. *Cell*. **151**, 807–820

84. Psakhye, I., Castellucci, F., and Branzei, D. (2019) SUMO-Chain-Regulated Proteasomal Degradation Timing Exemplified in DNA Replication Initiation. *Mol Cell*. **76**, 632-645.e6

85. Walser, F., Mulder, M. P. C., Bragantini, B., Burger, S., Gubser, T., Gatti, M., Botuyan, M. V., Villa, A., Altmeyer, M., Neri, D., Ovaa, H., Mer, G., and Penengo, L. (2020) Ubiquitin Phosphorylation at Thr12 Modulates the DNA Damage Response. *Mol Cell*. **80**, 423-436.e9

86. Nishi, H., Shaytan, A., and Panchenko, A. R. (2014) Physicochemical mechanisms of protein regulation by phosphorylation. *Front Genet*. **5**, 1–10

87. Blackford, A. N., and Jackson, S. P. (2017) ATM, ATR, and DNA-PK: The Trinity at the Heart of the DNA Damage Response. *Mol Cell*. **66**, 801–817

88. Matsuoka, S., Rotman, G., Ogawa, A., Shiloh, Y., Tamai, K., and Elledge, S. J. (2000) Ataxia telangiectasia-mutated phosphorylates Chk2 in vivo and in vitro. *Proc Natl Acad Sci U S A*. **97**, 10389–10394

89. Zou, L., and Elledge, S. J. (2003) Sensing DNA damage through ATRIP recognition of RPA-ssDNA complexes. *Science (1979)*. **300**, 1542–1548

90. Byun, T. S., Pacek, M., Yee, M., Walter, J. C., and Cimprich, K. A. (2005) Functional uncoupling of MCM helicase and DNA polymerase activities activates the ATR-dependent checkpoint. *Genes Dev*. **19**, 1040–1052

91. Myers, J. S., and Cortez, D. (2006) Rapid activation of ATR by ionizing radiation requires ATM and Mre11. *Journal of Biological Chemistry*. **281**, 9346–9350

92. Liu, Q., Guntuku, S., Cui, X. S., Matsuoka, S., Cortez, D., Tamai, K., Luo, G., Carattini-Rivera, S., DeMayo, F., Bradley, A., Donehower, L. A., and Elledge, S. J. (2000) Chk1 is an essential kinase that is regulated by Atr and required for the G2/M DNA damage checkpoint. *Genes Dev*. **14**, 1448–1459

93. Singleton, B. K., Torres-Arzayus, M. I., Rottinghaus, S. T., Taccioli, G. E., and Jeggo, P. A. (1999) The C terminus of Ku80 activates the DNA-dependent protein kinase catalytic subunit. *Mol Cell Biol*. **19**, 3267–3277

94. Lee, J.-H., and Paull, T. T. (2005) ATM Activation by DNA Double-Strand Breaks Through the Mre11-Rad50-Nbs1 Complex. *Science (1979)*. **308**, 551–554

95. Uziel, T., Lerenthal, Y., Moyal, L., Andegeko, Y., Mittelman, L., and Shiloh, Y. (2003) Requirement of the MRN complex for ATM activation by DNA damage. *EMBO J*. **22**, 5612–21

96. Matthews, H. K., Bertoli, C., and de Bruin, R. A. M. (2022) Cell cycle control in cancer. *Nat Rev Mol Cell Biol*. **23**, 74–88

97. Malumbres, M. (2014) Cyclin-dependent kinases. *Genome Biol*. **15**, 122

98. Aylon, Y., Liefshitz, B., and Kupiec, M. (2004) The CDK regulates repair of double-strand breaks by homologous recombination during the cell cycle. *EMBO Journal*. **23**, 4868–4875

99. Ira, G., Pellicioll, A., Balijja, A., Wang, X., Florani, S., Carotenuto, W., Liberi, G., Bressan, D., Wan, L., Hollingsworth, N. M., Haber, J. E., and Folani, M. (2004) DNA end resection, homologous recombination and DNA damage checkpoint activation require CDK1. *Nature*. **431**, 1011–1017

100. Deans, A. J., Khanna, K. K., McNees, C. J., Mercurio, C., Heierhorst, J., and McArthur, G. A. (2006) Cyclin-dependent kinase 2 functions in normal DNA repair and is a therapeutic target in BRCA1-deficient cancers. *Cancer Res*. **66**, 8219–8226

101. Simoneau, A., Robellet, X., Ladouceur, A. M., and D'Amours, D. (2014) Cdk1-dependent regulation of the Mre11 complex couples DNA repair pathways to cell cycle progression. *Cell Cycle*. **13**, 1078–1090

102. Falck, J., Forment, J. V., Coates, J., Mistrik, M., Lukas, J., Bartek, J., and Jackson, S. P. (2012) CDK targeting of NBS1 promotes DNA-end resection, replication restart and homologous recombination. *EMBO Rep*. **13**, 561–568

103. Wohlbold, L., Merrick, K. A., De, S., Amat, R., Kim, J. H., Larochelle, S., Allen, J. J., Zhang, C., Shokat, K. M., Petrini, J. H. J., and Fisher, R. P. (2012) Chemical Genetics Reveals a Specific Requirement for Cdk2 Activity in the DNA Damage Response and Identifies Nbs1 as a Cdk2 Substrate in Human Cells. *PLoS Genet*. 10.1371/journal.pgen.1002935

104. Huertas, P., Cortés-Ledesma, F., Sartori, A. A., Aguilera, A., and Jackson, S. P. (2008) CDK targets Sae2 to control DNA-end resection and homologous recombination. *Nature*. **455**, 689–692

105. Wang, H., Shi, L. Z., Wong, C. C. L., Han, X., Hwang, P. Y. H., Truong, L. N., Zhu, Q., Shao, Z., Chen, D. J., Berns, M. W., Yates, J. R., Chen, L., and Wu, X. (2013) The Interaction of CtIP and Nbs1 Connects CDK and ATM to Regulate HR-Mediated Double-Strand Break Repair. *PLoS Genet*. **9**, 25–27

106. Chen, X., Niu, H., Chung, W. H., Zhu, Z., Papusha, A., Shim, E. Y., Lee, S. E., Sung, P., and Ira, G. (2011) Cell cycle regulation of DNA double-strand break end resection by Cdk1-dependent Dna2 phosphorylation. *Nat Struct Mol Biol*. **18**, 1015–1019

107. Tomimatsu, N., Mukherjee, B., Catherine Hardebeck, M., Ilcheva, M., Vanessa Camacho, C., Louise Harris, J., Porteus, M., Llorente, B., Khanna, K. K., and Burma, S. (2014) Phosphorylation of EXO1 by CDKs 1 and 2 regulates DNA end resection and repair pathway choice. *Nat Commun*. **5**, 3561

108. Yu, X., and Chen, J. (2004) DNA Damage-Induced Cell Cycle Checkpoint Control Requires CtIP, a Phosphorylation-Dependent Binding Partner of BRCA1 C-Terminal Domains. *Mol Cell Biol*. **24**, 9478–9486

109. Przetocka, S., Porro, A., Bolck, H. A., Walker, C., Lezaja, A., Trenner, A., von Aesch, C., Himmels, S.-F., D'Andrea, A. D., Ceccaldi, R., Altmeyer, M., and Sartori, A. A. (2018)

CtIP-Mediated Fork Protection Synergizes with BRCA1 to Suppress Genomic Instability upon DNA Replication Stress. *Mol Cell*. 10.1016/j.molcel.2018.09.014

110. Soniat, M. M., Myler, L. R., Kuo, H. C., Paull, T. T., and Finkelstein, I. J. (2019) RPA Phosphorylation Inhibits DNA Resection. *Mol Cell*. **75**, 145-153.e5
111. Hershko, A., Ciechanover, A., and Varshavsky, A. (2000) The ubiquitin system. *Nat Med*. **6**, 1073–1081
112. Wiborg, O., Pedersen, M. S., Wind, A., Berglund, L. E., Marcker, K. A., and Vuust, J. (1985) The human ubiquitin multigene family: some genes contain multiple directly repeated ubiquitin coding sequences. *EMBO J*. **4**, 755–759
113. Han, S.-W., Jung, B.-K., and Ryu, K.-Y. (2021) Regulation of polyubiquitin genes to meet cellular ubiquitin requirement. *BMB Rep*. **54**, 189–195
114. Goldstein, G., Scheid, M., Hammerling, U., Schlesinger, D. H., Niall, H. D., and Boyse, E. A. (1975) Isolation of a polypeptide that has lymphocyte-differentiating properties and is probably represented universally in living cells. *Proc Natl Acad Sci U S A*. **72**, 11–15
115. Goldknopf, I. L., and Busch, H. (1977) Isopeptide linkage between nonhistone and histone 2A polypeptides of chromosomal conjugate-protein A24. *Proc Natl Acad Sci U S A*. **74**, 864–868
116. Komander, D., Clague, M. J., and Urbé, S. (2009) Breaking the chains: Structure and function of the deubiquitinases. *Nat Rev Mol Cell Biol*. **10**, 550–563
117. Fang, S., and Weissman, A. M. (2004) Ubiquitin-proteasome system. *Cell Mol Life Sci*. **61**, 1546–1561
118. Morreale, F. E., and Walden, H. (2016) Types of Ubiquitin Ligases. *Cell*. **165**, 248-248.e1
119. Freemont, P. S. (2000) RING for destruction? *Curr Biol*. **10**, R84-7
120. Buchwald, G., van der Stoop, P., Weichenrieder, O., Perrakis, A., van Lohuizen, M., and Sixma, T. K. (2006) Structure and E3-ligase activity of the Ring-Ring complex of polycomb proteins Bmi1 and Ring1b. *EMBO J*. **25**, 2465–2474
121. Li, Z., Cao, R., Wang, M., Myers, M. P., Zhang, Y., and Xu, R. M. (2006) Structure of a Bmi-1-Ring1B polycomb group ubiquitin ligase complex. *Journal of Biological Chemistry*. **281**, 20643–20649

122. Stewart, M. D., Duncan, E. D., Coronado, E., DaRosa, P. A., Pruneda, J. N., Brzovic, P. S., and Klevit, R. E. (2017) Tuning BRCA1 and BARD1 activity to investigate RING ubiquitin ligase mechanisms. *Protein Science*. **26**, 475–483

123. Grice, G. L., and Nathan, J. A. (2016) The recognition of ubiquitinated proteins by the proteasome. *Cellular and Molecular Life Sciences*. **73**, 3497–3506

124. Spence, J., Sadis, S., Haas, A. L., and Finley, D. (1995) A ubiquitin mutant with specific defects in DNA repair and multiubiquitination. *Mol Cell Biol*. **15**, 1265–1273

125. Hurley, J. H., Lee, S., and Prag, G. (2006) Ubiquitin-binding domains. *Biochemical Journal*. **399**, 361–372

126. Dikic, I., Wakatsuki, S., and Walters, K. J. (2009) Ubiquitin-binding domains — from structures to functions. *Nat Rev Mol Cell Biol*. **10**, 659–671

127. Cao, R., Tsukada, Y.-I., and Zhang, Y. (2005) Role of Bmi-1 and Ring1A in H2A ubiquitylation and Hox gene silencing. *Mol Cell*. **20**, 845–854

128. Wei, J., Zhai, L., Xu, J., and Wang, H. (2006) Role of Bmi1 in H2A ubiquitylation and Hox gene silencing. *J Biol Chem*. **281**, 22537–22544

129. Wang, H., Wang, L., Erdjument-Bromage, H., Vidal, M., Tempst, P., Jones, R. S., and Zhang, Y. (2004) Role of histone H2A ubiquitination in Polycomb silencing. *Nature*. **431**, 873–878

130. Ismail, H., Andrin, C., McDonald, D., and Hendzel, M. J. (2010) BMI1-mediated histone ubiquitylation promotes DNA double-strand break repair. *Journal of Cell Biology*. **191**, 45–60

131. Ismail, I. H., Gagné, J. P., Caron, M. C., McDonald, D., Xu, Z., Masson, J. Y., Poirier, G. G., and Hendzel, M. J. (2012) CBX4-mediated SUMO modification regulates BMI1 recruitment at sites of DNA damage. *Nucleic Acids Res*. **40**, 5497–5510

132. Ismail, I. H., Gagne, J.-P., Genois, M.-M., Strickfaden, H., McDonald, D., Xu, Z., Poirier, G. G., Masson, J.-Y., and Hendzel, M. J. (2015) The RNF138 E3 ligase displaces Ku to promote DNA end resection and regulate DNA repair pathway choice. *Nat Cell Biol*. **17**, 1446–1457

133. Schmidt, C. K., Galanty, Y., Sczaniecka-Clift, M., Coates, J., Jhujh, S., Demir, M., Cornwell, M., Beli, P., and Jackson, S. P. (2015) Systematic E2 screening reveals a UBE2D-RNF138-CtIP axis promoting DNA repair. *Nat Cell Biol*. **17**, 1458–1470

134. Matunis, M. J., Coutavas, E., and Blobel, G. (1996) A novel ubiquitin-like modification modulates the partitioning of the Ran-GTPase-activating protein RanGAP1 between the cytosol and the nuclear pore complex. *Journal of Cell Biology*. **135**, 1457–1470

135. Mahajan, R., Delphin, C., Guan, T., Gerace, L., and Melchior, F. (1997) A small ubiquitin-related polypeptide involved in targeting RanGAP1 to nuclear pore complex protein RanBP2. *Cell*. **88**, 97–107

136. Hendriks, I. A., D'Souza, R. C. J., Yang, B., Verlaan-De Vries, M., Mann, M., and Vertegaal, A. C. O. (2014) Uncovering global SUMOylation signaling networks in a site-specific manner. *Nat Struct Mol Biol*. **21**, 927–936

137. Rodriguez, M. S., Dargemont, C., and Hay, R. T. (2001) SUMO-1 conjugation in vivo requires both a consensus modification motif and nuclear targeting. *J Biol Chem*. **276**, 12654–12659

138. Kamitani, T., Nguyen, H. P., and Yeh, E. T. H. (1997) Preferential modification of nuclear proteins by a novel ubiquitin-like molecule. *Journal of Biological Chemistry*. **272**, 14001–14004

139. Hendriks, I. A., Lyon, D., Su, D., Skotte, N. H., Daniel, J. A., Jensen, L. J., and Nielsen, M. L. (2018) Site-specific characterization of endogenous SUMOylation across species and organs. *Nat Commun*. 10.1038/s41467-018-04957-4

140. Hendriks, I. A., Lyon, D., Young, C., Jensen, L. J., Vertegaal, A. C. O., and Nielsen, M. L. (2017) Site-specific mapping of the human SUMO proteome reveals co-modification with phosphorylation. *Nat Struct Mol Biol*. **24**, 325–336

141. Vertegaal, A. C. O. (2022) Signalling mechanisms and cellular functions of SUMO. *Nat Rev Mol Cell Biol*. **23**, 715–731

142. Wilson, V. G. (2017) *SUMO Regulation of Cellular Processes* (Wilson, V. G. ed), Advances in Experimental Medicine and Biology, Springer International Publishing, Cham, 10.1007/978-3-319-50044-7

143. Luo, K., Zhang, H., Wang, L., Yuan, J., and Lou, Z. (2012) Sumoylation of MDC1 is important for proper DNA damage response. *EMBO Journal*. **31**, 3008–3019

144. Yin, Y., Seifert, A., Chua, J. S., Maure, J.-F., Golebiowski, F., and Hay, R. T. (2012) SUMO-targeted ubiquitin E3 ligase RNF4 is required for the response of human cells to DNA damage. *Genes Dev*. **26**, 1196–1208

145. Vyas, R., Kumar, R., Clermont, F., Helfricht, A., Kalev, P., Sotiropoulou, P., Hendriks, I. A., Radaelli, E., Hochepied, T., Blanpain, C., Sablina, A., Van Attikum, H., Olsen, J. V., Jochemsen, A. G., Vertegaal, A. C. O., and Marine, J. C. (2013) RNF4 is required for DNA double-strand break repair in vivo. *Cell Death Differ*. **20**, 490–502

146. Kumar, R., and Fang, C. C. (2017) Dynamics of RIF1 SUMOylation is regulated by PIAS4 in the maintenance of Genomic Stability. *Sci Rep*. **7**, 1–17

147. Galanty, Y., Belotserkovskaya, R., Coates, J., Polo, S., Miller, K. M., and Jackson, S. P. (2009) Mammalian SUMO E3-ligases PIAS1 and PIAS4 promote responses to DNA double-strand breaks. *Nature*. **462**, 935–939

148. Wu, C. S., Ouyang, J., Mori, E., Nguyen, H. D., Maréchal, A., Hallet, A., Chen, D. J., and Zou, L. (2014) SUMOylation of ATRIP potentiates DNA damage signaling by boosting multiple protein interactions in the ATR pathway. *Genes Dev*. **28**, 1472–1484

149. Morris, J. R., Boutell, C., Keppler, M., Densham, R., Weekes, D., Alamshah, A., Butler, L., Galanty, Y., Pangon, L., Kiuchi, T., Ng, T., and Solomon, E. (2009) The SUMO modification pathway is involved in the BRCA1 response to genotoxic stress. *Nature*. **462**, 886–890

150. Chung, I., and Zhao, X. (2015) DNA break-induced sumoylation is enabled by collaboration between a SUMO ligase and the ssDNA-binding complex RPA. *Genes Dev*. **29**, 1593–1598

151. Dhingra, N., Wei, L., and Zhao, X. (2019) Replication protein A (RPA) sumoylation positively influences the DNA damage checkpoint response in yeast. *Journal of Biological Chemistry*. **294**, 2690–2699

152. Dou, H., Huang, C., Singh, M., Carpenter, P. B., and Yeh, E. T. H. (2010) Regulation of DNA Repair through DeSUMOylation and SUMOylation of replication protein A complex. *Mol Cell*. **39**, 333–345

153. Eladad, S., Ye, T. Z., Hu, P., Leversha, M., Beresten, S., Matunis, M. J., and Ellis, N. A. (2005) Intra-nuclear trafficking of the BLM helicase to DNA damage-induced foci is regulated by SUMO modification. *Hum Mol Genet*. **14**, 1351–1365

154. Ouyang, K. J., Woo, L. L., Zhu, J., Huo, D., Matunis, M. J., and Ellis, N. A. (2009) SUMO modification regulates BLM and RAD51 interaction at damaged replication forks. *PLoS Biol*. **7**, e1000252

155. Ouyang, K. J., Yagle, M. K., Matunis, M. J., and Ellis, N. A. (2013) BLM SUMOylation regulates ssDNA accumulation at stalled replication forks. *Front Genet*. **4**, 1–11

156. Ranjha, L., Levikova, M., Altmannova, V., Krejci, L., and Cejka, P. (2019) Sumoylation regulates the stability and nuclease activity of Saccharomyces cerevisiae Dna2. *Commun Biol*. 10.1038/s42003-019-0428-0

157. Bologna, S., Altmannova, V., Valtorta, E., Koenig, C., Liberali, P., Gentili, C., Anrather, D., Ammerer, G., Pelkmans, L., Krejci, L., and Ferrari, S. (2015) Sumoylation regulates EXO1 stability and processing of DNA damage. *Cell Cycle*. **14**, 2439–2450

158. Shima, H., Suzuki, H., Sun, J., Kono, K., Shi, L., Kinomura, A., Horikoshi, Y., Ikura, T., Ikura, M., Kanaar, R., Igarashi, K., Saitoh, H., Kurumizaka, H., and Tashiro, S. (2013) Activation of the SUMO modification system is required for the accumulation of RAD51 at sites of DNA damage. *J Cell Sci*. **126**, 5284–5292

159. Hariharasudhan, G., Jeong, S. Y., Kim, M. J., Jung, S. M., Seo, G., Moon, J. R., Lee, S., Chang, I. Y., Kee, Y., You, H. J., and Lee, J. H. (2022) TOPORS-mediated RAD51 SUMOylation facilitates homologous recombination repair. *Nucleic Acids Res*. **50**, 1501–1516

160. González-Prieto, R., Eifler-Olivi, K., Claessens, L. A., Willemstein, E., Xiao, Z., Talavera Ormeno, C. M. P., Ovaa, H., Ulrich, H. D., and Vertegaal, A. C. O. (2021) Global non-covalent SUMO interaction networks reveal SUMO-dependent stabilization of the non-homologous end joining complex. *Cell Rep*. 10.1016/j.celrep.2021.108691

161. Hang, L. E., Lopez, C. R., Liu, X., Williams, J. M., Chung, I., Wei, L., Bertuch, A. A., and Zhao, X. (2014) Regulation of Ku-DNA association by yku70 C-terminal tail and SUMO modification. *Journal of Biological Chemistry*. **289**, 10308–10317

162. Yurchenko, V., Xue, Z., and Sadofsky, M. J. (2006) SUMO Modification of Human XRCC4 Regulates Its Localization and Function in DNA Double-Strand Break Repair. *Mol Cell Biol*. **26**, 1786–1794

163. Johnson, P. R., and Hochstrasser, M. (1997) SUMO-1: Ubiquitin gains weight. *Trends Cell Biol*. **7**, 408–413

164. Martin, S., Wilkinson, K. A., Nishimune, A., and Henley, J. M. (2007) Emerging extranuclear roles of protein SUMOylation in neuronal function and dysfunction. *Nat Rev Neurosci*. **8**, 948–959

165. Lapenta, V., Chiurazzi, P., Van Der Spek, P., Pizzuti, A., Hanaoka, F., and Brahe, C. (1997) SMT3A, a human homologue of the S. cerevisiae SMT3 gene, maps to chromosome 21qter and defines a novel gene family. *Genomics*. **40**, 362–366

166. Salas-Lloret, D., and González-Prieto, R. (2022) Insights in Post-Translational Modifications: Ubiquitin and SUMO. *Int J Mol Sci*. 10.3390/ijms23063281

167. Saitoh, H., and Hinchey, J. (2000) Functional heterogeneity of small ubiquitin-related protein modifiers SUMO-1 versus SUMO-2/3. *Journal of Biological Chemistry*. **275**, 6252–6258

168. Wang, L., Wansleeben, C., Zhao, S., Miao, P., Paschen, W., and Yang, W. (2014) SUMO2 is essential while SUMO3 is dispensable for mouse embryonic development. *EMBO Rep*. **15**, 878–885

169. Evdokimov, E., Sharma, P., Loskett, S. J., Lualdi, M., and Kuehn, M. R. (2008) Loss of SUMO1 in mice affects RanGAP1 localization and formation of PML nuclear bodies, but is not lethal as it can be compensated by SUMO2 or SUMO3. *J Cell Sci*. **121**, 4106–4113

170. Vertegaal, A. C. O., Andersen, J. S., Ogg, S. C., Hay, R. T., Mann, M., and Lamond, A. I. (2006) Distinct and overlapping sets of SUMO-1 and SUMO-2 target proteins revealed by quantitative proteomics. *Mol Cell Proteomics*. **5**, 2298–2310

171. Hickey, C. M., Wilson, N. R., and Hochstrasser, M. (2012) Function and regulation of SUMO proteases. *Nat Rev Mol Cell Biol*. **13**, 755–766

172. Gong, L., Kamitani, T., Fujise, K., Caskey, L. S., and Yeh, E. T. H. (1997) Preferential interaction of sentrin with a ubiquitin-conjugating enzyme, Ubc9. *Journal of Biological Chemistry*. **272**, 28198–28201

173. Hendriks, I. A., and Vertegaal, A. C. O. (2016) A comprehensive compilation of SUMO proteomics. *Nat Rev Mol Cell Biol*. **17**, 581–595

174. Nacerddine, K., Lehembre, F., Bhaumik, M., Artus, J., Cohen-Tannoudji, M., Babinet, C., Pandolfi, P. P., and Dejean, A. (2005) The SUMO pathway is essential for nuclear integrity and chromosome segregation in mice. *Dev Cell*. **9**, 769–779

175. Matic, I., Schimmel, J., Hendriks, I. A., van Santen, M. A., van de Rijke, F., van Dam, H., Gnad, F., Mann, M., and Vertegaal, A. C. O. (2010) Site-Specific Identification of SUMO-2 Targets in Cells Reveals an Inverted SUMOylation Motif and a Hydrophobic Cluster SUMOylation Motif. *Mol Cell*. **39**, 641–652

176. Pichler, A., Gast, A., Seeler, J. S., Dejean, A., and Melchior, F. (2002) The nucleoporin RanBP2 has SUMO1 E3 ligase activity. *Cell*. **108**, 109–120

177. Kagey, M. H., Melhuish, T. A., and Wotton, D. (2003) The polycomb protein Pc2 is a SUMO E3. *Cell*. **113**, 127–137

178. Rabellino, A., Andreani, C., and Scaglioni, P. P. (2017) The Role of PIAS SUMO E3-Ligases in Cancer. *Cancer Res*. **77**, 1542–1547

179. Shi, X., Du, Y., Li, S., and Wu, H. (2022) The Role of SUMO E3 Ligases in Signaling Pathway of Cancer Cells. *Int J Mol Sci*. 10.3390/ijms23073639

180. Tatham, M. H., Jaffray, E., Vaughan, O. A., Desterro, J. M. P., Botting, C. H., Naismith, J. H., and Hay, R. T. (2001) Polymeric Chains of SUMO-2 and SUMO-3 are Conjugated to Protein Substrates by SAE1/SAE2 and Ubc9. *Journal of Biological Chemistry*. **276**, 35368–35374

181. Matic, I., van Hagen, M., Schimmel, J., Macek, B., Ogg, S. C., Tatham, M. H., Hay, R. T., Lamond, A. I., Mann, M., and Vertegaal, A. C. O. (2008) In vivo identification of human small ubiquitin-like modifier polymerization sites by high accuracy mass spectrometry and an in vitro to in vivo strategy. *Molecular and Cellular Proteomics*. **7**, 132–144

182. Hecker, C. M., Rabiller, M., Haglund, K., Bayer, P., and Dikic, I. (2006) Specification of SUMO1- and SUMO2-interacting motifs. *Journal of Biological Chemistry*. **281**, 16117–16127

183. Keusekotten, K., Bade, V. N., Meyer-Teschendorf, K., Sriramachandran, A. M., Fischer-Schrader, K., Krause, A., Horst, C., Schwarz, G., Hofmann, K., Dohmen, R. J., and Praefcke, G. J. K. (2014) Multivalent interactions of the SUMO-interaction motifs in RING finger protein 4 determine the specificity for chains of the SUMO. *Biochemical Journal*. **457**, 207–214

184. Weisshaar, S. R., Keusekotten, K., Krause, A., Horst, C., Springer, H. M., Göttsche, K., Dohmen, R. J., and Praefcke, G. J. K. (2008) Arsenic trioxide stimulates SUMO-2/3 modification leading to RNF4-dependent proteolytic targeting of PML. *FEBS Lett*. **582**, 3174–3178

185. Lallemand-Breitenbach, V., Jeanne, M., Benhenda, S., Nasr, R., Lei, M., Peres, L., Zhou, J., Raught, B., and de Thé, H. (2008) Arsenic degrades PML or PML-RARα through a SUMO-triggered RNF4/ ubiquitin-mediated pathway. *Nat Cell Biol*. **10**, 547–555

186. Tatham, M. H., Geoffroy, M. C., Shen, L., Plechanovova, A., Hattersley, N., Jaffray, E. G., Palvimo, J. J., and Hay, R. T. (2008) RNF4 is a poly-SUMO-specific E3 ubiquitin ligase required for arsenic-induced PML degradation. *Nat Cell Biol*. **10**, 538–546

187. Galanty, Y., Belotserkovskaya, R., Coates, J., and Jackson, S. P. (2012) RNF4, a SUMO-targeted ubiquitin E3 ligase, promotes DNA double-strand break repair. *Genes Dev*. **26**, 1179–1195

188. Kumar, R., González-Prieto, R., Xiao, Z., Verlaan-De Vries, M., and Vertegaal, A. C. O. (2017) The STUbL RNF4 regulates protein group SUMOylation by targeting the SUMO conjugation machinery. *Nat Commun*. 10.1038/s41467-017-01900-x

189. Sriramachandran, A. M., Meyer-Teschendorf, K., Pabst, S., Ulrich, H. D., Gehring, N. H., Hofmann, K., Praefcke, G. J. K., and Dohmen, R. J. (2019) Arkadia/RNF111 is a SUMO-targeted ubiquitin ligase with preference for substrates marked with SUMO1-capped SUMO2/3 chain. *Nat Commun*. **10**, 1–12

190. Li, Y. J., Stark, J. M., Chen, D. J., Ann, D. K., and Chen, Y. (2010) Role of SUMO:SIM-mediated protein-protein interaction in non-homologous end joining. *Oncogene*. **29**, 3509–3518

191. Zhou, Y. B., Gerchman, S. E., Ramakrishnan, V., Travers, A., and Muyldermans, S. (1998) Position and orientation of the globular domain of linker histone H5 on the nucleosome. *Nature*. **395**, 402–405

192. West, M. H. P., and Bonner, W. M. (1980) Histone 2A, a Heteromorphous Family of Eight Protein Species. *Biochemistry*. **19**, 3238–3245

193. Thatcher, T. H., and Gorovsky, M. A. (1994) Phylogenetic analysis of the core histones H2A, H2B, H3, and H4. *Nucleic Acids Res*. **22**, 174–179

194. Rogakou, E. P., Pilch, D. R., Orr, A. H., Ivanova, V. S., and Bonner, W. M. (1998) DNA double-stranded breaks induce histone H2AX phosphorylation on serine 139. *Journal of Biological Chemistry*. **273**, 5858–5868

195. Iacovoni, J. S., Caron, P., Lassadi, I., Nicolas, E., Massip, L., Trouche, D., and Legube, G. (2010) High-resolution profiling of γh2AX around DNA double strand breaks in the mammalian genome. *EMBO Journal*. **29**, 1446–1457

196. Mattiroli, F., and Penengo, L. (2021) Histone Ubiquitination: An Integrative Signaling Platform in Genome Stability. *Trends in Genetics*. **37**, 566–581

197. Allis, C. D., and Jenuwein, T. (2016) The molecular hallmarks of epigenetic control. *Nat Rev Genet*. **17**, 487–500

198. Millán-Zambrano, G., Burton, A., Bannister, A. J., and Schneider, R. (2022) Histone post-translational modifications — cause and consequence of genome function. *Nat Rev Genet*. **23**, 563–580

199. Guillemette, B., Drogaris, P., Lin, H. H. S., Armstrong, H., Hiragami-Hamada, K., Imhof, A., Bonneil, É., Thibault, P., Verreault, A., and Festenstein, R. J. (2011) H3 lysine 4 is acetylated at active gene promoters and is regulated by H3 lysine 4 methylation. *PLoS Genet*. 10.1371/journal.pgen.1001354

200. Lee, T. I., Jenner, R. G., Boyer, L. A., Guenther, M. G., Levine, S. S., Kumar, R. M., Chevalier, B., Johnstone, S. E., Cole, M. F., Isono, K., Koseki, H., Fuchikami, T., Abe, K., Murray, H. L., Zucker, J. P., Yuan, B., Bell, G. W., Herbolsheimer, E., Hannett, N. M., Sun, K., Odom, D. T., Otte, A. P., Volkert, T. L., Bartel, D. P., Melton, D. A., Gifford, D. K., Jaenisch, R., and Young, R. A. (2006) Control of developmental regulators by Polycomb in human embryonic stem cells. *Cell*. **125**, 301–313

201. Boyer, L. A., Plath, K., Zeitlinger, J., Brambrink, T., Medeiros, L. A., Lee, T. I., Levine, S. S., Wernig, M., Tajonar, A., Ray, M. K., Bell, G. W., Otte, A. P., Vidal, M., Gifford, D. K., Young, R. A., and Jaenisch, R. (2006) Polycomb complexes repress developmental regulators in murine embryonic stem cells. *Nature*. **441**, 349–353

202. Saredi, G., Huang, H., Hammond, C. M., Alabert, C., Bekker-Jensen, S., Forne, I., Reverón-Gómez, N., Foster, B. M., Mlejnkova, L., Bartke, T., Cejka, P., Mailand, N., Imhof, A., Patel, D. J., and Groth, A. (2016) H4K20me0 marks post-replicative chromatin and recruits the TONSL-MMS22L DNA repair complex. *Nature*. **534**, 714–718

203. Pesavento, J. J., Yang, H., Kelleher, N. L., and Mizzen, C. A. (2008) Certain and Progressive Methylation of Histone H4 at Lysine 20 during the Cell Cycle. *Mol Cell Biol*. **28**, 468–486

204. Becker, J. R., Clifford, G., Bonnet, C., Groth, A., Wilson, M. D., and Chapman, J. R. (2021) BARD1 reads H2A lysine 15 ubiquitination to direct homologous recombination. *Nature*. **596**, 433–437

205. Nakamura, K., Saredi, G., Becker, J. R., Foster, B. M., Nguyen, N. V., Beyer, T. E., Cesa, L. C., Faull, P. A., Lukauskas, S., Frimurer, T., Chapman, J. R., Bartke, T., and Groth, A.

(2019) H4K20me0 recognition by BRCA1–BARD1 directs homologous recombination to sister chromatids. *Nat Cell Biol*. **21**, 311–318

206. Dai, L., Dai, Y., Han, J., Huang, Y., Wang, L., Huang, J., and Zhou, Z. (2021) Structural insight into BRCA1-BARD1 complex recruitment to damaged chromatin. *Mol Cell*. **81**, 2765-2777.e6
207. Hu, Q., Botuyan, M. V., Zhao, D., Cui, G., Mer, E., and Mer, G. (2021) Mechanisms of BRCA1–BARD1 nucleosome recognition and ubiquitylation. *Nature*. **596**, 438–443
208. Tang, J., Cho, N. W., Cui, G., Manion, E. M., Shanbhag, N. M., Botuyan, M. V., Mer, G., and Greenberg, R. A. (2013) Acetylation limits 53BP1 association with damaged chromatin to promote homologous recombination. *Nat Struct Mol Biol*. **20**, 317–325
209. Hsiao, K. Y., and Mizzen, C. A. (2013) Histone H4 deacetylation facilitates 53BP1 DNA damage signaling and double-strand break repair. *J Mol Cell Biol*. **5**, 157–165
210. Burma, S., Chen, B. P., Murphy, M., Kurimasa, A., and Chen, D. J. (2001) ATM Phosphorylates Histone H2AX in Response to DNA Double-strand Breaks. *Journal of Biological Chemistry*. **276**, 42462–42467
211. Rogakou, E. P., Boon, C., Redon, C., and Bonner, W. M. (1999) Megabase chromatin domains involved in DNA double-strand breaks in vivo. *Journal of Cell Biology*. **146**, 905–915
212. Mailand, N., Bekker-Jensen, S., Faustrup, H., Melander, F., Bartek, J., Lukas, C., and Lukas, J. (2007) RNF8 ubiquitylates histones at DNA double-strand breaks and promotes assembly of repair proteins. *Cell*. **131**, 887–900
213. Huen, M. S. Y., Grant, R., Manke, I., Minn, K., Yu, X., Yaffe, M. B., and Chen, J. (2007) RNF8 transduces the DNA-damage signal via histone ubiquitylation and checkpoint protein assembly. *Cell*. **131**, 901–914
214. Kolas, N. K., Chapman, J. R., Nakada, S., Ylanko, J., Chahwan, R., Sweeney, F. D., Panier, S., Mendez, M., Wildenhain, J., Thomson, T. M., Pelletier, L., Jackson, S. P., and Durocher, D. (2007) Orchestration of the DNA-damage response by the RNF8 ubiquitin ligase. *Science (1979)*. **318**, 1637–1640
215. Wang, B., and Elledge, S. J. (2007) Ubc13/Rnf8 ubiquitin ligases control foci formation of the Rap80/Abraxas/Brca1/Brcc36 complex in response to DNA damage. *Proc Natl Acad Sci U S A*. **104**, 20759–20763

216. Thorslund, T., Ripplinger, A., Hoffmann, S., Wild, T., Uckelmann, M., Villumsen, B., Narita, T., Sixma, T. K., Choudhary, C., Bekker-Jensen, S., and Mailand, N. (2015) Histone H1 couples initiation and amplification of ubiquitin signalling after DNA damage. *Nature*. **527**, 389–393

217. Doil, C., Mailand, N., Bekker-Jensen, S., Menard, P., Larsen, D. H., Pepperkok, R., Ellenberg, J., Panier, S., Durocher, D., Bartek, J., Lukas, J., and Lukas, C. (2009) RNF168 binds and amplifies ubiquitin conjugates on damaged chromosomes to allow accumulation of repair proteins. *Cell*. **136**, 435–446

218. Stewart, G. S., Panier, S., Townsend, K., Al-Hakim, A. K., Kolas, N. K., Miller, E. S., Nakada, S., Ylanko, J., Olivarius, S., Mendez, M., Oldreive, C., Wildenhain, J., Tagliaferro, A., Pelletier, L., Taubenheim, N., Durandy, A., Byrd, P. J., Stankovic, T., Taylor, A. M. R., and Durocher, D. (2009) The RIDDLE syndrome protein mediates a ubiquitin-dependent signaling cascade at sites of DNA damage. *Cell*. **136**, 420–434

219. Gatti, M., Pinato, S., Maspero, E., Soffientini, P., Polo, S., and Penengo, L. (2012) A novel ubiquitin mark at the N-terminal tail of histone H2As targeted by RNF168 ubiquitin ligase. *Cell Cycle*. **11**, 2538–2544

220. Mattiroli, F., Vissers, J. H. A., van Dijk, W. J., Ikpa, P., Citterio, E., Vermeulen, W., Marteijn, J. A., and Sixma, T. K. (2012) RNF168 ubiquitinates K13-15 on H2A/H2AX to drive DNA damage signaling. *Cell*. **150**, 1182–1195

221. Sakasai, R., and Tibbetts, R. (2008) RNF8-dependent and RNF8-independent regulation of 53BP1 in response to DNA damage. *J Biol Chem*. **283**, 13549–13555

222. Hu, Y., Wang, C., Huang, K., Xia, F., Parvin, J. D., and Mondal, N. (2014) Regulation of 53BP1 protein stability by RNF8 and RNF168 is important for efficient DNA double-strand break repair. *PLoS One*. **9**, e110522

223. Fradet-Turcotte, A., Canny, M. D., Escribano-Díaz, C., Orthwein, A., Leung, C. C. Y., Huang, H., Landry, M.-C., Kitevski-LeBlanc, J., Noordermeer, S. M., Sicheri, F., and Durocher, D. (2013) 53BP1 is a reader of the DNA-damage-induced H2A Lys 15 ubiquitin mark. *Nature*. **499**, 50–54

224. Wilson, M. D., Benlekbir, S., Fradet-Turcotte, A., Sherker, A., Julien, J.-P., McEwan, A., Noordermeer, S. M., Sicheri, F., Rubinstein, J. L., and Durocher, D. (2016) The structural basis of modified nucleosome recognition by 53BP1. *Nature*. **536**, 100–103

225. Botuyan, M. V., Lee, J., Ward, I. M., Kim, J.-E., Thompson, J. R., Chen, J., and Mer, G. (2006) Structural basis for the methylation state-specific recognition of histone H4-K20 by 53BP1 and Crb2 in DNA repair. *Cell*. **127**, 1361–1373

226. Bohgaki, M., Bohgaki, T., El Ghamrasni, S., Srikumar, T., Maire, G., Panier, S., Fradet-Turcotte, A., Stewart, G. S., Raught, B., Hakem, A., and Hakem, R. (2013) RNF168 ubiquitylates 53BP1 and controls its response to DNA double-strand breaks. *Proc Natl Acad Sci U S A*. **110**, 20982–20987

227. Himmels, S. F., and Sartori, A. A. (2016) Controlling DNA-end resection: An emerging task for ubiquitin and SUMO. *Front Genet*. **7**, 1–7

228. Bunting, S. F., Callén, E., Wong, N., Chen, H. T., Polato, F., Gunn, A., Bothmer, A., Feldhahn, N., Fernandez-Capetillo, O., Cao, L., Xu, X., Deng, C. X., Finkel, T., Nussenzweig, M., Stark, J. M., and Nussenzweig, A. (2010) 53BP1 inhibits homologous recombination in brca1-deficient cells by blocking resection of DNA breaks. *Cell*. **141**, 243–254

229. Bothmer, A., Robbiani, D. F., Feldhahn, N., Gazumyan, A., Nussenzweig, A., and Nussenzweig, M. C. (2010) 53BP1 regulates DNA resection and the choice between classical and alternative end joining during class switch recombination. *Journal of Experimental Medicine*. **207**, 855–865

230. Callen, E., Zong, D., Wu, W., Wong, N., Stanlie, A., Ishikawa, M., Pavani, R., Dumitrache, L. C., Byrum, A. K., Mendez-Dorantes, C., Martinez, P., Canela, A., Maman, Y., Day, A., Kruhlak, M. J., Blasco, M. A., Stark, J. M., Mosammaparast, N., McKinnon, P. J., and Nussenzweig, A. (2020) 53BP1 Enforces Distinct Pre- and Post-resection Blocks on Homologous Recombination. *Mol Cell*. **77**, 26-38.e7

231. Zong, D., Callén, E., Pegoraro, G., Lukas, C., Lukas, J., and Nussenzweig, A. (2015) Ectopic expression of RNF168 and 53BP1 increases mutagenic but not physiological non-homologous end joining. *Nucleic Acids Res*. **43**, 4950–4961

232. Pierce, A. J., Hu, P., Han, M., Ellis, N., and Jasin, M. (2001) Ku DNA end-binding protein modulates homologous repair of double-strand breaks in mammalian cells. *Genes Dev*. 10.1101/gad.946401

233. Cejka, P., and Symington, L. S. (2021) DNA End Resection: Mechanism and Control. *Annu Rev Genet*. **55**, 285–307

234. Setiaputra, D., and Durocher, D. (2019) Shieldin - the protector of DNA ends. *EMBO Rep*. **20**, e47560

235. Mirman, Z., Sasi, N. K., King, A., Chapman, J. R., and de Lange, T. (2022) 53BP1–shieldin-dependent DSB processing in BRCA1-deficient cells requires CST–Polα–primase fill-in synthesis. *Nat Cell Biol*. **24**, 51–61

236. Paiano, J., Zolnerowich, N., Wu, W., Pavani, R., Wang, C., Li, H., Zheng, L., Shen, B., Sleckman, B. P., Chen, B. R., and Nussenzweig, A. (2021) Role of 53BP1 in end protection and DNA synthesis at DNA breaks. *Genes Dev*. **35**, 1356–1368

237. Densham, R. M., and Morris, J. R. (2019) Moving Mountains—The BRCA1 Promotion of DNA Resection. *Front Mol Biosci*. 10.3389/fmolb.2019.00079

238. Isono, M., Niimi, A., Oike, T., Hagiwara, Y., Sato, H., Sekine, R., Yoshida, Y., Isobe, S. Y., Obuse, C., Nishi, R., Petricci, E., Nakada, S., Nakano, T., and Shibata, A. (2017) BRCA1 Directs the Repair Pathway to Homologous Recombination by Promoting 53BP1 Dephosphorylation. *Cell Rep*. **18**, 520–532

239. Kalb, R., Mallery, D. L., Larkin, C., Huang, J. T. J., and Hiom, K. (2014) BRCA1 is a histone-H2A-specific ubiquitin ligase. *Cell Rep*. **8**, 999–1005

240. Zhang, J., Dai, Q., Park, D., and Deng, X. (2016) Targeting DNA replication stress for cancer therapy. *Genes (Basel)*. 10.3390/genes7080051

241. Zeman, M. K., and Cimprich, K. A. (2014) Causes and consequences of replication stress. *Nat Cell Biol*. **16**, 2–9

242. Gaillard, H., García-Muse, T., and Aguilera, A. (2015) Replication stress and cancer. *Nat Rev Cancer*. **15**, 276

243. Macheret, M., and Halazonetis, T. D. (2015) DNA replication stress as a hallmark of cancer. *Annu Rev Pathol*. **10**, 425–448

244. Kotsantis, P., Silva, L. M., Irmscher, S., Jones, R. M., Folkes, L., Gromak, N., and Petermann, E. (2016) Increased global transcription activity as a mechanism of replication stress in cancer. *Nat Commun*. **7**, 13087

245. Jeggo, P. A., and Löbrichf, M. (2015) How cancer cells hijack DNA double-strand break repair pathways to gain genomic instability. *Biochemical Journal*. **471**, 1–11

246. Neelsen, K. J., and Lopes, M. (2015) Replication fork reversal in eukaryotes: From dead end to dynamic response. *Nat Rev Mol Cell Biol*. **16**, 207–220

247. Quinet, A., Lemaçon, D., and Vindigni, A. (2017) Replication Fork Reversal: Players and Guardians. *Mol Cell*. **68**, 830–833

248. Kolinjivadi, A. M., Sannino, V., de Antoni, A., Techer, H., Baldi, G., and Costanzo, V. (2017) Moonlighting at replication forks - a new life for homologous recombination proteins BRCA1, BRCA2 and RAD51. *FEBS Lett*. **591**, 1083–1100

249. Schlacher, K., Christ, N., Siaud, N., Egashira, A., Wu, H., and Jasin, M. (2011) Double-Strand Break Repair-Independent Role for BRCA2 in Blocking Stalled Replication Fork Degradation by MRE11. *Cell*. **145**, 529–542

250. Schlacher, K., Wu, H., and Jasin, M. (2012) A distinct replication fork protection pathway connects Fanconi anemia tumor suppressors to RAD51-BRCA1/2. *Cancer Cell*. **22**, 106–116

251. Ying, S., Hamdy, F. C., and Helleday, T. (2012) Mre11-dependent degradation of stalled DNA replication forks is prevented by BRCA2 and PARP1. *Cancer Res*. **72**, 2814–2821

252. Lemaçon, D., Jackson, J., Quinet, A., Brickner, J. R., Li, S., Yazinski, S., You, Z., Ira, G., Zou, L., Mosammaparast, N., and Vindigni, A. (2017) MRE11 and EXO1 nucleases degrade reversed forks and elicit MUS81-dependent fork rescue in BRCA2-deficient cells. *Nat Commun*. **8**, 860

253. Schaeper, U., Subramanian, T., Lim, L., Boyd, J. M., and Chinnadurai, G. (1998) Interaction between a cellular protein that binds to the C-terminal region of adenovirus E1A (CtBP) and a novel cellular protein is disrupted by E1A through a conserved PLDLS motif. *J Biol Chem*. **273**, 8549–8552

254. Fusco, C., Reymond, A., and Zervos, A. S. (1998) Molecular cloning and characterization of a novel retinoblastoma-binding protein. *Genomics*. **51**, 351–358

255. Wong, A. K., Ormonde, P. A., Pero, R., Chen, Y., Lian, L., Salada, G., Berry, S., Lawrence, Q., Dayananth, P., Ha, P., Tavtigian, S. V, Teng, D. H., and Bartel, P. L. (1998) Characterization of a carboxy-terminal BRCA1 interacting protein. *Oncogene*. **17**, 2279–2285

256. You, Z., Shi, L. Z., Zhu, Q., Wu, P., Zhang, Y. W., Basilio, A., Tonnu, N., Verma, I. M., Berns, M. W., and Hunter, T. (2009) CtIP Links DNA Double-Strand Break Sensing to Resection. *Mol Cell*. **36**, 954–969

257. Andres, S. N., and Williams, R. S. (2017) CtIP/Ctp1/Sae2, molecular form fit for function. *DNA Repair (Amst)*. **56**, 109–117

258. Davies, O. R., Forment, J. V., Sun, M., Belotserkovskaya, R., Coates, J., Galanty, Y., Demir, M., Morton, C. R., Rzechorzek, N. J., Jackson, S. P., and Pellegrini, L. (2015) CtIP tetramer assembly is required for DNA-end resection and repair. *Nat Struct Mol Biol*. **22**, 150–157

259. Wilkinson, O. J., Martín-González, A., Kang, H., Northall, S. J., Wigley, D. B., Moreno-Herrero, F., and Dillingham, M. S. (2019) CtIP forms a tetrameric dumbbell-shaped particle which bridges complex DNA end structures for double-strand break repair. *Elife*. **8**, 1–22

260. Öz, R., Howard, S. M., Törnkvist, H., Ceppi, I., Kk, S., Kristiansson, E., Cejka, P., and Westerlund, F. (2020) Phosphorylated CtIP bridges DNA to promote annealing of broken ends. 10.1073/pnas.2008645117

261. Andres, S. N., Appel, C. D., Westmoreland, J. W., Williams, J. S., Nguyen, Y., Robertson, P. D., Resnick, M. A., and Williams, R. S. (2015) Tetrameric Ctp1 coordinates DNA binding and DNA bridging in DNA double-strand-break repair. *Nat Struct Mol Biol*. **22**, 158–166

262. Andres, S. N., Li, Z. M., Erie, D. A., and Williams, R. S. (2019) Ctp1 protein–DNA filaments promote DNA bridging and DNA double-strand break repair. *Journal of Biological Chemistry*. **294**, 3312–3320

263. You, Z., and Bailis, J. M. (2010) DNA damage and decisions: CtIP coordinates DNA repair and cell cycle checkpoints. *Trends Cell Biol*. **20**, 402–409

264. Qvist, P., Huertas, P., Jimeno, S., Nyegaard, M., Hassan, M. J., Jackson, S. P., and Børglum, A. D. (2011) CtIP mutations cause Seckel and Jawad syndromes. *PLoS Genet*. 10.1371/journal.pgen.1002310

265. Li, S., Ting, N. S. Y., Zheng, L., Chen, P., Ziv, Y., Shiloh, Y., Lee, E. Y. P., and Lee, W. (2000) Functional link of BRCA1 and ataxia telangiectasia gene product in DNA damage response. **406**, 2–7

266. Matsuoka, S., Ballif, B. A., Smogorzewska, A., McDonald, E. R. 3rd, Hurov, K. E., Luo, J., Bakalarski, C. E., Zhao, Z., Solimini, N., Lerenthal, Y., Shiloh, Y., Gygi, S. P., and Elledge, S. J. (2007) ATM and ATR Substrate Analysis Reveals Extensive Protein Networks Responsive to DNA Damage. *Science*. **316**, 1160–1166

267. Peterson, S. E., Li, Y., Wu-Baer, F., Chait, B. T., Baer, R., Yan, H., Gottesman, M. E., and Gautier, J. (2013) Activation of DSB Processing Requires Phosphorylation of CtIP by ATR. *Mol Cell*. **49**, 657–667

268. Wang, H., Qiu, Z., Liu, B., Wu, Y., Ren, J., Liu, Y., Zhao, Y., Wang, Y., Hao, S., Li, Z., Peng, B., and Xu, X. (2018) PLK1 targets CtIP to promote microhomology-mediated end joining. *Nucleic Acids Res*. **46**, 10724–10739

269. Ceppi, I., Cannavo, E., Bret, H., Camarillo, R., Vivalda, F., Thakur, R. S., Romero-Franco, A., Sartori, A. A., Huertas, P., Guérois, R., and Cejka, P. (2023) PLK1 regulates CtIP and DNA2 interplay in long-range DNA end resection. *Genes Dev*. **37**, 119–135

270. Wang, H., Li, Y., Truong, L. N., Shi, L. Z., Hwang, P. Y. H., He, J., Do, J., Cho, M. J., Li, H., Negrete, A., Shiloach, J., Berns, M. W., Shen, B., Chen, L., and Wu, X. (2014) CtIP maintains stability at common fragile sites and inverted repeats by end resection-independent endonuclease activity. *Mol Cell*. **54**, 1012–1021

271. Chanut, P., Britton, S., Coates, J., Jackson, S. P., and Calsou, P. (2016) Coordinated nuclease activities counteract Ku at single-ended DNA double-strand breaks. *Nat Commun*. 10.1038/ncomms12889

272. Makharashvili, N., Tubbs, A. T., Yang, S. H., Wang, H., Barton, O., Zhou, Y., Deshpande, R. A., Lee, J. H., Lobrich, M., Sleckman, B. P., Wu, X., and Paull, T. T. (2014) Catalytic and Non-catalytic Roles of the CtIP Endonuclease in Double-Strand Break End Resection. *Mol Cell*. **54**, 1022–1033

273. Kakarougkas, A., Downs, J. A., and Jeggo, P. A. (2015) The PBAF chromatin remodeling complex represses transcription and promotes rapid repair at DNA double-strand breaks. *Mol Cell Oncol*. 10.4161/23723548.2014.970072

274. Kruhlak, M., Crouch, E. E., Orlov, M., Montão, C., Gorski, S. A., Nussenzweig, A., Misteli, T., Phair, R. D., and Casellas, R. (2007) The ATM repair pathway inhibits RNA polymerase I transcription in response to chromosome breaks. *Nature*. **447**, 730–734

275. Pankotai, T., Bonhomme, C., Chen, D., and Soutoglou, E. (2012) DNAPKcs-dependent arrest of RNA polymerase II transcription in the presence of DNA breaks. *Nat Struct Mol Biol*. **19**, 276–282

276. Shanbhag, N. M., Rafalska-Metcalf, I. U., Balane-Bolivar, C., Janicki, S. M., and Greenberg, R. A. (2010) ATM-Dependent chromatin changes silence transcription in cis to DNA double-strand breaks. *Cell*. **141**, 970–981

277. Burgess, R. C., Burman, B., Kruhlak, M. J., and Misteli, T. (2014) Activation of DNA Damage Response Signaling by Condensed Chromatin. *Cell Rep*. **9**, 1703–1717

278. Kruhlak, M. J., Celeste, A., Dellaire, G., Fernandez-Capetillo, O., Müller, W. G., McNally, J. G., Bazett-Jones, D. P., and Nussenzweig, A. (2006) Changes in chromatin structure and mobility in living cells at sites of DNA double-strand breaks. *Journal of Cell Biology*. **172**, 823–834

279. Khurana, S., Kruhlak, M. J., Kim, J., Tran, A. D., Liu, J., Nyswaner, K., Shi, L., Jailwala, P., Sung, M.-H., Hakim, O., and Oberdoerffer, P. (2014) A macrohistone variant links dynamic chromatin compaction to BRCA1-dependent genome maintenance. *Cell Rep*. **8**, 1049–1062

280. Ayrapetov, M. K., Gursoy-Yuzugullu, O., Xu, C., Xu, Y., and Price, B. D. (2014) DNA double-strand breaks promote methylation of histone H3 on lysine 9 and transient formation of repressive chromatin. *Proc Natl Acad Sci U S A*. **111**, 9169–9174

281. Aranda, S., Mas, G., and Di Croce, L. (2015) Regulation of gene transcription by Polycomb proteins. *Sci Adv*. **1**, e1500737

282. Grossniklaus, U., and Paro, R. (2014) Transcriptional silencing by polycomb-group proteins. *Cold Spring Harb Perspect Biol*. **6**, a019331

283. Lewis, E. B. (1978) A gene complex controlling segmentation in Drosophila. *Nature*. **276**, 565–570

284. Struhl, G. (1981) A gene product required for correct initiation of segmental determination in Drosophila. *Nature*. **293**, 36–41

285. Levine, S. S., King, I. F. G., and Kingston, R. E. (2004) Division of labor in polycomb group repression. *Trends Biochem Sci*. **29**, 478–485

286. Simon, J. A., and Kingston, R. E. (2009) Mechanisms of polycomb gene silencing: knowns and unknowns. *Nat Rev Mol Cell Biol*. **10**, 697–708

287. Pasini, D., Bracken, A. P., Jensen, M. R., Lazzerini Denchi, E., and Helin, K. (2004) Suz12 is essential for mouse development and for EZH2 histone methyltransferase activity. *EMBO J*. **23**, 4061–4071

288. Wang, H., Wang, L., Erdjument-Bromage, H., Vidal, M., Tempst, P., Jones, R. S., and Zhang, Y. (2004) Role of histone H2A ubiquitination in Polycomb silencing. *Nature*. **431**, 873–878

289. de Napoles, M., Mermoud, J. E., Wakao, R., Tang, Y. A., Endoh, M., Appanah, R., Nesterova, T. B., Silva, J., Otte, A. P., Vidal, M., Koseki, H., and Brockdorff, N. (2004) Polycomb group proteins Ring1A/B link ubiquitylation of histone H2A to heritable gene silencing and X inactivation. *Dev Cell*. **7**, 663–676

290. Vidal, M. (2009) Role of polycomb proteins Ring1A and Ring1B in the epigenetic regulation of gene expression. *Int J Dev Biol*. **53**, 355–370

291. Dellino, G. I., Schwartz, Y. B., Farkas, G., McCabe, D., Elgin, S. C. R., and Pirrotta, V. (2004) Polycomb silencing blocks transcription initiation. *Mol Cell*. **13**, 887–893

292. King, I. F. G., Francis, N. J., and Kingston, R. E. (2002) Native and recombinant polycomb group complexes establish a selective block to template accessibility to repress transcription in vitro. *Mol Cell Biol*. **22**, 7919–7928

293. Morey, L., and Helin, K. (2010) Polycomb group protein-mediated repression of transcription. *Trends Biochem Sci*. **35**, 323–332

294. Tamburri, S., Lavarone, E., Fernández-Pérez, D., Conway, E., Zanotti, M., Manganaro, D., and Pasini, D. (2020) Histone H2AK119 Mono-Ubiquitination Is Essential for Polycomb-Mediated Transcriptional Repression. *Mol Cell*. **77**, 840-856.e5

295. Bergink, S., Salomons, F. A., Hoogstraten, D., Groothuis, T. A. M., De Waard, H., Wu, J., Yuan, L., Citterio, E., Houtsmuller, A. B., Neefjes, J., Hoeijmakers, J. H. J., Vermeulen, W., and Dantuma, N. P. (2006) DNA damage triggers nucleotide excision repair-dependent monoubiquitylation of histone H2A. *Genes Dev*. **20**, 1343–1352

296. Pan, M. R., Peng, G., Hungs, W. C., and Lin, S. Y. (2011) Monoubiquitination of H2AX protein regulates DNA damage response signaling. *Journal of Biological Chemistry*. **286**, 28599–28607

297. Ginjala, V., Nacerddine, K., Kulkarni, A., Oza, J., Hill, S. J., Yao, M., Citterio, E., van Lohuizen, M., and Ganesan, S. (2011) BMI1 Is Recruited to DNA Breaks and Contributes to DNA Damage-Induced H2A Ubiquitination and Repair. *Mol Cell Biol*. **31**, 1972–1982

298. Wu, C.-Y., Kang, H.-Y., Yang, W.-L., Wu, J., Jeong, Y. S., Wang, J., Chan, C.-H., Lee, S.-W., Zhang, X., Lamothe, B., Campos, A. D., Darnay, B. G., and Lin, H.-K. (2011) Critical

Role of Monoubiquitination of Histone H2AX Protein in Histone H2AX Phosphorylation and DNA Damage Response. *Journal of Biological Chemistry*. **286**, 30806–30815

299. Facchino, S., Abdouh, M., Chatoo, W., and Bernier, G. (2010) BMI1 confers radioresistance to normal and cancerous neural stem cells through recruitment of the DNA damage response machinery. *J Neurosci*. **30**, 10096–10111
300. Chagraoui, J., Hébert, J., Girard, S., and Sauvageau, G. (2011) An anticlastogenic function for the Polycomb Group gene Bmi1. *Proc Natl Acad Sci U S A*. **108**, 5284–5289
301. Chou, D. M., Adamson, B., Dephoure, N. E., Tan, X., Nottke, A. C., Hurov, K. E., Gygi, S. P., Colaiácovo, M. P., and Elledge, S. J. (2010) A chromatin localization screen reveals poly (ADP ribose)-regulated recruitment of the repressive polycomb and NuRD complexes to sites of DNA damage. *Proc Natl Acad Sci U S A*. **107**, 18475–18480
302. Ui, A., Nagaura, Y., and Yasui, A. (2015) Transcriptional elongation factor ENL phosphorylated by ATM recruits polycomb and switches off transcription for DSB repair. *Mol Cell*. **58**, 468–482
303. Yamada, M., Ohnishi, J., Ohkawara, B., Iemura, S., Satoh, K., Hyodo-Miura, J., Kawachi, K., Natsume, T., and Shibuya, H. (2006) NARF, an Nemo-like kinase (NLK)-associated ring finger protein regulates the ubiquitylation and degradation of T cell factor/lymphoid enhancer factor (TCF/LEF). *Journal of Biological Chemistry*. **281**, 20749–20760
304. Giannini, A. L., Gao, Y., and Bijlmakers, M. J. (2008) T-cell regulator RNF125/TRAC-1 belongs to a novel family of ubiquitin ligases with zinc fingers and a ubiquitin-binding domain. *Biochemical Journal*. **410**, 101–111
305. Brooks, W. S., Banerjee, S., and Crawford, D. F. (2014) RNF138 / NARF is a cell cycle regulated E3 ligase that poly-ubiquitinates G2E3. *JSM Cell*. **2**, 1005
306. Fu, S. J., Jeng, C. J., Ma, C. H., Peng, Y. J., Lee, C. M., Fang, Y. C., Lee, Y. C., Tang, S. C., Hu, M. C., and Tang, C. Y. (2017) Ubiquitin ligase RNF138 promotes episodic ataxia type 2-associated aberrant degradation of human Cav2.1 (P/Q-type) calcium channels. *Journal of Neuroscience*. **37**, 2485–2503
307. Yu, X., Li, W., Deng, Q., Liu, H., Wang, X., Hu, H., Cao, Y., Xu-Monette, Z. Y., Li, L., Zhang, M., Lu, Z., Young, K. H., and Li, Y. (2021) MYD88 L265P elicits mutation-specific ubiquitination to drive NF-κB activation and lymphomagenesis. *Blood*. **137**, 1615–1627

308. Lu, Y., Huang, R., Ying, J., Li, X., Jiao, T., Guo, L., Zhou, H., Wang, H., Tuersuntuoheti, A., Liu, J., Chen, Q., Wang, Y., Su, L., Guo, C., Xu, F., Wang, Z., Lu, Y., Li, K., Liang, J., Huang, Z., Chen, X., Yao, J., Hu, H., Cheng, X., Wan, Y., Chen, X., Zhang, N., Miao, S., Cai, J., Wang, L., Liu, C., Song, W., and Zhao, H. (2022) RING finger 138 deregulation distorts NF-κB signaling and facilities colitis switch to aggressive malignancy. *Signal Transduct Target Ther*. 10.1038/s41392-022-00985-1

309. Liu, W., Wang, Z., Liu, S., Zhang, X., Cao, X., and Jiang, M. (2023) RNF138 inhibits late inflammatory gene transcription through degradation of SMARCC1 of the SWI/SNF complex. *Cell Rep*. 10.1016/j.celrep.2023.112097

310. Huang, L., Xu, W., Liu, H., Xue, M., Liu, X., Zhang, K., Hu, L., Li, J., Liu, X., Xiang, Z., Zheng, J., Li, C., Chen, W., Bu, Z., Xiong, T., and Weng, C. (2021) African Swine Fever Virus pI215L Negatively Regulates cGAS-STING Signaling Pathway through Recruiting RNF138 to Inhibit K63-Linked Ubiquitination of TBK1. *The Journal of Immunology*. **207**, 2754–2769

311. Xu, L., Lu, Y., Han, D., Yao, R., Wang, H., Zhong, S., Luo, Y., Han, R., Li, K., Fu, J., Zong, S., Miao, S., Song, W., and Wang, L. (2017) Rnf138 deficiency promotes apoptosis of spermatogonia in juvenile male mice. *Cell Death Dis*. **8**, e2795-11

312. Kim, W., Youn, H., Lee, S., Kim, E., Kim, D., Lee, J. S., Lee, J. M., and Youn, B. (2018) RNF138-mediated ubiquitination of rpS3 is required for resistance of glioblastoma cells to radiation-induced apoptosis. *Exp Mol Med*. **50**, e434-14

313. Lu, Y., Han, D., Liu, W., Huang, R., Ou, J., Chen, X., Zhang, X., Wang, X., Li, S., Wang, L., Liu, C., Miao, S., Wang, L., Ma, C., and Song, W. (2018) RNF138 confers cisplatin resistance in gastric cancer cells via activating Chk1 signaling pathway. *Cancer Biol Ther*. **19**, 1128–1138

314. Yard, B. D., Reilly, N. M., Bedenbaugh, M. K., and Pittman, D. L. (2016) RNF138 interacts with RAD51D and is required for DNA interstrand crosslink repair and maintaining chromosome integrity. *DNA Repair (Amst)*. **42**, 82–93

315. Han, D., Liang, J., Lu, Y., Xu, L., Miao, S., Lu, L. Y., Song, W., and Wang, L. (2016) Ubiquitylation of Rad51d mediated by E3 ligase Rnf138 promotes the homologous recombination repair pathway. *PLoS One*. **11**, 1–16

316. Mimori, T., and Hardin, J. A. (1986) Mechanism of interaction between Ku protein and DNA. *J Biol Chem*. **261**, 10375–10379

317. Lee, K. J., Saha, J., Sun, J., Fattah, K. R., Wang, S. C., Jakob, B., Chi, L., Wang, S. Y., Taucher-Scholz, G., Davis, A. J., and Chen, D. J. (2015) Phosphorylation of Ku dictates DNA double-strand break (DSB) repair pathway choice in S phase. *Nucleic Acids Res*. **44**, 1732–1745

318. Shao, Z., Davis, A. J., Fattah, K. R., So, S., Sun, J., Lee, K. J., Harrison, L., Yang, J., and Chen, D. J. (2012) Persistently bound Ku at DNA ends attenuates DNA end resection and homologous recombination. *DNA Repair (Amst)*. **11**, 310–316

319. Carballar, R., Martínez-Láinez, J. M., Samper, B., Bru, S., Bállega, E., Mirallas, O., Ricco, N., Clotet, J., and Jiménez, J. (2020) CDK-mediated Yku80 Phosphorylation Regulates the Balance Between Non-homologous End Joining (NHEJ) and Homologous Directed Recombination (HDR). *J Mol Biol*. **432**, 10–12

320. Postow, L., Ghenoiu, C., Woo, E. M., Krutchinsky, A. N., Chait, B. T., and Funabiki, H. (2008) Ku80 removal from DNA through double strand break-induced ubiquitylation. *Journal of Cell Biology*. **182**, 467–479

321. Sullivan, M. R., and Bernstein, K. A. (2018) RAD-ical new insights into RAD51 regulation. *Genes (Basel)*. 10.3390/genes9120629

322. Tubbs, A., and Nussenzweig, A. (2017) Endogenous DNA Damage as a Source of Genomic Instability in Cancer. *Cell*. **168**, 644–656

323. Symington, L. S. (2014) End Resection at Double-Strand Breaks: Mechanism and Regulation. *Cold Spring Harb Perspect Biol*. **6**, a016436

324. Cannavo, E., and Cejka, P. (2014) Sae2 promotes dsDNA endonuclease activity within Mre11–Rad50–Xrs2 to resect DNA breaks. *Nature*. **514**, 122–125

325. Caron, M.-C., Sharma, A. K., O'Sullivan, J., Myler, L. R., Ferreira, M. T., Rodrigue, A., Coulombe, Y., Ethier, C., Gagne, J.-P., Langelier, M.-F., Pascal, J. M., Finkelstein, I. J., Hendzel, M. J., Poirier, G. G., and Masson, J.-Y. (2019) Poly(ADP-ribose) polymerase-1 antagonizes DNA resection at double-strand breaks. *Nat Commun*. **10**, 2954

326. Tkáč, J., Xu, G., Adhikary, H., Young, J. T. F., Gallo, D., Escribano-Díaz, C., Krietsch, J., Orthwein, A., Munro, M., Sol, W., Al-Hakim, A., Lin, Z. Y., Jonkers, J., Borst, P., Brown,

G. W., Gingras, A. C., Rottenberg, S., Masson, J. Y., and Durocher, D. (2016) HELB Is a Feedback Inhibitor of DNA End Resection. *Mol Cell*. **61**, 405–418

327. Sogo, J. M., Lopes, M., and Foiani, M. (2002) Fork reversal and ssDNA accumulation at stalled replication forks owing to checkpoint defects. *Science*. **297**, 599–602
328. Cotta-Ramusino, C., Fachinetti, D., Lucca, C., Doksani, Y., Lopes, M., Sogo, J., and Foiani, M. (2005) Exo1 processes stalled replication forks and counteracts fork reversal in checkpoint-defective cells. *Mol Cell*. **17**, 153–159
329. Zellweger, R., Dalcher, D., Mutreja, K., Berti, M., Schmid, J. A., Herrador, R., Vindigni, A., and Lopes, M. (2015) Rad51-mediated replication fork reversal is a global response to genotoxic treatments in human cells. *J Cell Biol*. **208**, 563–579
330. Hashimoto, Y., Ray Chaudhuri, A., Lopes, M., and Costanzo, V. (2010) Rad51 protects nascent DNA from Mre11-dependent degradation and promotes continuous DNA synthesis. *Nat Struct Mol Biol*. **17**, 1305–1311
331. Thangavel, S., Berti, M., Levikova, M., Pinto, C., Gomathinayagam, S., Vujanovic, M., Zellweger, R., Moore, H., Lee, E. H., Hendrickson, E. A., Cejka, P., Stewart, S., Lopes, M., and Vindigni, A. (2015) DNA2 drives processing and restart of reversed replication forks in human cells. *J Cell Biol*. **208**, 545–562
332. Mijic, S., Zellweger, R., Chappidi, N., Berti, M., Jacobs, K., Mutreja, K., Ursich, S., Ray Chaudhuri, A., Nussenzweig, A., Janscak, P., and Lopes, M. (2017) Replication fork reversal triggers fork degradation in BRCA2-defective cells. *Nat Commun*. **8**, 859
333. Ray Chaudhuri, A., Callen, E., Ding, X., Gogola, E., Duarte, A. A., Lee, J.-E., Wong, N., Lafarga, V., Calvo, J. A., Panzarino, N. J., John, S., Day, A., Crespo, A. V., Shen, B., Starnes, L. M., de Ruiter, J. R., Daniel, J. A., Konstantinopoulos, P. A., Cortez, D., Cantor, S. B., Fernandez-Capetillo, O., Ge, K., Jonkers, J., Rottenberg, S., Sharan, S. K., and Nussenzweig, A. (2016) Replication fork stability confers chemoresistance in BRCA-deficient cells. *Nature*. **535**, 382–387
334. Dungrawala, H., Rose, K. L., Bhat, K. P., Mohni, K. N., Glick, G. G., Couch, F. B., and Cortez, D. (2015) The Replication Checkpoint Prevents Two Types of Fork Collapse without Regulating Replisome Stability. *Mol Cell*. **59**, 998–1010

335. Gu, B., and Chen, P. L. (2009) Expression of PCNA-binding domain of CtIP, a motif required for CtIP localization at DNA replication foci, causes DNA damage and activation of DNA damage checkpoint. *Cell Cycle*. **8**, 1409–1420

336. Przetocka, S., Porro, A., Bolck, H. A., Walker, C., Lezaja, A., Trenner, A., von Aesch, C., Himmels, S.-F., D'Andrea, A. D., Ceccaldi, R., Altmeyer, M., Sartori, A. A., D'Andrea, A. D., Ceccaldi, R., Altmeyer, M., and Sartori, A. A. (2018) CtIP-Mediated Fork Protection Synergizes with BRCA1 to Suppress Genomic Instability upon DNA Replication Stress. *Mol Cell*. **72**, 1–15

337. Yeo, J. E., Lee, E. H., Hendrickson, E. A., and Sobeck, A. (2014) CtIP mediates replication fork recovery in a FANCD2-regulated manner. *Hum Mol Genet*. **23**, 3695–3705

338. Moldovan, G. L., Pfander, B., and Jentsch, S. (2007) PCNA, the Maestro of the Replication Fork. *Cell*. **129**, 665–679

339. Dantuma, N. P., and van Attikum, H. (2016) Spatiotemporal regulation of posttranslational modifications in the DNA damage response. *EMBO J*. **35**, 6–23

340. Yu, X., Fu, S., Lai, M., Baer, R., Chen, J., Breast, B., and Susceptibility, C. (2006) BRCA1 ubiquitinates its binding partner CtIP. *Genes Dev*. **1**, 1721–1726

341. Li, S., Ting, N. S. Y., Zheng, L., Chen, P., Ziv, Y., Shiloh, Y., Lee, E. Y. P., and Lee, W. (2000) Functional link of BRCA1 and ataxia telangiectasia gene product in DNA damage response. *Nature*. **406**, 210–215

342. Garvin, A. J., and Morris, J. R. (2017) SUMO, a small, but powerful, regulator of double-strand break repair. *Philos Trans R Soc Lond B Biol Sci*. **372**, 20160281

343. Soria-Bretones, I., Cepeda-García, C., Checa-Rodriguez, C., Heyer, V., Reina-San-Martin, B., Soutoglou, E., and Huertas, P. (2017) DNA end resection requires constitutive sumoylation of CtIP by CBX4. *Nat Commun*. **8**, 113

344. Yuan, J., and Chen, J. (2009) N terminus of CtIP is critical for homologous recombination-mediated double-strand break repair. *Journal of Biological Chemistry*. **284**, 31746–31752

345. Liu, B., Gross, M., ten Hoeve, J., and Shuai, K. (2001) A transcriptional corepressor of Stat1 with an essential LXXLL signature motif. *Proc Natl Acad Sci U S A*. **98**, 3203–3207

346. Hendriks, I. A., D'Souza, R. C., Chang, J. G., Mann, M., and Vertegaal, A. C. O. (2015) System-wide identification of wild-type SUMO-2 conjugation sites. *Nat Commun*. **6**, 7289

347. Tatham, M. H., Rodriguez, M. S., Xirodimas, D. P., and Hay, R. T. (2009) Detection of protein SUMOylation in vivo. *Nat Protoc*. **4**, 1363–1371

348. Franken, N. A. P., Rodermond, H. M., Stap, J., Haveman, J., and van Bree, C. (2006) Clonogenic assay of cells in vitro. *Nat Protoc*. **1**, 2315–2319

349. Yu, Z., Vogel, G., Coulombe, Y., Dubeau, D., Spehalski, E., Hébert, J., Ferguson, D. O., Masson, J. Y., and Richard, S. (2012) The MRE11 GAR motif regulates DNA double-strand break processing and ATR activation. *Cell Res*. **22**, 305–320

350. He, Y. J., Meghani, K., Caron, M.-C., Yang, C., Ronato, D. A., Bian, J., Sharma, A., Moore, J., Niraj, J., Detappe, A., Doench, J. G., Legube, G., Root, D. E., D'Andrea, A. D., Drané, P., De, S., Konstantinopoulos, P. A., Masson, J.-Y., and Chowdhury, D. (2018) DYNLL1 binds to MRE11 to limit DNA end resection in BRCA1-deficient cells. *Nature*. **563**, 522–526

351. Fukuda, I., Ito, A., Hirai, G., Nishimura, S., Kawasaki, H., Saitoh, H., Kimura, K. ichi, Sodeoka, M., and Yoshida, M. (2009) Ginkgolic Acid Inhibits Protein SUMOylation by Blocking Formation of the E1-SUMO Intermediate. *Chem Biol*. **16**, 133–140

352. Pierce, A. J., Johnson, R. D., Thompson, L. H., and Jasin, M. (1999) XRCC3 promotes homology-directed repair of DNA damage in mammalian cells. *Genes Dev*. **13**, 2633–2638

353. Colombo, R., Boggio, R., Seiser, C., Draetta, G. F., and Chiocca, S. (2002) The adenovirus protein Gam1 interferes with sumoylation of histone deacetylase 1. *EMBO Rep*. **3**, 1062–1068

354. Chiocca, S., Baker, A., and Cotten, M. (1997) Identification of a novel antiapoptotic protein, GAM-1, encoded by the CELO adenovirus. *J Virol*. **71**, 3168–3177

355. Boggio, R., Colombo, R., Hay, R. T., Draetta, G. F., and Chiocca, S. (2004) A mechanism for inhibiting the SUMO pathway. *Mol Cell*. **16**, 549–561

356. Boggio, R., Passafaro, A., and Chiocca, S. (2007) Targeting SUMO E1 to ubiquitin ligases: A viral strategy to counteract sumoylation. *Journal of Biological Chemistry*. **282**, 15376–15382

357. Chen, W.-T., Alpert, A., Leiter, C., Gong, F., Jackson, S. P., and Miller, K. M. (2013) Systematic Identification of Functional Residues in Mammalian Histone H2AX. *Mol Cell Biol*. **33**, 111–126

358. Liu, L. F., Desai, S. D., Li, T. K., Mao, Y., Sun, M., and Sim, S. P. (2000) Mechanism of action of camptothecin. *Ann N Y Acad Sci*. **922**, 1–10

359. Ray Chaudhuri, A., Hashimoto, Y., Herrador, R., Neelsen, K. J., Fachinetti, D., Bermejo, R., Cocito, A., Costanzo, V., and Lopes, M. (2012) Topoisomerase I poisoning results in PARP-mediated replication fork reversal. *Nat Struct Mol Biol*. **19**, 417–423

360. Singh, A., and Xu, Y.-J. (2016) The Cell Killing Mechanisms of Hydroxyurea. *Genes (Basel)*. **7**, 99

361. Xiao, Z., Chang, J.-G., Hendriks, I. A., Sigurðsson, J. O., Olsen, J. V., and Vertegaal, A. C. O. (2015) System-wide Analysis of SUMOylation Dynamics in Response to Replication Stress Reveals Novel Small Ubiquitin-like Modified Target Proteins and Acceptor Lysines Relevant for Genome Stability. *Molecular & Cellular Proteomics*. **14**, 1419–1434

362. Yu, X., and Baer, R. (2000) Nuclear localization and cell cycle-specific expression of CtIP, a protein that associates with the BRCA1 tumor suppressor. *Journal of Biological Chemistry*. **275**, 18541–18549

363. Hustedt, N., and Durocher, D. (2017) The control of DNA repair by the cell cycle. *Nat Cell Biol*. **19**, 1–9

364. Tadesse, S., Caldon, E. C., Tilley, W., and Wang, S. (2019) Cyclin-Dependent Kinase 2 Inhibitors in Cancer Therapy: An Update. *J Med Chem*. **62**, 4233–4251

365. Bach, S., Knockaert, M., Reinhardt, J., Lozach, O., Schmitt, S., Baratte, B., Koken, M., Coburn, S. P., Tang, L., Jiang, T., Liang, D.-C., Galons, H., Dierick, J.-F., Pinna, L. A., Meggio, F., Totzke, F., Schächtele, C., Lerman, A. S., Carnero, A., Wan, Y., Gray, N., and Meijer, L. (2005) Roscovitine Targets, Protein Kinases and Pyridoxal Kinase. *Journal of Biological Chemistry*. **280**, 31208–31219

366. Byth, K. F., Thomas, A., Hughes, G., Forder, C., McGregor, A., Geh, C., Oakes, S., Green, C., Walker, M., Newcombe, N., Green, S., Growcott, J., Barker, A., and Wilkinson, R. W. (2009) AZD5438, a potent oral inhibitor of cyclin-dependent kinases 1, 2, and 9, leads to pharmacodynamic changes and potent antitumor effects in human tumor xenografts. *Mol Cancer Ther*. **8**, 1856–1866

367. Vassilev, L. T., Tovar, C., Chen, S., Knezevic, D., Zhao, X., Sun, H., Heimbrook, D. C., and Chen, L. (2006) Selective small-molecule inhibitor reveals critical mitotic functions of human CDK1. *Proc Natl Acad Sci U S A*. **103**, 10660–10665

368. Traven, A., and Heierhorst, J. (2005) SQ/TQ cluster domains: concentrated ATM/ATR kinase phosphorylation site regions in DNA-damage-response proteins. *BioEssays*. **27**, 397–407

369. Warbrick, E. (1998) PCNA binding through a conserved motif. *BioEssays*. **20**, 195–199

370. Bernier-Villamor, V., Sampson, D. A., Matunis, M. J., and Lima, C. D. (2002) Structural basis for E2-mediated SUMO conjugation revealed by a complex between ubiquitin-conjugating enzyme Ubc9 and RanGAP1. *Cell*. **108**, 345–356

371. Mohiuddin, M., Evans, T. J., Rahman, M. M., Keka, I. S., Tsuda, M., Sasanuma, H., and Takeda, S. (2018) SUMOylation of PCNA by PIAS1 and PIAS4 promotes template switch in the chicken and human B cell lines. *Proc Natl Acad Sci U S A*. **115**, 12793–12798

372. Sarangi, P., Steinacher, R., Altmannova, V., Fu, Q., Paull, T. T., Krejci, L., Whitby, M. C., and Zhao, X. (2015) Sumoylation Influences DNA Break Repair Partly by Increasing the Solubility of a Conserved End Resection Protein. *PLoS Genet*. **11**, e1004899

373. Bowman, E. A., and Kelly, W. G. (2014) RNA polymerase II transcription elongation and Pol II CTD Ser2 phosphorylation: A tail of two kinases. *Nucleus*. **5**, 224–236

374. Dohadwala, M., da Cruz e Silva, E. F., Hall, F. L., Williams, R. T., Carbonaro-Hall, D. A., Nairn, A. C., Greengard, P., and Berndt, N. (1994) Phosphorylation and inactivation of protein phosphatase 1 by cyclin-dependent kinases. *Proc Natl Acad Sci U S A*. **91**, 6408–6412

375. Sakamoto, Y., Watanabe, S., Ichimura, T., Kawasuji, M., Koseki, H., Baba, H., and Nakao, M. (2007) Overlapping roles of the methylated DNA-binding protein MBD1 and polycomb group proteins in transcriptional repression of HOXA genes and heterochromatin foci formation. *J Biol Chem*. **282**, 16391–16400

376. Lin, X., Liang, M., Liang, Y.-Y., Brunicardi, F. C., and Feng, X.-H. (2003) SUMO-1/Ubc9 promotes nuclear accumulation and metabolic stability of tumor suppressor Smad4. *J Biol Chem*. **278**, 31043–31048

377. Densham, R. M., Garvin, A. J., Stone, H. R., Strachan, J., Baldock, R. A., Daza-Martin, M., Fletcher, A., Blair-Reid, S., Beesley, J., Johal, B., Pearl, L. H., Neely, R., Keep, N. H., Watts, F. Z., and Morris, J. R. (2016) Human BRCA1-BARD1 ubiquitin ligase activity counteracts chromatin barriers to DNA resection. *Nat Struct Mol Biol*. **23**, 647–655

378. Stewart, G. S., Panier, S., Townsend, K., Al-Hakim, A. K., Kolas, N. K., Miller, E. S., Nakada, S., Ylanko, J., Olivarius, S., Mendez, M., Oldreive, C., Wildenhain, J., Tagliaferro, A., Pelletier, L., Taubenheim, N., Durandy, A., Byrd, P. J., Stankovic, T., Taylor, A. M., and Durocher, D. (2009) The RIDDLE syndrome protein mediates a ubiquitin-dependent signaling cascade at sites of DNA damage. *Cell*. **136**, 420–434

379. Wang, H., Wang, L., Erdjument-Bromage, H., Vidal, M., Tempst, P., Jones, R. S., and Zhang, Y. (2004) Role of histone H2A ubiquitination in Polycomb silencing. *Nature*. **431**, 873–878

380. Yuan, G., Ma, B., Yuan, W., Zhang, Z., Chen, P., Ding, X., Feng, L., Shen, X., Chen, S., Li, G., and Zhu, B. (2013) Histone H2A ubiquitination inhibits the enzymatic activity of H3 lysine 36 methyltransferases. *Journal of Biological Chemistry*. 10.1074/jbc.M113.475996

381. Simon, J. A., and Kingston, R. E. (2013) Occupying Chromatin: Polycomb Mechanisms for Getting to Genomic Targets, Stopping Transcriptional Traffic, and Staying Put. *Mol Cell*. 10.1016/j.molcel.2013.02.013

382. Fitieh, A., Locke, A. J., Motamedi, M., and Ismail, I. H. (2021) The role of polycomb group protein BMI1 in DNA repair and genomic stability. *Int J Mol Sci*. 10.3390/ijms22062976

383. de Napoles, M., Mermoud, J. E., Wakao, R., Tang, Y. A., Endoh, M., Appanah, R., Nesterova, T. B., Silva, J., Otte, A. P., Vidal, M., Koseki, H., and Brockdorff, N. (2004) Polycomb group proteins ring1A/B link ubiquitylation of histone H2A to heritable gene silencing and X inactivation. *Dev Cell*. 10.1016/j.devcel.2004.10.005

384. Cao, R., Tsukada, Y. I., and Zhang, Y. (2005) Role of Bmi-1 and Ring1A in H2A ubiquitylation and hox gene silencing. *Mol Cell*. 10.1016/j.molcel.2005.12.002

385. Wei, J., Zhai, L., Xu, J., and Wang, H. (2006) Role of Bmi1 in H2A ubiquitylation and Hox gene silencing. *Journal of Biological Chemistry*. 10.1074/jbc.M600826200

386. Kakarougkas, A., Downs, J. A., and Jeggo, P. A. (2015) The PBAF chromatin remodeling complex represses transcription and promotes rapid repair at DNA double-strand breaks. *Mol Cell Oncol*. **2**, e970072

387. Kakarougkas, A., Ismail, A., Chambers, A. L., Riballo, E., Herbert, A. D., Kunzel, J., Lobrich, M., Jeggo, P. A., and Downs, J. A. (2014) Requirement for PBAF in transcriptional repression and repair at DNA breaks in actively transcribed regions of chromatin. *Mol Cell*. **55**, 723–732

388. Izhar, L., Adamson, B., Ciccia, A., Lewis, J., Pontano-Vaites, L., Leng, Y., Liang, A. C., Westbrook, T. F., Harper, J. W., and Elledge, S. J. (2015) A Systematic Analysis of Factors Localized to Damaged Chromatin Reveals PARP-Dependent Recruitment of Transcription Factors. *Cell Rep*. **11**, 1486–1500

389. Sanchez, A., De Vivo, A., Uprety, N., Kim, J., Stevens Jr., S. M., and Kee, Y. (2016) BMI1-UBR5 axis regulates transcriptional repression at damaged chromatin. *Proc Natl Acad Sci U S A*. **113**, 11243–11248

390. Shanbhag, N. M., Rafalska-Metcalf, I. U., Balane-Bolivar, C., Janicki, S. M., and Greenberg, R. A. (2010) ATM-dependent chromatin changes silence transcription in cis to DNA double-strand breaks. *Cell*. **141**, 970–981

391. Ui, A., Nagaura, Y., and Yasui, A. (2015) Transcriptional elongation factor ENL phosphorylated by ATM recruits polycomb and switches off transcription for DSB repair. *Mol Cell*. **58**, 468–482

392. Ismail, I. H., McDonald, D., Strickfaden, H., Xu, Z., and Hendzel, M. J. (2013) A small molecule inhibitor of polycomb repressive complex 1 inhibits ubiquitin signaling at DNA double-strand breaks. *J Biol Chem*. **288**, 26944–26954

393. Campbell, S., Ismail, I. H., Young, L. C., Poirier, G. G., and Hendzel, M. J. (2013) Polycomb repressive complex 2 contributes to DNA double-strand break repair. *Cell Cycle*. 10.4161/cc.25795

394. Lagarou, A., Mohd-Sarip, A., Moshkin, Y. M., Chalkley, G. E., Bezstarosti, K., Demmers, J. A., and Verrijzer, C. P. (2008) dKDM2 couples histone H2A ubiquitylation to histone H3 demethylation during Polycomb group silencing. *Genes Dev*. **22**, 2799–2810

395. Densham, R. M., and Morris, J. R. (2019) Moving Mountains-The BRCA1 Promotion of DNA Resection. *Front Mol Biosci*. **6**, 79

396. Marini, F., Rawal, C. C., Liberi, G., and Pellicioli, A. (2019) Regulation of DNA Double Strand Breaks Processing: Focus on Barriers. *Front Mol Biosci*. 10.3389/fmolb.2019.00055

397. Symington, L. S. (2014) End resection at double-strand breaks: Mechanism and regulation. *Cold Spring Harb Perspect Biol*. 10.1101/cshperspect.a016436

398. Pan, M. R., Hsieh, H. J., Dai, H., Hung, W. C., Li, K., Peng, G., and Lin, S. Y. (2012) Chromodomain helicase DNA-binding protein 4 (CHD4) regulates homologous

recombination DNA repair, and its deficiency sensitizes cells to poly(ADP-ribose) polymerase (PARP) inhibitor treatment. *J Biol Chem*. **287**, 6764–6772

399. Janicki, S. M., Tsukamoto, T., Salghetti, S. E., Tansey, W. P., Sachidanandam, R., Prasanth, K. V., Ried, T., Shav-Tal, Y., Bertrand, E., Singer, R. H., and Spector, D. L. (2004) From silencing to gene expression: Real-time analysis in single cells. *Cell*. **116**, 683–698
400. Mali, P., Yang, L., Esvelt, K. M., Aach, J., Guell, M., DiCarlo, J. E., Norville, J. E., and Church, G. M. (2013) RNA-guided human genome engineering via Cas9. *Science*. **339**, 823–826
401. Ventii, K. H., Devi, N. S., Friedrich, K. L., Chernova, T. A., Tighiouart, M., Van Meir, E. G., and Wilkinson, K. D. (2008) BRCA1-associated protein-1 is a tumor suppressor that requires deubiquitinating activity and nuclear localization. *Cancer Res*. **68**, 6953–6962
402. Cooper, S., Grijzenhout, A., Underwood, E., Ancelin, K., Zhang, T., Nesterova, T. B., Anil-Kirmizitas, B., Bassett, A., Kooistra, S. M., Agger, K., Helin, K., Heard, E., and Brockdorff, N. (2016) Jarid2 binds mono-ubiquitylated H2A lysine 119 to mediate crosstalk between Polycomb complexes PRC1 and PRC2. *Nat Commun*. **7**, 1–8
403. Sowa, M. E., Bennett, E. J., Gygi, S. P., and Harper, J. W. (2009) Defining the human deubiquitinating enzyme interaction landscape. *Cell*. **138**, 389–403
404. Elmroth, K., Nygren, J., Mårtensson, S., Ismail, I. H., and Hammarsten, O. (2003) Cleavage of cellular DNA by calicheamicin gamma1. *DNA Repair (Amst)*. **2**, 363–374
405. Zhou, Y., Caron, P., Legube, G., and Paull, T. T. (2014) Quantitation of DNA double-strand break resection intermediates in human cells. *Nucleic Acids Res*. **42**, 1–11
406. Cohen, S., Puget, N., Lin, Y. L., Clouaire, T., Aguirrebengoa, M., Rocher, V., Pasero, P., Canitrot, Y., and Legube, G. (2018) Senataxin resolves RNA:DNA hybrids forming at DNA double-strand breaks to prevent translocations. *Nat Commun*. 10.1038/s41467-018-02894-w
407. Wu, Y., Li, Q., and Chen, X.-Z. (2007) Detecting protein-protein interactions by Far western blotting. *Nat Protoc*. **2**, 3278–3284
408. Pierce, A. J., Johnson, R. D., Thompson, L. H., and Jasin, M. (1999) XRCC3 promotes homology-directed repair of DNA damage in mammalian cells. *Genes Dev*. **13**, 2633–2638
409. Kreso, A., van Galen, P., Pedley, N. M., Lima-Fernandes, E., Frelin, C., Davis, T., Cao, L., Baiazitov, R., Du, W., Sydorenko, N., Moon, Y.-C., Gibson, L., Wang, Y., Leung, C., Iscove,

N. N., Arrowsmith, C. H., Szentgyorgyi, E., Gallinger, S., Dick, J. E., and O'Brien, C. A. (2014) Self-renewal as a therapeutic target in human colorectal cancer. *Nat Med*. **20**, 29–36

410. Nishida, Y., Maeda, A., Chachad, D., Ishizawa, J., Qiu, Y. H., Kornblau, S. M., Kimura, S., Andreeff, M., and Kojima, K. (2015) Preclinical activity of the novel B-cell-specific Moloney murine leukemia virus integration site 1 inhibitor PTC-209 in acute myeloid leukemia: Implications for leukemia therapy. *Cancer Sci*. **106**, 1705–1713
411. Yong, K. J., Basseres, D. S., Welner, R. S., Zhang, W. C., Yang, H., Yan, B., Alberich-Jorda, M., Zhang, J., de Figueiredo-Pontes, L. L., Battelli, C., Hetherington, C. J., Ye, M., Zhang, H., Maroni, G., O'Brien, K., Magli, M. C., Borczuk, A. C., Varticovski, L., Kocher, O., Zhang, P., Moon, Y.-C., Sydorenko, N., Cao, L., Davis, T. W., Thakkar, B. M., Soo, R. A., Iwama, A., Lim, B., Halmos, B., Neuberg, D., Tenen, D. G., and Levantini, E. (2016) Targeted BMI1 inhibition impairs tumor growth in lung adenocarcinomas with low CEBPα expression. *Sci Transl Med*. **8**, 350ra104
412. Haring, S. J., Mason, A. C., Binz, S. K., and Wold, M. S. (2008) Cellular functions of human RPA1. Multiple roles of domains in replication, repair, and checkpoints. *J Biol Chem*. **283**, 19095–19111
413. Liu, S., Opiyo, S. O., Manthey, K., Glanzer, J. G., Ashley, A. K., Amerin, C., Troksa, K., Shrivastav, M., Nickoloff, J. A., and Oakley, G. G. (2012) Distinct roles for DNA-PK, ATM and ATR in RPA phosphorylation and checkpoint activation in response to replication stress. *Nucleic Acids Res*. **40**, 10780–10794
414. Maréchal, A., and Zou, L. (2015) RPA-coated single-stranded DNA as a platform for post-translational modifications in the DNA damage response. *Cell Res*. **25**, 9–23
415. Kakarougkas, A., Ismail, A., Chambers, A. L., Riballo, E., Herbert, A. D., Künzel, J., Löbrich, M., Jeggo, P. A., and Downs, J. A. (2014) Requirement for PBAF in Transcriptional Repression and Repair at DNA Breaks in Actively Transcribed Regions of Chromatin. *Mol Cell*. **55**, 723–732
416. Manfrini, N., Clerici, M., Wery, M., Colombo, C. V., Descrimes, M., Morillon, A., d'Adda di Fagagna, F., and Longhese, M. P. (2015) Resection is responsible for loss of transcription around a double-strand break in Saccharomyces cerevisiae. *Elife*. 10.7554/eLife.08942
417. Caron, P., Pankotai, T., Wiegant, W. W., Tollenaere, M. A. X., Furst, A., Bonhomme, C., Helfricht, A., de Groot, A., Pastink, A., Vertegaal, A. C. O., Luijsterburg, M. S., Soutoglou,

E., and van Attikum, H. (2019) WWP2 ubiquitylates RNA polymerase II for DNA-PK-dependent transcription arrest and repair at DNA breaks. *Genes Dev*. **33**, 684–704

418. Ismail, I. H., Davidson, R., Gagné, J.-P., Xu, Z. Z., Poirier, G. G., and Hendzel, M. J. (2014) Germline mutations in BAP1 impair its function in DNA double-strand break repair. *Cancer Res*. **74**, 4282–4294
419. Scheuermann, J. C., de Ayala Alonso, A. G., Oktaba, K., Ly-Hartig, N., McGinty, R. K., Fraterman, S., Wilm, M., Muir, T. W., and Müller, J. (2010) Histone H2A deubiquitinase activity of the Polycomb repressive complex PR-DUB. *Nature*. **465**, 243–247
420. Uckelmann, M., Densham, R. M., Baas, R., Winterwerp, H. H. K., Fish, A., Sixma, T. K., and Morris, J. R. (2018) USP48 restrains resection by site-specific cleavage of the BRCA1 ubiquitin mark from H2A. *Nat Commun*. **9**, 229
421. Soutoglou, E., and Misteli, T. (2008) Activation of the cellular DNA damage response in the absence of DNA lesions. *Science*. **320**, 1507–1510
422. Luijsterburg, M. S., Acs, K., Ackermann, L., Wiegant, W. W., Bekker-Jensen, S., Larsen, D. H., Khanna, K. K., van Attikum, H., Mailand, N., and Dantuma, N. P. (2012) A new non-catalytic role for ubiquitin ligase RNF8 in unfolding higher-order chromatin structure. *EMBO J*. **31**, 2511–2527
423. Hernández-Muñoz, I., Taghavi, P., Kuijl, C., Neefjes, J., and van Lohuizen, M. (2005) Association of BMI1 with polycomb bodies is dynamic and requires PRC2/EZH2 and the maintenance DNA methyltransferase DNMT1. *Mol Cell Biol*. **25**, 11047–11058
424. Murina, O., von Aesch, C., Karakus, U., Ferretti, L. P., Bolck, H. A., Hänggi, K., and Sartori, A. A. (2014) FANCD2 and CtIP cooperate to repair DNA interstrand crosslinks. *Cell Rep*. **7**, 1030–1038
425. Sanchez, A., De Vivo, A., Uprety, N., Kim, J., Stevens, S. M. J., and Kee, Y. (2016) BMI1-UBR5 axis regulates transcriptional repression at damaged chromatin. *Proc Natl Acad Sci U S A*. **113**, 11243–11248
426. Caron, P., van der Linden, J., and van Attikum, H. (2019) Bon voyage: A transcriptional journey around DNA breaks. *DNA Repair (Amst)*. **82**, 102686
427. Sewalt, R. G., Gunster, M. J., van der Vlag, J., Satijn, D. P., and Otte, A. P. (1999) C-Terminal binding protein is a transcriptional repressor that interacts with a specific class of vertebrate Polycomb proteins. *Mol Cell Biol*. **19**, 777–787

428. Satijn, D. P., Gunster, M. J., van der Vlag, J., Hamer, K. M., Schul, W., Alkema, M. J., Saurin, A. J., Freemont, P. S., van Driel, R., and Otte, A. P. (1997) RING1 is associated with the polycomb group protein complex and acts as a transcriptional repressor. *Mol Cell Biol*. **17**, 4105–4113

429. Han, J., Wan, L., Jiang, G., Cao, L., Xia, F., Tian, T., Zhu, X., Wu, M., Huen, M. S. Y., Wang, Y., Liu, T., and Huang, J. (2021) ATM controls the extent of DNA end resection by eliciting sequential posttranslational modifications of CtIP. *Proc Natl Acad Sci U S A*. 10.1073/pnas.2022600118

430. Locke, A. J., Hossain, L., McCrostie, G., Ronato, D. A., Fitieh, A., Rafique, T. A., Mashayekhi, F., Motamedi, M., Masson, J. Y., and Ismail, I. H. (2021) SUMOylation mediates CtIP's functions in DNA end resection and replication fork protection. *Nucleic Acids Res*. **49**, 928–953

431. Palijan, A., Fernandes, I., Verway, M., Kourelis, M., Bastien, Y., Tavera-Mendoza, L. E., Sacheli, A., Bourdeau, V., Mader, S., and White, J. H. (2009) Ligand-dependent corepressor LCoR is an attenuator of progesterone-regulated gene expression. *J Biol Chem*. **284**, 30275–30287

432. Unno, J., Itaya, A., Taoka, M., Sato, K., Tomida, J., Sakai, W., Sugasawa, K., Ishiai, M., Ikura, T., Isobe, T., Kurumizaka, H., and Takata, M. (2014) FANCD2 binds CtIP and regulates DNA-end resection during DNA interstrand crosslink repair. *Cell Rep*. **7**, 1039–1047

433. Marini, F., Rawal, C. C., Liberi, G., and Pellicioli, A. (2019) Regulation of DNA Double Strand Breaks Processing: Focus on Barriers. *Front Mol Biosci*. **6**, 1–8

434. Khanna, K. K., and Jackson, S. P. (2001) DNA double-strand breaks: signaling, repair and the cancer connection. *Nat Genet*. **27**, 247–254

435. Takata, M., Sasaki, M. S., Sonoda, E., Morrison, C., Hashimoto, M., Utsumi, H., Yamaguchi-Iwai, Y., Shinohara, A., and Takeda, S. (1998) Homologous recombination and non-homologous end-joining pathways of DNA double-strand break repair have overlapping roles in the maintenance of chromosomal integrity in vertebrate cells. *EMBO J*. **17**, 5497–5508

436. Scully, R., Panday, A., Elango, R., and Willis, N. A. (2019) DNA double-strand break repair-pathway choice in somatic mammalian cells. *Nat Rev Mol Cell Biol*. **20**, 698–714

437. Bekker-Jensen, S., and Mailand, N. (2015) RNF138 joins the HR team. *Nat Cell Biol*. **17**, 1375–1377

438. Békés, M., Okamoto, K., Crist, S. B., Jones, M. J., Chapman, J. R., Brasher, B. B., Melandri, F. D., Ueberheide, B. M., LazzeriniDenchi, E., and Huang, T. T. (2013) DUB-Resistant Ubiquitin to Survey Ubiquitination Switches in Mammalian Cells. *Cell Rep*. **5**, 826–838

439. Ma, H., McLean, J. R., Chao, L. F. I., Mana-Capelli, S., Paramasivam, M., Hagstrom, K. A., Gould, K. L., and McCollum, D. (2012) A highly efficient multifunctional tandem affinity purification approach applicable to diverse organisms. *Molecular and Cellular Proteomics*. **11**, 501–511

440. Meierhofer, D., Wang, X., Huang, L., and Kaiser, P. (2008) Quantitative analysis of global ubiquitination in HeLa cells by mass spectrometry. *J Proteome Res*. **7**, 4566–4576

441. Robert, X., and Gouet, P. (2014) Deciphering key features in protein structures with the new ENDscript server. *Nucleic Acids Res*. **42**, W320-4

442. Jumper, J., Evans, R., Pritzel, A., Green, T., Figurnov, M., Ronneberger, O., Tunyasuvunakool, K., Bates, R., Žídek, A., Potapenko, A., Bridgland, A., Meyer, C., Kohl, S. A. A., Ballard, A. J., Cowie, A., Romera-Paredes, B., Nikolov, S., Jain, R., Adler, J., Back, T., Petersen, S., Reiman, D., Clancy, E., Zielinski, M., Steinegger, M., Pacholska, M., Berghammer, T., Bodenstein, S., Silver, D., Vinyals, O., Senior, A. W., Kavukcuoglu, K., Kohli, P., and Hassabis, D. (2021) Highly accurate protein structure prediction with AlphaFold. *Nature*. **596**, 583–589

443. Mirdita, M., Schütze, K., Moriwaki, Y., Heo, L., Ovchinnikov, S., and Steinegger, M. (2022) ColabFold: making protein folding accessible to all. *Nat Methods*. **19**, 679–682

444. Tunyasuvunakool, K., Adler, J., Wu, Z., Green, T., Zielinski, M., Žídek, A., Bridgland, A., Cowie, A., Meyer, C., Laydon, A., Velankar, S., Kleywegt, G. J., Bateman, A., Evans, R., Pritzel, A., Figurnov, M., Ronneberger, O., Bates, R., Kohl, S. A. A., Potapenko, A., Ballard, A. J., Romera-Paredes, B., Nikolov, S., Jain, R., Clancy, E., Reiman, D., Petersen, S., Senior, A. W., Kavukcuoglu, K., Birney, E., Kohli, P., Jumper, J., and Hassabis, D. (2021) Highly accurate protein structure prediction for the human proteome. *Nature*. **596**, 590–596

445. Evans, R., O'Neill, M., Pritzel, A., Antropova, N., Senior, A., Green, T., Žídek, A., Bates, R., Blackwell, S., Yim, J., Ronneberger, O., Bodenstein, S., Zielinski, M., Bridgland, A., Potapenko, A., Cowie, A., Tunyasuvunakool, K., Jain, R., Clancy, E., Kohli, P., Jumper, J.,

and Hassabis, D. (2022) Protein complex prediction with AlphaFold-Multimer. *bioRxiv*. 10.1101/2021.10.04.463034

446. Whitman, B. T., Murray, C. R. A., Whitford, D. S., Paul, S. S., Fahlman, R. P., Glover, M. J. N., and Owttrim, G. W. (2022) Degron-mediated proteolysis of CrhR-like DEAD-box RNA helicases in cyanobacteria. *J Biol Chem*. **298**, 101925
447. Vaughn, J. P., Davis, P. L., Jarboe, M. D., Huper, G., Evans, A. C., Wiseman, R. W., Berchuck, A., Iglehart, J. D., Futreal, P. A., and Marks, J. R. (1996) BRCA1 expression is induced before DNA synthesis in both normal and tumor-derived breast cells. *Cell Growth & Differentiation*. **7**, 711–5
448. Scully, R., Chen, J., Ochs, R. L., Keegan, K., Hoekstra, M., Feunteun, J., and Livingston, D. M. (1997) Dynamic Changes of BRCA1 Subnuclear Location and Phosphorylation State Are Initiated by DNA Damage. *Cell*. **90**, 425–435
449. Ruffner, H., and Verma, I. M. (1997) BRCA1 is a cell cycle-regulated nuclear phosphoprotein. *Proc Natl Acad Sci U S A*. 10.1073/pnas.94.14.7138
450. Ma, H. T., and Poon, R. Y. C. (2017) Synchronization of HeLa Cells - Cell Cycle Synchronization: Methods and Protocols (Banfalvi, G. ed), pp. 189–201, Springer New York, New York, NY, 10.1007/978-1-4939-6603-5_12
451. Wang, C., Xu, H., Lin, S., Deng, W., Zhou, J., Zhang, Y., Shi, Y., Peng, D., and Xue, Y. (2020) GPS 5.0: An Update on the Prediction of Kinase-specific Phosphorylation Sites in Proteins. *Genomics Proteomics Bioinformatics*. **18**, 72–80
452. Boeing, S., Williamson, L., Encheva, V., Gori, I., Saunders, R. E., Instrell, R., Aygün, O., Rodriguez-Martinez, M., Weems, J. C., Kelly, G. P., Conaway, J. W., Conaway, R. C., Stewart, A., Howell, M., Snijders, A. P., and Svejstrup, J. Q. (2016) Multiomic Analysis of the UV-Induced DNA Damage Response. *Cell Rep*. **15**, 1597–1610
453. Elia, A. E. H., Boardman, A. P., Wang, D. C., Huttlin, E. L., Everley, R. A., Dephoure, N., Zhou, C., Koren, I., Gygi, S. P., and Elledge, S. J. (2015) Quantitative Proteomic Atlas of Ubiquitination and Acetylation in the DNA Damage Response. *Mol Cell*. **59**, 867–881
454. Udeshi, N. D., Svinkina, T., Mertins, P., Kuhn, E., Mani, D. R., Qiao, J. W., and Carr, S. A. (2013) Refined Preparation and Use of Anti-diglycine Remnant (K-ε-GG) Antibody Enables Routine Quantification of 10,000s of Ubiquitination Sites in Single Proteomics Experiments *. *Molecular & Cellular Proteomics*. **12**, 825–831

455. Mertins, P., Qiao, J. W., Patel, J., Udeshi, N. D., Clauser, K. R., Mani, D. R., Burgess, M. W., Gillette, M. A., Jaffe, J. D., and Carr, S. A. (2013) Integrated proteomic analysis of post-translational modifications by serial enrichment. *Nat Methods*. **10**, 634–637

456. Pommier, Y. (2006) Topoisomerase I inhibitors: Camptothecins and beyond. in *Nature Reviews Cancer*, pp. 789–802, **6**, 789–802

457. Mukherjee, B., Tomimatsu, N., and Burma, S. (2015) Immunofluorescence-Based Methods to Monitor DNA End Resection. in *Stress Responses: Methods and Protocols* (Oslowski, C. M. ed), pp. 67–75, Springer New York, New York, NY, 10.1007/978-1-4939-2522-3_5

458. Raderschall, E., Golub, E. I., and Haaf, T. (1999) Nuclear foci of mammalian recombination proteins are located at single-stranded DNA regions formed after DNA damage. *Proc Natl Acad Sci U S A*. **96**, 1921

459. Alani, E., Thresher, R., Griffith, J. D., and Kolodner, R. D. (1992) Characterization of DNA-binding and strand-exchange stimulation properties of y-RPA, a yeast single-strand-DNA-binding protein. *J Mol Biol*. **227**, 54–71

460. Chen, H., Lisby, M., and Symington, L. S. (2013) RPA Coordinates DNA End Resection and Prevents Formation of DNA Hairpins. *Mol Cell*. **50**, 589–600

461. Cruet-Hennequart, S., Glynn, M. T., Murillo, L. S., Coyne, S., and Carty, M. P. (2008) Enhanced DNA-PK-mediated RPA2 hyperphosphorylation in DNA polymerase eta-deficient human cells treated with cisplatin and oxaliplatin. *DNA Repair (Amst)*. **7**, 582–596

462. Binz, S. K., Sheehan, A. M., and Wold, M. S. (2004) Replication Protein A phosphorylation and the cellular response to DNA damage. *DNA Repair (Amst)*. **3**, 1015–1024

463. Mukherjee, S., Chakraborty, P., and Saha, P. (2016) Phosphorylation of Ku70 subunit by cell cycle kinases modulates the replication related function of Ku heterodimer. *Nucleic Acids Res*. **44**, 7755–7765

464. Mariani, V., Biasini, M., Barbato, A., and Schwede, T. (2013) lDDT: a local superposition-free score for comparing protein structures and models using distance difference tests. *Bioinformatics*. **29**, 2722–2728

465. Dhingra, N., and Zhao, X. (2021) Advances in SUMO-based regulation of homologous recombination. *Curr Opin Genet Dev*. **71**, 114–119

466. Dhingra, N., and Zhao, X. (2019) Intricate SUMO-based control of the homologous recombination machinery. *Genes Dev*. **33**, 1346–1354

467. Lisby, M., Barlow, J. H., Burgess, R. C., and Rothstein, R. (2004) Choreography of the DNA Damage Response: Spatiotemporal Relationships among Checkpoint and Repair Proteins. *Cell*. **118**, 699–713

468. Kim, J. S., Krasieva, T. B., Kurumizaka, H., Chen, D. J., Taylor, A. M. R., and Yokomori, K. (2005) Independent and sequential recruitment of NHEJ and HR factors to DNA damage sites in mammalian cells. *Journal of Cell Biology*. **170**, 341–347

469. Yang, G., Liu, C., Chen, S.-H., Kassab, M. A., Hoff, J. D., Walter, N. G., and Yu, X. (2018) Super-resolution imaging identifies PARP1 and the Ku complex acting as DNA double-strand break sensors. *Nucleic Acids Res*. **46**, 3446–3457

470. Shim, E. Y., Hong, S. J., Oum, J.-H., Yanez, Y., Zhang, Y., and Lee, S. E. (2007) RSC mobilizes nucleosomes to improve accessibility of repair machinery to the damaged chromatin. *Mol Cell Biol*. **27**, 1602–1613

471. Mimitou, E. P., and Symington, L. S. (2010) Ku prevents Exo1 and Sgs1-dependent resection of DNA ends in the absence of a functional MRX complex or Sae2. *EMBO J*. **29**, 3358–3369

472. Deshpande, R. A., Myler, L. R., Soniat, M. M., Makharashvili, N., Lee, L., Lees-Miller, S. P., Finkelstein, I. J., and Paull, T. T. (2020) DNA-dependent protein kinase promotes DNA end processing by MRN and CtIP. *Sci Adv*. **6**, eaay0922

473. Deshpande, R. A., Marin-Gonzalez, A., Barnes, H. K., Woolley, P. R., Ha, T., and Paull, T. T. (2023) Genome-wide analysis of DNA-PK-bound MRN cleavage products supports a sequential model of DSB repair pathway choice. *Nat Commun*. **14**, 1–17

474. Elegheert, J., Behiels, E., Bishop, B., Scott, S., Woolley, R. E., Griffiths, S. C., Byrne, E. F. X., Chang, V. T., Stuart, D. I., Jones, E. Y., Siebold, C., and Aricescu, A. R. (2018) Lentiviral transduction of mammalian cells for fast, scalable and high-level production of soluble and membrane proteins. *Nat Protoc*. **13**, 2991–3017

475. Fottner, M., Brunner, A. D., Bittl, V., Horn-Ghetko, D., Jussupow, A., Kaila, V. R. I., Bremm, A., and Lang, K. (2019) Site-specific ubiquitylation and SUMOylation using genetic-code expansion and sortase. *Nat Chem Biol*. **15**, 276–284

476. Chen, Y.-J., Chuang, Y.-C., Chuang, C.-N., Cheng, Y.-H., Chang, C.-R., Leng, C.-H., and Wang, T.-F. (2016) S. cerevisiae Mre11 recruits conjugated SUMO moieties to facilitate the

assembly and function of the Mre11-Rad50-Xrs2 complex. *Nucleic Acids Res*. **44**, 2199–2213

477. Acharya, A., Kasaciunaite, K., Göse, M., Kissling, V., Guérois, R., Seidel, R., and Cejka, P. (2021) Distinct RPA domains promote recruitment and the helicase-nuclease activities of Dna2. *Nat Commun*. 10.1038/s41467-021-26863-y
478. D'Alessandro, G., and d'Adda di Fagagna, F. (2017) Transcription and DNA Damage: Holding Hands or Crossing Swords? *J Mol Biol*. **429**, 3215–3229
479. Zong, D., Oberdoerffer, P., Batista, P. J., and Nussenzweig, A. (2020) RNA: a double-edged sword in genome maintenance. *Nat Rev Genet*. 10.1038/s41576-020-0263-7
480. Fitieh, A., Locke, A. J., Mashayekhi, F., Khaliqdina, F., Sharma, A. K., and Ismail, I. H. (2022) BMI-1 regulates DNA end resection and homologous recombination repair. *Cell Rep*. **38**, 110536
481. Michelini, F., Pitchiaya, S., Vitelli, V., Sharma, S., Gioia, U., Pessina, F., Cabrini, M., Wang, Y., Capozzo, I., Iannelli, F., Matti, V., Francia, S., Shivashankar, G. V., Walter, N. G., and Di Fagagna, F. D. A. (2017) Damage-induced lncRNAs control the DNA damage response through interaction with DDRNAs at individual double-strand breaks. *Nat Cell Biol*. **19**, 1400–1411
482. Ohle, C., Tesorero, R., Schermann, G., Dobrev, N., Sinning, I., and Fischer, T. (2016) Transient RNA-DNA Hybrids Are Required for Efficient Double-Strand Break Repair. *Cell*. **167**, 1001-1013.e7
483. Sharma, S., Anand, R., Zhang, X., Francia, S., Michelini, F., Galbiati, A., Williams, H., Ronato, D. A., Masson, J.-Y., Rothenberg, E., Cejka, P., and d'Adda di Fagagna, F. (2021) MRE11-RAD50-NBS1 Complex Is Sufficient to Promote Transcription by RNA Polymerase II at Double-Strand Breaks by Melting DNA Ends. *Cell Rep*. **34**, 108565
484. Aymard, F., Bugler, B., Schmidt, C. K., Guillou, E., Caron, P., Briois, S., Iacovoni, J. S., Daburon, V., Miller, K. M., Jackson, S. P., and Legube, G. (2014) Transcriptionally active chromatin recruits homologous recombination at DNA double-strand breaks. *Nat Struct Mol Biol*. **21**, 366–374
485. Ouyang, J., Yadav, T., Zhang, J. M., Yang, H., Rheinbay, E., Guo, H., Haber, D. A., Lan, L., and Zou, L. (2021) RNA transcripts stimulate homologous recombination by forming DR-loops. *Nature*. **594**, 283–288

486. Liu, S., Hua, Y., Wang, J., Li, L., Yuan, J., Zhang, B., Wang, Z., Ji, J., and Kong, D. (2021) RNA polymerase III is required for the repair of DNA double-strand breaks by homologous recombination. *Cell*. **184**, 1314-1329.e10

487. Grau, D. J., Chapman, B. A., Garlick, J. D., Borowsky, M., Francis, N. J., and Kingston, R. E. (2011) Compaction of chromatin by diverse Polycomb group proteins requires localized regions of high charge. 10.1101/gad.17288211.Lys

488. Francis, N. J., Kingston, R. E., and Woodcock, C. L. (2004) Chromatin Compaction by a Polycomb Group Protein Complex. **306**, 1574–1578

489. Eskeland, R., Leeb, M., Grimes, G. R., Kress, C., Boyle, S., Sproul, D., Gilbert, N., Fan, Y., Skoultchi, A. I., Wutz, A., and Bickmore, W. A. (2010) Ring1B Compacts Chromatin Structure and Represses Gene Expression Independent of Histone Ubiquitination. *Mol Cell*. **38**, 452–464

490. Kundu, S., Ji, F., Sunwoo, H., Jain, G., Lee, J. T., Sadreyev, R. I., Dekker, J., and Kingston, R. E. (2017) Polycomb Repressive Complex 1 Generates Discrete Compacted Domains that Change during Differentiation. *Mol Cell*. **65**, 432-446.e5

491. Wertz, I. E., O'Rourke, K. M., Zhou, H., Eby, M., Aravind, L., Seshagiri, S., Wu, P., Wiesmann, C., Baker, R., Boone, D. L., Ma, A., Koonin, E. V, and Dixit, V. M. (2004) De-ubiquitination and ubiquitin ligase domains of A20 downregulate NF-κB signalling. *Nature*. **430**, 694–699

492. Yang, C., Zang, W., Tang, Z., Ji, Y., Xu, R., Yang, Y., Luo, A., Hu, B., Zhang, Z., Liu, Z., and Zheng, X. (2018) A20/TNFAIP3 regulates the DNA damage response and mediates tumor cell resistance to DNA-damaging therapy. *Cancer Res*. **78**, 1069–1082

493. Thompson, L. L., Rutherford, K. A., Lepage, C. C., and McManus, K. J. (2021) The SCF complex is essential to maintain genome and chromosome stability. *Int J Mol Sci*. 10.3390/ijms22168544

494. Li, F., Mladenov, E., Mortoga, S., and Iliakis, G. (2020) SCFSKP2 regulates APC/CCDH1-mediated degradation of CTIP to adjust DNA-end resection in G2-phase. *Cell Death Dis*. 10.1038/s41419-020-02755-9

495. Tomimatsu, N., Mukherjee, B., Harris, J. L., Boffo, F. L., Hardebeck, M. C., Potts, P. R., Khanna, K. K., and Burma, S. (2017) DNA-damage-induced degradation of EXO1

exonuclease limits DNA end resection to ensure accurate DNA repair. *Journal of Biological Chemistry* . **292**, 10779–10790

496. Postow, L., and Funabiki, H. (2013) An SCF complex containing Fbxl12 mediates DNA damage-induced Ku80 ubiquitylation. *Cell Cycle*. **12**, 587–595
497. Wu, J., Zhang, X., Zhang, L., Wu, C. Y., Rezaeian, A. H., Chan, C. H., Li, J. M., Wang, J., Gao, Y., Han, F., Jeong, Y. S., Yuan, X., Khanna, K. K., Jin, J., Zeng, Y. X., and Lin, H. K. (2012) Skp2 E3 Ligase Integrates ATM Activation and Homologous Recombination Repair by Ubiquitinating NBS1. *Mol Cell*. **46**, 351–361
498. Evans, P. C., Ovaa, H., Hamon, M., Kilshaw, P. J., Hamm, S., Bauer, S., Ploegh, H. L., and Smith, T. S. (2004) Zinc-finger protein A20, a regulator of inflammation and cell survival, has de-ubiquitinating activity. *Biochemical Journal*. **378**, 727–734
499. Luo, K., Deng, M., Li, Y., Wu, C., Xu, Z., Yuan, J., and Lou, Z. (2015) CDK-mediated RNF4 phosphorylation regulates homologous recombination in S-phase. *Nucleic Acids Res*. **43**, 5465–5475
500. Raaphorst, F. M. (2003) Self-renewal of hematopoietic and leukemic stem cells: a central role for the Polycomb-group gene Bmi-1. *Trends Immunol*. **24**, 522–524
501. Xu, J., Li, L., Shi, P., Cui, H., and Yang, L. (2022) The Crucial Roles of Bmi-1 in Cancer: Implications in Pathogenesis, Metastasis, Drug Resistance, and Targeted Therapies. *Int J Mol Sci*. 10.3390/ijms23158231
502. Wang, M.-C., Li, C.-L., Cui, J., Jiao, M., Wu, T., Jing, L. I., and Nan, K.-J. (2015) BMI-1, a promising therapeutic target for human cancer. *Oncol Lett*. **10**, 583–588
503. Rouhigharabaei, L., Ferreiro, J. F., Put, N., Michaux, L., Tousseyn, T., Lefebvre, C., Gardiner, A., De Kelver, W., Demuynck, H., Verschuere, J., Théate, I., Vicente, C., Vandenberghe, P., Cools, J., and Wlodarska, I. (2013) BMI1, the polycomb-group gene, is recurrently targeted by genomic rearrangements in progressive B-cell leukemia/lymphoma. *Genes Chromosomes Cancer*. **52**, 928–944
504. Nishida, Y., Maeda, A., Kim, M. J., Cao, L., Kubota, Y., Ishizawa, J., AlRawi, A., Kato, Y., Iwama, A., Fujisawa, M., Matsue, K., Weetall, M., Dumble, M., Andreeff, M., Davis, T. W., Branstrom, A., Kimura, S., and Kojima, K. (2017) The novel BMI-1 inhibitor PTC596 downregulates MCL-1 and induces p53-independent mitochondrial apoptosis in acute myeloid leukemia progenitor cells. *Blood Cancer J*. **7**, e527

505. Bishop, A. J. R., and Schiestl, R. H. (2002) Homologous recombination and its role in carcinogenesis. *J Biomed Biotechnol*. **2002**, 75–85

506. Reliene, R., Bishop, A. J. R., and Schiestl, R. H. (2007) Involvement of Homologous Recombination in Carcinogenesis. *Adv Genet*. **58**, 67–87

507. Seeler, J.-S., and Dejean, A. (2017) SUMO and the robustness of cancer. *Nat Rev Cancer*. **17**, 184

508. Kazandjian, D. (2016) Multiple myeloma epidemiology and survival: A unique malignancy. *Semin Oncol*. **43**, 676–681

509. Rajkumar, S. V. (2019) Multiple myeloma: Every year a new standard? *Hematol Oncol*. **37**, 62–65

510. Driscoll, J. J., Pelluru, D., Lefkimmiatis, K., Fulciniti, M., Prabhala, R. H., Greipp, P. R., Barlogie, B., Tai, Y. T., Anderson, K. C., Shaughnessy, J. D., Annunziata, C. M., and Munshi, N. C. (2010) The sumoylation pathway is dysregulated in multiple myeloma and is associated with adverse patient outcome. *Blood*. **115**, 2827–2834

511. Felix, R. S., Colleoni, G. W. B., Caballero, O. L., Yamamoto, M., Almeida, M. S. S., Andrade, V. C. C., Chauffaille, M. de L. L. F., Silva, W. A. da, Begnami, M. D., Soares, F. A., Simpson, A. J., Zago, M. A., and Vettore, A. L. (2009) SAGE analysis highlights the importance of p53csv, ddx5, mapkapk2 and ranbp2 to multiple myeloma tumorigenesis. *Cancer Lett*. **278**, 41–48

512. Xu, J., Sun, H. Y., Xiao, F. J., Wang, H., Yang, Y., Wang, L., Gao, C. J., Guo, Z. K., Wu, C. T., and Wang, L. S. (2015) SENP1 inhibition induces apoptosis and growth arrest of multiple myeloma cells through modulation of NF-κB signaling. *Biochem Biophys Res Commun*. **460**, 409–415

513. Langston, S. P., Grossman, S., England, D., Afroze, R., Bence, N., Bowman, D., Bump, N., Chau, R., Chuang, B.-C., Claiborne, C., Cohen, L., Connolly, K., Duffey, M., Durvasula, N., Freeze, S., Gallery, M., Galvin, K., Gaulin, J., Gershman, R., Greenspan, P., Grieves, J., Guo, J., Gulavita, N., Hailu, S., He, X., Hoar, K., Hu, Y., Hu, Z., Ito, M., Kim, M.-S., Lane, S. W., Lok, D., Lublinsky, A., Mallender, W., McIntyre, C., Minissale, J., Mizutani, H., Mizutani, M., Molchinova, N., Ono, K., Patil, A., Qian, M., Riceberg, J., Shindi, V., Sintchak, M. D., Song, K., Soucy, T., Wang, Y., Xu, H., Yang, X., Zawadzka, A., Zhang, J.,

and Pulukuri, S. M. (2021) Discovery of TAK-981, a First-in-Class Inhibitor of SUMO-Activating Enzyme for the Treatment of Cancer. *J Med Chem*. **64**, 2501–2520

514. He, X., Riceberg, J., Soucy, T., Koenig, E., Minissale, J., Gallery, M., Bernard, H., Yang, X., Liao, H., Rabino, C., Shah, P., Xega, K., Yan, Z., Sintchak, M., Bradley, J., Xu, H., Duffey, M., England, D., Mizutani, H., Hu, Z., Guo, J., Chau, R., Dick, L. R., Brownell, J. E., Newcomb, J., Langston, S., Lightcap, E. S., Bence, N., and Pulukuri, S. M. (2017) Probing the roles of SUMOylation in cancer cell biology by using a selective SAE inhibitor. *Nat Chem Biol*. **13**, 1164
515. Du, L., Liu, W., Pichiorri, F., and Rosen, S. T. (2023) SUMOylation inhibition enhances multiple myeloma sensitivity to lenalidomide. *Cancer Gene Ther*. **30**, 567–574
516. Du, L., Liu, W., Aldana-Masangkay, G., Pozhitkov, A., Pichiorri, F., Chen, Y., and Rosen, S. T. (2022) SUMOylation inhibition enhances dexamethasone sensitivity in multiple myeloma. *Journal of Experimental & Clinical Cancer Research*. **41**, 8
517. Farmer, H., McCabe, N., Lord, C. J., Tutt, A. N. J., Johnson, D. A., Richardson, T. B., Santarosa, M., Dillon, K. J., Hickson, I., Knights, C., Martin, N. M. B., Jackson, S. P., Smith, G. C. M., and Ashworth, A. (2005) Targeting the DNA repair defect in BRCA mutant cells as a therapeutic strategy. *Nature*. **434**, 917–921
518. Bryant, H. E., Schultz, N., Thomas, H. D., Parker, K. M., Flower, D., Lopez, E., Kyle, S., Meuth, M., Curtin, N. J., and Helleday, T. (2005) Specific killing of BRCA2-deficient tumours with inhibitors of poly(ADP-ribose) polymerase. *Nature*. **434**, 913–917
519. Rose, M., Burgess, J. T., O'Byrne, K., Richard, D. J., and Bolderson, E. (2020) PARP Inhibitors: Clinical Relevance, Mechanisms of Action and Tumor Resistance. *Front Cell Dev Biol*. **8**, 1–22
520. Pandey, N., and Black, B. E. (2021) Rapid Detection and Signaling of DNA Damage by PARP-1. *Trends Biochem Sci*. **46**, 744–757
521. Haince, J.-F., McDonald, D., Rodrigue, A., Déry, U., Masson, J.-Y., Hendzel, M. J., and Poirier, G. G. (2008) PARP1-dependent kinetics of recruitment of MRE11 and NBS1 proteins to multiple DNA damage sites. *J Biol Chem*. **283**, 1197–1208
522. Hopkins, T. A., Shi, Y., Rodriguez, L. E., Solomon, L. R., Donawho, C. K., DiGiammarino, E. L., Panchal, S. C., Wilsbacher, J. L., Gao, W., Olson, A. M., Stolarik, D. F., Osterling, D. J., Johnson, E. F., and Maag, D. (2015) Mechanistic Dissection of PARP1 Trapping and the

Impact on In Vivo Tolerability and Efficacy of PARP Inhibitors. *Mol Cancer Res*. **13**, 1465–1477

523. Patel, A. G., Sarkaria, J. N., and Kaufmann, S. H. (2011) Nonhomologous end joining drives poly(ADP-ribose) polymerase (PARP) inhibitor lethality in homologous recombination-deficient cells. *Proc Natl Acad Sci U S A*. **108**, 3406–3411
524. Maya-Mendoza, A., Moudry, P., Merchut-Maya, J. M., Lee, M., Strauss, R., and Bartek, J. (2018) High speed of fork progression induces DNA replication stress and genomic instability. *Nature*. **559**, 279–284
525. Cong, K., and Cantor, S. B. (2022) Exploiting replication gaps for cancer therapy. *Mol Cell*. **82**, 2363–2369
526. Grellety, T., Peyraud, F., Sevenet, N., Tredan, O., Dohollou, N., Barouk-Simonet, E., Kind, M., Longy, M., Blay, J.-Y., and Italiano, A. (2020) Dramatic response to PARP inhibition in a PALB2-mutated breast cancer: moving beyond BRCA. *Annals of Oncology*. **31**, 822–823
527. Wang, J., Ding, Q., Fujimori, H., Motegi, A., Miki, Y., and Masutani, M. (2016) Loss of CtIP disturbs homologous recombination repair and sensitizes breast cancer cells to PARP inhibitors. *Oncotarget*. **7**, 7701–7714
528. Mardis, E. R. (2019) The Impact of Next-Generation Sequencing on Cancer Genomics: From Discovery to Clinic. *Cold Spring Harb Perspect Med*. 10.1101/cshperspect.a036269
529. de Bruijn, I., Kundra, R., Mastrogiacomo, B., Tran, T. N., Sikina, L., Mazor, T., Li, X., Ochoa, A., Zhao, G., Lai, B., Abeshouse, A., Baiceanu, D., Ciftci, E., Dogrusoz, U., Dufilie, A., Erkoc, Z., Garcia Lara, E., Fu, Z., Gross, B. E., Haynes, C. D., Heath, A., Higgins, D. M., Jagannathan, P., Kalletla, K., Kumari, P., Lindsay, J. R., Lisman, A., Leenknegt, B., Lukasse, P., Madala, D., Madupuri, R., van Nierop, P., Plantalech, O., Quach, J., Resnick, A., Rodenburg, S. Y. A., Satravada, B. A., Schaeffer, F., Sheridan, R., Singh, J., Sirohi, R., Sumer, S. O., van Hagen, S., Wang, A., Wilson, M., Zhang, H., Zhu, K., Rusk, N., Brown, S., Lavery, J. A., Panageas, K. S., Rudolph, J. E., LeNoue-Newton, M. L., Warner, J. L., Guo, X., Hunter-Zinck, H., Yu, T. V, Pillai, S., Nichols, C., Gardos, S. M., Philip, J., Bpc Core Team, G., Project Genie Consortium, A., Kehl, K. L., Riely, G. J., Schrag, D., Lee, J., Fiandalo, M. V, Sweeney, S. M., Pugh, T. J., Sander, C., Cerami, E., Gao, J., and Schultz, N. (2023) Analysis and Visualization of Longitudinal Genomic and Clinical Data from

the AACR Project GENIE Biopharma Collaborative in cBioPortal. *Cancer Res*. 10.1158/0008-5472.CAN-23-0816

530. Gao, J., Aksoy, B. A., Dogrusoz, U., Dresdner, G., Gross, B., Sumer, S. O., Sun, Y., Jacobsen, A., Sinha, R., Larsson, E., Cerami, E., Sander, C., and Schultz, N. (2013) Integrative analysis of complex cancer genomics and clinical profiles using the cBioPortal. *Sci Signal*. **6**, pl1
531. Cerami, E., Gao, J., Dogrusoz, U., Gross, B. E., Sumer, S. O., Aksoy, B. A., Jacobsen, A., Byrne, C. J., Heuer, M. L., Larsson, E., Antipin, Y., Reva, B., Goldberg, A. P., Sander, C., and Schultz, N. (2012) The cBio cancer genomics portal: an open platform for exploring multidimensional cancer genomics data. *Cancer Discov*. **2**, 401–404
532. Zarrizi, R., Higgs, M. R., Voßgröne, K., Rossing, M., Bertelsen, B., Bose, M., Kousholt, A. N., Rösner, H., Network, the C., Ejlertsen, B., Stewart, G. S., Nielsen, F. C., and Sørensen, C. S. (2020) Germline RBBP8 variants associated with early-onset breast cancer compromise replication fork stability. *Journal of Clinical Investigation*. **130**, 4069–4080
533. Adli, M. (2018) The CRISPR tool kit for genome editing and beyond. *Nat Commun*. **9**, 1911
534. Charpentier, M., Khedher, A. H. Y., Menoret, S., Brion, A., Lamribet, K., Dardillac, E., Boix, C., Perrouault, L., Tesson, L., Geny, S., De Cian, A., Itier, J. M., Anegon, I., Lopez, B., Giovannangeli, C., and Concordet, J. P. (2018) CtIP fusion to Cas9 enhances transgene integration by homology-dependent repair. *Nat Commun*. **9**, 1–11
535. Tran, N.-T., Bashir, S., Li, X., Rossius, J., Chu, V. T., Rajewsky, K., and Kühn, R. (2019) Enhancement of Precise Gene Editing by the Association of Cas9 With Homologous Recombination Factors . *Frontiers in Genetics*
536. Carusillo, A., Haider, S., Schäfer, R., Rhiel, M., Türk, D., Chmielewski, K. O., Klermund, J., Mosti, L., Andrieux, G., Schäfer, R., Cornu, T. I., Cathomen, T., and Mussolino, C. (2023) A novel Cas9 fusion protein promotes targeted genome editing with reduced mutational burden in primary human cells. *Nucleic Acids Res*. **51**, 4660–4673
537. Chen, Y. J., Chuang, Y. C., Chuang, C. N., Cheng, Y. H., Chang, C. R., Leng, C. H., and Wang, T. F. (2016) S. cerevisiae Mre11 recruits conjugated SUMO moieties to facilitate the assembly and function of the Mre11-Rad50-Xrs2 complex. *Nucleic Acids Res*. **44**, 2199–2213

Appendix

STAR Protocols

CellPress
OPEN ACCESS

Protocol

Quantification of protein enrichment at site-specific DNA double-strand breaks by chromatin immunoprecipitation in cultured human cells

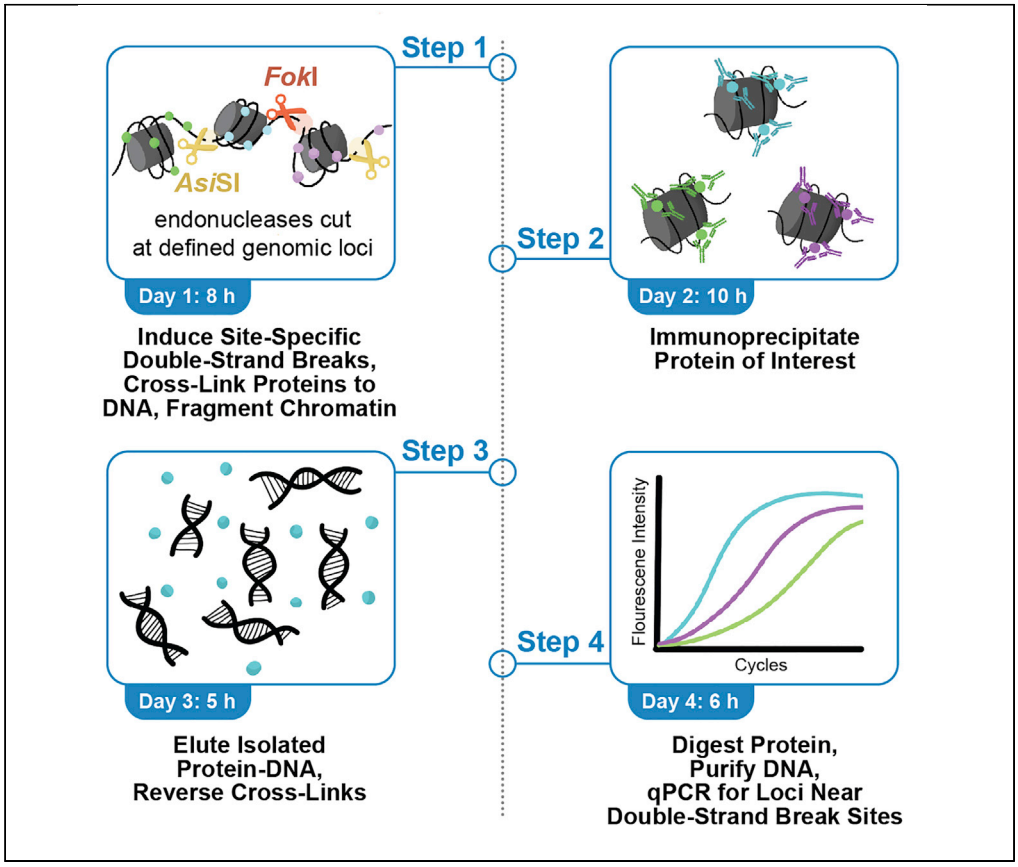

Here, we present a chromatin-immunoprecipitation-based protocol to quantify the recruitment of proteins adjacent to site-specific DNA double-strand breaks (DSBs), such as proteins involved in DSB repair. We describe steps to induce DSBs in U2OS osteosarcoma cells stably expressing the restriction endonucleases *FokI* or *AsiSI*. We then detail the procedures of chromatin isolation and immunoprecipitation, followed by protein elution and quantitative-PCR-based quantification of DNA. This protocol cannot be used on DSBs generated at random loci by DNA damaging agents.

Publisher's note: Undertaking any experimental protocol requires adherence to local institutional guidelines for laboratory safety and ethics.

Ajit K. Sharma, Amira Mohammed Fitieh, Andrew J. Locke, Jana Yasser Hafez Ali, Ismail Hassan Ismail

iismail@ualberta.ca

Highlights

A sensitive approach to measure protein association near DNA double-strand breaks (DSBs)

The DSBs are induced in U2OS cells stably expressing the endonucleases *FokI* or *AsiSI*

Involves ChIP and subsequent qPCR

Primers used for qPCR target genomic loci proximal to the endonuclease-generated DSBs

Sharma et al., STAR Protocols 4, 101917
March 17, 2023
https://doi.org/10.1016/j.xpro.2022.101917

STAR Protocols

CellPress
OPEN ACCESS

Protocol

Quantification of protein enrichment at site-specific DNA double-strand breaks by chromatin immunoprecipitation in cultured human cells

Ajit K. Sharma,[1,3] Amira Mohammed Fitieh,[1,2,3] Andrew J. Locke,[1,3] Jana Yasser Hafez Ali,[1] and Ismail Hassan Ismail[1,2,4,5,*]

[1]Department of Oncology, Faculty of Medicine & Dentistry, University of Alberta, Cross Cancer Institute, 11560 University Avenue, Edmonton, AB T6G 1Z2, Canada

[2]Biophysics Department, Faculty of Science, Cairo University, 12613 Giza, Egypt

[3]These authors contributed equally

[4]Technical contact

[5]Lead contact

*Correspondence: iismail@ualberta.ca
https://doi.org/10.1016/j.xpro.2022.101917

SUMMARY

Here, we present a chromatin-immunoprecipitation-based protocol to quantify the recruitment of proteins adjacent to site-specific DNA double-strand breaks (DSBs), such as proteins involved in DSB repair. We describe steps to induce DSBs in U2OS osteosarcoma cells stably expressing the restriction endonucleases *Fok*I or *Asi*SI. We then detail the procedures of chromatin isolation and immunoprecipitation, followed by protein elution and quantitative-PCR-based quantification of DNA. This protocol cannot be used on DSBs generated at random loci by DNA damaging agents.

For complete details on the use and execution of this protocol, please refer to Fitieh et al. (2022).[1]

BEFORE YOU BEGIN

This protocol uses chromatin immunoprecipitation (ChIP) to quantify the association of proteins with DNA near DSBs induced by the restriction endonucleases *Fok*I or *Asi*SI. Upon induction of these DSBs, proteins bound to DNA are cross-linked to it, the DNA is fragmented by sonication, and the chromatin fraction of the cells is isolated. Immunoprecipitation is then performed to isolate the protein of interest and its associated DNA. The cross-links are reversed, and the associated DNA is recovered. Quantitative polymerase chain reaction (qPCR) is then performed on this DNA using primers that target genomic loci proximal to the endonuclease-induced DSBs.

The protocol relies on U2OS osteosarcoma cells that stably express fusion proteins containing *Fok*I or *Asi*SI, whose endonuclease activities can be induced on nuclear DNA at specific loci. *Fok*I endonuclease is activated upon dimerization,[2] and its nuclease domain is sequence non-specific,[3,4] thus its activity can be targeted to specific sequences when fused to DNA recognition domains from other proteins. Here, the fusion for *Fok*I comprises the *Fok*I nuclease domain, tagged with a destabilization domain (DD) derived from FK506- and rapamycin binding protein (FKBP12),[5] along with an altered estrogen receptor hormone-binding domain (ER),[6,7] the fluorescent protein mCherry, and the *E. coli* lactose repressor protein (LacI) ("ER-mCherry-LacI-*Fok*I-DD").[8,9] Roger Greenberg's group stably expressed this fusion in U2OS 2-6-3 cells, where a single genomic locus was engineered with tandem *E. coli lac* operator sequence (*lacO*) repeats,[10] referring to the cells as U2OS-DSB

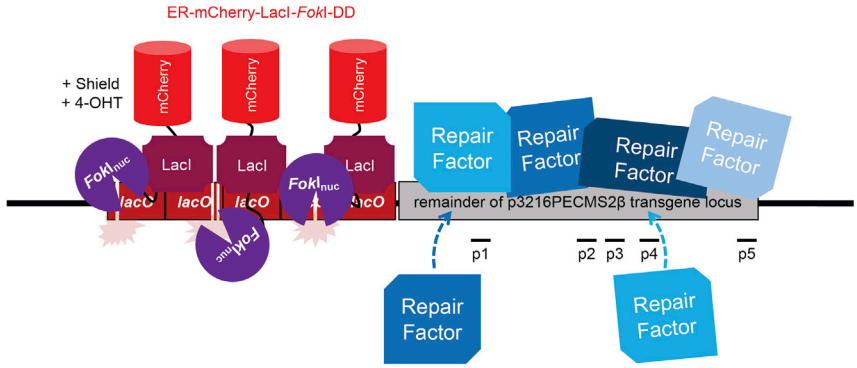

Figure 1. U2OS-DSB reporter cells

Schematic diagram of the *lacO* array and the action of the *Fok*I nuclease domain (*Fok*I$_{nuc}$)-containing fusion protein ER-mCherry-LacI-*Fok*I-DD in U2OS-DSB reporter cells.[8,9] p1, p2, p3, p4, and p5 are loci adjacent to the array and can be amplified by qPCR with the appropriate primers. (Please note that the *lacO* array is part of the p3216PECMS2β transgene locus, which enables inducible transcription of a transgenic messenger RNA (mRNA) upon treatment with doxycycline.[10] Transcription downstream of the *lacO* array can be induced if reverse tetracycline-responsive transcriptional activator (rtTA, via the pTet-On plasmid) is expressed in the cells and doxycycline is added to the culture media.[9,10] A focus of the induced mRNA product can be visualized if yellow fluorescent protein-tagged MS2 viral coat protein is also expressed in the cells. The induced mRNA also codes for a cyan fluorescent protein-tagged protein product.[9,10] This reporter, in combination with mCherry-LacI-*Fok*I, has been used to study transcription in the context of local DSBs.[1,9])

reporter cells[8] (Figure 1). The *lacO* repeats are recognized by the LacI portion of the fusion protein, allowing *Fok*I activity to accumulate at the *lacO* array. To restrict *Fok*I activity, the DD actively targets the fusion for proteasome-dependent degradation. This can be prevented when the small molecule Shield-1 is bound to the DD.[5] Additional control is provided by the ER portion, which ensures nuclear translocation of the fusion occurs only in the presence of 4-hydroxytamoxifen (4-OHT). Therefore, ER-mCherry-LacI-*Fok*I-DD activity can be induced at the *lacO* array upon the combined presence of Shield-1 and 4-OHT.

Alternatively, a stable U2OS cell line with inducible *Asi*SI activity (*Asi*SI-ER U2OS, also known as DIvA cells[11,12]) was generated by Gaëlle Legube's group. It stably expresses a fusion of the *Asi*SI restriction endonuclease and the aforementioned ER domain, again enabling 4-OHT-inducible translocation from the cytoplasm to the nucleus and thus inducible DSBs[13,14] (Figure 2). As *Asi*SI cleaves double-stranded DNA at the 8 base pair (bp) sequence 5′-GCGATCGC-3′, it is a "rare cutter", and digesting genomic DNA should produce DNA fragments >1 Mbp.[13,14] In *Asi*SI-ER U2OS, *Asi*SI-ER generates ~200 DSBs in diploid cells in G_1 phase.[12,14] 80 of these sites are significantly cleaved upon 4-OHT treatment.[12]

While the *Asi*SI-ER U2OS and U2OS-DSB systems both utilize restriction enzymes to generate DSBs, in U2OS-DSB cells the DSBs are highly concentrated at the single *lacO* array. On the other hand, in *Asi*SI-ER U2OS cells the DSBs are distributed throughout the genome and on every chromosome, allowing for the study of protein recruitment to DSBs at numerous loci.

Preparation before the experiment

1. Locate required reagents and equipment.

   Note: Different DNA primer sets are used for the U2OS-DSB and *Asi*SI-ER U2OS systems (Tables 1 and 2). Primers can be custom synthesized and dissolved according to guidelines from the manufacturer and should be stored at −20°C.

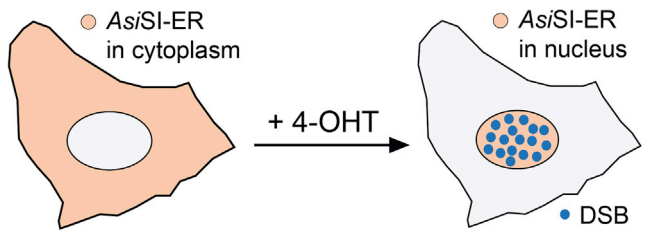

Figure 2. *Asi*SI-ER U2OS cells

Addition of 4-OHT to the culture media induces *Asi*SI-ER to translocate to the nucleus and generate sequence-specific DSBs at defined genomic loci.

2. As ChIP can be a lengthy procedure, we recommend that the sonication conditions (step 13), amount of chromatin (step 17), amount of antibody used for immunoprecipitation (step 21), and qPCR (step 32) are tested and optimized, in that sequence, prior to proceeding with a full-scale experiment.

Cell culture

Timing: 2 weeks

3. Maintain the U2OS-DSB or *Asi*SI-ER U2OS cell cultures.
   a. Culture these adherent cells in 100 mm culture dishes at 37°C in a humidified atmosphere with 5% CO_2. Grow the cells in low-glucose Dulbecco's Modified Eagle Medium (DMEM) supplemented with 10% fetal bovine serum (FBS).

⚠ CRITICAL: when handling the cells, always work under a certified biosafety cabinet with sterilized equipment and solutions and using aseptic technique. U2OS cells are classified as Biosafety Level 1.

Note: add selection markers to the culture media to maintain the genetic constructs stably expressed by the cells. These are 2 μg/mL puromycin and 100 μg/mL hygromycin for U2OS-DSB reporter cells and 2 μg/mL puromycin for *Asi*SI-ER U2OS cells.

Note: Do not add chilled media to cells; always use media pre-warmed to 37°C.

Note: The media should be replenished every 3–4 days.

Table 1. U2OS-DSB reporter locus qPCR primers

Locus	Primer name	Sequence (5′-3′)	Source
3′ (downstream) of the *lacO* array in U2OS-DSB reporter cells, getting further 3′ as p1 → p5	p1 For[a]	GGAAGATGTCCCTTGTATCACCAT	Tang et al. and Shanbhag et al.[8,9]
	p1 Rev[a]	TGGTTGTCAACAGAGTAGAAAGTGAA	
	p2 For	GCTGGTGTGGCCAATGC	
	p2 Rev	TGGCAGAGGGAAAAAGATCTCA	
	p3 For	GGCATTTCAGTCAGTTGCTCAA	
	p3 Rev	TTGGCCGATTCATTAATGCA	
	p4 For[a]	CCACCTGACGTCTAAGAAACCAT	
	p4 Rev[a]	GATCCCTCGAGGACGAAAGG	
	p5 For	CCACCTGACGTCTAAGAAACCAT	
	p5 Rev	GATCCCTCGAGGACGAAAGG	
Chromosome 7 (negative control)	chr7 For	GCTCGTGCCGTTTTGCA	
	chr7 Rev	GGGTTGACCATGGCTAATAGTACA	

[a]We have used these primers to examine CtIP, RPA2, and RAD51 recruitment near the *lacO* locus in U2OS-DSB reporter cells.

Table 2. *Asi*SI-ER U2OS *Asi*SI site-proximal qPCR primers

Primer name	Sequence (5′-3′)	Source
chr1_89231183 For[a]	GATTGGCTATGGGTGTGGAC	Iacovoni et al.[13]
chr1_89231183 Rev[a]	CATCCTTGCAAACCAGTCCT	
chr6_90404906 For[a]	TGCCGGTCTCCTAGAAGTTG	
chr6_90404906 Rev[a]	GCGCTTGATTTCCCTGAGT	
chr21_21292316 For[a]	TGGCTGGAACTGCTTTCTTT	
chr21_21292316 Rev[a]	GGTGAGTGAATGAGCTGCAA	
HR-DSB2 For[b]	CCGCCAGAAAGTTTCCTAGA	Aymard et al. and Arnould et al.[11,15]
HR-DSB2 Rev[b]	CTCACCCTTGCAGCACTTG	
Control region For[c]	AGCACATGGGATTTTGCAGG	Arnould et al.[15]
Control region Rev[c]	TTCCCTCCTTTGTGTCACCA	

[a]Other primers to regions proximal and distal to *Asi*SI cut sites on chromosomes 1, 6, and 22 are available.[13] The ones provided here are ones which we have used previously.[1]

[b]Use this primer set as a positive control in ChIP for detecting RAD51 recruitment near an *Asi*SI-generated DSB in *Asi*SI-ER U2OS cells (steps 16 and 32).

[c]The genomic region this primer binds is not adjacent to an *Asi*SI-generated DSB in *Asi*SI-ER U2OS cells and thus can be used as a negative control for ChIP.

b. When 90% confluence is reached, routinely subculture at 1:5 to 1:10 dilutions.
   i. Wash once in sterile phosphate-buffered saline (PBS).
   ii. Detach cells with trypsin-EDTA solution for 5 min at 37°C.
   iii. Resuspend cells in DMEM/FBS media, discard the unwanted volume, and top up to a final culture volume of 10 mL with DMEM/FBS media.

c. Cultures should be restarted from liquid nitrogen stocks once 30 passages have elapsed.

4. Prior to starting the protocol, seed the cells into 150 mm dishes to attain 90% confluence at the time you wish to induce DSBs. The cells should be cultured in low-glucose DMEM supplemented with 10% charcoal-stripped FBS at least 5 days before inducing DSBs.

Note: Charcoal-stripped FBS is used here instead of regular FBS to avoid trace levels of estrogen, which may induce activity of the *Fok*I or *Asi*SI restriction endonucleases in samples where 4-OHT is not added.

⚠ CRITICAL: Ensure separate 150 mm dishes are seeded for all conditions required for your experiment, including dishes for "not induced" controls (where Shield-1 and/or 4-OHT are not added to the media, preventing DSB induction), DSB-induced samples, and for any experimental manipulations (e.g., RNA interference, overexpression of proteins, pharmacological inhibition, etc.) of interest. Note, however, that one 150 mm dish may yield enough protein for multiple chromatin immunoprecipitations for different DNA binding proteins.

Before starting the protocol

Timing: 1–2 days

5. Prepare stock solutions and buffers as required (materials and equipment) the day before performing the desired steps. If they are required to be ice-cold, chill them at 4°C at least 12 h prior to performing the steps. While it is preferable to have all buffers freshly prepared, for convenience, some may be stored long-term, as indicated in materials and equipment.
6. The day of, ensure any temperature-controlled equipment is at the correct temperature prior to beginning the procedure.

Note: Centrifuges must be pre-chilled to 4°C at least 30 min before they are needed.

Note: The Bioruptor Pico sonicator's water tank must be pre-chilled to 4°C at least 45 min before it is needed.

KEY RESOURCES TABLE

REAGENT or RESOURCE	SOURCE	IDENTIFIER
Antibodies		
Rabbit anti-RAD51, H-92 (3–4 µg per ChIP)	Santa Cruz Biotechnology	Cat#sc-8349; RRID: AB_2253533
Mouse anti-RPA2, 9H8 (2.5 µg per ChIP)	Abcam	Cat#ab2175; RRID: AB_302873
Mouse anti-CtIP, 14-1 (3.5 µg per ChIP)	Active Motif	Cat#61141; RRID: AB_2714164
RNA polymerase II phospho-S5 at CTD repeats (YSPTSPS), 4H8 (2 µg per ChIP)	Abcam	Cat#ab5408; RRID: AB_304868
Mouse IgG1 isotype control	Thermo Fisher	Cat#02-6100; RRID: AB_2532935
Rabbit IgG isotype control	Thermo Fisher	Cat#02-6102; RRID: AB_2532938
Chemicals, peptides, and recombinant proteins		
DMEM, low glucose, pyruvate (Gibco)	Thermo Fisher	Cat#11885084
Fetal bovine serum (Gibco)	Thermo Fisher	Cat#26140079
Charcoal-stripped fetal bovine serum	Sigma-Aldrich	Cat#F6765
Puromycin dihydrochloride	Sigma-Aldrich	Cat#P8833
Hygromycin B solution, 50 mg/mL	Thermo Fisher	Cat#10687010
Trypsin-EDTA solution	Sigma-Aldrich	Cat#T4049
DMSO	Sigma-Aldrich	Cat#D8418
Shield-1 ligand	Clontech/Takara	Cat#632189; CAS:914805-33-7
4-Hydroxytamoxifen	Sigma-Aldrich	Cat#H7904; CAS:68047-06-3
Potassium chloride	Sigma-Aldrich	Cat#P3911
Sodium phosphate dibasic (Na_2HPO_4)	Sigma-Aldrich	Cat#S9763
Potassium phosphate monobasic (KH_2PO_4)	Sigma-Aldrich	Cat#P0662
Concentrated hydrochloric acid	Sigma-Aldrich	Cat#H1758
HEPES	Sigma-Aldrich	Cat#H4034
Sucrose	Sigma-Aldrich	Cat#S5016
EDTA	Sigma-Aldrich	Cat#E9884
1 M magnesium chloride solution	Sigma-Aldrich	Cat#M1028
Triton X-100	Sigma-Aldrich	Cat#T8787
cOmplete Protease Inhibitor Cocktail, EDTA-free tablets	Sigma-Aldrich	Cat#11873580001
phosSTOP phosphatase inhibitor cocktail tablets	Sigma-Aldrich	Cat#4906837001
Sodium deoxycholate	Sigma-Aldrich	Cat#D6750
Sodium dodecyl sulfate	Sigma-Aldrich	Cat#436143
Glycogen, 20 mg/mL	Thermo Fisher	Cat#RO561
Yeast tRNA, 10 mg/mL	Thermo Fisher	Cat#AM7119
Bovine serum albumin (BSA)	Sigma-Aldrich	Cat#B6917
Tris base	Sigma-Aldrich	Cat#252859
Lithium chloride	Sigma-Aldrich	Cat#L9650
IGEPAL CA-630	Sigma-Aldrich	Cat#I3021
Sodium bicarbonate	Sigma-Aldrich	Cat#S6014
Glacial acetic acid	Sigma-Aldrich	Cat#695092
Glycerol	Sigma-Aldrich	Cat#G5516
Bromophenol blue	Sigma-Aldrich	Cat#114391
37% formaldehyde solution	Sigma-Aldrich	Cat#F8775
Glycine	Sigma-Aldrich	Cat#50046
Agarose	Sigma-Aldrich	Cat#A9539
Ethidium bromide, 10 mg/mL in H_2O	Sigma-Aldrich	Cat#E1510
Dynabeads Protein A for Immunoprecipitation	Thermo Fisher	Cat#10001D
Dynabeads Protein G for Immunoprecipitation	Thermo Fisher	Cat#10003D
40% Acrylamide/Bis solution 29:1	Bio-Rad	Cat#1610146

(*Continued on next page*)

Continued

REAGENT or RESOURCE	SOURCE	IDENTIFIER
2-mercaptoethanol	Sigma-Aldrich	Cat#M3148
RNase A, DNase and protease-free, 10 mg/mL	Thermo Fisher	Cat#EN0531
Proteinase K solution, 20 mg/mL	Thermo Fisher	Cat#25530049
Critical commercial assays		
Pierce BCA Protein Assay Kit	Thermo Fisher	Cat#23225
QIAquick PCR Purification Kit	Qiagen	Cat#28104
Pico488 dsDNA Quantification Kit	Lumiprobe	Cat#1102-200
BrightGreen 2× qPCR MasterMix-ROX	abm (Applied Biological Materials)	Cat#MasterMix-R (discontinued but BlasTaq 2× qPCR MasterMix, Cat#G891, is functionally equivalent)
Experimental models: Cell lines		
U2OS cells (*Homo sapiens* osteosarcoma, from 15-year-old female) – genes expressed: osteosarcoma derived growth factor; blood type A; Rh^+; HLA:(A2; Aw30; B12; Bw35; $B40^{+/-}$)	ATCC	Cat#HTB-96
*Asi*SI-ER U2OS cells (stable cell line derived from U2OS cells)	Gaelle Legube[13]	N/A
U2OS-DSB reporter cells (stable cell line derived from U2OS cells)	Roger A. Greenberg[8]	N/A
Software and algorithms		
QuantStudio 6 Flex Real-Time PCR System Software	Applied Biosystems	Version 1.3 https://www.thermofisher.com/ca/en/home/global/forms/life-science/quantstudio-6-7-flex-software.html
Prism	GraphPad	Version 9 https://www.graphpad.com/
Oligonucleotides		
See Tables 1 and 2 for qPCR primer sequences	Gaelle Legube and Roger A. Greenberg[8,9,11,13,15] Custom synthesis by Millipore-Sigma	N/A
Other		
Allegra X-12R refrigerated centrifuge	Beckman-Coulter	Cat#B08867
Benchtop centrifuge 5804 R	Eppendorf	Cat#022623508
Model 200 Rocking Platform	VWR	Cat# 40000-304
Hematology/Chemistry Mixer Model 346	Fisher Scientific	Cat#14-059-346
ThermoMixer F1.5	Eppendorf	Cat#5384000020
Millex-GP Syringe Filter Unit with PES Membrane, 0.22 µm	Millipore-Sigma	Cat#SLGP033RS
Heracell Vios 160i CR CO_2 Incubator	Thermo Fisher	Cat#51033775
100 mm Dishes	Sarstedt	Cat#83.3902
150 mm Dishes	Sarstedt	Cat#83.3903
Cell scrapers (Nunc)	Thermo Fisher	Cat#179693PK
Bioruptor Pico Sonication Device	Diagenode	Cat#B01060010 (discontinued, replaced by Cat#B01080010)
1.5 mL Bioruptor Pico Microtubes with cap	Diagenode	Cat#C30010016
MagJET Separation Rack, 12 × 1.5 mL tube	Thermo Fisher	Cat#MR02
Mini-PROTEAN Tetra Vertical Electrophoresis Cell, 4-Gel, for 1.0 mm Thick Handcast Gels, with Mini Trans-Blot Module and PowerPac Basic Power Supply	Bio-Rad	Cat#1658033FC
Trans-Blot Transfer Medium (nitrocellulose membrane), 0.2 µm	Bio-Rad	Cat#162-0112
Mini-Sub Cell GT Horizontal Electrophoresis System, 7 × 10 cm Tray, with Mini-Gel Caster	Bio-Rad	Cat#1704467

(*Continued on next page*)

Continued		
REAGENT or RESOURCE	SOURCE	IDENTIFIER
FLUOstar Omega Microplate Reader	BMG LABTECH	N/A
NanoDrop ND-1000 Spectrophotometer	Thermo Scientific	N/A(discontinued, but replaced by NanoDrop One Microvolume UV-Vis Spectrophotometer, Cat#ND-ONE-W)
QuantStudio 6 Flex Real-Time PCR System	Applied Biosystems	Cat#4485692

MATERIALS AND EQUIPMENT

1× PBS		
Reagent	Final concentration	Amount
NaCl	137 mM	8 g
KCl	2.7 mM	0.2 g
Na_2HPO_4	10 mM	1.44 g
KH_2PO_4	1.8 mM	0.24 g
concentrated $HCl_{(aq)}$	use to adjust final pH to 7.4	
ddH_2O	N/A	dissolve solids in, then complete to 1,000 mL final volume
1× PBS must be sterilized by autoclaving or filter sterilization with a 0.2 μm filter prior to use in this protocol.		

Sterilized 1× PBS can be stored at 20°C–22°C for up to a year upon autoclaving or filter sterilization with a 0.2 μm filter.

Lysis Buffer		
Reagent	Final concentration	Amount
HEPES, 1 M	25 mM, adjust to pH 7.9	2.5 mL
NaCl, 5 M	50 mM	1 mL
Sucrose, 2 M	300 mM	15 mL
EDTA, 0.5 M, pH 8.0	1 mM	200 μL
$MgCl_2$, 1 M	3 mM	300 μL
Triton X-100, 25%	0.5%	2 mL
ddH_2O	N/A	to complete to 100 mL
Prepare this buffer the day before beginning the protocol and refrigerate to 4°C. Alternatively, it can be stored at 4°C for up to 2 weeks upon filter sterilization with a 0.2 μm filter.		

⚠ CRITICAL: immediately before use, add cOmplete protease inhibitor cocktail to 2× final concentration and PhosSTOP phosphatase inhibitor cocktail to 1× final concentration to the required volume.

2 M sucrose stock solution should be stored at −20°C and thawed and mixed immediately before use.

Sonication Buffer		
Reagent	Final concentration	Amount
HEPES, 1 M	50 mM, adjust to pH 7.9	5 mL
NaCl, 5 M	140 mM	2.8 mL
Sucrose, 2 M	300 mM	15 mL
EDTA, 0.5 M, pH 8.0	1 mM	200 μL
Sodium deoxycholate, 10%	0.1%	1 mL
Sodium dodecyl sulfate, 10%	1%	10 mL
Triton X-100, 25%	1%	4 mL
ddH_2O	N/A	to complete to 100 mL
Prepare this buffer the day before beginning the protocol and refrigerate to 4°C. Alternatively, it can be stored at 4°C for up to 2 weeks upon filter sterilization with a 0.2 μm filter.		

⚠ CRITICAL: immediately before use, add cOmplete protease inhibitor cocktail to 2× final concentration and PhosSTOP phosphatase inhibitor cocktail to 1× final concentration to the required volume.

2 M sucrose stock solution should be stored at −20°C and thawed and mixed immediately before use.

Dilution Buffer		
Reagent	Final concentration	Amount
HEPES, 1 M	50 mM, adjust to pH 7.9	25 mL
NaCl, 5 M	140 mM	14 mL
EDTA, 0.5 M, pH 8.0	1 mM	1 mL
Sodium deoxycholate, 10%	0.1%	5 mL
Triton X-100, 25%	1%	20 mL
ddH_2O	N/A	to complete to 500 mL
Prepare this buffer the day before beginning the protocol and refrigerate to 4°C. Alternatively, it can be stored at 4°C for up to 1 month upon filter sterilization with a 0.2 μm filter.		

⚠ CRITICAL: for step 17 only, immediately before use, add cOmplete protease inhibitor cocktail to 2× final concentration and PhosSTOP phosphatase inhibitor cocktail to 1× final concentration to the required volume.

Blocking Buffer	
Reagent	Amount
Glycogen, 20 mg/mL	10 μL
Yeast tRNA, 10 mg/mL	20 μL
Bovine serum albumin, 20 mg/mL in ddH_2O	10 μL
Dilution Buffer	960 μL
Total	**1 mL**
Prepare this buffer immediately before use and keep on ice.	

Glycogen, tRNA, and bovine serum albumin stock solutions should be stored at −20°C.

Low Salt Wash Buffer		
Reagent	Final concentration	Amount
Tris, 1 M	20 mM, adjust to pH 8.1	2 mL
NaCl, 5 M	50 mM	1 mL
EDTA, 0.5 M, pH 8.0	2 mM	400 μL
Sodium dodecyl sulfate, 10%	0.1%	1 mL
Triton X-100, 25%	1%	4 mL
ddH_2O	N/A	to complete to 100 mL
Prepare this buffer the day before beginning the protocol and refrigerate to 4°C. Alternatively, it can be stored at 4°C for up to 1 month upon filter sterilization with a 0.2 μm filter.		

High Salt Wash Buffer		
Reagent	Final concentration	Amount
Tris, 1 M	20 mM, adjust to pH 8.1	2 mL
NaCl, 5 M	500 mM	10 mL
EDTA, 0.5 M, pH 8.0	2 mM	400 μL

(*Continued on next page*)

Continued		
Reagent	Final concentration	Amount
Sodium dodecyl sulfate, 10%	0.1%	1 mL
Triton X-100, 25%	1%	4 mL
ddH_2O	N/A	to complete to 100 mL
Prepare this buffer the day before beginning the protocol and refrigerate to 4°C. Alternatively, it can be stored at 4°C for up to 1 month upon filter sterilization with a 0.2 μm filter.		

LiCl Wash Buffer		
Reagent	Final concentration	Amount
Tris, 1 M	10 mM, adjust to pH 8.0	1 mL
LiCl, 1 M	250 mM	25 mL
EDTA, 0.5 M, pH 8.0	1 mM	200 μL
Sodium deoxycholate, 10%	0.1%	1 mL
IGEPAL CA-630, 25%	1%	4 mL
ddH_2O	N/A	to complete to 100 mL
Prepare this buffer the day before beginning the protocol and refrigerate to 4°C. Alternatively, it can be stored at 4°C for up to 1 month upon filter sterilization with a 0.2 μm filter.		

Alternatives: IGEPAL CA-630 can be substituted with Nonidet P-40.

TE Buffer		
Reagent	Final concentration	Amount
Tris, 1 M	10 mM, adjust to pH 8.0	1 mL
EDTA, 0.5 M, pH 8.0	1 mM	200 μL
ddH_2O	N/A	to complete to 100 mL
Prepare this buffer the day before beginning the protocol and refrigerate to 4°C. Alternatively, it can be stored at 4°C for up to 6 months upon filter sterilization with a 0.2 μm filter.		

Elution Buffer		
Reagent	Final concentration	Amount
Tris, 1 M	50 mM, adjust to pH 8.0	2.5 mL
EDTA, 0.5 M, pH 8.0	1 mM	100 μL
$NaHCO_3$	100 mM	420 mg
Sodium dodecyl sulfate, 10%	1%	5 mL
ddH_2O	N/A	to complete to 50 mL
Prepare this buffer the day of use and store at 20°C–22°C.		

50× TAE Buffer		
Reagent	Final concentration	Amount
Tris base	2 M	242.3 g
Glacial acetic acid	1 M	57.1 mL
EDTA, 0.5 M, pH 8.0	50 mM	100 mL
ddH_2O	N/A	to complete to 1 L
This buffer can be stored at 20°C–22°C for at least 1 year.		

Dilute 50× TAE to 1× concentration in ddH_2O (final concentrations: 40 mM Tris, 20 mM acetic acid, 1 mM EDTA). 1× TAE can be stored at 20°C–22°C for at least 1 year.

4× Laemmli Sample Buffer

Reagent	Final concentration	Amount
Tris base	250 mM, adjust to pH 6.8	6.06 g
Sodium dodecyl sulfate	8%	16 g
Glycerol	40%	80 mL
Bromophenol blue	0.2%	~400 mg
ddH_2O	N/A	to complete to 200 mL

This buffer can be stored at 20°C–22°C for at least 1 year.

This buffer can be diluted to 2× concentration in ddH_2O upon warming to 37°C and gently mixing to ensure all components have been dissolved. 2× Laemmli Buffer can be stored at 20°C–22°C for at least 1 year.

> *Note:* For SDS-PAGE to validate efficient immunoprecipitation (step 21), mix samples of the input and flow-through controls for immunoprecipitation with 4× Laemmli Sample Buffer to obtain a final concentration of 1× Laemmli Sample Buffer. Meanwhile, add 2× Laemmli Sample Buffer to the washed Protein A or G-coupled Dynabeads. 2-mercaptoethanol at a final concentration of 5% must then be added fresh to each of the immunoprecipitation eluate, input control, and flow-through fractions prior to heating them at 95°C.

Stock solutions

- 1 M HEPES: dissolve 23.83 g of HEPES in ddH_2O to a final volume of 100 mL. This solution can be stored at 4°C for at least 6 months.
- 5 M NaCl: dissolve 29.22 g of NaCl in ddH_2O to a final volume of 100 mL. This solution can be stored at 4°C for at least 1 year.
- 2 M sucrose: dissolve 342.3 g of sucrose in 200 mL of ddH_2O with gentle heating, then top up to a final volume of 500 mL. This solution can be stored at −20°C for at least 1 year.
- 0.5 M EDTA, pH 8.0: dissolve 14.61 g of EDTA in ddH_2O to a final volume of 100 mL. Concentrated NaOH must be added to the mixture for EDTA to dissolve. This solution can be stored at 4°C for at least 1 year.
- 25% Triton X-100: dissolve 25 mL of Triton X-100 in ddH_2O to a final volume of 100 mL. This solution can be stored at 4°C for at least 6 months.
- 10% sodium deoxycholate: dissolve 5 g of sodium deoxycholate in ddH_2O to a final volume of 50 mL. This solution can be stored at 20°C–22°C, protected from light, for up to 1 month.

  ⚠ CRITICAL: Respiratory protection (such as an N95 particulate respirator) must be worn while weighing sodium deoxycholate as it is a respiratory irritant.

- 10% sodium dodecyl sulfate: dissolve 5 g of sodium dodecyl sulfate in ddH_2O to a final volume of 50 mL. This solution can be stored at 20°C–22°C for at least 1 year.

  ⚠ CRITICAL: Respiratory protection (such as an N95 particulate respirator) must be worn while weighing sodium dodecyl sulfate as it is a respiratory irritant.

- 50× cOmplete protease inhibitor cocktail: dissolve 1 cOmplete tablet in 1 mL of ddH_2O. This solution must be kept on ice while in use and at −20°C for storage for up to 2 months.
- 20× PhosSTOP protease inhibitor cocktail: dissolve 2 PhosSTOP tablets in 1 mL of ddH_2O. This solution must be kept on ice while in use and at −20°C for storage for up to 2 months.

- 20 mg/mL bovine serum albumin: dissolve 200 mg of bovine serum albumin in 10 mL of ddH_2O. This solution can be stored at −20°C for at least 1 year.
- 1 M Tris: dissolve 12.11 g of Tris base in ddH_2O to a final volume of 100 mL. This solution can be stored at 4°C for at least 6 months.
- 1 M LiCl: dissolve 4.24 g of LiCl in ddH_2O to a final volume of 100 mL. This solution can be stored at 20°C–22°C for at least 6 months.
- 25% IGEPAL CA-630: dissolve 25 mL of IGEPAL CA-630 in ddH_2O to a final volume of 100 mL. This solution can be stored at 4°C for at least 6 months.
- 1 M glycine, dissolved in PBS: dissolve 3.75 g glycine in 1× PBS to a final volume of 50 mL. Prepare this solution the day of the protocol and refrigerate to 4°C.

The majority of the listed primer pairs are adjacent to known cleavage sites by *Asi*SI[13] or *Fok*I[8] in the genomes of the respective U2OS stable cell lines. All have been validated by the groups who generated the enzyme-expressing cell lines. Primer sequences to *Asi*SI sites other than the ones cited here (and antibodies suitable for ChIP) may be sourced from publications by the Legube group referencing *Asi*SI-ER U2OS or DIvA cells.

STEP-BY-STEP METHOD DETAILS

Day 1: Isolation of chromatin after induction of enzyme-mediated double-strand breaks

Timing: 8 h

On this day, enzyme-mediated DSBs are induced in cells, after which DNA-binding proteins are cross-linked to DNA. The cells are then harvested, lysed, and the resulting DNA is sheared by sonication.

Note: This protocol is described for cultured U2OS cells grown in 150 mm dishes, containing ~12–18 × 10^7 cells per dish.

1. In the biosafety cabinet, remove media from each 150 mm dish of cells and wash once with sterile phosphate-buffered saline (PBS).
   a. Aspirate media by tipping the dish towards the vacuum aspirator.
   b. Gently wash the cells once by adding 20 mL sterile PBS warmed to 20°C–22°C.

   Note: Aim the pipettor to the wall of the dish to avoid dislodging the cells.

   c. Remove the PBS by tipping the dish towards the vacuum aspirator.

   Note: These approaches for applying and removing solutions from cells should be maintained for the rest of the protocol.

2. Induce DSBs.
   a. For U2OS-DSB reporter cells (which stably express ER-mCherry-LacI-*Fok*I-DD), replace the dish with 20 mL of 37°C (low-glucose DMEM + 10% charcoal-stripped FBS) containing 0.5 μM Shield-1 and 300 nM 4-OHT for 3 h.
   b. For *Asi*SI-ER U2OS cells (which stably express *Asi*SI-ER), replace the dish with 20 mL of 37°C (DMEM + 10% charcoal-stripped FBS) containing 300 nM 4-OHT for 3 h.

   Note: If multiple dishes are being treated, prepare a master mix of pre-warmed DMEM + 10% charcoal-stripped FBS with 0.5 μM Shield-1 and/or 300 nM 4-OHT to be split over all the dishes. This will prevent variations in 4-OHT or Shield-1 concentration between samples. Avoid introducing too many air bubbles into the media.

⚠ CRITICAL: An essential control for quantification of ChIP signal is to include not induced samples (with no *Asi*SI- or *Fok*I-mediated DSBs) such that one can compare the relative recruitment of proteins when DSBs are induced. For not induced samples, replace the dish with warmed DMEM + 10% charcoal-stripped FBS but *do not* include Shield-1 or 4-OHT.

c. Keep the cells incubating at 37°C in a humidified atmosphere with 5% CO_2 for the duration of the induction.

3. Remove media by vacuum aspiration and gently wash each dish twice with 20 mL of ice-cold PBS.

Note: Keep the bottle of refrigerated PBS on ice for the washes.

4. Replace each dish with 20 mL of serum-free low-glucose DMEM warmed to 20°C–22°C.
5. Cross-link proteins to DNA.
   a. Immediately add 556 μL of 37% formaldehyde to each dish to reach a final concentration of 1% formaldehyde.
   b. Gently swirl the dish immediately, then continue mixing by placing the dish on a laboratory rocker set at 10–15 rpm for 10 min at 20°C–22°C.

⚠ CRITICAL: The efficiency of ChIP is sensitive to cross-linking time so this time should be adhered to. Excessive cross-linking may mask or damage the epitopes needed for the immunoprecipitation or lead to false positive ChIP signals.

Note: ChIP experiments targeting histone post-translational modifications and DNA repair proteins typically require 10 min for cross-linking. On the other hand, ChIP that targets transcription factors may require a longer cross-linking time (up to 30 min), due to lower protein abundance, weak interactions, or transient occupancy time with DNA.

⚠ CRITICAL: Formaldehyde (both the liquid and emitted vapor) is a strong irritant, is highly toxic, and is flammable. It is a known carcinogen and repeated exposure may trigger an allergic reaction. Avoid inhaling vapors, ingestion, and contact with skin. Formaldehyde must be handled under the fume hood and with appropriate personal protective equipment, especially gloves, lab coat, and face/eye protection. After use, formaldehyde-containing solutions and consumables they contacted should be disposed of as chemical hazardous waste. Your institution's environmental health and safety office may have a protocol for disposal of formaldehyde-contaminated solutions or solids.

Note: Formaldehyde is an effective DNA-protein cross-linker,[16] but its small spacer length (2 Å)[17] may preclude its utility for ChIP experiments on proteins that do not bind directly to DNA but interact with it through protein-protein interactions. More efficient protein-protein cross-linkers can be used in addition to formaldehyde, depending on your need to cross-link over various intermolecular distances.[17–19]

6. Quench the cross-linking reaction.
   a. Add to each dish 3 mL of 1 M glycine (dissolved in PBS) to obtain a final concentration of 125 mM glycine.

Note: This will quench unreacted formaldehyde and stop the cross-linking reaction.

   b. Place on the rocker at 10–15 rpm for another 10 min at 20°C–22°C.

c. Remove the formaldehyde-containing DMEM by pipette-aid or vacuum aspiration. Store and dispose of this waste in accordance with the environmental health and chemical safety practices at your institution.

7. Place each dish on ice. Wash gently 3 times with 20 mL of ice-cold PBS supplemented with 1× cOmplete protease inhibitor cocktail.

Note: cOmplete protease inhibitor cocktail comes in tablets that can be directly dissolved in the PBS.

8. Collect the cells from each 150 mm dish on ice.
   a. On ice, add 10 mL of ice-cold PBS supplemented with 1× cOmplete onto the dish and scrape the cells off the surface using a plastic cell scraper.

Note: The dish can be tilted to pool and collect the cell suspension.

   b. When the entire surface of the dish has been contacted by the scraper, transfer the cell suspension into a 50 mL conical tube on ice.
   c. Add another 10 mL of ice-cold PBS with 1× cOmplete to the dish.
   d. Pipette up and down over the dish surface to rinse off residual cells, then transfer these into the same 50 mL conical tube.

Note: When pipetting over the dish surface, avoid generating an excess of air bubbles.

9. Spin down the cell suspension and remove the supernatant from the cell pellet.
   a. Spin the cell suspension at 250 *g* for 5 min in a centrifuge pre-chilled to 4°C.
   b. Carefully remove the supernatant (the PBS), leaving behind the cell pellet.

Note: Remove most of the supernatant first with the vacuum aspirator. Nearer to the pellet, remove the remaining supernatant with a P1000 micropipette.

Pause point: formaldehyde-cross-linked cell pellets can be flash frozen in liquid nitrogen and stored at −80°C for up to 3 months.

10. Lyse the cells.
    a. Add 1 mL of ice-cold Lysis Buffer (supplemented with 2× cOmplete and 1× PhosSTOP) to each cell pellet.
    b. Slowly pipette up and down 20 times using a P1000 micropipette.
    c. Incubate on ice for 10 min.
    d. Centrifuge at 900 *g* for 10 min at 4°C.

Note: To check if the Lysis Buffer is working suitably, a 100 mm dish of cells seeded in parallel can be treated on ice with 10 mL of ice-cold Lysis Buffer, then be gently rinsed twice with PBS. Examine the dish surface at 4–10× magnification under a brightfield microscope before and after treatment with Lysis Buffer. Before treatment, U2OS cells should have a morphology typical of adherent cells – a visible periphery extended outwards from a central, rounded nucleus, representative of the plasma membrane. Treatment with Lysis Buffer should cause the periphery to disappear but leave the shape of the nucleus intact (Figure 3).

11. Wash the resulting nuclei in Lysis Buffer.
    a. Carefully remove the supernatant with a P1000 micropipette.
    b. Gently resuspend the nuclear pellet by pipetting up and down 20 times in 400 µL of ice-cold Lysis Buffer (with cOmplete and PhosSTOP) to wash once.
    c. Centrifuge at 900 *g* for 10 min at 4°C.

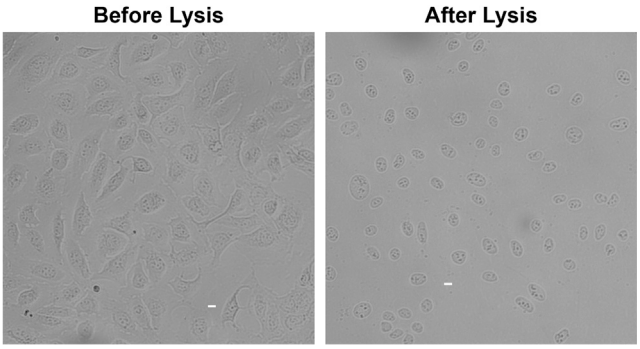

Figure 3. Checking for effective lysis

Brightfield images of *Asi*SI-ER U2OS cells before (left) and after treatment with ice-cold Lysis Buffer twice for 3 min and two washes in PBS (right). Note the disappearance of the plasma membrane and the remaining shape of the nuclei after lysis. Scale bar: 10 μm.

d. Carefully remove the supernatant with a P1000 micropipette.

12. Resuspend the nuclear pellet in Sonication Buffer.
    a. With a P1000 micropipette, slowly resuspend the resulting pellet of nuclei in 1.6 mL of ice-cold Sonication Buffer (with cOmplete and PhosSTOP) by pipetting up and down 20 times.

Note: Avoid generating too many air bubbles.

    b. Incubate for 30 min on ice.

Note: The Sonication Buffer contains 1% sodium dodecyl sulfate (SDS) to facilitate efficient, uniform, and reproducible sonication. This concentration of SDS may interfere with the immunoprecipitation by denaturing the antibody and/or epitopes recognized. As such, after sonication and before immunoprecipitation, the SDS will be diluted ten-fold with Dilution Buffer to attain a concentration of 0.1% SDS, which is conducive to immunoprecipitation.

13. Shear the chromatin by sonication.
    a. Resuspend the nuclear suspension with a P1000 micropipette.
    b. Split the volume evenly over five 1.5 mL Bioruptor Pico microtubes, at 300 μL each.
    c. Sonicate the nuclei at 4°C using a pre-chilled Bioruptor Pico (Diagenode) at high power for 15 cycles of 30 s on, then 30 s off.

Note: after every 5 cycles, stop the sonicator and flick or vortex the tubes to assure the nuclei are uniformly distributed.

Note: the Bioruptor Pico sonicator's water tank must be pre-chilled to 4°C at least 45 min before it is needed. Samples should be kept at 3°C–5°C during the entire sonication process.

Note: If using Diagenode sonicator models, use only microfuge tubes provided by Diagenode as they are more efficient in conducting sound waves and improve shearing efficiency. In this protocol, we used 1.5 mL Bioruptor Pico microtubes with caps (#C30010016).

Note: Ensure any empty spots in the carousel of the Bioruptor Pico are filled by microtubes with water at equal volume to the samples.

⚠ CRITICAL: Effective sonication is critical for ChIP and will yield chromatin fragments of ~200–500 bp (1–3 nucleosomes in length). In our hands, the sonication settings listed are sufficient to generate DNA fragments of suitable size, however other sonicator

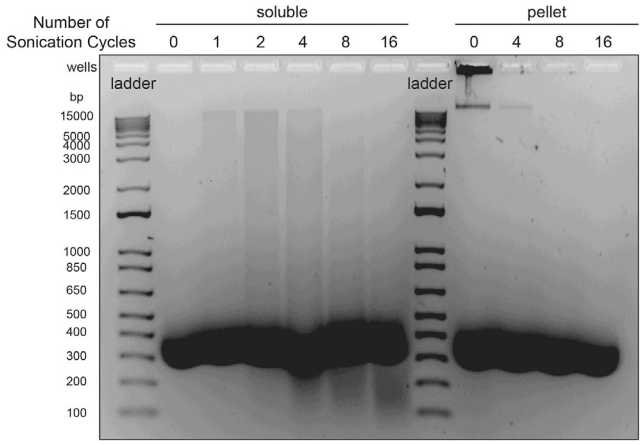

Figure 4. Optimizing sonication conditions

Formaldehyde-cross-linked and lysed *Asi*SI-ER U2OS cells were sonicated in a Bioruptor Pico for 0, 1, 2, 4, 8, or 16 cycles on high power, each cycle for 30 s on and 30 s off. After centrifugation, soluble and insoluble (pellet) fractions were collected. The cross-links were then reversed in the presence of RNase A for 16 h and the samples digested with Proteinase K for 3 h. The samples were then electrophoresed in 1.8% agarose and visualized by ethidium bromide staining. Shearing of DNA can be seen with increasing sonication cycles, along with release of insoluble DNA into the soluble fraction. 15 cycles were ultimately chosen for the ChIP protocol to ensure some larger fragments remaining after 8 cycles were sheared. As purification of DNA (step 30) was omitted prior to electrophoresis, the intense non-specific signal between 300 – 450 bp likely arises from components present in the Sonication Buffer. The image was acquired on an AlphaImager (Alpha Innotech).

models may yield different fragmentation efficiencies. It is imperative the sonication conditions are tested and optimized (described below) prior to proceeding with a full-scale ChIP experiment, even if one has access to a Bioruptor Pico. Closely follow recommendations from the sonicator's manufacturer to maximize sonication efficiency.

Note: To verify that the sonication conditions are efficiently shearing DNA, chromatin samples before and after sonication should be processed to reverse cross-links and digest away RNA and protein (steps 28 – 29) and be purified for DNA (step 30). Resolve the DNA samples by electrophoresis at 100 V in 1.8% agarose gel in 1× TAE (Tris-acetate-EDTA) buffer, stain with 0.5 μg/mL ethidium bromide, and visualize DNA on an ultraviolet transilluminator (Figure 4). Suitably fragmented DNA should appear as a smear between ~200 – 500 bp. If the DNA fragments are too long (inefficient sonication), the power, the number of sonication cycles, the sonication time in each cycle, and the frequency of resuspending the nuclei can be increased. The cell suspension can also be divided over more 1.5 mL Bioruptor Pico microtubes to reduce the number of nuclei per tube and maximize sonication efficiency. If the fragment sizes are too small, the time per sonication, the number of cycles, and/or the power of the Bioruptor can be decreased.

14. Collect the fragmented chromatin.
    a. Centrifuge the sonicated nuclear suspensions at 20000 *g* for 15 min at 4°C in a pre-chilled microfuge.
    b. Transfer the supernatant (containing fragmented chromatin) and pool into a fresh and pre-chilled microfuge tube, one tube per 150 mm dish.

Pause point: Fragmented chromatin can be flash frozen in liquid nitrogen and stored at −80°C for at least 3 months. The samples can be aliquoted into multiple tubes on ice prior to freezing to avoid freeze-thaw cycles.

Day 2 – Immunoprecipitation

Timing: 8–10 h (excluding a long incubation at the end)

On this day, the target protein of interest will be isolated from the fragmented chromatin by antibody pull-down (immunoprecipitation).

Note: to avoid protein degradation, all solutions and samples must be kept on ice or at 4°C.

15. Determine the protein concentration of the fragmented chromatin (step 14) using the Pierce BCA (bicinchoninic acid) Protein Assay kit. Measure the absorbance of the samples at 562 nm (A_{562}) using a spectrophotometer.

Note: the Pierce BCA Protein Assay Kit is compatible with all reagents (particularly the concentrations of the detergents) used in the Sonication Buffer.

Note: if the protein concentration determined is above the working range of the bovine serum albumin (BSA) standard curve generated with the kit, dilute a small portion of the fragmented chromatin (e.g., 1–2%) with Sonication Buffer and re-measure A_{562}, multiplying the resulting concentration by the dilution factor (e.g., 1 part sample + 9 parts Sonication Buffer gives a dilution factor of 10).

16. Equilibrate the Protein A or Protein G-coupled Dynabeads.
    a. Calculate the volume of Protein A or G-coupled Dynabeads (Invitrogen, referred to here as "the beads") required for Day 2.

Note: You will require 100 µL of beads per immunoprecipitation, which includes 40 µL for preclearing (step 19) and 60 µL for the immunoprecipitation itself (steps 20, 21, and 23). Include an additional 10% volume of beads on top of the required volume.

Note: A master mix of Protein A or G Dynabeads suspended in Dilution Buffer will be prepared in step 16e.

Note: Dynabeads are super-paramagnetic beads and thus will be held at the bottom of a microfuge tube when it is placed on a magnetic rack. They are coupled to Protein A or Protein G. The use of Protein A or Protein G depends on the host and isotype of the chosen antibody; Protein G generally binds to mouse and rat IgGs with higher affinity than Protein A, while Protein A binds to rabbit immunoglobulins with higher affinity than Protein G. Please consult with the manufacturer as to which is better suited for your choice of antibody.

⚠ CRITICAL: Each condition must be immunoprecipitated twice: once using the antibody recognizing the protein of interest and once with a species-/isotype-matched control IgG (referred to as the isotype control, a pool of immunoglobulins purified from animal serum) as a negative control. The isotype control is essential as it is used for normalizing ChIP signal.

Note: For each condition, one may wish to perform a positive control immunoprecipitation (i.e., targeting an established DSB signaling or repair protein used by the groups who generated the endonuclease-expressing cell lines), along with its isotype control immunoprecipitation. A suitable positive control is immunoprecipitating the homologous recombination effector protein RAD51, and performing qPCR with primer pairs as indicated in step 32. While we have successfully performed ChIP for RAD51 with the H-92 antibody (#sc-8349, Santa Cruz), this antibody was recently discontinued. The Legube group has validated an antibody from Abcam (#ab176458, RRID: AB_2665405) as a replacement.[15]

b. Wash the Protein A or G Dynabeads.

Note: As much as possible, Protein A or G Dynabeads should be kept on ice or at 4°C.

i. Vortex the stock bottle of Protein A or G Dynabeads.
ii. Pipette the volume of beads required into a 2 mL microfuge tube.

Note: To aid in pipetting, trim the micropipette tip at the front end with clean scissors to widen its diameter.

iii. Add 1.5 mL of ice-cold Dilution Buffer and vortex for 10 s.
iv. Tumble the beads end-over-end at 10–15 rpm on a rotating mixer for 5 min in a cold room set to 4°C.
v. Place the tube on a magnetic rack (e.g., a MagJET Separation Rack, Thermo Scientific) for 30 s.

Note: If it is preferred to have the entire portion of beads collected at the bottom of the tube, the researcher can centrifuge the beads at 3000 *g* for 2 min at 4°C prior to placing the tube on the magnetic rack.

vi. Carefully remove the supernatant by gentle vacuum aspiration with the tube still on the magnetic rack.

c. Immediately add another 1.5 mL of ice-cold Dilution Buffer to the beads, vortex for 10 s, and tumble end-over-end for another 5 min as per step 16b.
d. Place the tube on the magnetic rack for 30 s, and carefully remove the supernatant by gentle vacuum aspiration with the tube still on the magnetic rack.
e. Resuspend the beads in ice-cold Dilution Buffer, using the same volume as the volume of beads picked up in step 16a.

Note: Always keep the bead suspension on ice. This master mix of beads will be used in upcoming steps.

Note: The master mix of beads must be resuspended by vortexing for 5 s before a portion of beads is taken out.

17. Dilute fragmented chromatin in Dilution Buffer.
    a. Determine the volume of fragmented chromatin required to obtain 1 mg of protein, based on the protein concentration determined in step 15.

Note: The amount of chromatin required for an immunoprecipitation may vary and can be altered depending on the abundance of the protein targeted. In general, we use 500 μg to 1 mg of chromatin per immunoprecipitation, however for detection of histones and their modifications 25–100 μg of chromatin may be sufficient.

    b. Resuspend the chromatin by vortex and pipette the required volume of fragmented chromatin (step 17a) into a fresh and pre-chilled 2 mL microfuge tube, 1 tube per immunoprecipitation.

Note: As the microfuge tubes only hold 2 mL, the volume of chromatin needed cannot exceed 180 μL (with the later addition of 9 volumes of Dilution Buffer, the final volume will be 1.8 mL). If more than 180 μL of chromatin is needed, the immunoprecipitation reaction can be split evenly among multiple 2 mL microfuge tubes.

Note: For efficient mixing, the final volume of diluted chromatin should be at minimum 400 μL (40 μL fragmented chromatin and 360 μL of Dilution Buffer to be added next). If the chromatin is concentrated such that the required amount can be attained with less than 40 μL, dilute the chromatin in Sonication Buffer before adding it to the 2 mL tube such that at least 40 μL (and less than 180 μL) is used.

c. Add 9 volumes of ice-cold Dilution Buffer (supplemented with 2× cOmplete and 1× PhosSTOP) to each 2 mL tube and mix by vortexing.

⚠ CRITICAL: Diluting the fragmented chromatin in Dilution Buffer is essential as this ensures the SDS in Sonication Buffer is reduced to a concentration of 0.1%, where it interferes less with antibody-antigen binding.

18. Save chromatin for the input control.
    a. For each immunoprecipitation, vortex and save 1% (1/100) of the volume of diluted fragmented chromatin in a fresh and pre-chilled microfuge tube.

⚠ CRITICAL: Saving the input control is essential as it is used to normalize ChIP signal during the quantification.

Note: Other volumes can be saved, such as 5% (1/20) or 10% (1/10). The proportion saved determines the adjustment to the C_t value for the input control in the subsequent qPCR (Equation 1, quantification and statistical analysis).

Note: Save 10% of the diluted fragmented chromatin if you wish to perform immunoblot analysis to determine if the immunoprecipitation is working overall (step 21).

    b. Flash freeze the input control in liquid nitrogen and store at −20°C.
19. Pre-clear the diluted chromatin.
    a. For each immunoprecipitation, add 40 μL of equilibrated Protein A or G Dynabeads (prepared as a master mix in step 16) to the remaining diluted fragmented chromatin in the 2 mL tube.

⚠ CRITICAL: Always vortex the beads immediately before taking from the master mix.

Note: Always dispense the beads using a micropipette tip trimmed at the front end to widen its diameter.

    b. Tumble the mixture end-over-end at 10–15 rpm on a rotating mixer for 3 h in a cold room set to 4°C.

Note: This step removes components of chromatin that may bind non-specifically to the Protein A or G Dynabeads.

20. Block the remaining Protein A or G Dynabeads.
    a. To the remaining master mix of beads, centrifuge at 3000 *g* for 2 min at 4°C, place on the magnetic rack, and remove residual Dilution Buffer by gentle vacuuming with the tube still on the rack.

Note: Record the volume of the master mix of beads before vacuum aspiration, for step 20e.

    b. Add 1 mL of ice-cold Blocking Buffer to the beads.

c. Tumble the mixture end-over-end at 10–15 rpm on a rotating mixer for 1 h in a cold room set to 4°C.
d. Wash the beads once in Dilution Buffer:
   i. Centrifuge the beads at 3000 *g* for 2 min at 4°C.
   ii. Place the tube on the magnetic rack for 30 s.
   iii. Carefully remove the supernatant by vacuum aspiration with the tube still on the rack.
   iv. Add 1.5 mL of ice-cold Dilution Buffer.
   v. Vortex for 10 s.
   vi. Centrifuge again for 2 min at 3000 *g*, 4°C.
   vii. Place the tube on the magnetic rack for 30 s.
   viii. Carefully remove the supernatant by vacuum aspiration with the tube still on the rack.
e. Resuspend the beads in ice-cold Dilution Buffer in the same volume that they started with at step 20a to regenerate the bead master mix.

21. Assemble antibody—Protein A or G Dynabead complexes.

Note: This step ensures Protein A or G are pre-bound with antibody prior to incubation with chromatin, limiting non-specific immunoprecipitation.

a. Add 0.5 mL of Dilution Buffer to a fresh and pre-chilled 2 mL microfuge tube, one tube per immunoprecipitation.
b. Dispense into the tube 60 μL of blocked beads from the Protein A or G Dynabead master mix (step 20).

Note: Always dispense the beads using a micropipette tip trimmed at the front end to widen its diameter.

c. Add to each tube 2–4 μg of the desired antibody (i.e., antibody to the protein of interest, isotype control antibody, or positive control (step 16a)).

Note: The optimum amount of the antibody will vary and should be empirically determined using 2–4 μg as a starting point. For instance, in a pilot experiment to test this protocol up to immunoprecipitation, both 2 and 4 μg of antibody and isotype control can be used in separate immunoprecipitation reactions. After completing immunoprecipitation and the associated washes (step 25), add 100 μL of 2× Laemmli Sample Buffer supplemented with 5% 2-mercaptoethanol to the beads and heat at 95°C on a ThermoMixer (Eppendorf), 1,000 rpm for 10 min. The protein of interest—antibody—Protein A/G complexes will be eluted into the 2× Laemmli. In addition, add 4× Laemmli Sample Buffer and 2-mercaptoethanol to the input control (saved in step 18) and flow-through (step 24) to final concentrations of 1× and 5%, respectively, then heat and mix them as per the beads. All the samples can then be resolved by sodium dodecyl sulfate polyacrylamide gel electrophoresis (SDS-PAGE), electro-transferred to 0.2 μm nitrocellulose membrane (Bio-Rad), and immunoblotted for the immunoprecipitated protein of interest (Figure 5). The amount of antibody used for immunoprecipitation can then be adjusted accordingly. For example, if both 2 and 4 μg of antibody immunoprecipitate the target protein well above the isotype control and at similar efficiencies, 2 μg of antibody can be used in further iterations. If 4 μg is more efficient, that amount should be used in the future. If neither amount is effective, greater amounts can be attempted in further pilot experiments.

d. Tumble the mixture end-over-end at 10–15 rpm on a rotating mixer for 2 h in a cold room set to 4°C.

22. Collect the pre-cleared chromatin.

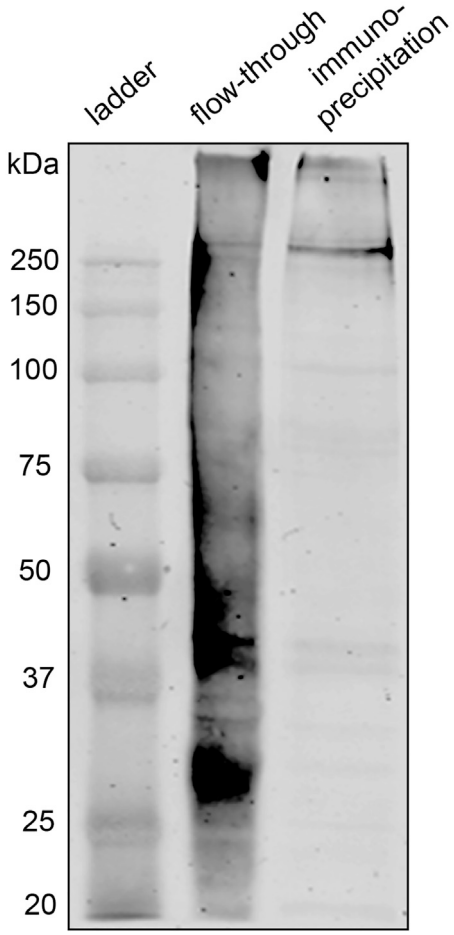

Figure 5. Confirming successful immunoprecipitation

Immunoblot for RNA polymerase II subunit Rpb1's C-terminal domain (CTD) repeats, phosphorylated at Ser 5. The flow-through (middle lane) and immunoprecipitation eluate (right lane) are from a ChIP experiment probing for Ser 5-phosphorylated Rpb1 CTD in *Asi*SI-ER U2OS cells. Note the enrichment of phosphorylated RNA polymerase in the immunoprecipitation eluate (immunoreactive band just above 250 kDa) and the abundant non-specific signal present in the flow-through fraction.

a. Continuing from step 19, centrifuge each microfuge tube of the diluted chromatin at 3000 *g* for 2 min at 4°C.
b. Place each tube on the magnetic rack and wait 30 s.
c. With the tubes on the rack, carefully transfer the supernatant into a fresh and pre-chilled 2 mL microfuge tube on ice using a P1000 micropipette, one tube per immunoprecipitation. Keep on ice.

Note: The remaining beads (the pellet) can be discarded.

23. Immunoprecipitation.
    a. Continuing from step 21, centrifuge the antibody-coupled Protein A or G Dynabeads at 3000 *g* for 2 min at 4°C.
    b. Place each tube on the magnetic rack for 30 s.
    c. With the tubes on the rack, carefully vacuum aspirate the supernatant.
    d. Immediately wash the beads twice in Dilution Buffer.
        i. Add to each tube of beads 1.5 mL of ice-cold Dilution Buffer.

ii. Vortex for 10 s.
iii. Centrifuge at 3000 *g* for 2 min at 4°C.
iv. Place each tube on the magnetic rack for 30 s.
v. Carefully remove the supernatant by vacuum aspiration with the tube still on the rack.
vi. Repeat the above sequence from i.-v. again.

e. Quickly add to each tube of antibody-coupled Protein A or G Dynabeads the entire volume of pre-cleared chromatin from the corresponding tube (step 22c).
f. Incubate the mixture for 12–18 h in the cold room at 4°C with constant end-over-end tumbling on a rotating mixer at 10–15 rpm.

Day 3 – Completing the immunoprecipitation and reversing cross-links

Timing: 4–5 h (excluding a long incubation at the end)

On this day, the immunoprecipitated fraction of chromatin is recovered and washed to remove non-specific binding. The formaldehyde cross-links from this fraction are then removed and the protein digested, leaving the DNA, which is then isolated in Day 4.

24. Save the flow-through fraction.

Note: This step will help troubleshoot if the immunoprecipitation step is not working. The collected supernatant can assist in immunoblot analysis (see step 21, Figure 5) as it contains chromatin that was not immunoprecipitated. Efficient immunoprecipitation will enrich the protein of interest in the fraction eluted from the beads, whereas the flow-through fraction should contain minimal levels of the target protein relative to the input control.

a. Recover the protein of interest—antibody—Protein A or G Dynabead complexes by centrifugation at 3000 *g* for 2 min at 4°C.
b. Place each tube on the magnetic rack for 30 s.
c. With the tubes on the rack, carefully collect the supernatant to a fresh and pre-chilled 2 mL microfuge tube using a P1000 micropipette, one tube per immunoprecipitation. Store the supernatant (the "flow-through") at −80°C.
d. Close the microfuge tubes containing the beads and keep on ice.

25. Wash the beads extensively to remove non-specific binding.
    a. Each wash consists of the following steps:
        i. Add the appropriate buffer into the microfuge tube on ice.
        ii. Vortex for 10 s.
        iii. Tumble end-over-end at 10–15 rpm in the cold room set to 4°C for 5 min.
        iv. Centrifuge at 3000 *g* for 2 min at 4°C to pellet the beads.
        v. Place each tube on the magnetic rack for 30 s.
        vi. Carefully remove the supernatant by vacuum aspiration with the tube still on the rack.
        vii. Place the beads on ice. Close the microfuge tube to prevent the beads from drying. Immediately proceed to the next wash.
    b. Wash the beads in the following buffers to remove non-specific binding:
        i. Wash the beads twice in 1.5 mL ice-cold Dilution Buffer.
        ii. Wash the beads once in 1.5 mL ice-cold Low Salt Wash Buffer.
        iii. Wash the beads once in 1.5 mL ice-cold High Salt Wash Buffer.
        iv. Wash the beads once in 1.5 mL ice-cold LiCl Wash Buffer.
        v. Wash the beads twice in 1.5 mL ice-cold TE Buffer.
26. Elute the target protein from the beads.
    a. Add 200 µL of Elution Buffer to each microfuge tube of beads.
    b. Incubate on the ThermoMixer at 800 rpm for 10 min at 65°C.
    c. Centrifuge at 20000 *g* at 20°C–22°C for 2 min.

d. With the tube on the magnetic rack for at least 30 s, transfer the supernatant to one fresh microfuge tube per immunoprecipitation.
e. Repeat the above sequence from a.-d., except transfer the supernatant into the same microfuge tube as in d., for a final volume of 400 μL.

Optional: The remaining beads can be stored at −80°C. In case elution is unsuccessful, the elution can be attempted again.

f. If the final volume is less, adjust with Elution Buffer to reach 400 μL final volume.

27. Prepare the input control. Thaw the input control from −80°C (one per immunoprecipitation, step 18). Add Elution Buffer to reach a final volume of 400 μL and vortex.
28. Reverse DNA-protein cross-links and digest with RNase A.
    a. Add 25.6 μL of 5 M NaCl to each input control and immunoprecipitation eluate tube for a final concentration of 300 mM NaCl, then vortex.
    b. Add to each tube 4.3 μL of DNase-free RNase A (stock concentration: 10 mg/mL) to a final concentration of 0.1 mg/mL RNase A, then vortex.
    c. Incubate at 65°C for at least 4 h on the ThermoMixer at 800 rpm.

Note: this incubation can also be performed for 12–18 h.

Pause point: samples can be stored at −20°C for at least 3 months after the 65°C incubation.

Day 4 – Genomic DNA extraction and analysis by qPCR

Timing: 5–6 h (excluding the wait time for qPCR)

On this day, the DNA associated with the immunoprecipitation will be cleaned up and quantified by qPCR.

29. Digest with Proteinase K.
    a. Centrifuge the input control and immunoprecipitation tubes at 20°C–22°C for 2 min at 20000 *g* to bring down any condensation.
    b. Add to each tube 4.35 μL of DNase-free Proteinase K (stock concentration: 20 mg/mL) to a final concentration of 0.2 mg/mL Proteinase K, then vortex.
    c. Incubate at 65°C for 2 h on the ThermoMixer at 800 rpm.
30. Purify DNA.
    a. Centrifuge the input control and immunoprecipitation tubes at 20°C–22°C for 2 min at 20000 *g* to bring down any condensation. Vortex.
    b. Purify the DNA from these samples using a QIAquick PCR Purification Kit (Qiagen) according to the manufacturer's instructions. Elute the DNA from each sample in 100 μL of the provided EB Buffer (10 mM Tris, pH 8.5).

Pause point: DNA samples can be stored at −20°C for at least 3 months after the purification.

31. Determine the DNA concentration for the input control and immunoprecipitation samples.
    a. Measure the fluorescence of the samples in combination with the Pico488 dsDNA Quantification Kit (Lumiprobe) according to the manufacturer's instructions.

Note: when bound to dsDNA, the Pico488 dye fluoresces with an excitation maximum of 503 nm and an emission maximum of 525 nm. This can be detected using a fluorometer or plate reader with fluorescence capability (e.g., FLUOstar Omega microplate reader, BMG LABTECH).

Table 3. qPCR reaction setup for ChIP

Components	Amount	Final concentration
BrightGreen 2× qPCR MasterMix	5 μL	1×
Forward Primer ("For", 10 μM)	0.3 μL	300 nM
Reverse Primer ("Rev", 10 μM)	0.3 μL	300 nM
Template DNA	30 ng template DNA per reaction	N/A
Nuclease-free ddH_2O	to complete to 10 μL	N/A

Note: DNA concentrations above 5 ng/μL are outside the linear range of the Pico488 kit.

b. For more concentrated samples (>5 ng/μL), the absorbance of the samples at 260 nm (A_{260}) can be detected with a spectrophotometer (e.g., NanoDrop ND-1000).

Note: EB Buffer (from the QIAquick PCR Purification Kit) should be used to blank the spectrophotometer.

Note: The Nanodrop ND-1000 should not be used to detect samples below 5 ng/ μL as that is near its detection limit. The spectrophotometer may be more useful for samples from immunoprecipitations of abundant DNA-binding proteins or the input control.

32. Perform quantitative PCR with the input control and immunoprecipitation samples as DNA templates with a SYBR Green-based detection system (such as BrightGreen from Abm Inc.). We used the QuantStudio 6 Flex Real-Time PCR System (Applied Biosystems) for qPCR amplification.

Note: PCR reaction mix and cycling conditions are listed in Tables 3 and 4. Primer sequences are listed in Tables 1 and 2.

Note: We recommend using RAD51 recruitment to induced DSBs as a positive control for ChIP (step 16). Primers compatible with RAD51 recruitment that we have tested include the pairs for positions p1 and p4 in U2OS-DSB reporter cells and the pair for the locus HR-DSB2.[15]

Note: As negative controls, we list primer pairs that amplify regions far from the induced DSB sites, such as Control Region for *Asi*SI-ER U2OS cells and Chromosome 7 for U2OS-DSB reporter cells. As these genomic loci are distal from the induced DSBs, the enrichment of DSB repair proteins (and hence the ChIP signal) should be minimal.

Note: A suitable negative control for qPCR is the "no template control", such that all components for the PCR reaction are provided except the template DNA (PCR master mix, forward and reverse primers, water). Amplification should not be detected for these samples during qPCR. If amplification does occur, this suggests the PCR master mix, tubes, or primers may be contaminated with genomic DNA, or that the primers chosen are dimerizing and being amplified by PCR ("primer dimers").

Note: As SYBR Green binds to nucleic acids without sequence specificity, the amplification of SYBR Green fluorescence upon qPCR may not mean the amplicon of interest has been amplified. Further validation may be required, such as resolving the PCR product by agarose gel electrophoresis to verify the size of the amplicon is as expected. The amplicon can also be sequenced by the Sanger method to ensure the correct genomic locus is being amplified. Amplicons also have a higher melting temperature than primer dimers. This is a result of increased thermostability, as an amplicon is typically longer than a primer dimer and both strands are

Table 4. qPCR cycling conditions

Steps	Temperature	Time	Cycles
Initial Denaturation	95°C	10 min	1
Denaturation	95°C	15 s	40 cycles
Annealing	58°C	30 s	
Extension	72°C	1 min	
Final extension	72°C	2 min	1
Hold	4°C	forever	

completely complementary. In contrast, primer dimers exhibit low complementarity to each other and are shorter (30–50 bp in size).

EXPECTED OUTCOMES

Chromatin immunoprecipitation is a sensitive method for accurately measuring the recruitment of DNA damage response proteins at restriction enzyme-generated DSB sites. We have successfully employed this protocol to measure RPA2, CtIP, and RAD51 association with DNA near breaks induced by *Fok*I, and active RNA polymerase near DSBs induced by *Asi*SI.[1] Similar approaches have been used by the groups that generated the cell lines to measure levels of γH2AX,[9,13,14] ATM phosphorylated at Ser1981[14]; DNAPKcs phosphorylated at Ser2056,[14,20] RAD51, XRCC4,[14,15] 53BP1, BRCA1, and acetylated histone H4[8] near site-specific DSBs. While not discussed here, a similar strategy can detect protein enrichment at a DSB generated at the DR-GFP reporter locus by the endonuclease I-*Sce*I.[21,22]

It is anticipated that an enrichment of well-established DSB repair players (e.g., γH2AX, RPA subunits, RAD51) should be detected by ChIP at the induced DSBs as a reflection of their accrual at DSB foci. While the ChIP signal (% of input) for DSB repair proteins may be low (0.1–1%), a substantial increase in signal should be detected relative to not induced samples and samples where the isotype control is used for immunoprecipitation. The degree of enrichment may also vary with the proximity of the selected locus to the DSB site.

Enrichment to site-specific DSBs should not be detected in other negative controls, such as when primers binding loci far removed from the DSB sites are used for qPCR, or when plain U2OS cells are used instead of the indicated reporter cells despite 4-OHT and/or Shield-1 treatment. Enrichment of the protein of interest near DSBs should also be reduced if formaldehyde cross-linking is eliminated from the protocol. As well, immunoprecipitating a protein that does not interact with DNA (e.g., free green fluorescent protein transfected in cells) should not result in qPCR signal enrichment when DSBs are induced.

QUANTIFICATION AND STATISTICAL ANALYSIS

The enrichment of a protein near a sequence-defined DSB is quantified using the Percent Input method. This method compares the ChIP-qPCR amplification signal from the immunoprecipitation for the target protein to that for the input control.

The amount of DNA amplified is represented by the C_t (threshold cycle) value, which denotes the number of PCR cycles needed to reach a threshold of detecting SYBR Green fluorescence above the background. As SYBR Green fluoresces upon binding double-stranded DNA, a plot of fluorescence over the number of PCR cycles represents the amount of DNA over the course of PCR amplification. The threshold fluorescence value for an experiment can be set via QuantStudio Real-Time PCR Software (Applied Biosystems, associated with the QuantStudio 6 Flex Real-Time PCR System), after which the C_t values for each qPCR reaction can be calculated by the program (Figure 6).

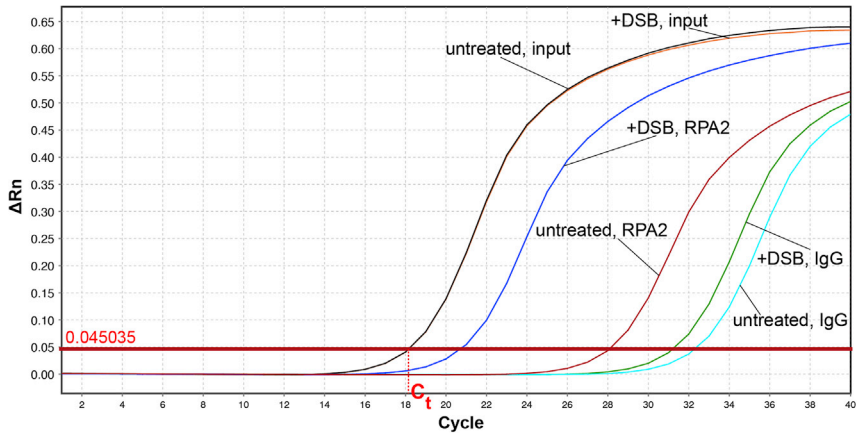

Figure 6. qPCR amplification

Representative qPCR linear amplification plot from QuantStudio Real-Time PCR Software. qPCR for locus p1 near the *lacO* array from a ChIP experiment for RPA2 enrichment with and without 4-OHT induction (+DSB) in U2OS-DSB reporter cells. The horizontal red line is the threshold set by the software to determine the C_t value for each reaction curve. The dotted line demonstrates calculation of the C_t value. IgG: isotype control.

Recall that a portion of chromatin was saved for the input control prior to immunoprecipitation, for instance 1% (1/100) (step 18). The C_t value for the input is then adjusted to what it would be if it was the same concentration as the chromatin that went into the immunoprecipitation (i.e., 100%), according to Equation 1. In other words, the additional doubling cycles needed to reach C_t because the input control was dilute are subtracted from the measured C_t for the input. The dilution factor of the input control determines the value of this adjustment (Table 5).

$$\text{Adjusted input to 100\%} = C_t\,(\text{input}) - \log_2(\text{dilution factor of input}) \qquad \text{(Equation 1)}$$

For instance, if the input is 1% (diluted 1:100),

$$\text{Adjusted input to 100\%} = C_t\,(\text{input}) - \log_2(100)$$

$$\text{Adjusted input to 100\%} = C_t\,(\text{input}) - 6.644$$

Similarly, if the input is 5% (diluted 1:20),

$$\text{Adjusted input to 100\%} = C_t\,(\text{input}) - \log_2(20)$$

$$\text{Adjusted input to 100\%} = C_t\,(\text{input}) - 4.322$$

Next, the qPCR signal from the immunoprecipitation (C_t (IP)) is normalized to that of the adjusted input control according to Equation 2. This yields the % of immunoprecipitated (IP) DNA (from a

Table 5. Sample Calculations – Applying Equation 1

Sample	C_t value	Dilution factor (DF)	Correction: $\log_2$(DF)	Adjusted input to 100% concentration
Input Control, Not Induced	24.147	100	6.644	17.503
Input Control, + 4-OHT (DSBs)	24.091	100	6.644	17.447

Immunoprecipitation was performed using anti-RAD51 antibody (Santa Cruz #sc-8349) or rabbit IgG control in AsiSI-ER U2OS cells induced with 4-OHT treatment or not. Subsequent qPCR was performed using the HR-DSB2 For and Rev primer set.

specific locus in the genome) relative to the amount of DNA (also from that locus) present in the input control (% input).

$$\text{Percent Input} = 100\% \times 2^{\left(\text{adjusted input to } 100\% - \text{Ct (IP)}\right)} \quad \text{(Equation 2)}$$

Two critical control samples that must be present when plotting ChIP data are the isotype control (species-/isotype-specific antibody control, IgG) and not induced control (with no *Asi*SI- or *Fok*I-mediated DSBs). Both are required for all experimental manipulations tested (e.g., RNA interference, pharmacological inhibitors, protein overexpression, etc.).

Below are sample calculations – Applying Equation 2

Sample	Adjusted input to 100% (from Table 5)	C_t value	Percent of input
IP for RAD51, Not Induced	17.503	27.413	0.1039
IP for RAD51, + 4-OHT	17.447	25.664	0.3361
IP for IgG Control, Not Induced	17.503	29.100	0.0323
IP for IgG Control, + 4-OHT	17.447	29.459	0.0242

Immunoprecipitation was performed using anti-RAD51 antibody (Santa Cruz #sc-8349) or rabbit IgG control in AsiSI-ER U2OS cells induced with 4-OHT treatment or not. Subsequent qPCR was performed using the HR-DSB2 For and Rev primer set.

ChIP data should be represented as the mean and standard deviation from three independent replicates (Figure 7). Our statistical analysis and graphs were generated using Prism (Graphpad) with error bars to represent the standard deviation from the mean value. To determine statistical significance, we used an unpaired *t*-test.

LIMITATIONS

This assay can only examine the recruitment of proteins in response to DSBs at loci in the genome that are cleaved by *Fok*I or *Asi*SI but not DSBs generated at random loci by DNA damaging agents, such as ionizing radiation. As *Fok*I and *Asi*SI are restriction endonucleases, their DSBs are a distinct type that is chemically "clean" and ligatable, unlike the DSBs generated by ionizing radiation and reactive oxygen species, for instance. Moreover, in U2OS-DSB reporter cells, the length of the 256-repeat *lacO* array likely causes an excessively large number of these DSBs to be generated in a confined region of the genome. Kinetic information for protein recruitment may also be more difficult to obtain with this assay, as loci are constantly cleaved by the endonucleases throughout the 3-h induction period. The latter problem has been overcome by the fusion of an auxin-inducible degron (AID) to the *Asi*SI-ER chimera, allowing degradation of the *Asi*SI enzyme upon auxin addition and enabling pulsed induction of DSBs (AID-DIvA cells).[11]

Like many molecular techniques, ChIP heavily depends on the quality and specificity of antibodies. One factor limiting resolution is the non-specific binding of antibodies. Additionally, the use of cross-linking may detect transient interactions between DNA and proteins that are not functionally significant. Conversely, transient interactions of proteins with DNA (e.g., some transcription factors) may not be fully captured. In the end, these factors may result in low ChIP signal for the protein of interest relative to the not induced or isotype controls, resulting in inconclusive data.

TROUBLESHOOTING

Problem 1

ChIP-qPCR signal is low.

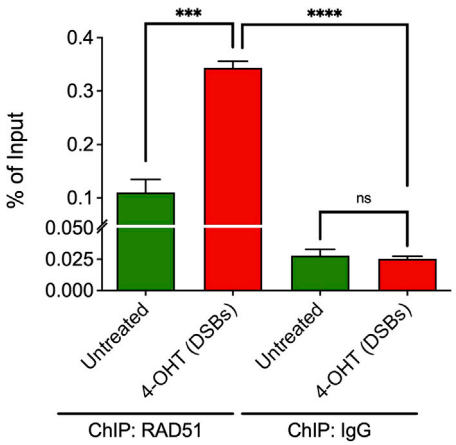

Figure 7. Representative ChIP results
Representative ChIP quantification for RAD51 recruitment to locus HR-DSB2 near an *Asi*SI cut site in *Asi*SI-ER U2OS cells induced with 4-OHT or left untreated. Data are represented as mean ± standard deviation for three independent replicates.

Potential solution

There are many reasons why ChIP data has a low signal; some may include cross-linking that has gone on too long, small chromatin fragment size, insufficient chromatin for immunoprecipitation, insufficient antibody for immunoprecipitation, or removal of the protein of interest during washes. To avoid these issues:

- When cross-linking, only incubate for 5–10 min, wash well with PBS, and be sure to quench the fixation reaction (step 5).
- Ensure chromatin is not sonicated to less than 150 bp (step 13).
- Do not use less than 25 μg of chromatin for immunoprecipitation (step 17). If enough chromatin cannot be obtained from one 150 mm dish for immunoprecipitation, scale up the number of dishes used (e.g., two to three 150 mm dishes that are combined to make one sample) to yield a better enrichment of target proteins and hence an improvement in qPCR signal (before you begin).
- Use ChIP grade antibodies for the immunoprecipitation step, preferably ones that have been validated by another research group using ChIP to study DSB repair (step 21).
- Use 2–4 μg of antibody for each immunoprecipitation reaction and raise this amount if the signal is still low (step 21).
- Prevent excess stringency in the wash buffers (step 25). Do not exceed a NaCl concentration of 500 mM as higher concentrations may prevent antibody binding.

One may also consider using alternative cross-linkers on top of the formaldehyde step for recruited proteins that do not directly bind to DNA (discussed in step 5).

Problem 2

The ChIP-qPCR data has a high background signal.

Potential solution

High background could result from the non-specific binding of the antibody to beads.

- Use ChIP grade antibodies with high specificity (step 21) and high-quality magnetic beads (step 16).

> ***Note:*** The specificity of an antibody can be tested by performing a pilot immunoprecipitation (step 21) comparing the isotype control and the antibody in immunoprecipating the target the protein of interest. Immunoprecipitations eluted in 2× Laemmli Sample Buffer supplemented

with 5% 2-mercaptoethanol and processed by SDS-PAGE can then be immunoblotted for the protein of interest. There should be a striking enrichment of the precipitated protein of interest when the chosen antibody is used relative to the isotype control.

- Increase the duration of each washing step during the immunoprecipitation protocol (step 25).
- Carefully increase the stringency of the wash solutions by gradually raising the salt (NaCl, LiCl) and detergent (Triton X-100, IGEPAL CA-630, SDS) concentrations when preparing the buffers (step 25).
- Ensure the pre-clearing (step 19) and bead blocking (step 20) steps have been performed correctly and in the right sequence.
- Another reason for high background signal could be ChIP buffer contamination. To prevent this, prepare buffers fresh and filter sterilize them before starting this protocol (before you begin).

High background may also result from large DNA fragment size. To avoid this, the sonication conditions should be optimized. DNA fragment sizes should not exceed 1,000 bp (step 13).

Another potential solution to high background is to pre-extract the cells using Lysis Buffer prior to cross-linking (after step 2 and before step 3). This step can extract away protein populations that are not or less tightly bound to chromatin, thereby reducing background and enhancing the specific signal for proteins recruited to DSBs. This method is commonly used during immunofluorescence staining for DNA damage-induced foci.[1] To do so, first wash the cells twice with 15 mL of ice-cold PBS, then *gently* replace the dish with 12 mL of ice-cold Lysis Buffer (supplemented with 2× cOmplete and 1× PhosSTOP) for 3 min. *Gently* replace the dish again with Lysis Buffer/cOmplete/PhosSTOP for another 3 min. Proceed to step 3. In our hands, ChIP signal for RPA2 improved with a pre-extraction step performed prior to formaldehyde cross-linking.

Problem 3

Issues with qPCR amplification: there is high amplification in every sample, or no amplification.

Potential solution

High PCR amplification in every sample may suggest contamination of qPCR solutions, primers, or the tubes. PCR amplification in a control where everything is added except the template DNA may indicate the PCR master mix itself is contaminated (step 32). In cases where amplification is not detected, ensure qPCR is performed on the input control (steps 18, 27, and 32) to ensure the primers are properly binding to their targets.

Problem 4

Enrichment of the protein of interest to enzyme-induced DSB sites is low or not detected.

Potential solution

- Ensure a suitable positive control (e.g., RAD51, as per steps 16 and 32) is included in the ChIP experiment to verify that DSBs are being induced and that the ChIP assay is functioning.
- Reduce the background ChIP signal, as in the solutions to problem 2 (for instance, consider a pre-extraction step prior to cross-linking).
- Alter the length of time that DSBs are induced (step 2), in case the peak of protein recruitment is outside the 3 h window suggested here. Alternatively, consider using auxin-inducible degron-controlled pulsed induction of DSBs with AID-DIvA cells[11] and monitor protein enrichment at various time points.
- As DSB repair can proceed through different pathways which can involve different players, consider approaches to enhance the occurrence of specific pathways. For instance, as the homologous recombination (HR) pathway is restricted to S or G2 phase,[23] one could synchronize cells to such phases[24] to increase the likelihood the DSB is repaired by HR.[21] Relatedly, as a subset of *Asi*SI

sites is prone to repair by HR,[11] selecting *Asi*SI cut sites outside of this subset may improve detection of accrual for a protein in a different pathway.

RESOURCE AVAILABILITY

Lead contact

Further information and requests for resources and reagents should be directed to and fulfilled by the lead contact, Ismail Hassan Ismail (iismail@ualberta.ca).

Materials availability

This study did not generate new unique reagents.

Data and code availability

This study did not generate/analyze datasets/code.

ACKNOWLEDGMENTS

CIHR (Canadian Institutes of Health Research), grant number 154485; CRS (Cancer Research Society), grant number 22019; and NSERC (Natural Sciences and Engineering Research Council of Canada), grant number RGPIN-2017-05752, funded this research.

AUTHOR CONTRIBUTIONS

A.K.S. established the protocol in the lab and wrote the first draft of the manuscript. A.J.L., A.M.F., J.Y.H.A., and I.H.I. extensively edited the first draft and generated the final version. A.J.L. and J.Y.H.A. made figures.

DECLARATION OF INTERESTS

The authors declare no competing interests.

REFERENCES

1. Fitieh, A., Locke, A.J., Mashayekhi, F., Khaliqdina, F., Sharma, A.K., and Ismail, I.H. (2022). BMI-1 regulates DNA end resection and homologous recombination repair. Cell Rep. *38*, 110536. https://doi.org/10.1016/j.celrep.2022.110536.

2. Bitinaite, J., Wah, D.A., Aggarwal, A.K., and Schildkraut, I. (1998). *Fok*I dimerization is required for DNA cleavage. Proc. Natl. Acad. Sci. USA *95*, 10570–10575. https://doi.org/10.1073/pnas.95.18.10570.

3. Li, L., Wu, L.P., and Chandrasegaran, S. (1992). Functional domains in Fok I restriction endonuclease. Proc. Natl. Acad. Sci. USA *89*, 4275–4279. https://doi.org/10.1073/pnas.89.10.4275.

4. Li, L., Wu, L.P., Clarke, R., and Chandrasegaran, S. (1993). C-terminal deletion mutants of the FokI restriction endonuclease. Gene *133*, 79–84. https://doi.org/10.1016/0378-1119(93)90227-t.

5. Banaszynski, L.A., Chen, L.C., Maynard-Smith, L.A., Ooi, A.G.L., and Wandless, T.J. (2006). A rapid, reversible, and tunable method to regulate protein function in living cells using synthetic small molecules. Cell *126*, 995–1004. https://doi.org/10.1016/j.cell.2006.07.025.

6. Littlewood, T.D., Hancock, D.C., Danielian, P.S., Parker, M.G., and Evan, G.I. (1995). A modified oestrogen receptor ligand-binding domain as an improved switch for the regulation of heterologous proteins. Nucleic Acids Res. *23*, 1686–1690. https://doi.org/10.1093/nar/23.10.1686.

7. Agger, K., Santoni-Rugiu, E., Holmberg, C., Karlström, O., and Helin, K. (2005). Conditional E2F1 activation in transgenic mice causes testicular atrophy and dysplasia mimicking human CIS. Oncogene *24*, 780–789. https://doi.org/10.1038/sj.onc.1208248.

8. Tang, J., Cho, N.W., Cui, G., Manion, E.M., Shanbhag, N.M., Botuyan, M.V., Mer, G., and Greenberg, R.A. (2013). Acetylation limits 53BP1 association with damaged chromatin to promote homologous recombination. Nat. Struct. Mol. Biol. *20*, 317–325. https://doi.org/10.1038/nsmb.2499.

9. Shanbhag, N.M., Rafalska-Metcalf, I.U., Balane-Bolivar, C., Janicki, S.M., and Greenberg, R.A. (2010). ATM-dependent chromatin changes silence transcription in cis to DNA double-strand breaks. Cell *141*, 970–981. https://doi.org/10.1016/j.cell.2010.04.038.

10. Janicki, S.M., Tsukamoto, T., Salghetti, S.E., Tansey, W.P., Sachidanandam, R., Prasanth, K.V., Ried, T., Shav-Tal, Y., Bertrand, E., Singer, R.H., and Spector, D.L. (2004). From silencing to gene expression: real-time analysis in single cells. Cell *116*, 683–698. https://doi.org/10.1016/S0092-8674(04)00171-0.

11. Aymard, F., Bugler, B., Schmidt, C.K., Guillou, E., Caron, P., Briois, S., Iacovoni, J.S., Daburon, V., Miller, K.M., Jackson, S.P., and Legube, G. (2014). Transcriptionally active chromatin recruits homologous recombination at DNA double-strand breaks. Nat. Struct. Mol. Biol. *21*, 366–374. https://doi.org/10.1038/nsmb.2796.

12. Clouaire, T., Rocher, V., Lashgari, A., Arnould, C., Aguirrebengoa, M., Biernacka, A., Skrzypczak, M., Aymard, F., Fongang, B., Dojer, N., et al. (2018). Comprehensive mapping of histone modifications at DNA double-strand breaks deciphers repair pathway chromatin signatures. Mol. Cell *72*, 250–262.e6. https://doi.org/10.1016/j.molcel.2018.08.020.

13. Iacovoni, J.S., Caron, P., Lassadi, I., Nicolas, E., Massip, L., Trouche, D., and Legube, G. (2010). High-resolution profiling of γh2AX around DNA double strand breaks in the mammalian genome. EMBO J. *29*, 1446–1457. https://doi.org/10.1038/emboj.2010.38.

14. Massip, L., Caron, P., Iacovoni, J.S., Trouche, D., and Legube, G. (2010). Deciphering the chromatin landscape induced around DNA double strand breaks. Cell Cycle *9*, 2963–2972. https://doi.org/10.4161/cc.9.15.12412.

15. Arnould, C., Rocher, V., and Legube, G. (2021). Analyzing homologous recombination at a genome-wide level. In Homologous Recombination: Methods and Protocols, A.

Aguilera and A. Carreira, eds. (Springer US), pp. 427–438. https://doi.org/10.1007/978-1-0716-0644-5_29.

16. Hoffman, E.A., Frey, B.L., Smith, L.M., and Auble, D.T. (2015). Formaldehyde crosslinking: a tool for the study of chromatin complexes. J. Biol. Chem. *290*, 26404–26411. https://doi.org/10.1074/jbc.R115.651679.

17. Tian, B., Yang, J., and Brasier, A.R. (2012). Two-step cross-linking for analysis of protein-chromatin interactions. Methods Mol. Biol. *809*, 105–120. https://doi.org/10.1007/978-1-61779-376-9_7.

18. Nowak, D.E., Tian, B., and Brasier, A.R. (2005). Two-step cross-linking method for identification of NF-kappaB gene network by chromatin immunoprecipitation. Biotechniques *39*, 715–725. https://doi.org/10.2144/000112014.

19. Kurdistani, S.K., and Grunstein, M. (2003). In vivo protein–protein and protein–DNA crosslinking for genomewide binding microarray. Methods *31*, 90–95. https://doi.org/10.1016/S1046-2023(03)00092-6.

20. Zhou, Y., Caron, P., Legube, G., and Paull, T.T. (2014). Quantitation of DNA double-strand break resection intermediates in human cells. Nucleic Acids Res. *42*, 1–11. https://doi.org/10.1093/nar/gkt1309.

21. Rodrigue, A., Lafrance, M., Gauthier, M.-C., McDonald, D., Hendzel, M., West, S.C., Jasin, M., and Masson, J.-Y. (2006). Interplay between human DNA repair proteins at a unique double-strand break in vivo. EMBO J. *25*, 222–231. https://doi.org/10.1038/sj.emboj.7600914.

22. Hsiao, K.Y., and Mizzen, C.A. (2013). Histone H4 deacetylation facilitates 53BP1 DNA damage signaling and double-strand break repair. J. Mol. Cell Biol. *5*, 157–165. https://doi.org/10.1093/jmcb/mjs066.

23. Hustedt, N., and Durocher, D. (2016). The control of DNA repair by the cell cycle. Nat. Cell Biol. *19*, 1–9. https://doi.org/10.1038/ncb3452.

24. Ma, H.T., and Poon, R.Y.C. (2017). Synchronization of HeLa cells. In BT - Cell Cycle Synchronization: Methods and Protocols, G. Banfalvi, ed. (Springer New York), pp. 189–201. https://doi.org/10.1007/978-1-4939-6603-5_12.